Studies in Mechanobiology, Tissue Engineering and Biomaterials 22

Georges Limbert *Editor*

Skin Biophysics

From Experimental Characterisation to Advanced Modelling

Springer

Studies in Mechanobiology, Tissue Engineering and Biomaterials

Volume 22

Series Editor
Amit Gefen
Department of Biomedical Engineering
Tel Aviv University
Ramat Aviv, Israel

More information about this series at http://www.springer.com/series/8415

Georges Limbert
Editor

Skin Biophysics

From Experimental Characterisation to Advanced Modelling

Springer

Editor
Georges Limbert
Department of Mechanical Engineering,
Faculty of Engineering and Physical
Sciences
University of Southampton
Southampton, UK

ISSN 1868-2006 ISSN 1868-2014 (electronic)
Studies in Mechanobiology, Tissue Engineering and Biomaterials
ISBN 978-3-030-13278-1 ISBN 978-3-030-13279-8 (eBook)
https://doi.org/10.1007/978-3-030-13279-8

This Springer imprint is published by the registered company Springer Nature Switzerland AG
The registered company address is: Gewerbestrasse 11, 6330 Cham, Switzerland

To Theo, Eva and Grace for making my life a happy, beautiful, fun, exciting and learning adventure.

Preface

> What spirit is so empty and blind, that it cannot recognise the fact that the foot is more noble than the shoe, and skin more beautiful than the garment with which it is clothed? [Michelangelo di Lodovico Buonarroti Simoni (1475–1564)]

From the soothing feeling of the sun warming one's face on a beach, through the perception of sand texture when walking towards the ocean, to the abrupt sense of cold one experiences when jumping into its waters, we all have an intuitive understanding of how our skin mediates our interactions with the outside world. Of course, these interactions extend beyond thermal and haptic sensing, contact mechanics and hydrodynamics. Skin, our largest organ, is the primary line of defence shielding our internal body structures from insults of the external environment. Interfacial and bulk exchanges take the form of mechanical, thermal, biological, chemical and electromagnetic processes which typically operate in concert and feature complex coupling effects. At the biophysical level, the skin is also an essential plant that synthesises vital compounds like vitamin D, hosts necessary immunologic biochemical and cellular processes and contains a rich sensory biophysical network that informs us in real time of any haptic cues or potentially threatening physical insults and noxious agents.

The more one studies skin physiology and biophysics the more one realises that there are multiple nested dimensions waiting to be unravelled, where psychology, human behaviour, health, well-being and biophysics are intrinsically connected, more often than not, in complex and mysterious ways. For example, the psychosocial role of the skin is multifaceted and strongly dependent upon the biophysical properties of this complex organ whose visual appearance continuously evolves across the life course, from birth to death. The skin tells a story about our health status, age, past traumas, emotions, ethnicity and our social and physical environments. These cues—mostly perceived at a subconscious level—are fundamental in human social interactions.

In the last few decades, we have witnessed a significant drive in efforts to move skin science research forward through engineering approaches, and more particularly within the biomechanics and biophysics communities, at both experimental and modelling levels. This is hardly surprising considering the special

place of the skin in human life and the multiple applications of skin science from cosmetics, pharmaceutics, surgery and medical devices, through consumer goods and automotive safety, to wearable electronics and biomimetics. The systemic complexity of skin biophysics can only be unravelled by adopting inter- and multidisciplinary research methods which integrate physical experiments, imaging and modelling. As a consequence, researchers must be trained in a wide range of topics from experimental physics, skin biology, continuum mechanics, soft matter physics, mathematical modelling and data analysis, through multiscale imaging protocols and image processing, to finite element methods and computational procedures.

A unified, structured and up-to-date review of cutting-edge research in experimental characterisation, imaging and modelling aspects of skin biophysics was long overdue. Despite a recent excellent book focused on computational skin biophysics, edited by Bernard Querleux of L'Oréal Research, a treatise simultaneously covering the three aforementioned topics was missing.

The frontier in skin biophysics research is presented in this volume through contributions of internationally leading groups in the field, from France, Ireland, New Zealand, South Africa, Switzerland, the UK and the USA. The aim of this book is to present the current state of the art and perspectives on future research directions, with a strong bias towards mechanics, structural and mechanical properties and constitutive models based on theories and concepts rooted in continuum mechanics. I take full responsibility and, cheekily, make no apologies for letting my personal research interests steer the coverage of skin biophysics in this particular direction. My experience in working in academia, and with industry, has consistently demonstrated that the methods and theories described in the book are not only critical research tools that are used for fundamental research or as part of the product life cycle but can also deliver practical engineering solutions that are used daily by hundreds of million people across the globe.

This book is addressed to postgraduate students in biomedical/mechanical/civil engineering, (bio)physics and applied mathematics, postdoctoral researchers as well as scientists and engineers working in academia and industry engaged in skin research, particularly, if at the cross-roads of physical experiments, imaging and modelling. The book will also be of interest to clinicians/biologists who wish to learn about the possibilities offered by modern engineering techniques for skin science research and, by so doing, provide them with an incentive to broaden their outlook, engage more widely with the non-clinical research communities and, ultimately, help cross-fertilising new ideas that will lead to better treatment plans and engineering solutions.

The book is divided into three main parts that covers Part I—Human skin structure and composition (Chapter 1), Part II—Mathematical and computational modelling (Chapters 2–5) and Part III—Experimental characterisation techniques (Chapters 6–10).

In the chapter entitled "Human Skin: Composition, Structure and Visualisation Methods", Graham, Eckersley, Ozols, Mellody and Sherratt discuss the molecular

composition and structure of the skin and associated invasive/non-invasive imaging techniques.

In the chapter entitled "Constitutive Modelling of Skin Mechanics", Limbert provides an expose of the current state-of-the-art constitutive theories and models for describing the passive mechanics of the skin.

Buganza-Tepole and Gosain present a constitutive modelling framework for skin growth in the chapter entitled "Constitutive Modelling of Skin Growth", while Bunganza-Tepole reviews frontier research in the constitutive description of skin wound healing in the chapter entitled "Constitutive Modelling of Wound Healing".

In the chapter entitled "Constitutive Modelling of Skin Ageing", Limbert, Pond and McBride examine the mechanical and structural aspects of both intrinsic and extrinsic ageing and present a multiphysics modelling framework to capture the chemo-mechanobiology of ageing.

State-of-the-art inverse characterisation methods which combine experimental characterisation and numerical techniques are presented by Weickenmeier and Mazza in the chapter entitled "Inverse Methods" and Flynn in the chapter entitled "Experimental Characterisation: Rich Deformations".

In the chapter entitled "Multiscale Characterization of Skin Mechanics Through in situ Imaging", Allain, Lynch and Schanne-Klein provide a review of multiscale characterisation techniques of skin mechanics through in situ imaging.

In the chapter entitled "Tension Lines of the Skin", Ní Annaidh and Destrade discuss experimental approaches to characterise skin tension lines which are proven to be essential in describing in vivo skin mechanics.

Finally, in the chapter entitled "Experimental Tribology of Human Skin", Masen, Veijgen and Klaassen review the current state of the art of experimental methods to characterise the tribological properties of the skin.

Southampton, UK Georges Limbert
December 2018

Acknowledgements

This book is the outcome of multiple interactions with many research colleagues over the years. I have learnt much from them, and they all have influenced my research in some ways.

First of all, I would like to express my sincere gratitude to Amit Gefen, the editor of the Springer series "Studies in Mechanobiology, Tissue Engineering and Biomaterials" who planted the seed in my head to edit "a book on the skin". Amit, the seed has germinated, and hopefully, has become a beautiful plant that many gardeners want to see!

I am particularly indebted to the contributors to this volume. They all enthusiastically accepted to provide their expertise, opinions and time and, by so doing, made this book a reality. I am very grateful for their outstanding contributions and also patience in coping with my numerous requests.

There are also many individuals who have sparked many of my interests, generously shared their expertise and contact, introduced me to areas of research unknown to me, both in the academia and industry, and welcomed me to their research groups, conferences and meetings, or who have simply been great friends and partners in crime (you know you are!) in the wonderful and hazardous world of academic research.

I would like to thank in particular (in alphabetic order) Stéphane Bordas, Michel Destrade, Thomas Franz, Christian Gasser, Helen Graham, Raphael Grytz, Eberhard Haug, Marie-Christine Ho Ba Tho, Ellen Kuhl, Kemal Levi, Marc A. Masen, Andrew McBride, David-John O'Callaghan, Cees Oomens, Timon Rabczuk, Daya Reddy, Roberto Santoprete, Michael Sherratt, Sebastian Skatulla, David Steigmann, Mark Taylor, Daniela Valdez-Jasso, Jeff Weiss and Philippe Young.

I would also like to thank Bibhuti Sharma, the book project coordinator for Springer Nature, for his first-class and dedicated assistance in the publishing process which was key in smoothing out any difficulties.

The Universities of Southampton and Cape Town are gratefully acknowledged for providing me with a supportive research environment.

Finally, I am deeply grateful to my family for their patience and support during many busy working weekends and research trips that took me away from home.

Contents

Human Skin: Composition, Structure and Visualisation Methods

Helen K. Graham, Alexander Eckersley, Matiss Ozols, Kieran T. Mellody, and Michael J. Sherratt

Abstract In this chapter we discuss the molecular composition and structure of the epidermis, dermal-epidermal junction, dermis and hypodermis. We highlight the contribution of long-lived dermal collagens, elastic fibres, proteoglycans and hyaluronic acid to skin function and also consider the role of apparently "minor" skin components. In order to characterise both healthy skin, and the progression of disease and ageing, it is necessary to use microscopical approaches but in addition to conventional ex vivo techniques, which image in two dimensions, valuable information can be gained by complimentary non-invasive and 3D imaging technologies.

1 Introduction

> The finest clothing made is a person's own skin, but, of course, society demands something more than this. Mark Twain

In the above quote the author highlights the importance of a person's skin in a personal and social context. The appearance, health and wellbeing of this organ are inextricably bound to an individual's psychological well-being whilst societal perception and personal interactions are influenced by its look, colour and the features of ageing. The remodelling which can accompany skin ageing impacts not only on appearance but also function with xerosis (dry skin) and skin

H. K. Graham · K. T. Mellody
Division of Musculoskeletal and Dermatological Sciences, School of Biological Sciences, Faculty of Biology, Medicine and Health, The University of Manchester, Manchester, UK
e-mail: helen.k.graham@manchester.ac.uk; kieran.mellody@manchester.ac.uk

A. Eckersley · M. Ozols · M. J. Sherratt (✉)
Division of Cell Matrix Biology and Regenerative Medicine, School of Biological Sciences, Faculty of Biology, Medicine and Health, The University of Manchester, Manchester, UK
e-mail: alexander.eckersley@manchester.ac.uk; matiss.ozols@manchester.ac.uk; michael.sherratt@manchester.ac.uk

G. Limbert (ed.), *Skin Biophysics*, Studies in Mechanobiology, Tissue Engineering and Biomaterials 22,
https://doi.org/10.1007/978-3-030-13279-8_1

injuries becoming increasingly common in older people [1]. However, an increased understanding of skin ageing also has the potential to increase our insight into ageing in other organs systems. Life expectancy within the United Kingdom is increasing and this rise in the elderly population poses a challenge for health-care services and funding due to the increase in age-associated multi-morbidities such as cancer, cardiovascular disease, chronic renal disease and diabetes. Such factors support the argument that ageing is a disease process [2], and highlight a pressing need to better understand its molecular mechanisms. The skin lends itself to these studies because it is relatively safe to biopsy and the clinical ageing phenotype is easily observable. In this chapter we discuss the composition and structure of the three distinct tissue-types that comprise healthy human skin and compare differing approaches to visualising skin anatomy.

2 Epidermis and the Dermal-Epidermal Junction

The skin is a multifunctional organ with a complex architecture that forms a protective barrier against harmful microbes and the external environment. It is composed of three distinct tissue layers: the epidermis, dermis and hypodermis (Fig. 1).

2.1 Epidermis

The outer epidermal layer is a highly cellular, yet avascular structure which provides the main barrier against environmental damage [3] such as protection from pathogens, ultraviolet radiation (UVR), pollution and dehydration [4]. Stem cells at the basal layer of the epidermis transdifferentiate into keratinocytes, the main epidermal cell-type that forms the superficial layers of the epidermis. Over the course of approximately 4 weeks, the cells lose their nuclei to become corneocytes that form the skin-air interface [5]. In addition to the family of keratin proteins that are alternatively expressed in abundance by keratinocytes at throughout the different stages of their differentiation, the epidermis is also rich in vimentin, desmin, a-internexin and nestin. The epidermis itself can be segmented into four micro-layers (moving in from the surface: *stratum corneum*, *stratum granulosum*, *stratum spinosum* and *stratum basale*). An additional layer of dead cells, known as the *stratum lucidum*, is situated superficial to the *granulosum* and beneath the *corneum* in areas of thick skin such as the heel and the palm of the hand.

The *stratum corneum* consists of a tightly bound sheet of corneocytes (dead, flattened keratinocytes) and acts as the primary defence against infection, injury and prevents dehydration [6]. It is able to endure high mechanical stress making it resistant to abrasive and penetrative forces [7]. The barrier function of this layer is attributable to both the terminally differentiated corneocytes and also to the sur-

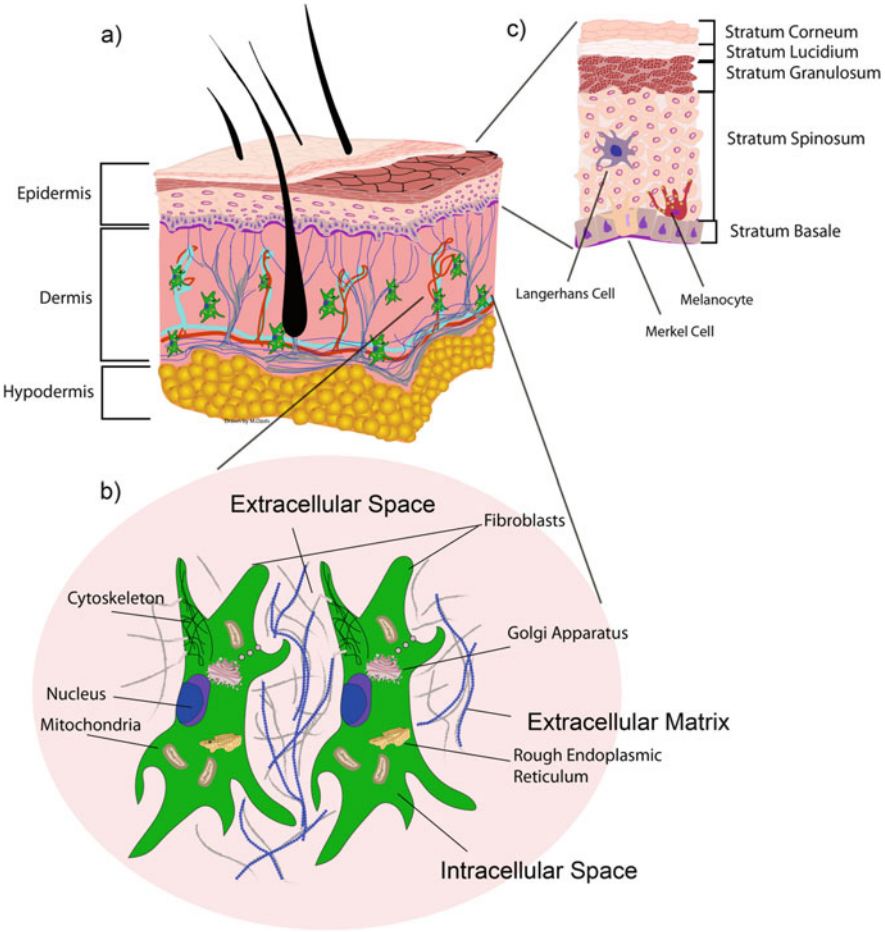

Fig. 1 Skin anatomy and composition. (**a**) Human skin is composed of three tissues, an outer cell-rich epidermis, an extracellular-matrix-rich dermis and a layer of fat-rich adipocytes. The dermis is vascularised and contains the major portions of skin organelles (such as hair follicles). (**b**) The major cellular components of the dermis are fibroblasts whose internal structures (cytoskeleton) interacts with the external extracellular matrix of collagens, fibronectin and elastic fibres. (**c**) The metabolically active epidermis is constantly regenerated via a stem cell layer (*stratum basale*) which feeds maturing chondrocytes in the upper layers

rounding lipid matrix (composed of ceramidines, fatty acids and cholesterol) which collectively act as a "bricks and mortar" providing water content maintenance and acting as a biosensor and first protection against damage [8, 9]. The *stratum granulosum* and the *stratum spinosum* consist mainly of lipid-releasing keratinocytes, which progress through distinct stages of differentiation into corneocytes [6]. The innermost layer of the epidermis, the *stratum basale* is made of a single layer of progenitor keratinocytes which act as both a source of proliferation, continuously

replacing cells in the more superficial layers of the epidermis [10], and as a physical barrier between the epidermis and the dermis. In addition to keratinocytes, the epidermis also contains melanocytes that produce melanin, a pigment that forms a protective umbrella-like cup over keratinocyte nuclei to prevent UV damage [11] and Langerhan's cells that act as sentinels of the cutaneous immune system [12]. The stem cells within the *stratum basale* are anchored to the basement membrane, by protein complexes called hemidesmosomes, via the transmembrane signalling α6β4 integrin [13]. Banded anchoring fibrils, rich in collagen VII, originate in the dermis and intercalate with the DEJ connecting it to the underlying stroma [14] whilst other dermal assemblies, such as the fibrillin-rich oxytalan fibres, also appear to play a role in dermal-epidermal adhesion [15].

2.2 Dermal-Epidermal Junction

The dermal-epidermal junction (DEJ) forms the interface between the cellular, metabolically active and avascular epidermis and the supporting extracellular-matrix rich, vascularised dermis. Central to the DEJ is a basement membrane composed of a highly specialised extracellular matrix (comprised of proteins such as laminins and collagen IV) that both mechanically anchors the two tissues and also plays a regulatory role in development and wound healing [16–18]. In addition to the basement membrane proteins, the DEJ also contains hemidesmosomes and collagen VII anchoring fibrils which anchor basal keratinocytes and the dermal matrix respectively [17]. Commonly, in young, healthy, human skin the DEJ is comprised of intercalating projections (papillae) which, much like the villi of the small intestine, maximise the surface area between the two layers. This increases the efficiency of nutrient delivery from the dermis to the epidermis [16]. Mechanically, this high surface area enhances the adhesion between the dermis and the epidermis and also protects the dermis from physical trauma by diffusing external forces along the area of contact [19]. Crucially, loss of these papillae is a key hallmark of ageing [20].

3 Dermis

The dermis is composed primarily of a dense extracellular matrix (ECM) that supports the cutaneous vasculature, sensory nerve cells and organelles such as sweat glands and hair follicles. Whilst these glands and organelles contain multiple cell populations, the dermal ECM itself is populated primarily by sparsely distributed fibroblasts (Fig. 1). These cells synthesise a complex structural matrix composed of load bearing collagens, resilient elastic fibres, negatively charged and therefore hydrophilic proteoglycans and hyaluronic acid. In addition to these major

components there are numerous less abundant ECM constituents including soluble proteases, protease inhibitors and cytokines.

3.1 Collagens

The collagen superfamily of proteins consists of 28 different types, encoded by more than 44 separate genes, which assemble into a variety of supramolecular structures [21]. Most collagens have specific spatial and temporal tissue distributions and exhibit both distinct and overlapping functional properties. Their primary structure is characterised by a Glycine-X-Y repeat sequence in which the X and Y may alter between repeats but are typically proline or hydroxyproline residues [22]. Collagens contain a triple helical domain that is stabilised by the hydroxylation of proline [23, 24]. The non-helical (globular) domains in some of the collagens are separated by more than one triple helical domain. The indispensability of these abundant proteins in the body to the integrity of connective tissues is demonstrated by the number of diseases associated with gene mutations affecting its structure and function (e.g., epidermolysis bullosa, Ehlers-Danlos syndrome and osteogenesis imperfecta) [25–28]. The function of fibrillar collagens and ultimately the dermis and skin is determined not only by the collagens themselves but also by associated proteins which mediate fibril structure and interaction. For example, decorin is a small leucine rich proteoglycan which 'decorates' the surface of collagen fibrils and is thought to prevent fibril fusion [29]. Although the dermis of decorin knockout mice contains abundant collagen fibrils, the skin itself is extremely fragile and prone to tears (Fig. 2). In the absence of decorin, the ordered packing and uniform diameter of fibrillary collagen is disrupted. Therefore it is clear that ECM structure is a major determinant of function.

The most common collagens in skin (and many other tissue and organs) are the interstitial fibrillar collagens—types I, III and V; the basement membrane localised—types IV and type XVII; and type VI which forms the heteromeric microfibrils that are abundant within the dermis. Collagen fibrils (are stabilised by covalent bonds between lysine residues that are catalysed by the copper dependent, extracellular enzyme lysyl oxidase (LOX), and which endow the tissue with tensile strength [30–36]. Collagen I is the most abundant of all the fibril forming collagens and can combine with type III in fibres of the reticular dermis [31, 37]. Compared with other tissues, such as tendon and cornea, the micro-architecture of collagen fibril bundles in human skin appears less well defined, although there are gradients in the abundance of the fibrillar collagens [20] and the bundles themselves are often reported to form local basket weave arrangements [38]. Collagen IV is a non-fibrillar collagen which assembles into a sheet-like structure within the DEJ and co-localises with laminin-332, fibronectin and nidogen to provide a scaffold for the deposition of ECM molecules including the anchoring collagen VII [30, 37, 39]. Collagen XVII

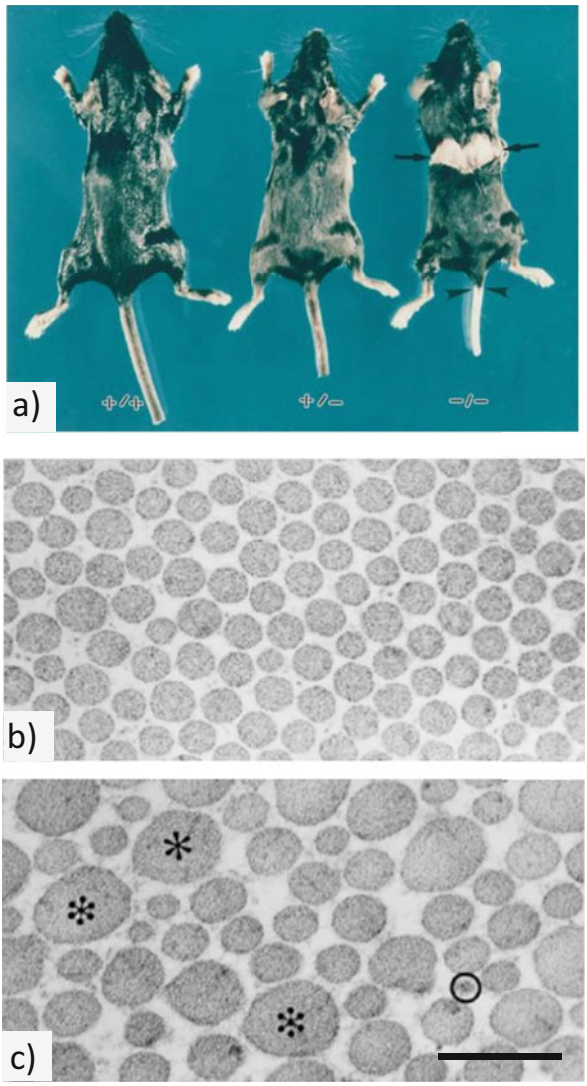

Fig. 2 Skin fragility and collagen fibril structure in decorin knockout mice. (**a**) Human compared with the wildtype (+/+) and heterozygous knockout (+/−), the skin of the homozygous decorin knockout mouse is prone to tears (arrows). (**b**) The dermis of the wild type mouse is composed of regularly spaced, uniform diameter collagen fibrils. (**c**) In contrast the fibril packing and diameter are poorly controlled in the homozygous knockout mouse. Dermal fibrils are both abnormally large (asterisk) and small (circles). Scale bar = 200 nm. Adapted from [29] with permission

is a hemidesmosome component which is involved in the migration of keratinocytes in wound healing [40]. Collagen VI is a unique collagen that forms a beaded microfibrillar meshwork encircling the fibres of principal fibrillary collagen I, and is important in regulating matrix assembly and fibroblast behaviour [41–43].

3.2 Elastic Fibres

Elastic fibres are integral ECM components of dynamic connective tissues such as, lungs, blood vessels, bladder and skin. They exhibit remarkable resilience and elasticity and are capable of unforced, passive deformation and recoil [44]. The elastic fibre is comprised of an amorphous elastin core (which constitutes 90% of the fibre mass) surrounded by a protective, biochemically active fibrillin microfibril sheath [45] which may strengthen and anchor the fibres [46]. Elastin is a multi-domain signalling protein encoded by a single gene on chromosome 7q11.2, elastogenic cells such as dermal fibroblasts, secrete elastin into the ECM in the form of its soluble precursor, tropoelastin [45]. Hydrophobic amino acids alternating with lysine residues are covalently cross-linked by LOX during elastic fibre assembly [32]. The N-terminus of elastin endows the protein with its elastic recoil whilst the C-terminus and a central region of the protein are actively involved in integrin-mediated cell adhesion and signalling respectively [47, 48]. In contrast to the single elastin gene there are three fibrillin isoforms, although fibrillin-1 is the most abundant isoform in adult tissue and forms the major component of the insoluble dermal fibrillin microfibrils. All three fibrillin isoforms are composed mainly of cbEGF domain repeats, interspersed by seven TGFβ-binding (TB) domains. In addition, there are two hybrid domains and a hydrophobic domain within the N-terminus; proline-rich in fibrillin-1, glycine-rich in fibrillin-2 and both proline- and glycine-rich in fibrillin-3. Fibrillin functions as a cell signalling molecule via an arginine-glycine-aspartic acid (RGD) recognition site and other cell binding domains within the molecule [49, 50]. It also has a role to play in regulating the availability of TGFβ within the ECM [51, 52].

Mature elastic fibres in the dermis are therefore composed of both cross-linked elastin and fibrillin microfibrils. In the dermis, elastic fibres exhibit a semi-structured micro-architecture [53]. Thick horizontal bundles of elastic fibres dominate the deep reticular dermis of the skin and connect to thinner, perpendicular elastic elaunin fibres and finally to oxytalan fibres in the papillary dermis. In contrast to elastic and elaunin fibres, oxytalan fibres are composed solely of fibrillin microfibrils and extend through the papillary dermis to the basement membrane where they are thought to interact with the heparin sulphate proteoglycan: perlecan [54]. Remodelling of this architecture is a key marker of age-related photodamage [15].

3.3 Proteoglycans and Hyaluronic Acid

Proteoglycans are proteins modified by linkage to one or more glycosaminoglycan (GAG) chains [55]. Hyaluronic acid (or hyaluronan) is a GAG chain which is found both intracellularly and within the ECM but is not linked to a protein core

[56]. The GAGs in skin are chondroitin sulfate, dermatan sulfate, keratan sulfate, heparan sulfate, heparin, and hyaluronic acid. Their negative charge is thought to be important in maintaining skin water content [57] whilst the flexibility of these GAG chains makes them an effective hygroscopic space filler allowing them to function as a "hydraulic shock absorber" [58]. The proteoglycans in skin include the heterogeneous small leucine-rich proteoglycans (SLRP) and versican which are expressed within the dermis, perlecan which is localised to basement membranes (including the dermal-epidermal junction) and cell-surface expressed glypians and syndecans [59]. In addition to their structural roles proteoglycans also perform regulatory roles interacting with a number of ligands within the ECM, notably TGF-β [60]. As such, they play an important role in sequestering cytokines and storing them in the surrounding ECM.

3.4 Non-structural Extracellular Components

Non-structural components of human skin including cytokines, cross-linking enzymes, protease and protease inhibitors play keys roles in constructing, maintaining and degrading structural proteins. Many skin proteins are highly interconnected commonly through the formation of di-sulphide bonds and transglutaminase and LOX mediated crosslinks [61]. LOX is also involved in the crosslinking of elastin in elastic fibres [62] whilst basement membrane laminins and fibronectin are also crosslinked via di-sulphide bonding [63]. These crosslinking mechanisms are not only important to the stability of the ECM, but also for rendering the network insoluble. Transglutaminase-2, for instance, is extremely important for maintaining ECM insolubility [61, 64].

Proteases are actively involved in the remodelling and modification of the ECM in tissue homeostasis, disease, inflammation and ageing [20, 65–70]. There are several families of proteases that exhibit diverse substrate specificity and some cleave ECM components to generate biologically active protein fragments, known as 'matrikines,' [59, 71–73]. Such proteases include the matrix metalloproteinases (MMPs), the a disintegrin-like and metalloproteinase domain with thrombospondin-type 1 motifs (ADAMTS) proteases, adamalysins, meprins and serine proteases [74]. MMPs are a zinc dependant family of proteases and are the main group involved in ECM degradation, they exhibit low substrate specificity and their activity is tightly controlled by endogenous inhibitors known as tissue inhibitors of metalloproteinases (TIMPs) [75]. The ADAMTs family have been found to be important in modulating fibrillin-rich microfibril formation and function [76]. There are at least two elastases in skin; neutrophil elastase and fibroblast-derived elastase. Neutrophil elastase is a serine protease that is capable of degrading the mature elastic fibre system and may be important in driving solar elastosis [65, 77, 78]. In contrast, fibroblast-derived elastase is a member of the metalloproteinases found in non-inflamed skin, acts on elaunin and oxytalin fibres but has limited specificity for mature elastic fibres [79]. These proteases, and others, are thought

to be important in matrix degradation and the de novo synthesis of the aberrant ECM that is characteristic of photodamaged skin.

Finally, skin contains cell signalling molecules (cytokines). Some of these molecules are sequestered by the dermal matrix awaiting release as a consequence of injury or inflammation. For example, latent bone morphogenetic proteins (BMPs) have been shown to associate with fibrillin microfibrils both in vitro and in vivo [80]. Fibrillin microfibrils act as natural storage for BMP, co-localising the growth factor to a specific site which minimizes diffusion and allows their quick mobilisation and subsequent influence on cell differentiation and migration [81]. Like latent BMPs, TGF-β is stored in the ECM by associating with fibrillin-1 via LTBPs 1, 3 and 4 [82]. TGF-β is a multifunctional cytokine which acts as a mediator of neurogenesis, angiogenesis, immuno-recruitment, wound healing, lineage determination, differentiation, proliferation, cell adhesion, apoptosis and ECM regulation [83]. The storage of TGF-β by fibrillin microfibrils suggests that they play a major role in controlling tissue homeostasis [84].

3.5 "Minor" Proteins and the Skin Proteome

Whilst the proteins discussed in the preceding sections clearly play vital roles in contributing to skin structure and function, it is also clear that skin is composed of many additional proteins, some of which are present only in low abundance. Both the identity and function of these proteins in human skin is not is not always well defined. Skin proteomic profiling has been attempted by several studies using mass spectrometry methods (MS). Crucially, however, there is little agreement as to the identity and number of skin proteins in the published studies of Mikesh et al. and Bliss et al. [85, 86]. We have recently taken an alternative approach using the peer reviewed literature as an information source and by adapting systematic review and bioinformatic techniques, we have defined a skin proteome of 2948 skin proteins, 437 of which are unique to this database and 2011 of which are supported by both mass spectrometry and immune-based evidence. This proteome can be found at: www.manchesterproteome.manchester.ac.uk.

3.6 Turnover and Longevity

Whereas intracellular proteins have biological half-lives ranging from minutes and hours [87–89] to a few days [90], several components of the ECM are known to be remarkably long-lived by comparison. In skin, the half-life of collagen type I was estimated to be 15 years whilst collagen type II in cartilage has an estimated half-life of 117 years [91]. Elastic fibres are also thought to be highly persistent in

tissues. The mean turnover for elastin was extrapolated in the late seventies using dietary estimates [92]. The permanence of elastin and its microfibrillar template in resident human tissues was demonstrated experimentally by Shapiro et al. [93] using two distinct methods. The first was using aspartic acid racemization whereby L-enantiomers of amino acids slowly and predictably convert to D-enantiomers over an individual's lifetime. This allowed the age of long-lived elastic fibre proteins to be determined. The second was by measuring the levels of radioactive isotope ^{14}C within purified elastin, which had been incorporated into the carbonaceous tissues of organisms in the late 1950s as a result of nuclear weapons tests and provides a useful dating tool in biogenic material. Using both these means, Shapiro et al. estimated the mean residence time of elastin, purified from human lung parenchyma, to be 74 years. In the same study, they went on to show that microfibrils and other non-elastin components of the elastic fibre (which are likely to be microfibrillar) also contributed a large proportion of total D-aspartate and are therefore similarly long lived. As a consequence it appears that the major structural ECM assemblies in the dermis (fibrillar collagens and elastic fibres) are likely to persist in the tissue for many years. Over a lifetime, these proteins are exposed to many stressors (e.g., mechanical forces, reactive oxidative species, photodamage) that result in accumulated damage to protein structure and function. Ageing in ECM-rich, predominantly acellular tissues such as the dermis may therefore be mediated by the rate of damage accumulation rather than in the decline of cell mediated repair mechanisms.

4 Hypodermis

The hypodermis is mainly composed of fatty acids which provide thermoregulation, insulation, store nutrition and protect deeper tissues from injuries [94]. The hypodermis, which is rich in white adipose tissue containing pre-adipocytes, adipocytes, macrophages and fibroblasts, forms the underlying layer of the skin. It has little ECM and its thickness varies according to anatomical site. Epidermal appendages, such as nerve endings and hairs, terminate within the hypodermis. Similar to the dermal elastic fibre system, the hypodermis seems to also be susceptible to damage from UVR with the subcutaneous tissue becoming thinner in photo-exposed regions of the body [95]. Recent studies suggest that the hypodermis may influence dermal physiology and structure. Ezure and Amano have shown that a raised body mass index (BMI) and the associated adipocyte hypertrophy is correlated with reduced elastic fibre staining in the dermis [96]. This correlation is intriguing and suggests that adipocytes may influence dermal structure, however the mechanism and reversibility of this remodelling is, as yet, not clear [97].

5 Characterising Cutaneous Structure

Much of our knowledge of skin structure is informed by ex vivo techniques which use light or, electron microscopy to visualise skin tissues (often in two dimensional sections). There is also promise in combining ex vivo 3D imaging of intact skin samples with prior longitudinal in vivo (non-invasive) imaging.

5.1 Conventional Imaging of Skin Sections

Traditional histological methods combined with light microscopy are commonly employed to study dermal organisation and architecture and have been vital to our understanding of skin ageing and skin pathologies over a number of decades. The process relies on effective removal and preservation of the specimen either by chemical fixation or controlled freezing, followed by staining of tissue sections (typically 4–8 micron thick) mounted on glass microscope slides and visualised by light microscopy. The unique chemistry of specific extracellular macromolecules can be exploited to attract and bind the histological stain which enables differentiation from cellular structures and provides optimal contrast of tissue architecture. For example, routinely used stains for evaluation of skin are Weigert's and orcein stain for elastic fibres; picrosirus red and Massons Trichrome stain for collagen fibres and haematoxylin and eosin (H&E) which differentiate the cell nucleus and cytoplasm from extracellular matrix. H&E is still extensively and routinely used for light microscopic evaluation of dermal morphology.

Immunohistochemical staining, first reported by Coons et al. [98] has become a powerful tool to detect amino acid sequences of proteins, cell-types or even infectious agents within tissue sections. The strategy relies upon the specific binding of a primary antibody to an epitope within the protein (antigen) of interest. A secondary antibody that binds antibody from the animal species that the primary IgG is derived from, labelled with either fluorescent tags or enzymes such as peroxidase or alkaline phosphatase can be applied to the tissue section to localise the primary antibody and therefore the epitope of interest. This method is considered to be highly specific, but can lack visual contrast. Counterstains such as nuclear fast red or haematoxylin can be used as counterstains to provide morphological information.

5.2 Three Dimensional and Non-invasive Imaging

Whilst often highly informative of composition, these two dimensional sectioning-based approaches commonly induce artefacts due to the chemical dehydration and

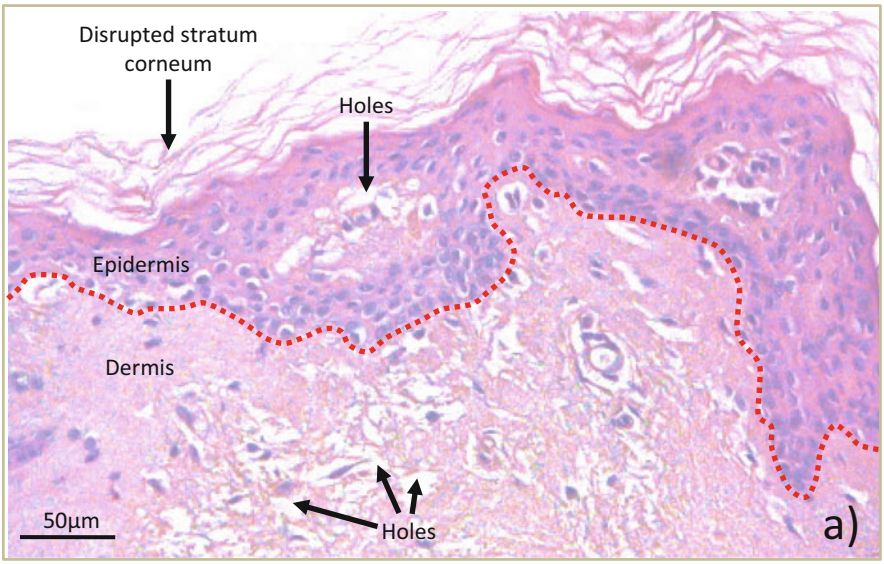

Fig. 3 Sectioning induced artefacts. This ethanol dehydrated, chemically fixed, paraffin embedded and H&E stained human skin section (imaged be light microscopy) illustrates the common artefacts induced by the preparation process. Often the *stratum corneum* will delaminate, whilst holes (either due to mechanical stresses or the loss of components such as cellular contents) can be found in the epidermis or more commonly in the dermis. Figure adapted from Walton et al. [99] with permission

fixation of the tissues and the mechanical disruption caused by sectioning (Fig. 3). These artefacts can manifest as disruption of the *stratum corneum* and as tears and holes in both the epidermis and dermis. In contrast micro-computed X-ray tomography (microCT) imaging of either unstained skin (imaged by phase contrast) [99] or iodine stained skin [100] can readily resolve recognisable three dimensional skin structures in intact biopsies (Figs. 3 and 4). To date we have only imaged chemically fixed skin samples but it seems likely based on our work on other tissues (i.e. the intervertebral disc) that it should be possible to image native (non-fixed) skin and also to apply digital image and volume correlation techniques to map strain in three dimensions [101, 102]. MicroCT imaging is not the only potential 3D imaging modality and the reader is referred to our recent review for a comprehensive comparison of alternative imaging techniques [103]. Whilst powerful, these ex vivo techniques are poorly suited to tracking longitudinal changes in skin. In our recent review we compare the potential for non-invasive techniques such as ultrasound, optical coherence tomography and confocal microscopy to characterise skin structure in situ [104].

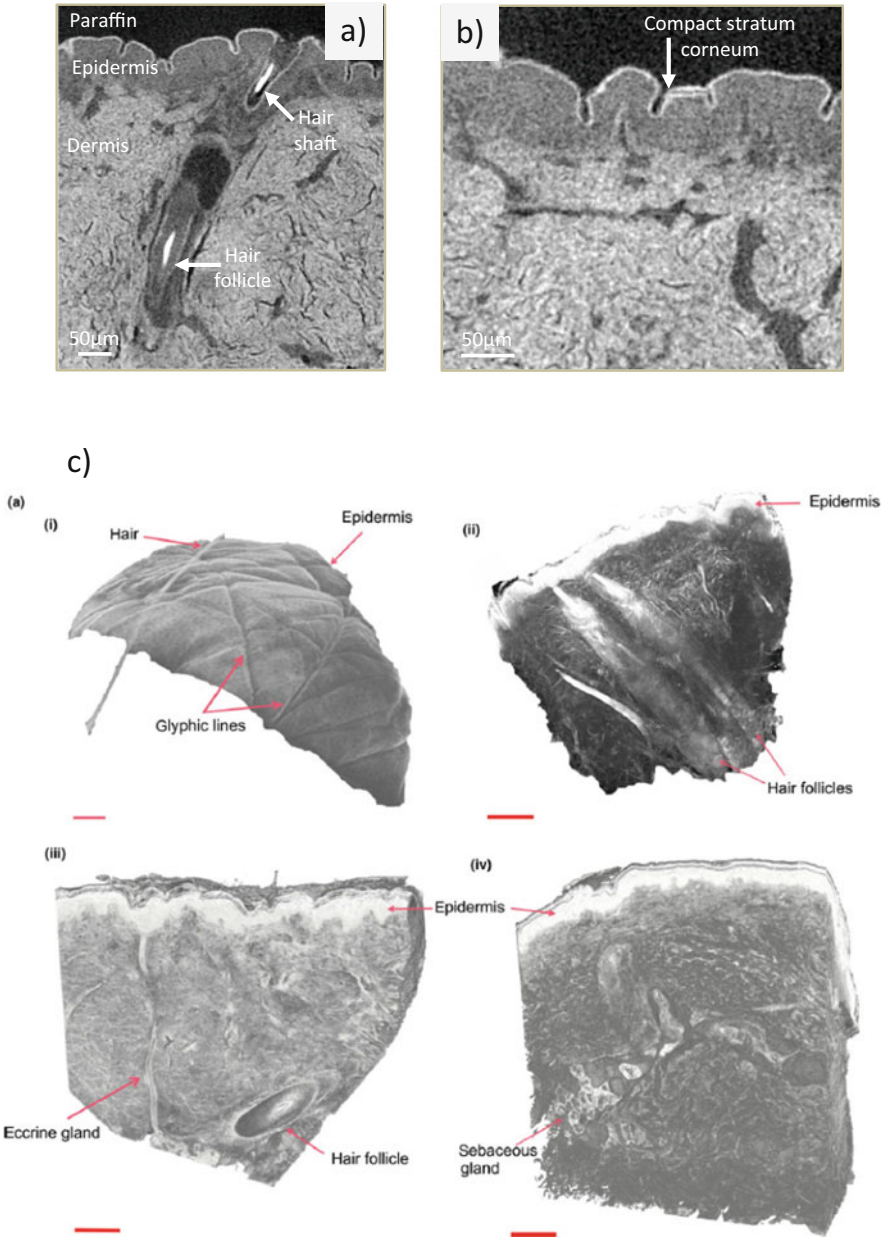

Fig. 4 MicroCT imaging of human skin. In common with clinical CT imaging, microCT employs many (typically thousands) of projections to reconstruct the 3D structure of an object. In the case of our microCT studies with a spatial resolution of approximately 1 μm. (**a** and **b**) Virtual, two dimensional slices through a three dimensional volume (tomogram) clearly showing major skin features including the intact *stratum corneum*, epidermis, dermis and hair follicles. (**c**) Tomograms can be visualised in three dimensions. Here iodine staining has been used to highlight the epidermis. Adapted from Walton et al. [99] and Newton et al. [100] with permission

6 Conclusions and Future Directions

The biophysical properties of human skin are determined by its structure and molecular composition. The major structural and compositional features of human skin, its and the differential expression of structural proteins such as keratins in the epidermis and collagens and elastic fibre components in the dermis have been established for many decades. However, the role played by "minor" skin components and the influence of nano- and micro-structure on its mechanical properties is poorly understood. As a consequence the functional consequences of the structural and compositional differences which are associated with anatomical site, ethnicity, environmental exposures and ageing are also poorly understood. Conventional, histological and immunohistochemical techniques will clearly remain important in characterising skin structure and composition but there is considerable opportunity to augment these techniques with new methods which can characterise: (1) the three dimensional structure and mechanical properties of intact, native skin and (2) the whole skin proteome and transcriptome.

Acknowledgements The authors would like to acknowledge the generous financial support of Walgreens Boots Alliance.

References

1. Al-Nuaiami Y, Sherratt MJ, Griffiths CEM (2014) Skin health in older age. Maturitas 7:256–264
2. Bulterijs S, Hull R, Bjork VE, Roy AG (2015) It is time to classify biological aging as a disease. Front Genet 6:205
3. D'Errico M, Lemma T, Calcagnile A, Proietti De Santis L, Dogliotti E (2007) Cell type and DNA damage specific response of human skin cells to environmental agents. Mutat Res 614:37–47
4. Fluhr JW, Feingold KR, Elias PM (2006) Transepidermal water loss reflects permeability barrier status: validation in human and rodent in vivo and ex vivo models. Exp Dermatol 15:483–492
5. Nelson WG, Sun TT (1983) The 50- and 58-kdalton keratin classes as molecular markers for stratified squamous epithelia: cell culture studies. J Cell Biol 97:244–251
6. Proksch E, Brandner JM, Jensen JM (2008) The skin: an indispensable barrier. Exp Dermatol 17:1063–1072
7. Madison KC (2003) Barrier function of the skin: "la raison d'etre" of the epidermis. J Invest Dermatol 121:231–241
8. Elias PM (1983) Epidermal lipids, barrier function, and desquamation. J Invest Dermatol 80:44s–49s
9. Harding CR (2004) The *stratum corneum*: structure and function in health and disease. Dermatol Ther 17:6–15
10. Bollag WB, Dodd ME, Shapiro BA (2004) Protein kinase D and keratinocyte proliferation. Drug News Perspect 17:117–126
11. Cichorek M, Wachulska M, Stasiewicz A, Tymińska A (2013) Skin melanocytes: biology and development. Adv Dermatol Allergol 30:30–41

12. Collin M, Milne P (2016) Langerhans cell origin and regulation. Curr Opin Hematol 23:28–35
13. Mainiero F, Pepe A, Yeon M, Ren Y, Giancotti FG (1996) The intracellular functions of alpha6beta4 integrin are regulated by EGF. J Cell Biol 134:241–253
14. Keene DR, Sakai LY, Lunstrum GP, Morris NP, Burgeson RE (1987) Type-VII collagen forms an extended network of anchoring fibrils. J Cell Biol 104(3):611–621. https://doi.org/10.1083/jcb.104.3.611
15. Watson RE, Griffiths CE, Craven NM, Shuttleworth CA, Kielty CM (1999) Fibrillin-rich microfibrils are reduced in photoaged skin. Distribution at the dermal-epidermal junction. J Invest Dermatol 112:782–787
16. Briggaman RA, Wheeler CEJR (1975) The epidermal-dermal junction. J Invest Dermatol 65:71–84
17. Burgeson RE, Christiano AM (1997) The dermal-epidermal junction. Curr Opin Cell Biol 9:651–658
18. Hashmi S, Marinkovich MP (2011) Molecular organization of the basement membrane zone. Clin Dermatol 29:398–341
19. Xiong X, Wu T, He S (2013) Physical forces make rete ridges in oral mucosa. Med Hypotheses 81:883–886
20. Naylor EC, Watson RE, Sherratt MJ (2011) Molecular aspects of skin ageing. Maturitas 69:249–256
21. Mienaltowski MJ, Birk DE (2014) Structure, physiology, and biochemistry of collagens. Adv Exp Med Biol 802:5–29
22. Ramshaw JA, Shah NK, Brodsky B (1998) Gly-X-Y tripeptide frequencies in collagen: a context for host-guest triple-helical peptides. J Struct Biol 122:86–91
23. Brodsky B, Ramshaw JA (1997) The collagen triple-helix structure. Matrix Biol 15:545–554
24. Dolz R, Engel J, Kuhn K (1988) Folding of collagen IV. Eur J Biochem 178:357–366
25. Bonadio J et al (1990) Transgenic mouse model of the mild dominant form of osteogenesis imperfecta. Proc Natl Acad Sci USA 87:7145–7149
26. Bruckner-Tudeman L, Has C (2014) Disorders of the cutaneous basement membrane zone—the paradigm of epidermolysis bullosa. Matrix Biol 33:29–34
27. Kivirikko KI (1993) Collagens and their abnormalities in a wide spectrum of diseases. Ann Med 25:113–126
28. Metsaranta M, Garofalo S, Decker G, Rintala M, De Crombrugghe B, Vuorio E (1992) Chondrodysplasia in transgenic mice harboring a 15-amino acid deletion in the triple helical domain of pro alpha 1(II) collagen chain. J Cell Biol 118:203–212
29. Danielson KG, Baribault H, Holmes DF, Graham H, Kadler KE, Iozzo RV (1997) Targetted disruption of decorin leads to abnormal collagen fibril morphology and skin fragility. J Cell Biol 136:729–743
30. Chanut-Delalande H, Bonod-Bidaud C, Cogne S, Malbouyres M, Ramirez F, Fichard A, Ruggiero F (2004) Development of a functional skin matrix requires deposition of collagen V heterotrimers. Mol Cell Biol 24:6049–6057
31. Fleischmajer R, Macdonald ED, Perlish JS, Burgeson RE, Fisher LW (1990) Dermal collagen fibrils are hybrids of type I and type III collagen molecules. J Struct Biol 105:162–169
32. Lucero HA, Kagan HM (2006) Lysyl oxidase: an oxidative enzyme and effector of cell function. Cell Mol Life Sci 63:2304–2316
33. Pinnell SR, Martin GR (1968) The cross-linking of collagen and elastin: enzymatic conversion of lysine in peptide linkage to alpha-aminoadipic-delta-semialdehyde (allysine) by an extract from bone. Proc Natl Acad Sci USA 61:708–716
34. Smith-Mungo LI, Kagan HM (1998) Lysyl oxidase: properties, regulation and multiple functions in biology. Matrix Biol 16:387–398
35. Vogel HG (1974) Correlation between tensile strength and collagen content in rat skin. Effect of age and cortisol treatment. Connect Tissue Res 2:177–182
36. Weber L, Kirsch E, Muller P, Krieg T (1984) Collagen type distribution and macromolecular organization of connective tissue in different layers of human skin. J Invest Dermatol 82:156–160

37. Gelse K, Poschl E, Aigner T (2003) Collagens—structure, function, and biosynthesis. Adv Drug Deliv Rev 55:1531–1546
38. Graham HK, Hodson NW, Hoyland JA, Millward-Sadler SJ, Garrod D, Scothern A, Griffiths CE, Watson RE, Cox TR, Erler JT, Trafford AW, Sherratt MJ (2010) Tissue section AFM: in situ ultrastructural imaging of native biomolecules. Matrix Biol 29:254–260
39. Abreeu-Velez AM, Howard MS (2012) Collagen IV in normal skin and in pathological processes. N Am J Med Sci 4:1–8
40. Loffek S, Hurskainen T, Jackow J, Sigloch FC, Schilling O, Tasanen K, Bruckner-Tuderman L, Franzke CW (2014) Transmembrane collagen XVII modulates integrin dependent keratinocyte migration via PI3K/Rac1 signaling. PLoS One 9:e87263
41. Godwin AR, Starborg T, Sherratt MJ, Roseman AM, Baldock C (2017) Defining the hierarchical organisation of collagen VI microfibrils at nanometre to micrometre length scales. Acta Biomater 52:21–32
42. Sabatelli P, Gara SK, Grumati P, Urciuolo A, Gualandi F, Curci R, Squarzoni S, Zamparelli A, Martoni E, Merlini L, Paulsson M, Bonaldo P, Wagener R (2011) Expression of the collagen VI alpha 5 and alpha 6 chains in normal human skin and in skin of patients with collagen VI-related myopathies. J Invest Dermatol 131:99–107
43. Theocharidis G, Drymoussi Z, Kao AP, Barber AH, Lee DA, Braun KM, Connelly JT (2016) Type VI collagen regulates dermal matrix assembly and fibroblast motility. J Invest Dermatol 136:74–83
44. Baldwin AK, Cain SA, Lennon R, Godwin A, Merry CL, Kielty CM (2014) Epithelial-mesenchymal status influences how cells deposit fibrillin microfibrils. J Cell Sci 127(Pt 1):158–171. https://doi.org/10.1242/jcs.134270
45. Kielty CM, Sherratt MJ, Shuttleworth CA (2002) Elastic fibres. J Cell Sci 115:2817–2828
46. Sherratt MJ, Baldock C, Haston JL, Holmes DF, Jones CJP, Shuttleworth CA, Wess TJ, Kielty CM (2003) Fibrillin microfibrils are stiff reinforcing fibres in compliant tissues. J Mol Biol 332(1):183–193. https://doi.org/10.1016/S0022-2836(03)00829-5
47. Bax DV, Mahalingam Y, Cain S, Mellody K, Freeman L, Younger K, Shuttleworth CA, Humphries MJ, Couchman JR, Kielty CM (2007) Cell adhesion to fibrillin-1: identification of an Arg-Gly-Asp-dependent synergy region and a heparin-binding site that regulates focal adhesion formation. J Cell Sci 120:1383–1392
48. Lee P, Bax DV, Bilek MM, Weiss AS (2014) A novel cell adhesion region in tropoelastin mediates attachment to integrin alphaVbeta5. J Biol Chem 289:1467–1477
49. Bax DV, Bernard SE, Lomas A, Morgan A, Humphries J, Shuttleworth CA, Humphries MJ, Kielty CM (2003) Cell adhesion to fibrillin-1 molecules and microfibrils is mediated by alpha 5 beta 1 and alpha v beta 3 integrins. J Biol Chem 278:34605–34616
50. Sakamoto H, Broekelmann T, Cheresh DA, Ramirez F, Rosenbloom J, Mecham RP (1996) Cell-type specific recognition of RGD- and non-RGD-containing cell binding domains in fibrillin-1. J Biol Chem 271:4916–4922
51. Chaudhry SS, Cain SA, Morgan A, Dallas SL, Shuttleworth CA, Kielty CM (2007) Fibrillin-1 regulates the bioavailability of TGFbeta1. J Cell Biol 176:355–367
52. Massam-Wu T, Chiu M, Choudhury R, Chaudhry SS, Baldwin AK, Mcgovern A, Baldock C, Shuttleworth CA, Kielty CM (2010) Assembly of fibrillin microfibrils governs extracellular deposition of latent TGF beta. J Cell Sci 123:3006–3018
53. Cotta-Pereira G, Rodrigo G, Bittencourt-Sampaio S (1976) Oxytalan, elaunin and elastic fibers in the human skin. J Investig Dermatol 66:143–148
54. Tiedemann K, Sasaki T, Gustafsson E, Göhring W, Bätge B, Notbohm H, Timpl R, Wedel T, Schlötzer-Schrehardt U, Reinhardt DP (2005) Microfibrils at basement membrane zones interact with perlecan via fibrillin-1. J Biol Chem 280:11404–11412
55. Schaefer L, Schaefer RM (2010) Proteoglycans: from structural compounds to signaling molecules. Cell Tissue Res 339:237–246
56. Hascall VC, Majors AK, De La Motte CA, Evanko SP, Wang A, Drazba JA, Strong SA, Wight TN (2004) Intracellular hyaluronan: a new frontier for inflammation? Biochim Biophys Acta 1673:3–12

57. Oh JH, Kim YK, Jung JY, Shin JE, Kim KH, Cho KH, Eun HC, Chung JH (2011) Intrinsic aging- and photoaging-dependent level changes of glycosaminoglycans and their correlation with water content in human skin. J Dermatol Sci 62:192–201
58. Evanko SP, Tammi M, Tammi RH, Wight TN (2007) Hyaluronan-dependent pericellular matrix. Adv Drug Deliv Rev 59:1351–1365
59. Maquart FX, Monboisse JC (2014) Extracellular matrix and wound healing. Pathol Biol (Paris) 62:91–95
60. Lyon M, Rushton G, Gallagher JT (1997) The interaction of the transforming growth factor-βs with heparin/heparan sulfate is isoform-specific. J Biol Chem 272:18000–18006
61. Hynes RO, Naba A (2012) Overview of the matrisome—an inventory of extracellular matrix constituents and functions. Cold Spring Harb Perspect Biol 4:a004903
62. Rucker RB, Kosonen T, Clegg MS, Mitchell AE, Rucker BR, Uriu-Hare JY, Keen CL (1998) Copper, lysyl oxidase, and extracellular matrix protein cross-linking. Am J Clin Nutr 67:996S–1002S
63. Yurchenco PD (2011) Basement membranes: cell scaffoldings and signaling platforms. Cold Spring Harb Perspect Biol 3
64. Lorand L, Graham RM (2003) Transglutaminases: crosslinking enzymes with pleiotropic functions. Nat Rev Mol Cell Biol 4:140–156
65. Doring G (1994) The role of neutrophil elastase in chronic inflammation. Am J Respir Crit Care Med 150:S114–S117
66. Kahari VM, Saarialho-Kere U (1997) Matrix metalloproteinases in skin. Exp Dermatol 6:199–213
67. Mccarty SM, Percival SL (2013) Proteases and delayed wound healing. Adv Wound Care (New Rochelle) 2:438–447
68. Mezentsev A, Nikolaev A, Bruskin S (2014) Matrix metalloproteinases and their role in psoriasis. Gene 540:1–10
69. Singh D, Srivastava SK, Chaudhuri TK, Upadhyay G (2015) Multifaceted role of matrix metalloproteinases (MMPs). Front Mol Biosci 2:19
70. Zeeuwen PLJM (2004) Epidermal differentiation: the role of proteases and their inhibitors. Eur J Cell Biol 83:761–773
71. Duca L, Floquet N, Alix AJ, Haye B, Debelle L (2004) Elastin as a matrikine. Crit Rev Oncol Hematol 49:235–244
72. Maquart FX, Simeon A, Pasco S, Monboisse JC (1999) Regulation of cell activity by the extracellular matrix: the concept of matrikines. J Soc Biol 193:423–428
73. Wells JM, Gaggar A, Blalock JE (2015) MMP generated Matrikines. Matrix Biol 44–46:122–129
74. Bonnans C, Chou J, Werb Z (2014) Remodelling the extracellular matrix in development and disease. Nat Rev Mol Cell Biol 15:786–801
75. Murphy G (2011) Tissue inhibitors of metalloproteinases. Genome Biol 12:233
76. Hubmacher D, Apte SS (2015) ADAMTS proteins as modulators of microfibril formation and function. Matrix Biol 47:34–43
77. Rijken F, Bruijnzeel PL (2009) The pathogenesis of photoaging: the role of neutrophils and neutrophil-derived enzymes. J Investig Dermatol Symp Proc 14:67–72
78. Starcher B, Conrad M (1995) A role for neutrophil elastase in solar elastosis. Ciba Found Symp 192:338–346
79. Godeau G, Hornebeck W (1988) Morphometric analysis of the degradation of human skin elastic fibres by human leukocyte elastase (EC 3-4-21-37) and human skin fibroblast elastase (EC 3-4-24). Pathol Biol (Paris) 36:1133–1138
80. Sengle G, Charbonneau NL, Ono RN, Sasaki T, Alvarez J, Keene DR, Bächinger HP, Sakai LY (2008) Targeting of bone morphogenetic protein growth factor complexes to fibrillin. J Biol Chem 283:13874–13888
81. Jensen SA, Robertson IB, Handford PA (2012) Dissecting the fibrillin microfibril: structural insights into organization and function. Structure 20(2):215–225
82. Kaartinen V, Warburton D (2003) Fibrillin controls TGF-β activation. Nat Genet 33:331–332

83. Massagué J (1998) TGF-β signal transduction. Annu Rev Biochem 67:753–791
84. Lemaire R, Bayle J, Lafyatis R (2006) Fibrillin in Marfan syndrome and tight skin mice provides new insights into transforming growth factor-beta regulation and systemic sclerosis. Curr Opin Rheumatol 18:582–587
85. Bliss E, Heywood WE, Benatti M, Sebire NJ, Mills K (2016) An optimised method for the proteomic profiling of full thickness human skin. Biol Procedures Online 18:15
86. Mikesh LM, Aramadhaka LR, Moskaluk C, Zigrino P, Mauch C, Fox JW (2013) Proteomic anatomy of human skin. J Proteomics 84:90–200
87. Aziz N, Detels R, Quint JJ, Li Q, Gietson D, Butch AW (2016) Stability of cytokines, chemokines and soluble activation markers in unprocessed blood stored under different conditions. Cytokine 84:17–24
88. Brinster RL, Brunner S, Joseph X, Levey IL (1979) Protein degradation in the mouse blastocyst. J Biol Chem 254:1927–1931
89. Kuehl L, Sumsion EN (1970) Turnover of several glycolytic enzymes in rat liver. J Biol Chem 245:6616–6623
90. Price JC, Guan S, Burlingame A, Prusiner SB, Ghaemmaghami S (2010) Analysis of proteome dynamics in the mouse brain. Proc Natl Acad Sci 107:14508–14513
91. Verzijl N, DeGroot J, Ben ZC, Brau-Benjamin O, Maroudas A, Bank RA, Mizrahi J, Schalkwijk CG, Thorpe SR, Baynes JW, Bijlsma JW, Lafeber FP, TeKoppele JM (2000) Age-related accumulation of Maillard reaction products in human articular cartilage collagen. Biochem J 350:381–387
92. Stenhouse MJ, Baxter MS (1977) Bomb 14C as a biological tracer. Nature 267:828
93. Shapiro SD, Endicott SK, Province MA, Pierce JA, Campbell EJ (1991) Marked longevity of human lung parenchymal elastic fibers deduced from prevalence of D-aspartate and nuclear weapons-related radiocarbon. J Clin Investig 87:1828–1834
94. Kanitakis J (2009) Anatomy histology and immunohistochemistry of normal human skin: the epidermis. Eur J Dermatol 12(4):1–13
95. Fenske NA, Lober CW (1986) Structural and functional changes of normal aging skin. J Am Acad Dermatol 15:571–585
96. Ezure T, Amano S (2015) Increment of subcutaneous adipose tissue is associated with decrease of elastic fibres in the dermal layer. Exp Dermatol 24:924–929
97. Sherratt MJ (2015) Body mass index and elastic fibre remodelling. Exp Dermatol 24:922–923
98. Coons AH, Creech HJ, Jones RN (1941) Immunological properties of an antibody containing a fluorescent group. Proc Soc Exp Biol 47:200–202
99. Walton LA, Bradley RS, Withers PJ, Newton VL, Watson REB, Austin C, Sherratt MJ (2015) Morphological characterisation of unstained and intact tissue micro-architecture by X-ray computed micro- and nano-tomography. Sci Rep 5:10074
100. Newton VL, Bradley RS, Seroul P, Cherel M, Griffiths CE, Rawlings AV, Voegeli R, Watson RE, Sherratt MJ (2017) Novel approaches to characterize age-related remodelling of the dermal-epidermal junction in 2D, 3D and in vivo. Skin Res Technol 23:131–148
101. Disney CM, Lee PD, Hoyland JA, Sherratt MJ, Bay BK (2018) A review of techniques for visualising soft tissue microstructure deformation and quantifying strain Ex Vivo. J Microsc 272(3):165–179. doi: https://doi.org/10.1111/jmi.12701
102. Disney CM, Madi K, Bodey AJ, Lee PD, Hoyland JA, Sherratt MJ (2017) Visualising the 3D microstructure of stained and native intervertebral discs using X-ray microtomography. Sci Rep 7:16279
103. Shearer T, Bradley RS, Hidalgo-Bastida A, Sherratt MJ, Cartmell SH (2016) Commentary: 3D visualisation of soft biological structures by microCT. J Cell Sci 129:13
104. Newton VL, Mcconnell JC, Hibbert SA, Graham HK, Watson RE (2015) Skin aging: molecular pathology, dermal remodelling and the imaging revolution. G Ital Dermatol Venereol 150:665–674

Constitutive Modelling of Skin Mechanics

Georges Limbert

Abstract The objective of this chapter is to provide a structured review of constitutive models of skin mechanics valid for finite deformations, with special emphasis on state-of-the-art anisotropic formulations which are essential in most advanced modelling applications. The fundamental structural and material characteristics of the skin, necessary for understanding its mechanics and for the formulation of constitutive equations, are briefly presented.

1 Introduction

Due to its privileged nature, as both an internal and external organ of the human body, the skin is crucial in how we interact with our inner and outer environments. Mechanics plays a fundamental role in conditioning the biophysical behaviour of skin, not only at a basic mechanical level, but also by being involved in a complex and intricate interplay with other physical processes such as cell activity, tissue biochemistry or electromagneto-chemical coupling (e.g. photo-ageing) [1, 2]. Additionally, the skin is a sensory interface containing a large network of nociceptors which respond to mechanical stimuli [1, 3, 4]. Contact interactions of the skin with internal structures (e.g. adipose tissue, muscles and bony structures) as well as with external devices (e.g. razor, clothing fabric, prosthesis, wearable electronics) are revealing examples of physical phenomena where the intrinsic mechanical and structural properties of the skin are essential. The ability to

G. Limbert (✉)
National Centre for Advanced Tribology at Southampton (nCATS) — Bioengineering Science Research Group, Department of Mechanical Engineering, Faculty of Engineering and Physical Sciences, University of Southampton, Southampton, UK

Laboratory of Biomechanics and Mechanobiology, Division of Biomedical Engineering, Department of Human Biology, Faculty of Health Sciences, University of Cape Town, Observatory, South Africa
e-mail: g.limbert@soton.ac.uk

G. Limbert (ed.), *Skin Biophysics*, Studies in Mechanobiology, Tissue Engineering and Biomaterials 22,
https://doi.org/10.1007/978-3-030-13279-8_2

understand, describe and predict the mechanical behaviour of skin is therefore an important and broad research topic which is relevant to many clinical, scientific and engineering applications. Mathematical and computational modelling is now an integral part of these research endeavours [5–7] and calls for the formulation of constitutive models with various degrees of sophistication [5].

Review articles have discussed various aspects of skin mechanics. Jor et al. [6] reviewed current (as of 2013) and future challenges associated with the modelling and experimental characterisation of skin mechanics. These authors highlighted the need for tight integration of modelling, instrumentation and imaging. They also recommended that focus should be directed toward the development of in vivo quantitative characterisation techniques so that research could be more seamlessly translated into the clinical setting. Recently, Li [8] conducted a short review of modelling approaches for the description of in vitro biomechanical properties of the skin. This researcher concluded that major research efforts should be devoted to the development of constitutive models of skin capable of accounting for viscoelastic effects, damage and fracture. Although Jor et al. [6] and Li [8] reviewed some popular constitutive models of the skin, they did not provide an extensive, detailed and *unified* review of formulations capable of representing the anisotropic behaviour of skin at finite strain and, from elasticity through anelasticity to damage and growth. This was addressed by Limbert [5] who provided a review on some aspects of the mathematical and computational modelling of skin biophysics with special focus on theories based on non-linear continuum mechanics [9–11]. Besides mechanics, other physical aspects were covered such as growth and thermoelasticity. In a recent review paper, Benítez and Montáns [7] covered experimental characterisation techniques and modelling approaches based on continuum mechanics formulations for elasticity, viscoelasticity, preconditioning (i.e. Mullins effect, damage) as well as computational implementation aspects. Although the paper was said to be a review on skin mechanics the treatment was much more general, geared toward soft tissue mechanics, and featured models that had not been applied to skin. Joodaki and Panzer [12] briefly discussed in vivo and in vitro mechanical characterisation tests for skin, its key mechanical and structural aspects such as non-linear behaviour, viscoelasticity, damage, failure and anisotropy. In the last part of this review paper they presented a selection of constitutive models for skin elasticity and viscoelasticity.

The objective of this chapter is to provide an extended, but by no means exhaustive, logically structured review of constitutive models of skin mechanics with special emphasis on state-of-the-art anisotropic formulations which are essential in most modelling applications. In the next section the fundamental structural characteristics of the skin and its mechanical properties will be presented. Then, non-linear isotropic and anisotropic constitutive models of the skin will be reviewed to provide a sound basis for researchers interested in the mathematical and computational modelling of skin mechanics. Further, a brief introduction on image-based modelling principles and selected applications will be provided. Finally, potential future directions for research will be discussed.

2 Fundamental Structural and Material Properties of the Skin

2.1 Skin Structure

In mammals the skin is part of the integumentary system that includes the skin itself as the largest organ of the body, and various appendages such as hair, nails and hooves, nerve receptors and glands. In humans, the skin accounts for up to 16% of an adult's total body weight whilst covering an average surface area of about 1.6 m^2 [13]. The skin is a complex biological system featuring a broad array of coupled physical processes acting in concert, or sequentially, as for instance, in the case of wound healing where a cascade of biochemical and mechanobiological events is triggered by an injury [14]. From the mechanical and material science point of view, the skin is primarily a multiphasic and multiscale structure which, as a result, encompasses a rich set of mechanical properties and constitutive behaviours [15, 16]. The biological nature of this structure renders these properties very dynamic, particularly over the life course, and like most biological tissues, there is a strong variability according to body site, individuals, age, sex, ethnicity and exposure to specific environmental conditions [17, 18]. At the meso-macroscopic level, the skin is generally considered as a multi-layer assembly made up of three main distinct structures: the epidermis, dermis and hypodermis (Fig. 1) [13, 16, 19, 20].

The epidermis—which is avascular—is a terminally differentiated stratified squamous epithelium about 200 μm thick. Ninety-five percent of the cells contained

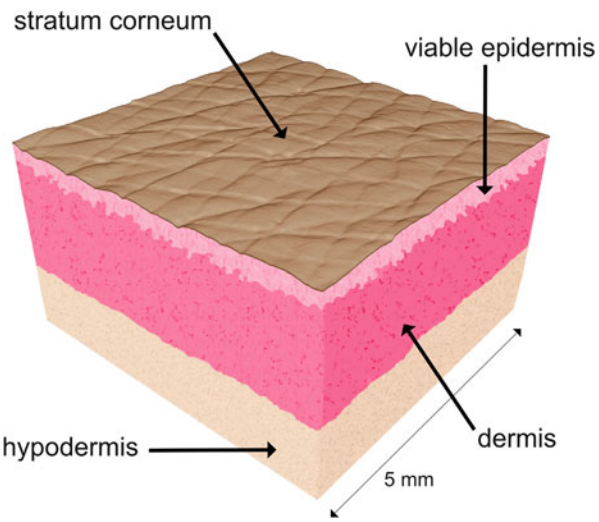

Fig. 1 Schematic representation of the multi-layer nature of the skin featuring the epidermis (constituted of the *stratum corneum* and viable epidermis), dermis and hypodermis. Dimensions are not necessarily up to scale

in the epidermis are keratinocytes which undergo mitosis at the 0.5–1 μm thick epidermal basement membrane (also known as *basal lamina*) [21]. From this basement membrane which separates the epidermis from the dermis, the cells subsequently migrate from towards the skin surface, forming four main well delineated layers during their transit, namely the *stratum basale* (also called the *stratum germinativum*), the *stratum spinosum*, the *stratum granulosum* and *the stratum corneum*. This latter layer consists of a one to three cell-thick layer of dead keratinocytes representing a 15–30 μm thickness. The epidermis includes other cells such as melanocytes, Langerhans's cells and Merkel cells [13]. The complex formed by the living epidermis, at the exclusion of the *stratum corneum*, is called the **living** or **viable epidermis**. The ***stratum corneum*** is the prime line of defence against external threats such as mechanical, thermal, chemical, electromagnetic or biological insult. In particular, the mechanical properties of the *stratum corneum* are key in conditioning transmission of loads and subsequent deformations of the other underlying skin layers across several length scales [22, 23].

These purely mechanical aspects are essential for certain biophysical processes such as the stimulation of mechano-receptors that transduce mechanical energy into neural signalling (e.g. tactile perception [3] and pain [4]) or mechanobiological transduction involved in metabolic processes (e.g. homoeostatic regulation of the skin barrier function [24]).

Any variation in the mechanical properties of the *stratum corneum*—like those occurring daily as a results of fluctuations in internal and external environmental conditions (e.g. relative humidity, temperature) [25]—is likely to affect the material mechanical response and also the subsequent altered external surface topography. This has obvious and important consequences for the tribological response of the skin [23].

The **living epidermis** is connected to the underlying dermis through a three-dimensional (3D) interlocking wavy interface, called the dermal-epidermal junction (DEJ) which is the *basal lamina*. Papillae are the protrusions of the papillary dermis into the epidermis. These finger-like structures increase the contact surface area between the reticular dermis and the living epidermis, and are thus believed to favour biochemical mass exchanges between these layers e.g. transport of oxygen and nutrients [21, 26, 27]. The DEJ controls the transit of biomolecules between the dermis and epidermis according to their dimension and charge. It allows the passage of migrating and invading cells under normal (i.e. melanocytes and Langerhans cells) or pathological (i.e. lymphocytes and tumour cells) conditions [27]. The behaviour of keratinocytes is influenced by the DEJ via modulation of cell polarity, proliferation, migration and differentiation.

As principally constituted of a dense array of stiff collagen fibres with various degrees of crimp, the **dermis** (Fig. 2) is the main load-bearing structural component of the skin when subjected to tension-inducing loads (e.g. in-plane tension, out-of-plane indentation and suction). It is 15–40 times as thick as the epidermis [13] and much thinner on the eyelids than on the back. The dermis can be broken down into three main layers: the papillary layer juxtaposed to the epidermis, the sub-papillary layer underneath and the reticular layer which is connected to the

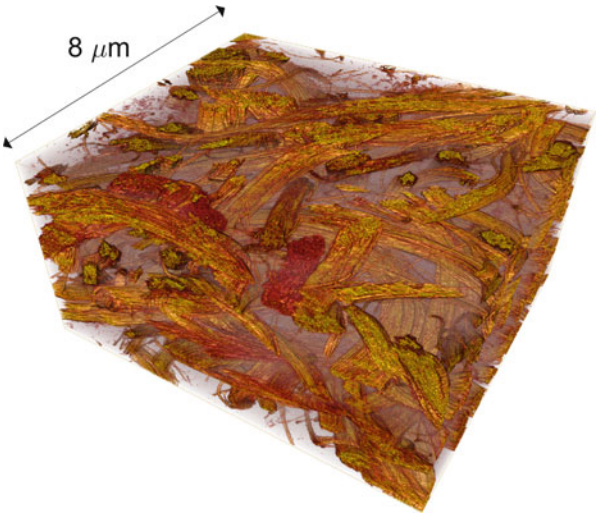

Fig. 2 Volume rendering of the collagen fibre network in human reticular dermis obtained through serial block-face scanning electron microscopy. Ethically-approved fresh abdominal skin extracted during a cosmetic surgery procedure from a 39 years-old female Caucasian patient with no known medical conditions was commercially obtained (TCS Cellworks, Buckingham, UK). Chlorhexidine was used for skin decontamination prior to surgery. The 1.5 cm × 1.5 cm full-thickness skin sample did not feature hair follicle, scars or stretch marks. The skin sample was cut into 1 mm slices and processed for serial block-face imaging using a high contrast fixation protocol (SBEM Protocol v7_01_10, https://ncmir.ucsd.edu/sbem-protocol) and embedded in Spurr resin (Agar Scientific, Stansted, UK). The tissue block was then trimmed appropriately, glued onto a small aluminium pin, sputter coated in gold/palladium and imaged in the serial block-face imaging system 3View® (Gatan, Inc., Pleasanton, CA, USA) mounted inside a Zeiss Sigma VP field emission scanning electron microscope with variable pressure mode (Carl Zeiss Microscopy GmbH, Jena, Germany) and imaged at 2.5 kV. The acquisition was done at a defined sampling XY resolutions of 2500 × 2500 pixels resulting in an 8 nm pixel size. In total there were 376 images with a 50 nm spacing in the Z direction

underlying subcutaneous tissue. The papillary layer is defined by the rete ridges protruding into the epidermis and contains thin collagen fibres, a rich network of blood capillaries, sensory nerve endings and cytoplasms. The sub-papillary layer which is the zone below the epidermis and papillary layer features similar structural and biological components to the papillary layer. Besides a dominant content of types I and III collagen (respectively 80% and 15% of total collagen content), the reticular layer is innervated and vascularised, contains elastic fibres (e.g. elastin) and the dermal matrix made of cells in the interstitial space. Cells present in the reticular dermis include fibroblasts, plasma cells, macrophages and mast cells.

Collagen fibres account for approximately 70% of the weight of dry dermis. Collagen fibres in the papillary and sub-papillary dermis are thin (because of their low aggregate content of fibrils) and sparsely distributed while reticular fibres are thick, organised in bundles and densely distributed. Fibrils are typically

very long, 100–500 nm in diameter featuring a cross striation pattern with a 60–70 nm spatial periodicity. The diameter of thick collagen bundles can span 2–15 μm. Birefringence techniques are considered promising tools to characterise the orientation and supramolecular organisation of collagen bundles in skin [28].

The **dermal matrix** is composed of an extra-cellular matrix, ground substance which is a gel-like amorphous phase mainly constituted of proteoglycans and glycoproteins (e.g. fibronectin) as well as blood and lymph-derived fluids which are involved in the transport of substances crucial to cellular and metabolic activities. Proteoglycans are composed of multiple glycosaminoglycans (i.e. mucopolysaccharides) interlaced with back bone proteins. Dermal fibroblasts produced glycosamine which is rich in hyaluronic acid and therefore plays an essential role in moisture retention.

Unlike collagen fibres, **elastic fibres** are extremely elastic and can fully recover from strains in excess of 100% [29]. Their diameter ranges from 1–3 μm. Their mechanical entanglement with the collagen network of the dermis is what gives the skin its resilience and recoil ability. This is evidenced by the correlation between degradation of elastin/abnormal collagen synthesis associated with ageing and the apparent stiffening of the dermis [30]. The diameter of elastic fibres in the dermis is inversely proportional to their proximity to the papillary layer where they tend to align perpendicular to the DEJ surface.

The **subcutaneous tissue** is the layer between the dermis and the fascia which is a band of connective tissue, primarily collagen, that attaches, stabilises, encloses, and separates muscles and other internal organs. The thickness of subcutaneous tissue is highly variable intra- and inter-individually. This layer is mainly composed of adipocytes. Its role is to provide mechanical cushioning, heat generation and insulation as well as a reserve of nutrients.

An important feature of skin mechanics is that, in vivo, skin is in a state of complex in-plane heterogeneous tension patterns which depend on individuals, their age, body location and position. This was first evidenced by French anatomist and military surgeon Baron Guillaume Dupuytren. In 1834, Dupuytren examined the chest of a man who had stabbed himself with a round-tipped awl in a failed suicide attempt, and noticed that the inflicted wounds were elliptical and not circular [31–33]. Later, in 1838, French surgeon Joseph-François Malgaigne reported that this type of elliptical wound patterns were oriented according to body location. Although these two surgeons had evidenced the existence of tension lines in vivo, it was the Austrian anatomist Karl Langer [31–33] who provided a sound explanation and comprehensive anatomical basis to it. This was achieved by conducting a large number of punctures on cadavers, using a round awl, and meticulously mapping the direction and dimensions of the created elliptical wounds on the body. Because these experiments were conducted on cadavers with extremities in extension, Langer observed that tension lines varied with the position of the cadaver. Real in vivo conditions are also likely to differ from cadaveric conditions because of *rigor mortis* which stiffens muscles and joints. Moreover, tension lines are also dependent upon skin dysfunctions and diseases such as the Elhers-Danlos syndrome which manifests as a hyper-extensibility of soft tissues, and skin in particular. Experimental

characterisation of Langer lines is discussed in more details in chapter "Tension Lines of the Skin".

2.2 Mechanical Properties of the Skin

Following the brief review of the structural properties of the skin, and, as will be discussed in the next section in more details, depending on the length scale considered, the skin can be viewed as a structure or a material (i.e. a homogeneous structure). Here, in this basic review of mechanical properties, we will mainly focus on the latter. Due to its characteristic dimensions and interfacial nature, the skin is often described as a membrane in the general sense. From the mechanical point of view, it would be more accurate to describe it as a multi-layer shell structure because it possesses a non-negligible bending stiffness despite mainly sustaining membrane strains.

Due to its significant thickness compared to that of the *stratum corneum* and viable epidermis, combined with its high content in collagen fibres, the dermis is the main contributor to the tensile mechanical properties of the skin. The intricate fibrous collagen architecture of the dermis and its close mechanical connectivity to elastin fibres lead to anisotropic and non-linear macroscopic mechanical properties which is consistent with the strain stiffening effect typically observed in biological soft tissues under tension [9].

The *measured* mechanical anisotropy of the skin is not only due to the structural characteristics of the skin layers and their microstructural constituents but is also the result of its mechanical interplay with the Langer lines. In-plane anisotropy of the skin is correlated with the distribution and orientation of Langer lines [34] while out-of-plane (or across-the-thickness) anisotropy is due to the distinct mechanical properties and complex 3D structure of the skin layers. This presents a number of challenges for the experimental characterisation of the mechanical properties of skin [6, 35] as well as their mathematical and computational realisation. Intuitively, one would expect that the inclusion or not of pre-stress/pre-strain in a mathematical or computational model of the skin would significantly influence its mechanical response. Flynn et al. [36] determined a relation between the in vivo relaxed skin tension lines (RSTL) on a human face and the directional dependency of the skin stiffness using a combination of contact measurement techniques and inverse finite element methods. These authors demonstrated the need to account for these tension lines in the characterisation of the anisotropic properties of the human skin. Recently, Deroy et al. [37] developed a non-destructive and non-invasive experimental protocol based on elastic surface wave propagation to determine the orientation of skin tension lines. The method was validated on canine cadaveric specimens. The Cutiscan CS 100® (Courage-Khazaka Electronic GmbH, Köln, Germany) is a device offering the possibility of qualitatively measuring mechanical anisotropy of the skin in vivo [38].

A variety of methods have been used to measure the mechanical properties of skin: e.g. uniaxial and biaxial tensile tests [34, 39–41], multiaxial tests [15, 42], application of torsion loads [43], indentation [44], suction [38, 45–50] and bulge testing [51]. More recent techniques have focused on the experimental characterisation of the mechanical properties of the epidermis [52–54] which are particularly relevant for cosmetic and pharmaceutical applications. Beside intra- and inter-individual biological variability as well as sensitivity to environmental conditions, the nature of these experimental techniques combined with their operating spatial scale (e.g. macroscopic or cellular levels) are the main reasons there is a such a wide variability in mechanical properties reported in the literature. Differences for the mechanical properties of the skin or those of its individual layers can span several order of magnitude (see Table 1 in [22]).

Given its complex hierarchical structure, and like most soft tissues, the skin exhibits a wide range of viscoelastic phenomena including creep, relaxation, hysteresis [18, 39, 55, 56] and strain rate dependency [41].

3 Modelling Approaches

The brief review of the structural and macroscopic mechanical properties of the skin in the previous section have highlighted three main characteristics, namely, non-linear behaviour, structural non-homogeneity and mechanical anisotropy. However, many studies only considered the isotropic constitutive behaviour of skin which could be a rational assumption depending on the type of loading conditions. A brief summary of isotropic constitutive models of skin will be provided. Mathematical and computational models of the skin can be classified into three main categories: ***phenomenological***, ***structural*** and ***structurally-based phenomenological*** models.

Phenomenological models are based on the assumption that the skin is a homogeneous material where the microstructure and multiple phases as well their associated mechanical properties are not accounted for explicitly. These phenomenological models aim to capture the overall—generally macroscopic—behaviour of the tissue without accounting for the individual behaviour of its elemental constituents and their mutual interactions [57]. Typically, if one considers mechanical behaviour only, a phenomenological model is a set of mathematical relations that describe the evolution of stress as a function of strain [9]. Provided the formulation is appropriate, it is generally always possible to fit such a constitutive law to a set of experimental data. However, the main drawback of this approach is that the resulting constitutive parameters often do not have a direct physical interpretation, and the model effectively acts as a "black box" without the flexibility of integrating and studying mechanistic structural effects.

Structural models of the skin represent the tissue as a composite material made of an *explicitly* defined assembly of key microstructural elements (e.g. collagen fibres arranged in bundles with a certain degree of crimp and dispersion, within a matrix mainly composed of proteoglycans). The way these structural elements

interact can also be specified by developing appropriate equations (e.g. mutual shear interactions of collagen fibrils and fibres or small-range electromagnetic interactions between proteoglycans and collagen fibres [58]).

In this approach, not only the mechanical properties of the individual basic structures need to be determined or known but also the way they are geometrically arranged to form the macroscopic tissue, and how they interact mechanically, thermally or through any other type of physical phenomenon. The overall mechanical properties of the tissue are the result of this—generally nonlinear—coupling between geometry and mechanics. Structural models can be viewed as geometrical assemblies of phenomenological models. For this reason, one could argue that, strictly speaking, structural models are not fully structural, and that classification as a structural or phenomenological model is a matter of length scale. Only if models are built ab initio from the first principles of quantum chemistry could one talk about structural models. In that respect, the constitutive parameters of phenomenological models describing the behaviour of elemental microstructural components may also not have a direct physical interpretation but, typically, they do. For example, if collagen fibres are part of the formulation, their elastic modulus, waviness and degree of dispersion around a main orientation are indeed constitutive parameters with have a direct physical interpretation and that, often, can be experimentally determined. One of the main drawbacks of structural models lays in the necessity to have accurate information about the geometrical and material characteristics of each elemental building block as well as their mutual spatial and interfacial arrangement. This presents obvious experimental characterisation challenges which, however, are progressively overcome as technologies in this field improve, and new characterisation techniques emerge. Moreover, in a computational finite element environment, structural models spanning several orders of magnitude in terms of length scale require significantly high mesh density to explicitly capture the geometry of the structural constituents. Inevitably, despite tremendous advances in the computing power of modern processors, this can lead to prohibitively computationally expensive analyses and lengthy run times.

A judicious compromise between strictly phenomenological and structural models is a third-class of models, formulated by combining certain characteristics of phenomenological models to those of structural ones. These models could be denoted under the general appellation of ***structurally-based phenomenological models*** or ***structurally-based continuum models***. The continuum composite approach of Spencer [59] is a good example of that philosophy. In this type of constitutive formulation for fibre-reinforced composite materials, fibres are not *explicitly* modelled at the geometric level but their mechanical contribution to the overall (i.e. continuum) behaviour is *implicitly* accounted for by strain energy density terms directly related to microstructural metrics (e.g. stretch along the fibre direction). Nowadays, models adopting this type of constitutive hypotheses dominate the literature as they have been very successful at representing the biomechanics of many biological tissues [10, 11]. The mathematical formulation of these models can be viewed as mutltiscale as it accounts for structural geometrical/mechanical

features/effects arising from a smaller length scale than that at which the gross physical response is represented in a continuum sense.

Multiscale formulations in the homogenisation theory/computational mechanics sense are also possible but require more advanced finite element formulations for practical calculations [60, 61].

3.1 Image-Based Microstructural Models of the Skin: Principles and Applications

Given the hierarchical structure of biological tissues, especially the skin, capturing certain key aspects of their microstructure in computational models opens up the possibility of conducting hypothesis-driven research about the links between their structure and function [9] in a very systematic and mechanistic way. One can isolate and study the influence of certain microstructural and/or material parameters on the global response of the system [22, 23, 62] to formulate hypotheses and theories that can further our fundamental understanding of skin physiology and also assist in the design of physical experiments.

According to the classification of models presented in the previous section, image-based models could be best described as computational (micro)structural models where the constitutive model used for representing the material behaviour of each substructure could be a phenomenological, structural or structurally-based phenomenological model. Image-based modelling has become ubiquitous in many research domains where capturing complex multiphasic structures at various length scales is essential for conducting physics-based numerical analyses [63]. In the context of biological tissues and structures, any type of imaging modalities (1D, 2D, 3D, 4D) can be used, including digital optical photography [22], computed tomography [64], magnetic resonance imaging [65] and laser confocal microscopy [66].

Developing an image-based computational model is the process of acquiring the geometry of a physical system through a single or a combination of imaging modalities, bring it into the digital world under the form of an image or a series of images, conduct image-processing on these files to identify and isolate regions of interest (i.e. segmentation of the distinct skin layers or segmentation of individual microstructural phases within a layer) (Fig. 3) and mesh these digital regions into finite elements so that the partial differential equations governing the physics considered could be solved using the finite element method.

Image-based microstructural finite element models of the skin can provide unique insights into the interplay between material and structural properties of the skin even when considering only two-dimensional geometries. For sake of illustration, and drawn for the author's research portfolio, three applications concerning **the role of the *stratum corneum* on skin mechanics** [22], **deformation-induced skin friction** [23, 62, 67] and **micro-wrinkle formation** [68, 69] are briefly discussed.

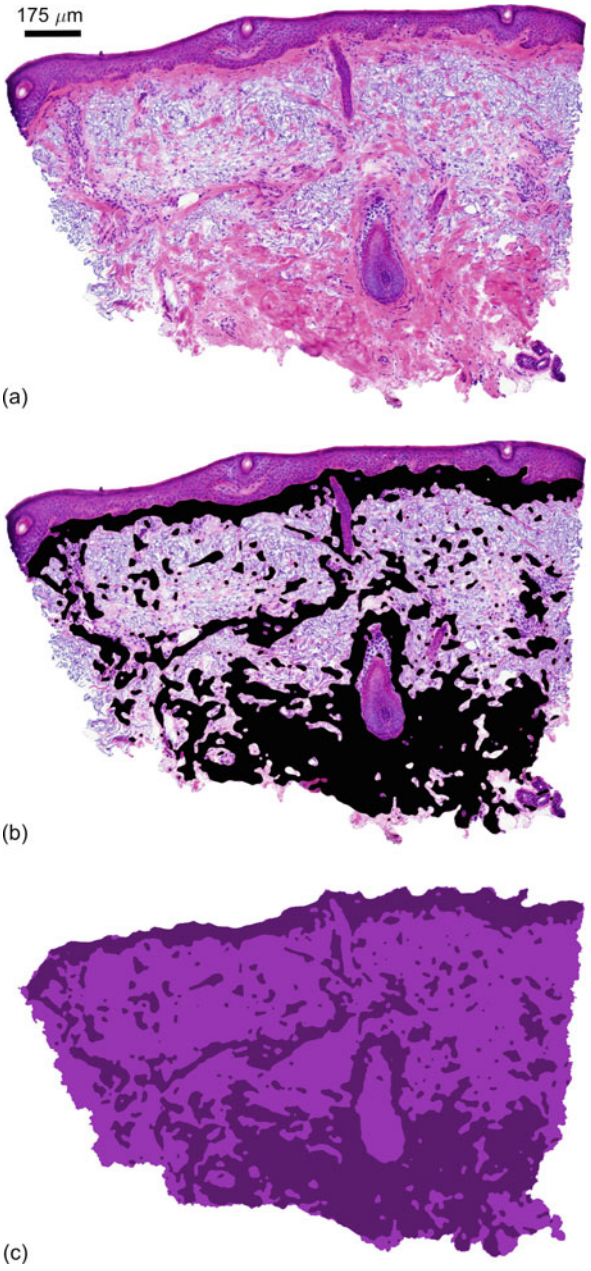

Fig. 3 (**a**) Digital image of a histological section obtained from a human facial skin biopsy (site: forehead) of a 68-year old Caucasian woman (courtesy of Bradley Jarrold, The Procter & Gamble Company, Cincinnati, USA); (**b**) Result of image segmentation of the intact collagen phase within the dermis (coloured in black) overlaid over original digital histological section (**a**); (**c**) Segmented intact collagen and elastotic tissue phases, coloured respectively in dark and light pink

Leyva-Mendivil et al. [22] unveiled and quantified structural folding mechanisms driven by the mechanics of the *stratum corneum* in combination with its intricate surface topography when the skin is subjected to plane-strain compression. It was shown that *macroscopic* strains may significantly be modulated at the *microscopic* (i.e. local) level. The convoluted shape of the *stratum corneum* can effectively acts as a strain reducer.

These authors subsequently used a similar approach to show that the *macroscopic* coefficient of friction between the skin and a rigid slider moving across its surface is noticeably higher that the *local* coefficient of friction applied as an input parameter to the finite element analyses [67]. This demonstrated that the deformation-induced component of skin friction could be significant, unlike what has been widely assumed in the tribology community [70–74] where adhesion-induced friction is deemed to be the dominant contributor to macroscopic friction. Similar observations were made in a similar computational contact homogenisation study by Stupkiewicz et al. [75]: geometrical effects alone can have a significant impact on the macroscopic frictional response of elastic contacts. To date, despite much experimental and modelling studies investigating shear stress at the surface of the skin in relation to skin injuries and pressure ulcers [52, 54, 76], very little efforts have been made to develop methodologies to gain a more accurate and mechanistic understanding of how shear stresses are induced at the level of skin microrelief asperities and how they propagate from the skin surface to the deeper layers where they are likely to mechanically stress living cells. Ultimately, excessive stress or strain can lead to cell damage and death, which, at a meso/macroscopic level translates into tissue damage and loss of structural integrity. A more recent study was conducted by Leyva-Mendivil et al. [62] to investigate these aspects and, again, demonstrated the importance of accounting for skin microstructure in this type of study. Building upon this computational modelling approach Leyva-Mendivil et al. [67] recently investigated the role of contact pressure on skin friction. Results confirmed the potentially major role of finite deformations of skin asperities on the resulting macroscopic friction. This effect was shown to be modulated by the level of contact pressure and relative size of skin surface asperities compared to those of a rigid slider. The numerical study also corroborated experimental observations by Adams et al. [71] concerning the existence of two contact pressure regimes where macroscopic friction steeply and non-linearly increases up to a critical value, and then remains approximately constant as pressure increases further.

Understanding the biophysics of skin wrinkling is of critical importance in cosmetics, dermatology, surgery and for a wide range of industrial applications (e.g. consumer goods). Throughout the past decade, bi-layered model systems [77] have evolved as a valuable tool to study the mechanisms of skin wrinkling in idealised two-dimensional geometries. However, these idealised systems can only generate regular wrinkling patterns and fail to accurately predict the surface topology of real human skin (Fig. 4).

In their image-based finite element study, Limbert and Kuhl [68] reconstructed the microrelief of a 0.25 cm^2 skin patch of a healthy human 40-year old male subject using laser scanning profilometry to characterise the impact of initial surface

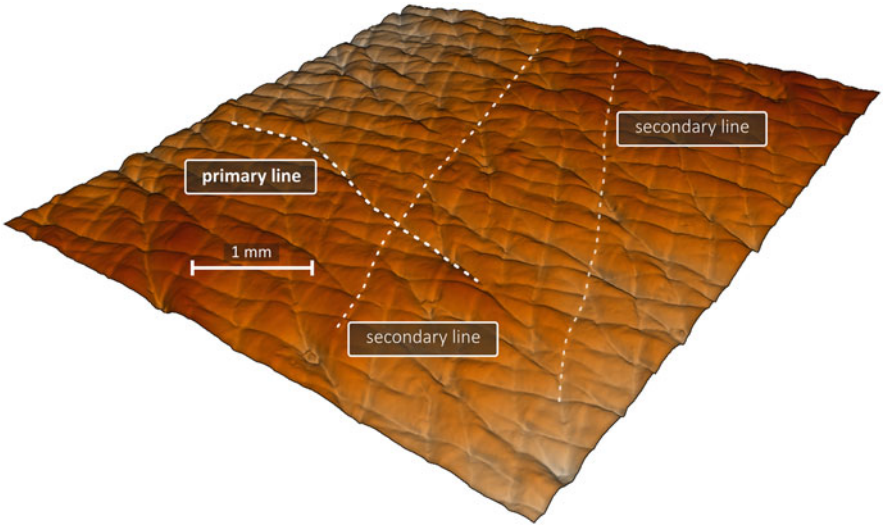

Fig. 4 Synthetic image representing the typical microrelief of human skin surface (ridges and furrows) in its undeformed configuration, reconstructed from laser scanning profilometry of a silicone replica of a human volar forearm skin patch (5 mm × 5 mm). Some of the primary and secondary lines are delineated by rectangles overlaid over the skin surface. The profilometric acquisition features a 400 × 400 grid of points that was fitted to a NURBS surface (adapted from Limbert and Kuhl [68])

imperfections on pattern formation upon compression-induced wrinkling. The skin patch was modelled as a bi-layered system with a 20 μm thick *stratum corneum* layer on top of a 2.6 mm thick skin substrate.

In a systematic sensitivity analysis, the authors studied the effects of a fully three-dimensional microrelief geometry on wrinkling pattern formation for different stiffness ratios between layer and substrate where realistic variations of stiffness ratio were taken as surrogate measures of hydration level of the *stratum corneum* [25]. For moderate stiffness ratios up to 20, and for the particular surface considered, external compression simply magnified the underlying microrelief pattern. For stiffness ratios larger than 100, external compression induced a well-defined periodic wrinkling pattern at wavelengths that agree well with analytical predictions. While analytical models and computational simulations of idealised model systems provide valuable insight into the wrinkling pattern of regular structures at high stiffness contrasts, they cannot predict surface topologies of realistic skin surfaces with irregular microstructures. Especially for human skin with an inherently irregular surface topology, realistic three-dimensional modelling can become critically important since surface instabilities are highly sensitive to initial imperfections [78]. This sensitivity analysis with varying *stratum corneum* stiffnesses unravelled important implications in understanding the effects of drying or ageing on altered surface pattern formation (Fig. 5).

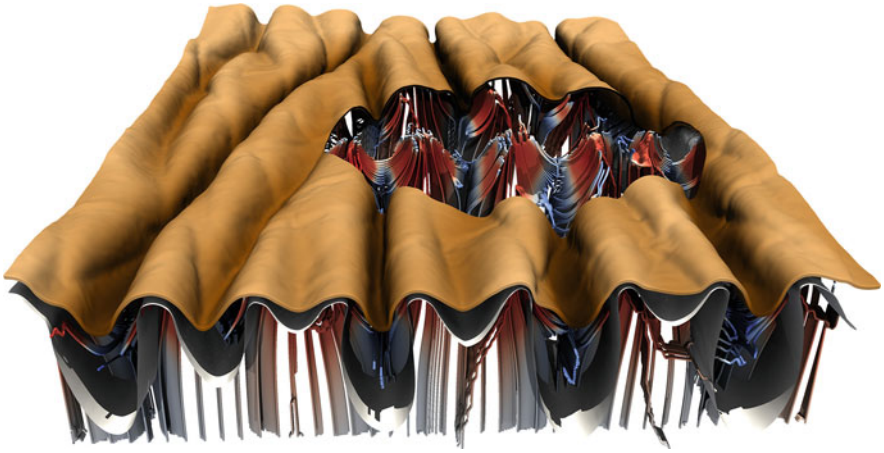

Fig. 5 Finite element model of a bi-layer model of human skin upon application of a 25% uniaxial compressive deformation (new original plot adapted from Limbert and Kuhl [68]). The top light-brown thin layer is the *stratum corneum* while the coloured streamlines represent the path of minimum (i.e. compressive) principal strain within the (transparent) substrate (i.e. living epidermis + dermis) and the white undulated surface is an iso-surface of 20% compressive Green-Lagrange strain within the substrate

4 Constitutive Models of the Skin

In this section, we present what are considered state-of-the-art mechanical constitutive models of the skin. The focus is on non-linear elasticity and viscoelasticity theories. For sake of completeness, isotropic elastic models of the skin found in the literature are also covered. Anelastic phenomena such as plasticitys [79], softening and damage [80] are presented. Other types of constitutive laws such as mechanobiological models for growth [81] and chemo-mechanobiological models of wound healing [14, 82–84] are covered respectively in chapters "Constitutive Modelling of Skin Growth" and "Constitutive Modelling of Skin Wound Healing". To enable a sound theoretical basis to formulate constitutive model a brief review of hyperelasticity theory is provided below.

4.1 Basic Continuum Mechanics for Isotropic and Anisotropic Hyperelastic Solids

Non-linear continuum mechanics provides a flexible mathematical framework to model a wide range of constitutive behaviours [85, 86] from non-linear elasticity and finite strain plasticity to thermoelasticity and biological growth. Accounting for finite deformations is essential for many applications in skin mechanics, and it is therefore sensible to develop constitutive equations a priori valid for finite kinematics. To this end, in this section, essential definitions of kinematic and kinetic

quantities are provided, and, without loss of generality, particularised for Cartesian coordinate systems. Because of the popularity of their use in the constitutive modelling of biological tissues [10], particularly those featuring anisotropic mechanical properties, tensor invariants and structural tensors are also introduced. Invariant formulations typically postulate the existence of a strain energy function depending on a set of tensorial invariants of a given deformation or strain measure [86–89]. Introducing a dependency of the strain energy to tensor agencies characterising local microstructural features (e.g. local collagen fibre bundle orientation) is a very efficient way to incorporate microstructural information within a macroscopic continuum constitutive formulation. This class of material models corresponds to that of the microstructurally-based models defined in the previous section. In order to ensure a direct physical interpretation of constitutive parameters it is judicious to select a set of tensor invariants that characterise particular deformation modes the tissue is known to be subjected to and that can also be physically measured [90, 91]. For collagenous tissues, a standard assumption is to consider the tissue as a *continuum* composite material made of one or several families of (oriented) collagen fibres embedded in a highly compliant isotropic solid matrix composed mainly of proteoglycans. A preferred fibre alignment is defined by the introduction of a so-called *structural* or *structure tensor* which appears as an argument of the strain energy function [87, 89]. These notions are detailed in the next sections.

4.1.1 Kinematics of a Continuum and Deformation Invariants

A key basic kinematic entity in continuum mechanics is represented by the gradient of the deformation φ, $\mathbf{F}$, defined as $\mathbf{F}(\mathbf{X}) := \partial\varphi(\mathbf{X})/\partial\mathbf{X} = \partial\varphi_i/\partial X_I \mathbf{e_i} \otimes \mathbf{E_I}$. The Einstein summation convention for indices is used throughout. $\mathbf{X}$ is the position of a material point in the *Lagrangian*—or *reference*—configuration while $\mathbf{x} = \varphi(\mathbf{X})$ is its material placement in the *Eulerian*—or *current*—configuration. $\{\mathbf{E}_I\}_{I=1,2,3}$ and $\{\mathbf{e}_i\}_{i=1,2,3}$ are fixed orthonormal bases in the *Lagrangian* and *Eulerian* configurations respectively. ".", ":", $\otimes$ and "T" respectively denote the scalar product of second-order tensors, double-contraction tensor product, tensor outer product and transpose operators. $\mathbf{F}$ maps infinitesimal line vectors from the material to spatial configuration while cofactor$(\mathbf{F}) = J\,\mathbf{F}^{-\mathrm{T}}$ and $J =$ determinant$(\mathbf{F})$ respectively maps oriented infinitesimal surface and volume. The right (material) and left (spatial) Cauchy-Green deformation tensors are respectively defined as $\mathbf{C} = \mathbf{F}^{\mathrm{T}}.\mathbf{F}$ and $\mathbf{b} = \mathbf{F}.\mathbf{F}^{\mathrm{T}}$. Because these two tensors only contain information about change of length, and therefore exclude local material rotations, they are appropriate to define valid constitutive equations that satisfy the Principle of Material Frame Indifference [86]. The Green-Lagrange strain tensor is defined from the deformation tensor $\mathbf{C}$ as $\mathbf{E} = (\mathbf{C} - \mathbf{I})/2$ where $\mathbf{I}$ is the second-order identity tensor. The classical three principal invariants of $\mathbf{C}$ which define the isotropic (or non-directional) response of a given material are defined as follows [85]:

$$I_1 = \text{trace}\,(\mathbf{C}) = \mathbf{C} : \mathbf{I}; \quad I_2 = \frac{1}{2}\left[I_1 - \mathbf{C}^2 : \mathbf{I}\right]; \quad I_3 = \text{determinant}\,(\mathbf{C}) \qquad (1)$$

To characterise a general orthotropic symmetry one can introduce three unit vectors $\boldsymbol{n}_0^i$ associated respectively with the principal material directions i in the reference configuration. Because these material directions are *signed* directional properties one introduces the concept of structural tensors $\mathfrak{B}_0^i$ [86–89] which are even functions of these unit vectors: $\mathfrak{B}_0^i = \boldsymbol{n}_0^i \otimes \boldsymbol{n}_0^i \{i = 1, 2, 3\}$ (no summation on i). The spatial counterparts of these structural tensors are defined as: $\mathfrak{B}_t^i = 1/\lambda_i^2 \ \mathbf{F}.\mathfrak{B}_0^i.\mathbf{F}^{\mathrm{T}} = 1/\lambda_i^2 \ \mathbf{F}.\left(\boldsymbol{n}_0^i \otimes \boldsymbol{n}_0^i\right).\mathbf{F}^{\mathrm{T}} = \boldsymbol{n}_t^i \otimes \boldsymbol{n}_t^i \ \{i = 1, 2, 3\}$ (no summation on i) where $\boldsymbol{n}_t^i \ \{i = 1, 2, 3\}$ are the unit vectors in the spatial configuration and $\lambda_i \ \{i = 1, 2, 3\}$ are the stretches along these directions.

For material *isotropy* all material directions are equivalent so that:

$$\mathfrak{B}_0^1 = \mathfrak{B}_0^2 = \mathfrak{B}_0^3 = \boldsymbol{n}_0^1 \otimes \boldsymbol{n}_0^1 = \boldsymbol{n}_0^2 \otimes \boldsymbol{n}_0^2 = \boldsymbol{n}_0^3 \otimes \boldsymbol{n}_0^3 = \mathbf{I} \otimes \mathbf{I} \tag{2}$$

For *transverse isotropy*, if the preferred material direction is given by $\boldsymbol{n}_0^3$:

$$\mathfrak{B}_0^3 = \boldsymbol{n}_0^3 \otimes \boldsymbol{n}_0^3, \ \mathfrak{B}_0^1 = \mathfrak{B}_0^2 = \frac{1}{2}\left(\mathbf{I} - \mathfrak{B}_0^3\right) \tag{3}$$

For *orthotropic symmetry* the preferred material directions are orthogonal to each other.

In the context of soft tissue mechanics, depending on the spatial scale of investigation, a single unit vector $\boldsymbol{n}_0^i$ can represent the local orientation of a single collagen microfibril or fibril, that of a single fibre bundle or that of a family of fibres. This gives rise to a *transverse isotropy* symmetry if one assumes that these fibres are embedded in an isotropic matrix. Two additional tensorial invariants characteristic of transverse isotropy symmetry can be defined [86, 87, 89]:

$$I_4^i = \mathbf{C} : \mathfrak{B}_0^i = \lambda_i^2, \quad I_5^i = \mathbf{C}^2 : \mathfrak{B}_0^i \tag{4}$$

I_4^i is a very convenient invariant with a direct physical interpretation as it is the square of the stretch along the corresponding fibre direction.

4.1.2 Constitutive Equations for Invariant-Based Hyperelasticity

As a general procedure to formulate constitutive equations for hyperelastic materials, one can postulate the existence of a strain energy density ψ, *isotropic* function of its deformation or strain invariant arguments. Stress and elasticity tensors are obtained by respectively first and second order differentiation [86]. Hyperelastic formulations can serve as a basis for inelastic formulations such as finite strain plasticity, finite strain viscoelasticity and growth, or any combination of these constitutive behaviours. The Lagrangian second Piola-Kirchhoff stress tensor, S, is readily obtained by differentiation of the strain energy density function with respect to the right Cauchy-Green deformation tensor whilst

applying the chain rule of differentiation for the n deformation invariants I_i: $\mathbf{S} = 2\,(\partial\psi/\partial I_i)\,(\partial I_i/\partial \mathbf{C})\ \ \{i = 1\ \ldots\ n\}$.

The (spatial) Cauchy stress tensor, often referred as *true* stress tensor, is obtained by push-forward operation of the second Piola-Kirchhoff stress tensor $\mathbf{S}$ from the reference to the current configuration [86]:

$$\boldsymbol{\sigma} = \frac{1}{J}\,(\varphi_*\,\mathbf{S}) = \frac{1}{J}\mathbf{F}.\mathbf{S}.\mathbf{F}^{\mathrm{T}} = \frac{2}{J}\mathbf{F}.\left(\frac{\partial\psi}{\partial\mathbf{C}}\right).\mathbf{F}^{\mathrm{T}} = \frac{2}{J}\sum_{i=1}^{n\ \text{invariants}}\left(\frac{\partial\psi}{\partial I_i}\mathbf{F}.\frac{\partial I_i}{\partial\mathbf{C}}.\mathbf{F}^{\mathrm{T}}\right) \tag{5}$$

while, the (volume ratio)-weighted Cauchy stress is the Kirchhoff stress tensor:

$$\boldsymbol{\tau} = J\boldsymbol{\sigma} = 2\frac{\partial\psi}{\partial\mathbf{b}}.\mathbf{b} = 2\sum_{i=1}^{n\ \text{invariants}}\left(\frac{\partial\psi}{\partial I_i}\frac{\partial I_i}{\partial\mathbf{b}}\right).\mathbf{b} \tag{6}$$

Remarks about the associated material and spatial elasticity tensors in the context of finite element procedures are provided in the **Supplementary Material** of the review paper by Limbert [5]. The particular form of the tangent stiffness required for the implementation of constitutive models in the commercial software package Abaqus/Standard (Simulia, Dassault Systèmes, Johnston, RI, USA) is also derived. Additional information about tangent stiffness is also provided by Benítez and Montáns [7].

4.1.3 A Note on the Modelling of Fibre Dispersion

It is clear that the complex microarchitecture of the collagen network in skin cannot be accurately captured by the rather strong assumption of *uniform* fibre alignment, even at a local level. A better assumption, more in line with physical observations, is to assume that, at a local level, fibres are distributed around a main orientation, $\boldsymbol{n}_0$ with a certain probability to lay within a particular range of angular deviation from that main direction. This is embodied by the notion of *fibre dispersion* which can be accounted for by means of two main modelling approaches [92]. The first one, termed the "***angular integration approach***" is due to Lanir [93] while the second approach, known as the "***generalised structure tensor***" approach is due to Gasser et al. [94].

In the **angular integration approach**, also known as the *microsphere* approach, the strain energy function of a single fibre, $\psi_{fibre}(\lambda)$, is considered a function of the fibre stretch λ. This strain energy is then integrated over the unit sphere $\mathbb{U}^2$ to represent the strain energy of a bundle of these fibres per unit reference volume, ψ_{bundle}. This could effectively be viewed as an homogenisation procedure where mesoscopic (or macroscopic) quantities are obtained by integration of fibre level

microscopic quantities (e.g. strain energy of a single fibre $\psi_{fibre}(\lambda)$). It follows that:

$$\psi_{_{bundle}} = n \int_{\mathbb{U}^2} \rho^{\boldsymbol{n}_0}(\boldsymbol{v}_0)\, \psi_{_{fibre}}(\lambda)\, dA \tag{7}$$

where dA is the elemental unit sphere surface area, n is the number of fibres per unit reference volume, $\boldsymbol{v}_0$ is a unit vector bearing the direction of an arbitrary fibre, defined with respect to $\boldsymbol{n}_0$, a unit vector representing a mean direction around which fibre dispersion occurs, and $\rho^{\boldsymbol{n}_0}$ is the relative angular distribution of fibres around the mean direction which must satisfy the following normalisation condition [92]:

$$\frac{1}{4\pi} \int_{\mathbb{U}^2} \rho^{\boldsymbol{n}_0}(\boldsymbol{v}_0) dA = 1 \tag{8}$$

The homogenised second Piola-Kirchhoff stress tensor associated with a fibre bundle can then simply be defined as:

$$\mathbf{S}_{_{bundle}} = 2 \frac{\partial \psi_{_{bundle}}}{\partial \mathbf{C}} = 2\, n \int_{\mathbb{U}^2} \rho^{\boldsymbol{n}_0}(\boldsymbol{v}_0) \frac{\partial \psi_{_{fibre}}(\lambda)}{\partial \mathbf{C}} dA \tag{9}$$

Similarly, the associated Lagrangian elasticity tensor is:

$$\mathbb{C}^{\mathbf{E}}_{_{bundle}} = 2 \frac{\partial \mathbf{S}_{_{bundle}}}{\partial \mathbf{C}} = 4\, n \int_{\mathbb{U}^2} \rho^{\boldsymbol{n}_0}(\boldsymbol{v}_0) \frac{\partial^2 \psi_{_{fibre}}(\lambda)}{\partial \mathbf{C} \otimes \partial \mathbf{C}} dA \tag{10}$$

As pointed out by Holzapfel and Ogden [92], in Eq. (7), it is assumed that the elastic properties of all fibres are defined by the same strain energy function ψ_{fibre}. This is was not the case in Lanir's study [93] where a probability distribution characterising the degree of fibre crimp, and therefore, the degree of mechanical activation, was considered, effectively leading to a modulation of ψ_{fibre} for each fibre.

In the **generalised structure tensor approach**, introduced by Gasser et al. [94], the idea is to use a homogenised structure tensor $\mathbf{H}$ which is obtained by integration of the structure tensor $\boldsymbol{v}_0 \otimes \boldsymbol{v}_0$ associated with an arbitrary fibre of direction $\boldsymbol{v}_0$, deviating from the mean fibre direction $\boldsymbol{n}_0$, over the unit sphere. This effectively amounts to defining a statistical strain-like invariant ($\mathbf{C} : \mathbf{H} - 1$) (see Sect. 4.3.4). In that case, the strain energy of a bundle of fibres per unit reference volume ψ_{bundle} is defined as:

$$\psi_{bundle} = \psi_{bundle}\,(\mathbf{C}, \mathbf{H}) \tag{11}$$

where:

$$\mathbf{H} = \frac{1}{4\pi} \int_{\mathbb{U}^2} \rho^{\boldsymbol{n}_0}(\boldsymbol{v}_0)\, \boldsymbol{v}_0 \otimes \boldsymbol{v}_0\, dA \tag{12}$$

with satisfaction of the normalisation condition (8) leading to $\mathbf{H} : \mathbf{I} = 1$.

Holzapfel and Ogden [92] recently discussed important theoretical aspects of the angular integration and generalised structure tensor approaches for fibre dispersion. They demonstrated the equivalence of these two formulations in terms of predictive power and therefore, implicitly recommend the latter approach because it has been proven very effective in describing experimental data for a broad range of biological fibrous tissues, is conceptually simple, much simpler to implement in a numerical context, and also, much less demanding with regards to computational cost. Moreover, and of particular significance, these authors developed a formulation based on the generalised structure tensor approach which exclude *compressed* fibres within a dispersion group. By so doing, they proved that it is indeed possible, unlike what has previously been claimed in the literature. More recent work on models that exclude compressed fibres is due to Li et al. [95, 96] who also defined a novel tensor invariant that excludes them a priori [96].

In his seminal paper, Lanir [93] developed a microstructurally-based plane stress model of skin in which he introduced a planar fibre angular density distribution $\mathcal{R}_k(\theta)$ where $\mathcal{R}_k(\theta)\, d\theta$ is the fraction of all fibres of type k (collagen or elastin) oriented between θ and $(\theta + d\theta)$ in the reference configuration. In that case, θ represents the deviation from the mean fibre orientation $\boldsymbol{n}_0$. Lanir selected a circular normal distribution, also known as von Mises type distribution:

$$\mathcal{R}\left(\theta, \mu, \kappa\right) = \frac{\exp\left(\kappa \ \left[\cos\left(\theta\right) - \mu\right]\right)}{2\pi\, I_0\left(\kappa\right)} \tag{13}$$

where $I_0(\kappa)$ is the modified Bessel function of order 0. Naturally, other forms of angular distribution functions are possible [94, 97, 98]. Fibre dispersion over the unit sphere is described by a spatial density function $\rho(\theta, \varphi)$ where θ and φ represent the Eulerian angles describing the direction of any material vector $\boldsymbol{v}_0$ [94] so that one can write $\rho(\theta, \varphi) = \rho(\boldsymbol{v}_0) = \rho[\boldsymbol{v}_0(\theta, \varphi)]$:

$$\boldsymbol{v}_0\left(\theta, \varphi\right) = \left(\sin\theta\cos\varphi\right)\ \mathbf{e}_x + \left(\sin\theta\sin\varphi\right)\ \mathbf{e}_y + \left(\cos\theta\right)\ \mathbf{e}_z \tag{14}$$

$dA = \ \sin\theta\, d\theta\, d\varphi$ represents the infinitesimal surface area of the unit sphere defined by the angular range $[(\theta, \theta + d\theta), (\varphi, \varphi + d\varphi)]$. Without loss of generality, if one assumes that any vector $\boldsymbol{v}_0(\theta, \varphi)$ is aligned with the base vector $\mathbf{e}_z$, rotational symmetry around $\mathbf{e}_z$ is obtained and the fibre density distribution becomes independent of φ so that $\rho = \rho(\theta) = \rho[\boldsymbol{v}_0(\theta)]$. The normalisation condition is then reduced to:

$$\int_0^{\pi} \rho\left[\boldsymbol{v}_0\left(\theta\right)\right]\ dA = 2 \tag{15}$$

The dispersion of collagen fibres around a preferred mean direction (transverse isotropy) can be accounted for by the use of a modified version of the standard π-periodic von Mises distribution function with dispersion parameter b

[97, 99]:

$$\rho\left(\theta\right) = 4\sqrt{\frac{b}{2\pi}}\frac{\exp\left(b\ \left[\cos\left(2\theta\right)+1\right]\right)}{\operatorname{erfi}\left(\sqrt{2b}\right)} \tag{16}$$

where erfi is the imaginary error function defined as:

$$\operatorname{erfi}(x) = -i\frac{2}{\sqrt{\pi}}\int_0^{i\,x} \mathrm{e}^{-t^2}dt \tag{17}$$

Ogden [100] showed that the dispersion parameter κ of the structure tensor approach of Gasser et al. [94] can be expressed as:

$$\kappa = \frac{1}{2} + \frac{1}{8b} - \frac{1}{4}\sqrt{\frac{2}{\pi b}}\frac{\exp(2b)}{\operatorname{erfi}\left(\sqrt{2b}\right)} \tag{18}$$

Instead of using a MacLaurin series expansion to approximate the imaginary error function (which is often not standard in low-level programming languages), Limbert [5] proposed an original formulation based on a global Padé decomposition established by Winitzki [101]. This approximation offers the simultaneous advantages of low computing requirement and high accuracy.

More details about the formula can be found in the **Supplementary Material** in Limbert [5]. For completeness, a very accurate four-term Padé approximant of the imaginary error functionerfi, $\operatorname{erfi}_4^{\text{Padé}}$ is provided below:

$$\operatorname{erfi}_4^{\text{Padé}}(x) = \frac{\mathrm{e}^{x^2}}{\sqrt{\pi}}\frac{f(x)}{g(x)} \tag{19}$$

$$f(x) = x\left(\frac{654729075}{512} + \frac{126351225x^2}{256} + \frac{4999995x^4}{32} + \frac{637065x^6}{16} + \frac{134805x^8}{16} + \frac{12255x^{10}}{8} + \frac{495x^{12}}{2} + 37x^{14} + \frac{11x^{16}}{2} + x^{18}\right) \tag{20}$$

$$g(x) = \frac{654729075}{1024} + \frac{172297125x^2}{256} + \frac{91216125x^4}{256} + \frac{2027025x^6}{16} + \frac{1091475x^8}{32} + \frac{59535x^{10}}{8} + \frac{11025x^{12}}{8} + 225x^{14} + \frac{135x^{16}}{4} + 5x^{18} + x^{20} \tag{21}$$

4.2 Non-linear Isotropic Models of the Skin

In this section, a selection of some of the most popular non-linear isotropic elastic models of skin are presented. They are all based on the definition of strain energy functions and valid for finite kinematics, unlike Hookean elasticity despite its wide spread use in the literature, particularly in earlier studies.

4.2.1 Veronda-Westmann's Model

To identify the highly non-linear behaviour of cat's skin in tension, Veronda and Westmann [57] formulated the following strain energy function:

$$\psi = c_1 \{\exp [c_2 (I_1 - 3)] - 1\} - \frac{c_1 c_2}{2} (I_2 - 3) + f (I_3) \tag{22}$$

where c_1 is a shear-like modulus, c_2 is a dimensionless parameter that scales the response connected to the second invariant while $f(I_3)$ is a bulk energy associated with volumetric deformations and that characterises the degree of compressibility of the material.

4.2.2 Models Based on Mooney-Rivlin's/Neo-Hookean Formulation

This model, widely used for rubber mechanics [102], is based on the following strain energy function:

$$\psi = c_1 (I_1 - 3) - c_2 (I_2 - 3) + f (I_3) \tag{23}$$

where c_1 and c_2 are a shear-like moduli. If $c_2 = 0$, the strain energy degenerates to that of a neo-Hookean material with ground state shear modulus $\mu = c_1/2$. Experimental results of uniaxial tensile testing on human abdominal skin by Jansen and Rottier [103] were used by Shergold and Fleck [104] to identify Mooney-Rivlin parameters. They found that the response resulted in $c_2 \simeq 0$ which meant that the identified model was effectively neo-Hookean. Another study using a neo-Hookean strain energy potential was conducted by Delalleau et al. [105]. More recent research used neo-Hookean elasticity to model the mechanical response of individual skin layers can be found [22, 23, 62, 67, 68].

4.2.3 Models Based on Polynomial Strain Energy

This type of strain energy function can be viewed as a generalisation of Mooney-Rivlin's model and is defined as:

$$\psi = \sum_{i+j=1}^{N} c_{ij} (I_1 - 3)^i (I_2 - 3)^j + f (I_3) \tag{24}$$

where c_{ij} are shear-like moduli. If $j = 0$ the strain energy function degenerates to that of a Yeoh's material defined as:

$$\psi = \sum_{i=1}^{N} c_i (I_1 - 3)^i + f (I_3) \tag{25}$$

where c_i are shear-like moduli.

Hendriks et al. [47] used an inverse characterisation technique based on finite element simulations and in vivo suction experiments to identify the constitutive parameters of a two-term polynomial strain energy defined as:

$$\psi = c_{10}\,(I_1 - 3) + c_{11}\,(I_1 - 3)\,(I_2 - 3) + f\,(I_3) \tag{26}$$

Lapeer et al. [106] identified constitutive parameters of the general polynomial formulation and those of its reduced form (i.e. Yeoh's model) from tensile tests on human female abdominal skin.

Models based on polynomial strain energies (Eq. 24) can suffer from material stability issues depending on the choice of constitutive parameters, and, in the author's opinion, should be avoided.

This does not apply to the Yeoh's formulation [107] which is unconditionally stable provided its constitutive parameters are all positive. This result was also empirically determined by Lapeer et al. [106].

4.2.4 Models Based on Ogden's Formulation

This constitutive model was originally developed to represent the mechanical behaviour of elastomers [108, 109]. It is based on the definition of a strain energy function defined in terms of the principal stretches (i.e. the eigenvalues of the deformation gradient $\mathbf{F}$, $\lambda_i \;\; \{i = 1, 2, 3\}$, in a three-dimensional setting):

$$\psi = \sum_{i=1}^{n} 2\frac{\mu_i}{\alpha_i^2}\left(\lambda_1^{\alpha_i} + \lambda_2^{\alpha_i} + \lambda_3^{\alpha_i} - 3\right) \tag{27}$$

where μ_i are shear-like moduli, α_i are adimensional parameters that control the shape of the stress-strain curve and n is the order of the series. This model offers great flexibility for describing the typical strain hardening behaviour of biological tissues but this flexibility might be paid off by unwanted "over-fitting" in the presence of experimental noise.

For $n = 1$ and $\alpha_1 = 1$ the Ogden strain energy becomes that of a neo-Hookean material while the incompressible Mooney-Rivlin model is recovered for $n = 2$, $\alpha_1 = 2$, $\alpha_2 = \; - 2$ and $\lambda_1\lambda_2\lambda_3 = 1$. Shergold and Fleck [110] used a one-term Ogden's strain energy function to model the mechanical behaviour of skin in the context of deep penetration. In a subsequent study [104] these authors identified an Ogden hyperelastic formulation with experimental data on pig skin obtained for different strain rates. They concluded that the parameter $\alpha = \alpha_1$ was mostly independent of the strain rate and that this was due to the fact that α is conditioned by the evolution of the collagen meshwork in skin which makes it independent of strain rate. A similar observation was made by Lim et al. [111] for pig skin. Evans and Holt [112] conducted in vivo testing of human skin using digital image

correlation and successfully fitted their data to a one-term Ogden model for in-plane deformations. Flynn et al. [113] used a one- and two-term Ogden strain energy to model skin under rich deformations (i.e. in- and out-of-plane deformations) applied and controlled by a force-sensitive micro-robotic device. They used an inverse technique based on finite element simulations to determine constitutive parameters including the values of pre-stress (also converted to residual strains) associated with Langer lines. The underlying assumption for using an isotropic constitutive model was to consider that anisotropy was a by-product of the existence of Langer lines. Measurements were conducted on anterior forearm and posterior upper arm of human volunteers. A similar study was later performed by these authors [114] to characterise the in vivo mechanical behaviour of facial skin under rich sets of deformation.

4.2.5 Models Based on Arruda-Boyce's Formulation

Chain network models such as the Arruda-Boyce eight-chain model originates from concepts borrowed from statistical mechanics, namely, entropic elasticity of macromolecules [115]. In this theory, long molecular chains are assumed to rearrange their conformation under the influence of random thermal fluctuations so that their possible geometrical configurations can only be known in a statistical sense. Polymer chains in rubber are typically described as *uncorrelated* [116] as their conformation is reminiscent of a random walk. The term *freely jointed* chains is also used. In contrast, biopolymer chains such as collagen assemblies feature smoothly varying curvature and are therefore considered *correlated*. These chains are best described using the concept of worm-like chains of Kratky and Porod [117]. In the context of soft tissue mechanics, several authors used this approach to describe the structure and mechanics of the basic building block of collagen assemblies, the tropocollagen molecule, the so-called collagen triple-helix [116, 118–123]. Both freely-jointed and worm-like entropic chains are assumed to be made of beads connected by N rigid links of equal length d, the so-called Kuhn length [124], so that the maximum length of a chain, the contour length, is $L = Nd$. The mechanics of macromolecular polymer structures is not only governed by the mechanical properties of individual chains but also by their electromagnetic and mechanical interactions which can take the form of covalent bonds, entanglement and physical cross-links. These combined effects give rise to strong network properties which can be implicitly captured by network models such as the eight-chain model of Arruda and Boyce [125]. The central idea behind these formulations is that there exists a representative nano-/microscopic unit cell able to capture network properties. The eight-chain model assumes that the unit cell is made of eight entropic chains of equal lengths connected from the centre of the cell to each of its corners (Fig. 6), each equipped with their own strain energy ψ_{chain}.

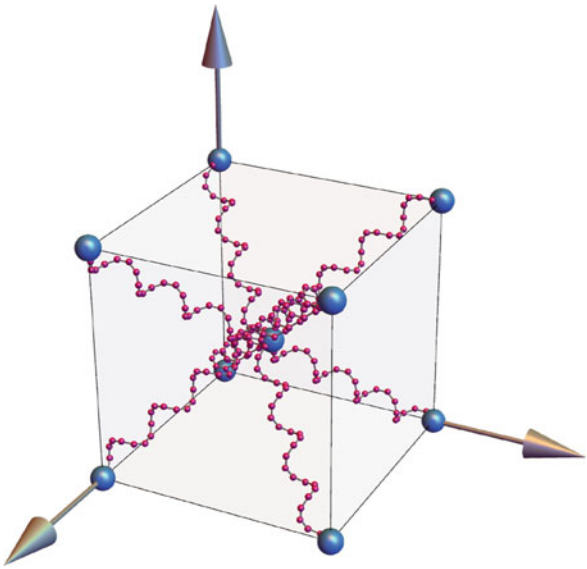

Fig. 6 Schematic representation of the eight chain network model of Arruda and Boyce [115]. The light grey solid volume represents the bulk material admitting the strain energy function ψ_{bulk} while the eight single polymer chains are governed by the strain energy function ψ_{chain} defined in Eq. (28)

For uncorrelated and correlated chains one can consider respectively the freely jointed chain energy (Eq. 28) and the worm-like chain energy (Eq. 30) The unit cell is further assumed to feature a solid phase conferring isotropic bulk properties through the strain energy ψ_{bulk}. Affinity of deformations is assumed.

The freely jointed chain model for uncorrelated chains is defined by the following strain energy function:

$$\psi_{\text{chain}} = \widehat{\psi}^{FJC}_{Langevin}(r) = \widehat{\psi}^{FJC}_{0} + \mathfrak{K}\,\theta N \left\{ \frac{r}{L}\mathcal{L}^{-1}(r) + \ln\left[\frac{\mathcal{L}^{-1}(r)}{\sinh\left(\mathcal{L}^{-1}(r)\right)} \right] \right\} \tag{28}$$

where $\widehat{\psi}^{FJC}_{0}$ is the ground state chain energy in the unperturbed state, r the current end-to-end distance of the chain and $\mathcal{L}^{-1}$ is the inverse of the Langevin function defined as $\mathcal{L}(x) = \coth(x) - 1/x$, $\mathfrak{K} = 1.3806503 \times 10^{-23}\left[\text{m}^2\text{kg s}^{-2}\text{K}^{-1}\right]$ is the Boltzmann constant and θ is the absolute temperature [K]. $\mathcal{L}^{-1}$ can be approximated using a Padé approximant [126] as:

$$\mathcal{L}^{-1}(x) \simeq \frac{3 - x^2}{1 - x^2}x \tag{29}$$

For a more in-depth analysis and alternative approximations of the inverse Langevin function, see recent papers by Nguessong et al. [127], Jedynak [128], Marchi and Arruda [129] and Darabi and Itskov [130].

The worm-line chain model for correlated chains is defined by the following strain energy function:

$$\psi_{\text{chain}} = \widehat{\psi}^{WLC}(r) = \widehat{\psi}_0^{WLC} + \frac{\Re\,\theta L}{\Lambda}\left[2\frac{r^2}{L^2} + \frac{1}{\left(1-\frac{r}{L}\right)} - \frac{r}{L}\right] \tag{30}$$

where L, Λ, r_0 and r are respectively the contour, persistence, initial end-to-end length and the current end-to-end length of the chain. Similarly to the freely jointed chain model, $\widehat{\psi}_0^{WLC}$ is the chain energy in the unperturbed state.

Bischoff et al. [118] later extended the eight-chain model of Arruda and Boyce [125] to orthotropy by considering distinct values of the characteristic dimensions of the unit cell (i.e. the three orthogonal edges of the cuboid). Rather than detailing the link between the Arruda-Boyce model and deformation invariants associated with the entropic chains and the unit cell here, a more in-depth description will be provided in Sect. 4.3.2 because the Bischoff-Arruda-Grosh formulation [118] is a generalisation of that of Arruda and Boyce.

Bischoff et al. [131] successfully modelled skin using the tensile test data on human skin on normal and hypertrophic scar tissue of Dunn et al. [132], those of Belkof and Haut [133] on rat skin and in vivo extensometry data of Gunner et al. [134] to identify constitutive parameters of the Arruda-Boyce model. Bischoff et al. [131] argued that the anisotropy of skin could be captured using an isotropic model coupled with an appropriate residual stress state (i.e. effects of Langer lines). This approach was demonstrated by running finite element analyses using the Abaqus/Standard (Simulia, Dassault Systèmes, Johnston, RI, USA) which offers the capability to apply pre-stress [131].

4.3 Non-linear Anisotropic Elastic Models of the Skin

In this section, a selection of some of the seminal and/or current state-of-the-art non-linear elastic models of skin are presented. As mentioned earlier in this review, the anisotropic mechanical properties of the skin are critical for most applications, so the focus of this review is therefore on constitutive models capturing these characteristics.

4.3.1 Lanir's Model

A very significant microstructurally-based continuum model of skin was first proposed by Lanir [93] who assumed that skin was a continuum composite made of an isotropic ground substance matrix in which oriented collagen and elastin fibres were embedded. These fibres obeyed an angular distribution $\mathcal{R}_k(\theta)$ (see Sect. 4.1.3).

The total strain energy function of the material is defined as:

$$\psi = (1 - \mathcal{V}_c - \mathcal{V}_e)\,\frac{\mu}{2}\,(I_1 - 3) + \sum_k \mathcal{V}_k \sum_\theta \mathcal{R}_k\,(\theta)\,\frac{K_k}{2}(\lambda - 1)^2 \tag{31}$$

μ is a shear modulus defining a neo-Hookean hyperelastic potential for the matrix, $\mathcal{V}_k$, K_k and $\mathcal{R}_k$ are respectively the volume fraction, fibre stiffness and fibre orientation probability density function of each fibrous phase k (collagen: $k = c$ and elastin: $k = e$).

Collagen and elastin fibres are assumed to be linear elastic and unable to sustain compression along their axis:

$$\begin{aligned} &f_k\,(\lambda) = K_k\,(\lambda - 1)\,,\ \lambda \geq 1 \\ &f_k\,(\lambda) = 0,\ \text{otherwise} \end{aligned} \tag{32}$$

In Lanir's model, collagen fibres are assumed to be undulated and can only resist loads when fully straightened. The degree of crimp of collagen fibres oriented in the direction θ is not uniform and follows a Gaussian distribution $D(x)$, where x is the stretch required to straighten an uncrimped fibre. The Cauchy stress in skin is given as:

$$\boldsymbol{\sigma} = \frac{1}{J}\sum_k \mathcal{V}_k \int_0^\pi \left[\mathcal{R}_k\,(\theta)\,f_k^*\,(\lambda)\,\mathbf{F}\frac{\partial \lambda}{\partial \mathbf{E}}\mathbf{F}^{\mathrm{T}}\right] d\theta - p\mathbf{1} \tag{33}$$

$f_k^*\,(\lambda)$ is the force per unit undeformed cross sectional area of an individual fibre at stretch λ and p is a hydrostatic pressure that represents the mechanical contribution of the isotropic matrix. For collagen fibres $f_k^*\,(\lambda)$ is expressed as follows:

$$f_{k=c}^*\,(\lambda) = f_c^*\,(\lambda) = \int_1^\lambda D(x)\,f_c\left(\frac{\lambda}{x}\right) dx \tag{34}$$

As elastin fibres are assumed to be undulation-free, $f_e^*\,(\lambda) = f_e\,(\lambda)$. Although Lanir [93] did not identify its model with experimental data, Meijer et al. [135] exploited it by characterising in-plane mechanical properties of human forearm skin using an hybrid numerical-experimental approach. Collagen fibre stiffness and mean undulation were estimated from the physical tests while the other constitutive parameters were extracted from the literature. Very low values of collagen fibre stiffness ranging from 51 to 86 MPa were determined from the identification procedure. As an explanation, the partial mechanical recruitment of fibres for the specific limited strain range applied during the physical test was invoked. Lanir's model was used as a constitutive framework for an in vitro porcine skin model in a study by Jor et al. [136]. Constitutive parameters were determined through numerical optimisation, and, as it is often the case

in identification procedures, multiple comparable solutions were obtained. The mean orientation of collagen fibres was determined to lay within the 2°–13° range which is consistent with observations. Young's modulus ranges for the ground substance matrix and collagen fibres were respectively 5–12 kPa and 48–366 MPa.

Fixing structural parameters that can be experimentally measured (e.g. fibre splay distribution) is a way to accelerate numerical identification and eliminate feasible but unrealistic solutions, thus reducing the issue of non-unicity in parameter sets.

4.3.2 Models Based on Bischoff-Arruda-Grosh's Formulation

This class of models is based on the notion of entropic elasticity and the micromechanics of macromolecule mechanical networks [125]. Bischoff et al. [118] extended the eight-chain model of Arruda and Boyce [125] developed for polymer elasticity to orthotropy, by considering distinct values $a = \|\mathbf{a}\|$, $b = \|\mathbf{b}\|$ and $c = \|\mathbf{c}\|$ for the three characteristic dimensions of the original cuboid microscopic unit cell defined by Arruda and Boyce (Fig. 7). Earlier, Bischoff et al. [131] had demonstrated that, despite being mechanically isotropic, the Arruda-Boyce model could reproduce load-induced anisotropy. However, the model could not capture the mechanical response of rabbit skin under biaxial extension [55]. Bischoff-Arruda-Grosh (BAG)'s strain energy function per unit volume is decomposed into chain

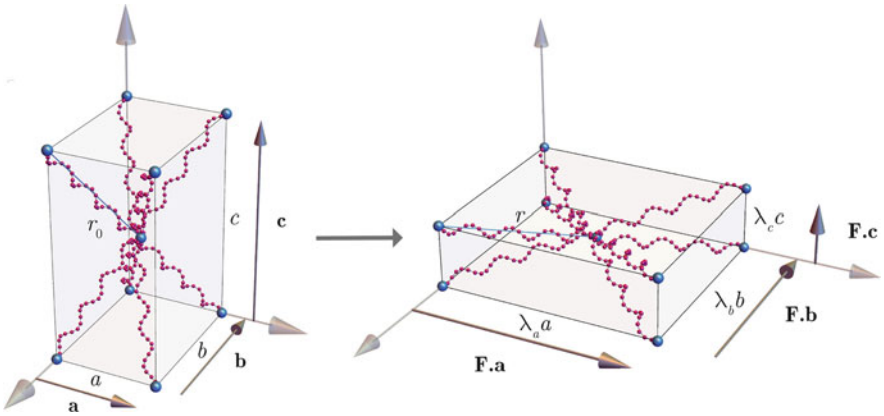

Fig. 7 Schematic representation of the orthotropic eight chain network model of Bischoff et al. [118]. The light grey solid volume represents the bulk material admitting the strain energy function ψ_{bulk} while the eight single polymer chains are governed by the strain energy function ψ_{chain}. When $\|\mathbf{a}\| = \|\mathbf{b}\| = \|\mathbf{c}\|$ the Bischoff et al.'s model [118] degenerates to the Arruda-Boyce's model while the Kuhl et al.'s model [116] is recovered if two cell dimensions are identical (e.g. $\|\mathbf{a}\| = \|\mathbf{b}\|$). r_0 and r are respectively the end-to-end length of each chain in the undeformed and deformed configurations

and bulk energies:

$$\psi = \psi_{\text{chain}} + \psi_{\text{bulk}} \tag{35}$$

$$\psi_{\text{chain}} = \psi_0 + \frac{n\,\Re\,\theta}{4}\left\{N\sum_{i=1}^{4}\left[\frac{\overline{r}_i}{N}\beta_i + \ln\left(\frac{\beta_i}{\sinh\beta_i}\right)\right] - \frac{\mathcal{L}^{-1}\left(1/\sqrt{N}\right)}{\sqrt{N}}\ln\left(\lambda_{\mathbf{a}}^{a^2}\lambda_{\mathbf{b}}^{b^2}\lambda_{\mathbf{c}}^{c^2}\right)\right\} \tag{36}$$

where ψ_0 a reference energy of the chain in the reference configuration, calculated so that the reference state is stress free, n is the volumetric chain density, $\overline{r}_i = r_i/d$ is the end-to-end length of deformed chain normalised by the chain link length d, $\sqrt{N}$ is the length of each *undeformed* chain:

$$N = \frac{1}{4}\left(a^2 + b^2 + c^2\right) \tag{37}$$

$\lambda_{\mathbf{i}}$ are the stretches along the principal material axes ($\mathbf{a}$, $\mathbf{b}$, $\mathbf{c}$) defined as:

$$\lambda_{\mathbf{i}} = \sqrt{\mathbf{C} : (\mathbf{i} \otimes \mathbf{i})},\ (\mathbf{i} = \mathbf{a}, \mathbf{b} \text{ or } \mathbf{c}) \tag{38}$$

$$\beta_i = \mathcal{L}^{-1}\left(\frac{\overline{r}_i}{N}\right) \tag{39}$$

Finally, the bulk energy is defined as:

$$\psi_{\text{bulk}} = \frac{\kappa}{\alpha^2}\left\{\cosh\left[\alpha\left(J-1\right)\right] - 1\right\} \tag{40}$$

where κ is the bulk modulus and α, a parameter that controls the shape of the pressure-J curve. Bischoff et al. [118] calibrated their constitutive model using data from biaxial testing on rabbit skin [55] and obtained an excellent fit with only seven parameters. The parameters were $n = 3.75.10^{22}$ (m^{-3}), $N = 1.25$, $\kappa = 50$ [kPa], $\alpha = 1$ and $\{a, b, c\} = \{1.37, 1.015, 1.447\}$.

Flynn et al. developed a series of skin models based on BAG's formulation to investigate the wrinkling behaviour of skin [137], scar tissue contraction [121] and wrinkling/ageing of the skin [138]. Kuhl et al. [116] particularised BAG's model to the case of transverse isotropy by setting two of the unit cell dimensions equal and fitted their model to the ubiquitous rabbit skin data from Lanir and Fung [55] but the fit was not as good as that provided by the original BAG's model.

4.3.3 Model Based on Limbert-Middleton's/Itskov-Aksel's Formulation

A polyconvex anisotropic strain energy function for soft tissues was developed by Limbert and Middleton [139] and independently formulated by Itskov et al. [140]. The constitutive framework was based on the generalised structure tensor invariant formulation proposed by Itskov and Aksel [141]. Rabbit skin biaxial tensile test data from Lanir and Fung [55] were used by Limbert and Middleton to identify sets of constitutive parameters. It was shown that a three-term series formulation was sufficient to obtain a very good fit between the experimental measurements and the predictions of the model. The starting point of the formulation which features novel invariants (compared to those described in Sect. 4.1.1) is the definition of a generalised structure tensor (indexed by k) as the weighted sum of three-mutually orthogonal structural tensors [140]:

$$\mathfrak{B}^{i}_{0\,[k]} = \sum_{i=1}^{3} w^{i}_{k}\mathfrak{B}^{i}_{0} = w^{1}_{k}\mathfrak{B}^{1}_{0} + w^{2}_{k}\mathfrak{B}^{2}_{0} + w^{3}_{k}\mathfrak{B}^{3}_{0}, \quad \{\, k = 1, 2, \ldots, n\} \tag{41}$$

where ω^{i}_{k} $(i = 1, 2, 3;\ k = 1, 2, \ldots, n)$ are non-negative scalars dependent on the principal material directions. The generalised structure tensors must satisfy the normalisation condition so that:

$$trace\left(\mathfrak{B}^{i}_{0\,[k]}\right) = 1 \ \ if \ \ \sum_{i=1}^{3}\omega^{i}_{k} = 1 \tag{42}$$

Itskov and Aksel [141] proposed the following two sets of invariants to describe the generalised orthotropic behaviour of hyperelastic materials:

$$I_{[k]} = \sum_{i=1}^{3}\omega^{i}_{k}\left(\mathfrak{B}^{i}_{0\,[k]} : \mathbf{C}\right) \tag{43}$$

$$J_{[k]} = I_3\left[\omega^{1}_{k}\mathrm{trace}\left(\mathbf{C}^{-1}\mathfrak{B}^{1}_{0\,[k]}\right) + \omega^{2}_{k}\mathrm{trace}\left(\mathbf{C}^{-1}\mathfrak{B}^{2}_{0\,[k]}\right) + \omega^{3}_{k}\mathrm{trace}\left(\mathbf{C}^{-1}\mathfrak{B}^{3}_{0\,[k]}\right)\right] \tag{44}$$

The original strain energy function proposed by Itskov and Aksel [141] was designed to model the mechanics of transversely isotropic calendered rubber sheets at high strains which it did very well:

$$\psi = \frac{1}{4}\sum_{k=1}^{n}\mu_k\left[\frac{1}{\alpha_k}\left(I^{\alpha_k}_{[k]} - 1\right) + \frac{1}{\beta_k}\left(J^{\beta_k}_{[k]} - 1\right) + \frac{1}{\chi_k}\left(I_3{}^{-\chi_k} - 1\right)\right] \tag{45}$$

This function was subsequently modified by Limbert and Middleton [139] to capture the typical exponential behaviour of the toe region of the stress-strain curve

of biological soft tissues:

$$\psi = \frac{1}{4}\sum_{k=1}^{n}\mu_k\left[\frac{1}{\alpha_k}\left(e^{(I_{[k]}-1)^{\alpha_k}}-1\right)+\frac{1}{\beta_k}\left(J_{[k]}^{\beta_k}-1\right)+\frac{1}{\chi_k}\left(I_3{}^{-\chi_k}-1\right)\right] \quad (46)$$

For both strain energy functions ψ, the polyconvexity condition is fulfilled if the material coefficients μ_k, α_k. β_k and χ_k satisfy the following inequalities:

$$\mu_k \geq 0, \quad \alpha_k \geq 1, \quad \beta_k \geq 1, \quad \chi_k \geq -\frac{1}{2} \quad \{k = 1, 2, \ldots, n\} \quad (47)$$

Although the function developed by Limbert and Middleton was able to fit very well the data from Lanir and Fung [55] it featured 12 parameters with no direct physical interpretation which, depending on the intended application, might be a limiting factor.

4.3.4 Models Based on Gasser-Ogden-Holzapfel's Anisotropic Hyperelastic Formulation

Gasser-Ogden-Holzapfel (GOH)'s constitutive formulation [94] was designed to capture the orthotropic hyperelastic behaviour of arterial tissues whilst accounting for fibre splay around two main directions corresponding to each collagen fibre families, characteristic of arterial microstructure. It is an extension of the original model developed by Gasser and his colleagues [142] and is based on the introduction of a new structure tensor $\mathbf{H}_i$ accounting for fibre dispersion of fibre family i:

$$\mathbf{H}_i = \kappa_i \mathbf{1} + (1 - 3\,\kappa_i)\;\boldsymbol{n}_0^i \otimes \boldsymbol{n}_0^i = \kappa_i \mathbf{1} + (1 - 3\,\kappa_i)\;\mathfrak{B}_0^i \quad (48)$$

where κ_i is a measure of fibre dispersion. The deceptively simple form for $\mathbf{H}_i$ was derived by introducing a statistical distribution which was integrated analytically. One can observe that $\mathbf{H}_i$ is a simple weighting of isotropy and transverse isotropy. When $\kappa_i = 0$, $\mathbf{H}_i$ collapses to the classical structure tensor $\mathfrak{B}_0^i$ that corresponds to perfect alignment of fibres without dispersion. If κ_i reaches its maximum value $\kappa_i = 1/3$, isotropic symmetry is recovered. The structural tensor is assumed to be only defined when fibres exhibit tension ($\mathbf{H}_i : \mathbf{C} - 1 > 0$). The strain energy function of GOH's model was defined as:

$$\psi = \frac{\mu}{2}(I_1 - 3) + \sum_{i=1}^{2}\frac{k_{i1}}{k_{ki2}}\left(\exp\left\{k_{ki2}[\mathbf{H}_i : \mathbf{C} - 1]^2\right\} - 1\right) \quad (49)$$

where μ, k_{i1}, k_{ki2} are material parameters. μ is a shear modulus defining a neo-Hookean hyperelastic potential whilst k_{i1} and k_{ki2} are respectively a stress-like and unitless scaling parameters.

The GOH model was used in the context of skin mechanics by Ní Annaidh et al. [34] who conducted a series of physical uniaxial tensile tests up to failure using digital image correlation (DIC) to measure stress-strain characteristics and mean collagen fibre distribution [40]. The physical characterisation was conducted on cadaveric human skin specimens at various body locations and along several orientations (defined with respect to Langer lines). GOH's model was fitted to the experimental tensile stress-strain curves and implemented into the finite element environment of Abaqus (Simulia, Dassault Systèmes, Johnston, RI, USA). The physical experiments were replicated by means of finite element analysis and demonstrated very good performance of the numerical model.

Combining 3D DIC and bulge tests, Tonge et al. [51] determined in-plane anisotropic mechanical properties of post-mortem human skin using cyclic full-field measurements. Two main directions of anisotropy were considered and a series of full skin samples (located on the back torso) obtained from six male and female donors (43, 44, 59, 61, 62 and 83 years-old) were used. The effect of preconditioning and humidity of the sample on the stress-strain response was investigated and was shown to be negligible. Age of the donors had a significant effect on the stiffness and directional properties of the skin. Specimens for older donors exhibited a stiffer and more isotropic response compared to those of younger donors. The authors also found that the bulge test method was limited by its inability to accurately determine stress and material parameters due to significant bending effects. In a companion paper, Tonge et al. [143] analysed the results of their bulge tests [51] using an analytical method based on thin shell theory which considered the effects of bending stiffness of the skin. The method accounts for through-the-thickness linear strain gradients. These authors fitted the shell version of GOH's model featuring a fully-integrated fibre distribution to their experimental data. Two cases were considered for the GOH model—2D and 3D fibre distributions—whilst the fully-integrated fibre model was restricted to 2D planar fibre orientation. It was found that both the 2D and 3D GOH model were unable to capture the anisotropic mechanics of skin from bulge tests unlike the 2D fully-integrated fibre model which was shown to capture it very well. Tonge et al. [143] attributed the differences between their results and those of Ní Annaidh et al. [34, 40] mainly to the younger age of their donors, lower strain level considered in their tests and their assumption about fibre orientation. Tonge et al. [143] considered only one fibre family aligned with the principal stretch direction while Ní Annaidh et al. [34, 40] assumed that skin was made of two fibre families, symmetric about the loading axis. In the context of surgical simulation procedures, the GOH model was used by Buganza-Tepole et al. [144] to model the mechanics of skin. In that study, computed stress profiles in skin flap were used as a surrogate measure of likelihood of tissue necrosis, following reconstructive surgery.

4.3.5 Models Based on Flynn-Rubin-Nielsen's Formulation

To address the issue of computationally expensive integration methods required for microstructural models of soft tissues featuring statistical distributions of material or structural characteristics (e.g. integration of fibre splay angular distribution over the unit sphere, distribution of engaged fibres), Flynn et al. [145] proposed a new model termed "*discrete fibre icosahedral structural model*". The model relies on the use of a *discrete* rather than *continuous* fibre orientation distribution kernel which allows closed-form solutions for strain energy and stress.

Six discrete directions are considered: they are oriented parallel to the lines connecting opposing vertices of a regular icosahedron (i.e. a 20-faced polyhedron). Six unit vectors $\boldsymbol{n}_0^i \{i = 1, \ldots, 6\}$ corresponding to distinct fibre bundles are thus defined as:

$$\begin{aligned}
&\boldsymbol{n}_0^1 = \tfrac{2}{\sqrt{5}}\mathbf{e}_1 + \tfrac{1}{\sqrt{5}}\mathbf{e}_3; && \boldsymbol{n}_0^2 = \tfrac{1}{2}\left(1-\tfrac{1}{\sqrt{5}}\right)\mathbf{e}_1 + \sqrt{\tfrac{1}{2}\left(1+\tfrac{1}{\sqrt{5}}\right)}\mathbf{e}_2 + \tfrac{1}{\sqrt{5}}\mathbf{e}_3 \\
&\boldsymbol{n}_0^3 = -\tfrac{1}{2}\left(1+\tfrac{1}{\sqrt{5}}\right)\mathbf{e}_1 + \sqrt{\tfrac{1}{2}\left(1-\tfrac{1}{\sqrt{5}}\right)}\mathbf{e}_2 + \tfrac{1}{\sqrt{5}}\mathbf{e}_3, && \boldsymbol{n}_0^4 = -\tfrac{1}{2}\left(1+\tfrac{1}{\sqrt{5}}\right)\mathbf{e}_1 - \sqrt{\tfrac{1}{2}\left(1-\tfrac{1}{\sqrt{5}}\right)}\mathbf{e}_2 + \tfrac{1}{\sqrt{5}}\mathbf{e}_3 \\
&\boldsymbol{n}_0^5 = \tfrac{1}{2}\left(1-\tfrac{1}{\sqrt{5}}\right)\mathbf{e}_1 - \sqrt{\tfrac{1}{2}\left(1+\tfrac{1}{\sqrt{5}}\right)}\mathbf{e}_2 + \tfrac{1}{\sqrt{5}}\mathbf{e}_3, && \boldsymbol{n}_0^6 = \mathbf{e}_3
\end{aligned} \tag{50}$$

From these six unit vectors, Flynn et al. [145] defined six structural tensors:

$$\mathfrak{B}_0^i = \boldsymbol{n}_0^i \otimes \boldsymbol{n}_0^i \{i = 1, \ldots, 6\} \text{ (no summation on } i), \text{ with } \sum_{i=1}^{6} \mathfrak{B}_0^i = 2\mathbf{I} \tag{51}$$

Flynn et al. [145] introduced a strain energy function per unit mass of the collection of six fibre bundles which features separate contributions for collagen and elastin fibres:

$$\psi = \sum_{i=1}^{6} w_i \left[\psi_c\left(\lambda_i\right) + \psi_e\left(\lambda_i\right)\right] + U(J) \tag{52}$$

with

$$\psi_e\left(\lambda_i\right) = \frac{1}{\rho_0}\sum_{i=1}^{6} w_i \frac{E_e}{4}\left\langle \lambda_i^2 - 1 \right\rangle \tag{53}$$

where w_i are positive weights, associated with each of the six structural tensors, that balance the respective structural contributions of each fibre direction and ρ_0 is the mass density in the reference configuration. $\langle\rangle$ are the Macaulay brackets defined as follows: $\langle x \rangle = 1/2(x + |x|)$.

Because collagen fibres are typically crimped in the macroscopic stress-free reference configuration [93, 145], it is sensible to introduce a so-called *undulation parameter* $x \geq 1$, which is the value of stretch at which a fibre starts to bear tension:

$$\int_1^{\infty} D(x)dx \tag{54}$$

This means that the fraction of fibres that are fully taut (i.e. straight) at a stretch λ is given by the following integral, where D is an undulation probability distribution:

$$\int_1^{\lambda} D(x)dx \tag{55}$$

The stiffness of any of the six collagen bundles is:

$$\frac{d}{d\lambda}\left(\frac{\lambda\rho_0}{J}\frac{d\psi_c\,(\lambda)}{d\lambda}\right) = E_c\int_1^{\lambda} D(x)dx \tag{56}$$

Assuming that all the collagen fibres are slack and are stress-free for stretch lower or equal to unity, and further assuming that deformations are isochoric:

$$\frac{d\psi_c\,(\lambda)}{d\lambda} = \frac{1}{\lambda\rho_0}\int_1^{\lambda}\left[E_c\int_1^{\lambda} D(x)dx\right]dy \tag{57}$$

Flynn et al. [145] considered two undulation probability distributions: step and triangle distributions. They offer the advantage of being simple enough so that a closed-form analytical expression can be obtained for ψ_c. A unit step distribution takes the following form

$$D(x) = \begin{cases} 0, \; x < x_1 \;\text{ or }\; x > x_3 \\ \frac{1}{x_3 - x_1}, \; \text{otherwise} \end{cases} \tag{58}$$

If one injects the definition of the unit step distribution function D into Eq. (57), one arrives to the following expression for the strain energy function of a single collagen fibre bundle:

$$\psi_c\,(\lambda) = \begin{cases} 0, \; \lambda < x_1 \\ \frac{E_c}{\rho_0}\frac{1}{4(x_3 - x_1)}\left[(\lambda - x_1)\,(\lambda - 3\,x_1) + 2\,x_1^2 \ln\left(\frac{\lambda}{x_1}\right)\right], \; x_1 \leq \lambda < x_3 \\ \frac{E_c}{\rho_0}\left\{\frac{1}{4(x_3 - x_1)}\left[(x_3 - x_1)\,(x_3 - 3\,x_1) + 2\,x_1^2 \ln\left(\frac{x_3}{x_1}\right)\right]\right. \\ \quad \left. + \left(\frac{x_3 - x_1}{2} - x_3\right)\ln\left(\frac{\lambda}{x_3}\right) + \lambda - x_3\right\}, x_3 < \lambda \end{cases} \tag{59}$$

This strain energy function was used by Flynn et al. [145] to model the biaxial tensile response of rabbit skin [55] (8.7% error) and uniaxial response of porcine skin [146] (7.6% error). The constitutive model was later extended by Flynn and Rubin [147] to address shortcomings linked to the relation between fibre weight and anisotropic response, namely, the fact that for equal weights w_i the mechanical response is not necessarily isotropic. These authors introduced a generalised strain invariant γ:

$$\gamma = \left(\mathbf{C} + \mathbf{C}^{-1}\right) . \sum_{i=1}^{6} w_i \mathfrak{B}_0^i - 2 \tag{60}$$

where w_i are positive weights, associated with each of the six structural tensors $\mathfrak{B}_0^i = \boldsymbol{n}_0^i \otimes \boldsymbol{n}_0^i$, that balance the respective structural contributions of each fibre direction.

Unlike for the earliest model of Flynn et al. [145], here, equal weights can only lead to isotropy of mechanical properties. Finally, Flynn and Rubin [147] proposed the following strain energy density:

$$\psi = \frac{\sigma_0}{2\rho_0}\left[\gamma + \sum_{m=1}^{M} \frac{\gamma_m}{m}\left(\frac{\gamma}{\gamma_m}\right)\right] \tag{61}$$

where ρ_0 is the mass density in the reference configuration, σ_0 is a stress-like material parameter, γ_m are dimensionless positive material parameters and M is the order of the polynomial expansion.

Using the same experimental data as in their 2011 paper [55, 146], Flynn and Rubin [147] identified constitutive parameters of their new strain energy function (Eq. 61). The fit was not as good as in their previous study [145] as the fitting errors for rabbit and pig skin data were respectively 12 and 17%. However, in that case, the weights were a pure measure of anisotropy.

4.3.6 Model Based on Limbert's Formulation

Most of the microstructurally-based constitutive models of soft tissues assume an additive decomposition of the strain energy function into decoupled matrix and fibre elastic potentials. This means that fibre-fibre and matrix-fibre interactions are not *explicitly* captured in the constitutive formulation. The network models based on BAG's formulation captures only *implicitly* and *globally* these interactions. To address this first shortcoming, Limbert [148] developed a novel invariant-based multi-scale constitutive framework to characterise the transversely isotropic and orthotropic elastic responses of biological soft tissues. The constitutive equations were particularised to model skin. The model was not only capable to accurately reproduce the experimental multi-axial behaviour of rabbit skin, as in [149] but

could also a posteriori predict stiffness values of individual tropocollagen molecules in agreement with physical and molecular-dynamics-based computational experiments [148]. A desirable feature of the constitutive formulation is that the constitutive parameters can be directly extracted from physical measurements by segregating the orthogonal deformation modes of its constituents and the response is based on physical geometrical/structural parameters that can be measured experimentally or determined ab initio from molecular dynamic simulations.

Limbert's formulation is based on the constitutive framework of Lu and Zhang [150] for transversely isotropic materials which make use of four invariants that characterise decoupled deformations modes solely related to purely volumetric (J), deviatoric stretch in the fibre direction $\left(\overline{\lambda}\right)$, cross-fibre shear $\left(\alpha_1^i\right)$ and fibre-to-fibre/matrix-to-fibre shear $\left(\alpha_2^i\right)$ stress responses. Orthotropic symmetry is accounted for by introducing a second family of fibres. The index $i = 1, 2$ identifies each fibre family:

$$J = \sqrt{I_3}; \quad \overline{\lambda}_i = I_3^{-\frac{1}{6}} \sqrt{I_4^i}; \quad \alpha_1^i = \frac{I_1 I_4^i - I_5^i}{\sqrt{I_3 I_4^i}}; \quad \alpha_2^i = \frac{I_5^i}{\left(I_4^i\right)^2} \tag{62}$$

Limbert proposed the following strain energy function:

$$\psi = \psi^v(J) + \sum_{i=1}^{2} \left[\psi_i^{\overline{\lambda}} \left(\overline{\lambda}_i\right) + \widehat{\psi}_i^1 \left(\alpha_1^i\right) + \tilde{\psi}_i^2 \left(\alpha_2^i, \overline{\lambda}_i\right) \right] \tag{63}$$

ψ^v, $\psi_i^{\overline{\lambda}}$, $\widehat{\psi}_i^1$ and $\tilde{\psi}_i^2$ are respectively the volumetric, deviatoric fibre, cross-fibre shear and fibre-to-fibre/fibre-to-matrix shear energies. The functional forms of the energies and the constitutive parameters are detailed below.

$$\widehat{\psi}_i^1 \left(\alpha_1^i\right) = \frac{1}{2} \mu_1^i \left(\alpha_1^i - 2\right); \; \tilde{\psi}_i^2 \left(\alpha_2^i, \overline{\lambda}_i\right) = \frac{1}{2} \mu_2^i \left(\alpha_2^i - 1\right)^2 \underbrace{\frac{1}{1 + a_i \, \mathrm{e}^{-b_i \left(\overline{\lambda}_i - \overline{\lambda}_i^c\right)}}}_{\text{Sigmoid coupling function}} \tag{64}$$

A notable feature of this constitutive approach is that collagen fibres and matrix are allowed to interact via explicit decoupled shear interactions whilst collagen fibres behave like a worm-like chain model [116, 117].

$$\psi_i^{\overline{\lambda}} \left(\overline{\lambda}_i\right) = \begin{cases} \aleph_i \mu_0^i \left(\overline{\lambda}_i^{\,2} + \frac{2}{\overline{\lambda}_i} - 3\right) + \xi_0^i \aleph_i \ln\left(\overline{\lambda}_i^{\,r_{0\,i}^2}\right) & \text{if } \overline{\lambda}_i \leq 1 \\ \aleph_i \Re \theta \frac{L_i}{4 L_p^i} \left(2 \frac{\overline{\lambda}_i^{\,2} r_{0\beta}^2}{L_i^2} + \left(1 - \frac{\overline{\lambda}_i r_{0\,i}}{L_i}\right)^{-1} - \frac{\overline{\lambda}_i r_{0\,i}}{L_i} \right) + \xi_0^i \aleph_i \ln\left(\overline{\lambda}_i^{\,r_{0\beta}^2}\right) & \text{if } \overline{\lambda}_i > 1 \end{cases} \tag{65}$$

The constitutive model resulted in a set of 23 constitutive parameters $\mathbf{p} = \mathbf{p}^1 \cup \mathbf{p}^2 = \left\{\Re, \theta, \kappa, \mu_0^i, \mu_1^i, \mu_2^i, \aleph_i, L_i, L_p^i, r_i, a_i, b_i, \overline{\lambda}_i^c\right\}_{i=1,2}$. Moreover, all the constitutive parameters of this multiscale formulation have a direct physical interpretation. Limbert [148] determined the parameter set $\mathbf{p}^2$ using a numerical global optimisation algorithm while the parameter set $\mathbf{p}^1$ was assumed a priori based on existing data [116] and data obtained via visual inspection of the biaxial stress-strain curves [149]. For a more detailed interpretation of the constitutive parameters the reader is referred to the papers by Limbert [5, 148]. Although the model slightly under-predicts the response of rabbit skin along the head-tail direction at low stretch (<1.35), an excellent fit was obtained. Limbert implemented the non-linear constitutive model as tri-linear hexahedral finite element using an enhanced strain formulation [151] which has been proven to be superior to a standard displacement-based formulation, particularly for shear-dominated problems and nearly incompressible materials. Moreover, analytically-exact direct sensitivity analyses subroutines were also implemented to assess the sensitivity of the shear response of the model to its constitutive parameters during a simulated indentation test [148]. From the persistence lengths of tropocollagen molecules determined from the optimisation procedure (22 and 65 nm for fibre families 1 and 2) Limbert [148] calculated equivalent Young's moduli of respectively 293 and 865 MPa. These values lie within one order of magnitude less of what has been determined experimentally and obtained through computational modelling studies (see for example Gautieri et al. [152]). However, using the same equation used by Limbert to calculate Young's modulus, Sun et al. [153] estimated Young's modulus of collagen molecules to range between 350 MPa and 12 GPa. Limbert's model [148] features a set of 23 constitutive parameters $\mathbf{p} = \mathbf{p}^1 \cup \mathbf{p}^2$ where $\mathbf{p}^1 = \left\{\Re, \theta, \kappa, \mu_0, a_{\boldsymbol{n}_0}, b_{\boldsymbol{n}_0}, a_{\boldsymbol{m}_0}, b_{\boldsymbol{m}_0}, \aleph_{\boldsymbol{n}_0}, \aleph_{\boldsymbol{m}_0}, \overline{\lambda}_{\boldsymbol{n}_0}^c, \overline{\lambda}_{\boldsymbol{m}_0}^c\right\}$ and $\mathbf{p}^2 = \left\{\mu_1, \mu_2, L_{\boldsymbol{n}_0}, L_p^{\boldsymbol{n}_0}, r_{\boldsymbol{n}_0}, \aleph_{\boldsymbol{m}_0}, L_{\boldsymbol{m}_0}, L_p^{\boldsymbol{m}_0}, r_{\boldsymbol{m}_0}\right\}$. Limbert [148] determined the parameter set $\mathbf{p}^2$ using a numerical global optimisation algorithm while the parameter set $\mathbf{p}^1$ was assumed a priori based on existing data [116] and data obtained via visual inspection of biaxial stress-strain curves for rabbit skin [149].

4.3.7 Models Based on Weiss-Maker-Govindjee's Transversely Isotropic Hyperelastic Formulation

Groves et al. [154] used Weiss-Maker-Govindjee's model [155] to describe the anisotropic mechanics of skin by identifying constitutive parameters from a series of uniaxial tensile tests. The original model proposed by Weiss et al. [155] was formulated to capture the transversely isotropic hyperelastic response of ligaments of the knee joint but without including fibre dispersion which is not significant in these soft tissues.

The strain energy function used by Groves et al. [154] was defined as the sum of the Veronda-Westmann (VW) potential ψ^{VW} [57] and a piece-wise anisotropic fibre

function ψ_i^{fibre} [155], to model the isotropic and anisotropic responses respectively:

$$\psi\left(I_1, I_2, I_4^1, I_4^2, I_4^3\right) = \psi^{VW}\left(I_1, I_2\right) + \sum_{i=1}^{3} \psi_i^{fibre}\left(I_4^i = \lambda^i\right) \tag{66}$$

where:

$$\psi^{VW} = c_1\left\{\exp\left[c_2\left(I_1 - 3\right)\right] - 1\right\} - \frac{c_1 c_2}{2}\left(I_2 - 3\right) \tag{67}$$

c_1 is a shear-like modulus while c_2 is a dimensionless parameter that scales the response connected to the second invariant.and

$$\frac{\partial \psi_i^{fibre}\left(\lambda^i\right)}{\partial \lambda^i} = \frac{1}{\lambda^i}\begin{cases} 0 & if\ \lambda^i \leq 1 \\ c_3\left\{\exp\left[c_4\left(\lambda^i - 1\right)\right] - 1\right\} & if\ 1 < \lambda^i < \overline{\lambda}^i \\ c_5\lambda^i + c_6 & if\ \lambda^i \geq \overline{\lambda}^i \end{cases} \tag{68}$$

$\overline{\lambda}^i = \sqrt{\overline{I}_4^i}$ represents the stretch at which the (collagen) fibres are assumed to be fully taut. c_3 is an elastic modulus-like parameter scaling the exponential response, c_4 controls the rate of un-crimping of the fibres, c_5 is the elastic modulus of the taut fibre while c_6 is a correcting factor to ensure continuity of the stiffness response at $\lambda^i = \overline{\lambda}^i$.

In their experimental procedure, Groves et al. [154] used eight human discoid skin samples from two female donors (aged 56 and 68) following mastectomy and fourteen post-mortem murine skin samples obtained from eight mice (aged 18–24 months). For each sample, tensile tests were simultaneously conducted along three axis (0°, 45° and 90°). Using an inverse analysis based on finite element simulations of the testing procedure constitutive parameters were determined. For each sample, three sets of four parameters (c_3, c_4, $\sqrt{\overline{I}_4^i}$ and an additional parameter characterising the deviation from the assumed fibre orientation) for each fibre energy function were obtained in addition to the two parameters of the VW function. Although Groves et al. [154] demonstrated a good fit between their three-fibre family model and their experimental data, they also acknowledged the limitations of using a Simplex optimisation algorithm for their inverse analysis which could only capture *local* minima of their cost function.

4.3.8 Model Based on Yang-Sherman-Gludovat-Schaible-Stewart-Ritchie-Meyers's Formulation

Yang et al. [156] investigated the tear resistance of rabbit skin by conducting a very comprehensive multi-modality study. This study combined physical tensile tests, scanning electron microscope, in situ synchrotron X-ray characterisation and

constitutive modelling. The constitutive model used to represent the tensile elastic response of skin is based on the mechanics of a wire made of circular segments and captures almost four hierarchical levels of the skin (from 0.5 nm to 10 μm): (I) sub-nanometre level (collagen molecule), (II) nanometre level (collagen fibrils), (III) micrometre level (collagen fibres, arranged in an undulating geometry) and (IV) mesoscale level (collagen fibres with two main orientations, effectively creating a meshwork with orthotropic mechanical symmetry) collagen that is. The stress response of a planar spring made of circular wire segments, σ_0, is given by

$$\sigma_0 = \int_{r_c}^{r} E' \underbrace{\left\{ \frac{\cos(\theta_0)}{r_c r} \left[r \sin\left(\frac{r_c \theta_0}{r} \right) - r_c \theta_0 \cos\left(\frac{r_c \theta_0}{r} \right) \right] \right\}}_{d\varepsilon} dr \tag{69}$$

where E' is a pseudo-modulus (determined from the geometry of the wire), θ_0 is the initial central angle of the quarter of the circular segments (Fig. 8) and r_c is the initial circle radius. $d\varepsilon$ is the strain increment induced by a change in radius r as a segment is stretched. The derivation and explicit form of E' was not provided in this paper, nor in a review paper by the same group [157] on the material science of collagen where it is mentioned, but in a later study [158] (**Supplementary Material**). The formulation of the pseudo-modulus was derived from the mechanics of circular beam with round cross section where the total energy of the system is expressed as the sum of components due to bending, normal force and shear force. This elastic constitutive model was augmented by a viscoelastic component by adding a dashpot to the elastic spring defined in Eq. (69). The mechanical behaviour of a dashpot is simply represented by a Newtonian response $\sigma = \eta\, d\varepsilon/dt$ where σ, η and $d\varepsilon/dt$ are respective the unidimensional stress, viscosity and unidimensional strain rate. The constitutive model was shown to provide very good agreement for reproducing the mechanics of steel wire and that of rabbit skin for different orientations of tension

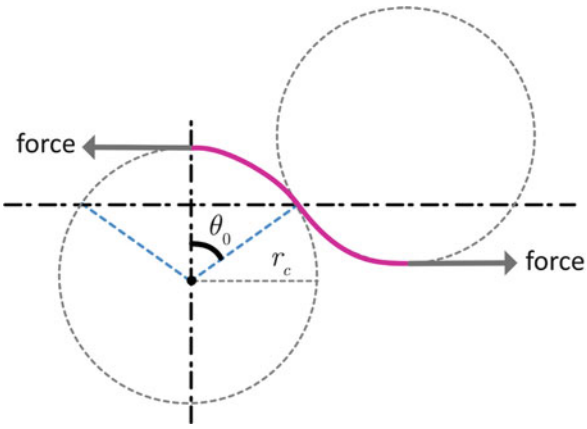

Fig. 8 Schematic illustration describing the geometry of a wire made of circular segment as in the constitutive model of Wang and co-authors [158, 159]. Adapted from Wang et al. [159]

but its ability to generalise to more geometrically complex collagen assemblies and more complex loading scenarios remains to be established.

4.4 Nonlinear Viscoelastic Models of the Skin

The skin exhibits a wide range of viscoelastic effects including stress relaxation, creep, rate-dependency of stress and hysteresis [9]. A large number of researchers have characterised the viscoelastic properties of skin under various testing conditions [56, 160–167]. Observed macroscopic viscoelastic effects can be attributed to two main mechanisms that operate in concert. Viscoelasticity of the skin can originate from the intrinsic viscoelastic characteristics of its nano- and microstructural constituents (e.g. proteoglycans, elastic fibres) and also from the time-dependent rearrangement of its microstructure under macroscopic loads which takes a finite amount of time to occur (e.g. flow of interstitial fluid across the porous structures, progressive sliding of collagen fibrils past each other). Proteoglycan macromolecules such as decorin bound on the collagen fibrils and play an important role in these interactions which are mediated by the side chains of glycosaminoglycans. Because the forces acting between fibrils are of a non-covalent nature, these links can break and reconnect [56, 168, 169]. One should also note that there are other complex physics phenomena at play. For example, the thermal motion of ions, including Na+ and K+, displacing toward the negatively charged ends of glycosaminoglycans of fibril-associated proteoglycans, induce an attractive force between two collagen fibrils.

To date, there are only very few nonlinear viscoelastic anisotropic constitutive models of skin, see [56, 119, 170–172] and references therein. This is partly due to the considerable challenges of experimentally characterising the behaviour of skin, particularly in vivo, and the success of simpler theories such as quasi-linear viscoelasticity (QLV) [9, 173]. The literature on general viscoelastic constitutive models is rich and, here, only a brief account of the most common approaches to model biological soft tissues (following the classification of Ehret [174]) is reported. More recent and state-of-the-art nonlinear viscoelastic models of skin are presented.

4.4.1 Quasi-linear Viscoelasticity and Its Derivatives

The application of QLV theory to soft tissue mechanics has been particularly popularised by the work of Fung and co-workers [9, 173]. The idea behind QLV is to assume that the time-dependent stress response $\sigma(t)$ following uniaxial loading can be expressed as a convolution integral of the form:

$$\sigma(t) = \int_{-\infty}^{t} G(t-\tau)\,\frac{\partial \sigma_e(\tau)}{\partial t} d\tau \tag{70}$$

where σ_e is the instantaneous elastic stress and G the reduced relaxation function. This function controls how the current stress response is modulated by past loading history.

The notion of quasi-linearity stems from the linear relation of the integrand terms and the analogy with rate equations of linear viscoelasticity. The uniaxial relationship can be extended to a full 3D representation by introducing second-order and fourth order tensors describing respectively the stress and reduced relaxation function [9]. This represents a flexible framework where anisotropic properties, and decoupling between deviatoric and volumetric responses can be captured by appropriate constitutive equations. A recent update of QLV for transversely isotropic hyperelastic materials can be found in the work of Balbi et al. [175].

Bischoff [176] applied QLV at the collagen fibre level to model porcine skin by developing an anisotropic microstructurally-motivated constitutive model which also includes fibre dispersion. A notable feature of the model is the ability to capture a fibre-level viscoelastic orthotropic response with only seven parameters. However, the authors recognised the need for additional experiments to fully characterise the mechanical response as numerical identification procedures are plagued by non-unicity of constitutive parameters. Additional characterisation tests would likely lead to convergence toward a single set of optimal parameters.

4.4.2 Explicitly Rate-Dependent Models

By design, these types of model—also called viscoelastic models of the *differential* type—capture strain-rate sensitivity and *short-term* viscous effects following application of load [177]. They are based on *differential* rather than *integral* equations like for QLV, and are therefore inappropriate to capture long-term memory viscoelastic effects such as relaxation. Long-term memory effects encompass the whole deformation history of the material. The so-called *principle of fading memory* [178] states that deformations that occurred in the recent time history have greater influence on the actual stresses than those which occurred in a more distant past history.

Explicitly rate-dependent models of soft tissues are particularly well suited to high strain rate situations such as those occurring during vehicle accidents, sport activities, impact and blast scenarios [177, 179–182]. These models generally postulate the existence of a viscous potential ψ^v from which the viscous dissipative effects (denoted by scalar $\mathcal{D}$) arise by differentiation with respect to the rate of the Cauchy-Green deformation tensor $\dot{\mathbf{C}} = \partial \mathbf{C}/\partial t$:

$$\mathcal{D} = \frac{\partial \psi^v}{\partial \dot{\mathbf{C}}} : \dot{\mathbf{C}} \tag{71}$$

The total second Piola-Kirchhoff stress tensor which include purely elastic effects through a potential ψ^e, and purely viscous effects through ψ^v, is obtained by differentiation of the total potential ψ assuming that $\dot{\mathbf{C}}$ is a parameter or internal

variable:

$$\mathbf{S} = 2\left(\frac{\partial \psi^e}{\partial \mathbf{C}} + \frac{\partial \psi^v}{\partial \dot{\mathbf{C}}}\right) \tag{72}$$

The framework proposed by Pioletti et al. [177] for modelling the rate-dependent isotropic viscohyperelastic behavior of ligaments and tendons was later extended by Limbert and Middleton [180] to transverse isotropy using tensor formalism. This model was subsequently combined with damage equations to model the failure of human skin in response to puncturing biting loads [179].

4.4.3 Internal Variables Based on Deformation/Strain Decomposition

Unidimensional (small-strain) rheological models based on combinations of spring and dashpot elements are efficient means to conceptualise particular viscoelastic behaviours [86]. The arrangement of a dashpot and a spring in series constitutes a Maxwell element with elastic modulus E and viscosity η and the total strain ε in the element can be decomposed into elastic and inelastic strains as $\varepsilon = \varepsilon_e + \varepsilon_i$ and the total strain rate is:

$$\frac{\partial \varepsilon}{\partial t} = \frac{1}{E}\frac{\sigma}{\eta} + \frac{\partial \sigma}{\partial t} \tag{73}$$

A very simple approach to account for the viscoelastic properties of skin would be to assume that it is a generalised standard viscoelastic solid made of n Maxwell elements so that it can be described by a strain energy function of the form $\psi = \mathcal{P}(t)\psi^{\infty}$ where ψ^{∞} is the time-independent or instantaneous strain energy which is convolved with a time-dependent kernel represented by a n-term Prony series $\mathcal{P}$ defined through characteristic times and moduli τ_i and c_i as:

$$\mathcal{P}(t) = 1 + \sum_{i=1}^{n} c_i \left[1 - \exp\left(-\frac{t}{\tau_i}\right)\right] \tag{74}$$

Borrowing the concept of linear strain decomposition and applying it to the 3D finite strain regime, it is possible to establish a multiplicative decomposition of the deformation gradient into an elastic and inelastic parts as $\mathbf{F} = \mathbf{F}^e.\mathbf{F}^i$ [183, 184]. From this definition one can define the fictitious *elastic* and *inelastic* right Cauchy-Green deformation tensors as:

$$\mathbf{C}^e = \mathbf{F}^{e\,\mathrm{T}}.\mathbf{F}^e;\ \mathbf{C}^i = \mathbf{F}^{i\,\mathrm{T}}.\mathbf{F}^i \tag{75}$$

One can then postulate the existence of a free energy $\psi(\mathbf{C}^e, \mathbf{C}^i)$ decomposed into *equilibrium* and *non-equilibrium terms* where $\mathbf{C}^i$ is treated as an internal variable [183]:

$$\psi\left(\mathbf{C}\right) = \psi\left(\mathbf{C}^e, \mathbf{C}^i\right) = \psi^{equilibrium}\left(\mathbf{C}^e\right) + \psi^{n.equilibrium}\left(\mathbf{C}^i\right) \tag{76}$$

Naturally, one can generalise this concept to n Maxwell elements so that one introduces n internal (tensor) variables $\mathbf{C}_k^i$, arguments of n non-equilibrium potentials $\psi_k^{n.equilibrium}$:

$$\psi\left(\mathbf{C}, \mathbf{C}_k^i\right) = \psi^{equilibrium}\left(\mathbf{C}\right) + \sum_{k=1}^{n} \psi_k^{n.equilibrium}\left(\mathbf{C}_k^i\right) \tag{77}$$

The second Piola-Kirchhoff stress is then obtained as the sum of equilibrium and non-equilibrium terms as:

$$\mathbf{S} = \mathbf{S}^{equilibrium} + \sum_{k=1}^{n} \mathbf{S}_k^{n.equilibrium} = 2\left[\frac{\partial \psi^{equilibrium}(\mathbf{C}^e)}{\partial \mathbf{C}^e} + \sum_{k=1}^{n} \frac{\psi_k^{n.equilibrium}(\mathbf{C}_k^i)}{\partial \mathbf{C}_k^i}\right] \tag{78}$$

A notable feature of the present formulation is that non-equilibrium or viscous deformations are not restricted to the small strain regime unlike the vast majority of viscoelastic models of biological soft tissues found in the literature.

Bischoff et al. [119] combined this type of formulation with their previous orthotropic eight-chain model [118] to model the viscoelastic behaviour of soft tissues. The model was fitted to the experimental data on rabbit skin [55]. Vassoler et al. [185] recently proposed a variational framework making use of the multiplicative decomposition of the deformation gradient into elastic and inelastic parts to represent the mechanics of fibre-reinforced biological composites and this would be appropriate for skin.

Limbert (2014, private communication) extended his decoupled invariant orthotropic hyperelastic model to finite strain viscoelasticity following a similar approach to that described in this section. The particular approach for anisotropic viscoelastic effects follows the tensor formalism of Nguyen et al. [186] and Nedjar [187] who introduced viscosity tensors. An essential feature of the model is that the matrix and the fibre phase are treated separately, each featuring their own deformation gradient. The non-linear creep and/or relaxation response is based on the multiplicative viscoelastic split of the deformation gradient combined with the assumption of the existence of viscoelastic potentials for each phase. The deformation gradient and its multiplicative decomposition apply to all the continua (matrix and fibre phase) linking them *implicitly*. Separate flow rules are specified for the matrix and fibre families. The flow rules of the fibre families are combined to provide an anisotropic flow rule of the fibre phase. Details of the constitutive

formulation and finite element implementation of the present constitutive model for the dermis can be found in Nguyen et al.'s paper [186]. One should point out that, besides the *matrix* phase, the multiplicative decomposition of the deformation gradient applies to the *fibre phase*, not to the individual families of fibres (two, in our case).

$$\mathbf{F} = \mathbf{F}^{e}_{matrix\ (k)}\mathbf{F}^{v}_{matrix\ (k)} = \mathbf{F}^{e}_{fibre\ (p)}\mathbf{F}^{v}_{fibre\ (p)} \tag{79}$$

The elastic right Cauchy-Green deformation tensors associated with the matrix and fibre phases are defined as:

$$\mathbf{C}^{e}_{matrix} = \left(\mathbf{F}^{v}_{matrix}\right)^{-\mathrm{T}}\left(\mathbf{F}^{T}\mathbf{F}\right)\left(\mathbf{F}^{v}_{matrix}\right)^{-1} \tag{80}$$

and

$$\mathbf{C}^{e}_{fibre} = \left(\mathbf{F}^{v}_{fibre}\right)^{-\mathrm{T}}\left(\mathbf{F}^{T}\mathbf{F}\right)\left(\mathbf{F}^{v}_{fibre}\right)^{-1} \tag{81}$$

The general formulation of the free energy density can be expressed as the sum of equilibrium and non-equilibrium energies depending on the total and viscous deformation tensors and the fibre orientation vectors (defined by $\boldsymbol{n}_0$ and $\boldsymbol{m}_0$ If one considers two family of collagen fibres):

$$\psi(\mathbf{C}, \mathbf{C}^{v}_{matrix}, \mathbf{C}^{v}_{fibre}, \boldsymbol{n}_0, \boldsymbol{m}_0) = \underbrace{\psi^{\infty}(\mathbf{C}, \boldsymbol{n}_0, \boldsymbol{m}_0)}_{\text{equilibrium part}} + \underbrace{\psi^{v}(\mathbf{C}^{e}_{matrix}, \mathbf{C}^{e}_{fibre}, \boldsymbol{n}_0, \boldsymbol{m}_0)}_{\text{non-equilibrium part}} \tag{82}$$

where

$$\psi^{\infty}(\mathbf{C}, \boldsymbol{n}_0, \boldsymbol{m}_0) = \psi^{\infty}_{M}(I_1, I_2, I_3) + \psi^{\infty}_{F}(I_4, I_5, I_6, I_7) \tag{83}$$

$$\psi^{v}\left(\mathbf{C}^{e}_{matrix}, \mathbf{C}^{e}_{fibre}, \boldsymbol{n}_0, \boldsymbol{m}_0\right) = \mathcal{W}^{v}_{M}\left(I^{e}_{1\ (\mathrm{M})}, I^{e}_{2\ (\mathrm{M})}, I^{e}_{3\ (\mathrm{M})}\right) + \mathcal{W}^{v}_{F}\left(I^{e}_{4\ (F)}, I^{e}_{5\ (F)}, I^{e}_{6\ (F)}, I^{e}_{7\ (F)}\right) \tag{84}$$

with

$$I_4 = \mathbf{C} : (\boldsymbol{n}_0 \otimes \boldsymbol{n}_0)\,;\ I_5 = \mathbf{C}^2 : (\boldsymbol{n}_0 \otimes \boldsymbol{n}_0)\,;\ I_6 = \mathbf{C} : (\boldsymbol{m}_0 \otimes \boldsymbol{m}_0)\,;\ I_7 = \mathbf{C}^2 : (\boldsymbol{m}_0 \otimes \boldsymbol{m}_0) \tag{85}$$

$$I^{e}_{1(k)} = \mathbf{C}^{e}_{(k)} : \mathbf{I};\ I^{e}_{2(k)} = \frac{1}{2}\left({\mathbf{C}^{e}_{(k)}}^{2} : \mathbf{I} - I^{e}_{1(k)}\right);\ I^{e}_{3(k)} = \text{determinant}\left(\mathbf{C}^{e}_{(k)}\right) \tag{86}$$

$$I^{e}_{4(k)} = \mathbf{C}^{e}_{(k)} : (\boldsymbol{n}_0 \otimes \boldsymbol{n}_0)\,;\ I^{e}_{5(k)} = {\mathbf{C}^{e}_{(k)}}^{2} : (\boldsymbol{n}_0 \otimes \boldsymbol{n}_0)\,;\ I^{e}_{6(k)} = \mathbf{C}^{e}_{(k)} : (\boldsymbol{m}_0 \otimes \boldsymbol{m}_0)\,;\ I^{e}_{7(k)} = \mathbf{C}^{e}_{(k)} \tag{87}$$

where

$$k = matrix \text{ or } fibre \tag{88}$$

Finally, the specific form of the free energy using the decoupled invariants introduced in Sect. 4.3.6 is defined as follows:

$$\psi(\mathbf{C}, \mathbf{C}^v_{matrix}, \mathbf{C}^v_{fibre}, \boldsymbol{n}_0, \boldsymbol{m}_0) = \underbrace{\psi^\infty_M(J) + \sum_{\beta=1}^{2}\left[\psi^\infty_\beta(\overline{\lambda}_\beta, \alpha^\beta_1, \alpha^\beta_2)\right]}_{equilibrium\ part} + \underbrace{\Phi^v_M(J^e) + \sum_{\beta=1}^{2}\left[\Phi^v_\beta(\overline{\lambda}^e_\beta, \alpha^\beta_{1e}, \alpha^\beta_{2e})\right]}_{non-equilibrium\ part} \tag{89}$$

where invariants with superscript/subscript "e" refer to those associated with the *elastic* right Cauchy-Green deformation tensor $\mathbf{C}^e$. The equilibrium part of the free energy is identical to the total elastic energy defined in Eq. (63). The reduced dissipation inequality is:

$$\underbrace{-2\frac{\partial \psi^v_M}{\partial \mathbf{C}^v_{matrix}}}_{\mathbf{S}^v_M} : \frac{1}{2}\dot{\mathbf{C}}^v_{matrix} \underbrace{-2\frac{\partial \psi^v_F}{\partial \mathbf{C}^v_{fibre}}}_{\mathbf{S}^v_F} : \frac{1}{2}\dot{\mathbf{C}}^v_{fibre} \geq 0 \tag{90}$$

where $\mathbf{S}^v_M$ and $\mathbf{S}^v_F$ are the stresses driving the viscous relaxation of the matrix and fibre phases. To satisfy the positive dissipation criterion for the matrix/fibre phase, the following evolution equations are proposed [183, 186]:

$$\frac{1}{2}\dot{\mathbf{C}}^v_{matrix} = \mathbb{V}^{-1}_M : \mathbf{S}^v_M; \qquad \frac{1}{2}\dot{\mathbf{C}}^v_{matrix} = \mathbb{V}^{-1}_M : \mathbf{S}^v_M \tag{91}$$

where $\mathbb{V}^{-1}_M$ and $\mathbb{V}^{-1}_F$ are the inverse of positive definite fourth-order isotropic/anisotropic viscosity tensors for the matrix and fibre phases $\mathbb{V}_M$ and $\mathbb{V}_F$ defined as:

$$\mathbb{V}^{-1}_M = \frac{1}{2\eta_{M_S}}\left(\mathbf{C}^v_{matrix} \odot \mathbf{C}^v_{matrix} - \frac{1}{3}\mathbf{C}^v_{matrix} \otimes \mathbf{C}^v_{matrix}\right) + \frac{1}{9\eta_{M_B}}\mathbf{C}^v_{matrix} \otimes \mathbf{C}^v_{matrix} \tag{92}$$

$$\mathbb{V}_F = \eta_{F_1}\frac{\boldsymbol{n}_0 \otimes \boldsymbol{n}_0}{\mathbf{C}^v_{fibre} : (\boldsymbol{n}_0 \otimes \boldsymbol{n}_0)} \otimes \frac{\boldsymbol{n}_0 \otimes \boldsymbol{n}_0}{\mathbf{C}^v_{fibre} : (\boldsymbol{n}_0 \otimes \boldsymbol{n}_0)} + \eta_{F_2}\frac{\boldsymbol{m}_0 \otimes \boldsymbol{m}_0}{\mathbf{C}^v_{fibre} : (\boldsymbol{m}_0 \otimes \boldsymbol{m}_0)} \otimes \frac{\boldsymbol{m}_0 \otimes \boldsymbol{m}_0}{\mathbf{C}^v_{fibre} : (\boldsymbol{m}_0 \otimes \boldsymbol{m}_0)} \tag{93}$$

where the non-standard tensor product $\odot$ is defined as:

$$(\bullet \odot \circ)_{ijkl} = \left(\bullet \overline{\otimes} \circ + \bullet \underline{\otimes} \circ\right)_{ijkl} = \frac{1}{2}\left(\bullet_{ik}\circ_{jl} + \bullet_{il}\circ_{jk}\right) \tag{94}$$

and η_{M_S} and η_{M_B} are the deviatoric and bulk viscosities of the matrix while η_{F_1} and η_{F_2} are the viscosities associated with the two families of fibres.

Particular non-equilibrium viscous potentials are defined as follows (Limbert, 2014, private communication):

$$\Phi_M^v\left(J^e,\alpha_1^e\right)=\frac{1}{2}\kappa^v\left(J^e-1\right)^2+\frac{1}{2}\mu_M^v\left(\alpha_1^e-2\right) \tag{95}$$

$$\Phi_\beta^v\left(\overline{\lambda}_\beta^e\right)=\frac{1}{2}\mu_\beta^v\left(\overline{\lambda}_\beta^{e\,2}-1\right)^2 \tag{96}$$

κ^v, μ_M^e, μ_1^v and μ_2^v are material parameters that define the properties of the elastic part of the non-equilibrium Maxwell component. This non-linear orthotropic visco-hyperelastic constitutive model was implemented into a commercial finite element code and constitutive parameters were identified from proprietary experimental data.

Flynn and Rubin [188] extended the original Flynn-Rubin's [147] and Flynn-Rubin-Nielsen's [145] formulations to phenomenologically model dissipative effects in soft tissues. They followed the theoretical and numerical approach of Hollenstein et al. [189] which can capture both rate-independent and rate-dependent anelastic response including stress relaxation effects. The model was applied to stress relaxation data of rabbit skin [55] with various degrees of success depending on the magnitude of stretch [188].

4.4.4 Internal Variables Based on Stress Decomposition

Another popular approach for describing the viscous non-linear elasticity of biological soft tissues is to considers a set of non-measurable (i.e. internal variable) strain-like internal variables $\mathbf{E}_k$ in the reference configuration, the free energy of a viscoelastic material can be defined as follows [86]:

$$\psi\left(\mathbf{C},\mathbf{E}_k\right)=\psi^{equilibrium}\left(\mathbf{C}\right)+\sum_{k=1}^{n}\psi_k^{n.equilibrium}\left(\mathbf{C},\mathbf{E}_k\right) \tag{97}$$

where, in analogy with Eq. (77), the free energy (and stress) can be split into equilibrium and non-equilibrium contributions associated respectively with elastic and viscous deformation mechanisms:

$$\mathbf{S}=\mathbf{S}^{equilibrium}+\sum_{k=1}^{n}\mathbf{Q}_k^{n.equilibrium} \tag{98}$$

The over-stress $\mathbf{Q}_k^{n.equilibrium}$ are work-conjugate to $\mathbf{E}_k$. Drawing a parallel with rheological elements of linear viscoelasticity, and instead of formulating evolution equations for the strain-like variables $\mathbf{E}_k$, one can formulate rate equations in terms of the stress-like internal variables $\mathbf{Q}_k^{n.equilibrium}$. These equations can be solved by means of convolution integrals [183, 190]. Using a multi-modal Maxwell

element rheological analogy, this type of formulation was applied by Holzapfel and Gasser [190] to model the viscoelastic orthotropic behavior of arteries. Peña et al. [191, 192] developed a similar approach to model the ligaments of the knee but conceptually used a combination of Kelvin-Voigt elements. Ehret et al. [193] proposed a microstructurally-motivated finite strain viscoelastic model for soft tissues which is very relevant for skin mechanics. Gasser and Forsell [194] developed a finite strain viscoelastic framework using an elastic and Maxwell body configurations which respectively correspond to an elastic and viscous phase. The model was motivated by the desire to gain an insight into the passive mechanics of the myocardium tissue during pacing lead perforation. The non-equilibrium energy in Eq. (97) could have been equivalently defined in terms of internal stress-like variables $\mathbf{Q}_k^{n.equilibrium}$ as proposed by Simo [195]. Only in special cases, the approach based on the multiplicative decomposition of the deformation gradient is consistent with the one based on convolution integrals [195].

4.5 Softening and Damage

Preconditioning effects are often associated with viscoelasticity [9]. They are linked to short-term rearrangement of the tissue microstructure and, in some instances, permanent deformation and/or damage of the microstructure. Preconditioning of biological soft tissues before in vitro tensile tests is often recommended. On one hand, it is a way to re-load the tissue into a state closer to in vivo conditions, on the other hand, depending on the amount of pre-conditioning, this could lead to microstructural rearrangements going beyond what would be physiologically experienced by the tissue. Muñoz et al. [196] observed a typical softening effect—known as the Mullins effect in the context of filled rubber mechanics—during cyclic uniaxial testing of murine skin at large deformations. A similar effect was reported by Edsberg et al. [197] for human skin under cyclic pressures. Ehret and Itskov [198] developed a constitutive framework to capture the Mullins effects observed in biological soft tissues and fitted it to the experimental data of Muñoz et al. [196] demonstrating an excellent agreement. Ehret et al. [199] later applied their constitutive model to porcine dermis and corroborated observations made by Muñoz et al., namely the occurrence of significant residual deformations upon cycling loading. Recently, Li and Luo [80] proposed an invariant-based softening damage and failure constitutive model for human and animal skins. The nine-parameter model is based on a combination of the GOH model [94] and the energy-limiter approach of Volokh [200, 201]. The performance of the model was tested on a series of orthogonal uniaxial tensile tests on human, swine, bovine and rabbit skins and exhibited excellent results.

The main drawback of the model is its conservative nature: upon unloading the material would fully recover its original shape and return to its virgin undamaged state, effectively healing. This shortcoming could easily be rectified [202].

Considering its soft interfacial and protective nature, it is reasonable to assume that, at an evolutionary level, the skin of mammals in general, and that of humans, in particular, must have evolved damage resistance strategies through optimisation of their ultrastructure. Recently, Yang et al. [156] have discovered four microstructural mechanisms that explain the extreme tear resistance of rabbit skin by conducting a very comprehensive multi-modality study (see Sect. 4.3.8).

4.6 Plasticity

Mazza et al. [203, 204] developed a non-linear elasto-visco-plastic model to simulate ageing of the human face [203, 204]. It is based on the constitutive formulation of Rubin and Bodner [205] to model the dissipative response of soft tissues. In this study the dissipative effects were a combination of elastic and visco-plastic mechanisms. Rubin and Bodner [205] demonstrated the relevance of their model by capturing very well the cyclic dissipative response of superficial musculoaponeurotic system tissue. The constitutive equations were implemented as a user subroutine in the commercial finite element code Abaqus (Simulia, Dassault Systèmes, Providence, RI, USA) to simulate gravimetric descent of facial tissue [203]. Mazza et al. [203, 204] extended the model of Rubin and Bodner [205] by including an ageing parameter equipped with its own time evolution equation. This ageing-driven parameter was a modulator of tissue. A four-layer model of facial skin combined with a face-like geometrical base was developed and highlighted the great potential of this kind of computational models to study the effects of skin ageing on facial appearance. The Rubin and Bodner's constitutive model [205] was generalised by Weickenmeier and Jabareen [79], in terms of the viscoplasticity equations and hardening parameter, whilst establishing a robust finite element framework featuring a strongly objective integration scheme. In this paper, this modelling framework was applied to identify the mechanical properties of facial skin by combining suction measurements obtained via a Cutometer® MPA 580 (Courage and Khazaka Electronic GmbH, Köln, Germany) and inverse finite element techniques. The procedure is described in more details in a subsequent paper by Weickenmeier et al. [48]. With regard to the anelastic behaviour of skin, recent work from Prof. Mazza's group highlighted the location dependence of facial tissue mechanical response using a combination of cutometry tests and ultrasound measurement of tissue thickness [49]. They observed a more pronounced creep behaviour in the forehead compared to the jaw and parotid as well as a lack of positive correlation between skin thickness and tissue stiffness. From this later observation they suggested that the interplay of the mechanics of collagen fibres and fluid motion could be a significant factor.

5 Conclusion

This review has covered what appears to be the largest collection of constitutive models of skin mechanics which, and of particular significance, are all valid for finite deformations. Over the last few decades, researchers have demonstrated creative ingenuity in progressively incorporating important microstructural information and physical mechanisms into continuum constitutive models. These models have now reached a high level of sophistication, and can capture a wide range of relevant biophysical features. Most of them have been implemented in commercial and/or commercial finite element codes so that large-scale computer experiments could be conducted. Nevertheless, as very rightly pointed out by Jor et al. [6] in their review paper on the computational and experimental characterisation of skin, a significant limiting factor in the development and adoption of advanced constitutive theories is the scarcity and relevance of captured experimental data. Models are as good as the quality and statistical significance of the experimental data that feed them. Practical, economical and ethical reasons typically limit the scope and scale of physical characterisation experiments. These constraints are in direct conflict with many aspects associated with skin biology and biophysics, namely a large intra- and inter-individual variability of biophysical properties, an extreme sensitivity of the skin to environmental conditions and the fact that the in vivo and ex vivo biophysical environments of the skin are fundamentally different. Moreover, the question of how to best integrate multi-modality/multiscale imaging and characterisation data together with modelling techniques naturally arises. Intra-individually, the skin is a complex heterogeneous adaptive structure which varies according to body location, health status and history, diet, age, lifestyle, *external* environmental conditions (e.g. temperature, humidity, pollution level, water quality, sun exposure, contact with external surfaces) and *internal* environmental conditions (e.g. hormones, pregnancy, water and glucose levels, tension lines). Besides intra-individual variability, there is a significant source of variability, particularly that associated with sex, age and ethnicity. There are therefore formidable challenges in *representatively* characterising the skin ultrastructure as well as its biophysical properties.

Should the skin be described as an individual-specific system, or rather, as a statistical system describing particular populations? Or, perhaps, as a combination of both? This issue is, of course, not unique to the skin, but pervasive throughout many biological tissues and organs. These questions are of particular relevance in many practical applications concerned with skin mechanics, for example, pre-operative surgical planning where one would want to have access to generic robust tissue models (and fast modelling techniques) whilst also accounting for patient-specific data (e.g. age and ethnicity-dependent mechanical properties) and considering patient-specific intervention.

Recent approaches following this line of thought have been applied in soft tissue [206] and skin mechanics [207] whereby variability is accounted for, and

uncertainties arising from this variability, propagated through to the resulting mechanical response.

The reliance of structural and structurally-based phenomenological models on accurate descriptions of the skin ultrastructure and the associated mechanical properties of its sub-components, means that imaging and characterisation techniques needs to span multiple spatial and temporal scales if one wants to capture more reliably the complex biophysics of the skin. Additionally, and as a corollary to that, multiscale modelling techniques must be developed in concert with these physical experimental protocols. This approach has the necessary advantage of avoiding the "*post mortem* analysis" of data [208], particularly, if one considers "big data". Said otherwise, the focus should be on *relevant* not *big* data where a lot of potentially useless information is collected, and, more importantly, where relevant data might not be collected.

Computational multiscale methods combining atomistic, molecular and continuum techniques are increasingly becoming common place in the modelling of skin biophysics [58, 209, 210], whether it is within an academic or industrial context. Moreover, integration of imaging and physical testing (i.e. in situ imaging) [211] is a very promising approach that should be followed, as much can be learnt about microstructural mechanisms under real loading conditions [6] (see also chapter "Multiscale Characterisation of Skin Mechanics Through In situ Imaging").

Perhaps, in the same way that statistical information is currently being integrated into constitutive models (e.g. fibre dispersion, degree of crimp of collagen fibres), additional stochastic elements could be added into constitutive equations effectively developing what could be termed *stochastic partial differential equations* [212]. This would be another approach to encompass variability, directly into the constitutive equations, rather than at the input data level when conducting probabilistic simulations. Stochastic finite element techniques based on perturbation theory [213] offer interesting alternatives to computationally-intensive Monte-Carlo simulations to compute the statistical response of biological tissues featuring stochastic fields (e.g. material properties, geometrical heterogeneities).

As currently witnessed in the computational mechanics community [214, 215], data mining and machine learning techniques [216] are likely to play an increasing role in the future to make sense of large and complex heterogeneous data sets, whether they originate from physical or computer experiments, expert knowledge (e.g. anatomists, clinicians, nurses, vets) or from any other means (e.g. patient's observations or traditional knowledge). Building upon these techniques, the development and adoption of data-driven model-free simulations are to be closely monitored as these paradigm-shifting scientific methods could make a huge impact in skin science in the very near future.

Acknowledgements/Funding Statement The author would like to gratefully acknowledge the financial support he has received over the last few years to support research on skin biophysics and applications from the Royal Society, The Royal Academy of Engineering, The British High Commission in South Africa, EPSRC, Procter & Gamble, L'Oréal, Roche and the US Air Force.

He would also like to thank Dr. Anton Page of the Biomedical Imaging Unit at the University of Southampton and Mr. Sandy Monteith of Gatan UK for respectively preparing the skin sample for serial block-face imaging and for organising the electron microscopy acquisition at Gatan USA in San Diego.

References

1. Burns T et al (2004) Rook's textbook of dermatology, 7th edn. Blackwell Science, Oxford
2. Silver FH, Siperko LM, Seehra GP (2003) Mechanobiology of force transduction in dermal tissue. Skin Res Technol 9(1):3–23
3. Dandekar K, Raju BI, Srinivasan MA (2003) 3-D finite-element models of human and monkey fingertips to investigate the mechanics of tactile sense. J Biomech Eng-Trans ASME 125(5):682–691
4. Xu F, Lu T (2011) Introduction to skin biothermomechanics and thermal pain. Springer, Heidelberg, p 414
5. Limbert G (2017) Mathematical and computational modelling of skin biophysics – a review. Proc R Soc A Math Phys Eng Sci 473(2203):1–39
6. Jor JWY et al (2013) Computational and experimental characterization of skin mechanics: identifying current challenges and future directions. Wiley Interdiscip Rev Syst Biol Med 5(5):539–556
7. Benítez JM, Montáns FJ (2017) The mechanical behavior of skin: structures and models for the finite element analysis. Comput Struct 190:75–107
8. Li W (2015) Modelling methods for in vitro biomechanical properties of the skin: a review. Biomed Eng Lett 5(4):241–250
9. Fung YC (1981) Biomechanics: mechanical properties of living tissues. Springer, New York
10. Humphrey JD (2003) Continuum biomechanics of soft biological tissues. Proc R Soci A Math Phys Eng Sci 459(2029):3–46
11. Lanir Y (2016) Multi-scale structural modeling of soft tissues mechanics and mechanobiology. J Elast 129(1–2):7–48
12. Hamed J, Matthew BP (2018) Skin mechanical properties and modeling: a review. Proc Inst Mech Eng Part H J Eng Med 232:323–343. https://doi.org/10.1177/0954411918759801
13. Shimizu H (2007) Shimizu's textbook of dermatology. Hokkaido University Press - Nakayama Shoten, Sapporo, p 564
14. Buganza Tepole A, Kuhl E (2014) Computational modeling of chemo-bio-mechanical coupling: a systems-biology approach toward wound healing. Comput Methods Biomech Biomed Eng 19:13–30
15. Kvistedal YA, Nielsen PMF (2009) Estimating material parameters of human skin in vivo. Biomech Model Mechanobiol 8(1):1–8
16. Lanir Y (1987) Skin mechanics. In: Skalak R, Chien S (eds) Handbook of bioengineering. McGraw-Hill, New York
17. Vierkötter A, Krutmann J (2012) Environmental influences on skin aging and ethnic-specific manifestations. Dermato-endocrinol 4(3):227–231
18. Silver FH, Freeman JW, DeVore D (2001) Viscoelastic properties of human skin and processed dermis. Skin Res Technol 7(1):18–23
19. Limbert G (2014) State-of-the-art constitutive models of skin biomechanics. In: Querleux B (ed) Computational biophysics of the skin. Pan Stanford, Singapore, pp 95–131
20. Marieb EN, Hoehn K (2010) Human anatomy & physiology, 8th edn. Pearson International Edition, San Francisco, p 1114
21. Chan LS (1997) Human skin basement membrane in health and autoimmune diseases. Front Biosci 2:343–352

22. Leyva-Mendivil MF et al (2015) A mechanistic insight into the mechanical role of the stratum corneum during stretching and compression of the skin. J Mech Behav Biomed Mater 49(0):197–219
23. Leyva-Mendivil MF et al (2017) Skin microstructure is a key contributor to its friction behaviour. Tribol Lett 65(1):12
24. Biniek K, Levi K, Dauskardt RH (2012) Solar UV radiation reduces the barrier function of human skin. Proc Natl Acad Sci USA 109(42):17111–17116
25. Wu KS, van Osdol WW, Dauskardt RH (2006) Mechanical properties of human stratum corneum: effects of temperature, hydration, and chemical treatment. Biomaterials 27(5):785–795
26. Ciarletta P, Ben Amar M (2012) Papillary networks in the dermal-epidermal junction of skin: a biomechanical model. Mech Res Commun 42:68–76
27. Burgeson RE, Christiano AM (1997) The dermal-epidermal junction. Curr Opin Cell Biol 9:651–658
28. Ribeiro JF et al (2013) Skin collagen fiber molecular order: a pattern of distributional fiber orientation as assessed by optical anisotropy and image analysis. PLoS One 8(1):e54724
29. Gosline J et al (2002) Elastic proteins: biological roles and mechanical properties. Philos Trans R Soc Lond B Biol Sci 357(1418):121–132
30. Sherratt MJ (2013) Age-related tissue stiffening: cause and effect. Adv Wound Care 2(1):11–17
31. Langer K (1861) Zur Anatomie und Physiologie der Haut. Über die Spaltbarkeit der Cutis. Sitzungsbericht der Mathematisch-naturwissenschaftlichen Classe der Wiener Kaiserlichen Academie der Wissenschaften Abt, p 44
32. Langer K (1978) On the anatomy and physiology of the skin: I. The cleavability of the cutis. Br J Plast Surg 31(1):3–8
33. Langer K (1978) On the anatomy and physiology of the skin: II. Skin tension (with 1 figure). Br J Plast Surg 31(2):93–106
34. Ní Annaidh A et al (2011) Characterization of the anisotropic mechanical properties of excised human skin. J Mech Behav Biomed Mater 5(1):139–148
35. Alexander H, Cook TH (1977) Accounting for natural tension in the mechanical testing of human skin. J Invest Dermatol 69:310–314
36. Flynn C, Stavness I, Lloyd J, Fels S (2015) A finite element model of the face including an orthotropic skin model under in vivo tension. Comput Methods Biomech Biomed Eng 18:571–582. https://doi.org/10.1080/10255842.2013.820720
37. Deroy C et al (2016) Non-invasive evaluation of skin tension lines with elastic waves. Skin Res Technol 23:326–335
38. Rosado C et al (2016) About the in vivo quantitation of skin anisotropy. Skin Res Technol 23:429–436. https://doi.org/10.1111/srt.12353
39. Wan Abas WAB (1994) Biaxial tension test of human skin in vivo. Biomed Mater Eng 4:473–486
40. Ní Annaidh A et al (2012) Automated estimation of collagen fibre dispersion in the dermis and its contribution to the anisotropic behaviour of skin. Ann Biomed Eng 40(8):1666–1678
41. Ottenio M et al (2015) Strain rate and anisotropy effects on the tensile failure characteristics of human skin. J Mech Behav Biomed Mater 41:241–250
42. Kvistedal YA, Nielsen PMF (2004) Investigating stress-strain properties of in-vivo human skin using multiaxial loading experiments and finite element modeling. In: Proceedings of the 26th annual international conference of the IEEE engineering in medicine and biology society, vols 1–7, 26, pp 5096–5099
43. Batisse D et al (2002) Influence of age on the wrinkling capacities of skin. Skin Res Technol 8(3):148–154
44. Delalleau A et al (2006) Characterization of the mechanical properties of skin by inverse analysis combined with the indentation test. J Biomech 39:1603–1610
45. Diridollou S et al (2000) In vivo model of the mechanical properties of the human skin under suction. Skin Res Technol 6(4):214–221

46. Dobrev Hq (2000) Use of Cutometer to assess epidermal hydration. Skin Res Technol 6(4):239–244
47. Hendriks FM et al (2003) A numerical-experimental method to characterize the non-linear mechanical behaviour of human skin. Skin Res Technol 9(3):274–283
48. Weickenmeier J, Jabareen M, Mazza E (2015) Suction based mechanical characterization of superficial facial soft tissues. J Biomech 48(16):4279–4286
49. Pensalfini M et al (2018) Location-specific mechanical response and morphology of facial soft tissues. J Mech Behav Biomed Mater 78(Suppl C):108–115
50. Müller B et al (2018) A novel ultra-light suction device for mechanical characterization of skin. PLoS One 13(8):e0201440
51. Tonge TK et al (2013) Full-field bulge test for planar anisotropic tissues: Part I – Experimental methods applied to human skin tissue. Acta Biomater 9(4):5913–5925
52. Geerligs M et al (2011) Linear shear response of the upper skin layers. Biorheology 48(3–4):229–245
53. Geerligs M et al (2011) In vitro indentation to determine the mechanical properties of epidermis. J Biomech 44:1176–1181
54. Lamers E et al (2013) Large amplitude oscillatory shear properties of human skin. J Mech Behav Biomed Mater 28:462–470
55. Lanir Y, Fung YC (1974) Two-dimensional mechanical properties of rabbit skin—II: Experimental results. J Biomech 7:171–182
56. Wong WLE, Joyce TJ, Goh KL (2016) Resolving the viscoelasticity and anisotropy dependence of the mechanical properties of skin from a porcine model. Biomech Model Mechanobiol 15(2):433–446
57. Veronda DR, Westmann R (1970) Mechanical characterization of skin – finite deformations. J Biomech 3:111–124
58. Marino M (2016) Molecular and intermolecular effects in collagen fibril mechanics: a multiscale analytical model compared with atomistic and experimental studies. Biomech Model Mechanobiol 15(1):133–154
59. Spencer AJM (1984) Constitutive theory for strongly anisotropic solids. In: Spencer AJM (ed) Continuum theory of the mechanics of fibre-reinforced composites. Springer, Vienna, pp 1–32
60. Šolinc U, Korelc J (2015) A simple way to improved formulation of FE^2 analysis. Comput Mech 56(5):905–915
61. Saeb S, Steinmann P, Javili A (2016) Aspects of computational homogenization at finite deformations: a unifying review from Reuss' to Voigt's bound. Appl Mech Rev 68(5):050801–050801-33
62. Leyva-Mendivil MF et al (2017) Implications of multi-asperity contact for shear stress distribution in the viable epidermis – an image-based finite element study. Biotribology 11:110–123
63. Young PG et al (2008) An efficient approach to converting three-dimensional image data into highly accurate computational models. Philos Trans R Soc A Math Phys Eng Sci 366(1878):3155–3173
64. Limbert G et al (2010) Trabecular bone strains around a dental implant and associated micromotions—a micro-CT-based three-dimensional finite element study. J Biomech 43(7):1251–1261
65. Linder-Ganz E et al (2007) Assessment of mechanical conditions in sub-dermal tissues during sitting: a combined experimental-MRI and finite element approach. J Biomech 40(7):1443–1454
66. Limbert G et al (2013) On the mechanics of bacterial biofilms on non-dissolvable surgical sutures: a laser scanning confocal microscopy-based finite element study. Acta Biomater 9(5):6641–6652
67. Leyva-Mendivil MF, Lengiewicz J, Limbert G (2017) Skin friction under pressure. The role of micromechanics. Surf Topogr: Metrol Prop 6:014001

68. Limbert G, Kuhl E (2018) On skin microrelief and the emergence of expression microwrinkles. Soft Matter 14(8):1292–1300
69. Limbert G (2018) Investigating the influence of relative humidity on expression microwrinkles. J Aesthet Nurs 7(4):204–207
70. Gerhardt LC et al (2008) Influence of epidermal hydration on the friction of human skin against textiles. J R Soc Interface 5(28):1317–1328
71. Adams MJ, Briscoe BJ, Johnson SA (2007) Friction and lubrication of human skin. Tribol Lett 26(3):239–253
72. Derler S et al (2009) Friction of human skin against smooth and rough glass as a function of the contact pressure. Tribol Int 42(11–12):1565–1574
73. Kwiatkowska M et al (2009) Friction and deformation behaviour of human skin. Wear 267(5–8):1264–1273
74. Wolfram LJ (1983) Friction of skin. J Soc Cosmet Chem 34:465–476
75. Stupkiewicz S, Lewandowski MJ, Lengiewicz J (2014) Micromechanical analysis of friction anisotropy in rough elastic contacts. Int J Solids Struct 51(23–24):3931–3943
76. Goldstein B, Sanders J (1998) Skin response to repetitive mechanical stress: a new experimental model in pig. Arch Phys Med Rehabil 79(3):265–272
77. Budday S, Kuhl E, Hutchinson JW (2015) Period-doubling and period-tripling in growing bilayered systems. Philos Mag(Abingdon) 95(28–30):3208–3224
78. Cao Y, Hutchinson JW (2012) From wrinkles to creases in elastomers: the instability and imperfection-sensitivity of wrinkling. Proc R Soc A Math Phys Eng Sci 468:94–115
79. Weickenmeier J, Jabareen M (2014) Elastic–viscoplastic modeling of soft biological tissues using a mixed finite element formulation based on the relative deformation gradient. Int J Numer Methods Biomed Eng 30(11):1238–1262
80. Li W, Luo XY (2016) An invariant-based damage model for human and animal skins. Ann Biomed Eng 44(10):3109–3122
81. Buganza Tepole A et al (2011) Growing skin: a computational model for skin expansion in reconstructive surgery. J Mech Phys Solids 59(10):2177–2190
82. Vermolen FJ, Gefen A, Dunlop JWC (2012) In vitro "wound" healing: experimentally based phenomenological modeling. Adv Eng Mater 14(3):B76–B88
83. Sherratt JA, Dallon JC (2002) Theoretical models of wound healing: past successes and future challenges. C R Biol 325(5):557–564
84. Buganza Tepole A (2017) Computational systems mechanobiology of wound healing. Comput Methods Appl Mech Eng 314:46–70
85. Marsden JE, Hughes TJR (1994) Mathematical foundations of elasticity. Dover, New York, p 556
86. Holzapfel GA (2000) Nonlinear solid mechanics. A continuum approach for engineering. Wiley, Chichester, p 470
87. Boehler L (1978) de comportement anisotrope des milieux continus. J Méc 17(2):153–190
88. Limbert G, Taylor M (2002) On the constitutive modeling of biological soft connective tissues. A general theoretical framework and tensors of elasticity for strongly anisotropic fiber-reinforced composites at finite strain. Int J Solids Struct 39(8):2343–2358
89. Spencer AJM (1992) Continuum theory of the mechanics of fibre-reinforced composites. Springer, New York
90. Criscione JC et al (2000) An invariant basis for natural strain which yields orthogonal stress response terms in isotropic hyperelasticity. J Mech Phys Solids 48(12):2445–2465
91. Criscione JC, Douglas AS, Hunter WC (2001) Physically based strain invariant set for materials exhibiting transversely isotropic behavior. J Mech Phys Solids 49(4):871–897
92. Holzapfel GA, Ogden RW (2016) On fiber dispersion models: exclusion of compressed fibers and spurious model comparisons. J Elast 129(1–2):49–68
93. Lanir Y (1983) Constitutive equations for fibrous connective tissues. J Biomech 16(1):1–22
94. Gasser TC, Ogden RW, Holzapfel GA (2006) Hyperelastic modelling of arterial layers with distributed collagen fibre orientations. J R Soc Interface 3(6):15–35

95. Li K, Ogden RW, Holzapfel GA (2018) A discrete fibre dispersion method for excluding fibres under compression in the modelling of fibrous tissues. J R Soc Interface 15(138)
96. Li K, Ogden RW, Holzapfel GA (2018) Modeling fibrous biological tissues with a general invariant that excludes compressed fibers. J Mech Phys Solids 110:38–53
97. Alastrué V et al (2009) Anisotropic micro-sphere-based finite elasticity applied to blood vessel modelling. J Mech Phys Solids 57(1):178–203
98. Holzapfel GA et al (2015) Modelling non-symmetric collagen fibre dispersion in arterial walls. J R Soc Interface 12(106)
99. Sáez P et al (2012) Anisotropic microsphere-based approach to damage in soft fibered tissue. Biomech Model Mechanobiol 11(5):595–608
100. Ogden RW (2016) Nonlinear continuum mechanics and modelling the elasticity of soft biological tissues with a focus on artery walls. In: Holzapfel GA, Ogden RW (eds) Lecture notes from the summer school "Biomechanics: trends in modeling and simulation, September, 2014, Graz. Springer, Heidelberg
101. Winitzki S (2003) Uniform approximations for transcendental functions. In: Kumar V et al (eds) Computational science and its applications—ICCSA 2003: Proceedings of international conference, Part I, Montreal, 18–21 May 2003. Springer, pp 780–789
102. Ogden RW (1984) Non-linear elastic deformations. Ellis Horwood, West Sussex
103. Jansen LH, Rottier PB (1958) Some mechanical properties of human abdominal skin measured on excised strips: a study of their dependence on age and how they are influenced by the presence of striae. Dermatologica 117:65–83
104. Shergold OA, Fleck NA, Radford D (2006) The uniaxial stress versus strain response of pig skin and silicone rubber at low and high strain rates. Int J Impact Eng 32(9):1384–1402
105. Delalleau A et al (2008) A nonlinear elastic behavior to identify the mechanical parameters of human skin in vivo. Skin Res Technol 14(2):152–164
106. Lapeer RJ, Gasson PD, Karri V (2010) Simulating plastic surgery: from human skin tensile tests, through hyperelastic finite element models to real-time haptics. Prog Biophys Mol Biol 103(2–3):208–216
107. Yeoh OH (1993) Some forms of the strain energy function for rubber. Rubber Chem Technol 66(5):754–771
108. Ogden RW (1972) Large deformation isotropic elasticity – correlation of theory and experiment for compressible rubberlike solids. Proc R Soc Lond A Math Phys Sci 328(1575):567
109. Ogden RW (1972) Large deformation isotropic elasticity – correlation of theory and experiment for incompressible rubberlike solids. Proc R Soc Lond A Math Phys Sci 326(1567):565
110. Shergold OA, Fleck NA (2004) Mechanisms of deep penetration of soft solids, with application to the injection and wounding of skin. Proc R Soc A Math Phys Eng Sci 460(2050):3037–3058
111. Lim J et al (2011) Mechanical response of pig skin under dynamic tensile loading. Int J Impact Eng 38(2):130–135
112. Evans SL, Holt CA (2009) Measuring the mechanical properties of human skin in vivo using digital image correlation and finite element modelling. J Strain Anal Eng Des 44(5):337–345
113. Flynn C, Taberner A, Nielsen P (2011) Modeling the mechanical response of in vivo human skin under a rich set of deformations. Ann Biomed Eng 39(7):1935–1946
114. Flynn C et al (2013) Simulating the three-dimensional deformation of in vivo facial skin. J Mech Behav Biomed Mater 28(0):484–494
115. Flory PJ (1969) Statistical mechanics of chain molecules. Wiley, Chichester
116. Kuhl E et al (2005) Remodeling of biological tissue: mechanically induced reorientation of a transversely isotropic chain network. J Mech Phys Solids 53:1552–1573
117. Kratky O, Porod G (1949) Röntgenuntersuchungen gelöster Fadenmoleküle. Recl Trav Chim Pays-Bas Belg 68:1106–1122
118. Bischoff JE, Arruda EA, Grosh K (2002) A microstructurally based orthotropic hyperelastic constitutive law. J Appl Mech Trans ASME 69(5):570–579
119. Bischoff JE, Arruda EM, Grosh K (2004) A rheological network model for the continuum anisotropic and viscoelastic behavior of soft tissue. Biomech Model Mechanobiol 3(1): 56–65

120. Garikipati K et al (2004) A continuum treatment of growth in biological tissue: the coupling of mass transport and mechanics. J Mech Phys Solids 52(7):1595–1625
121. Flynn C, McCormack BAO (2008) A simplified model of scar contraction. J Biomech 41(7):1582–1589
122. Flynn CO, McCormack BAO (2009) A three-layer model of skin and its application in simulating wrinkling. Comput Methods Biomech Biomed Engin 12(2):125–134
123. Kuhl E, Holzapfel GA (2007) A continuum model for remodeling in living structures. J Mater Sci 42(21):8811–8823
124. Kuhn W (1936) Beziehungen zwischen Molekühlgrösse, statistischer Molekülgestalt und elastischen Eigenschaften hochpolymerer Stoffe. Kolloid Z 76:258–271
125. Arruda EM, Boyce MC (1993) A three-dimensional constitutive model for the large stretch behavior of rubber elastic-materials. J Mech Phys Solids 41(2):389–412
126. Cohen A (1991) A Padé approximant to the inverse Langevin function. Rheol Acta 30(3):270–273
127. Nguessong AN, Beda T, Peyraut F (2014) A new based error approach to approximate the inverse langevin function. Rheol Acta 53(8):585–591
128. Jedynak R (2015) Approximation of the inverse Langevin function revisited. Rheol Acta 54(1):29–39
129. Marchi BC, Arruda EM (2015) An error-minimizing approach to inverse Langevin approximations. Rheol Acta 54(11):887–902
130. Darabi E, Itskov M (2015) A simple and accurate approximation of the inverse Langevin function. Rheol Acta 54(5):455–459
131. Bischoff JE, Arruda EM, Grosh K (2000) Finite element modeling of human skin using an isotropic, nonlinear elastic constitutive model. J Biomech 33(6):645–652
132. Dunn MG, Silver FH, Swann DA (1985) Mechanical analysis of hypertrophic scar tissue: structural basis for apparent increased rigidity. J Invest Dermatol 84(1):9–13
133. Belkoff SM, Haut RC (1991) A structural model used to evaluate the changing microstructure of maturing rat skin. J Biomech 24(8):711–720
134. Gunner CW, Hutton WC, Burlin TE (1979) The mechanical properties of skin in vivo—a portable hand-held extensometer. Br J Dermatol 100(2):161–163
135. Meijer R, Douven LFA, Oomens CWJ (1999) Characterisation of anisotropic and non-linear behaviour of human skin in vivo. Comput Methods Biomech Biomed Eng 2(1):13–27
136. Jor JWY et al (2011) Estimating material parameters of a structurally based constitutive relation for skin mechanics. Biomech Model Mechanobiol 10(5):767–778
137. Flynn C, McCormack BAO (2008) Finite element modelling of forearm skin wrinkling. Skin Res Technol 14(3):261–269
138. Flynn CO, McCormack BAO (2010) Simulating the wrinkling and aging of skin with a multilayer finite element model. J Biomech 43(3):442–448
139. Limbert G, Middleton J (2005) A polyconvex anisotropic strain energy function. Application to soft tissue mechanics. In: ASME summer bioengineering conference, Vail
140. Itskov M, Ehret AE, Mavrilas D (2006) A polyconvex anisotropic strain-energy function for soft collagenous tissues. Biomech Model Mechanobiol 5(1):17–26
141. Itskov M, Aksel N (2004) A class of orthotropic and transversely isotropic hyperelastic constitutive models based on a polyconvex strain energy function. Int J Solids Struct 41(14):3833–3848
142. Holzapfel GA, Gasser TC, Ogden RW (2000) A new constitutive framework for arterial wall mechanics and a comparative study of material models. J Elast 61:1–48
143. Tonge TK, Voo LM, Nguyen TD (2013) Full-field bulge test for planar anisotropic tissues: Part II – A thin shell method for determining material parameters and comparison of two distributed fiber modeling approaches. Acta Biomater 9(4):5926–5942
144. Buganza Tepole A, Gosain AK, Kuhl E (2014) Computational modeling of skin: using stress profiles as predictor for tissue necrosis in reconstructive surgery. Comput Struct 143:32–39
145. Flynn C, Rubin MB, Nielsen P (2011) A model for the anisotropic response of fibrous soft tissues using six discrete fibre bundles. Int J Numer Methods Biomed Eng 27(11):1793–1811

146. Ankersen J et al (1999) Puncture resistance and tensile strength of skin simulants. Proc Inst Mech Eng Part H J Eng Med 213(H6):493–501
147. Flynn C, Rubin MB (2012) An anisotropic discrete fibre model based on a generalised strain invariant with application to soft biological tissues. Int J Eng Sci 60:66–76
148. Limbert G (2011) A mesostructurally-based anisotropic continuum model for biological soft tissues—decoupled invariant formulation. J Mech Behav Biomed Mater 4(8):1637–1657
149. Bischoff JE, Arruda EM, Grosh K (2002) Finite element simulations of orthotropic hyperelasticity. Finite Elem Anal Des 38(10):983–998
150. Lu J, Zhang L (2005) Physically motivated invariant formulation for transversely isotropic hyperelasticity. Int J Solids Struct 42(23):6015–6031
151. Korelc J, Šolinc U, Wriggers P (2010) An improved EAS brick element for finite deformation. Comput Mech 46(4):641–659
152. Gautieri A et al (2011) Hierarchical structure and nanomechanics of collagen microfibrils from the atomic scale up. Nano Lett 11:757–766
153. Sun YL et al (2002) Direct quantification of the flexibility of type I collagen monomer. Biochem Biophys Res Commun 295(2):382–386
154. Groves RB et al (2013) An anisotropic, hyperelastic model for skin: experimental measurements, finite element modelling and identification of parameters for human and murine skin. J Mech Behav Biomed Mater 18(0):167–180
155. Weiss JA, Maker BN, Govindjee S (1996) Finite element implementation of incompressible transversely isotropic hyperelasticity. Comput Methods Appl Mech Eng 135:107–128
156. Yang W et al (2015) On the tear resistance of skin. Nat Commun 6:6649
157. Sherman VR, Yang W, Meyers MA (2015) The materials science of collagen. J Mech Behav Biomed Mater 52:22–50
158. Sherman VR et al (2017) Structural characterization and viscoelastic constitutive modeling of skin. Acta Biomater 53:460–469
159. Wang S et al (2012) Mechanics of epidermal electronics. J Appl Mech 79(3):031022–031022
160. Barbenel JC, Evans JH (1973) The time-dependent mechanical properties of skin. J Invest Dermatol 69(3):165–172
161. Pereira JM, Mansour JM, Davis BR (1990) Analysis of shear-wave propagation in skin – application to an experimental procedure. J Biomech 23(8):745–751
162. Pereira JM, Mansour JM, Davis BR (1991) Dynamic measurement of the viscoelastic properties of skin. J Biomech 24(2):157–162
163. Lanir Y (1979) The rheological behavior of the skin: experimental results and a structural model. Biorheology 16:191–202
164. Wu JZ et al (2006) Estimation of the viscous properties of skin and subcutaneous tissue in uniaxial stress relaxation tests. Biomed Mater Eng 16(1):53–66
165. Khatyr F et al (2004) Model of the viscoelastic behaviour of skin in vivo and study of anisotropy. Skin Res Technol 10(2):96–103
166. Boyer G et al (2009) Dynamic indentation on human skin in vivo: ageing effects. Skin Res Technol 15(1):55–67
167. Boyer G et al (2007) In vivo characterization of viscoelastic properties of human skin using dynamic micro-indentation. Annu Int Conf IEEE Eng Med Biol Soc 1–16:4584–4587
168. Goh KL, Listrat A, Béchet D (2014) Hierarchical mechanics of connective tissues: integrating insights from nano to macroscopic studies. J Biomed Nanotechnol 10(10):2464–2507
169. Redaelli A et al (2003) Possible role of decorin glycosaminoglycans in fibril to fibril force transfer in relative mature tendons—a computational study from molecular to microstructural level. J Biomech 36(10):1555–1569
170. Kearney SP et al (2015) Dynamic viscoelastic models of human skin using optical elastography. Phys Med Biol 60(17):6975–6990
171. Lokshin O, Lanir Y (2009) Viscoelasticity and preconditioning of rat skin under uniaxial stretch: microstructural constitutive characterization. J Biomech Eng 131(3):031009–031010
172. Lokshin O, Lanir Y (2009) Micro and macro rheology of planar tissues. Biomaterials 30(17):3118–3127

173. Fung YC (1973) Biorheology of soft tissues. Biorheology 10:139–155
174. Ehret A (2011) Generalised concepts for constitutive modelling of soft biological tissues. PhD Thesis RWTH Aachen University, pp 1–230
175. Balbi V, Shearer T, Parnell WJ (2018) A modified formulation of quasi-linear viscoelasticity for transversely isotropic materials under finite deformation. Proc R Soc A Math Phys Eng Sci 474(2217):20180231
176. Bischoff J (2006) Reduced parameter formulation for incorporating fiber level viscoelasticity into tissue level biomechanical models. Ann Biomed Eng 34(7):1164–1172
177. Pioletti DP et al (1998) Viscoelastic constitutive law in large deformations: application to human knee ligaments and tendons. J Biomech 31(8):753–757
178. Coleman BD, Noll W (1961) Foundations of linear viscoelasticity. Rev Mod Phys 3(2):239–249
179. Limbert G (2004) Development of an advanced computational model for the simulation of damage to human skin. Welsh Development Agency (Technology and Innovation Division) – FIRST Numerics, Cardiff, pp 1–95
180. Limbert G, Middleton J (2004) A transversely isotropic viscohyperelastic material: application to the modelling of biological soft connective tissues. Int J Solids Struct 41(15):4237–4260
181. Limbert G, Middleton J (2005) An anisotropic viscohyperelastic constitutive model of the posterior cruciate ligament suitable for high loading-rate situations. In: IUTAM symposium on impact biomechanics: from fundamental insights to applications. Dublin
182. Limbert G, Middleton J (2006) A constitutive model of the posterior cruciate ligament. Med Eng Phys 28(2):99–113
183. Reese S, Govindjee S (1998) A theory of finite viscoelasticity and numerical aspects. Int J Solids Struct 35:3455–3482
184. Lubarda VA (2004) Constitutive theories based on the multiplicative decomposition of deformation gradient: thermoelasticity, elastoplasticity and biomechanics. Appl Mech Rev 57:95–108
185. Vassoler JM, Reips L, Fancello EA (2012) A variational framework for fiber-reinforced viscoelastic soft tissues. Int J Numer Methods Eng 89(13):1691–1706
186. Nguyen TD, Jones RE, Boyce BL (2007) Modeling the anisotropic finite-deformation viscoelastic behavior of soft fiber-reinforced composites. Int J Solids Struct 44(25–26):8366–8389
187. Nedjar B (2007) An anisotropic viscoelastic fibre–matrix model at finite strains: continuum formulation and computational aspects. Comput Meth Appl Mech Eng 196(9–12):1745–1756
188. Flynn C, Rubin MB (2014) An anisotropic discrete fiber model with dissipation for soft biological tissues. Mech Mater 68:217–227
189. Hollenstein M, Jabareen M, Rubin MB (2013) Modeling a smooth elastic–inelastic transition with a strongly objective numerical integrator needing no iteration. Comput Mech 52(3):649–667
190. Holzapfel GA, Gasser TC (2001) A viscoelastic model for fiber-reinforced composites at finite strains: continuum basis, computational aspects and applications. Comput Methods Appl Mech Eng 190(34):4379–4403
191. Pena E et al (2007) An anisotropic visco-hyperelastic model for ligaments at finite strains. Formulation and computational aspects. Int J Solids Struct 44(3–4):760–778
192. Pena E et al (2008) On finite-strain damage of viscoelastic-fibred materials. Application to soft biological tissues. Int J Numer Methods Eng 74(7):1198–1218
193. Ehret AE, Itskov M, Weinhold GW (2009) A micromechanically motivated model for the viscoelastic behaviour of soft biological tissues at large strains. Nuovo Cimento Della Societa Italiana Di Fisica C-Geophysics and Space Physics 32(1):73–80
194. Gasser TC, Forsell C (2011) The numerical implementation of invariant-based viscoelastic formulations at finite strains. An anisotropic model for the passive myocardium. Comput Methods Appl Mech Eng 200(49-52):3637–3645

195. Simo JC (1987) On a fully three-dimensional finite-strain viscoelastic damage model: formulation and computational aspects. Comput Methods Appl Mech Eng 60:153–173
196. Muñoz MJ et al (2008) An experimental study of the mouse skin behaviour: damage and inelastic aspects. J Biomech 41(1):93–99
197. Edsberg LE et al (1999) Mechanical characteristics of human skin subjected to static versus cyclic normal presures. J Rehabil Res Dev 36(2):133–141
198. Ehret AE, Itskov M (2009) Modeling of anisotropic softening phenomena: application to soft biological tissues. Int J Plast 25:901–919
199. Ehret AE et al (2011) Porcine dermis in uniaxial cyclic loading: sample preparation, experimental results and modeling. J Mech Mater Struct 6(7–8):1125–1135
200. Volokh KY (2007) Prediciton of arterial failure based on a microstructural bi-layer fiber-matrix model with softening. In: Proceeding of the ASME summer bioengineering conference – 2007, pp 129–130
201. Volokh KY (2011) Modeling failure of soft anisotropic materials with application to arteries. J Mech Behav Biomed Mater 4(8):1582–1594
202. Volokh KY (2014) On irreversibility and dissipation in hyperelasticity with softening. J Appl Mech Trans ASME 81(7):074501
203. Mazza E et al (2005) Nonlinear elastic-viscoplastic constitutive equations for aging facial tissues. Biomech Model Mechanobiol 4(2–3):178–189
204. Mazza E et al (2007) Simulation of the aging face. J Biomech Eng Trans ASME 129(4):619–623
205. Rubin MB, Bodner SR (2002) A three-dimensional nonlinear model for dissipative response of soft tissue. Int J Solids Struct 39(19):5081–5099
206. Mihai LA, Woolley TE, Goriely A (2018) Stochastic isotropic hyperelastic materials: constitutive calibration and model selection. Proc R Soc A Math Phys Eng Sci 474(2211):201708
207. Lee T et al (2018) Propagation of material behavior uncertainty in a nonlinear finite element model of reconstructive surgery. Biomech Model Mechanobiol b(6):1857–1873
208. Azencott C-A et al (2017) The inconvenience of data of convenience: computational research beyond post-mortem analyses. Nat Methods 14:937
209. Buehler MJ (2006) Large-scale hierarchical molecular modeling of nanostructured biological materials. J Comput Theor Nanosci 3(5):603–623
210. Rim JE, Pinsky PM, van Osdol WW (2009) Multiscale modeling framework of transdermal drug delivery. Ann Biomed Eng 37(6):1217–1229
211. Bancelin S et al (2015) Ex vivo multiscale quantitation of skin biomechanics in wild-type and genetically-modified mice using multiphoton microscopy. Sci Rep 5:17635
212. Liu W, Röckner M (2015) Stochastic partial differential equations: an introduction, 1st edn. Springer, New York, p 272
213. Kamiński M (2007) Generalized perturbation-based stochastic finite element method in elastostatics. Comput Struct 85(10):586–594
214. Kirchdoerfer T, Ortiz M (2016) Data-driven computational mechanics. Comput Methods Appl Mech Eng 304:81–101
215. Oishi A, Yagawa G (2017) Computational mechanics enhanced by deep learning. Comput Methods Appl Mech Eng 327:327–351
216. Barber D (2012) Bayesian reasoning and machine learning. Cambridge University Press, Cambridge, p 697

Constitutive Modelling of Skin Growth

Adrian Buganza Tepole and Arun K. Gosain

Abstract Skin, like all biological materials, adapts to mechanical cues. When expanded beyond its physiological regime over extended time periods, skin grows. This intuitive knowledge has been leveraged clinically in a widely used surgical technique called tissue expansion, in which a surgeon inserts a balloon-like device and inflates it gradually over months to grow skin for reconstructive purposes. However, it is currently not possible to anticipate how much of the deformation due to the expander is growth and how much of it is elastic strain, and tissue expansion protocols remain arbitrary, based on each physician's experience and training, leading to an unacceptable frequency of complications. Here we show a continuum mechanics framework to describe skin growth based on the multiplicative split of the deformation gradient in to growth and elastic tensors. We present the corresponding finite element implementation, in which the growth component is an internal variable stored and updated at the integration points of the finite element mesh. The model is applied to study the deformation and growth patterns of skin for different expander shapes, as well as in patient specific scenarios, showing excellent qualitative agreement with clinical experience. Experimental methods to calibrate and validate the translation of the model to the clinical setting are briefly discussed. We expect that the proposed modeling framework will increase our fundamental understanding of how skin grows in response to stretch, and it will soon lead to personalized treatment plans to achieve the desired patterns of skin growth while minimizing complications.

A. B. Tepole (✉)
School of Mechanical Engineering and Weldon School of Biomedical Engineering, Purdue University, West Lafayette, IN, USA
e-mail: abuganza@purdue.edu

A. K. Gosain
Feinberg School of Medicine, Northwestern University, Chicago, IL, USA

G. Limbert (ed.), *Skin Biophysics*, Studies in Mechanobiology, Tissue Engineering and Biomaterials 22,
https://doi.org/10.1007/978-3-030-13279-8_3

1 Introduction

Unlike structural materials, living tissues have the capacity to adapt to the environment, and in particular to mechanical cues. There are two main mechanisms by which tissues respond chronically to mechanical input: growth and remodeling. Growth is the addition of mass, and remodeling is associated to permanent changes in microstructure [1]. Skin growth is encountered in our everyday lives; we all probably have noticed changes in skin surface area when we gain or lose weight. Pregnancy also induces remarkable and evident skin adaptation, both growth and remodeling [2]. Yet, this intuitive notion about our everyday tissue adaptation had not captivated our scientific interest or the ambition to systematically control skin growth for medical applications until recently.

The first reported case of tissue expansion dates to 1957 when Dr. Neumann implanted a balloon in the neck of a patient who had lost an ear. He then inflated the balloon with water over a period of 8 weeks. When the balloon was taken out, skin had grown approximately 50% with respect to the initial area of skin, and the new tissue was used to reconstruct the ear [3]. This was the first example of tissue expansion, a technique that has since revolutionized reconstructive surgery [4–6]. At the core of tissue expansion is the ability to leverage the remarkable adaptation of skin growth in response to stretch beyond the physiological limit for the creation of skin flaps.

Currently, tissue expansion is used ubiquitously in the field of plastic and reconstructive surgery, to resurface large portions of skin after removal of giant birth defects (termed nevus), to reconstruct breasts after mastectomy, to create new skin for burn patients, and to grow skin needed after the excision of skin cancer [7, 8]. Tissue expanders are produced by different manufactures and they come in different sizes and shapes. The popularity of this procedure hinges on its crucial capacity to grow new tissue that has the same mechanical properties, appearance, and blood supply as the surrounding skin, making it particularly ideal for aesthetic reasons [9]. Yet, despite the demand for this procedure, there are still no tools to predict how skin adapts to stretch, and the current treatment planning continues to rely extensively on the surgeon's experience and training rather than on engineering design tools. Unfortunately, complications and suboptimal outcomes are still common and there is no gold standard for the treatment strategy of individual patients. Instead, there are many arbitrary tissue expansion protocols [10–12].

In this chapter we show the latest progress in modeling skin growth in response to stretch beyond the physiological regime, how simulations of skin growth can be used to increase our fundamental understanding of tissue adaptation, and as a stepping stone towards the incorporation of computational tools in routine clinical practice with the end goal of aiding in the decision making process and minimizing complications from tissue expansion.

Figure 1 shows the case of an 11-year old who had a giant nevus in the right shoulder that was to be resected. Nevi are giant birthmarks associated with increased

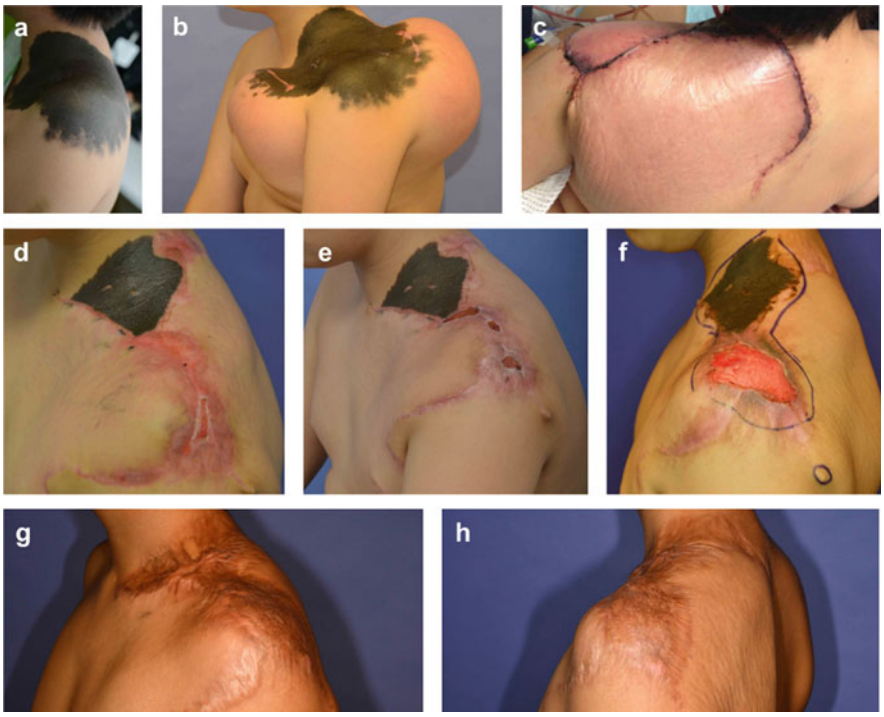

Fig. 1 Complications after tissue expansion. (**a**) 11-year-old patient with giant nevus. (**b**) Tissue expanders were used to grow skin by chronic overstretch. (**c**) Expanded tissue was advanced to correct the defect. (**d–f**) Excessive tension due to insufficient skin growth led to a chronic wound. (**g–h**) After full thickness graft there was scarring and contracture at the neck and shoulder

risk of malignancy and constitute a concern for psychological development during childhood and are hence typically resected early in life [13]. In the case shown, two tissue expanders were placed and gradually inflated over several months. At the end of the inflation, the expanders were removed and the newly grown skin was used to reconstruct the adjacent area. Unfortunately, the amount of grown skin was less than needed and the resulting flaps were closed under significant tension, leading to wound dehiscence and necrosis. Ultimately, a full thickness graft was needed, but the secondary intention healing concluded in a hypertrophic scar with contracture. Had there been tools to predict and monitor the amount of newly grown skin and the resulting flap deformation, this patient would have received an uneventful treatment plan without complications.

Schematically, the underlying biological control of skin adaptation is shown in Fig. 2. In vivo, the skin is in a homeostatic configuration, possibly with some residual stress [14]. The tissue expanders, gradually inflated over a long time period, impose supra-physiological deformations that trigger local adaptation, i.e. growth. As a result, homeostasis is regained locally. When the expander is removed, the

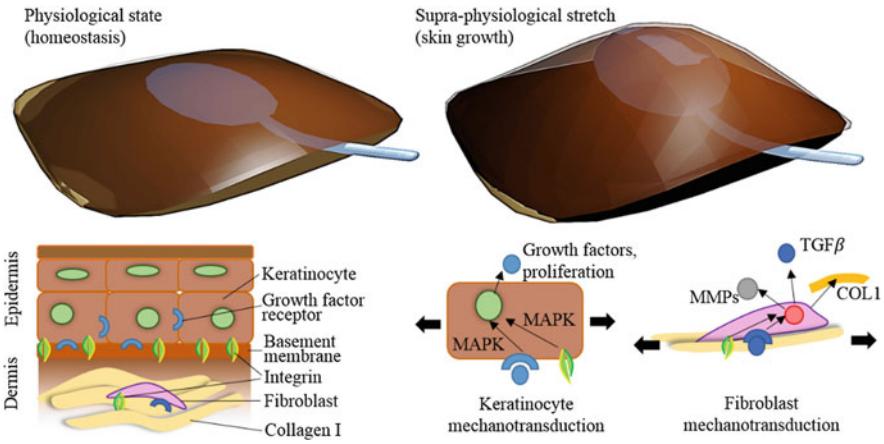

Fig. 2 Skin mechanotransduction. In the physiological state the skin is in local homeostasis. There are two main cell types present in skin, keratinocytes in the epidermis and fibroblast in the dermis. These cells response to mechanical cues and modify their immediate environment to regain homeostasis, leading to skin growth

grown skin is used for reconstructive purposes [15]. From the surgeon's point of view, the primary challenge in anticipating the amount of new skin comes from the fact that the observed deformation is a combination of prestrain, elastic deformation, and growth [16]. The continuum mechanics framework for finite volumetric growth presented here is an ideal approach to model the interplay between the different components of the deformation.

While it is evident that skin grows in response to stretch, the underlying biological mechanisms remain poorly understood. Figure 2 shows our current understanding of the biological pathways involved in skin mechanoadaptation. As for all living matter, the cells resident in the tissue are the ones responsible for sensing the local stress or deformation, transforming these mechanical inputs into chemical signals, and responding in consequence by altering their proliferation rate and remodeling their extra cellular matrix (ECM). The process by which cells interpret stress and strain, turning them into chemical signals inside the cell, is called mechanotransduction [17]. We emphasize the notion of a local homeostatic configuration determined by a single cell in their immediate micro-environment. In other words, as illustrated in Fig. 2, skin growth can be modeled as a local process determined by the cell response. This assumption aligns well with experimental evidence showing that growth is greater in zones of higher deformation [16].

The skin is made out of two layers, the epidermis is at the top and the dermis is at the bottom [18]. Keratinocytes are the most abundant cell population in the epidermis, while the main resident cells of the dermis are the fibroblasts. At the interface between dermis and epidermis there is a basement membrane made out of collagen type IV and laminin that serves as an anchoring matrix for the first layer of keratinocytes [19]. This initial layer of the epidermis is also called the basal

layer. Basal keratinocytes are tasked with the constant renewal of the epidermis [20]. When a basal keratinocyte divides asymmetrically creating a daughter cell that is not in contact with the basement membrane, this cell continues a process of terminal differentiation as it makes its way to the outer surface where it is released by desquamation [21]. Other layers of the epidermis are thus non proliferative. Not surprisingly, basal keratinocytes are the most important mechanosensitive cells in the epidermis [22]. Mechanosensing by these cells is associated primarily with integrin signaling [23]. Integrins are proteins that serve as anchoring points between the cell membrane and the surrounding ECM, and have been recognized as a general mechanosensing tool across cell types [24]. In the epidermis, integrins concentrate in the basal layer [25]. In the rest of the epidermis, cell-cell adhesion is regulated by desmosomes [26]. There are also indirect mechanotransduction pathways. For instance, integrin signaling has been shown to crosstalk with growth factor receptors such as epithelial growth factor receptor (EGF-R) [23, 27]. Both of these pathways ultimately leads to increase keratinocyte proliferation through mitogen-activated protein (MAP) kinase signaling [28].

In the dermis, fibroblasts are a hallmark example of mechanosensitive cells [29]. The dermis is primarily made out of collagen type I, and fibroblasts constitute a scarce cell population in this environment [30]. Fibroblasts sense mechanical signals through integrins which serve as their attachment points to the ECM. Upon stretch, integrin signaling is linked to three crucial cell processes needed for ECM remodeling. First, fibroblasts collagen remodeling is widely regulated by the transforming growth factor beta (TGF-β) signaling pathway. In response to applied stretch, TGF-β1 is upregulated [31]. Activation of this pathway then contributes to the regulation of the collagen network. Collagen production is the second process of interest. For skin growth, new ECM must be created, which entails production of collagen by fibroblasts. In response to stretch, fibroblasts show increased collagen deposition [32]. Thirdly, to facilitate ECM remodeling, matrix metalloproteinases (MMP) are needed to degrade collagen crosslinking. MMP-2 and MMP-9 are particularly upregulated in response to mechanical loading [33]. The biological control of skin growth is, in summary, a complex process driven by local cell mechanosensing and action of cells in their immediate microenvironment.

Parallel to the interest in the underlying biological adaptation, modeling skin growth requires equally assiduous attention to this tissue's mechanical behavior. Skin is a nonlinear, transversely isotropic, and hyperelastic material that can undergo extreme deformations during tissue expansion [34, 35]. The theoretical framework to describe skin growth for finite deformations is the multiplicative decomposition of the deformation gradient into growth and elastic contributions within a continuum mechanics description [36]. This split was initially introduced to model tissue growth in response to stress by Rodriguez and coworkers just over two decades ago [37], and it was inspired by the multiplicative split of the deformation gradient used to model plasticity at finite strains [38]. The multiplicative split into growth and elastic components has been used to model the growth of tumors, the heart, blood vessels, and heart valves, to name a few examples [39–42]. An axisymmetric model of skin growth was first considered 10 years ago [43]. The growth component of the

deformation reflects the local biological adaptation. The elastic part is associated with the residual stresses induced by growth, as well as stress and deformation due to external loading. The application of this theoretical framework to predict skin growth in realistic scenarios has required the development of novel finite element methods specifically tailored to growing tissues undergoing extreme changes over time. In the case of skin, particular attention is needed to account for the mechanical behavior of this structure as a thin, nonlinear membrane [44].

The rest of this chapter is organized as follows, in the next section we cover the standard description of volumetric growth theory within continuum mechanics. Then we introduce the corresponding finite element discretization. Examples are shown next. We finish the chapter with a conclusions section.

2 Growth Theory

2.1 Kinematics

We start by introducing the reference geometry defined by material coordinates $\boldsymbol{X} \in \mathcal{B}_0$ that are mapped by φ to the current configuration $\boldsymbol{x} \in \mathcal{B}$. The local deformation is captured by the deformation gradient $\boldsymbol{F} = \partial \boldsymbol{x}/\partial \boldsymbol{X}$. The framework of volumetric growth assumes the split of the deformation gradient into growth and elastic contributions

$$\boldsymbol{F} = \boldsymbol{F}^e \cdot \boldsymbol{F}^g \tag{1}$$

Conceptually, this split involves the notion of a microscopic configuration where additional kinematic assumptions can be made [45]. Cells can change their immediate microenvironment in response to mechanical cues. These permanent changes in the local ECM define the growth component of the deformation $\boldsymbol{F}^g$. Seen in this way, the multiplicative split introduces an intermediate incompatible configuration [46]. The tensor field $\boldsymbol{F}^e$ is the local deformation required to assemble the grown differential volume elements into the current, observed, geometry. Therefore, while $\boldsymbol{F}$ is the gradient of a deformation field, neither $\boldsymbol{F}^g$ or $\boldsymbol{F}^e$ are compatible with a deformation, i.e., they are not gradients of any field. A complimentary explanation is to imagine that all we know is the current configuration and we proceed to cut this geometry into small pieces and remove all external loading. Due to residual stresses in the material, the individual pieces would deform elastically to achieve their local equilibrium or, equivalently, their stress-free state. Measuring the deformation between the stress-free state of each of these individual pieces to the current configuration would yield $\boldsymbol{F}^e$. This view of the elastic component of the deformation has led to experiments to determine the residual stresses in soft tissues. Perhaps the most well-known example of this investigation is the opening angle experiment used to determine the residual stress in arteries [47]. The residual stress field,

however, is not necessarily homogeneous over an entire tissue. In that case, a single cutting line is insufficient to reconstruct the residual stress distribution. Recent experiments on skin have characterized a non-homogeneous elastic deformation field by implementing the thought experiment described above: A sizable skin patch was cut into multiple small pieces, revealing a spatially-varying elastic deformation field induced by tissue expansion [46].

The volume change also follows the multiplicative split

$$J = J^e J^g \tag{2}$$

Where the total volume change is $J = \det(\boldsymbol{F})$, and the elastic and growth components are $J^e = \det(\boldsymbol{F}^e)$, and $J^g = \det(\boldsymbol{F}^g)$. Skin is a thin membrane and in response to stretch it grows primarily in plane. Thus, we are interested in the area change

$$\vartheta = \|\mathrm{cof}(\boldsymbol{F}) \cdot \boldsymbol{n}_0\| = \vartheta^e \vartheta^g \tag{3}$$

Which can also be decomposed into a growth term ϑ^g, and an elastic area contribution ϑ^e. The operator $\mathrm{cof}(\circ) = \det(\circ)(\circ)^T$ is the cofactor of the second order tensor $(\circ)$, and applied to the surface normal in the reference configuration $\boldsymbol{n}_0$ it yields the area change. In what follows we derive equilibrium equations in the reference configuration. We introduce the right Cauchy Green deformation tensor

$$\boldsymbol{C} = \boldsymbol{F}^T \cdot \boldsymbol{F} \tag{4}$$

However, the growth component of the deformation does not produce stress. Returning to our imaginary experiment in which we cut the current configuration into small pieces, only the elastic component of the deformation produces stress [48, 49]. The deformation tensor for the elastic component is

$$\boldsymbol{C}^e = \boldsymbol{F}^{g-T} \cdot \boldsymbol{C} \cdot \boldsymbol{F}^{g-1} \tag{5}$$

We remark that there are three main deformation measures, but only two of them are independent. In other words, the current configuration described by the deformation map φ is the observed geometry. For instance, in tissue expansion, this deformation map is a combination of both elastic deformation due to the inflation of the balloon, and permanent skin growth. Determining one of the two components of the deformation is enough to fully characterize the local kinematics. This will be important in the finite element implementation. We also note that we focus on the deformations measured with respect to the reference configuration. Alternatively, the strains could be calculated with respect to the current, deformed state [50].

2.2 Balance Equations

Mass is not conserved in growing tissues and the analysis of skin as an open thermodynamic system is required [51]. The permanent changes in volume due to the growth tensor $\boldsymbol{F}^g$ are associated with an addition of mass. Let ρ_0 denote the material density field. Since mass it is not conserved for this system, we have

$$\dot{\rho}_0 = \mathrm{Div}(\boldsymbol{R}) + R_0 \tag{6}$$

Density can change due to a flux $\boldsymbol{R}$ or a source term R_0. The operator $\mathrm{Div}(\circ)$ is the divergence operator in the reference configuration. Consequently, the mass-specific form for the balance of linear momentum balance is

$$\rho \dot{\boldsymbol{v}} = \mathrm{Div}(\boldsymbol{F} \cdot \boldsymbol{S}) + \rho_0 \boldsymbol{b} \tag{7}$$

With $\dot{\boldsymbol{v}} = \dot{\varphi}$, $\boldsymbol{S}$ is the second Piola-Kirchhoff stress tensor, and the momentum flux is then $\boldsymbol{F} \cdot \boldsymbol{S}$. The momentum source per unit reference mass is $\boldsymbol{b}$. We remark that for open systems, the mass-specific version of the dissipation inequality contains an extra entropy source to account for the growing system, see [52] for a detailed review of the open system treatment in the context of biological growth.

2.3 Constitutive Models for Skin Growth

The multiplicative split of the deformation into growth and elastic contributions requires the definition of separate constitutive relations. The momentum flux is associated with the elastic deformation, and the biological process of mechanosensing and adaptation is linked to the growth tensor. To describe the mechanical behavior of skin we adopt a Neo-Hookean strain energy density function [53]. Other constitutive models for the elastic part are possible and have been explored. For instance, in our previous work we have also used a worm-like chain model, as well as the strain energy function proposed by Holzapfel, Ogden and Gasser, which allows consideration of skin anisotropy [54, 55]. An increasingly detailed and accurate understanding of skin mechanical behavior needs to be taken into consideration for the continuous updating of skin growth models [34]. For this chapter we restrict ourselves with the Neo-Hookean description.

The Helmholtz free energy $\psi = \widehat{\psi}(\boldsymbol{C}, \boldsymbol{F}^g)$, through the use of the dissipation inequality, yields the definition of the second Piola-Kirchhoff stress tensor as the thermodynamically conjugate tensor to the right Cauchy-Green deformation tensor

$$\boldsymbol{S} = 2\rho_0 \frac{\partial \psi}{\partial \boldsymbol{C}} = 2 \frac{\partial \psi}{\partial \boldsymbol{C}^e} : \frac{\partial \boldsymbol{C}^e}{\partial \boldsymbol{C}} = \boldsymbol{F}^{g-1} \cdot \boldsymbol{S}^e \cdot \boldsymbol{F}^{g-T} \tag{8}$$

For a classical Neo-Hookean solid the free energy takes the form

$$\rho_0 \psi = \frac{1}{2}\lambda \ln^2\left(J^e\right) + \frac{1}{2}\mu\left(\boldsymbol{C}^e : \boldsymbol{I} - 3 - 2\ln\left(J^e\right)\right) \tag{9}$$

The strain energy in (9) is parameterized by the Lame constants λ and μ. It can be further seen from (8) that the elastic deformation is the only one that produces stress, leading to the definition of elastic second Piola-Kirchhoff stress tensor

$$\boldsymbol{S}^e = 2\rho_0 \frac{\partial \psi}{\partial \boldsymbol{C}^e} = \left(\lambda \ln\left(J^e\right) - \mu\right)\boldsymbol{C}^{e-1} + \mu \boldsymbol{I} \tag{10}$$

For implementation of the finite element algorithm, the definition of the elastic constitutive moduli is also needed

$$\boldsymbol{L}^e = 2\frac{\partial \boldsymbol{S}^e}{\partial \boldsymbol{C}^e} = \lambda \boldsymbol{C}^{e-1} \otimes \boldsymbol{C}^{e-1} + \left(\mu - \lambda \ln\left(J^e\right)\right)\left[\boldsymbol{C}^e \overline{\otimes} \boldsymbol{C}^e + \boldsymbol{C}^e \underline{\otimes} \boldsymbol{C}^e\right] \tag{11}$$

For the growth component of the deformation we postulate that growth occurs primarily in plane [56, 57]. Recall that the normal to the skin surface is denoted $\boldsymbol{n}_0$, the growth tensor for area growth takes the form

$$\boldsymbol{F}^g = \sqrt{\vartheta^g}\boldsymbol{I} + \left(1 - \sqrt{\vartheta^g}\right)\boldsymbol{n}_0 \otimes \boldsymbol{n}_0 \tag{12}$$

The rate of change of the area growth, $\dot{\vartheta}^g$, is used to define the mass source in (6), $R_0 = \rho_0\left(1 + 2\sqrt{\dot{\vartheta}^g}/\sqrt{\vartheta^g}\right)$. The area growth variable is defined with a constitutive law for its rate of change. It is assumed that the rate of area growth is proportional to the elastic area strain at a point [58, 59]. This form of the growth tensor is assumed based on our knowledge of fibroblast and keratinocyte mechanosensing and experimental evidence that skin grows more in areas subjected to larger strains during tissue expansion [60, 61]. Specifically, we postulate the growth law

$$\dot{\vartheta^g} = k^g\left(\vartheta^g\right)\phi^g\left(\vartheta^e\right) \tag{13}$$

In which $k^g(\vartheta^g)$ is a weighting function to capture saturation of the growth rate at higher growth, and the function $\phi^g(\vartheta^e)$ captures the mechanosensing response and it is thus a function of the elastic area change. The weighting function is further expanded as

$$k^g\left(\vartheta^g\right) = \frac{1}{\tau}\left(\frac{\vartheta^{max} - \vartheta^g}{\vartheta^{max} - 1}\right)^{\gamma} \tag{14}$$

Where the parameter τ represents a time scale for growth, ϑ^{max} prevents unbounded growth, and γ characterizes the nonlinearity of the curve. The growth criterion is

$$\phi^g\left(\vartheta^e\right) = \left\langle \vartheta^e - \vartheta^{crit} \right\rangle \tag{15}$$

The parameter ϑ^{crit} is related to the physiological regime. In our everyday activities, skin undergoes constant deformation that may not trigger growth. Moreover, skin is naturally prestrained [14]. Therefore, growth takes place only when the elastic stretch goes beyond the physiological limits [62, 63]. The notation $\langle \circ \rangle$ is used for the Macaulay brackets.

The constitutive equations introduced in this section are clearly nonlinear, and solution of the equilibrium problem and update of the growth variable require iterative methods. The discretization and computational algorithm based on the finite element method are described in the next section. However, anticipating the need for the consistent linearization of the stress with respect to the deformation we have already introduced the elastic constitutive moduli $\boldsymbol{L}^e$. We now proceed to define the constitutive moduli with respect to the initial configuration

$$\boldsymbol{L} = 2\frac{\partial \boldsymbol{S}}{\partial \boldsymbol{C}} = \left(\boldsymbol{F}^{g-1}\overline{\otimes}\boldsymbol{F}^{g-1}\right) : \boldsymbol{L}^e : \left(\boldsymbol{F}^{g-T}\overline{\otimes}\boldsymbol{F}^{g-T}\right) + 2\left(\frac{\partial \boldsymbol{S}}{\partial \boldsymbol{F}^g} : \frac{\partial \boldsymbol{F}^g}{\partial \vartheta^g}\right) \otimes \frac{\partial \vartheta^g}{\partial \boldsymbol{C}} \tag{16}$$

The second term in (16) benefits from additional discussion. The second Piola-Kirchhoff stress is the pull-back of the elastic stress defined in the intermediate configuration. At constant total deformation $\boldsymbol{F}$, the derivative of the stress $\boldsymbol{S}$ with respect to the growth tensor consists of two terms, the derivative of the pull-back operation itself, which is clearly a function of $\boldsymbol{F}^g$, but also the derivative of $\boldsymbol{S}^e$, which can be obtained from the use of the chain rule. We have

$$\frac{\partial \boldsymbol{S}}{\partial \boldsymbol{F}^g} = -\left(\boldsymbol{F}^{g-1}\overline{\otimes}\boldsymbol{S} + \boldsymbol{S}\underline{\otimes}\boldsymbol{F}^{g-1}\right) - \left(\boldsymbol{F}^{g-1}\overline{\otimes}\boldsymbol{F}^{g-1}\right) : \tfrac{1}{2}\boldsymbol{L}^e : \left(\boldsymbol{F}^{g-T}\underline{\otimes}\boldsymbol{C}^e + \boldsymbol{C}^e\overline{\otimes}\boldsymbol{F}^{g-T}\right) \tag{17}$$

The last terms in Eq. (16) relating the growth multiplier ϑ^g to the total deformation $\boldsymbol{C}$, are computed based on the specific form of the growth tensor and the growth rate [64].

3 Finite Element Discretization

In the development of the theoretical framework in Sect. 2, all quantities of interest were presented with respect to the reference configuration. To solve the equilibrium Eq. (7) in a quasi-static approach, a finite element discretization based on a total

Lagrangian formulation is thus adopted. An alternative framework to simulate the growth of skin in tissue expansion is an Eulerian description, see [50].

In the finite element formulation, given the split of the total deformation into two contributions, each with its own set of constitutive relations, two independent variables need to be considered. Having a constitutive relation for the growth rate, we naturally choose ϑ^g as one of the independent variables. Then, considering a classical finite element methodology in the Lagrangian setting, it is straightforward to consider the total deformation as the second independent variable.

For the deformation, the degrees of freedom are given by the displacements at the nodes of the finite element mesh. We note that growth is considered as a local process, completely specified by the deformation at a point. In consequence, the growth multiplier is discretized as an internal variable at the integration points of the finite element mesh [36]. In what follows we distinguish between the solution of the local problem dictated by (13), and that of the global momentum equilibrium problem expressed in (7).

3.1 Local Problem: Growth Update

The growth update is done in each element independently. Consider the discretization of the time domain into n_{stp} subintervals

$$\mathcal{T} = \bigcup_{n=1}^{n_{stp}} [t_n, t_{n+1}] \tag{18}$$

For a given time step $[t_n, t_{n+1}]$, we are interested in calculating the update of the area growth at the end of the time step ϑ^g_{n+1}, given its value at the beginning of the time step ϑ^g_n, and the current total deformation $\boldsymbol{F}$ at t_{n+1}. The subscript $(\circ)_{t+1}$ to denote the end of the current time step will be omitted from now on. Recall that the constitutive equation for growth reported in (13) is the definition of the growth rate given the growth and elastic area changes. We adopt a backward Euler scheme to update the growth multiplier such that

$$\vartheta^g = \vartheta^g_n + \Delta t \dot{\vartheta}^g \tag{19}$$

Since this is an implicit scheme for time integration, and the growth rate is a nonlinear function of the current growth and elastic area changes, we solve for the update of the area growth using Newton-Raphson iterations. Recasting (19) into a residual $\mathrm{R}^{\vartheta} = \vartheta^g - \vartheta^g_n - \Delta t \dot{\vartheta}^g \doteq 0$, we then get the derivative needed for the local Newton iterations

$$\mathrm{K}^{\vartheta} = \frac{\partial \mathrm{R}^{\vartheta}}{\partial \vartheta^g} = 1 - \left(\frac{\partial k^g}{\partial \vartheta^g} \phi^g + \frac{k^g \partial \phi^g}{\partial \vartheta^g} \right) \Delta t \tag{20}$$

Where the functions $k^g(\vartheta^g)$ and $\phi^g(\vartheta^e)$ were defined in (14) and (15) above. Note that the growth criterion depends on the elastic area change, but the residual is constructed for the new growth multiplier under constant total deformation $\boldsymbol{F}$, i.e., constant ϑ. Therefore, Eq. (3) should be used to introduce $\vartheta^e = \vartheta/\vartheta^g$.

3.2 Global Problem: Total Deformation

We solve for the deformation of the finite element mesh to satisfy mechanical equilibrium (7). The growth of soft tissues occurs slowly in time such that inertia effects can be neglected. We thus set $\dot{\boldsymbol{v}} = 0$. We also ignore the contribution of body forces $\boldsymbol{b} = \boldsymbol{0}$. Then, consider the weak form of the mechanical equilibrium problem following integration by parts

$$\int_{\mathcal{B}_0} \nabla \delta\boldsymbol{\varphi} : (\boldsymbol{F} \cdot \boldsymbol{S})\, dV_0 = 0 \tag{21}$$

Appropriate boundary conditions should also be considered. There is no special treatment required for the boundary conditions, prescribed displacements or boundary loads can be applied in the same way as for standard finite element formulations in the finite deformation regime. In (21), the virtual displacements or test functions $\delta\varphi$ were used to transform (19) into its weak form. To discretize (19) in space we consider the partition of the domain $\mathcal{B}_0$ into n_{el} elements

$$\mathcal{B}_0 = \bigcup_{\mathrm{e}=1}^{n_{el}} \mathcal{B}_0^e \tag{22}$$

The geometry of each finite element is in turn defined by nodal positions and nodal basis functions. We apply the isoparametric Bubnov-Galerkin interpolation such that the deformation field φ^{el} and the test functions $\delta\varphi^{\mathrm{el}}$ inside of an element are interpolated with the same basis functions

$$\boldsymbol{\varphi}^{\mathrm{el}} = \sum_{i=1}^{n_{en}} N^i \boldsymbol{\varphi}_i,\ \delta\boldsymbol{\varphi}^{\mathrm{el}} = \sum_{j=1}^{n_{en}} N^j \delta\boldsymbol{\varphi}_j \tag{23}$$

Where φ_i, $\delta\varphi_j$ are the nodal values used to discretize the deformation and test function fields; N^i, N^j are the nodal shape functions, and n_{en} are the number of nodes per element. The gradients of the deformation field and the test function inside of an element follow directly from (23)

$$\nabla\boldsymbol{\varphi}^{\mathrm{el}} = \sum_{i=1}^{n_{en}} \boldsymbol{\varphi}_i \otimes \nabla N^i,\ \nabla\delta\boldsymbol{\varphi}^{\mathrm{el}} = \sum_{j=1}^{n_{en}} \delta\boldsymbol{\varphi}_j \otimes \nabla N^j \tag{24}$$

The discretized deformation and test function fields are used in the weak form of the equilibrium equation to define the global residual

$$\mathbf{R}_I^{\varphi} = \mathbf{A}_{e=1}^{n_{el}} \int_{\mathcal{B}e} \nabla N^i \cdot (\boldsymbol{F} \cdot \boldsymbol{S})\, dV_e \doteq 0 \tag{25}$$

The operator $\mathbf{A}_{e=1}^{n_{el}}$ is called the assembly operator and it links the residual associated with the node i, local to an element e, to the residual in terms of the global node numbering I. In order to find the deformation field φ that leads to the vanishing of the residual, a global Newton-Raphson iteration is needed. Note that the discretized residual (25) is highly nonlinear because of the definition of the second Piola-Kirchhoff stress in (8), compounded with the nonlinearity of the growth process. Therefore, we introduce the consistent tangent

$$\mathbf{K}_{IJ}^{\varphi} = \frac{\partial \mathbf{R}_I^{\varphi}}{\partial \varphi_J} = \mathbf{A}_{e=1}^{n_{el}} \int_{\mathcal{B}e} \left[\left(\nabla N^i \cdot \boldsymbol{F} \right)^{\text{sym}} \cdot \boldsymbol{L} \cdot \left(\boldsymbol{F}^T \cdot \nabla N^j \right)^{\text{sym}} + \nabla N^i \cdot \boldsymbol{S} \cdot \nabla N^j \boldsymbol{I} \right] dV \tag{26}$$

In summary, given the deformation φ_n and the growth ϑ_n^g at time t_n, we want to solve for the total deformation φ and the new growth ϑ^g at time t_{n+1}. To do so, an initial guess for the deformation is given $\varphi^{(0)}$. With this guess, the growth multiplier is updated at every integration point with the local Newton iterations. Then, the residual and algorithmic tangent defined in (25) and (26) are computed and used to generate the increment $\Delta\boldsymbol{\varphi} = -\mathbf{K}_{IJ}^{\varphi -1} \mathbf{R}^{\varphi}$. The deformation field then is updated $\varphi^{(1)} = \varphi^{(0)} + \Delta\varphi$. This process is iterated until convergence is achieved.

4 Examples

The above modeling framework has been used to study the fundamental mechanisms and implications of the growth process, as well as to showcase its potential for medical application [50, 65]. More recently, this theoretical framework has been paired with experiments on large animal models to get an even more in depth knowledge of the processes at the cellular scale [66]. Computational modeling of skin growth has helped us gain key insights and rationalize decision making during tissue expansion [58]. In particular, an important motivation for our work has been the lack of a gold standard for the expansion protocols [4, 67, 68]. Today, expander size and shape are chosen arbitrarily, based on the surgeons training and experience. Hence, in this section we start by presenting the simulation of skin growth for different expander geometries [54]. Ideal cases are tremendously useful to get generalizable knowledge and propose protocol guidelines. However, in clinical scenarios, every patient has a unique geometry and requires an individualized procedure. Thus, in the second portion of this section we also present the application

of our modeling framework to study skin growth in a patient-specific case of scalp reconstruction [69].

4.1 Expander Shape

Tissue expanders come in different sizes and shapes. The most common ones are spherical, crescent, rectangular and square. Anticipating the relative area growth from these different expanders has been challenging and, instead, empirical correction factors have been introduced [70]. Unfortunately, our inability to predict skin response to chronic hyper-stretch can lead to cases where not enough skin is harvested at the end of expansion and wound complications ensue [71]. In the opposite case, expansion can be aggressive and occur over a significant amount of time, resulting in excess skin that gets discarded at the time of surgery [6]. Here we present the virtual inflation of different expander shapes and show that even with the same material parameters and filled to an equal volume over the same time period, different shapes produce vastly different growth contours and overall area gain.

Figure 3 shows the finite element discretization of four different expanders. In all cases, the reference configuration was a flat, square sheet of tissue with dimensions $12 \times 12\ \text{cm}^2$, and with a thickness of 0.2 cm. A total of 1728 trilinear brick elements were used to discretize the geometry.

The material parameters used in the simulation were the Lame constants $\lambda = 0.577$ MPa, $\mu = 0.0385$ MPa. For the growth constitutive equations, the critical area strain was set to $\vartheta^{crit} = 1.01$, the maximum area growth was limited to $\vartheta^{max} = 2.4$, the timescale of growth was $\tau = 1.0$, and the nonlinearity parameter used was $\gamma = 2$. Note that the time used is non-dimensional since we are

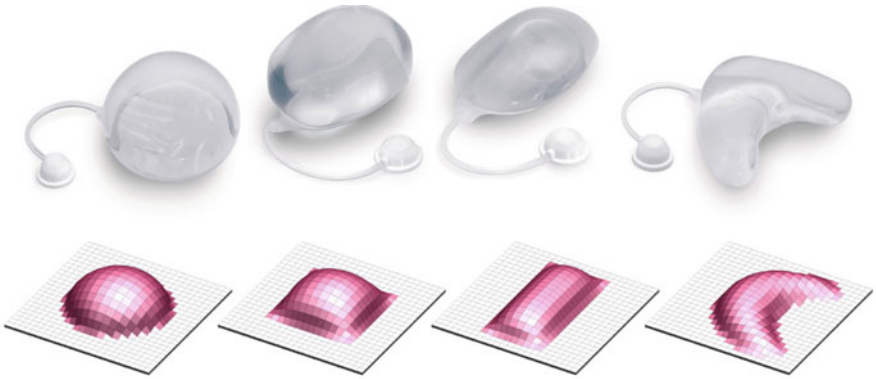

Fig. 3 Finite element modeling of different expander shapes. Four different expander shapes were simulated. The same discretization consisting of 1728 triliniear brick elements was used for all cases. The shapes depicted are, from left to right: sphere, square, rectangle, and crescent. In all cases the initial geometry was a flat sheet of tissue [53]

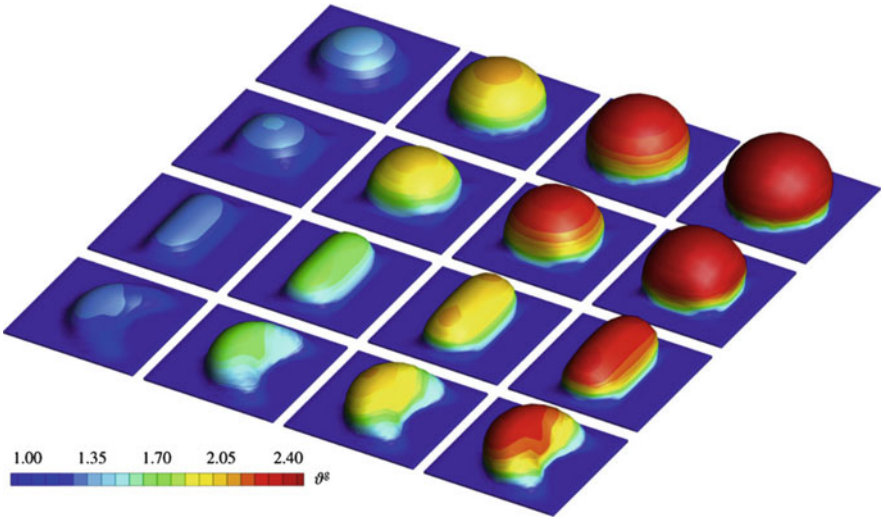

Fig. 4 Area growth due to tissue expansion. The snapshots show four consecutive time points during a virtual inflation process simulated with custom finite element tools tailored for skin growth modeling. The contours depict the amount of area growth. The apex of the expander is stretched more and also shows the greatest growth. Growth is progressively less toward the periphery of the expanded area. The same trend in the area growth distribution is seen for different expander shapes. However, total growth is different across expander geometries. The sphere expander achieves the most area gain compared to the other shapes [53]

concerned with the relative behavior across different expander shapes and not direct comparison to a clinical case.

The virtual inflation was prescribed by gradually applying a pressure of 0.002 MPa over 40 loading steps spanning a nondimensional time of $t = 4$. The skin is then left to grow under a constant pressure over the next 460 steps of $\Delta t = 0.1$ until $t = 50$. Figure 4 shows the relative area gain contours for each of the expanders over time. The area gain is calculated by measuring the total area being expanded. The initial area is measured based on the highlighted faces in Fig. 3 and is thus $A_0 = NdA$, where N is the number of faces that are part of the expanded skin and dA is the area of each face. In the beginning of the simulation all faces are square and have the same area. The final area is obtained with the sum of the growth multipliers as $A_f = \left(\sum \vartheta_e^g\right) dA$, where the subscript denotes area growth per element.

The sphere expander grows the most compared to the other expander shapes, achieving a relative area gain A_f/A_0 of 1.59, followed by the square expander which grows 1.37 in area compared to the initial state. Even though we did not calibrate the model directly to experimental or clinical evidence, this amount of growth does align with values reported in the literature. For instance, in the first tissue expansion performed by Neumann [3], an expander was filled over a span of 2 months to produce an are gain of approximately 1.5 times the initial area. The rectangular expander in our simulations grows 1.2 times in area, and the

crescent expander grows the least, achieving only 1.11 fractional area gain. These simulations underscore the importance of computational models to guide basic design principles of tissue expansion treatment. Area gain is not the only factor considered when deciding a tissue expansion protocol, but anticipating changes in area gain due to different expanders based on predictive models is a requirement for the improvement of this technique [66].

Subsequent work from our group has verified experimentally that different expanders produce different growth patterns, and that the spherical expander induces greater growth compared to the crescent expander [46]. Furthermore, we have confirmed experimentally that the growth pattern resembles the elastic and total deformation fields, with greater area growth in zones undergoing larger deformation [16]. This validates our phenomenological approach to a certain degree. Clearly, more experiments are needed to fully calibrate the computational model, especially regarding the underlying biological control, but even at the current stage, this framework is able to provide valuable and quantitative insight of how the parameters of the tissue expansion protocol are connected to the final shape and amount of newly grown skin.

4.2 Pediatric Tissue Expansion

Undoubtedly, the primary motivation for modeling skin growth in response to stretch is to transform clinical practice and improve surgery outcomes. The modeling framework presented here has been applied to study the growth of skin in patient specific geometries. In this section we present two cases of scalp reconstruction concerning the excision of a giant nevus following prolonged inflation of tissue expanders over the scalp. Reconstruction of birth defects is a common application of tissue expansion [13]. In the head and neck region, careful planning is essential but also extremely complicated [6]. In fact, currently, no predictive tool exists to aid the surgeon during preoperative planning of skin expansion. Therefore, the two cases shown here are a n important advancement towards personalized planning of tissue expansion based on computational modeling. The two inflation protocols presented are particularly interesting because a giant nevus of a similar size and location needed to be removed in both cases. Yet, despite the similarities between the two defects, different expansion protocols were performed [8, 72]. We were interested in comparing both strategies with computational modeling tools in order to assess if one alternative is more adequate than the other in terms of fractional area gain.

Starting from CT scan data, we reconstructed the skin geometry and recreated both procedures virtually with our custom finite element implementation [73]. The same material and growth parameters were used in the two cases, and the differences in growth patterns and total area growth were quantified. Figure 5 shows the photographs of the two clinical cases of interest. The top row shows a one-year old baby girl with a giant nevus in the left scalp [72]. Three tissue expanders were

Fig. 5 Tissue expansion for nevus resection. Two cases of tissue expansion are shown for two clinical cases. In the top row, the case of a one-year old baby girl is shown. Three expanders were placed, one in the forehead and two in the scalp [72]. The bottom row shows the case of a one-year old boy with a similar giant nevus. In this case, an expander was placed in the cheek, a second expander was positioned in the forehead, and a third expander was located in the top of the scalp [8]

placed, one in the forehead, one in the top of the scalp, and one in the posterior scalp. The second case is a one-year old boy with a similar giant nevus in the right scalp [8]. Three tissue expanders were used to grow the skin needed for the correction of the defect. In this case, one expander was placed in the cheek, one in the forehead, and one on the top of the scalp.

Figure 6 shows the contours of the growth multiplier for several time points of the simulation. Both cases are depicted in the same figure to allow for side-by-side comparison. For the case study I, following the clinical scenario, one virtual expander was placed in the posterior scalp. The skin in this region consisted of 2270

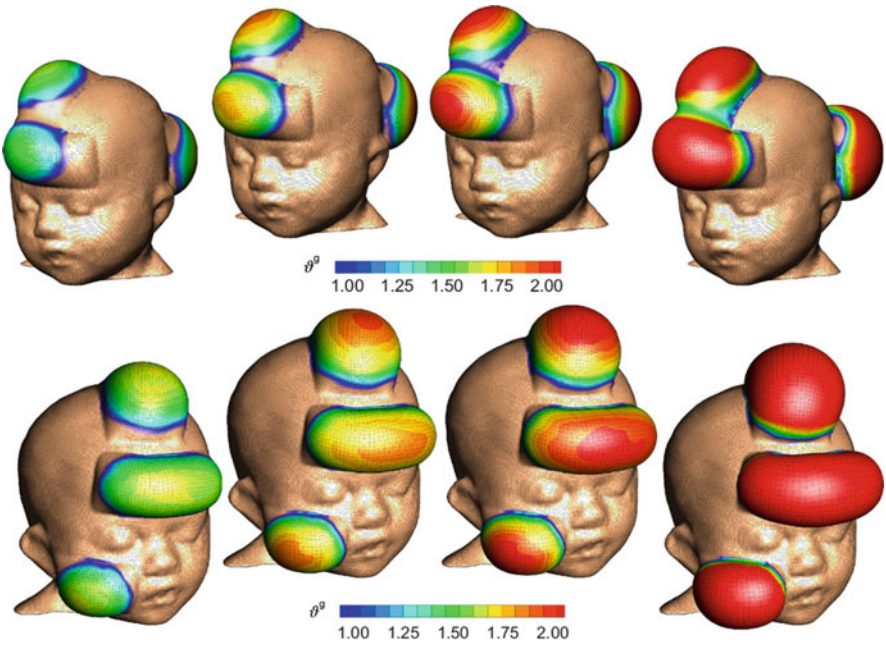

Fig. 6 Pediatric patient-specific model of tissue expansion. The top row shows the area growth contours for case I. Three expanders were placed in the forehead and scalp regions. Growth is greater at the apex of the expanded region and less toward the periphery of the expander. Area growth increases for the four time points shown. At the end of the simulation a total fractional area gain of 1.68 is achieved, and the absolute area available for reconstruction is 251.2 cm^2. The bottom row shows four snapshots for case II. A similar defect needed to be resected but in this case one expander was placed in the cheek. Area growth contours obey the same trends as seen in case I. The overall fractional area gain in this case was 1.76, however, the absolute area available for reconstruction at the end of the expansion was 227.1 cm^2. Adapted from [50] with permission

trilinear brick elements and spanned an area of 53.1 cm^2. Two more expanders were placed in the top of the scalp and the forehead. The expanded skin in this area was discretized with 3820 brick elements covering an area of 96.3 cm^2. For the case study II, aligned with the clinical case, one expander was placed in the posterior scalp, where the area of skin affected by expansion consisted of 2088 elements and covered 50.5 cm^2. An expander in the forehead and one in the cheek were then placed. The expanded forehead region was 48.8 cm^2 in area and was made up of 1800 elements. In the cheek the skin was modeled with 1200 elements and had an initial area of 29.3 cm^2.

Growth in the patient specific geometries follows the trends observed in the ideal settings of the previous section. As the expanded region is pressurized, the regions in the apex of the expander experience the greatest deformation. In consequence, skin grows more at the apex of the expander and progressively less towards the

periphery. This phenomenon is a consequence of the growth constitutive law, Eq. (13), itself based on our current understanding of skin mechanobiology.

There is always an interplay between the total, observed deformation, and the underlying tissue growth. In other words, at the beginning of the expansion process, most of the deformation is reversible, but as the process continues, skin will grow to restore the elastic stretch to ϑ^{crit}. The comparison of these two cases highlights the importance of considering patient-specific geometries when planning a procedure.

Quantitatively, for the top row of Fig. 6 corresponding to case I, the total area of expanded skin in this case starts at 149.4 cm^2, and progressively increases to 190.2 cm^2, 207.4 cm^2, 220.4 cm^2 and reaches 251.2 cm^2 by the end of the inflation process. The total fractional area gain for this case was 1.68. The different expanded regions grew differently for case I. The posterior scalp increased 1.73 in area, while the forehead and top scalp regions grew 1.66 in area. The bottom row of Fig. 6, corresponding to the case II, showed an overall fractional area gain of 1.77. The initial area of the expanded region for case II was 128.7 cm^2, and at the snapshots shown, the area increased to 176.0 cm^2, 191.3 cm^2, 202.1 cm^2 and 227.1 cm^2. Similar to case I, different expanders induced different area growth. The top of the scalp contributed 1.74 area gain, the forehead grew 1.82 the original surface, and the cheek grew by 1.72 times its initial area.

This example shows that placing the expanders in distinct anatomical regions can increase the overall area gain. At the same time, the absolute area useful for reconstruction was greater in case I. In other words, case I was not as efficient in terms of growth rate, but allowed for a greater area to be expanded and ultimately produced more skin compared to case II. We remark that the parameters used in the simulation were manually selected to match the clinical experience. A more careful calibration is needed to make more powerful predictions and impact treatment guidelines. On the other hand, these simulations were done with the same exact parameters, thus isolating the contribution of treatment strategy to area gain. This kind of insight is extremely valuable to design better tissue expansion treatments.

5 Conclusions

The future of reconstructive surgery is tied to new developments in our ability to predict skin adaptation under non-physiological regimes. Growth is one of the fundamental processes of skin tissues. Mathematical modeling of skin growth is particularly relevant in the context of tissue expansion, a reconstructive surgery technique that leverages the ability of living matter to adapt to mechanical cues [74]. Despite the popularity of this technique, we are still unable to control skin adaptation at will in order to grow skin patches of the desired area and shape. For instance, tissue expanders are the standard treatment for breast reconstruction after mastectomy, but complications and suboptimal outcomes characterized by unnatural breast shape are still common and impact cancer survivors' quality of life [68]. Tissue expansion is also widely used for reconstruction of large birth

defects such as nevus. Following skin growth, flap design is done with extreme care. However, our inability to anticipate the amount of newly grown skin and the new relaxed configuration of the skin after expander removal, can lead to excessive mechanical stress after flap closure. Tension in the flap causes delayed healing, wound dehiscence, necrosis, or hypertrophic scarring [6]. Solving these challenges relies on our ability to accurately describe skin deformation and adaptation with computational models. The progress in this area is already leading to personalized treatment and data-driven approaches in medicine [50, 54].

In this chapter we summarized the modeling framework to describe skin growth in response to supra-physiological stretch. The theoretical basis of this framework is the multiplicative split of the deformation gradient into growth and elastic contributions. This split has been adopted in the biomechanics community to model a wide variety of tissues with excellent agreement against experimental evidence [42]. Here we have specialized the general volumetric growth approach to skin tissues, characterized by area growth. The numerical solution of tissue expansion cases is achieved with custom finite element formulations [53].

In addition to modeling skin growth for its importance in tissue expansion, skin is an ideal model system to gain fundamental insight into how living tissues respond to mechanical cues. This is, at the same, a point for improvement of the current modeling approaches of finite volumetric growth: new, detailed mechanosensing models are lacking. Taking a step back, recall that the constitutive models needed to close the balance equations and fully define the problem involve two contributions. One set of constitutive relations corresponds to the elastic component of the deformation. The other constitutive law is needed for the growth component. The constitutive law for the elastic component has received significant attention over the past five decades, and many models of skin's mechanical behavior have been proposed, see [34] for a thorough and recent overview of skin mechanics. The biological aspect of growth mechanics remains poorly understood.

In this chapter we presented a phenomenological relationship connecting the elastic strain to the growth rate at one point. This simple relationship, albeit phenomenological, is indeed inspired on biological knowledge and clinical observation, and, while simple, has predicted growth patterns that were later confirmed experimentally [16, 46, 66]. However, clinical interest is turning towards therapies that control both the mechanical fields (amount and timing of expansion), as well as the cellular mechanisms implicated in skin growth due to overstretch [75]. The potential of these new techniques crucially relies on improving our understanding of how exactly the resident skin cells are sensing the mechanical cues, and how these inputs control the cell action on their local microenvironment. This remains an exciting are of research.

In terms of the computational implementation of the continuum mechanics framework, here we focused on a finite element formulation. New numerical analysis tools such as isogeometric methods are an appealing alternative to simulate skin growth. Isogeometric analysis uses basis functions that are C^1 continuous over the entire domain, enabling novel thin shell formulations for nonlinear membranes based on Kirchhoff-Love kinematics [44, 76].

Finally, in addition to sound modeling approaches and robust numerical tools, the need for extensive experimental calibration of these models cannot be understated. Work on large animal models such as the swine are currently being stablished for this purpose. Skin is advantageously exposed to the outside world and its deformation can be captured with new 3D imaging techniques that are easily incorporated into the operating room. We have used multi-view stereo to track the deformation of large porcine skin patches over long time periods. Sacrificing the animal at the end of the experiment reveals the elastic and growth components of the deformation [66]. Animal models of tissue expansion were proposed decades ago, however, they lacked a rigorous framework to distinguish the different components of the deformation [77, 78]. Our experiments have confirmed that skin grows more in the apex of the expander, and that different expander shapes induce different growth patterns. The next step in experimental calibration of the skin growth models is the acquisition of human data.

In conclusion, modeling of skin growth has advanced tremendously in the past 10 years. It is currently an exciting field with new challenges in theory, numerics, and experimentation. Addressing the gaps in the field will help us achieve personalized and predictive tools for optimal preoperative planning and improved reconstructive surgery outcomes.

References

1. Taber LA (1995) Biomechanics of growth, remodeling, and morphogenesis. Appl Mech Rev 48:487
2. Marcus J, Horan DB, Robinson JK (1990) Tissue expansion: past, present, and future. J Am Acad Dermatol 23:813–825
3. Neumann CG (1957) The expansion of an area of skin by progressive distention of a subcutaneousballoon: use of the method for securing skin for subtotal reconstruction of the ear. Plast Reconstr Surg 19:124–130
4. Manders EK, Schenden MJ, Furrey JA, Hetzler PT, Davis TS, Graham WP (1984) Soft-tissue expansion: concepts and complications. Plast Reconstr Surg 74(4):493–507
5. Bozkurt A, Groger A, O'Dey D, Vogeler F, Piatkowski A, Fuchs PC et al (2008) Retrospective analysis of tissue expansion in reconstructive burn surgery: evaluation of complication rates. Burns 34:1113–1118
6. LoGiudice J, Gosain AK (2003) Pediatric tissue expansion: indications and complications. J Craniofac Surg 14:866
7. Khalatbari B, Bakhshaeekia A (2013) Ten-year experience in face and neck unit reconstruction using tissue expanders. Burns 39:522–527
8. Gosain AK, Zochowski CG, Cortes W (2009) Refinements of tissue expansion for pediatric forehead reconstruction: a 13-year experience. Plast Reconstr Surg 124:1559–1570
9. Baker SR (1991) Fundamentals of expanded tissue. Head Neck 13:327–333
10. Pusic AL, Cordeiro PG (2003) An accelerated approach to tissue expansion for breast reconstruction: experience with intraoperative and rapid postoperative expansion in 370 reconstructions. Plast Reconstr Surg 111:1871–1875
11. Ronert MA, Hofheinz H, Manassa E, Asgarouladi H, Olbrisch RR (2004) The beginning of a new era in tissue expansion: self-filling osmotic tissue expander—four-year clinical experience. Plast Reconstr Surg 114:1025–1031

12. Schmidt SC, Logan SE, Hayden JM, Ahn ST, Mustoe TA (1991) Continuous versus conventional tissue expansion: experimental verification of a new technique. Plast Reconstr Surg 87:10–15
13. Gosain AK, Chepla KJ (2012) Giant nevus sebaceus: definition, surgical techniques, and rationale for treatment. Plast Reconstr Surg 130:296e–304e
14. Buganza Tepole A, Gart M, Purnell CA, Gosain AK, Kuhl E (2015) Multi-view stereo analysis reveals anisotropy of prestrain, deformation, and growth in living skin. Biomech Model Mechanobiol 14:1007–1019
15. De Filippo RE, Atala A (2002) Stretch and growth: the molecular and physiologic influences of tissue expansion. Plast Reconstr Surg 109:2450–2462
16. Buganza Tepole A, Gart M, Gosain AK, Kuhl E (2014) Characterization of living skin using multi-view stereo and isogeometric analysis. Acta Biomater 10:4822–4831
17. Eyckmans J, Boudou T, Yu X, Chen CS (2011) A hitchhiker's guide to mechanobiology. Dev Cell 21:35–47
18. McGrath JA, Eady RAJ, Pope FM (2004) Anatomy and organization of human skin. In: Rook's textbook of dermatology. Blackwell Science Ltd, Oxford, pp 45–128
19. Fuchs E, Raghavan S (2002) Getting under the skin of epidermal morphogenesis. Nat Rev Genet 3:199–209
20. Epstein WL, Maibach HI (1965) Cell renewal in human epidermis. Arch Dermatol 92:462
21. Lechler T, Fuchs E (2005) Asymmetric cell divisions promote stratification and differentiation of mammalian skin. Nature 437:275–280
22. Reichelt J (2007) Mechanotransduction of keratinocytes in culture and in the epidermis. Eur J Cell Biol 86:807–816
23. Margadant C, Charafeddine RA, Sonnenberg A (2010) Unique and redundant functions of integrins in the epidermis. FASEB J 24:4133–4152
24. Stupack DG, Cheresh DA (2002) Get a ligand, get a life: integrins, signaling and cell survival. J Cell Sci 115:3729–3738
25. Hertle M, Adams J, Watt F (1991) Integrin expression during human epidermal development in vivo and in vitro. Development 112:193–206
26. Runswick SK, O'Hare MJ, Jones L, Streuli CH, Garrod DR (2001) Desmosomal adhesion regulates epithelial morphogenesis and cell positioning. Nat Cell Biol 3:823–830
27. Schultz GS, Wysocki A (2009) Interactions between extracellular matrix and growth factors in wound healing. Wound Repair Regen 17:153–162
28. Kippenberger S, Bernd A, Loitsch S, Guschel M, Müller J, Bereiter-Hahn J et al (2000) Signaling of mechanical stretch in human keratinocytes via MAP kinases. J Invest Dermatol 114:408–412
29. Grinnell F (2003) Fibroblast biology in three-dimensional collagen matrices. Trends Cell Biol 13:264–269
30. Driskell RR, Lichtenberger BM, Hoste E, Kretzschmar K, Simons BD, Charalambous M et al (2013) Distinct fibroblast lineages determine dermal architecture in skin development and repair. Nature 504:277–281
31. Jiang C, Shao L, Wang Q, Dong Y (2012) Repetitive mechanical stretching modulates transforming growth factor-β induced collagen synthesis and apoptosis in human patellar tendon fibroblasts. Biochem Cell Biol 90:667–674
32. Silver FH, Siperko LM, Seehra GP (2003) Mechanobiology of force transduction in dermal tissue. Skin Res Technol 9:3–23
33. Prajapati RT, Chavally-Mis B, Herbage D, Eastwood M, Brown RA (2000) Mechanical loading regulates protease production by fibroblasts in three-dimensional collagen substrates. Wound Repair Regen 8:226–237
34. Limbert G (2017) Mathematical and computational modelling of skin biophysics: a review. Proc R Soc A Math Phys Eng Sci 473:20170257
35. Buganza Tepole A, Vaca EE, Purnell CA, Gart M, McGrath J, Kuhl E et al (2017) Quantification of strain in a porcine model of skin expansion using multi-view stereo and isogeometric kinematics. J Vis Exp 2017(122):55052

36. Himpel G, Kuhl E, Menzel A (2005) Computational modelling of isotropic multiplicative growth. Comput Model Eng Sci 8:119–134
37. Rodriguez EK, Hoger A, McCulloch AD (1994) Stress-dependent finite growth in soft elastic tissues. J Biomech 27:455–467
38. Lee EH (1969) Elastic-plastic deformation at finite strains. J Appl Mech 36(1):1–6
39. Göktepe S, Abilez OJ, Parker KK (2010) A multiscale model for eccentric and concentric cardiac growth through sarcomerogenesis. J Theor Biol 265(3):433–442
40. Roose T, Chapman SJ, Maini PK (2007) Mathematical models of avascular tumor growth. Siam Rev 49:179–208
41. Cowin SC (1996) Strain or deformation rate dependent finite growth in soft tissues. J Biomech 29:647–649
42. Ambrosi D, Ateshian GA, Arruda EM, Cowin S, Dumais J, Goriely A et al (2011) Perspectives on biological growth and remodeling. J Mech Phys Solids 59:863
43. Socci L, Pennati G, Gervaso F, Vena P (2006) An axisymmetric computational model of skin expansion and growth. Biomech Model Mechanobiol 6:177–188
44. Buganza Tepole A, Kabaria H, Bletzinger K-U, Kuhl E (2015) Isogeometric Kirchhoff-Love shell formulations for biological membranes. Comput Methods Appl Mech Eng 293:328–347
45. Cermelli P, Gurtin ME (2001) On the characterization of geometrically necessary dislocations in finite plasticity. J Mech Phys Solids 49:1539–1568
46. Buganza Tepole A, Gart M, Purnell CA, Gosain AK, Kuhl E (2016) The incompatibility of living systems: characterizing growth-induced incompatibilities in expanded skin. Ann Biomed Eng 44:1734–1752
47. Liu SQ, Fung YC (1988) Zero-stress states of arteries. J Biomech Eng 110:82–84
48. Ambrosi D, Mollica F (2002) On the mechanics of a growing tumor. Int J Eng Sci 40:1297–1316
49. Rausch MK, Kuhl E (2013) On the effect of prestrain and residual stress in thin biological membranes. J Mech Phys Solids 61:1955–1969
50. Zöllner AM, Buganza Tepole A, Kuhl E (2012) On the biomechanics and mechanobiology of growing skin. J Theor Biol 297:166–175
51. Kuhl E, Steinmann P (2003) Mass- and volume-specific views on thermodynamics for open systems. Proc R Soc A Math Phys Eng Sci 459:2547–2568
52. Kuhl E, Steinmann P (2003) On spatial and material settings of thermo-hyperelastodynamics for open systems. Acta Mech 160:179–217
53. Buganza Tepole A, Joseph Ploch C, Wong J, Gosain AK, Kuhl E (2011) Growing skin: a computational model for skin expansion in reconstructive surgery. J Mech Phys Solids 59:2177–2190
54. Buganza Tepole A, Kuhl E, Gosain AK (2012) Stretching skin: the physiological limit and beyond. Int J Non Linear Mech 47:938–949
55. Buganza Tepole A (2017) Computational systems mechanobiology of wound healing. Comput Methods Appl Mech Eng 314:46–70
56. Rivera R, LoGiudice J, Gosain AK (2005) Tissue expansion in pediatric patients. Clin Plast Surg 32:35–44
57. Chin MS, Ogawa R, Lancerotto L, Pietramaggiori G, Schomacker KT, Mathews JC et al (2010) In vivo acceleration of skin growth using a servo-controlled stretching device. Tissue Eng Part C Methods 16:397–405
58. Pamplona DC, Velloso RQ, Radwanski HN (2014) On skin expansion. J Mech Behav Biomed Mater 29:655–662
59. Austad ED, Pasyk KA, McClatchey KD, Cherry GW (1982) Histomorphologic evaluation of guinea pig skin and soft tissue after controlled tissue expansion. Plast Reconstr Surg 70:704–710
60. Erba P, Miele LF, Adini A, Ackermann M, Lamarche JM, Orgill BD et al (2011) A morphometric study of mechanotransductively induced dermal neovascularization. Plast Reconstr Surg 128:288e–299e

61. Derderian CA, Bastidas N, Lerman OZ, Bhatt KA, Lin S-E, Voss J et al (2005) Mechanical strain alters gene expression in an in vitro model of hypertrophic scarring. Ann Plast Surg 55:69–75. discussion 75
62. Flynn C, Taberner AJ, Nielsen PMF, Fels S (2013) Simulating the three-dimensional deformation of in vivo facial skin. J Mech Behav Biomed Mater 28:484–494
63. Flynn C, Taberner A, Nielsen P (2011) Mechanical characterisation of in vivo human skin using a 3D force-sensitive micro-robot and finite element analysis. Biomech Model Mechanobiol 10:27–38
64. Göktepe S, Abilez OJ, Kuhl E (2010) A generic approach towards finite growth with examples of athlete's heart, cardiac dilation, and cardiac wall thickening. J Mech Phys Solids 58:1661–1680
65. Zöllner AM, Holland MA, Honda KS, Gosain AK, Kuhl E (2013) Growth on demand: reviewing the mechanobiology of stretched skin. J Mech Behav Biomed Mater 28:495–509
66. Lee T, Vaca EE, Ledwon JK, Bae H, Topczewska JM, Turin SY et al (2018) Improving tissue expansion protocols through computational modeling. J Mech Behav Biomed Mater 82:224–234
67. Patel P a, Elhadi HM, Kitzmiller WJ, Billmire D a, Yakuboff KP (2014) Tissue expander complications in the pediatric burn patient: a 10-year follow-up. Ann Plast Surg 72:150–154
68. Cordeiro PG, McCarthy CM (2006) A single surgeon's 12-year experience with tissue expander/implant breast reconstruction: part I. A prospective analysis of early complications. Plast Reconstr Surg 118:825–831
69. Zöllner AM, Tepole AB, Gosain AK (2011) Growing skin: tissue expansion in pediatric forehead reconstruction. Biomech Model Mechanobiol 11:855–877
70. van Rappard JH, Molenaar J, van Doorn K, Sonneveld GJ, Borghouts JM (1988) Surface-area increase in tissue expansion. Plast Reconstr Surg 82:833–839
71. McCauley RL (2005) Tissue expansion reconstruction of the scalp. Semin Plast Surg 19:143–152
72. Gosain AK, Cortes W (2007) Pediatric tissue expansion for forehead reconstruction: a 13-year review and an algorithm for its use. Am Soc Plast Surg. Baltimore, Abstract 13288
73. Zöllner AM, Buganza Tepole A, Kuhl E (2012) On the biomechanics and mechanobiology of growing skin. J Theor Biol 297:166–175
74. Baker SR, Swanson NA (1990) Clinical applications of tissue expansion in head and neck surgery. Laryngoscope 100(3):313–319
75. Yang M, Li Q, Sheng L, Li H, Weng R, Zan T (2011) Bone marrow—derived mesenchymal stem cells transplantation accelerates tissue expansion by promoting skin regeneration during expansion. Ann Surg 253:202–209
76. Chen L, Nguyen-Thanh N, Nguyen-Xuan H, Rabczuk T, Bordas SPA, Limbert G (2014) Explicit finite deformation analysis of isogeometric membranes. Comput Methods Appl Mech Eng 277:104–130
77. Beauchene JG, Chambers MM, Peterson AE, Scott PG (1989) Biochemical, biomechanical, and physical changes in the skin in an experimental animal model of therapeutic tissue expansion. J Surg Res 47:507–514
78. Bartell TH, Mustoe TA (1989) Animal models of human tissue expansion. Plast Reconstr Surg 83:681–686

Constitutive Modelling of Wound Healing

Adrian Buganza Tepole

Abstract Wound healing is a complex process spanning several temporal and spatial scales and requiring precise coordination of cell populations through mechanical and biochemical regulatory networks. The dermis, which is the load bearing layer of the skin, is rebuilt after injury by fibroblasts through collagen deposition and active contraction. Fibroblast activity is controlled by cytokine gradients established during the initial inflammatory response, as well as by mechanical cues. However, even though we know the individual components of the wound healing system, in particular the factors associated with fibroblast-driven remodeling, we are still unable to achieve perfect skin regeneration and, instead, wounds lead to scars with inferior mechanical properties compared to healthy skin. Computational models offer the unique ability to quantitatively analyze the dynamics of wound healing in order to attain a deeper understanding of this system. Here we show a continuum framework to describe the essential bio-chemo-mechanical couplings during wound healing, together with a finite element implementation of a model problem. We account for nonlinear mechanical behavior and anisotropy of skin through a microstructure-based strain energy function, as well as the split of the deformation gradient into elastic and permanent deformations. These microstructure features evolve in time according to the spatiotemporal evolution of cell and cytokine concentration fields, which obey reaction diffusion differential equations. The model problem exhibits emergent features of wound healing dynamics, such as wound contraction by fibroblasts in the periphery of the injury. Moreover, the proposed framework can be readily extended to more comprehensive regulatory networks and used to simulate other realistic geometries. Thus, we expect that the formulation presented here will enable further advances in wound healing research.

A. Buganza Tepole (✉)
School of Mechanical Engineering and Weldon School of Biomedical Engineering, Purdue University, West Lafayette, IN, USA
e-mail: abuganza@purdue.edu

G. Limbert (ed.), *Skin Biophysics*, Studies in Mechanobiology, Tissue Engineering and Biomaterials 22,
https://doi.org/10.1007/978-3-030-13279-8_4

1 Introduction

One of the most remarkable properties of skin is its ability to heal following injury. This crucial adaptive mechanism is needed since skin is our first line of defense against outside harm, and we certainly damage this tissue throughout our life. Moreover, skin healing is needed following any surgical procedure. In the US alone there are more than 34 million surgeries each year, and skin self-repair is needed after each of them [1]. Unfortunately, despite the impressive capability of skin to regain some of its functionality, wound healing is not perfect and it does not result in tissue with the exact same properties as healthy skin, but rather it leads to a scar [2, 3].

The process of wound healing is an orchestra of different cell types, growth factors, and structural components, which all come together in synchrony to form the new tissue [4]. Such a complex dynamical system is tuned to restore tissue function and prevent infection in a timely manner, but the fine balance between these processes is difficult to achieve. Indeed, excessive inflammation signals are linked to a fibrotic response by resident skin cells, and lead to hypertrophic scars and contracture [5, 6]. These complications add up to a 4 billion dollar annual burden on the US healthcare system [7].

Interestingly, in the fetus wounds heal without a scar [8, 9]. Extensive research over the past decades has provided valuable information of the different elements involved in the wound healing process. Inflammation and extra-cellular matrix (ECM) composition, for example, have been compared between fetuses and adults [10]. Consequently, numerous scaffolds have been manufactured, controlling different aspects of the wound milieu such as microstructure or growth factor profiles that try to mimic the fetal healing environment [11, 12]. Great progress has been done in the area of skin tissue engineering and wound dressing design. Yet, we are still unable to control wound dynamics at will. The shortcomings of current treatment strategies can be explained by the point of view of systems biologists: the list of elements of a biological process is just a partial picture of the problem, and the dynamics of the regulatory networks are key to understand, and eventually control, the wound healing process [13]. Furthermore, given the complexity of the system, intuition is not enough, and computational models are particularly important in this context. Mathematical models can be used to tease out the strength of the interactions between the different elements of the wound healing regulatory network, test new hypotheses, and pose optimization problems to improve treatment.

Wound healing spatiotemporal dynamics are particularly fascinating from a mechanical point of view. Skin is a thin membrane made out of two layers, epidermis at the top and dermis at the bottom [14]. The dermis is the main load bearing layer. It is made primarily out of collagen fibers that form an inter-weaving network in the healthy skin [15]. Fibroblasts are the main resident cells of the dermis and are responsible for the continuous remodeling of the tissue [16]. Upon wounding, the collagen network is destroyed and replaced by a fibrin matrix of inferior mechanical

properties [17]. This temporary matrix has to be remodeled by an influx of new cells from the surrounding healthy tissue. Incoming fibroblasts are not only tasked with depositing new collagen, but also have to rebuild the fiber network architecture. Additionally, they close the wound by pulling on the collagen matrix leading to contraction and contracture of the tissue [18]. Briefly, as fibroblasts migrate into the wound, the inflammation-rich environment leads to fibroblast differentiation into a contractile phenotype called the myofibroblast [19]. Traction forces by these cells compact the collagen fibers and bring the wound edges closer together. The acute contraction is coupled with longer-term remodeling, in other words, the acute changes gradually become permanent. More details about wound mechanics and mechanobiology are saved for Sect. 4.4 on the model description. Here we simply emphasize the stunning coupling between the fibroblast population, the inflammation response, and the mechanical environment.

Mathematical modeling of wounds is not a new field. The seminal work by Sherratt and Murray dates back to 1990 [20]. In their first paper, these authors introduced the concept of a traveling wave of epidermal cells during re-epithelialization. Work by Tranquillo and Murray around the same time was also pioneering [21]. These authors explored the role of fibroblast-driven contraction. Wound models have undergone a steady evolution since those initial efforts. A notable trend has been the sophistication of the models in terms of the number of cells and cytokines considered. The consideration of detailed tissue mechanics, however, has lagged behind these developments. Wound models had considered simplistic assumptions for the skin mechanical behavior until recently [22]. This chapter is focused precisely on this aspect of wound healing modeling.

The structure of the chapter is as follows. In the next section we review the wound healing process and introduce all the different elements of the dynamical system. In Sect. 4.3 we briefly review the modeling strategies. In Sect. 4.4, we fully describe a continuum-framework for wound mechanobiology. Section 4.5 deals with the implementation of the continuum-framework into a custom finite element formulation. Section 4.6 shows examples and highlights the main features of the modeling framework. Finally, we conclude the chapter with a conclusions section.

2 Wound Healing in Time and Space

Wounds heal in four overlapping temporal stages. Immediately after injury, a fibrin-rich clot forms in a process called hemostasis. This fast response occurs in the order of seconds to minutes and it is aimed at preventing blood loss and creating a provisional matrix for cell infiltration [23]. The blood clot is rich in platelets which degranulate, releasing a first wave of pro-inflammatory signals, particularly platelet derived growth factor (PDGF) [24]. The second stage of wound healing is called inflammation and takes place from minutes to a few days. Within this phase there are two waves of incoming cells. Neutrophils are recruited first to the wound site [25]. These cells are equipped to kill pathogens by releasing chemokines such as inter-

leukins and tumor necrosis factor alpha (TNFα) [26]. In addition to help sterilize the wound site, cytokines released by neutrophils establish a gradient to direct the infiltration of the second wave of inflammatory cells : the macrophages. These cells further contribute to cleaning the fibrin clot by phagocytizing debris, pathogens, and neutrophils. Concomitantly, macrophages establish yet another chemical signal gradient, primarily by releasing transforming growth factor beta 1 (TGFβ1). For a more comprehensive review of inflammation please see these detailed reviews on the topic [5, 27, 28].

The third temporal stage of wound healing will be the starting point for our modeling framework in Sect. 4.4. This third phase is termed proliferation and takes from days to weeks [29]. Our interest in this stage stems from the fact that it is in the proliferation stage that skin is rebuilt. At the epidermis level, keratinocytes proliferate and migrate inward in the process called re-epithelialization [30]. At the dermis level, the fibrin clot is filled with incoming fibroblasts and endothelial cells. Endothelial cells establish a vascular network in the process of angiogenesis [31]. The new vasculature is needed in order to guarantee nutrient supply for this stage of the healing process which, as can be expected, is characterized by a high metabolic activity and a large number of cells. Fibroblasts, the prime example of a mechanosensitive cell, are responsible for dermis remodeling in the proliferative stage [32]. From the point of view of skin biomechanics, fibroblasts' actions are the central piece to understand how skin regains its mechanical functionality after injury.

The last stage of wound healing is remodeling. Fibroblasts are again under the spotlight for this process. Towards the end of the proliferative phase the skin has regained its functionality. The epidermis has been restored and the fibrin clot has been replaced with a collagen ECM. However, the new tissue has properties that do not match those of the healthy dermis [2, 33]. With the decrease in metabolic needs, a majority of the cells undergo apoptosis [34]. During this last phase, a scarce fibroblast population remains in the scar, and it slowly remodels the collagen network towards a more physiological state. Scar remodeling spans months to even years [35]. Unfortunately, even after such a long time window, the scar tissue does not revert completely to the healthy state.

3 Mathematical Modeling of Wound Healing

Given the large number of cells and chemical species present during wound healing, the different cellular processes that occur, the tissue mechanics aspects, and the multiple spatial and temporal scales, modeling efforts have been very diverse. To better dissect the advantages and disadvantages of the different strategies, we divide the modeling efforts according to three main features. First, we distinguish between discrete and continuum models. This separation is closely related to the scale of interest. Discrete models are usually concerned with the cell (microscopic) scale while continuum models typically deal with the tissue (macroscopic) scale.

Secondly, we discuss the modeling approaches according to the emergent behavior of interest, namely, the cellular process being emphasized. Three processes of the proliferative phase have been the focus of investigation in the past two decades: re-epithelialization, angiogenesis, and dermis remodeling. Models of inflammation have also been developed, but they will not be considered here. The reader is referred to [36, 37]. Lastly, we focus on the complexity of the spatial domain being simulated. Starting from point (zero-dimensional or 0D) models, other simple domains considered have been one-dimensional (1D) or axisymmetric (1.5D). Most of the emphasis has been on two-dimensional (2D) models, and there are a few examples of three-dimensional (3D) models which are the models of greatest complexity in terms of domain representation. Table 1 summarizes how different published mathematical models of wound healing fit within our categories [38].

We start by discussing discrete modeling approaches. As the name suggests, this strategy is characterized by accounting for individual cells. These formulations are also called agent-based models (ABMs) and they have been very popular because, by accounting for individual cell action, they are more closely related to experimental evidence of cell behavior and cell-ECM interactions. Furthermore, a fundamental feature of ABMs is that even though only rules for individual cells are prescribed, the simulations of entire cell populations exhibit emergent behavior [64, 65].

The discrete modeling framework has been used to study the three different processes in Table 1. At the level of the epidermis, modeling individual keratinocytes, researchers have identified traveling wave patterns consistent with experimental observations in wound scratch assays. In terms of angiogenesis, these cell-centered approaches have been able to test hypothesis regarding fractal pattern self-assembly characteristic of microvasculature geometries. Modeling individual fibroblast migration into a wound has helped test hypotheses of how cell influx affects collagen network orientation in the scar (see Table 1 for references).

Table 1 Classification of mathematical models of wound healing

Scale	Complexity	Re-epithelialization	Angiogenesis	Dermis contraction and remodeling
Cell-discrete	0/1/1.5D			
	2D	[39, 40]	[41, 42]	[43–46]
	3D	[47]	[48–50]	
Tissue-continuum	0/1/1.5D	[20, 51]	[52–56]	[21, 57, 58]
	2D	[59, 60]	[61]	[62, 63]
	3D			[22]

Published models of wound healing can be classified according to three criteria: (i) discrete or continuum formulations; (ii) emergent behavior of interest (epithelialization, angiogenesis, remodeling); and (iii) domain or implementation complexity, from zero to three dimensional spatial dimensions. References to representative publications have been selected. See [38] for a review

There are advantages and limitations for the discrete approach. As mentioned already, this modeling strategy is particularly suitable for the microscopic scale because it accounts for individual cell action. As a consequence, ABMs are not directly applicable to large domains. Some efforts have been made to link ABMs to the tissue scale. For example, Ziraldo et al. [66] used rules akin to those applicable to individual cells, but instead of simulating the cells, they considered mesh elements (much larger than the cell dimension) as the agents.

Another reason why ABMs are limited to small domains is that the computational cost increases dramatically as the domain size increases. The algorithmic complexity is also much greater going from two to three dimensions. Because of this challenges, discrete models have been used almost exclusively in two-dimensional simulations, see Table 1.

The alternative to discrete models are continuum descriptions. In the continuum assumption, the cells and cytokines are described not individually but as concentration or density fields. The evolution of these fields in time and space is described with reaction diffusion partial differential equations (PDEs).

The immediate consequence of describing the wound process with continuous fields is that these descriptions are directly related to the tissue scale, therefore they enable us to explore hypotheses closely related to real clinical scenarios. The obvious drawback is that the direct connection to individual cell actions, cell-cell and cell-ECM interactions, is lost. Therefore, the main challenge for these descriptions is to link the flux and reaction terms that appear in a reaction-diffusion PDE system, to cellular events. Several forms of constitutive equations have been proposed to capture cell and cytokine dynamics. Yet, rigorous up-scaling from the cell-scale remains an area of active research.

Continuum descriptions are of particular relevance to study wound mechanics. Re-epithelialization and angiogenesis have been modeled with reaction-diffusion PDEs (see Table 1 for relevant references), however, it is wound mechano-adaptation that truly benefits from this modeling strategy. Most ABMs have been limited to simplified mechanical descriptions. Some efforts have been made to couple individual cell action from ABMs to accurate mechanical description of soft tissues [46, 67], but this has been limited to small domains. Continuum models had also disregarded detailed tissue mechanics until recently [22, 63]. In terms of algorithmic complexity, similar to discrete approaches, the vast majority of the work has focused on two-dimensional descriptions and regular geometries. In contrast to discrete models, extending the continuum framework to arbitrary three-dimensional geometries is easily achievable through new finite element discretizations [22].

In this chapter we present a continuum description of wound mechanics. We present a general description of the healing modeling framework in this setting and then make particular assumptions for a simple system of only a single cell population and a single chemical concentration.

4 Mathematical Framework of Wound Healing Mechanobiology

A continuum description of wound healing is presented. First, all the relevant variables are introduced in a kinematics subsection. The variables of interest are divided into four classes: tissue deformation, tissue microstructure, cell fields, and chemical fields. Then, the balance equations satisfied for each of the different classes of variables are discussed. Tissue displacements satisfy momentum balance while cells and chemicals obey mass balance captured with reaction-diffusion equations. The microstructure changes locally in time according to ordinary differential equations that describe local cell-ECM interactions.

4.1 Kinematics

Let $\boldsymbol{X} \in B_0 \subset \mathbb{R}^3$ denote the material coordinates that specify the initial geometry of the wound. The material points get mapped to the deformed state $\boldsymbol{x} \in B_t \subset \mathbb{R}^3$ through the deformation mapping $\boldsymbol{x} = \varphi(\boldsymbol{X})$. The deformation gradient $\boldsymbol{F} = \partial \boldsymbol{x}/\partial \boldsymbol{X}$ describes the local geometric changes. To account for one of the most general frameworks of biological tissues, here we consider the multiplicative split of the deformation gradient into growth and elastic contributions

$$\boldsymbol{F} = \boldsymbol{F}^e \cdot \boldsymbol{F}^g \tag{1}$$

Where $\boldsymbol{F}^g$ denotes local permanent volume changes, and $\boldsymbol{F}^e$ is an elastic deformation tensor that maps the differential volume elements from the intermediate configuration to the current, observed state of the wound at time t. We emphasize that the multiplicative split of the deformation gradient has been typically used in the context of growing tissues. Here, however, the phenomenon of interest is permanent wound contraction, which can be interpreted as a negative growth process.

In addition to tissue displacements, the mechanical behavior of the skin tissue will be expressed in terms of microstructure variables. In the spirit of a general description, let $\boldsymbol{\Theta}$ denote the vector of microstructure variables. This vector includes, for example, mass fraction of collagen or fibrin fibers, orientation and dispersion of the fiber network, fiber diameter and stiffness, etc. We will introduce specific quantities later in this section.

In a standard continuum mechanics description, these variables would be enough to define the problem. During wound healing, however, the mechanical response changes in time and space due to the action of cells, which is in turn coordinated by a signaling network characterized by cytokine concentration fields. Let $\boldsymbol{\rho}(\boldsymbol{X}, t)$ denote the vector of cell density fields, and let $\boldsymbol{c}(\boldsymbol{X}, t)$ correspond to the vector of chemical concentrations in the domain. In the next section we will particularize the notation to the fibroblast population only and the TGFβ1 concentration only, but for

now we will continue with the general model description that could include several cell types and chemical species.

In order to describe the kinematics of the problem, some of the structural parameters need to be introduced at this point, specifically, those variables that are related to a geometric component of the microstructure. We consider the permanent area changes θ^g, the preferred fiber orientation in the reference configuration $\boldsymbol{a}_0$, and the fiber dispersion κ.

The growth tensor introduced through the multiplicative split is both a kinematic and a constitutive assumption. It requires additional constraints related to the geometry of the microstructure. In fact, the form of this tensor is specified as

$$\boldsymbol{F}^g = \theta^g \boldsymbol{I}_S + \boldsymbol{N} \otimes \boldsymbol{N} \tag{2}$$

Where $\boldsymbol{I}_s = \boldsymbol{I} - \boldsymbol{N} \otimes \boldsymbol{N}$ denotes the surface identity tensor, $\boldsymbol{N}$ is the normal to the skin surface, and $\boldsymbol{I}$ is the standard identity tensor in three dimensions. Thus, as can be intuited from Eq. (2), we will ignore through-thickness heterogeneity and will treat the skin as a thin membrane. This approach simplifies the model slightly while at the same time presents an important improvement to generalize a standard flat two-dimensional formulation. Some events during healing do require the description of a three-dimensional domain to capture the complexity of through-thickness cellular phenomena (such as epidermis stratification) [47]. However, from the point of view of a description that emphasizes skin mechanics, a thin membrane is very appealing. Indeed, skin can be described in this way using Kirchhoff-Love kinematics and discretized with shell elements and surface meshes instead of volume discretizations [68]. This kinematic assumption allows to capture realistic geometries in a three dimensional embedding with surface meshes. We have done both volume and plate simulations [22, 63].

The preferred fiber orientation and dispersion parameters are used to define the structural tensor in the reference configuration

$$\boldsymbol{A}_0 = \kappa \boldsymbol{I}_s + (1 - 2\kappa)\, \boldsymbol{a}_0 \otimes \boldsymbol{a}_0 \tag{3}$$

Upon deformation, the push-forward of the structural tensor leads to

$$\boldsymbol{A} = \boldsymbol{F} \cdot \boldsymbol{A}_0 \cdot \boldsymbol{F}^T = \kappa \boldsymbol{b} + (1 - 2\kappa)\, \boldsymbol{a} \otimes \boldsymbol{a} \tag{4}$$

With $\boldsymbol{b} = \boldsymbol{F} \cdot \boldsymbol{F}^T$ the left Cauchy-Green deformation tensor, and $\boldsymbol{a} = \boldsymbol{F} \cdot \boldsymbol{a}_0$ the push-forward of the preferred orientation field. The tensor $\boldsymbol{A}$ is, however, not a valid structural tensor in that it does not specify just a distribution of fiber orientations, but also contains information about fiber stretching. To obtain a valid structural tensor in the current configuration we normalize Eq. (4) to get

$$\widehat{\boldsymbol{A}} = \frac{\boldsymbol{A}}{\mathrm{tr}\,(\boldsymbol{A})} = \widehat{\kappa} \boldsymbol{i}_s + (1 - 2\,\widehat{\kappa})\, \widehat{\boldsymbol{a}} \otimes \widehat{\boldsymbol{a}} \tag{5}$$

In which $\widehat{\kappa}$ is the fiber dispersion in the current configuration, $\widehat{\boldsymbol{a}} = \boldsymbol{a}/\|\boldsymbol{a}\|$is the normalized fiber orientation in the current configuration, and $\boldsymbol{i}_s$ is the surface identity for the deformed surface. It must be noted that the growth tensor defined in Eq. (2) does not change the fiber orientation or dispersion, and therefore the structural tensor in Eq. (3) is also the structural tensor for the intermediate configuration.

The total deformation gradient defines a total measure of strain. For instance, the usual right Cauchy-Green deformation tensor $\boldsymbol{C} = \boldsymbol{F}^T \cdot \boldsymbol{F}$ can be used. In the context of growth and remodeling, it is more convenient to focus on the elastic deformation changes. We introduce the elastic part of the right Cauchy-Green deformation tensor

$$\boldsymbol{C}^e = \boldsymbol{F}^{eT} \cdot \boldsymbol{F}^e = \boldsymbol{C}_s^e + \lambda_N^e \boldsymbol{N} \otimes \boldsymbol{N} \tag{6}$$

Which has been decomposed into a surface component and a normal strain component. The decomposition in Eq. (6) is only valid when transverse-shear is ignored. As mentioned above, thin biological membranes such as skin have been deemed appropriate for Kirchhoff–Love kinematics, i.e., the normal to the surface stays normal throughout the deformation and, hence, no transverse shear occurs in this setting.

Another characteristic of skin as for most biological tissues, is the notion of incompressibility. Continuing with the use of the thin shell formulation, the normal strain can be explicitly calculated to satisfy this constraint

$$\lambda_N = \left\| \boldsymbol{F}^e \cdot \boldsymbol{N} \right\| = \left(\theta^e\right)^{-1} \tag{7}$$

Where the elastic area change θ^e was introduced. Alternatively, the elastic area change can be directly computed from the surface component of the right Cauchy-Green deformation tensor

$$\theta^e = \sqrt{\det\left(\boldsymbol{C}_s^e + \boldsymbol{N} \otimes \boldsymbol{N}\right)} \tag{8}$$

Other invariants of the surface component of the elastic deformation are also needed for the definition of the strain energy function. In particular, two invariants are of interest, one corresponding to the isotropic behavior and one pseudo-invariant to describe the fiber deformation

$$I_{1,s}^e = \operatorname{tr}\left(\boldsymbol{C}_s^e\right), I_{4,s}^e = \boldsymbol{a}_0 \cdot \boldsymbol{C}_s^e \cdot \boldsymbol{a}_0 \tag{9}$$

Note that the fourth pseudo-invariant is calculated using the elastic deformation tensor but with the reference fiber orientation. This is due to the definition of the growth tensor which leaves the structural tensor unchanged. In addition to the surface invariants, the trace of the full right Cauchy-Green deformation tensor $I_1^e = \operatorname{tr}\left(\boldsymbol{C}^e\right)$ will appear later on in order to couple the in plane component of the stress to the normal stress. This concludes the definition of all the essential kinematic ingredients of our formulation.

4.2 Balance Laws

4.2.1 Mechanical Equilibrium

To satisfy mechanical equilibrium we impose the balance of linear momentum which, in the current configuration takes the form $\nabla \cdot \boldsymbol{\sigma} = \mathbf{0}$. The stress, continuing with the aim of keeping the formulation very general, will be composed of a passive response, a pressure to impose the vanishing of the normal stress and incompressibility (together with the normal strain), and an active response that is a consequence of cell action

$$\boldsymbol{\sigma} = \boldsymbol{\sigma}^{\text{pas}} + \boldsymbol{\sigma}^{\text{act}} + p\boldsymbol{I} \tag{10}$$

The passive component of the stress is determined directly by the elastic deformation tensor. Recall that in the present derivation we treat skin as an incompressible, thin membrane, with hyperelastic mechanical behavior defined by a strain energy function. Therefore, the passive component of the stress tensor can be deduced from the strain energy function

$$\boldsymbol{\sigma}^{\text{pas}} = \frac{2}{J^e}\boldsymbol{F}^e \cdot \frac{\partial \psi}{\partial \boldsymbol{C}^e} \cdot \boldsymbol{F}^{eT} = \frac{1}{J^e}\boldsymbol{F}^e \cdot \boldsymbol{S}^{e,\text{pas}} \cdot \boldsymbol{F}^{eT} \tag{11}$$

Where the volume change $J^e = \det(\boldsymbol{F}^e) = 1$ when incompressibility is enforced, and we have introduced the strain energy denoted by ψ. Moreover, even though we have started with the description of stress in the current configuration, it may be of value to also consider the Lagrangian description. We have accordingly introduced the passive component of the second Piola-Kirchhoff stress tensor referred to the middle configuration. To get the stress referred to the initial configuration we can perform the corresponding pull-back operation

$$\boldsymbol{S}^{\text{pas}} = \boldsymbol{F}^{g-1} \cdot \boldsymbol{S}^{e,\text{pas}} \cdot \boldsymbol{F}^{g-T} \tag{12}$$

The active stress will be defined with a particular form in the following section. Nonetheless, here we can assume that this stress will be aligned with the structural tensor since fibers contract the ECM by pulling on the fiber network [69, 70].

$$\boldsymbol{\sigma}^{\text{act}} = T(\boldsymbol{\Theta}, \boldsymbol{\rho}, \boldsymbol{c})\,\widehat{\boldsymbol{A}} \tag{13}$$

Where the function $T(\circ)$ stands for cell traction, and can be a function of different structural elements as well as the cell and chemical concentration fields. The structural tensor used is the one corresponding to the current configuration. For completeness we pull-back this active stress to the initial configuration

$$\boldsymbol{S}^{\text{act}} = \frac{\theta^g}{\text{tr}(\boldsymbol{A})}\boldsymbol{A}_0 \tag{14}$$

The last component of the stress tensor is the pressure component. In the context of incompressibility of thin membranes, the normal strain can be analytically solved to satisfy this constraint. Then, the pressure can also be obtained analytically to satisfy $\sigma_n = 0$. The second Piola-Kirchhoff stress tensor, defined in the initial configuration, is finally assembled as

$$\boldsymbol{S} = \boldsymbol{S}^{\text{pas}} + \boldsymbol{S}^{\text{act}} + p\boldsymbol{C}^{-1} \tag{15}$$

Where the passive and active components have been defined in Eqs. (12) and (14) respectively, and the pressure can be also determined analytically to satisfy the vanishing of the normal stress in the reference configuration, $S_N = 0$. The mechanical equilibrium in the Lagrangian setting is $\nabla_X \cdot \boldsymbol{P} = \boldsymbol{0}$, where the divergence operator is now with respect to the reference coordinates $\boldsymbol{X}$, and $\boldsymbol{P} = \boldsymbol{F} \cdot \boldsymbol{S}$ is the first Piola-Kirchhoff stress tensor.

4.2.2 Mass Balance of Biological Fields

The cell populations and the chemical concentrations evolve in time satisfying mass balance. In particular, reaction and diffusion phenomena are the most important to consider. We then have that for each of the elements ρ_i of $\boldsymbol{\rho}$, and c_i of $\boldsymbol{c}$, the following reaction-diffusion systems dictate the transient response of the system

$$\begin{aligned} \dot{\rho}_i + \nabla \cdot \boldsymbol{q}_{\rho i} &= \mathrm{s}_{\rho i} \\ \dot{c}_i + \nabla \cdot \boldsymbol{q}_{ci} &= s_{ci} \end{aligned} \tag{16}$$

Where $\dot{(\circ)}$ is the material time derivative, $\nabla \cdot (\circ)$ is the divergence operator in the current configuration, and $\boldsymbol{q}$ and s are flux and source terms respectively. In the general case, the flux of cells can be a function of some or all of the other biological fields, i.e. $\boldsymbol{q}_{\rho i}(\boldsymbol{\rho}, \boldsymbol{c})$, whereas the flux term for the cytokines is going to be modeled as standard diffusion $\boldsymbol{q}_{ci}(c_i)$. The source terms could exhibit even more general couplings. Here we assume that a cell population is influenced by some or all other cell fields and cytokines, but also the state of stress and microstructure at a point. In other words, the source term for a cell population will be of the form $s_{\rho i}(\boldsymbol{\rho}, \boldsymbol{c}, \boldsymbol{\Theta}, \boldsymbol{\sigma}^e)$. The same will be assumed for the chemical concentration fields. Cytokines are produced by different cell populations, usually in response to other chemicals, but their production could also be altered by the state of stress, which leads us to propose a general source term $s_{ci}(\boldsymbol{\rho}, \boldsymbol{c}, \boldsymbol{\Theta}, \boldsymbol{\sigma}^e)$.

Alternative to a description in the current configuration, the reaction diffusion system of Eq. (16) can be recast in the Lagrangian setting

$$\begin{aligned} J\dot{\rho}_{\mathrm{i}} = \nabla_X \cdot \boldsymbol{Q}_{\rho i} &= J s_{\rho i} \\ J\dot{c}_i + \nabla_X \cdot \boldsymbol{Q}_{ci} &= J s_{ci} \end{aligned} \tag{17}$$

Where the divergence operator $\nabla_X \cdot (\circ)$ is now with respect to the reference coordinates $\boldsymbol{X}$, and the fluxes in this description are related to the Eulerian description by $\boldsymbol{Q}_{\rho i} = J\boldsymbol{F}^{-1}\boldsymbol{q}_{\rho i}$, and $\boldsymbol{Q}_{ci} = J\boldsymbol{F}^{-1}\boldsymbol{q}_{ci}$. For completeness we can define the source terms fully in the reference configuration as $S_{\rho i} = Js_{\rho i}$, $S_{ci} = Js_{ci}$, and the reference cell and chemical fields $\rho_{0i} = J\rho_i$, $c_{0i} = Jc_i$.

4.2.3 Local Remodeling

The structural and geometric components of the microstructure, all stored in the vector $\boldsymbol{\Theta}$, change locally. In other words, these variables change according to ordinary differential equations. For instance, for the variables that have been introduced already, θ^g, $\boldsymbol{a}_0$, κ, the transient response is going to be fully determined by functions $\dot{\theta}^g\,(\boldsymbol{\rho}, \boldsymbol{c}, \boldsymbol{\Theta}, \boldsymbol{\sigma}^e)$, and so on. Thus, in general we expect functions $\Theta_i(\boldsymbol{\rho}, \boldsymbol{c}, \boldsymbol{\Theta}, \boldsymbol{\sigma}^e)$ for each component Θ_i of the vector $\boldsymbol{\Theta}$. Explicit definitions will be presented for the model problem of wound healing which is described next.

4.3 Model Problem of Wound Healing and Constitutive Equations

The framework described thus far considers potentially several cell types and chemical fields. Indeed, there are examples of previous work considering multiple biological variables. For example, in [71], which focuses on the modeling of angiogenesis, fields for VEGF, PDGF, macrophages, fibroblasts, capillary tips and oxygen are described with continuous variables which satisfy equations analogous to those presented in Sect. 4.4.2.2. The model presented here focuses on fibroblast driven remodeling in response to TGF-β1. We refer the interested reader to [72, 73] for an overview of multiple cells and growth factors present in wound healing. In the context of *healing mechanics*, fibroblasts and TGFβ1 are the indispensable biological variables to be considered, and they offer an excellent model problem that can be easily generalized to multiple cell populations. Then, we denote $\rho(\boldsymbol{x}, t)$ to represent the fibroblast density field, and $c(\boldsymbol{x}, t)$ to be the TGFβ1 concentration field.

In addition to narrowing the cell and chemical fields to specific modeling choices, the structural variables also have to be explicitly defined. Here we restrict our attention to the collagen mass fraction ϕ. This is in addition to the variables related to the geometry of the microstructure that have already been introduced.

In summary, for the model problem we have a reference body defined by the coordinates $\boldsymbol{X} \in B_0 \subset \mathbb{R}^3$, and a deformed geometry $\boldsymbol{x} = \varphi(\boldsymbol{X}, t) \in B_t \subset \mathbb{R}^3$ at time t. The microstructure is described with the vector $\boldsymbol{\Theta}(\boldsymbol{x}, t) = \{\theta^g, \boldsymbol{a}_0, \kappa, \phi\}$, where we have made it explicit that these variables change in time and space as the wound heals. The evolution of the wound is the result of two biological fields, the fibroblast population $\rho(\boldsymbol{x}, t)$ and the TGFβ1 concentration $c(\boldsymbol{x}, t)$. These variables satisfy linear momentum balance, mass balance, and local remodeling laws, as specified in Sect. 4.4.2. To close the problem, we introduce the corresponding constitutive equations.

4.3.1 Stress

The passive component of the stress tensor follows from the strain energy. Here we adopt a two-dimensional version of the popular Holzapfel-Gasser-Ogden strain energy function [74, 75]. This form of the strain energy was originally proposed to describe the mechanical behavior of arteries but has since then been used to describe a wide variety of collagen-based materials. Mechanical tests of skin samples have been successfully fitted with this strain energy function [15, 76, 77]. Other choices of strain energy function based on microstructure considerations are also possible [78]. We modify the original description in two important ways. First of all, the original formulation considers a fiber network distributed in three dimensions. Here, however, we are restricting the skin to a membrane description. Accordingly, the structural tensor in our kinematic description is restricted to the tangent plane of the surface [79]. The second change is the explicit dependence of the fiber contribution on the collagen mass fraction. We propose

$$\begin{aligned} \psi &= \psi^m + \phi\psi^f \\ \psi^m &= k_0\left(I_1^e - 2\right) \\ \psi^f &= \frac{k_1}{2k_2}\left(\exp(\, k_2\big(\kappa\, I_{1s}^e + (1-2\kappa)\, I_{4s}^e - 1\big)^2 - 1\right. \end{aligned} \tag{18}$$

ψ^m is the strain energy of the isotropic matrix in which the fiber network is embedded, and ψ^f is the fiber contribution. The response of the matrix is controlled by the parameter k_0, while the fiber contribution is parameterized with k_1 and k_2. Note that the isotropic part of the strain energy is in terms of the full three-dimensional invariant I_1^e, which is needed in order to being able to solve for the normal strain that satisfies incompressibility, and then for the pressure that satisfies the zero normal stress condition.

Given the strain energy, we can immediately obtain the second Piola-Kirchhoff stress tensor referred to the middle configuration

$$\boldsymbol{S}^{e,\text{pas}} = 2\frac{\partial\psi}{\partial\boldsymbol{C}^e} = k_0\boldsymbol{I} + \phi\left(\psi_1^f\,\boldsymbol{I}_s + \psi_4^f\,\boldsymbol{a}_0\otimes\boldsymbol{a}_0\right) \tag{19}$$

Requiring the derivatives of the strain energy with respect to the surface invariants of the right Cauchy-Green deformation tensor

$$\begin{aligned} \psi_1^f &= 2k_2\kappa\left(\kappa\, I_{1s}^e + (1-2\kappa)\, I_{4s}^e - 1\right)\psi^f \\ \psi_4^f &= 2k_2\,(1-2\kappa)\left(\kappa\, I_{1s}^e + (1-2\kappa)\, I_{4s}^e - 1\right)\psi^f \end{aligned} \tag{20}$$

The active stress in Eq. (13) requires a constitutive equation for the traction by the fibroblast population. For the model problem we consider that fibroblast can exert a baseline traction, and this will increase in response to TGFβ1. Specifically

we assume

$$T = \left(t_f + \frac{t_c c}{K_c + c} \right) \rho \tag{21}$$

Fibroblast thus have the basal traction t_ρ, and one traction component t_c, which is influenced by TGFβ1. The dependence on the TGFβ1 concentration is nonlinear. In fact, it is described with Michaelis-Menten kinetics. In other mathematical models of biological systems besides wounds, Michaelis–Menten and Hill functions are generally employed to capture cell signaling networks [37, 45, 71]. This approach reflects the fact that cells sense the chemical concentration through transmembrane receptors. There is a finite number of these receptors, then, as the input increases, the *sensing* process becomes saturated. Furthermore, inside of the cell, a cascade of reactions, many of them obeying Michaelis-Menten kinetics, occur [80]. The aggregate of this sequence of reactions can also be captured with Hill functions.

4.3.2 Flux and Source Terms for Fibroblasts and TGFβ1

The mass balance of the biological fields defined in Eq. (16) for the Eulerian formulation, or the equivalent Lagragian form in Eq. (17), require constitutive definitions for the flux and source terms. For the fibroblast, we adopt the Keller-Segel model of chemotaxis [81]

$$\boldsymbol{Q}_\rho = -D^{\rho\rho} \boldsymbol{C}^{-1} \nabla_X \rho - \rho D^{\rho c} \boldsymbol{C}^{-1} \nabla_X c \tag{22}$$

In this model of cell migration, fibroblasts show both diffusion, and advection in the direction of the chemical gradient. The strength of these two processes is dictated by the parameters $D^{\rho\rho}$ and $D^{\rho c}$. The fibroblast source term is here assumed to be of the form

$$s_\rho = \left(p_\rho + \frac{p_{\rho c} c}{K_{\rho c} + c} + p_{\rho e} H\left(\theta^e - \theta^e_{crit}\right) \right) \left(1 - \frac{\rho}{K_{\rho\rho}} \right) \rho - d_\rho \rho \tag{23}$$

There is a basal proliferation rate p_ρ, which can change in response to chemical or mechanical signals. The cell population exhibits self-inhibition dictated by $K_{\rho\rho}$, and a linear decay given by d_ρ. TGFβ1 concentration increases proliferation through Michelis-Menten kinetics with maximum rate $p_{\rho c}$. A key mechanobiological coupling is introduced as well, namely, the effect of the elastic stretch θ^e which increases proliferation through a logistic function

$$H\left(\theta^e - \theta^e_{crit}\right) = \frac{1}{1 + \exp\left(-\gamma_\theta \left(\theta^e - \theta^e_{crit}\right)\right)} \tag{24}$$

Proliferation rates with self-inhibition are regularly used to describe growing cell populations. The effect of TGFβ1 also aligns well with previous models. The mechanosensing term was decided based on the fact that it provides a smooth switching behavior beyond a critical strain value with a saturation point, similar to Hill functions used for growth factor signaling. Additionally, logistic functions such as Eq. (24) have been employed for ion channel activation, which is one mode of fibroblast mechanosensing [82, 83]. Nevertheless, more sophisticated descriptions of fibroblast mechanosensing are certainly needed [84].

The chemical concentration flux is standard Fickian diffusion

$$\boldsymbol{Q}_c = -D^{cc}\boldsymbol{C}^{-1}\nabla_X c \tag{25}$$

The source term for TGFβ1 is much more interesting as it includes key couplings between the different fields

$$s_c = \left(p_{c\rho}c + p_{ce}H\left(\theta^e - \theta^e_{crit}\right)\right)\left(\frac{\rho}{K_{cc}+c}\right) - d_c c \tag{26}$$

Once again, there is a basal production rate of the growth factor by the cell population $p_{c\rho}$, a saturation controlled by K_{cc}, and a decay d_c. The novelty we have proposed is to link the mechanical input to the inflammation signal. Persistent inflammation in response to excessive stress in a wound has been experimentally reported to be a crucial factor in fibrosis [85, 86], yet, before our recent efforts in the field, this coupling between the mechanical cues and the inflammation signal had not been considered.

4.3.3 Remodeling

The mass fraction of collagen is arguably the central component in the healing wound, as it links the biological fields with the mechanical function of the skin tissue. The dermis, the middle of layer of skin, is primarily made out of collagen, and this fiber network is regarded as the main load bearing mechanism of the skin. Previous modeling efforts that focused on mechanical function have also considered collagen fraction, for example in [45, 71]. For example, in our previous work we have proposed a collagen production equation of the form

$$\dot{\phi}_+ = \left(p_\phi + \frac{p_{\phi c}c}{K_{\phi c}+c} + p_{\phi e}H\left(\theta^e - \theta^e_{crit}\right)\right)\left(\frac{\rho}{K_{\phi\rho}+\phi}\right) \tag{27}$$

There is a basal production rate p_ϕ by fibroblasts, and a self-saturation controlled by $K_{\phi\rho}$. There are two important couplings. First, TGFβ1 is related to increased collagen deposition up to a maximum rate $p_{\phi c}$, a mechanism widely confirmed experimentally [87]. Secondly, stretch also induces collagen deposition up to a rate $p_{\phi e}$, a phenomenon which also has ample experimental backing [88]. Note that

Eq. (27) is focused on collagen deposition only. To obtain the net change in the collagen mass fraction we add the decay term

$$\dot{\phi} = \dot{\phi}_+ - \left(d_\phi + c\rho d_{\phi c}\right)\phi \tag{28}$$

Instead of just a standard decay term, we have considered the possibility of an additional mechanism. It has been determined that the TGFβ1 pathway in fibroblasts leads not only to an increase in collagen deposition, but, perhaps counterintuitively at first, to an upregulation of matrix metalloproteinases (MMPs), which degrade ECM proteins such as collagen [89]. This link is actually reasonable if we think of remodeling not just as the addition of collagen, but a constant turnover. An increase in MMPs can facilitate the reorganization of the ECM.

We conclude this section with the permanent area change or contracture. In response to significant inflammation such as that observed in burn wounds closed by secondary intention, a major, undesirable feature, is the compaction of the collagen network and contracture of the scar [90]. This plastic deformation is not just a minor aesthetic concern; it is associated with loss of mechanical function such as preventing joint movement or causing psychological sequelae due to disfigurement [91]. To model the contracture, or permanent area change, we propose

$$\dot{\theta}^g = \frac{\dot{\phi}_+}{\tau_g}\left(\theta^e - \theta^e_{phys}\right) \tag{29}$$

This negative growth or contracture takes place when the elastic deformation deviates from the physiological or homeostatic state here described by θ^e_{phys}.This process occurs in a timescale given by τ_g. In previous work related to finite growth using the multiplicative split, the growth rate, or more generally the rate of the permanent deformation, is simply given by the difference of the elastic strain with respect to some homeostatic value as in Eq. (29), but the coupling to the collagen deposition rate is not considered [92–94]. The rationale for including it here is related to a modeling framework backed by Humphrey, Ateshian, and other authors [95–97] which postulate that constituent turnover is the essential mechanism of growth and remodeling processes. These authors model growth with the theory of mixtures rather than with a kinematic approach. In their formulation, each constituent, deposited at each instant of time, is followed individually to determine their contribution to the state of stress and deformation [95]. Since each constituent element is tracked individually, they can be gradually removed according to their own decay function. In practice, this idea becomes computationally expensive for even modest spatial domains. Our choice of the phenomenological equation (29) is hence inspired by this idea of coupling constituent deposition with gradual remodeling instead of purely geometric approaches. In this way, the permanent deformations occur as fibroblasts deposit the new collagen that essentially cements the elastic deformation in place [19].

This concludes the model description. To summarize, we have introduced the wound healing in a general way with a continuum approach that is basically made

out of two main categories. These two categories are, broadly, the mechanics and the biology fields. Within the mechanics category there are two types of variables considered, one is the geometry and its deformation, and the other one includes the variables related to microstructure. These two kinds of variables satisfy the mechanical equilibrium and describe the evolution of the wound from the perspective of mechanical function. Within the second category we have the cell and cytokine fields. The biological fields obey reaction diffusion systems of equations. The closure of the system is accomplished with the definition of constitutive equations. For the stress we introduced a well-established description of skin's mechanical behavior. The biological fields encapsulate the control of the wound healing process. Here we use some standard features of the wound healing regulatory network that can be found in other models, but also include key couplings between mechanical cues and cell action. The last set of constitutive equations are those of remodeling, which further link biology and mechanics by describing how cells change their local ECM. While we restricted the problem to just fibroblast and TGFβ1 for the constitutive equations, the framework is general and can be extended to multiple cell and chemical species.

5 Finite Element Discretization

Stepping back to the general formulation, we again consider the possibility of several cell and chemical fields. The continuum equations introduced in the previous section are very well suited for the finite element discretization in order to model arbitrary geometries. We start by formulating the weak form of the balance laws

$$\int_{B_0} \frac{1}{2}\boldsymbol{S} : D\left(\boldsymbol{C}\right)[\delta \boldsymbol{u}]\, dV - \int_{\partial B_0} \boldsymbol{t}\cdot \delta \boldsymbol{u}\, dA = 0 \tag{30}$$

$$\int_{B_0} \left(J\left(\dot{\rho}_i - s_{\rho i}\right)\delta\rho_i - \nabla_X \delta\rho_i \cdot Q_{\rho i}\right) dV + \int_{\partial B_0} Q_{\rho i,n}\delta\rho_i\, dA = 0$$

$$\int_{B_0} \left(J\left(\dot{c}_i - s_{ci}\right)\delta c_i - \nabla_X \delta c_i \cdot Q_{ci}\right) dV + \int_{\partial B_0} Q_{ci,n}\delta c_i\, dA = 0$$

Where the bottom two rows of Eq. (30) should be repeated for all the cell and chemical species of the model. We seek solutions $\boldsymbol{u}(\boldsymbol{X}, t)$, $\boldsymbol{\rho}(\boldsymbol{X}, t)$, $\boldsymbol{c}(\boldsymbol{X}, t)$ that satisfy Eq. (30) for all variations $\delta\boldsymbol{u}(\boldsymbol{X}, t)$, $\delta\boldsymbol{\rho}(\boldsymbol{X}, t)$, $\delta\boldsymbol{c}(\boldsymbol{X}, t)$. There are some restrictions on the solution and weighting functions but we will avoid the definition of the proper spaces to which these functions belong to, see [63]. Initial and boundary conditions should also be specified. For the microstructure variables no weak form is necessary since these variables evolve according to ordinary differential equations and those will be incorporated directly at the integration point of the finite element formulation. Also note that we have started from the strong form of the Lagrangian

formulation in order to arrive at Eq. (30). Alternatively, formulations in the Eulerian description could also be formulated. Lastly, we remark that the weak form for the mechanical equilibrium problem in Eq. (30) is valid for both three-dimensional as well as shell descriptions of the body B_0.

To discretize the weak form and also the change in time of the structural variables we first proceed by discretizing in time. Let Δt denote the time step. For the integration of the equations suppose we already know the fields $\boldsymbol{u}(\boldsymbol{X},t)$, $\boldsymbol{\rho}(\boldsymbol{X},t)$, $\boldsymbol{c}(\boldsymbol{X},t)$ at time t and we want to know the fields at time $t+\Delta t$. For the sake of simplifying the notation, the fields at time $t+\Delta t$ are simply going to be refer to as $\boldsymbol{u}$, $\boldsymbol{\rho}$, $\boldsymbol{c}$; whereas the fields at time t are denoted as $\boldsymbol{u}^{(t)}$, $\boldsymbol{\rho}^{(t)}$, $\boldsymbol{c}^{(t)}$. We adopt an implicit Euler scheme and discretize the weak form in Eq. (30) in time. The semi-discrete residuals are as follows

$$\int_{B_0} \frac{1}{2}\boldsymbol{S} : D\left(\boldsymbol{C}\right)[\delta \boldsymbol{u}]\, dV - \int_{\partial B_0} \boldsymbol{t}\cdot \delta \boldsymbol{u} dA = 0 \tag{31}$$

$$\int_{B_0} \left(\left(\frac{\rho_{0i} - \rho_{0i}^{(t)}}{\Delta t} - S_{\rho i} \right) \delta\rho_i - \nabla_X \delta\rho_i \cdot Q_{\rho i} \right) dV + \int_{\partial B_0} Q_{\rho i,n} \delta\rho_i dA = 0$$

$$\int_{B_0} \left(\left(\frac{c_{0i} - c_{0i}^{(t)}}{\Delta t} - S_{ci} \right) \delta c_i - \nabla_X \delta c_i \cdot Q_{ci} \right) dV + \int_{\partial B_0} Q_{ci,n} \delta c_i dA = 0$$

Note that the flux and source terms, as well as the stress, are evaluated at the time $t+\Delta t$, hence the implicit nature of the discretization. For the structural variables a similar time discretization is used. The material parameters at time t are denoted $\boldsymbol{\Theta}^{(t)}$, whereas the new values at the next time step are simply referred to as $\boldsymbol{\Theta}$.

To discretize the system in space we use finite elements. Note here that there are several options, for example, shell, plate, or volume elements can be used. The semi-discrete weak form of Eq. (31) is not restricted to a planar or a three-dimensional formulation. In the kinematics description developed in this chapter we did restrict the formulation to that of a thin membrane. However, we have previously done the first three-dimensional description of a wound [22]. Then, in [63] we use a planar discretization with quadrilateral elements.

The spatial domain is discretized with a mesh consisting of nodes $\{a\}$ and elements $\{e\}$. Inside of an element e, for each node a, there is an associated basis function N_a^e. The fields $\boldsymbol{u}$, $\boldsymbol{\rho}$, $\boldsymbol{c}$ are linearly interpolated inside of an element using these basis functions. For example $\boldsymbol{u}^e = N_a^e \boldsymbol{u}_a^e$ is the displacement inside of the element e defined by the sum of the nodal values of the displacement $\boldsymbol{u}_a^e$ multiplied by the corresponding basis functions. In a standard finite element solver, the global residual is assembled by integrating the residual over each element. To carry out the integrals in Eq. (31), the functions are sampled at the integration points of the element, denoted as b. Gauss integration points, for example, are a common choice. Importantly, the microstructure variables $\boldsymbol{\Theta}$ are discretized directly at the integration points. Recall that the microstructure variables are allowed to change

in space, but their evolution is given by ordinary differential equations because no diffusion is considered for these variables. Therefore, the residuals obtained from the finite element discretization of Eq. (31) are

$$\boldsymbol{R}_A^u = \mathrm{A}_{e=1}^{n_{el}} \int_{B_0^e} \nabla_X N_a^e \cdot (\boldsymbol{F} \cdot \boldsymbol{S})\, dV = 0 \tag{32}$$

$$\boldsymbol{R}_A^{\rho i} = \mathrm{A}_{e=1}^{n_{el}} \int_{B_0} \left(\left(\frac{\rho_{0i} - \rho_{0i}^{(t)}}{\Delta t} - S_{\rho i} \right) N_a^e - \nabla_X N_a^e \cdot \boldsymbol{Q}_{\rho i} \right) dV = 0$$

$$\boldsymbol{R}_A^{ci} = \mathrm{A}_{e=1}^{n_{el}} \int_{B_0} \left(\left(\frac{c_{0i} - c_{0i}^{(t)}}{\Delta t} - S_{ci} \right) N_a^e - \nabla_X N_a^e \cdot \boldsymbol{Q}_{ci} \right) dV = 0$$

In Eq. (32), the subscript A in the residual denotes the global node number corresponding to the node a of element e. Also, the operator $\mathrm{A}_{e=1}^{n_{el}}$ denotes the standard assembly process, i.e., the mapping from the local residual at node a of element e to the global node number A. The local residuals corresponding to the microstructural variables are not expanded here. Since the variables $\boldsymbol{\Theta}$ are integrated locally, their residuals are standard for the integration of a system of ordinary differential equations with a backward Euler scheme. Nonetheless, we do need to introduce the corresponding notation. Thus, we denote $\boldsymbol{R}_b^{\Theta}$ the vector of residuals of the microstructure variables at the integration point b.

The corresponding system of equations obtained from Eq. (32) and the residuals at the integration points completely define the discrete problem. The system is nonlinear and its solution could be accomplished with more than one strategy. For example, one approach would be a staggered solution scheme in which the mechanical equilibrium problem and the reaction-diffusion system are solved sequentially. Alternatively, a monolithic approach could be done. The advantage of the monolithic solution is that it explicitly considers all the couplings during time integration. The disadvantage, however, is that it also requires the linearization of all the couplings. This has been the approach we have taken in the past, see [38, 63] for the full linearization of the system. Here we will not write down the explicit form of all the tangent matrices, but there is one aspect of the linearization that we do wish to emphasize: the coupling between the fields $\boldsymbol{u}$, $\boldsymbol{\rho}$, $\boldsymbol{c}$ at the nodes, to the microstructure $\boldsymbol{\Theta}$ at the integration points.

Consider the displacement field $\boldsymbol{u}$. The computation of the tangent requires the derivative of the stress with respect to each of the global (or nodal) degrees of freedom. The explicit derivative with respect to the fields $\boldsymbol{u}$, $\boldsymbol{\rho}$, $\boldsymbol{c}$ discretized at the nodes is straightforward. However, additional terms are needed. Namely, the derivatives of the stress with respect to $\boldsymbol{\Theta}$ can also be computed explicitly, but then the derivatives of $\boldsymbol{\Theta}$ with respect to $\boldsymbol{u}$, $\boldsymbol{\rho}$, $\boldsymbol{c}$ are needed. This last step can benefit from further discussion. Therefore, the derivative of the stress with respect to the

nodal degrees of freedom can be expanded as

$$\mathbb{C}^{uu} = \frac{\partial \boldsymbol{S}}{\partial \boldsymbol{C}} + \frac{\partial \boldsymbol{S}}{\partial \boldsymbol{\Theta}} \frac{\partial \boldsymbol{\Theta}}{\partial \boldsymbol{C}}, \mathbb{C}^{u\rho} = \frac{\partial \boldsymbol{S}}{\partial \boldsymbol{\rho}} + \frac{\partial \boldsymbol{S}}{\partial \boldsymbol{\Theta}} \frac{\partial \boldsymbol{\Theta}}{\partial \boldsymbol{\rho}}, \mathbb{C}^{uc} = \frac{\partial \boldsymbol{S}}{\partial \boldsymbol{c}} + \frac{\partial \boldsymbol{S}}{\partial \boldsymbol{\Theta}} \frac{\partial \boldsymbol{\Theta}}{\partial \boldsymbol{c}} \tag{33}$$

Where the explicit derivative of the stress with respect to $\boldsymbol{C}$, $\boldsymbol{\rho}$, $\boldsymbol{c}$, $\boldsymbol{\Theta}$ is straightforward. To compute the derivatives of $\boldsymbol{\Theta}$ appearing at the end of the equations in Eq. (33) from the use of the chain rule, we first note that a Taylor expansion of the residuals of the microstructure variables at the integration points yields

$$\boldsymbol{R}_b^{\Theta} + \boldsymbol{K}^{\Theta\Theta} \cdot d\boldsymbol{\Theta} = 0 \tag{34}$$

In consequence, the derivative of Eq. (34) with respect to the nodal variables can be computed. For instance, let us consider the derivative of Eq. (34) with respect to the right Cauchy-Green deformation tensor

$$\frac{\partial \boldsymbol{R}_b^{\Theta}}{\partial \boldsymbol{C}} \cdot \frac{\partial \boldsymbol{\Theta}}{\partial \boldsymbol{C}} + \frac{\partial \boldsymbol{R}_b^{\Theta}}{\partial \boldsymbol{C}} = \boldsymbol{K}^{\Theta\Theta} \cdot \frac{\partial \boldsymbol{\Theta}}{\partial \boldsymbol{C}} + \frac{\partial \boldsymbol{R}_b^{\Theta}}{\partial \boldsymbol{C}} = 0 \tag{35}$$

From Eq. (35) we obtain a linear system from which we solve for the derivative of the microstructure variables with respect to the right Cauchy-Green deformation tensor

$$\frac{\partial \boldsymbol{\Theta}}{\partial \boldsymbol{C}} = -\left(\boldsymbol{K}^{\Theta\Theta}\right)^{-1} \cdot \frac{\partial \boldsymbol{R}_b^{\Theta}}{\partial \boldsymbol{C}} \tag{36}$$

Analogous formulas can be derived for $\partial\boldsymbol{\Theta}/\partial\boldsymbol{\rho}$ and $\partial\boldsymbol{\Theta}/\partial\boldsymbol{c}$. To summarize, the discrete residuals are nonlinear and their solution in a monolithic approach requires the linearization with respect to the degrees of freedom at the nodes of the mesh. The explicit derivatives of the residuals defined in Eq. (32) involve a fair amount of algebra but require standard derivations as in any nonlinear finite element code. The additional coupling between the microstructure variables and the nodal degrees of freedom is, on the other hand, not a standard derivation. However, we showed that doing a Taylor expansion of the residuals at the integration points, we can obtain formulas for the derivatives of the microstructure variables with respect to the nodal degrees of freedom.

6 Features of the Continuum Framework of Wound Mechanobiology

Here we present some of the results that have been obtained with the modeling framework and finite element discretization reviewed in the last two sections. We emphasize that the wound healing modeling community has produced a sequence

of formulations over the past two decades that have continuously pushed the boundaries of our mechanistic understanding of wound healing. Our contribution in this field has focused on the specialization of the continuum framework to three-dimensional domains and a detailed description of the wound remodeling and contracture via strong couplings between biological and microstructural variables. For a review of wound healing models please see for example [38, 98].

Figure 1 shows the healing of a circular wound of radius 1 cm in a three-dimensional domain of dimensions $4 \times 4 \times 1$ cm^3. For these simulations, the permanent volume changes were not considered. Instead, the collagen fraction ϕ was the only microstructure variable that was modeled and allowed to change to capture the recovery of the tissue's mechanical behavior. The biological fields simulated consisted of the fibroblast population density ρ, and the TGFβ1 concentration c. To showcase the coupling of the biological fields to the mechanical environment of the wound, we first imposed a prestrain of 10% in the x direction. At this initial point, all the tissue was considered healthy and the biological fields had constant values over the entire domain. Absolute values are not reported, instead, in this example we considered the healthy state to be described by normalized concentrations $\rho = 1, c = 0, \phi = 1$. After loading the tissue, the wound was created. This was accomplished by assigning $\rho = 0, c = 1, \phi = 0$ to the wounded region. The initial state of the wound is depicted in the first column of Fig. 1. In response to the creation of the wound, the strain shows an intriguing contour. Overall, strains at the core of the wound are higher than in the surrounding tissue, with some compression right at the edge of the wound along the x axis.

The columns of Fig. 1a shows the spatiotemporal evolution of the wound as captured by the fields ρ, c, ϕ and the strain component E_{xx}. As time progresses, the TGFβ1 concentration decays exponentially. The cell population invades the wound over the course of 5 days. The collagen fraction shows a delayed response compared to the fibroblast and TGFβ1 concentrations, but overall it increases monotonically. By day 4, the collagen content has gone back to approximately 0.8 of the healthy value. The bottom row of Fig. 1 illustrates the importance of spatial variations. This is particularly important for the strain contours. While overall the strain in the wound decreases as collagen is remodeled, it does not go back to the initial, unwounded state.

Figure 2 shows the healing of elliptical wounds predicted with our model. The initial setup of the simulation is analogous to what was presented for the circular wound. An initial domain of $4 \times 4 \times 1$ cm^3 was prestrained by 10% in the x direction and subsequently a wound was created by setting $\rho = 0$, $c = 1$, $\phi = 0$. However, in this case two elliptical wounds were simulated, with ratios between the major and minor axis of 3:2 and 3:1 respectively. The fibroblast and TGFβ1 concentration fields are not shown in Fig. 2 but they obey a similar trend to what was seen in the circular wound. In contrast, the evolution of the strain contours is the essential feature that can be observed with our formulation which stands out from what had been previously done.

Upon wounding, the strain in the wound core increases compared to the surrounding, healthy skin. There is a small region, along the x axis, near the edge

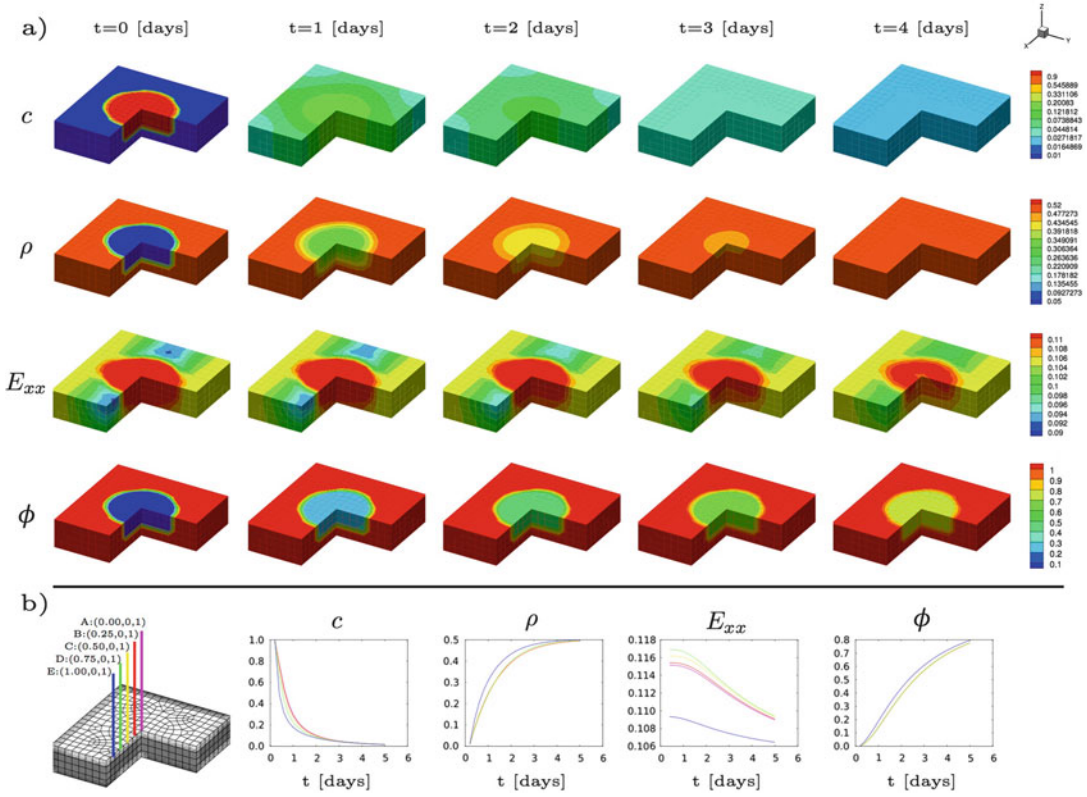

Fig. 1 Spatiotemporal evolution of a circular wound. A domain of $4 \times 4 \times 1$ cm^3 was prestretched $E_{xx} = 0.1$ in the x axis and then a wound was created by setting the fibroblast density $\rho = 0$, the TGFβ1 concentration to $c = 1$, and the collagen content $\phi = 0$ in the wounded region. The healthy state was in turn defined by $\rho = 1$, $c = 0$, $\phi = 1$ (first column of **a**). The wound healed over 5 days, snapshots of the relevant fields are shown in (**a**). Spatial variation is further emphasized in (**b**). This figure was obtained with permission from [22]

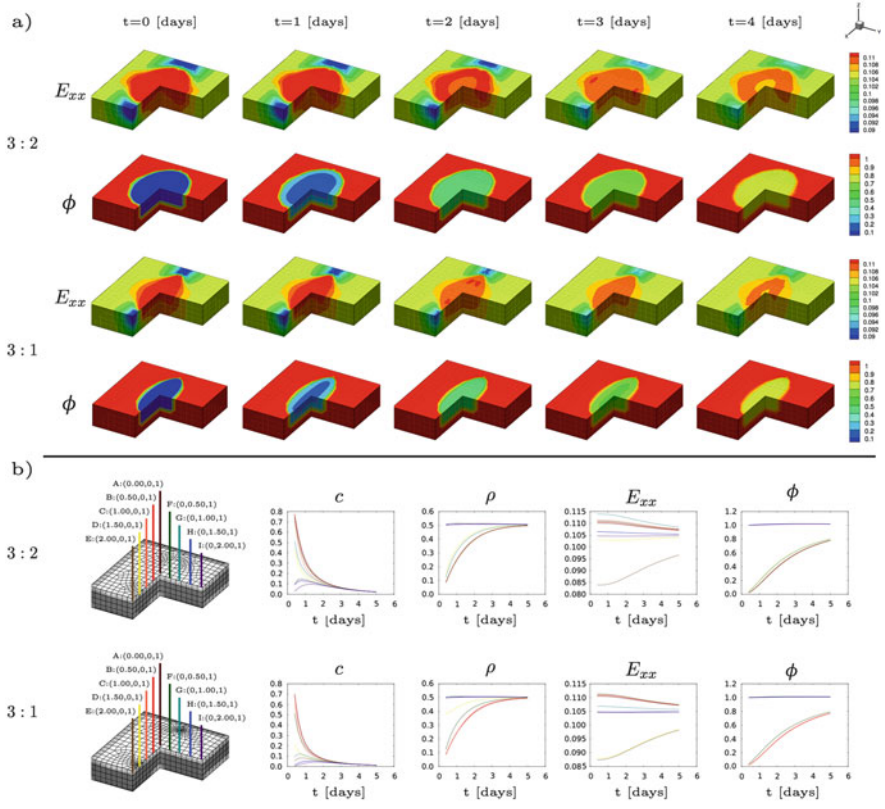

Fig. 2 Healing of elliptical wounds. After imposing a strain of $E_{xx} = 0.1$, a wound was created analogous to what was done in Fig. 1. Here, snapshots for the collagen fraction ϕ contours and the strain contours are shown for the first 5 days of healing (**a**). The elliptical wound with the higher aspect ratio between the major and minor axis shows the fastest healing. Nonetheless, the trends are similar between both cases. A clearer depiction of the importance of spatial variation is shown in (**b**), where plots of the fields of interest over time at specific locations are shown. This figure was reproduced with permission from [22]

of the wound, that is under compression when the wound is created. As the wound heals, the strain in the wound core decreases. This coupling is due to the fact that the collagen mass fraction is directly linked to the strain energy function, and, at the same time, it is controlled by the fibroblast population density. Surprisingly, the strain does not simply decrease homogeneously, but the interplay between the prestrain and the collagen deposition lead to a complex evolving pattern. It has been recently reported the fingerprint of the wound is indeed heterogeneous, and that the wound core may be partially stress-shielded from the surrounding tissue [99]. Additional work is needed to calibrate the model presented here to those recent results. Nevertheless, we now have a theoretical and computational framework uniquely suited for this kind of investigation.

The parameters employed to generate Figs. 1 and 2 are reported in [22]. These parameters were decided based partially on parameters used in previous models, as well as estimated to match experimental evidence reported in the literature. A more comprehensive test of the parameters is needed to investigate how sensitive is the model to the choice of parameters. One of the challenges in model calibration is that, typically, experimental studies only focus on one or a few aspects of the wound process, such that an incomplete picture emerges from any one particular study. This is complicated by the fact that different papers report various experimental setups and conditions that do not allow for exact comparison. At the same time, this partial picture made from disconnected experimental reports is precisely one of the greatest opportunities for computational models. Indeed, a model such as the one shown here can take pieces of information that seem disjoint and test out the theoretical implications of bringing these data together under a single framework.

Following our work in three-dimensions, we developed an updated framework which is the one described in Sect. 4.3 [63]. The most important improvement was the inclusion of active contraction by fibroblasts and the possibility to account for permanent deformations or contracture. This was also an opportunity for us to develop the model within the framework of thin shell analysis. As an initial numerical investigation, however, we restricted the simulations to a two-dimensional, planar domain. Figure 3 shows the spatiotemporal evolution of a circular wound with this updated model.

Similarly to what was shown before, the wound is described with a collagen fraction ϕ, a fibroblast cell density ρ, and the TGFβ1 concentration denoted c. As just mentioned, here we also include the evolution of the permanent contracture θ^g. In contrast to the previous simulations which were based on normalized concentrations, for this case we report absolute values for the cell and chemical concentrations. The domain is $100 \times 100\,\text{mm}^2$. The skin was modeled as anisotropic in this case, with a preferred fiber orientation aligned with the x axis of the domain. The wound is created just as before by reducing the cell density and increasing the inflammation signal in the wounded region. In this case however, no prestrain was initially applied and, instead, we simply fixed the edges of the domain and observed the contracture process dictated by fibroblast contraction. The bottom row of Fig. 3 shows precisely the change of the θ^g contours over time. The coupling of the different signals leads to a remarkable emergent pattern. Namely, the wound

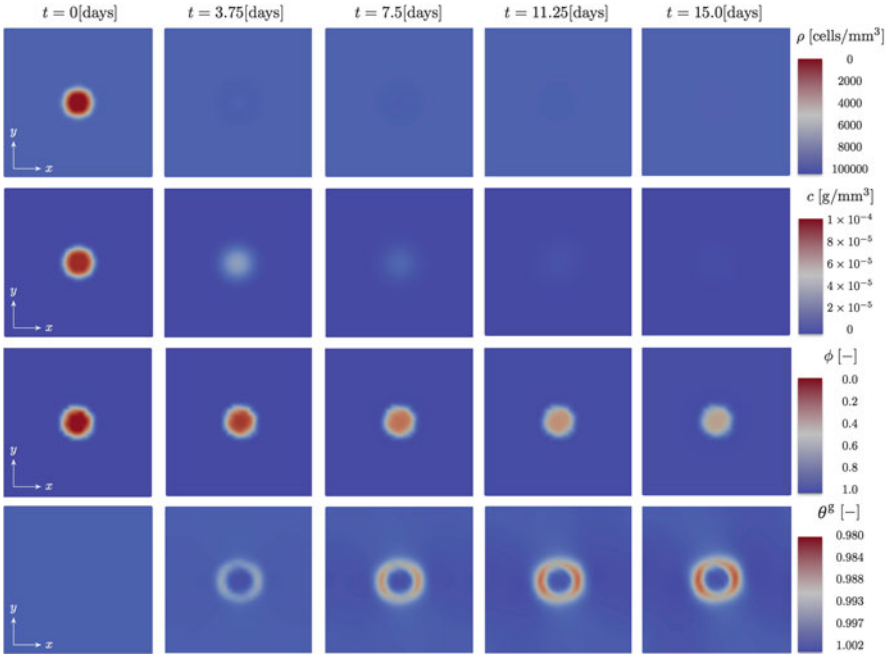

Fig. 3 Wound contraction. The framework outlined in Sects. 4.3 and 4.4 was used to simulate a circular wound of 20 mm diameter in a domain of 100 × 100 mm^2. The fields considered were fibroblast density ρ, TGFβ1 concentration c, collagen mass fraction ϕ, and permanent contracture θ^g. As the fibroblasts infiltrate the wound and deposit new collagen, and the TGFβ1 concentration diffuses out, a ring of wound contraction gradually appears at the edges of the wound over the first 15 days of healing. This figure was taken with permission from [63]

contracts primarily in a ring around the wounded area, and the contraction is more pronounced along the x axis compared to the orientation perpendicular to the fibers. This pattern of wound conctraction is in fact something expected based on experiments on mice [32].

The last result shown corresponds to the contraction of elliptical wounds. These simulations are closely related to the elliptical wounds in the three-dimensional setting we showed in Fig. 2. Here, however, we are interested in the permanent area changes or contracture θ^g. The wounds were created in the same manner as the circular and elliptical wounds of the previous three examples. The initial geometry, before creating the virtual injury, was also the same as for Fig. 3. Then an elliptical wound with a 2:1 aspect ratio was created. The wound was position either aligned or perpendicular to the preferred fiber orientation which corresponds to the x axis of our domain.

Figure 4-left shows the change in collagen mass fraction ϕ at $t = 0$ and $t = 15$ days for the two elliptical wounds. As can be seen from these contours, there is not a noticeable difference between these two columns. By day 15, both wounds

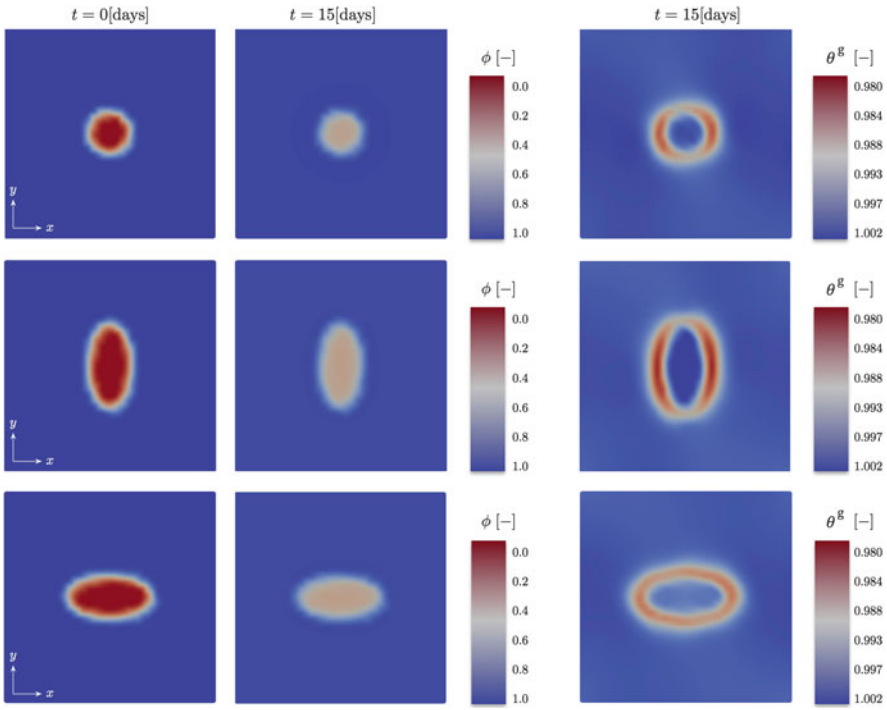

Fig. 4 Contracture of elliptical wounds. Elliptical wounds of aspect ratio 2:1 were created in a manner analogous to what is shown in Fig. 3. The wound was placed either aligned with the preferred fiber orientation (along the x axis), or orthogonal to the fiber orientation (along the y axis). The collagen content ϕ by day 15 is similar in both wounds, but the permanent contracture θ^g shows important differences. In the wound placed orthogonal to the fiber field the wound shows greater contracture. The elliptical wound aligned with the fiber direction showed the least permanent area changed (also compared to the circular wound in Fig. 3), and a more uniform θ^g contour, although still showing a ring around the edge of the wound. This figure was taken with permission from [63]

have a collagen fraction of approximately 0.5. The right-most column in Fig. 4 is the permanent contracture θ^g. Similar to the case of the circular wound, the elliptical geometries also show the gradual formation of a ring in which contracture is greatest. This pattern aligns well with the previous observation of the circular wound, and it similarly follows from the fact that as fibroblast infiltrate into the wound they face the gradient of TGFβ1 which induces their contractile phenotype. However, there are also some noticeable differences in the contracture pattern between the two elliptical wounds and the circular wound in Fig. 3. In the case in which the elliptical wound is aligned with the y axis, i.e. orthogonal to the fiber orientation, the contraction is much greater on the sides of the wound, and it is also greater compared to the circular wound. In the case where the ellipse is aligned with the fiber orientation (the x axis), the contracture is overall less than in the other

two cases, and it is also more uniform around the edge of the wound. This matches well with clinical experience that wounds aligned with the fiber direction show less contracture [100, 101].

We conclude this section by mentioning that the parameters used for the simulations shown in Figs. 3 and 4 are found in our paper [63]. The values of the parameters were assembled from a variety of sources, just as was the case for the parameters used in the code that generated Figs. 1 and 2. Once again we highlight the ability of our formulation to capture key mechanobiological couplings, essential to understand the scar formation process. In particular, our theoretical and computational framework follows a string of recent publications that have established how mechanical cues lead to hypertrophic scarring through decreased apoptosis and increased inflammation [85, 86, 102–104].

7 Conclusions

In this chapter we have presented a mathematical framework for skin wound healing with an emphasis on soft tissue mechanics and mechanobiology. It has been increasingly acknowledged that wounds under stress are linked to fibrosis, and that fibroblast biology and inflammation signaling are key to understand, and eventually predict, scar outcomes in individual patients [103]. At the same time, despite the evidence backing the relationship between stress, tissue mechanical function, inflammation, and fibroblast action, we are still unable to control the wound healing process at will. There have been many improvements in the treatment of cutaneous wounds, but the holy grail of scarless wound healing remains elusive [8].

Wound healing modeling has been an area of research interest for several decades, dating back to work by Sherrat, Murray, Tranquillo and Olsen, among others [20, 57, 105]. Mathematical models of wound healing have advanced since then. We showed here that a useful scheme to categorize the progress in wound healing modeling started by dividing these models into two main categories: discrete and continuum formulations. Discrete models are ideal to describe cell behavior at the microscopic scale and hence align well with in vitro experiments that emphasize cell biology and cell-ECM interactions [65]. The obvious drawback is the difficulty in connecting these models to realistic patient scenarios. Continuum models, on the other hand, are naturally applicable for the tissue behavior at the macroscopic scale [98]. An essential feature of continuum models is that they lend themselves perfectly for a detailed description of skin's mechanical behavior during healing [22]. Therefore, in this chapter, which emphasized the mechanical function of skin, we have presented a detailed model of tissue remodeling in a continuum framework [63].

Despite the excellent progress in wound healing models, coupling of the biological events to the latest advances in continuum mechanics modeling of growth and remodeling [94, 106], has been lagging. Models with increasing number of

cell types and cytokines have emerged [45, 71], but with relatively simplified models of the skin mechanical behavior. Our main contribution in this aspect has been to model skin as a hyperelastic material undergoing large deformations and described with a microstructurally-based strain energy function. Therefore, by incorporating microstructure parameters, we can explicitly couple the evolution of biological fields to the mechanical state of the wound. We have also incorporated the general framework of finite volumetric growth into our multi-field finite element formulation. A similar model of wound healing with contraction was proposed in [107], yet, it focused solely on the mechanics aspects and ignored any biological field.

An important limitation of continuum models is the difficulty to estimate the model parameters of the biological fields (cells and cytokines). The complexity of the interactions in the cell regulatory network of wound healing, even when focusing on a small range of behavior such as dermis remodeling, makes the model calibration problematic [38, 98]. A second limitation of continuum models is that going from cell behavior at the microscopic scale, to the continuum scale, constitutive equations for cell flux and source terms are needed. While current phenomenological equations for these fluxes and sources are grounded on experimental observations, more rigorous upscaling is certainly needed.

In conclusion, multi-field models of wound healing mechanics accounting for cell and cytokine fields can hold the key to understand fundamental couplings between mechanosensing and scar progression, especially as more data becomes available [99]. Predictive models based on this approach, especially continuum models, can potentially lead to the improvement of treatment in order to avoid or minimize hypertrophic scarring. Moreover, wound healing is not exclusive of skin but it happens across all connective tissues in a similar manner [108]. Thus, increasing understanding of cutaneous wound healing can have implications far beyond skin scarring, for example in the field of tissue engineering.

References

1. Aarabi S, Longaker MT, Gurtner GC (2007) Hypertrophic scar formation following burns and trauma: new approaches to treatment. PLoS Med 4:1464–1470
2. Van Zuijlen PPM, Ruurda JJB, Van Veen HA, Van Marle J, Van Trier AJM, Groenevelt F et al (2003) Collagen morphology in human skin and scar tissue: no adaptations in response to mechanical loading at joints. Burns 29:423–431
3. Corr DT, Gallant-Behm CL, Shrive NG, Hart DA (2009) Biomechanical behavior of scar tissue and uninjured skin in a porcine model. Wound Repair Regen 17:250–259
4. Singer AJ, Clark RA (1999) Cutaneous wound healing. N Engl J Med 341(10):738–746
5. Eming SA, Krieg T, Davidson JM (2007) Inflammation in wound repair: molecular and cellular mechanisms. J Invest Dermatol 127:514–525
6. van der Veer WM, Bloemen MCT, Ulrich MMW, Molema G, van Zuijlen PP, Middelkoop E et al (2009) Potential cellular and molecular causes of hypertrophic scar formation. Burns 35:15–29

7. Sen CK, Gordillo GM, Roy S, Kirsner R, Lambert L, Hunt TK et al (2009) Human skin wounds: a major and snowballing threat to public health and the economy. Wound Repair Regen 17:763–771
8. Walmsley GG, Maan ZN, Wong VW, Duscher D, Hu MS, Zielins ER et al (2015) Scarless wound healing: chasing the holy grail. Plast Reconstr Surg 135:907–917
9. Larson BJ, Longaker MT, Lorenz HP (2010) Scarless fetal wound healing: a basic science review. Plast Reconstr Surg 126:1172–1180
10. Colwell AS, Longaker MT (2003) Fetal wound healing. Front Biosci 8:s1240–s1248
11. Martino MM, Tortelli F, Mochizuki M, Traub S, Ben-David D, Kuhn GA et al (2011) Engineering the growth factor microenvironment with fibronectin domains to promote wound and bone tissue healing. Sci Transl Med 3:100ra89
12. Chantre CO, Campbell PH, Golecki HM, Buganza AT, Capulli AK, Deravi LF et al (2018) Production-scale fibronectin nanofibers promote wound closure and tissue repair in a dermal mouse model. Biomaterials 166:96–108
13. Vodovotz Y, Csete M, Bartels J, Chang S, An G (2008) Translational systems biology of inflammation. PLoS Comput Biol 4:e1000014
14. McGrath JA, Eady RAJ, Pope FM (2004) Anatomy and organization of human skin. In: Burns T, Breathnach S, Cox N, Griffiths C (eds) Rook's textbook of dermatology. Blackwell Science, Oxford, pp 45–128
15. Ní Annaidh A, Bruyère K, Destrade M, Gilchrist MD, Maurini C, Otténio M et al (2012) Automated estimation of collagen fibre dispersion in the dermis and its contribution to the anisotropic behaviour of skin. Ann Biomed Eng 40:1666–1678
16. Driskell RR, Lichtenberger BM, Hoste E, Kretzschmar K, Simons BD, Charalambous M et al (2013) Distinct fibroblast lineages determine dermal architecture in skin development and repair. Nature 504:277–281
17. Moreno-Arotzena O, Meier J, del Amo C, García-Aznar J (2015) Characterization of fibrin and collagen gels for engineering wound healing models. Materials (Basel) 8:1636–1651
18. Van De Water L, Varney S, Tomasek JJ (2013) Mechanoregulation of the myofibroblast in wound contraction, scarring, and fibrosis: opportunities for new therapeutic intervention. Adv Wound Care 2:122–141
19. Hinz B (2010) The myofibroblast: paradigm for a mechanically active cell. J Biomech 43:146
20. Sherratt JA, Murray JD (1990) Models of epidermal wound healing. Proc R Soc B Biol Sci 241:29–36
21. Tranquillo RT, Murray JD (1992) Continuum model of fibroblast-driven wound contraction: inflammation-mediation. J Theor Biol 158:135–172
22. Buganza Tepole A, Kuhl E (2014) Computational modeling of chemo-bio-mechanical coupling: a systems-biology approach toward wound healing. Comput Methods Biomech Biomed Engin 5842:1–18
23. Baum CL, Arpey CJ (2005) Normal cutaneous wound healing: clinical correlation with cellular and molecular events. Dermatol Surg 31:674–686
24. Breuing K, Andree C, Helo G, Slama J, Liu PY, Eriksson E (1997) Growth factors in the repair of partial thickness porcine skin wounds. Plast Reconstr Surg 100:657–664
25. Kim M-H, Liu W, Borjesson DL, Curry F-RE, Miller LS, Cheung AL et al (2008) Dynamics of neutrophil infiltration during cutaneous wound healing and infection using fluorescence imaging. J Invest Dermatol 128:1812–1820
26. Steenfos HH (1994) Growth factors and wound healing. Scand J Plast Reconstr Surg Hand Surg 28(2):95–105
27. Tsirogianni AK, Moutsopoulos NM, Moutsopoulos HM (2006) Wound healing: immunological aspects. Injury 37:S5–S12
28. Cooper L, Johnson C, Burslem F, Martin P (2005) Wound healing and inflammation genes revealed by array analysis of "macrophageless" PU.1 null mice. Genome Biol 6:R5
29. Gurtner GC, Werner S, Barrandon Y, Longaker MT (2008) Wound repair and regeneration. Nature 453:314–321

30. Pastar I, Stojadinovic O, Yin NC, Ramirez H, Nusbaum AG, Sawaya A et al (2014) Epithelialization in wound healing: a comprehensive review. Adv Wound Care 3:445–464
31. Chaplain MAJ (2000) Mathematical modelling of angiogenesis. J Neurooncol 50(1):37–51
32. Schmidt BA, Horsley V (2013) Intradermal adipocytes mediate fibroblast recruitment during skin wound healing. Development 140:1517–1527
33. Verhaegen PDHM, van Zuijlen PPM, Pennings NM, van Marle J, Niessen FB, van der Horst CMAM et al (2009) Differences in collagen architecture between keloid, hypertrophic scar, normotrophic scar, and normal skin: an objective histopathological analysis. Wound Repair Regen 17:649–656
34. Greenhalgh DG (1998) The role of apoptosis in wound healing. Int J Biochem Cell Biol 30:1019–1030
35. Doillon CJ, Dunn MG, Bender E, Silver FH (1985) Collagen fiber formation in repair tissue: development of strength and toughness. Coll Relat Res 5:481–492
36. Nagaraja S, Wallqvist A, Reifman J, Mitrophanov AY (2014) Computational approach to characterize causative factors and molecular indicators of chronic wound inflammation. J Immunol 192:1824–1834
37. Vodovotz Y, Clermont G, Chow C, An G (2004) Mathematical models of the acute inflammatory response. Curr Opin Crit Care 10:383–390
38. Buganza Tepole A, Kuhl E (2013) Systems-based approaches toward wound healing. Pediatr Res 73:553–563
39. Bindschadler M, McGrath JL (2007) Sheet migration by wounded monolayers as an emergent property of single-cell dynamics. J Cell Sci 120:876–884
40. Zhao J, Cao Y, DiPietro LA, Liang J (2017) Dynamic cellular finite-element method for modelling large-scale cell migration and proliferation under the control of mechanical and biochemical cues: a study of re-epithelialization. J R Soc Interface 14:20160959
41. Daub JT, Merks RMH (2013) A cell-based model of extracellular-matrix-guided endothelial cell migration during angiogenesis. Bull Math Biol 75:1377–1399
42. Stokes CL, Lauffenburger DA (1991) Analysis of the roles of microvessel endothelial cell random motility and chemotaxis in angiogenesis. J Theor Biol 152:377–403
43. McDougall S, Dallon J, Sherratt J, Maini P (2006) Fibroblast migration and collagen deposition during dermal wound healing: mathematical modelling and clinical implications. Philos Trans R Soc A Math Phys Eng Sci 364:1385–1405
44. Dallon JC, Sherratt JA, Maini PK (1999) Mathematical modelling of extracellular matrix dynamics using discrete cells: fiber orientation and tissue regeneration. J Theor Biol 199:449
45. Cumming BD, McElwain DLS, Upton Z (2009) A mathematical model of wound healing and subsequent scarring. J R Soc Interface 7:19–34
46. Rouillard AD, Holmes JW (2014) Coupled agent-based and finite-element models for predicting scar structure following myocardial infarction. Prog Biophys Mol Biol 115:235–243
47. Safferling K, Sütterlin T, Westphal K, Ernst C, Breuhahn K, James M et al (2013) Wound healing revised: a novel reepithelialization mechanism revealed by in vitro and in silico models. J Cell Biol 203:691–709
48. Das A, Lauffenburger D, Asada H, Kamm RD (2010) A hybrid continuum-discrete modelling approach to predict and control angiogenesis: analysis of combinatorial growth factor and matrix effects on vessel-sprouting morphology. Philos Trans A Math Phys Eng Sci 368:2937–2960
49. Shirinifard A, Gens JS, Zaitlen BL, Popławski NJ, Swat M, Glazier JA (2009) 3D multi-cell simulation of tumor growth and angiogenesis. PLoS One 4:e7190
50. Milde F, Bergdorf M (2008) A hybrid model for three-dimensional simulations of sprouting angiogenesis. Biophys J 95:3146–3160
51. Maini PK, McElwain DLS (2004) Traveling wave model to interpret a wound-healing cell migration assay for human peritoneal mesothelial cells. Tissue Eng 10:475–482
52. Levine HA, Sleeman BD (2001) Mathematical modeling of the onset of capillary formation initiating angiogenesis. J Math 42:195–238

53. Pettet GJ, Byrne HM, McElwain DLS, Norbury J (1996) A model of wound-healing angiogenesis in soft tissue. Math Biosci 136:35–63
54. Gaffney EA, Pugh K, Maini PK, Arnold F (2002) Investigating a simple model of cutaneous wound healing angiogenesis. J Math Biol 45:337–374
55. Byrne HM, Chaplain MAJ, Evans DL, Hopkinson I (2000) Mathematical modelling of angiogenesis in wound healing: comparison of theory and experiment. J Theor Med 2:175–197
56. Schugart RC, Friedman A, Zhao R, Sen CK (2008) Wound angiogenesis as a function of tissue oxygen tension: a mathematical model. Proc Natl Acad Sci 105:2628–2633
57. Olsen L, Sherratt JA (1995) A mechanochemical model for adult dermal wound contraction: on the permanence of the contracted tissue displacement profile. J Theor Biol 10(3):475–482
58. Murphy KE, McCue SW, McElwain DLS (2012) Clinical strategies for the alleviation of contractures from a predictive mathematical model of dermal repair. Wound Repair Regen 20:194–202
59. Haugh JM (2006) Deterministic model of dermal wound invasion incorporating receptor-mediated signal transduction and spatial gradient sensing. Biophys J 90(7):2297–2308
60. Javierre E, Vermolen FJ, Vuik C, Zwaag S (2008) A mathematical analysis of physiological and morphological aspects of wound closure. J Math Biol 59:605–630
61. Valero C, Javierre E, García-Aznar JM, Gómez-Benito MJ (2013) Numerical modelling of the angiogenesis process in wound contraction. Biomech Model Mechanobiol 12:349–360
62. Vermolen FJ, Javierre E (2010) Computer simulations from a finite-element model for wound contraction and closure. J Tissue Viability 19:43–53
63. Buganza Tepole A (2017) Computational systems mechanobiology of wound healing. Comput Methods Appl Mech Eng 314:46–70
64. Swat MH, Thomas GL, Belmonte JM, Shirinifard A, Hmeljak D, Glazier JA (2012) Multi-scale modeling of tissues using CompuCell3D. Methods Cell Biol 110:325–366
65. Merks RMH, Glazier JA (2005) A cell-centered approach to developmental biology. Phys A Stat Mech Appl 352:113–130
66. Ziraldo C, Solovyev A, Allegretti A, Krishnan S, Henzel MK, Sowa GA et al (2015) A computational, tissue-realistic model of pressure ulcer formation in individuals with spinal cord injury. PLoS Comput Biol 11:e1004309
67. Checa S, Rausch MK, Petersen A, Kuhl E, Duda GN (2015) The emergence of extracellular matrix mechanics and cell traction forces as important regulators of cellular self-organization. Biomech Model Mechanobiol 14:1–13
68. Tepole AB, Kabaria H, Bletzinger K-U, Kuhl E (2015) Isogeometric Kirchhoff-Love shell formulations for biological membranes. Comput Methods Appl Mech Eng 293:328–347
69. Abhilash AS, Baker BM, Trappmann B, Chen CS, Shenoy VB (2014) Remodeling of fibrous extracellular matrices by contractile cells: predictions from discrete fiber network simulations. Biophys J 107:1829–1840
70. Obbink-Huizer C, Oomens CWJ, Loerakker S, Foolen J, Bouten CVC, Baaijens FPT (2014) Computational model predicts cell orientation in response to a range of mechanical stimuli. Biomech Model Mechanobiol 13:227–234
71. Xue C, Friedman A, Sen CK (2009) A mathematical model of ischemic cutaneous wounds. Proc Natl Acad Sci 106:16537–16538
72. Wong VW, Akaishi S, Longaker MT, Gurtner GC (2011) Pushing back: wound mechanotransduction in repair and regeneration. J Invest Dermatol 131:2186–2196
73. Schreml S, Szeimies R-M, Prantl L, Landthaler M, Babilas P (2010) Wound healing in the 21st century. J Am Acad Dermatol 63:866–881
74. Holzapfel GA, Gasser TC, Ogden RW (2000) A new constitutive framework for arterial wall mechanics and a comparative study of material models. J Elast 61:1–48
75. Gasser TC, Ogden RW, Holzapfel GA (2006) Hyperelastic modelling of arterial layers with distributed collagen fibre orientations. J R Soc Interface 3:15–35
76. Tonge TK, Voo LM, Nguyen TD (2013) Full-field bulge test for planar anisotropic tissues: Part II-A thin shell method for determining material parameters and comparison of two distributed fiber modeling approaches. Acta Biomater 9:5926–5942

77. Li W, Luo XY (2016) An invariant-based damage model for human and animal skins. Ann Biomed Eng 44:3109–3122
78. Limbert G (2017) Mathematical and computational modelling of skin biophysics: a review. Proc R Soc A Math Phys Eng Sci 473:20170257
79. Cortes DH, Lake SP, Kadlowec JA, Soslowsky LJ, Elliott DM (2010) Characterizing the mechanical contribution of fiber angular distribution in connective tissue: comparison of two modeling approaches. Biomech Model Mechanobiol 9:651–658
80. Ronen M, Rosenberg R, Shraiman BI, Alon U (2002) Assigning numbers to the arrows: parameterizing a gene regulation network by using accurate expression kinetics. Proc Natl Acad Sci USA 99:10555–10560
81. Sherratt JA (1994) Chemotaxis and chemokinesis in eukaryotic cells: the Keller-Segel equations as an approximation to a detailed model. Bull Math Biol 56:129–146
82. Hu H, Sachs F (1997) Stretch-activated ion channels in the heart. J Mol Cell Cardiol 29:1511
83. Wang JHC, Thampatty BP, Lin JS, Im HJ (2007) Mechanoregulation of gene expression in fibroblasts. Gene 391:1–15
84. Moreo P, García-Aznar JM, Doblaré M (2008) Modeling mechanosensing and its effect on the migration and proliferation of adherent cells. Acta Biomater 4:613–621
85. Paterno J, Vial IN, Wong VW, Rustad KC, Sorkin M, Shi Y et al (2010) Akt-mediated mechanotransduction in murine fibroblasts during hypertrophic scar formation. Wound Repair Regen 19:49–58
86. Wong VW, Rustad KC, Akaishi S, Sorkin M, Glotzbach JP, Januszyk M et al (2011) Focal adhesion kinase links mechanical force to skin fibrosis via inflammatory signaling. Nat Med 18:1–6
87. Jiang C, Shao L, Wang Q, Dong Y (2012) Repetitive mechanical stretching modulates transforming growth factor-β induced collagen synthesis and apoptosis in human patellar tendon fibroblasts. Biochem Cell Biol 90:667–674
88. Powell HM, McFarland KL, Butler DL, Supp DM, Boyce ST (2010) Uniaxial strain regulates morphogenesis, gene expression, and tissue strength in engineered skin. Tissue Eng Part A 16:1083–1092
89. Kobayashi T, Kim H, Liu X, Sugiura H, Kohyama T, Fang Q et al (2014) Matrix metalloproteinase-9 activates TGF-β and stimulates fibroblast contraction of collagen gels. Am J Physiol Lung Cell Mol Physiol 306:L1006–L1015
90. Brissett AE, Sherris DA (2001) Scar contractures, hypertrophic scars, and keloids. Facial Plast Surg 17:263–271
91. Brown BC, McKenna SP, Siddhi K, McGrouther DA, Bayat A (2008) The hidden cost of skin scars: quality of life after skin scarring. J Plast Reconstr Aesthet Surg 61:1049–1058
92. Rodriguez EK, Hoger A, McCulloch AD (1994) Stress-dependent finite growth in soft elastic tissues. J Biomech 27:455–467
93. Zöllner AM, Buganza Tepole A, Kuhl E (2012) On the biomechanics and mechanobiology of growing skin. J Theor Biol 297:166–175
94. Menzel A, Kuhl E (2012) Frontiers in growth and remodeling. Mech Res Commun 42:1–14
95. Ateshian GA, Humphrey JD (2012) Continuum mixture models of biological growth and remodeling: past successes and future opportunities. Annu Rev Biomed Eng 14:97
96. Ateshian GA (2007) On the theory of reactive mixtures for modeling biological growth. Biomech Model Mechanobiol 6:423–445
97. Models M, Humphrey JD, Rajagopal KR (2002) A constrained mixture model for growth and remodeling of soft tissues. Math Model Meth Appl Sci 12:407–430
98. Valero C, Javierre E, García-Aznar JM, Menzel A, Gómez-Benito MJ (2014) Challenges in the modeling of wound healing mechanisms in soft biological tissues. Ann Biomed Eng 43(7):1654–1665
99. Pensalfini M, Haertel E, Hopf R, Wietecha M, Werner S, Mazza E (2017) The mechanical fingerprint of murine excisional wounds. Acta Biomater 65:226–236
100. Berard CW, Woodward SC, Herrmann JB, Pulaski EJ (1964) Healing of incisional wounds in rats the relationship of tensile strength and morphology to the normal skin wrinkle lines. Ann Surg 159:260–270

101. Chaudhry HR, Bukiet B, Siegel M, Findley T, Ritter AB, Guzelsu N (1998) Optimal patterns for suturing wounds. J Biomech 31:653–662
102. Wong VW, Levi K, Akaishi S, Schultz G, Dauskardt RH (2012) Scar zones: region-specific differences in skin tension may determine incisional scar formation. Plast Reconstr Surg 129:1272
103. Gurtner GC, Dauskardt RH, Wong VW, Bhatt KA, Wu K, Vial IN et al (2011) Improving cutaneous scar formation by controlling the mechanical environment: large animal and phase I studies. Ann Surg 254:217–225
104. Aarabi S, Bhatt KA, Shi Y, Paterno J, Chang EI, Loh SA et al (2007) Mechanical load initiates hypertrophic scar formation through decreased cellular apoptosis. FASEB J 21:3250–3261
105. Tranquillo RT, Murray JD (1992) Continuum model of fibroblast-driven wound contraction: inflammation-mediation. Biomech Model Mechanobiol 158:361–371
106. Kuhl E, Garikipati K, Arruda EM, Grosh K (2005) Remodeling of biological tissue: mechanically induced reorientation of a transversely isotropic chain network. J Mech Phys Solids 53:1552–1573
107. Wu M, Ben Amar M (2014) Growth and remodelling for profound circular wounds in skin. Biomech Model Mechanobiol 14:1–14
108. Richardson W, Holmes J (2016) Emergence of collagen orientation heterogeneity in healing infarcts and an agent-based model. Biophys J 110:2266–2277

Constitutive Modelling of Skin Ageing

Georges Limbert, Damien Pond, and Andrew McBride

Abstract The objective of this chapter is to review the main biomechanical and structural aspects associated with both intrinsic and extrinsic skin ageing, and to present potential research avenues to account for these effects in mathematical and computational models of the skin. This will be illustrated through recent work of the authors which provides a basis to those interested in developing mechanistic constitutive models capturing the mechanobiology of skin across the life course.

1 Introduction

The skin is not only the largest organ of the human body but is also one of the most complex multi-functional physiological systems in mammalian species [1]. Its main role is to ensure cohesion and protection of the internal body structures against mechanical, thermal, biological and radiological threats. It also has critically

G. Limbert (✉)
National Centre for Advanced Tribology at Southampton (nCATS) — Bioengineering Science Research Group, Department of Mechanical Engineering, Faculty of Engineering and Physical Sciences, University of Southampton, Southampton, UK

Laboratory of Biomechanics and Mechanobiology, Division of Biomedical Engineering, Department of Human Biology, Faculty of Health Sciences, University of Cape Town, Observatory, South Africa
e-mail: g.limbert@soton.ac.uk

D. Pond
Centre for Research in Computational and Applied Mechanics, University of Cape Town, Rondebosch, South Africa

A. McBride
Glasgow Computational Engineering Centre, Division of Infrastructure and Environment, School of Engineering, University of Glasgow, Glasgow, UK
e-mail: andrew.mcbride@glasgow.ac.uk

G. Limbert (ed.), *Skin Biophysics*, Studies in Mechanobiology, Tissue Engineering and Biomaterials 22,
https://doi.org/10.1007/978-3-030-13279-8_5

important thermo-regulation, biochemical synthesis and sensory functions [1, 2]. Moreover, the skin plays an important social and psychological role as it is a permanent reminder of our ethnicity, health status, age and past traumas, and therefore, provides direct and indirect cues to the people we interact with. By means of a rich library of mechanically-activated facial expressions, from micro-wrinkles to large macroscopic tissue folds, the skin is a powerful vehicle for conscious and subconscious communication. From these facts it is straightforward to conclude that, beyond physiology, the skin is crucial to human life and could be viewed as a "brain on the outside" [3]. Like any other organ of the body, the skin inexorably undergoes what is termed chronological or intrinsic ageing; a series of biochemical molecular degenerative changes occurring as the result of the mere passage of time and progression into older age. These alterations involve decreased proliferative capacity which leads to cellular senescence and altered biosynthetic activity of skin derived cells. Intrinsic ageing is triggered by two main mechanisms which can operate in concert, namely DNA damage and chromosomes' telomere shortening [4–7]. The fact that the skin of people of identical ages living in similar environments may appear younger- or older-looking is a testimony to the fundamental role of genetics in skin ageing. Genetics conditions the rate of skin ageing by controlling certain factors such as the biochemistry of skin cells, immunochemistry and hormonal mechanisms. Intrinsic ageing typically occurs in combination with extrinsic ageing which is the result of external environmental and lifestyle factors, particularly exposure to ultraviolet radiations (UVR) from sun light [8–10], and, increasingly, sunbeds [11, 12], as well as smoking [13, 14] and air pollution [14, 15]. Extrinsic ageing due to UVR exposure is called photoageing [9, 10], a term which was first coined by Kligman [10] using the American English spelling "aging". These aspects are discussed in more details in Sect. 3.

Ageing affects both the structure and the function of the skin (see Fig. 1). These alterations have important consequences for skin physiology [4, 16], rheology [17], surface physics and tribology [18–20]. Aged skin is more prone to developing disorders such as xerosis and pruritus [21], skin cancers [22] as well as debilitating, costly and life-threatening skin tears and pressure ulcers [23]. Even in their minor form, these afflictions can severely impact on quality of life for the elderly population. These facts must be considered alongside concerning demographics on the ageing of the population. Between 1984 and 2009 the UK population aged 65 and over increased by 1.7 million people [24]. Between 2001 and 2011, the UK population aged 85 and over increased by almost 25% (from 1.01 million to 1.25 million) [25]. As of 2016, these two age groups represented respectively 18 and 2.4% of the UK population [26]. By 2039, almost a quarter of the UK population will be 65 and over [25]. Globally, it has been estimated that the proportion of people over 60 will nearly double from 12% in 2015 to 22% by 2050 (i.e. 617 million to 1.6 billion) [27].

The significance of these statistics is embodied by two essential aspects: firstly, the need for medical treatment and care increases with longevity and, secondly, the ageing process itself results in degradation of physiological functions and

Fig. 1 Left inner forearm and right hand of an 82 year-old White Caucasian male subject with no known skin conditions, highlighting the wrinkled and leathery appearance of both intrinsically and extrinsically aged skin

biophysical properties of organs and tissues. In both cases, this puts an alarming economic and social burden on governments and healthcare services [28].

Average hospital spending for an 89 year-old man in the UK is roughly three times the average for a 70 year-old, and nine times the average figure for a 50 year-old, with costs typically escalating more rapidly for men than women [28]. In the case of skin, which accounts for up to 16% of an adult's total body weight whilst covering an average surface area of about $1.6\,m^2$ [2], ageing can lead to potentially life-threatening complications as mentioned previously in this section. As the skin is the prime line of defence against the external environment, it is clear that any significant alteration of its mechanical properties that could compromise its structural integrity and barrier function, has the potential to cause serious detrimental health effects.

From an economic point of view, both in the UK and globally, the ageing population is also rapidly becoming a significant market segment across many industrial sectors, spanning medical devices through consumer goods and personal care products to sport equipment and consumer electronics. For many of these products (e.g. wearable electronics, razors, incontinence products) the biophysical response of the skin, particularly for contact scenarios, is crucial in terms of comfort, performance and safety. It is therefore essential to engineer products that take into account altered biophysical characteristics of an aged skin (i.e. "inclusive design") so as to optimise their performance in terms of human factors. The goal should be

to understand how age-related alterations of skin biophysics can be accounted for in the development of new or improved products that will improve health, quality of life and enable the aged and ageing population to remain active longer. Particular research efforts should be devoted to gain a fundamental and quantitative insight into the mechanisms that drive and govern the ageing process. Unravelling the inherent complexity of the skin ageing process, firstly by identifying its biophysical drivers, underlying modulating factors and effects, and secondly, by gaining a mechanistic insight into their interplay, is a formidable challenge at both experimental and modelling levels. This stems from the fact that:

1. ageing is a *multi-factorial problem* which features multiple types of processes rooted in *biology*, *chemistry* and *physics*, and, more particularly, *mechanics*;
2. these processes are *non-linear* and lead to *complex non-linear feedback mechanisms*;
3. there is a *significant intra-individual* (primarily due to anatomical location and sun exposure) and *inter-individual* (as a consequence of age, sex or genetics) *variability*.

The multi-factorial nature of ageing and the complex non-linear interplay of its biophysical driving factors currently hinder our ability to develop a mechanistic understanding of ageing, and therefore, a rational basis to design prevention and treatment strategies against its degenerating effects.

The provision of mathematical and computational models of skin ageing holds the promise of offering a rational quantitative basis to develop such products whilst also enabling and accelerating innovation, and alleviating the reliance on animal models through a better quantitative understanding of human ageing.

The objective of this chapter is to provide a review of the main biomechanical and structural aspects associated with skin ageing and to present ideas on how to account for ageing in mathematical and computational models of the skin. This will be illustrated through recent work of the authors which could provide a starting point to those interested in developing mechanistic constitutive models capturing the mechanobiology of skin across the life course. Prior to that, some of the more popular theories of skin ageing will be briefly presented.

The chapter is organised as follows. The general structural and material properties of the skin are discussed in Sect. 2. Section 3 presents the key manifestations of ageing on the skin from the view point of structural biomechanics. Some of the most popular and accepted theories of skin ageing are also discussed. Finally a simplified mechanistic description of skin ageing unifying essential features of both intrinsic and photoageing is presented in Sect. 4. Background ideas and literature about modelling of ageing from the viewpoint of continuum mechanics are given in Sect. 5. A brief reminder of the essential equations of continuum mechanics necessary to describe the mechanical behaviour of skin is provided in Sect. 6. The structure of the constitutive model used to describe the mechanical response of skin at a fixed moment in time is presented in Sect. 7. Following the recent work of the authors [29], a mechanistic constitutive model of the skin linking microstructural constitutive parameters with intrinsic ageing is described in Sect. 8.

The intrinsic ageing model is implemented within the finite element method in Sect. 9 and the constitutive parameters associated with ageing identified. A novel chemo-mechanobiological constitutive model of skin ageing that includes features of both intrinsic and extrinsic ageing is developed in Sect. 10. Finally, Sect. 11 ends with concluding remarks about current and future prospects for the modelling of skin ageing.

2 Essential Structural and Material Properties of the Skin

2.1 Multi-Layer Nature of the Skin

The human skin is a complex multiscale structure that is often described at the mesoscopic scale as a multi-layer assembly composed of an epidermis, dermis and hypodermis (Fig. 2) [2, 30, 31] (see also the chapter "Human Skin: Composition, Structure and Visualisation Methods" of this book for a more comprehensive description of the molecular and structural properties of the skin).

The avascular epidermis is a terminally differentiated stratified squamous keratinocyte-dominated (95% of its composition) epithelium about 200 µm thick which also contains other cell types (e.g. melanocytes, Langerhans's cells and Merkel cells [2]). The epidermis consists of two main substructures, the *stratum corneum* and the viable, also called living, epidermis (Fig. 2). The *stratum corneum* consists of a one to three cell-thick layer of dead keratinocytes featuring a 10–30 µm total thickness. A 0.5–1 µm thick epidermal basement membrane (also known as

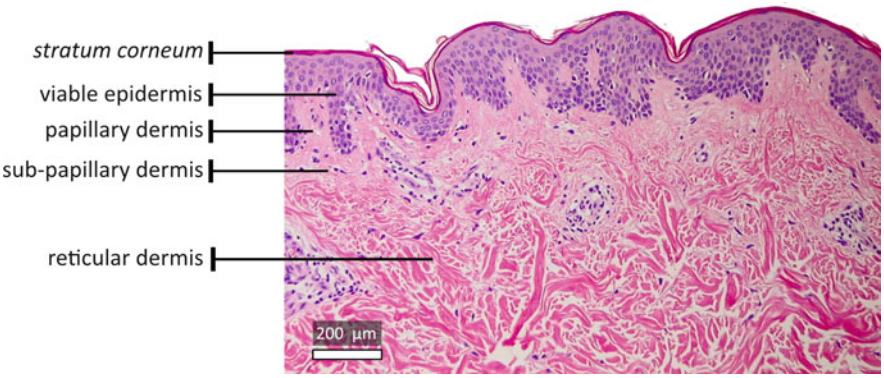

Fig. 2 Histological section of haematoxylin and eosin stained back human skin sample obtained from a 30 years-old healthy White Caucasian female volunteer following biopsy (10× magnification, image resolution: 1600 × 1200 pixels, imaged using a modified Nikon E950 camera). Image courtesy of Dr. Maria-Fabiola Leyva-Mendivil, University of Southampton, UK. The main skin layers, namely *stratum corneum*, viable epidermis, papillary dermis, sub-papillary dermis and reticular dermis are indicated

basal lamina) [32] separates the viable epidermis from the dermis. Keratinocytes undergo mitosis at this location before they progressively migrate toward the skin surface where they die, and eventually form the *stratum corneum*.

The dermis is 15–40 times as thick as the epidermis [2]. It is generally accepted that the bulk of the skin's response to loading is due to the dermal layer [17, 33]. The extracellular matrix (ECM) of the dermis which is mainly secreted by fibroblasts is a 3D network of fibrous proteins (mainly type I and III collagen and elastic fibres—namely, elastin and fibronectin) and glycosaminoglycan-rich proteoglycans [34]. The ECM provides strength, extensibility and elasticity to the skin and plays a significant bio-chemo-mechanical role in cell adhesion and regulation of cell signalling.

The expression of the macroscopic mechanical properties of the skin is due to its basic building components, their structural organisation and their mutual interactions. Three distinct zones can be identified within the dermis: the papillary layer juxtaposed to the epidermis, the sub-papillary layer underneath and the reticular layer (Fig. 2) which is connected to the underlying subcutaneous tissue. The papillary layer is defined by the rete ridges protruding into the epidermis and contains thin collagen fibres, sensory nerve endings, cytoplasms and a rich network of blood capillaries. The sub-papillary, layer which is the zone below the epidermis and papillary layer, features similar structural and biological components to those of the papillary layer.

The subcutaneous tissue is the layer between the dermis and the fascia which is a band of connective tissue, primarily collagen, that attaches, stabilises, encloses, and separates muscles and other internal organs. The thickness of subcutaneous tissue is highly variable intra- and inter-individually. This layer is mainly composed of adipocytes. Its role is to provide mechanical cushioning, heat generation and insulation as well as a reserve of nutrients.

2.2 Structural Elements of the Dermis

The ground substance is a gel-like amorphous phase mainly constituted of proteoglycans and glycoproteins (e.g. fibronectin) as well as blood and lymph-derived fluids which are involved in the transport of substances crucial to cellular and metabolic activities. Proteoglycans are composed of multiple glycosaminoglycans (i.e. mucopolysaccharides) interlaced with back bone proteins. Dermal fibroblasts produce glycosamine which is rich in hyaluronic acid and therefore play an essential role in moisture retention.

Collagen has been found to make up approximately 66–69% of the fractional volume of the dermis [17], and approximately 34% [35] and 70–80% [36] of the wet and dry weight of the skin, respectively. Experiments where collagen was isolated through enzymatic treatment [37–39], conclude that collagen is responsible for the tensile strength of the skin. Besides a dominant content of types I and III collagen (respectively 80% and 15% of total collagen content), the reticular layer

is innervated and vascularised, contains elastic fibres (e.g. elastin) and the dermal matrix made of cells in the interstitial space. Cells present in the reticular dermis include fibroblasts, plasma cells, macrophages and mast cells. Collagen fibres in the papillary and sub-papillary dermis are thin (because of their low aggregate content of fibrils) and sparsely distributed while reticular fibres are thick, organised in bundles and densely distributed. Fibrils are typically very long, 100–500 nm in diameter featuring a cross striation pattern with a 60–70 nm spatial periodicity. The diameter of thick collagen bundles can span 2–15 μm. Birefringence techniques have been used to characterise the orientation and supramolecular organisation of collagen bundles in skin [40]. Contributing approximately 2–4% of the dry weight of skin [41], elastin fibres are highly compliant with the ability to stretch elastically to twice their original length [42]. Their diameter ranges between 1 and 3 μm. Their mechanical intertwining with the collagen network of the dermis is what gives the skin its resilience and recoil ability. This is evidenced by the correlation between degradation of elastin, abnormal collagen synthesis associated with ageing and the apparent stiffening of the dermis [16]. The diameter of elastic fibres in the dermis is inversely proportional to their proximity to the papillary layer where they tend to align perpendicular to the dermal-epidermal junction surface.

2.3 Mechanical Behaviour of the Skin

At a macroscopic level, the mechanical properties of the skin are anisotropic and inhomogeneous, not only due to the complex hierarchical structure and materially non-linear constituents but also due to the existence of residual tension lines in the skin (i.e. the so-called "Langer lines") as first recognised by the Austrian anatomist Karl Langer in his seminal study [43]. These essential features of skin and their experimental characterisation are discussed in more detail in chapter "Tension Lines of the Skin" of this book.

Dispersion of collagen fibres around the main orientation directions and non-uniform fibre geometry means that under stretch not all fibres are straightened and stretched. This accounts for the anisotropic stiffness response when load is applied either along or across the preferential fibre direction. The magnitude of these directional effects have been the subject of several recent studies. It has been found that the Young's modulus parallel to the Langer lines was greater than that perpendicular by a ratio of approximately 2.21:1 [44]. Similarly, Reihsner et al. [36] found that the degree of anisotropy differs across anatomical site, an observation also made by Langer in his original study. In addition, they found that in situ stresses range from 0.2 to 1.6 N/mg along Langer lines and 0.1–1.3 N/mg perpendicularly, with the degree of anisotropy differing between principle stress components from 0.1 to 0.3 N/mg. It was shown that when the skin is stretched, the elastin fibres are the first to bear load [45], indicating that the contribution is important at low strain levels. Stress-strain curves of elastin-free skin [37] show that elastin supports the entire load up to 50% strain after which the strength rapidly increases due to the

collagen. The elastic modulus of elastin has been found at around 1 MPa which agrees with the Young's modulus of skin at low strain. Elastin is not strong enough to provide much tensile strength at higher strains [46]. Reihsner et al. [36] state that elastin is responsible for the recoiling of the skin and collagen after stress is applied. Following degradation of the elastin through the use of elastase, Oxlund et al. [37] found that the large strain response occurs sooner for a given tensile load. This suggests that in the absence of elastin, collagen fibres take on load at lower strain levels than when elastin is present.

The ground substance has been shown to play a role mainly on the viscoelastic properties of the skin because of high-water content and complex time-dependent interstitial fluid motion. Upon removal of various macromolecules within the ground substance, Oxlund and Andreassen [38] showed that there was no effect on the mechanical response of rat skin, while Oomens et al. [47] suggests that ground substance probably only plays a major role when soft tissue is subject to compression. Under uniaxial tension, skin exhibits a typical strain-hardening response, featuring three main characteristic zones (a), (b) and (c). Each portion of the stress-strain curve can be explained by particular structural deformation mechanisms associated with the skin dermal constituents. *(a) Low modulus portion of the strain-stress curve*: this occurs over the gradual straightening of crimped collagen fibres. During this stage, the greatest resistance to loading is generated by the elastin and ground substance, with collagen fibres offering very little resistance. The low modulus portion can be further divided into two phases: (1) Phase 1: wavy collagen fibres are still relaxed and elastin fibres take on the majority of the load; (2) Phase 2: collagen fibres start to uncrimp, then elongate and eventually start to bear load; *(b) Linear region of the strain-stress curve*: collagen fibres straighten and align with the load direction. Straightened collagen fibres strongly resist loading. This results in the rapid stiffening of the skin. The steep linear stress-strain relation is due to stretching and slippage between fibrils and molecules; *(c) Final yield region of the strain-stress curve*: tensile strength of collagen fibres is reached and fibres begin to sequentially break.

3 Manifestations of Skin Ageing and Underlying Biophysical Mechanisms

It is often thought that what one refers to as ageing of the skin is mostly due to the bio-structural alterations of the skin induced by extrinsic ageing, as a "well-maintained" skin, in terms of appropriate diet and skin care, and protected from UVR, exhibits a "remarkable resilience" [48] to intrinsic ageing. Intrinsic ageing can only be observed in old age subjects, and its extent and magnitude is strongly dependent upon ethnicity, individuals, even within the same ethnic group, and body locations. It is also characterised by a very gradual evolution of the skin appearance over decades, unlike extrinsic ageing which can take place over

much shorter periods of time. As would intuitively be expected, both intrinsic and extrinsic ageing operate in concert and influence each other [48]. For example, exogenous factors associated with a particular environment such as pro-oxidants and antioxidants have an impact on cell turnover through neuro-endocrine-immune biological response modifiers. While intrinsic ageing can be influenced by extrinsic ageing it could also be defined as a form of purely biological ageing, a process genetically determined and immutable [49]. Following a similar classifying logic, factors leading to extrinsic ageing can be split into three main types: environmental (e.g. effects of UVR, chemical pollution including that induced by the use of tobacco products, temperature), mechanical (e.g. repetitive muscle actions leading to tissue plasticity such as squinting and frowning) and lifestyle (e.g. diet and sleep patterns).

Intrinsic ageing is characterised by unblemished, smooth, stiffer, drier and less elastic skin [48] with fine wrinkles, with occasional exaggerated expression lines [34, 50], epidermal and dermal atrophy as well a reduction in the population of mast cells [51]. Extrinsic skin ageing manifests as deep wrinkles and leathery appearance due to photo-damage, pigmented lesions, actinic keratosis and patchy hyperpigmentations [52, 53]. The externally visible structural effects of extrinsic ageing on the skin can be viewed as exaggerated intrinsic ageing effects. It is worth to point out that UV exposure leads to additional photobiochemical effects which are not present in intrinsic ageing. Extrinsic ageing is most apparent on sun-exposed body locations such as the face, neck, chest and the dorsal surface of the arms [8]. It is estimated that 80% of the effects of facial skin ageing are due to chronic UV exposure.

A review of theories of skin ageing is out of the scope of the present chapter and the reader is referred to recent excellent review papers such as those by Gragnani et al. [53], Tobin [48] and Krutmann et al. [54] for detailed descriptions of established and suspected ageing mechanisms. There is very strong evidence that the main factors involved in skin ageing are oxydative stress (accumulation of oxidative damage to cells during their life due to excessive production of reactive oxygen species (ROS)), cellular senescence and telomeres' shortening due to apoptosis, diet, genetics, UV irradiation, smoking, pollution, intracellular signalling and skin lesions, age-related diseases, disorders and conditions of the skin, hormonal changes and the production of advanced glycation end products (AGEs) [53].

3.1 Ageing of the Skin Considered as a Homogeneous Structure

It is generally accepted that skin thickness decreases with age [39, 55]. Pawlaczyk et al. [56] found that there is an overall loss of 0.7–0.8 mm of thickness in older skin. It was found that skin thickness reaches a maximum around the fourth decade for men and third decade for women after which there is a gradual decrease [35], a result similar to that established by Diridollou et al. [57] who found that after an

initial increase during maturation (0–20 years), thickness remains constant to about the age of 60 followed by a decrease according to the following equation:

$$t = -6 \times 10^{-3} \times \text{age} + 1.3\,, \tag{1}$$

where t is in mm and the age is in years. Moreover, the rate of decrease is more significant in female subjects.

It is important to highlight that these observations about skin thickness apply to the skin as a whole composite structure. Individual skin layers may follow different trends depending on whether intrinsic and extrinsic ageing effects are considered separately or assumed to be combined. After 20 years of age, across all layers, the skin thickness starts to diminish at a rate that increases with age [58]. Between 30 and 80 years, the unexposed skin can lose up to 50% of its thickness and this effect is accentuated in zones exposed to sunlight such as the face or neck. Overall, epidermal thickness drops by about 6.4% per decade, and at a faster rate in women than men. It is generally believed that the reported reduction in dermal thickness is mainly caused by the loss of dermal collagen and elastin in elderly adults [59]. It was shown that in post-menopausal women a 1.13% per year skin thickness reduction is correlated with a 2% decrease per year in collagen content [60]. Besides decreased elastin and collagen content as well as their structural rearrangement, intrinsic ageing also has other consequences such as increase in trans-epidermal water loss, reduction in skin moisture content, diminished sebum production, arteriosclerotic changes in the small and large vessels, thinning of vessel walls [61], reduction in mast cells [51], melanocytes, Langerhans's cells, Meissner cells, Merkel cells and Pacinian corpuscules [61, 62] and increase in skin surface pH [63] after 70 years of age [64].

It is also accepted that skin ageing is characterised by an increase in macroscopic or apparent stiffness [56, 65, 66], although there is little agreement on the magnitude of the ground state Young's modulus and age of onset of stiffening. As mentioned by Xu and Lu [66], there is a sudden increase in the Young's modulus of the skin at age 30 of around 50%, whereas others quote an increase from the age of 45. It was observed by Escoffier et al. [55] that there is an increase of around 20% after the age of 70, which is backed by the findings of Lévêque et al. [35]. Furthermore, Alexander and Cook [65] found that the stiffness of skin starts to increase from the age of 25 but noted that the variation in results increases with age. This suggests that the process of skin ageing is a highly patient specific and may explain the large variation in results reported in the literature.

It was found by Escoffier et al. [55] and Lévêque et al. [35] that intrinsic skin extensibility (i.e. a standardised mean extensibility to account for varying skin thickness) decreases with age, while Alexander and Cook [65] found that intrinsic extensibility decreases by around 35% after the age of 65 which agrees with the findings of Xu and Lu [66] in that maximum skin elongation is found between ages 35 and 55. Similarly, skin elasticity (i.e. recoil ability) decreases with age [55, 66], which was also found by Henry et al. [67], but this may include the effects of UVR.

3.2 Ageing of the Epidermis

Intrinsic ageing induces thinning of the epidermis whilst also slowing its turnover. However, photoageing is manifested as a thickening of the epidermis because of its disruptive action on keratinocyte differentiation which leads to abnormal keratin intermediate filament expression. If one then superimposes the drying effect of photoageing on the *stratum corneum*, a reduced rate of desquamation is observed. As a consequence, the epidermis becomes thicker, stiffer and more fragile [68]. Overall, epidermal thickness drops by about 6.4% per decade at a faster rate in women than men [58]. Based on the observation that in areas of skin under high levels of external loading, such as on the hands and feet, the epidermis thickens, Silver et al. [69] suggested that epidermal thickness is controlled by the balance of external and internal forces acting on/within this layer. Intrinsic ageing slows down the turnover of keratinocytes and is also accompanied by a reduction in *stratum corneum* water content [70] because of alteration in lipid content of the epidermal barrier [71]. This factor leads to an increase in the stiffness of the *stratum corneum* which is correlated with humidity level [72–74]. For the skin to be considered clinically dry the normal water content of the *stratum corneum* (about 20%) must drop below 10% [70].

3.3 Ageing of the Dermal-Epidermal Junction (DEJ)

In young skin, there is an essential network of thin oxytalan fibres anchoring the papillary dermis to the viable epidermis. During intrinsic ageing, these oxytalan fibres are progressively shortened and resorbed leading to the disappearance of dermal papillae [75] and flattening of the dermal-epidermal junction (DEJ) [76–80]. This reduction in the amplitude of the papillae is also accompanied by a decrease in their density (unit per surface area) [77, 78]. The flattening of the DEJ leads to a reduction of up to 20% in epidermis thickness [81]. It was suggested that the flattening of the DEJ could be a facilitating factor in the formation of skin wrinkles by compromising the structural integrity of the basement membrane which links dermis to epidermis [82], increasing the likelihood of relative motion between these two layers. Besides these important structural effects, the flattening of the DEJ has important metabolic consequences as it reduces the surface area for nutritional exchange and metabolic byproducts evacuation between the dermis and epidermis. As a result, epidermal cell turnover is slowed down and free radicals accumulate. Skin exposed to UVR experiences an accelerated flattening of the DEJ when compared to sun protected skin [83]. It has also been shown through image analysis that intrinsically aged skin features the same density of veins and arteries as young skin but their diameters are reduced. In photoaged skin, the dermal vasculature is progressively lost and the diameter of veins and arteries is also reduced [84].

3.4 Ageing of Dermal Matrix

Important differences between the dermis of young, intrinsically aged and photoaged skin pertain to the level of structural organisation of fibrillar collagen which conditions its mechanobiological interactions with fibroblasts through their integrin attachments [34]. In young skin, the fibrillar collagen meshwork is made of small and thin bundles of tightly packed fibres in the papillary dermis while these bundles are thicker and more spaced in the reticular dermis [76, 85]. Fibroblasts are in a state of mechanical tension through the alignment along collagen fibres, the effect of which promotes a healthy homeostatic state for normal collagen fibre synthesis. The ratio of type III to I collagen increases with age [86, 87]. In intrinsically aged skin, there is a significantly reduced collagen turnover, thinning of fibre bundles and disappearance of the meshwork [88]. These structural changes affect the mechanobiological interactions of fibroblasts with collagen fibres leading to collapsed fibroblasts [88–90].

Lavker et al. [91] reported an increased density of the collagen network with age and explained it by the decrease in ground substance which effectively provides more space to fill in to collagen fibres. This has the effect of reducing dermis thickness. With age, the collagen and elastin fibre networks in the dermis become compacted leading to reduction in dermis thickness. Elastin fibres lose their elasticity while collagen fibres tend to unravel. As a consequence, the skin loses its extensibility, becomes less resilient and more lax [92]. The reported reduction in dermal thickness is mainly attributed to the loss of dermal collagen and elastin in elderly adults, as a result of progressive slowing down of dermal matrix turnover [59]. This reduced turnover stems from the imbalance between synthesis activity and degradation which increasingly dominate cell activity during the intrinsic ageing process.

The key regulators of collagen production are transforming growth factors-β (TGF-β) and activator protein-1 (AP-1) [93]. TGF-β is a multi-functional cytokine that helps regulate many biological functions such as cellular growth, differentiation and extracellular matrix synthesis, such as that associated with collagen and elastin constituents [94]. AP-1 is a transcription factor that inhibits collagen production and up-regulates matrix metalloproteinase (MMP) enzymes which act to break down extracellular matrix constituents. All fibroblasts have the capacity to synthesise collagen. Thus one of the main contributing factors to collagen synthesis is the proliferative capacity of resident fibroblasts. Synthesis of collagen is promoted through mechanical tension applied to dermal fibroblasts. The rate of collagen synthesis is conditioned by the level of mechanical tension [11].

Platelet derived growth factor (PDGF) is a substance that promotes fibroblast growth and proliferation, known as mitogen. PDGF binds to cell surface receptors, which activates mitogen-activated protein (MAP) kinase signalling. The result of this action is the signalling of downstream effectors, such as the activation of extracellular signal-related kinase (ERK), that promote cell growth and proliferation [93]. TGF-β is produced within the extracellular matrix and, when in active form,

is able to associate with TGF-β signalling receptors on the cell surface of dermal fibroblasts, referred as type I and type II receptors, or Tβ RI and Tβ RII respectively. This results in the activation of downstream pathways, notably the Smad protein pathways. Smads 2, 3 and 4 transduce the signals while Smad 7 acts as an inhibitor. Together with interaction with MAP kinase signalling, collagen synthesis is promoted [94].

The intrinsic ageing process is accompanied by a reduction of the fibroblast population [51] which induces a decrease in collagen production and is associated with an increased build-up of MMPs which can cleave elastic fibre molecules [93, 95]. MAP kinase activation is an important mediator of MMP production. Along with activation of the ERK pathways, signalling the jun-N-terminal kinase (JNK) are necessary for the regulation of MMPs. Activation of the JNK pathways results in the production of c-jun, while ERK signalling results in the production of c-fos, both of which are necessary for the production of AP-1. AP-1 is key to the production of MMP. There exists a class of proteins, known as tissue inhibitors of metalloproteinases (TIMPs), that control inhibition and regulation of MMPs. TIMP-1 is prominent in the skin. TIMPs are also regulated by downstream signalling through the MAP kinase. A simplified schematic representation of the key cellular mechanisms associated with dermal fibroblasts in intrinsic ageing is provided in Fig. 3.

Disruption of the homeostatic state between activation and inhibition of MMPs is a key ingredient in the pathophysiology of both intrinsic and extrinsic ageing. The ratio of type III to I collagen increases with age [86]. Macroscopically, alterations of the collagen network manifest themselves as reduced dermal volume and strength. Moreover, aged collagen fibres undergo non-enzymatic Maillard reactions that cross-link molecules by glycation [96, 97], and lead to non-degradable abnormal fibres [85] which belong to the class of advanced glycation end products (AGEs).

Chronic exposure to UV radiations induces a significant and incomplete ECM degradation. In photoaged skin, there is a massive increase in collagen fibre degradation. Acute UV exposure activates a key transcription factor in cells, namely AP-1, which triggers an increase in MMP 1, 2, 3 and 9 synthesis and cell activity linked to a decreased in type I procollagen synthesis [98]. It has also been suggested that via the inflammatory response associated with chronic UV exposure, immune cells could play a role in collagen network degradation [8, 99]. During the intrinsic ageing process collagen becomes less soluble, sparser and thinner while photoageing induces thickening, fragmentation and an increased solubility of collagen [87].

Elastin fibres are highly compliant with the ability to stretch elastically to twice their original length [42]. Their mechanical intertwining with the collagen network of the dermis is what gives the skin its resilience and recoil ability, by maintaining collagen fibres in a crimped state. This is evidenced by the correlation between degradation of elastin, abnormal collagen synthesis associated with ageing and the apparent stiffening of the dermis [16, 55]. It has been widely observed that, with age, there is a decrease in the initial portion of the elongation-stress curve of skin [36, 65, 100] which means that the onset of stiffening associated with recruitment of

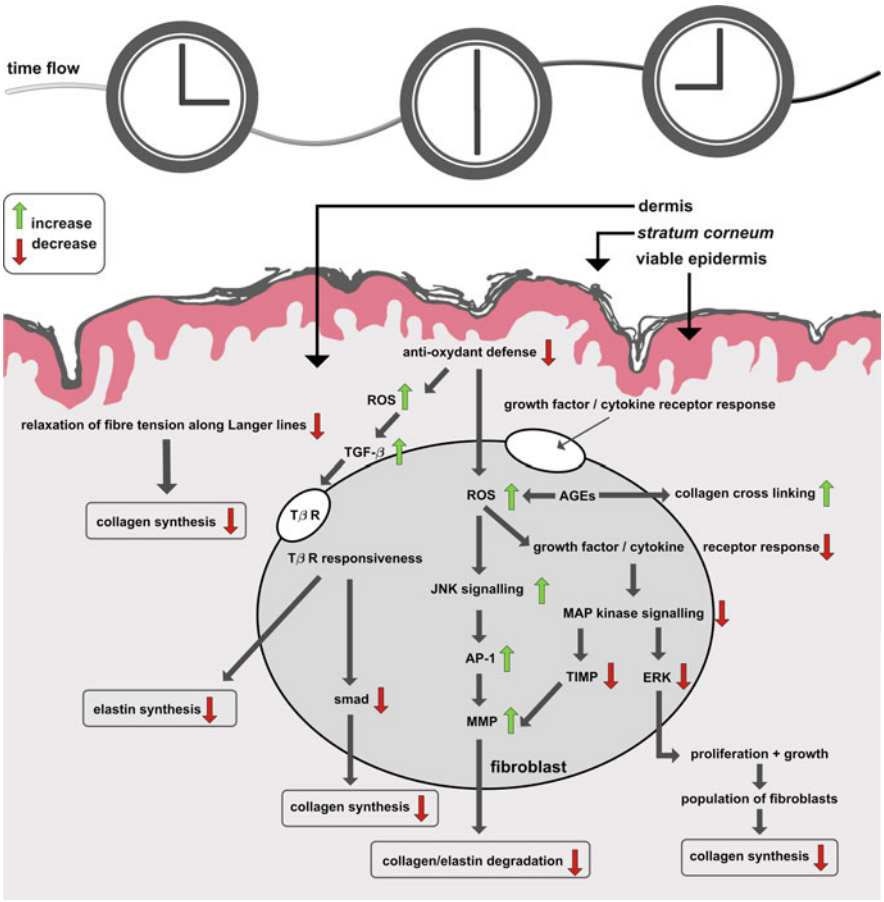

Fig. 3 Simplified schematic representation of the key cellular mechanisms associated with dermal fibroblasts in intrinsic ageing. A green/red arrow indicates an increase/a decrease [*ROS* Reactive Oxygen Species; *TGF-β* Transforming Growth Factor *β*; *Tβ* R TGF-*β* receptor; *AGE* Advanced Glycation End product; *JNK* Jun-N-terminal-Kinase; *MAP* Mitogen Activated Protein; *MMP* Matrix Metalloproteinase ; *TIMP* Tissue Inhibitor of MetalloProteinase; *AP-1* Activator Protein-1; *ERK* Extracellular signal-Related Kinase]

collagen fibres occurs at lower stretch. This is attributed to degradation of the elastin network and deposition of amorphous elastin [17, 36, 65, 100].

It has been reported that the slope of the linear portion of the elongation-stress curve tends to increase with age [65]. This suggests an apparent stiffening of the collagen fibre network with age but not necessarily a stiffening of the collagen fibres themselves. This aspect is supported by the experimental evidence obtained by Daly and Odland [100] and Reihsner et al. [36] who note that the final slope of the strain-stress curve of skin in tension remains constant with age, and that the stiffness of the collagen remains constant, possibly due to the reduction in the collagen content in

the dermal layer. There is therefore a suggestion that the alteration of the skin's apparent stiffness is not due to a stiffening of the collagen fibres, but rather to an alteration in the structure of the collagen network [29]. Escoffier et al. [55] and Reihsner et al. [36] report an increased collagen crosslinking with age, which would reduce any slippage between neighbouring fibres and stiffen up the collagen network. This would support the observations of Batisse et al. [72] who reported a stiffening with age of the whole dermis while noting a reduced density in the collagen fibres of the papillary dermis of aged skin as this might suggest that other stiffening mechanisms may be at play (e.g. increased collagen cross-linking with age [101]).

Anisotropy tends to increase with age suggesting that there is an increase in alignment along Langer lines with age [102, 103], or at least, a correlation between age, microstructurally-induced anisotropy and Langer lines, although Tonge et al. [41] found a decrease in overall anisotropy with age. The magnitude and directions of the Langer lines [43] are known to vary with age. There is a reduction in magnitude with age which is linked to the thinning of the hypodermis leading to a loss of firmness of the skin [101]. Also, with age, the skin tends to lose its in-plane isotropy [102] because of the strong mechanical effects introduced by dermal collagen realignment arising in combination with collagen cross-linking and density alteration.

Chronic UV irradiation spanning many years alters the normal structural and mechanical characteristics of the skin and ultimately causes premature skin ageing and cancer [8, 104]. Acute exposure to UV radiation sources trigger photochemical reactions in the skin which can manifest as sunburn, inflammation, immunity suppression, modified pigmentation and dermal connective tissue damage [104]. The photons carrying radiative energy quanta (of various wave lengths) are absorbed by molecules named chromophores in the skin where they create states of energetic excitations which engender the aforementioned photochemical reactions. These reactions induce the formation of stable photoproduct molecules [104] which, in turn, stimulate cellular signal transduction pathways which control cell proliferation and apoptosis, and also the secretion of cytokines. For most responses to UV and visible light exposure, the magnitude of the response is conditioned by the exposure dose at a given wave length. Wavelengths of radiations emitted by the sun shorter than 290 nm are mostly absorbed by the ozone layer in the stratosphere and do not reach sea level. Wavelengths in the range of 200–290 nm are strongly absorbed by DNA and therefore can be lethal to viable cells of the epidermis [104]. The UVB wave band (280–315 nm) is often referred as mid-UV or sunburn spectrum and constitutes about 0.5% of the total radiation reaching the Earth's surface. Most sunscreen agents reflect or absorb radiations operating in this waveband which is the testing benchmark upon which the sun protection factor (SPF) is based. Within the UVB spectrum, certain wave lengths have drastically different effects: radiations at 297 nm are nearly 100 times more erythemogenic than 313 nm radiations [105] and more effectively cause DNA damage and photocarcinogenesis [106]. Of the total amount of UV radiations reaching the Earth's surface, about 95% is made of

UVA waves (315–400 nm). The UVAII band (320–340 nm) is more damaging to unsensitised skin than the shorter wave length band UVAI (340–400 nm).

Extrinsic ageing through UV exposure leads to a partial degradation of existing elastic fibres by fibroblast and neutrophil elastase from the inflammatory infiltrate [107]. This is accompanied by higher turnover of tropoelastin and abnormal synthesis of new fibres [108].

The combined effects of the lysis of existing elastic fibres and synthesis of abnormal and non-functional elastic constituents provokes the accumulation of an amorphous and dense elastotic material in the upper and mid-dermis. The process leading to this altered quality of dermal tissue is called actinic damage [104, 109] which, superimposed on the loss of normal elastic fibres, has a drastic effect on the recoil capacity and resiliency of the dermal layer [110]. In photoageing, glycosaminoglycans (GAGs) which are key to skin hydration [111] are abnormally located on the elastotic material in the superficial dermis instead of being more uniformly distributed in the whole dermis. Moreover, hyaluronic acid (HA) and proteoglycans (versican and decorin) undergo structural alterations with age which lead to impairment of their water retention abilities [104]. A simplified schematic representation of the key cellular mechanisms associated with dermal fibroblasts in photoageing is provided in Fig. 4.

4 A Mechanistic Description of Both Intrinsic Ageing and Photoageing

It is clear that both intrinsic and extrinsic ageing are extremely complex coupled biophysical processes which involve a wide range of biochemical species and interacting cellular processes. Their effects are also modulated within the skin microstructural constituents which naturally encompass a great intra- and inter-individual variability. In order to develop a tractable mechanistic model of ageing it is critical to first extract some of their essential (i.e. dominant) features. Generally, using a simplified view, two main theories of skin ageing can be put forward: cellular senescence theory of ageing and free radical theory of ageing.

4.1 Cellular Senescence Theory of Ageing

According to this theory, the ageing process is a result of a combination of decreased cell proliferation ability, decreased matrix synthesis and increased expression of degrading enzymes of the collagenous matrix [112]. It has been shown that keratinocytes, fibroblasts and melanocytes all display an age-associated decrease in proliferative ability and irreversible cell arrest, which is a process termed as *cellular senescence*.

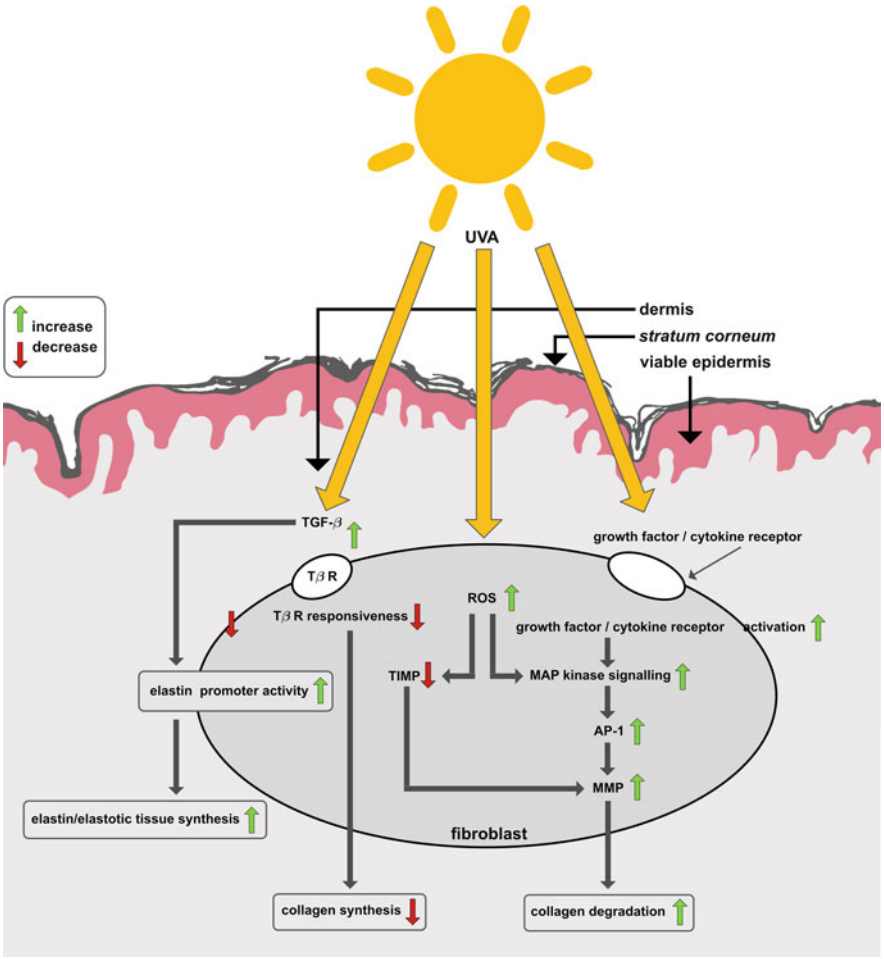

Fig. 4 Simplified schematic representation of the cellular mechanisms associated with dermal fibroblasts in photoageing. A green/red arrow indicates an increase/a decrease [*ROS* Reactive Oxygen Species; *TGF-β* Transforming Growth Factor *β*; *Tβ* R TGF-*β* receptor; *AGE* Advanced Glycation End product; *JNK* Jun-N-terminal-Kinase; *MAP* Mitogen Activated Protein; *MMP* Matrix Metalloproteinase; *TIMP* Tissue Inhibitor of MetalloProteinase; *AP-1* Activator Protein-1; *ERK* Extracellular signal-Related Kinase]

Essentially, cellular senescence is a change in the state of a cell, and not a deterioration of cell capabilities with time. Cells undergo a change that reduces, or completely arrests, cell growth and proliferation. Cell division plays a role in the gradual loss of replicative ability. On each cell division, there is a shortening of cellular telomeres. Telomeres are the end bits of DNA strands that have been shown to play a crucial part in ageing. This gradual change alters the physical expression of a cell's genotype, known as its phenotype [113]. As observed in senescent

fibroblasts, there is a selective repression of genes involved in growth regulation. As a consequence, this change results in the end of the replicative lifespan as the cell is no longer able to enter the first stages of mitosis. In pre-senescent fibroblasts, the level of MMP-1 and MMP-3 have been observed to expressed at very low levels. Additionally, TIMP levels have been shown to be high, further reducing MMP expression. The is reversed in senescent skin, where there is increased MMP and reduced TIMP expression. Coupled to this is the decreased rate of collagen synthesis in older skin, which further compounds the observed disorganisation and reduced presence of dermal collagen.

4.2 Free Radical Theory of Ageing

An alternate, and more popular view of ageing is that due to oxidative stress. Ageing results as an accumulation of oxidative damage due to a build-up of ROS. This ROS production is a result of aerobic metabolism. There has been significant research that supports the role of ROS and cumulative oxidative damage as a major contributor to the ageing process [11, 112, 114]. The main source of ROS in ageing is through mitochrondrial oxidative energy generation. Over the course of ageing, damage accumulation due to ROS results in reduced antioxidant capacity through mitochondrial deterioration which furthers ROS generation. This view of ageing is backed up by the observed higher levels of ROS in aged skin. Over the last few years there have been several conflicting results in studies on the effects of ROS [115]. For example, it was found that increased ROS may prolong the lifespan of yeast cells and that of *Caenorhabditis elegans* (a nematode), genetic manipulations in mice to increase mitochondrial ROS do not accelerate ageing, and mice with induced increased antioxidant defence do not experience an increased lifespan. There has also been research in the field of intracellular signalling that provides evidence that the role of ROS may in fact be as a survival response to physiological signals.

4.3 A Mechanistic Model of Both Intrinsic and Photoageing of the Skin

In order to consolidate the theories of ageing discussed in this section with the damaging properties of ROS established in previous studies, the following hypothesis is proposed and adopted for the development of the chemo-mechanobiological model of skin ageing as described in Sect. 10.

The primary effect of ROS is to trigger homoeostatic responses, such as cellular proliferation, in response to physiological stress. As chronological age advances, cellular damage increases while ROS levels increase as well in an attempt to maintain survival. Beyond a certain threshold, ROS eventually start to aggravate

age-associated damage. Whether the traditional theory of oxidative damage is adhered to or whether this new hypothesis is adopted, the cellular processes are the same. As a person ages, cells undergo a morphological change similar to that described in cellular senescence. Through the accumulation of ROS, the structural and functional capabilities degenerate, which only accelerates with advancing age. In skin, fibroblasts undergo this morphological change from mitotic cells to ones that are no longer able to undergo mitosis. This change is likely, as with senescence, to alter the phenotypical behaviour of the cell, thus negatively affecting type I procollagen production. Additionally, as mentioned, ROS has a direct impact on dermal collagen through the upregulation of AP-1 and MMPs

There is further evidence to support reduced antioxidant activity within the skin. Although results have been conflicting, in general they show that there is a reduction of antioxidant enzymes with age. It has also been demonstrated that aged fibroblasts are far more susceptible to the accumulation of oxidised proteins following oxidative stress, whereas young fibroblasts were able to remove these proteins more effectively [116].

Although the theory of cellular senescence has value, the free radical theory of ageing is thought to be far more relevant in terms of ageing in skin. By adopting this theory, a convenient and logical link is established between intrinsic ageing and photoageing (Fig. 5). Increased ROS production is a common biophysical process

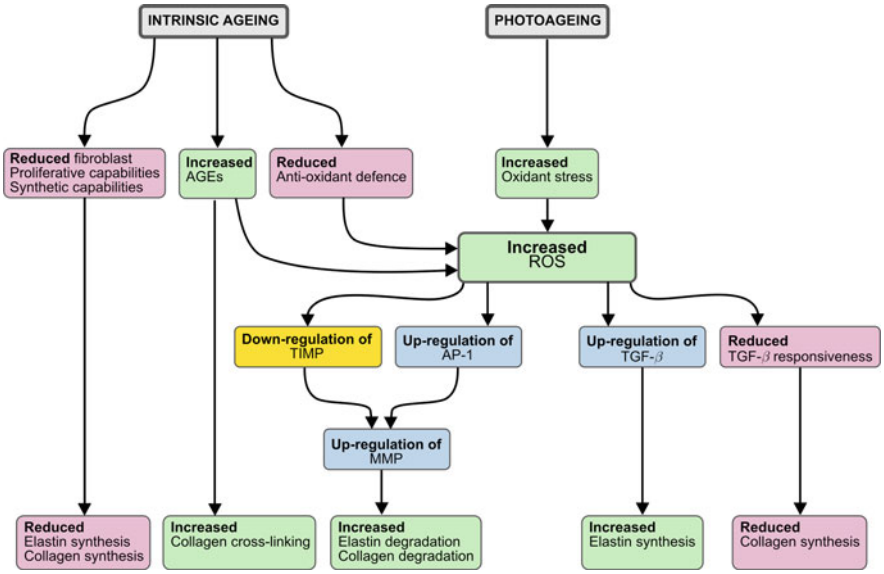

Fig. 5 Schematic and simplified representation of the underlying mechanisms and effects associated with the free radical theory of skin ageing in terms of collagen and elastin [*ROS* Reactive Oxygen Species; *TGF-β* Transforming Growth Factor *β*; T*β* R: *TGF-β* receptor; *AGE* Advanced Glycation End product; *MMP* Matrix Metalloproteinase; *TIMP* Tissue Inhibitor of MetalloProteinase; *AP-1* Activator Protein-1]

to both intrinsic ageing and photoageing. If this process—or its direct/indirect effects—can be modelled, then its influence on synthesis and degradation of two fundamental building blocks of the skin dermis affected by ageing can be approximated, namely collagen and elastin, and one is provided with a basis to formulate mechanistic constitutive equations of skin ageing that would link ageing, skin microstructure and macroscopic mechanical properties of the skin. This will be described in more details in subsequent sections.

5 Modelling of Skin Ageing

As a result of biochemical changes associated with ageing, the mechanical behaviour of the skin is significantly altered through time-dependent variations in the structural and mechanical properties of its elemental constituents (e.g. proteoglycans, collagen, elastin and keratin). The effects of skin ageing become apparent under the form of skin wrinkles—particularly on the face and hands—which are often unconsciously or consciously used as criteria to evaluate somebody's age. These morphological changes of the skin surface are manifestations of complex coupled biophysical phenomena where mechanics is believed to play a critical role like in many other remodelling and morphomechanical processes [117, 118]. Unravelling the inherent complexity of the skin ageing process, firstly by identifying its biophysical drivers, underlying factors and effects, and secondly, by gaining a mechanistic insight into their interplay, is a formidable challenge at both experimental and modelling levels. However, building upon the solid body of work on the constitutive modelling of the skin [119–121], there are opportunities to extend existing models and develop mechanistic constitutive formulations that could, first describe, and ultimately, predict ageing effects. These hypothesis-driven research tools have the potential to enable us to unveil the biophysical complexity of skin physiology as well as mechanobiological aspects associated with diseases and the ageing process. Various phenomenological and structurally-based mechanical models have been proposed and adopted to model the skin at finite deformations. For a good coverage of the relevant literature see the monograph by Xu and Lu [66], review papers by Jor et al. [120], Li [121] and Limbert [119] or book chapters by Flynn [122] and Limbert [30]. Structurally-based models attempt to reflect the contributions and mutual interactions from the primary constituents of the dermal layer, i.e. collagen, elastin and ground substance. Developing this type of models is desirable as it offers the ability to link the microscopic constituent characteristics (i.e. materials and structures) to the macroscopic response of the tissue [see 123–125].

Mazza et al. [126, 127] developed a non-linear constitutive model to simulate ageing of the human face. The elasto-visco-plastic constitutive equations are based on the constitutive formulation of Rubin and Bodner [128] to model the dissipative response of soft tissues. The dissipative material model was implemented in a commercial finite element code to simulate gravimetric descent of facial tissue.

Mazza et al. [126, 127] extended the model of Rubin and Bodner [128] by including an ageing parameter equipped with its own time evolution equation. This ageing-driven parameter was a modulator of tissue stiffness. A four-layer model of facial skin combined with a face-like geometrical base was developed and highlighted the usefulness of such a model to study the effects of skin ageing on facial appearance. Maceri et al. [129] proposed an age-dependent multiscale mechanical model for arterial walls that effectively coupled elastic nanoscale mechanisms linked to molecular and cross-link stretching to micro- and macroscopic structural effects. The model successfully captured the age-dependent evolution of arterial wall mechanics through alterations of its constitutive parameters including geometric characteristics of collagen fibres, cross-link stiffness of collagen fibrils and volume fraction of constituents.

However, to date, with the exception of the recent work of the authors [29], no mechanistic constitutive models for the skin has been developed that is capable of simultaneously capturing intrinsic ageing through evolution of its material and structural constitutive parameters whilst being embedded in the rigorous framework of non-linear continuum mechanics. The goal of the research presented in the paper by Pond et al. [29] was to develop an experimentally-based mathematical and computational model of the skin to study the interplay of its material and structural properties and their evolution as a result of the intrinsic ageing process. Plausible mechanisms associated with ageing-induced material and microstructural evolution were explored in an attempt to explain observed effects associated with ageing (e.g. macroscopic stiffening of the tissue). This approach is presented in subsequent sections while a novel chemo-mechanobiological constitutive model of skin ageing that includes features of both intrinsic and extrinsic ageing is developed in Sect. 10.

6 A Summary of Continuum Mechanics

The macroscopic response of skin to loading is mathematically described here using a continuum formulation. Prior to describing the model, the notation and key results from nonlinear continuum mechanics are summarised. For an extensive overview of continuum mechanics the reader is referred to [130], among others.

Notation

Direct notation is adopted throughout. The scalar product of two vectors $\boldsymbol{a}$ and $\boldsymbol{b}$ is denoted by $\boldsymbol{a} \cdot \boldsymbol{b}$. The scalar product of two second-order tensors $\boldsymbol{A}$ and $\boldsymbol{B}$ is denoted by $\boldsymbol{A} : \boldsymbol{B}$. The composition of two second-order tensors $\boldsymbol{A}$ and $\boldsymbol{B}$ is denoted by $\boldsymbol{AB}$. The action of a second-order tensor $\boldsymbol{A}$ on a vector $\boldsymbol{b}$ is a vector denoted by $\boldsymbol{Ab}$. The unit basis vectors in the Cartesian (standard-orthonormal) basis are $\{\boldsymbol{e}_1, \boldsymbol{e}_2, \boldsymbol{e}_3\}$.

The dyad of two vectors $\boldsymbol{a}$ and $\boldsymbol{b}$ is a second-order tensor and is denoted by $\boldsymbol{a} \otimes \boldsymbol{b}$. Additional notation will be defined when introduced.

6.1 Finite Strain Kinematics

Consider a continuum body representing a portion of the skin. The reference configuration is defined as the placement of this body at time $t = 0$, with that region denoted by Ω_0 with boundary $\partial\Omega_0$ and outward unit normal $\boldsymbol{N}$. As the body deforms, this region takes on subsequent configurations. At a current time t, the body occupies the region Ω, referred to as the current configuration with boundary $\partial\Omega$ and outward unit normal $\boldsymbol{n}$. A motion $\boldsymbol{\chi}$ is assumed such that each material point $\boldsymbol{X} \in \Omega_0$ uniquely maps to a spatial point $\boldsymbol{x} \in \Omega$ at time t, i.e.

$$\boldsymbol{x} = \boldsymbol{\chi}(\boldsymbol{X}, t) \qquad \forall \boldsymbol{X} \in \Omega_0 \,.$$

The deformation of the body is characterised by the deformation gradient $\boldsymbol{F}$, defined by

$$\boldsymbol{F}(\boldsymbol{X}, t) := \frac{\partial \boldsymbol{\chi}(\boldsymbol{X}, t)}{\partial \boldsymbol{X}} = \mathrm{Grad}\boldsymbol{\chi}(\boldsymbol{X}, t) \,.$$

The determinant of $\boldsymbol{F}$ is defined by $J := \det \boldsymbol{F} > 0$. The right Cauchy–Green tensor $\boldsymbol{C}$, defined by

$$\boldsymbol{C} := \boldsymbol{F}^T \boldsymbol{F} \,,$$

provides a stretch measure in the reference configuration. Additionally, the principal scalar invariants of $\boldsymbol{C}$ are defined by

$$I_1(\boldsymbol{C}) := \mathrm{tr}(\boldsymbol{C}) = \boldsymbol{I} : \boldsymbol{C} \,, \quad I_2(\boldsymbol{C}) := \frac{1}{2}\left[\mathrm{tr}(\boldsymbol{C})^2 - \mathrm{tr}(\boldsymbol{C}^2)\right] \,, \quad I_3(\boldsymbol{C}) := \det(\boldsymbol{C}) \,. \tag{2}$$

Consider now the case of transverse isotropy where the material properties depend on a single given direction—a defining feature of skin. The preferred material direction at a point $\boldsymbol{X}$ is given by $\boldsymbol{v}_0$. The fabric tensor is then defined by

$$\boldsymbol{A}_0 := \boldsymbol{v}_0 \otimes \boldsymbol{v}_0 \,,$$

and an additional invariant characteristic of transverse isotropic symmetry is given by

$$I_4(\boldsymbol{C}, \boldsymbol{v}_0) = \boldsymbol{v}_0 \cdot \boldsymbol{C}\boldsymbol{v}_0 = \lambda^2, \tag{3}$$

where λ is the principal stretch along vector $\boldsymbol{v}_0$ defined in the reference configuration.

6.2 Constitutive Relations for Invariant-Based Transversely Isotropic Hyperelasticity

A hyperelastic material is one for which a free energy ψ acts as a potential for the stress. For homogeneous materials, the free energy is a function of the deformation gradient $\boldsymbol{F}$ and any additional tensor agency (e.g. the fabric tensor). As a general procedure to formulate constitutive equations for hyperelastic materials, one can postulate the existence of a free energy ψ that is an isotropic function of the deformation. Hence, the first and second Piola–Kirchhoff stress tensors, $\boldsymbol{P}$ and $\boldsymbol{S}$, are defined by

$$\boldsymbol{P} := \frac{\partial \psi(\boldsymbol{F}, \boldsymbol{A}_0)}{\partial \boldsymbol{F}} \qquad \text{and} \qquad \boldsymbol{S} := 2\frac{\partial \psi(\boldsymbol{C}, \boldsymbol{A}_0)}{\partial \boldsymbol{C}},$$

where $\boldsymbol{P} = \boldsymbol{F}\boldsymbol{S}$. The dependence of the free energy on $\boldsymbol{C}$ can be be expressed in terms of the n_{inv} invariants of $\boldsymbol{C}$. The second Piola–Kirchhoff stress is thus given by

$$\boldsymbol{S} = 2\sum_{i=1}^{n_{\text{inv}}} \frac{\partial \psi(\boldsymbol{C})}{\partial I_i}\frac{\partial I_i}{\partial \boldsymbol{C}}. \tag{4}$$

6.3 Governing Relations

The balance of linear momentum, in the absence of inertial and body forces, and the natural boundary condition are given by

$$\text{Div}\,\boldsymbol{P} = \boldsymbol{0} \qquad \text{in } \Omega_0, \tag{5}$$

$$\boldsymbol{T} = \boldsymbol{P}\boldsymbol{N} = \overline{\boldsymbol{T}} \qquad \text{on } \partial\Omega_{0,\text{N}}, \tag{6}$$

where Div is the material divergence operator. The Piola traction $\boldsymbol{T}$ is prescribed on the Neumann part of the boundary $\partial\Omega_{0,\text{N}} \subset \partial\Omega_0$. Dirichlet boundary conditions on the motion $\boldsymbol{\chi} = \overline{\boldsymbol{\chi}}$ are prescribed on $\partial\Omega_{0,\text{D}}$ where $\partial\Omega_0 = \partial\Omega_{0,\text{D}} \cup \partial\Omega_{0,\text{N}}$ and $\partial\Omega_{0,\text{D}} \cap \partial\Omega_{0,\text{N}} = \emptyset$.

6.4 Weak Form of the Governing Relations

The weak form of the governing equations and the accompanying Neumann boundary conditions in Eqs. (5) and (6) is essential for establishing the approximate solution using the finite element method (FEM). Multiplying the strong form of the equilibrium equation (5) by an vector-valued test function $\delta\boldsymbol{u}$, where $\delta\boldsymbol{u} = \boldsymbol{0}$ on $\partial\Omega_{0,\mathrm{D}}$, and applying the divergence theorem yields the expression for the weak form of the equilibrium equation as

$$\int_{\Omega_0} \mathrm{Grad}\delta\boldsymbol{u} : \boldsymbol{P}\,\mathrm{d}V - \int_{\partial\Omega_{0,\mathrm{N}}} \delta\boldsymbol{u}\cdot\overline{\boldsymbol{T}}\,\mathrm{d}A = 0\,.$$

The weak form is the point of departure for the approximate solution of the equilibrium equation using the finite element method.

7 A Microstructurally-Based Constitutive Model of Skin

Based on the experimental data summarised in this chapter, it is assumed that elastin and ground substance are the main contributors to the low modulus portion of the stress-strain curve which is largely linear and isotropic. The second region of the loading curve is dominated by the mechanical response of collagen fibres. As the collagen fibres straighten and take on load, they exponentially resist further stretch which results in a rapid nonlinear strain stiffening behaviour. This behaviour is also strongly anisotropic due the inherent preferred alignment of collagen fibres along the direction of extension. As the stiffening response of the skin is dominated by the response of the collagen network, the formulation of an effective microstructurally-motivated constitutive model is essential. Hence, it is postulated that the free energy Ψ describing the overall mechanical behaviour of the dermis, assumed to be that of the skin because of the negligible contributions of the epidermis, is given by

$$\Psi = \Psi_{\mathrm{gs}} + \Psi_{\mathrm{elastin}} + \Psi_{\mathrm{collagen}}, \tag{7}$$

where Ψ_{gs}, Ψ_{elastin} and Ψ_{collagen} represent the free energy contributions from the ground substance, elastin and collagen, respectively.

To capture the behaviour of skin at low stretches, the elastin and ground substance free energies are given by the following compressible neo-Hookean type free energy:

$$\Psi_{\mathrm{gs}} + \Psi_{\mathrm{elastin}} = \left[\alpha_{\mathrm{gs}} + \alpha_{\mathrm{elastin}}\right]\left[I_1 - 3 + \frac{1}{\beta}\left[I_3^{-\beta} - 1\right]\right], \tag{8}$$

where

$$\alpha_{(\bullet)} = \frac{\mu_{(\bullet)}}{2}, \qquad \text{and} \qquad \beta = \frac{\nu}{1-2\nu}$$

are constitutive parameters, respectively associated with the shear and volumetric response, and $(\bullet)$ is either "gs" or "elastin". The shear modulus is denoted by μ, and ν is the Poisson's ratio of the composite material represented by the ground substance and elastin phases.

The nonlinear, anisotropic and network nature of the collagen response is captured through a transversely isotropic network eight-chain model proposed by Kuhl et al. [123]. This model is based on theories related to the micromechanics of macromolecule mechanical networks [131, 132] and is a particularisation of the orthotropic eight-chain model developed by Bischoff et al. [133]. In these mechanical descriptions of macromolecular networks, long molecular chains are assumed to rearrange their conformation under the influence of random thermal fluctuations (i.e. entropic forces). These type of idealised molecular chains are best described using the concept of wormlike chains by Kratky and Porod [134]. Wormlike chain models have been used to describe the structure and mechanical behaviour of collagen assemblies in the context of skin modelling [see e.g. 125, 133, 135–138] and other fibrous biological soft tissues [see e.g. 123, 124, 139, 140]. It is important to note that, in the development of microstructurally-based constitutive theories, these macromolecular chains could also be defined by or interpreted as either tropocollagen molecules, collagen micro-fibrils, fibrils, fibres or fibre bundles. If considering supra-molecular scales, it is clear that the wormlike chain energy is no longer associated with the notion of entropic elasticity and true molecular behaviour, but is rather a microstructurally-motivated macroscopic phenomenological energy that captures the strain-stiffening behaviour of collagenous structures. In the present approach, it is assumed that correlated chains represent collagen fibres (see Fig. 7).

The mechanics of macromolecular polymer structures is not only governed by the mechanical properties of individual chains but also by their electromagnetic and mechanical interactions which can take the form of covalent bonds, entanglement and physical cross-links. These combined effects give rise to strong isotropic and anisotropic network properties which can be implicitly and effectively captured by network models such as the eight-chain model of Arruda and Boyce [131] or Kuhl et al. [123]. The essential assumption underpinning these formulations is that there exists a representative microscopic unit cell able to capture network properties. The original eight-chain model of Arruda and Boyce [131] assumes that the unit cell is made of eight entropic chains of equal lengths connected from the centre of the cell to each of its corners (see Fig. 6), each equipped with their own entropic energy Ψ_{wormlike}. For correlated chains, the wormlike chain energy can be defined by

$$\Psi_{\text{wormlike}} = \Psi_0 + \frac{k\theta L}{4A}\left[2\frac{r^2}{L^2} + \frac{1}{[1-\frac{r}{L}]} - \frac{r}{L}\right], \tag{9}$$

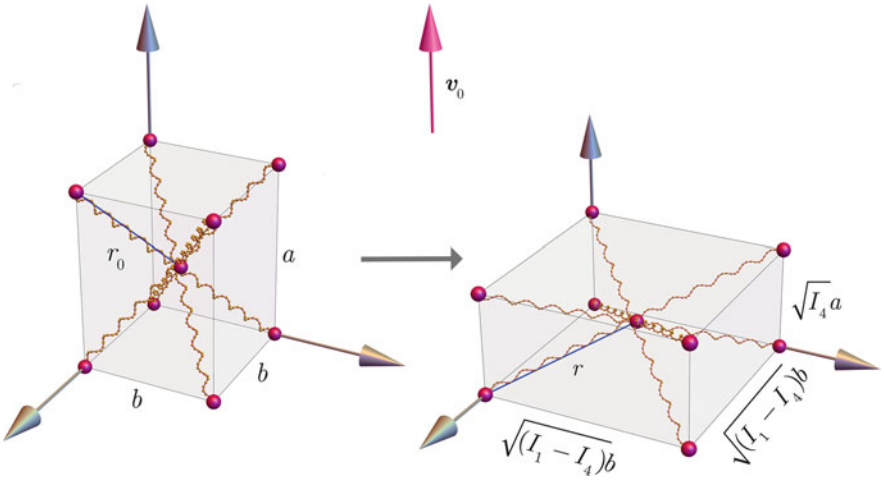

Fig. 6 Schematic representation of the transversely isotropic eight chain network model of Kuhl et al. [141]. The eight polymer chains are governed by a wormlike energy function ψ_{wormlike} (see Eq. (9)). The unit cell dimensions are a and b while unit vector $\boldsymbol{v}_0$, aligned with one of the principal directions of the unit cell, is the unit vector corresponding to the preferred orientation of the collagen network in the undeformed configuration [reproduced from 29]

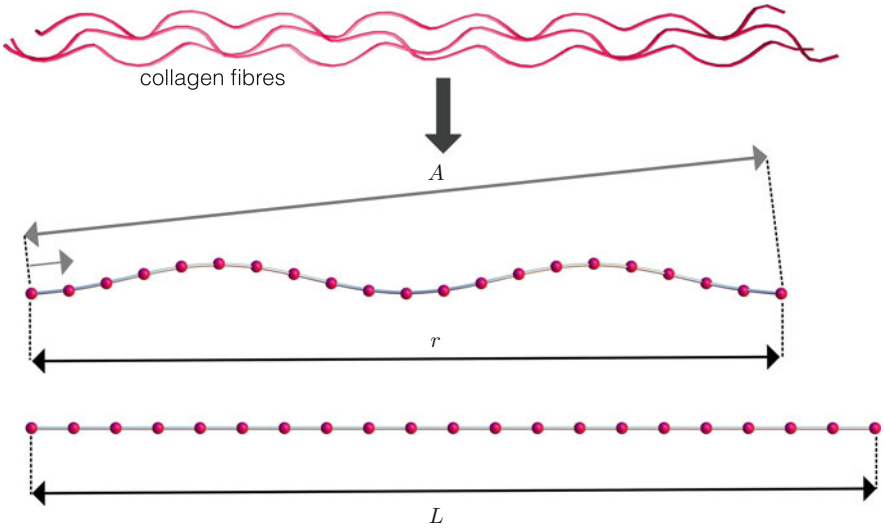

Fig. 7 Wormlike chain assembly. The successive chain link is correlated to the chain before it. A is the persistence length, r is the effective end-to-end length and L is the chain contour length [reproduced from 29]

where L, A, r_0 and r and are respectively the contour, persistence, initial end-to-end length and the current end-to-end length of the chain (see Fig. 7), and Ψ_0 is the wormlike chain energy in the unperturbed state. The wormlike chain has the defining

characteristic that the chain segments are correlated and exhibit a smoothly-varying curvature along the contour. This correlated form is captured by the persistence length A. The persistence length can be viewed as a measure of stiffness. Garikipati et al. [125] refer to it as a measurement of the degree to which a chain departs from a straight line, while Marko and Siggia [142] interpret it as the characteristic length over which a bend can be made with energy cost $k\theta$, where $k = 1.380{,}648{,}52\,\mathrm{J\,K^{-1}}$ is the Boltzmann constant and θ the absolute temperature.

In order to incorporate such chain models into an invariant-based constitutive framework it is necessary to relate the individual chain stretch to the macroscopic deformation. To this end, the principle of affinity is invoked so that the macroscopic and unit cell principal directions are identical. Due to the symmetry of the chain structure, the stretch of each chain can be found as a function of the principle stretches. In Fig. 6, a unit cell arrangement of dimensions $a \times b \times b$ is depicted. For the case of anisotropy $a \neq b$. Additionally, the unit cell is characterised by the unit vector $\boldsymbol{v}_0$ that corresponds to the (local) preferred orientation of the collagen network. The undeformed end-to-end length of each of the individual chains is given by

$$r_0 = \frac{1}{2}\sqrt{a^2 + 2b^2}\,.$$

The deformed end-to-end length r can be expressed using the invariants defined in Eqs. (2) and (3) by

$$r = \frac{1}{2}\sqrt{I_4 a^2 + [I_1 - I_4]b^2}\,.$$

The invariants I_1, I_3 and I_4 are measures of the macroscopic deformation of the polymer. It is assumed that the microscopic stretch along the direction $\boldsymbol{v}_0$ is captured by the macroscopic term I_4. This effectively couples the microscopic and macroscopic length scales. The relative stretch of a collagen fibre is defined by $\lambda_\mathrm{r} := r/r_0$, see Eq. (9).

The final term of Eq. (7), characterising the contribution of collagen to the free energy, is further decomposed as

$$\Psi_\mathrm{collagen} = \Psi_\mathrm{chain} + \Psi_\mathrm{repulsive}\,, \tag{10}$$

where Ψ_chain reflects the effective assembly of the eight chain energies, i.e. $\Psi_\mathrm{chain} := \gamma_\mathrm{chain}\Psi_\mathrm{wormlike}$ and $\Psi_\mathrm{repulsive}$ is a repulsive energy that ensures the initial configuration is stress free and that the chain does not collapse. γ_chain denotes the chain density per unit cell. Sáez et al. [140] interprets γ_chain as the number of molecules within a collagen fibril, while Bischoff et al. [133] describes it as the collagen fibre density. In the context of collagen this measure corresponds to the

Table 1 Constitutive parameters of Ψ_{collagen}

Parameter	Symbol	Units
Poisson's ratio	ν	–
Shear modulus	μ	N m^{-2}
Boltzmann constant	k	J K^{-1}
Absolute temperature	θ	K
Chain density	γ_{chain}	m^3
Contour length	L	–
Persistence length	A	–
Unit cell dimensions	a, b	–

number of fibres within a bundle. It follows that

$$\Psi_{\text{chain}} = \frac{\gamma_{\text{chain}} k L \theta}{4A}\left[2\frac{r^2}{L^2} + \frac{1}{1-\frac{r}{L}} - \frac{r}{L}\right],$$

$$\Psi_{\text{repulsion}} = -\frac{\gamma_{\text{chain}} k\theta}{4A}\left[\frac{1}{L} + \frac{1}{4r_0}\frac{1}{1-\frac{r_0}{L}} - \frac{1}{4r_0}\right]\left[\ln\left[I_4^{[a^2-b^2]/2}\right] + \frac{3}{2}\ln\left[I_1^{b^2}\right]\right].$$

All stretch quantities have been normalised by the link length L which is the length of a single link along the wormlike chain assembly.

A description of the constitutive parameters of Ψ_{collagen} is summarised in Table 1. The expression for the first Piola–Kirchhoff stress $\boldsymbol{P}$ then follows directly from Eq. (4).

8 Microstructurally-Based Mechanistic Model Indirectly Accounting for Intrinsic Ageing

A central hypothesis underpinning this study is that the effects of ageing (both intrinsic and extrinsic) on the mechanical properties of the tissue are directly linked to alterations in the microstructural characteristics of the collagen and elastin networks. In this section, some of the constitutive parameters introduced in Sect. 7 are motivated as plausible mechanistic descriptions of the intrinsic ageing process as evidenced by experimental observations (see Table 2). It is worth emphasising that, in reality, the material and structural effects of ageing are likely to be coupled and would therefore lead to a dependency between constitutive parameters. For the sake of simplicity, and in the absence of relevant experimental data, this interplay is not accounted for. In addition, the effect of intrinsic ageing on the ground substance manifests itself as a more pronounced viscoelastic response with age. As the constitutive model for the ground substance currently only captures the elastic response it is assumed that ageing does not affect the ground substance related parameters in Eq. (8).

Table 2 Description of the constitutive parameters, the evolution of which is associated with ageing

Constituent	Ageing effect	Parameter
Ground substance	Increased water content results in more pronounced viscoelasticity	n/a
Elastin	Loss of elasticity	α_{elastin}
	Destruction of elastin network	α_{elastin}
Collagen	Loss of mature collagen	γ_{chain}
	Increased crosslinking	γ_{chain}
	Flattening and unravelling of collagen network	a, b
	Alterations in anisotropy	a, b

The elastin network is observed to degrade with age. The loss of elastic integrity would logically lead to a reduced contribution from the elastin component to the composite strain energy function (7). One approach could be to introduce a volume fraction for elastin, ground substance and collagen. Degradation of the elastin network would then be modelled as a reduction in volume fraction of elastin. Instead, here, the value of α_{elastin} is assumed to decrease with age. It should be noted again that elastin is a highly-stable protein which undergoes little turnover before the age of 40. Thus α_{elastin} would remain constant for the first four decades.

Within the current model, there is no natural parameter that explicitly describes the level of collagen crosslinking at any point in time. It is believed that the increased crosslinking with age is one factor responsible for the increased stiffness of the skin. Through increasing γ_{chain}, it is expected that a stiffer response will be elicited. Although γ_{chain} describes the number of fibres within a bundle, it represents the closest link to the observed increase in crosslinking with age. It would be expected that a decrease in collagen density would contribute to a decrease in the overall stiffness of the skin as the collagen network loses integrity. Thus it is reasonable to assume that a decrease in γ_{chain} with age could describe a loss of collagen.

As discussed previously, the slope of the linear region of the stress-strain curve for skin, as a composite structure, remains constant with age but the onset of strain hardening occurs at lower strains. This suggests that there might be a mechanism that simply alters the structural characteristics of the collagen network and not the mechanical properties of collagen microfibrils. In their unloaded states collagen fibres are crimped. It is believed that this conformational state is due to the presence of highly cross-linked elastic fibres—mainly elastin fibres [143]—and is also the result of active tensions exerted by fibroblasts. Any reduction in fibroblast density in the collagen dermal network would have an effect on these active forces and on the rest state of collagen fibres. Such a reduction would tend to relax the residual strain/tension in the dermis. This would make collagen fibres less crimped and therefore their apparent length would be closer to their fully-taut length. Thus, when the skin is macroscopically loaded in tension, the dermal tissue will not exhibit a very pronounced toe region—corresponding to the progressive uncrimping of collagen fibres—but will rather reach the stiffer linear region more quickly. The

corollary of this observation is that for a given applied macroscopic strain, the response of the intrinsically-aged dermal collagen network will be stiffer. With age, due to dermal flattening and the loss of elastic recoil, the collagen fibres are observed to uncrimp [16]. In the chain network structure of the model, this is captured by adjustments to the end-to-end length of the collagen fibres through the parameters a and b. By increasing a and b there will be a reduction in the range of strain of the low modulus portion prior to the onset of the collagen response at lower stretches. Thus by increasing a and b the model should be capable of capturing the stiffening response. Additionally, the anisotropic response of the skin is observed to change with age. Tonge et al. [144] reports a loss of anisotropy in experiments using a bulge test. As the model developed here will be compared to the bulge test results at various ages, it is this behaviour that is intended to be captured. By reducing the ratio of a/b , either by increasing b or decreasing a or a combination of both, this should be achieved.

Undeniably, there is a reduction in the thickness of the skin with age (see Eq. (1)). Such an observation is backed by numerous sources in the literature [39, 55, 57], but there is still much debate over the exact relationship between age and skin thinning. The changes in the dermal thickness with age will be captured directly in the geometry of the computational model.

9 A Microstructurally-Based Model of Skin Intrinsic Ageing with Age-Dependent Constitutive Parameters

The objective is to now identify how the subset of constitutive parameters assumed to be associated with intrinsic ageing, identified in the previous section, can be determined at specific times in the ageing cycle using a combined experimental and computational approach.

9.1 Parameter Identification

Multiple mechanical skin tests have been proposed to characterise the skin response to loading. The variety of skin tests and different methods to perform them, as well as the natural skin variation that exists through factors such as ethnicity, gender, age and anatomical site, have resulted in a broad and varying characterisation of skin behaviour. In general, in vivo, in both physiological and supra-physiological conditions, the skin exhibits material nonlinearity, anisotropy, viscoelasticity and near incompressibility and can also sustain large deformations [119]. However, elicitation and relevance of these characteristics is highly variable. Although there are many experimental techniques to characterise certain aspects of skin mechanics [120], bulge tests are considered here. Performed in vitro, the bulge test applies a positive pressure to the underside of an excised skin sample. The skin sample is

fixed at a specified diameter aperture which allows for "bulge-like" deformation of the sample under pressure. Deformations are measured and linked to the state of stress so that constitutive parameters can be identified [41, 144]. The choice of the bulge experiment as a test-bed for the constitutive and computational and models developed here is motivated by the following factors:

- As the experiments are performed in vitro, the boundary conditions of the numerical model are simpler to define and impose.
- The large deformations induced in the physical tests ensure that the various components of the constitutive model are activated. At small deformations the elastin and ground substance will assume the dominant role, and ultimately, as macroscopic strains increase, the collagen fibres will become active and dictate the majority of the response at large deformations.
- The specimens were taken from the back of the patients, thus minimising any photoageing effects such as those observed on sun-exposed regions (e.g. the face).
- The experimental results published by Tonge et al. [41, 144] provide a broad range of kinematic measurements with which to compare the models.
- Crucially, the experiments by Tonge et al. [41, 144] were conducted on skin samples harvested from donors featuring a broad range of ages. This allows the correlation between age and mechanical properties (i.e. constitutive parameters) to be studied.

In the bulge test follows performed by Tonge et al., several 10×10 cm skin specimens were procured from the back torso of donors, ages ranging from 43 to 83 years. After excision, the adipose tissue was removed and tissue thickness measured. The thickness, gender, age and anatomical site of the samples are listed in Table 3. Thickness was measured at the middle of each edge of the sample and the average taken. This average was used as the uniform thickness of the sample in the numerical model.

The specimens were glued to a 7.5 cm diameter ring. The ring serves to constrain the skin specimen. The skin interior to the ring is subject to pressure loading while that exterior is fully constrained. The coordinate system for the samples was set such that the y-axis corresponded to the vertical body axis and the x-axis to the horizontal body axis, as shown in Fig. 8. Fibre and perpendicular directions can thus be defined by the angle Φ from the horizontal axis. Controlling for relative humidity

Table 3 Donor and specimen information from Tonge et al. [41]

Age	Gender	Site	Thickness [mm]
43	Male	Lower back	4.86
44	Male	Lower back	4.38
59	Female	Unknown	5.18
61	Male	Left upper back	2.01
62	Female	Unknown	2.95
83	Male	Unknown	2.43

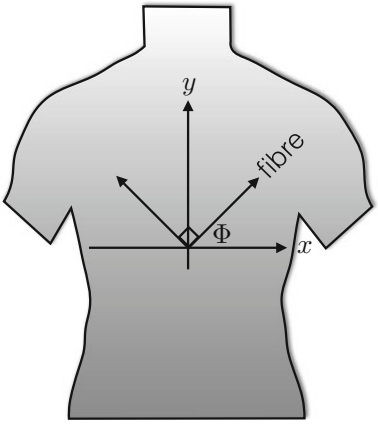

Fig. 8 Body axes: the y-axis corresponds to the vertical body axis and the x-axis to the horizontal body axis. Recreated from [144]

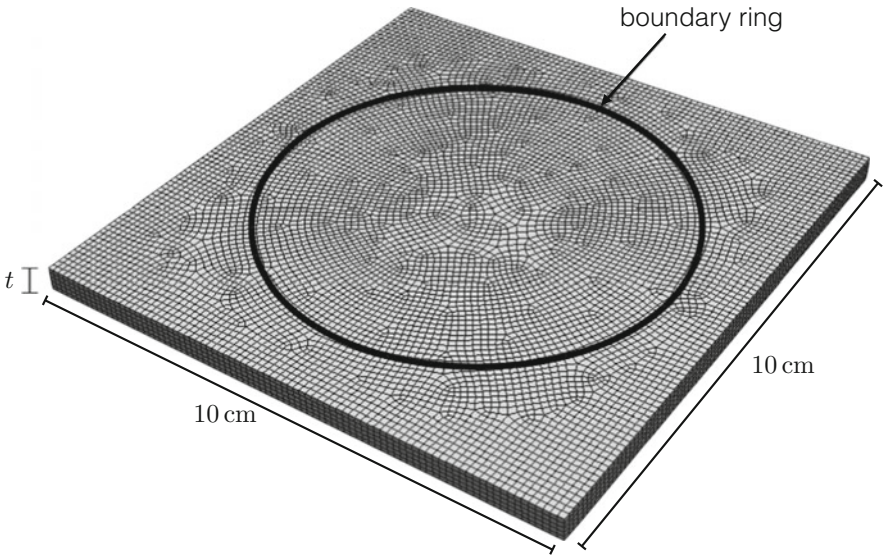

Fig. 9 Finite element mesh used for the bulge tests [adapted from 29]

and temperature, samples were inflated through a controlled applied pressure, with a maximum pressure of 5.516 kPa. Upon inflation the skin samples deformed to an elliptical dome. The dimensions of the ellipse are used to determine the dominant fibre direction with Φ defined accordingly.

A finite element updating technique [see e.g. 120, 145, 146] is used to identify the constitutive parameters of the transversely isotropic eight-chain model of the skin for various ages. Figure 9 shows the discretisation of the skin sample. The skin

thickness is set to the dermal thicknesses as specified in Table 3. The geometry is discretised using 8-noded hexahedral trilinear elements, with five elements through the thickness. Through a mesh sensitivity study, it was found that 46,416 nodes ensured a sufficiently converged solution. The nodes on the upper surface outside the boundary ring and the outer edges are fully constrained. The pressure loading condition is applied to the bottom surface. As proposed in the previous section, only the original network dimensions a and b, γ_{chain} and α_{elastin} are assumed to be variable. The rest of the parameters are assumed age invariant and are given by $L = 2.125$, $A = 1.82$, $\gamma_{\text{gs}} = 100\,\text{Pa}$, $\beta = 4.5$, $\theta = 310\,\text{K}$. Furthermore, only the tests for male specimens are simulated in order to exclude the influence of variations between genders.

In Fig. 10 the profile of the skin obtained from the finite element simulation of the bulge test on the 44 year-old male specimen is given at monotonically-increasing pressure loading from 34.37 Pa to 5.52 kPa. The profiles are given along and perpendicular to the fibre direction $\boldsymbol{v}_0$ as illustrated by the arrows in each subfigure. The bulge specimen undergoes a rapid initial displacement while the stress state is still within the low modulus portion of the stress-strain curve. This can be seen in the plot of the pressure versus the in-plane stretch where a small increment in pressure induces a large change in stretch (Fig. 11). During this phase, the elastin and ground substance contributions dominate the mechanical response and offer little resistance to inflation. The divergence of the pressure-stretch lines indicates the activation of the anisotropic collagen network. In terms of the material

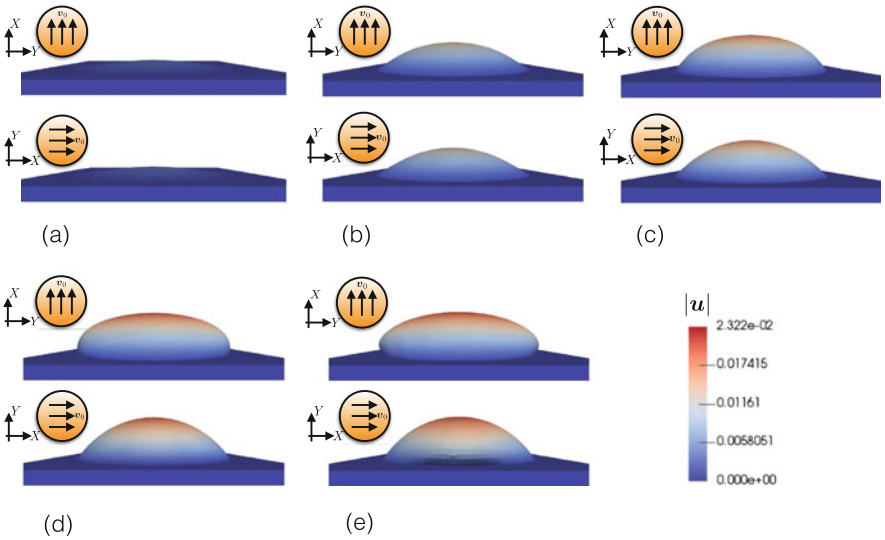

Fig. 10 Displacement profiles for the 44 years-old male skin specimen: (**a**) pressure = 34.37 Pa; (**b**) pressure = 206.4 Pa; (**c**) pressure = 502.1 Pa; (**d**) pressure = 1840 Pa; (**e**) pressure = 5520 Pa [reproduced from 29]

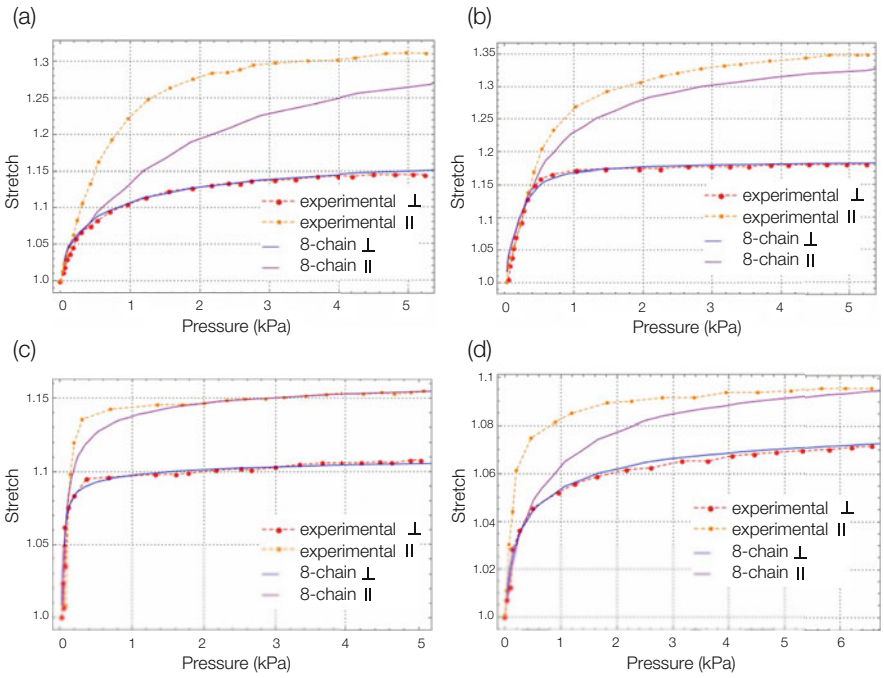

Fig. 11 Plots of in-plane stretch as a function of inflation pressure for the experimental measurements of Tonge et al. [144] overlaid over the theoretical curves obtained from the identification of constitutive parameters [reproduced from 29]. (**a**) Age 43. (**b**) Age 44. (**c**) Age 61. (**d**) Age 83

model, the collagen energy contribution is no longer negligible as the end-to-end chain length r undergoes significant stretch and approaches the contour length L. For the age 44 specimen, further stretch parallel to the fibre direction above 400 Pa does not occurs whereas perpendicular stretch continues to increase with pressure. This results in the response shown in Fig. 10c where at 502 Pa the profiles along the perpendicular and parallel directions differ. Mechanical anisotropy is amplified with increased pressure as the perpendicular stretch increases. As the specimen is deformed, exponentially more pressure is needed to attain further deformation which is characterised by the locking-type limits. In Fig. 10d and e displacement at high pressure occurs laterally in the perpendicular fibre direction.

The 8-chain model is now used to simulate the stretch behaviour of the skin at increasing pressure for increasing age, and the results summarised in Fig. 11. The stretch is measured parallel and perpendicular to the dominant fibre direction. In general, the stretch behaviour with increasing age is reasonably captured. The fit at age 43 is notably poor which suggests that there is an additional directional dependence not captured by the model or a missing constituent contribution (i.e. an incomplete constitutive model), or experimental error.

Table 4 Wormlike 8-chain model parameter values for the age 43, 44, 61 and 83 bulge test

Parameter	Age 43	Age 44	Age 61	Age 83
a	3.58	3.45	3.55	3.65
b	0.5	0.8	1.25	1.287
$\gamma_{\text{chain}}(\times 10^{22})$	$6\ \text{m}^{-3}$	$0.856\ \text{m}^{-3}$	$0.0856\ \text{m}^{-3}$	$0.856\ \text{m}^{-3}$
α_{elastin}	$1000\ \text{N m}^{-2}$	$1300\ \text{N m}^{-2}$	$1000\ \text{N m}^{-2}$	$500\ \text{N m}^{-2}$

Excluding the response of the age 43 test, the identified parameters shown in Table 4 are in agreement with the hypotheses advocated in Sect. 8. Note, γ_{chain} does not vary monotonically with age, with the same values obtained for age 44 and 83. This suggests that γ_{chain} is not age dependent. The difference in the initial end-to-end lengths as dictated by the increased values of a and b allows for the difference in maximum stretches observed in the experiments. Additionally the ratio between the two changes with age with $a{:}b =$ 4.313:1, 2.84:1, 2.836:1 at age 44, 61 and 83 respectively. This reduction, especially between age 44 and 61, is indicative of the expected reduction in anisotropy. The value of α_{elastin} decreases almost linearly with age, with an approximate reduction of $100\ \text{N m}^{-2}$ every 5 years.

9.2 Evolution of the Parameters in the Microstructurally-Based Mechanistic Model with Intrinsic Ageing

The factors discussed in the previous sections provide a means by which the skin constitutive model (and its associated finite element model replicating bulge tests) can capture ageing effects in a continuous sense through the modification of a few selected parameters. Using the a and b parameter values as found from the age 44, 61 and 83 fits, general ageing trends were established. It is clear that a mere three data points is insufficient in order to conclusively determine an ageing trend, but they are adequate for the current proof of concept. Shape-preserving fitting algorithms were used to find a continuous evolution of a and b as shown in Fig. 12a and b. As expected, there is a general increase in both parameters with age: a evolves almost linearly with age whereas b undergoes a large increase between age 44 and 61 followed by a plateau. This suggests that between age 44 and 61 there is a more significant loss of anisotropy due to a realignment or redistribution of the collagen fibres as a network as compared to later in life.

The skin thickness data as presented in Table 3 was used to determine a linear equation for the skin thickness as a function of age. From Fig. 12c it can observed that a very rough linear fit can been established as

$$t = -0.0047[\text{mm/year}] \times \text{age}\,[\text{years}] + 0.59\,[\text{mm}]\,. \tag{11}$$

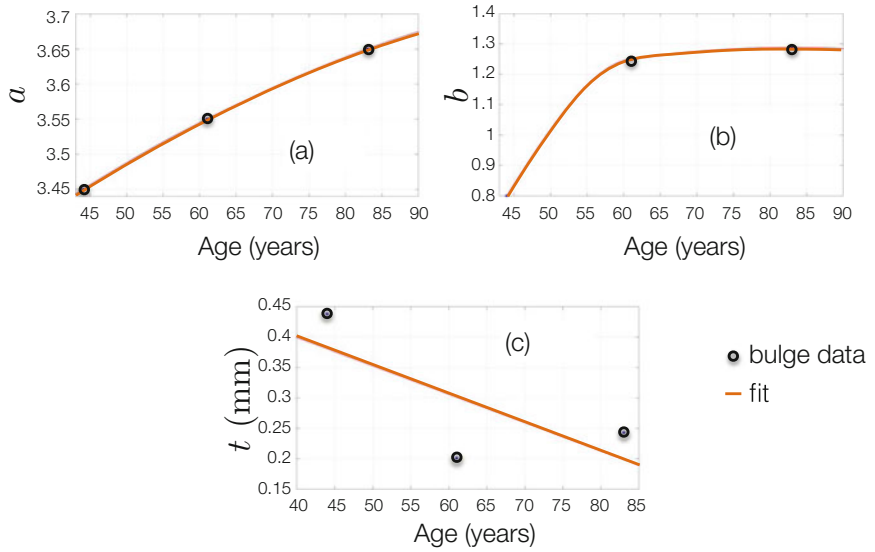

Fig. 12 Network dimension and skin thickness trends with age as found through bulge test fits [reproduced from 29]

Table 5 Modification of age dependent model parameters with intrinsic ageing

Age	a	b	α_{elastin}
49	3.483	0.984	1200
54	3.513	1.14	1100
59	3.54	1.236	1000
64	3.564	1.26	900
69	3.587	1.273	800
74	3.613	1.282	700
79	3.634	1.287	600
84	3.654	1.288	500
89	3.671	1.285	400

This should be compared with Eq. (1). The overall decrease in skin thickness is consistent with experimental values found in the literature.

With the established trends, bulge test simulations were run at 5 year increments. Table 5 contains the adjustments to the parameters of interest. As mentioned, α_{elastin} decreases from 1300 N/m^2 at age 44 by 100 N/m^2 every 5 years.

In Fig. 13 the simulated evolution of the stretch behaviour with age is given, and compared to the experimental data at ages 44, 61 and 83. As expected, the general ageing-induced trend is captured as the skin stiffens with age. The maximum stretch obtained drops significantly between ages 44 and 59, with less significant drops thereafter. This is to be expected primarily due to the trend in parameter b as given in Fig. 13b, where there is an initial sharp increase followed by a plateau. The convergence of the stretch values between ages 59 and 89 is due to the initial

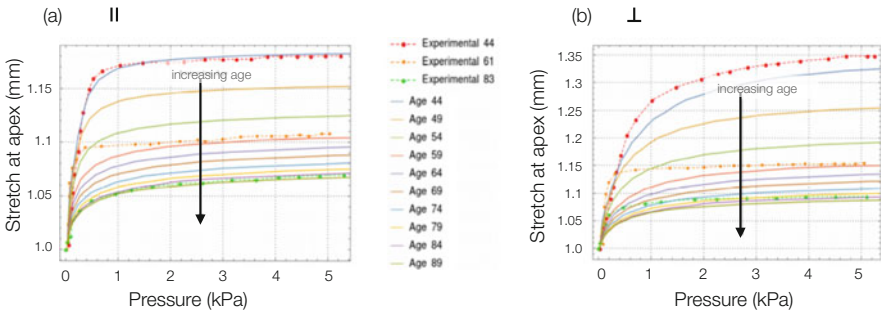

Fig. 13 Stretch at the apex of the pressurised skin as a function of applied pressure for 9 age values (see Table 5); (**a**) parallel to the fibre direction; (**b**) normal to the fibre direction [reproduced from 29]

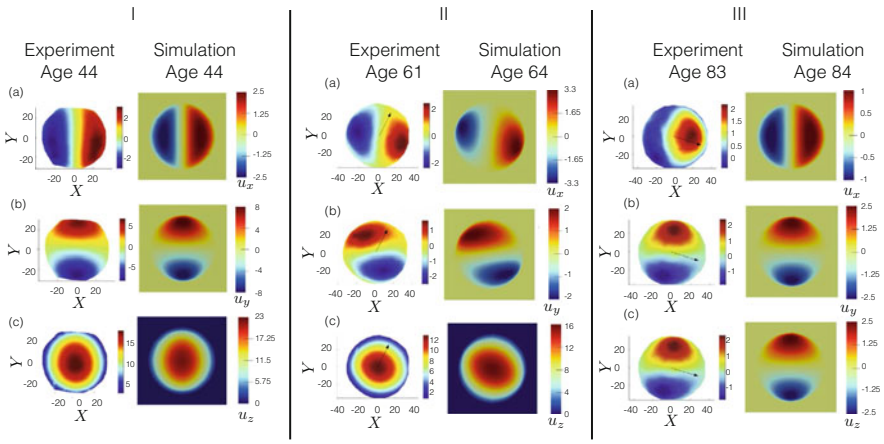

Fig. 14 Plots of deformed profile for the bulge test coloured by the various components of the displacement [mm]. The simulations are compared to the experimental results of Tonge et al. [144] for various different ages (I–III) [reproduced from 29]

end-to-end length r_0 approaching the contour length L. As r_0 increases with age, the amount of allowable macroscopic stretch is reduced.

The contour plots of the displacement components for the age 44 specimen are displayed in Fig. 14I, with the fibre direction along the x-axis. A comparison is given with the experimental results obtained by Tonge et al. [144]. As expected, the contour profiles for each displacement component are comparable and the overall behaviour of the simulations matches the experimental results. The age 44 simulations accurately capture the displacement along the x-axis (see Fig. 14Ia), but the displacements along the y- and z-axes, shown in Fig. 14Ib, Ic, are slightly overestimated by approximately 0.5 mm and 2 mm, respectively. This overestimation arises from a constituent contribution not captured in the model. It is also possible that the effect of the rig set-up is not appropriately captured in the simulation.

The guard ring may introduce a compressive force through the thickness that would limit the extent of the deformation.

Figure 14II and III shows the simulated contour profile of the bulge test for samples according to the proposed "ageing" of the various parameters. These profiles are compared to experimental results at approximately the same age, as extracted from the data obtained by Tonge et al. [144]. It is important to note that in the experimental specimens the Langer lines were not aligned with the body axes. The Langer lines were oriented at 64° and −24.6° to the x-axis for the age 61 and 83 specimens, respectively, as indicated in the figures. This alteration in the orientation is reflected in the simulated results.

The profile comparison between the age 64 simulated and age 61 experimental results are very similar to those of age 44. The alteration in the fibre orientation is captured quite satisfactorily, with the resulting axial assymmetry in the components of displacement along the x- and y-axes represented accurately. The z component of displacement in the out-of-plane direction is acceptably captured, although there seems to be an overestimation in the level of anisotropy in the simulated results. In terms of the magnitude of the displacements, the y-axis components of the age 61 experiment and age 64 simulation are similar, but the simulations overestimate the other two components. This is not too surprising considering the unsatisfactory fit with the pressure-stretch data at age 61 as shown in Fig. 13.

The age 84 simulations were orientated at −24.6° to the positive x-axis in order to replicate the age 83 experimental contour plots. There is sufficient agreement in the general profile of the simulated results when compared to the experimental data. The only discrepancy lies in the component along the x-axis of the experimental data as shown in Fig. 14IIIa, where the lack of symmetry suggests a possible defect in the skin specimen, such as a non-uniform skin thickness or an irregularity on a constituent level, such as an inconsistent collagen distribution or dispersion. Despite this, the displacements along the x- and y-axes of the age 84 simulated results are comparable to the experimental results, but there is again a minor overestimation in the z-axis component.

10 A Microstructurally-Based Chemo-Mechanobiological Model of Skin Ageing

A microstructurally-based model that attempts to capture the contribution of key constituents on the overall *mechanical response* of the skin has been presented in Sect. 7. An ageing type response was introduced in Sect. 9 by extending the mechanical model via the modification of parameters motivated to be involved. The proposed ageing model did not however incorporate the mechanisms directly involved in the turnover of collagen and elastin that occur during the ageing processes.

One extension to the skin model is now presented as a possible framework to describe a continuous ageing response. Evolution equations for the nano-constituents and their influence on collagen and elastin are proposed. With reference to Fig. 5, the focus here will be on chronological ageing, while further ideas will be given for an extension that incorporates photoageing.

10.1 Biological Remodelling

Continuum models that account for changes in the volume and constitutive properties of biological materials—key features of ageing—can be broadly classified as:

- Continuum models for growth, i.e. a change in volume [see e.g. 141, 147, 148].
- Continuum models for remodelling, i.e. a change in constituent density and constitutive parameters.

A remodelling approach to ageing is proposed here. Continuum models for remodelling were originally developed for hard tissue (bone) using the framework of continuum damage mechanics [see e.g. 149, 150]. These models have been extended to describe softening behaviour in soft biological tissue [see e.g. 151]. Evolution equations for the density field and the elasticity tensor follow from thermodynamic arguments.

An alternative remodelling framework not based on damage mechanics is *open-system thermodynamics*. This allows for isotropic remodelling via the introduction of density sources and fluxes [141, 148, 152]. The free energy Ψ has added dependence on the density thereby allowing for strengthening or weakening of the material microstructure. Anisotropic remodelling has been considered by Waffenschmidt et al. [153]. The general structure for remodelling is described by two coupled governing relations: one for the momentum balance (see Eq. (5)) and one for mass conservation. This framework has been successfully employed to different biological systems undergoing remodelling and more recently to soft tissue. Of particular relevance is the work on turnover in arteries by Sáez et al. [140], Lafortune and Aris [154]. The work by Sáez et al. is especially useful here in the context of skin ageing, as a theoretical and computational model for collagen turnover as a result of hypertension is proposed. The model focused on the variation of the nano-constituent factors, such as TIMP, MMP and TGF-β. This variation is driven by mechanical stimuli as a result of the muscular contractions. The remodelling framework of Sáez et al. thus provides a basis for an ageing model. The framework is now discussed in more detail prior to developing the ageing model for skin.

Hypertension is a chronic vascular disease where blood pressure becomes elevated. The increased pressure results in an increased mechanical load on the vasculature. In an attempt to maintain a homoeostatic stress state, smooth muscle cells (SMCs) start to grow. This causes thickening of the vessel walls. Thickening

is the result of alterations within the extracellular matrix (ECM) of vessel walls, primarily through changes in the deposition and degradation of collagen.

Extensive studies have shown that collagen deposition increases with hypertension. SMCs produce TGF-β and due to the added mechanical stress on the SMCs, there is increased expression of TGF-β. This results in the up-regulation of collagen deposition.

In terms of degradation of collagen, the ratio of MMP to TIMP is of primary concern. In hypertension, TIMP has been reported to increase, decreasing the total amount of MMP. Ultimately, collagen turnover increases as a result of hypertension and the mechanical loading imposed on the SMCs.

A key aspect of the model is how the collagen density ρ evolves. Density evolution introduces a mass source term $\mathscr{R}$ to the balance of mass. As proposed by Kuhl et al. [123], $\mathscr{R}$ takes the general form:

$$\dot{\rho} = \mathscr{R} := \left[\frac{\rho}{\rho^*}\right]^{-m} \Psi - \Psi^* , \tag{12}$$

where Ψ^* and ρ^* are the energy in the homoeostatic equilibrium state (also know as the attractor stimulus) and the initial density, respectively, and m is a parameter.

Additionally, Ψ_{col} takes on a density dependence, $\Psi_{\text{col}} = \Psi_{\text{col}}(\mathbf{C}, \mathbf{v}_0, \rho)$ similar to that in Eq. (12). This either strengthens or weakens the collagen contribution to the overall mechanical response according to the presence of collagen within the soft tissue.

Through activation of the SMCs, TGF-β and TIMP pathways are activated. It is these constituents that evolve according to Eq. (12). As mentioned, the system is driven by the mechanical loading on the SMCs which is captured through an energy, Ψ_{SMC} and source terms for TGF and TIMP given by

$$\mathscr{R}_{\text{TGF}-\beta} = \gamma_{\text{TGF}-\beta}\left[\frac{\rho_{\text{TGF}-\beta}}{\rho^*_{\text{TGF}-\beta}}\right]^{-m_{\text{TGF}-\beta}} \Psi_{\text{SMC}} - \Psi^*_{\text{TGF}-\beta} ,$$

$$\mathscr{R}_{\text{TIMP}} = \gamma_{\text{TIMP}}\left[\frac{\rho_{\text{TIMP}}}{\rho^*_{\text{TIMP}}}\right]^{-m_{\text{TIMP}}} \Psi_{\text{SMC}} - \Psi^*_{\text{TIMP}} ,$$

where $\gamma \in \mathbb{R}^+$ quantify the relative contribution to the SMC energy.

TIMP acts to inhibit and regulate MMP. Thus MMP evolves inversely to TIMP as

$$\mathscr{R}_{\text{MMP}} = \gamma_{\text{MMP}}\mathscr{R}_{\text{TIMP}} ,$$

where $\gamma_{\text{MMP}} \in \mathbb{R}^-$.

With the collagen sources defined, collagen evolves as

$$\mathscr{R}_{\text{col}} = \gamma_+\mathscr{R}_{\text{TGF}-\beta} + \gamma_-\mathscr{R}_{\text{MMP}} ,$$

Table 6 Evolution equation parameters for collagen turnover in hypertension [140]

Parameter	Symbol	Units
TGF-β sensitivity to SMC energy	$\gamma_{\text{TGF}-\beta}$	–
TIMP sensitivity to SMC energy	γ_{TIMP}	–
MMP sensitivity to TIMP	γ_{MMP}	–
Collagen sensitivity to TGF-β	γ_{+}	–
Collagen sensitivity to MMP	γ_{-}	–
$m_{\text{TGF}-\beta}$	TGF-β nonlinear remodelling	–
m_{TIMP}	TIMP nonlinear remodelling	–
ρ^{*}_{TIMP}	initial TIMP density	$\mu\text{g ml}^{-1}$
$\rho^{*}_{\text{TGF}-\beta}$	initial TGF-β density	$\mu\text{g ml}^{-1}$
ρ^{*}_{MMP}	initial MMP density	$\mu\text{g ml}^{-1}$
ρ^{*}_{col}	initial collagen density	$\mu\text{g ml}^{-1}$
$\Psi^{*}_{\text{TGF}-\beta}$	homoeostatic equilibrium state of TGF-β	N m^{-2}
Ψ^{*}_{TIMP}	homoeostatic equilibrium state of TIMP	N m^{-2}

where γ_{+} and γ_{-} characterise the sensitivity of collagen to TGF-β and MMP respectively.

The above system of time-dependent nonlinear equations can be solved using a time discretisation scheme and linearised through a Newton scheme to establish the collagen density evolution. The parameter units and interpretation are summarised in Table 6.

10.2 A Model for Skin Ageing

The model of Sáez et al. [140] provides a framework that can be extended to account for collagen and elastin remodelling due to intrinsic and extrinsic ageing. The interplay between factors such as TGF-β and MMP are critical for the ageing model. The primary difference between the model presented by Sáez et al. and an ageing model is how the processes are driven. In Sáez et al., the stimulus is related to the elastic energy density where changes in collagen turnover occur due to the mechanical loading of the SMCs of the vascular tissue. This offers a very natural driving process captured by the SMC free energy Ψ_{SMC}. The ageing process does not offer such an easy analogue.

Ageing, and accordingly the effects on collagen and elastin turnover, do not evolve with mechanical loading but instead evolve due to a more innate process. Additionally, in the Sáez et al. model the system is driven toward a state of equilibrium through the inclusion of the homoeostatic equilibrium terms, $\Psi^{*}_{\text{TGF}-\beta}$ and Ψ^{*}_{TIMP}. Within an ageing context, it does not make sense for the system to be driven to a state of equilibrium as this would be analogous to saying that ageing

stops. Due to these differences, and in order to develop a meaningful ageing model, several adjustments need to be made.

A primary challenge is the introduction of an alternative driving factor. In Sect. 4.3, the link between the loss of antioxidant defence with age and the increase in the the level of ROS was described. Accordingly ROS was found to be the common factor in the evolution of the primary constituents that related to collagen and elastin turnover (see Fig. 5). Therefore it is proposed that ROS provides a mechanism with which to drive the ageing process.

With reference to Eq. (12), the evolution equations are postulated to be of the form

$$\dot{\rho}^{\text{rel}} = \mathscr{R}\,,$$

where $\mathscr{R}$ represents the source term as before. As no initial values could be found in the literature for all the constituents that play a role in collagen and elastin turnover in the skin, relative quantities ρ^{rel} will be used to describe the constituent evolution, where the relative quantities are the current values normalised by the value at time $t = 0$ denoted by ρ^*. Hence

$$\rho^{\text{rel}} = \frac{\rho}{\rho^*}. \tag{13}$$

This normalisation further avoids any dimensional and scale issues. Accurate initial values are also not of concern (especially as this is an exercise in model development) as the relative initial value is always unity.

The proposed ageing model is now assessed by its ability to replicate key processes depicted in Fig. 5, with ROS as the independent variable driving the evolution equations. The primary factors that are dependent on ROS are TGF-β and TIMP. TGF-β levels have been found to increase with ROS accumulation in the extracellular matrix, while TIMP levels show a decline with ROS accumulation within the fibroblast cells. Thus their respective proposed source terms are given by

$$\mathscr{R}_{\text{TGF}} = \frac{\gamma^{+}_{\text{TGF}}}{\tau^{+}_{\text{TGF}}}\left[\frac{\rho^{\text{max}}_{\text{TGF}} - \rho^{\text{rel}}_{TGF}}{\rho^{\text{max}}_{\text{TGF}} - 1}\right]^{n_{\text{TGF}}}\left[\rho^{\text{rel}}_{\text{ROS}} - 1\right],$$

$$\mathscr{R}_{\text{TIMP}} = \frac{\gamma^{-}_{\text{TIMP}}}{\tau^{-}_{\text{TGF}}}\left[\frac{\rho^{\text{rel}}_{\text{TIMP}} - \rho^{\text{min}}_{\text{TIMP}}}{1 - \rho^{\text{min}}_{\text{TIMP}}}\right]^{m_{\text{TIMP}}}\left[\rho^{\text{rel}}_{\text{ROS}} - 1\right].$$

Additionally, through ROS and TIMP evolution, MMP levels will be affected. In order to simplify and reduce the number of the equations, the dependence on AP-1 as a governing factor in MMP turnover is absorbed into the dependence on ROS,

giving a source term for MMP as

$$\mathscr{R}_{\mathrm{MMP}} = \frac{\gamma^{-}_{\mathrm{MMP}}}{\tau^{-}_{\mathrm{MMP}}} \left[\frac{\rho^{\max}_{\mathrm{MMP}} - \rho^{\mathrm{rel}}_{\mathrm{MMP}}}{\rho^{\max}_{\mathrm{MMP}} - 1} \right]^{m_{\mathrm{MMP}}} \left[\rho^{\mathrm{rel}}_{\mathrm{TIMP}} - 1 \right] + \frac{\gamma^{+}_{\mathrm{MMP}}}{\tau^{+}_{\mathrm{MMP}}} \left[\frac{\rho^{\max}_{\mathrm{MMP}} - \rho^{\mathrm{rel}}_{\mathrm{MMP}}}{\rho^{\max}_{MMP} - 1} \right]^{n_{\mathrm{MMP}}} \left[\rho^{\mathrm{rel}}_{\mathrm{ROS}} - 1 \right].$$

Thus, the relative collagen and elastin mass density sources are given by

$$\mathscr{R}_{\mathrm{col}} = \frac{\gamma^{-}_{\mathrm{col}}}{\tau^{-}_{\mathrm{col}}} \left[\frac{\rho^{\mathrm{rel}}_{\mathrm{col}} - \rho^{\min}_{\mathrm{col}}}{1 - \rho^{\min}_{\mathrm{col}}} \right]^{m_{\mathrm{col}}} \left[\rho^{\mathrm{rel}}_{\mathrm{MMP}} - 1 \right] + \frac{\gamma^{+}_{\mathrm{col}}}{\tau^{+}_{\mathrm{col}}} \left[\frac{\rho^{\max}_{\mathrm{col}} - \rho^{\mathrm{rel}}_{\mathrm{col}}}{\rho^{\max}_{\mathrm{col}} - 1} \right]^{n_{\mathrm{col}}} \left[\rho^{\mathrm{rel}}_{\mathrm{TGF}} - 1 \right], \tag{14}$$

$$\mathscr{R}_{\mathrm{elas}} = \frac{\gamma^{-}_{\mathrm{elas}}}{\tau^{-}_{\mathrm{elas}}} \left[\frac{\rho^{\mathrm{rel}}_{\mathrm{elas}} - \rho^{\min}_{\mathrm{elas}}}{1 - \rho^{\min}_{\mathrm{elas}}} \right]^{m_{\mathrm{elas}}} \left[\rho^{\mathrm{rel}}_{\mathrm{MMP}} - 1 \right] + \frac{\gamma^{+}_{elas}}{\tau^{+}_{\mathrm{elas}}} \left[\frac{\rho^{\max}_{\mathrm{elas}} - \rho_{\mathrm{elas}}}{\rho^{\max}_{\mathrm{elas}} - 1} \right]^{n_{\mathrm{elas}}} \left[\rho^{\mathrm{rel}}_{\mathrm{TGF}} - 1 \right]. \tag{15}$$

In order to capture the reduction in collagen sensitivity to TGF-β, a ROS-dependent modification to $\gamma^{+}_{\mathrm{col}}$ is proposed as

$$\mathscr{R}_{\gamma^{+}_{\mathrm{col}}} = \frac{\gamma^{-}_{\gamma_{\mathrm{col}}}}{\tau^{-}_{\gamma_{\mathrm{col}}}} \left[\rho^{\mathrm{rel}}_{\mathrm{ROS}} - 1 \right].$$

The various model parameters are summarised in Table 7. τ is introduced as an adaptation speed parameter to allow for control over the reaction rate of one constituent relative to another, as well as to ensure dimensional consistency.

In the literature, it has been consistently reported that the features common to chronological ageing begin to manifest at around 40 years of age. Within the first

Table 7 Evolution equation parameters

Parameter	Symbol	Units
TGF-β sensitivity to ROS	$\gamma^{+}_{\mathrm{TGF}-\beta}$	–
TIMP sensitivity to ROS	$\gamma^{-}_{\mathrm{TIMP}}$	–
MMP sensitivity to TIMP	$\gamma^{-}_{\mathrm{MMP}}$	–
MMP sensitivity to ROS	$\gamma^{+}_{\mathrm{MMP}}$	–
Collagen sensitivity to TGF-β	$\gamma^{+}_{\mathrm{col}}$	–
Collagen sensitivity to MMP	$\gamma^{-}_{\mathrm{col}}$	–
Elastin sensitivity to TGF-β	$\gamma^{+}_{\mathrm{elas}}$	–
Elastin sensitivity to MMP	$\gamma^{-}_{\mathrm{elas}}$	–
m, n	Remodelling factors	–
τ	Adaptation speed	years
$\rho^{\max}$	Constituent relative maximum	–
$\rho^{\min}$	Constituent relative minimum	–

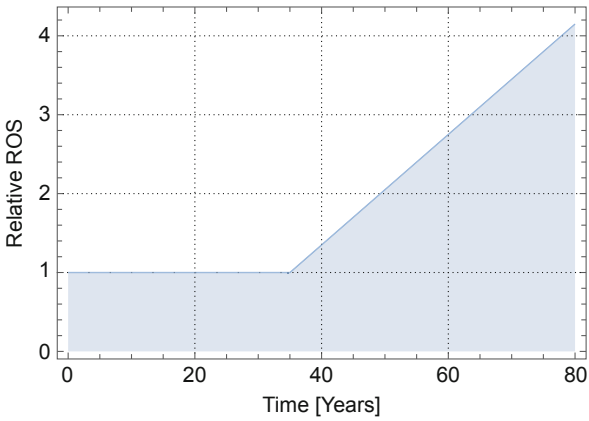

Fig. 15 Relative ROS evolution with time

four decades, ROS levels are relatively stable, where ROS production is balanced through oxidative defence. Thereafter, due to decline in the oxidative defence capabilities of the skin, ROS levels have been shown to gradually increase, with levels up to 4 times greater in aged skin as compared to young skin. As a simple model, a relative ROS evolution is proposed as depicted in Fig. 15 and governed by

$$\rho_{\text{ROS}}^{\text{rel}} = \begin{cases} 1 & t \leq 35 \\ 0.1(t-35)+1 & t > 35 \end{cases} . \tag{16}$$

That is, ROS is chosen to remain stable until age 35, whereafter it increases linearly with age.

The chosen parameter values are given in Table 8. All τ values were set to 1 year and the remodelling factors m and n to 0.8. Choices for the relative minimum and maximum values of the various constituents were determined from the literature discussed in Sect. 4. Where values could not be found, reasonable values were estimated to replicate the expected constituent response. In the absence of evolution data from actual experiments with which to calibrate the model, the proposed sensitivity parameters merely provide a proof of concept.

In Fig. 16, the simulated evolution of TGF-β, TIMP and MMP are shown. Within the first simulated 35 years, there is no change in the relative amounts of each factor. Thereafter, there is a gradual decline in the level of TIMP, while MMP and TGF-β increase. In Fig. 16d, the sensitivity of collagen to TGF-β is shown to reduce due to a decline in γ_{col}^{+}.

Through the dependence on MMP and TGF-β, collagen and elastin levels decline as depicted in Fig. 17a and b, respectively. As discussed previously, collagen has been shown to decline with age to approximately half the amount when compared to younger skin. As captured in Fig. 17a, despite the increase in TGF-β, the combination of increased MMP and reduced TGF-β sensitivity results in the relative amount of collagen declining towards the proposed relative minimum. As the relative minimum of 0.5 is approached, the rate of collagen degradation decreases.

Table 8 Evolution equation parameter values

Parameter	Value
$\gamma^{+}_{\mathrm{TGF}-\beta}$	0.005
$\gamma^{-}_{\mathrm{TIMP}}$	−0.005
$\gamma^{-}_{\mathrm{MMP}}$	−0.02
$\gamma^{+}_{\mathrm{MMP}}$	0.1
$\gamma^{+}_{\mathrm{col}}$	0.005
$\gamma^{-}_{\mathrm{col}}$	−0.02
$\gamma^{+}_{\mathrm{elas}}$	0.005
$\gamma^{-}_{\mathrm{elas}}$	−0.01
$\gamma^{-}_{\gamma_{\mathrm{col}}}$	−0.00003
$\rho^{\max}_{\mathrm{TGF}-\beta}$	4
$\rho^{\min}_{\mathrm{TIMP}}$	0.7
$\rho^{\max}_{\mathrm{MMP}}$	4
$\rho^{\max}_{\mathrm{col}}$	1.5
$\rho^{\min}_{\mathrm{col}}$	0.5
$\rho^{\max}_{\mathrm{elas}}$	3
$\rho^{\min}_{\mathrm{elas}}$	0.8

The evolution of elastin mimics that of collagen, although due to the inherently stable nature of elastin, the relative loss of elastin is not as severe.

Figures 16 and 17 provide an example of the evolution profile of the various constituents that have been identified to play a role in the ageing process. With this, it is essential to link the evolution of collagen and elastin back to the mechanical model. In order to accomplish this, inspiration is taken from that of the theory of constrained mixtures.

In the constrained mixture theory adopted here, the evolving constituent composition and organisation are innately linked to the overall mechanical behaviour of the soft tissue. The primary idea behind a constrained mixture formulation is to pay attention to the individual constituents within a tissue by accounting for the turnover rates of the constituents of interest, rather than focusing on the overall change of the tissue. For a detailed overview, the reader is referred to [155–159].

Denoting $\rho^{\mathrm{k}}(s)$ as the mass density of constituent k at time s, the free energy is proposed to take the form

$$\Psi = \Psi(\mathbf{F}, \rho^{\mathrm{k}}(s)) \,,$$

where any anisotropic behaviour has been omitted for simplicity. This structure of the free energy follows the general rule of mixtures where weighted contributions are used to predict the mean response of a composite material. That is,

$$\Psi(\mathbf{F}, \rho^{\mathrm{k}}(s)) = \sum_{k} \frac{\rho^{\mathrm{k}}(s)}{\rho(s)} \Psi^{\mathrm{k}},$$

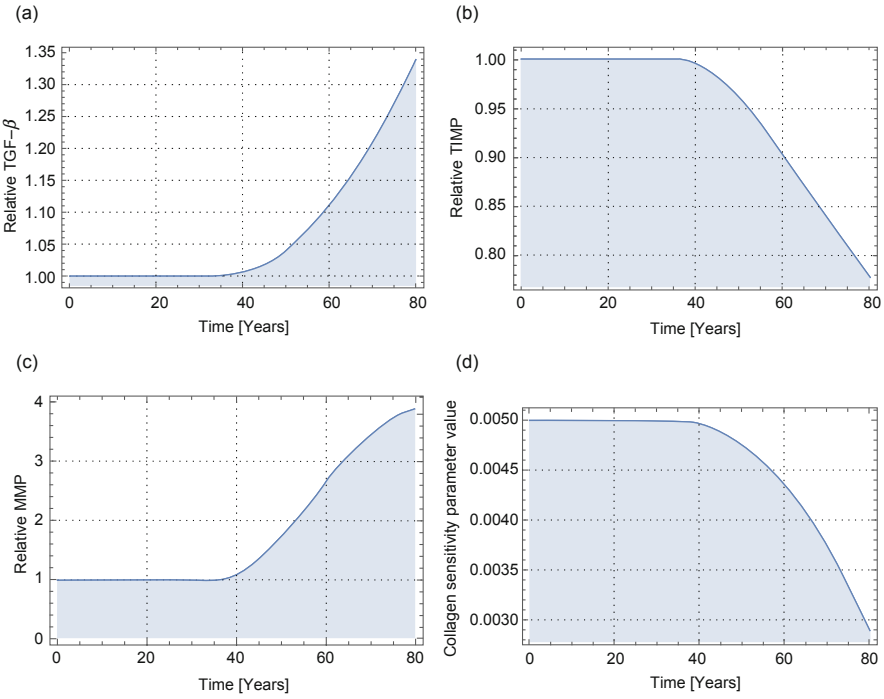

Fig. 16 Evolution of nano-constituents TGF-β, TIMP and MMP according to evolution equations. (**a**) Simulated TGF-β evolution with time. (**b**) Simulated TIMP evolution with time. (**c**) Simulated MMP evolution with time. (**d**) Simulated γ_{col}^{+} evolution with time

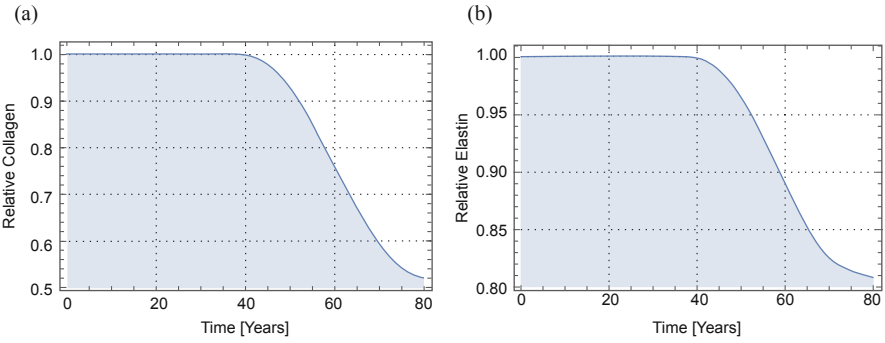

Fig. 17 Simulation evolution of collagen and elastin with time. (**a**) Evolution of collagen with time. (**b**) Evolution of elastin with time

where $\rho(s) = \sum_k \rho^{\text{k}}(s)$ and Ψ^{k} is the free energy contribution of constituent k. $\rho(s)$ is generally assumed to be constant [157]. Each constituent mass density $\rho^{\text{k}}(s)$ can thus be allowed to adapt in time according to some stimulus. Evolution

equations for each constituent can be proposed, in a manner similar to that proposed for the constituent evolutions. Thus, as an extension to Eq. (7), each constituent free energy is weighted by the corresponding relative mass density (Eq. (13)), that is

$$\Psi = \rho_{\text{gs}}^{\text{rel}}\Psi_{\text{gs}} + \rho_{\text{elas}}^{\text{rel}}\Psi_{\text{elas}} + \rho_{\text{col}}^{\text{rel}}\Psi_{\text{col}}\,. \tag{17}$$

The choice of using relative density weightings is motivated by the idea that in the absence of constituent remodelling, Eq. (17) reduces to Eq. (7). Equations (14) and (15) can be used as evolution equations for the relative collagen and elastin contributions, respectively, while $\rho_{\text{gs}}^{\text{rel}}$ evolves to ensure the overall density remains constant.

As mentioned, the model as presented in Eq. (7) does not have a natural connection to the amount of collagen and elastin present in the skin. This mixture-theory motivated extension addresses this issue. Additionally, with the form of the collagen free energy as presented in Eq. (10), this allows γ_{chn} to be a representation of the level of crosslinking within the collagen network.

10.3 A Model for Photoageing

In Sect. 4.3 photoageing was presented as a processes that not only compounds the effects of chronological ageing, but often induces structural changes more severe than those observed under normal ageing. Due to this, the extension of the mixture-type model to a one that accounts for photoageing is the logical next step.

From Fig. 5, the processes involved in chronological and photoageing are very similar, which makes the extension to account for photoageing a very natural one. The primary difference is the formation of what is referred to as elastotic tissue. This is similar to elastic tissue but highly-disorganised and irregular. Thus a simple extension of the free energy (17) would be

$$\Psi = \rho_{\text{gs}}^{\text{rel}}\Psi_{\text{gs}} + \rho_{\text{elas}}^{\text{rel}}\Psi_{\text{elas}} + \rho_{\text{col}}^{\text{rel}}\Psi_{\text{col}} + \rho_{\text{elastotic}}^{\text{rel}}\Psi_{\text{elastotic}}, \tag{18}$$

where $\Psi_{\text{elastotic}}$ is an elastotic free energy. The form of $\Psi_{\text{elastotic}}$ could be similar to that presented for the elastin free energy Ψ_{elas}, but experimental data would be needed to make an informed decision. The evolution process would similarly be driven by ROS generation, where ROS would take on a form such as

$$\text{ROS} = \text{ROS}_{\text{chrono}} + \text{ROS}_{\text{UV}}\,.$$

Here $\text{ROS}_{\text{chrono}}$ and ROS_{UV} are the ROS generated by the chronological and UV-exposure, respectively. $\text{ROS}_{\text{chrono}}$ would take on a form as proposed in Eq. (16) whereas ROS_{UV} would be motivated by actual UVA data obtained from measurement.

The evolution equations for TGF-β, TIMP and MMP would accordingly need to include terms dependent on $\mathrm{ROS}_{\mathrm{UV}}$. Additionally, an evolution equation for elastotic tissue would need to be proposed which would be very similar to that of the elastin evolution equation (15). Through such a framework, photoageing could be accounted for.

11 Discussion

In Sect. 8 of this chapter, a simple conceptual approach to implicitly capture intrinsic ageing of the skin through variation of age-dependent constitutive parameters has been presented. This method was implemented and described in Sect. 9 where a subset of microstructural parameters associated with intrinsic ageing were identified from experimental characterisation data available in the literature. A microstructurally-motivated constitutive formulation featuring distinct free energy contributions from the ground substance, elastin and collagen phases was devised. The mechanical behaviour of the ground substance and elastin was modelled by an isotropic, coupled, and compressible neo-Hookean strain energy. For collagen, the primary load-bearing constituent of skin in tension, a wormlike eight-chain model motivated by the fibrous and intertwined nature of the collagen network was selected. This approach captures well the inherent nonlinearity and anisotropy of the skin under finite deformations.

A subset of the constitutive parameters whose age-dependent variation has the most physically-justified influence on the response was identified. The effects of ageing were successfully replicated through experimentally-informed alterations of these constitutive parameters. The reduction in skin stiffness at low stretches (i.e. when the equivalent Young's modulus is low) through degradation of the elastin network was well captured through modification of the elastic strain energy associated with elastin. Results show that degradation of the elastin mesh work and variations in anisotropy of the collagen network are plausible mechanisms to explain manifestations of ageing in terms of macroscopic tissue stiffening. Whereas alterations in elastin affect the low-strain region of the skin stress-strain curve, those related to collagen have an impact on its (large strain) linear region.

Despite the ability of the constitutive model to capture ageing effects, some limitations can be identified and form the basis for future improvements.

Only three sample points from experimental bulge test data were used, corresponding to ages 44, 61 and 83. This limited sampling space does not represent an adequate range of data with which to make a conclusive parameter fit. Therefore, for a more comprehensive ageing model to be developed, it would be necessary to include data from a statistically significant number of specimens and over a larger range of age groups. Moreover, skin specimens would need to be controlled for several factors so as to limit variability, or at least, to characterise it so it could be accounted for in the modelling. Of significant importance would be control over anatomical site. Not only should skin from the same site of the patients be tested,

but also controlled for segregating the respective influence of intrinsic ageing and photoageing by considering photo-protected and photo-exposed zones.

The model does not explicitly account for the existence of crosslinks within the collagen network, and therefore, cannot provide a mechanistic description of their effect. Crosslinks prevent slippage between fibres and accordingly contributes toward the stiffness elicited by the collagen network under stretch [160]. With age, crosslinking has been observed to increase and this has often been considered as a possible reason for the increase in macroscopic stiffness [101]. It is worth pointing out that, in general, crosslinking of collagen might rather be a by-product of UV radiation exposure and/or glycation associated with diabetes [16] rather than the consequence of intrinsic ageing *per se*. Modifications of crosslinking properties are implicitly captured in the eight-chain model but modelling approaches explicitly accounting for crosslinks could also be considered. For example, for a more explicit description of fibre-to-fibre and matrix-to-fibre mechanical/physical interactions one could use dedicated tensor invariants [161, 162] that segregate deformation modes associated with such interactions, or one could use multiscale mechanistic micromechanical constitutive models that explicitly describe these interactions [163–166]. Micromorphic continuum models are also well suited to capture these effects [167, 168]. Other types of microstructurally-motivated strain energy function for the individual chains of the unit cell could also be used [169, 170].

Because the dermal layer is the main mechanical contributor of the skin under states of tension it was reasonable to model the skin as single homogeneous layer. In order to build a more realistic model, valid for different load cases (e.g. surface shear), it would be sensible to incorporate individual skin layers with realistic structural geometries [20, 119] and associated constitutive properties.

Although the ageing skin undergoes significant alterations of its mechanical and biostructural properties, other body tissues, structures and organs undergo comparable ageing processes. As a result, they can alter the mechanical environment experienced by the skin. For example, thinning/atrophy of adipose and muscular tissues [101], or even bone resorption, are factors that can modify the complex mechanobiology and associated residual strains of the skin as an organ covering the entire body, and more particularly on the face. This is consistent with variations of Langer lines' tension and direction with age, reported in the literature [43]. These aspects were not directly accounted for in the present constitutive model and. Also, with age, the skin tends to lose its in-plane isotropy [102] because of the strong mechanical effects introduced by dermal collagen realignment arising in combination with collagen cross-linking and density alteration. These effects are also linked to the relaxation of tension in Langer lines with ageing.

At this stage, the model presented in Sect. 9 does not account for ageing-triggered enzymatic degradation of elastic fibres, abnormal collagen deposition and remodelling. This was addressed in Sect. 10 where, in the framework of open-system thermodynamics and mixture theory, a biochemo-mechanical model of skin ageing was formulated based on a simplified mechanistic description of the biochemo-mechanics of both intrinsic and extrinsic ageing (Fig. 5) that was established in Sect. 4 of this chapter. The multiphysics constitutive model considered ROS, TGF-

β, TIMP, MMP as biochemical species whose interplay modulated the homeostatic state of collagen and elastin phases. ROS were taken as the main triggers to initiate ageing of the skin. Density of ROS was the independent variable driving the ageing process. Of particular significance in this model, disruption of the homeostatic state between activation and inhibition of MMPs—through modulation of ROS and TIMP levels—was a key ingredient in describing the pathophysiology of intrinsic skin ageing and photoageing by controlling the degradation of collagen and elastin in the skin.

This prototype model should be viewed as a first attempt at partly deconstructing and simplifying the systemic characteristics of skin ageing. Here, we have laid down the foundation of a thermodynamically-admissible constitutive formulation embedded in the rigorous framework of continuum mechanics that capture ageing-induced evolution of fundamental biochemical species associated with ageing. The chemical interplay of these quantities (ROS, TGF-β, TIMP, MMP) modulates the evolution of microstructural characteristics of the skin, namely its collagen and elastin content. The model's ability to describe the evolution of collagen and elastin relative levels as a function of enzymatic factors and cytokines levels, themselves modulated by ROS levels, was demonstrated. It should be noted that, in its current formulation, the constitutive model does not encompass a two-way coupling between mechanics and biochemistry. This was an intentional feature, justified by the absence of suitable experimental data to calibrate such a model. The one-way coupling means that, although changes in collagen and elastin (relative) density as a by-product of ageing implicitly alter the composite properties of the skin, mechanics does not influence evolution of collagen and elastin levels or that of other biochemical constituents (ROS, TGF-β, TIMP, MMP). Moreover, a constrained mixture theory extension (Eq. (17)) was considered to effectively link evolution of collagen and elastin content to their respective contributions to the strain energy density defined in Eq. (7). Finally, a possible extension of the constitutive model to specifically include the effects of photoageing under the form of a weighted elastotic tissue component to the strain energy density (Eq. (18)).

Naturally, at this stage, much work remains to be done. Particular research efforts should be directed toward the design of physical characterisation experiments aiming to provide qualitative and quantitative evidence to support the formulation and validation of chemo-mechanobiological constitutive models of ageing. In Sect. 10 simple rate equations were chosen to describe the density evolution of all chemical species present in the mixture model. Equations of this type do not present any conceptual difficulty and more sophisticated analytical forms could have been used. However, the main challenge in developing, testing and validating biophysics-based model lies in the (limited) availability of experimental data, particularly biological fields (e.g. concentration of TIMPs as a function of age) to derive constitutive parameters.

The multiscale aspects of tissue structure — both in length and time scales than span several orders of magnitude—coupled to evolution of biochemical species present a significant technical challenge for modellers, particularly if considering computational coupling techniques [171].

In the light of this review of the main biomechanical and biostructural aspects of skin ageing, and despite a synthetic and simplified outlook, one is still left with a sense of overwhelming complexity. The number of processes and driving factors, their interplay, their multiphysics nature and the scales at which these occur make the understanding and description skin ageing a very challenging task, at both the experimental and modelling levels. Additionally, the effects of intrinsic ageing are generally compounded by the influence of extrinsic ageing (e.g. photoageing), which only serves to add complexity to the problem.

Here, in this chapter, we have outlined possible modelling approaches to capture the static or dynamic effects of ageing through the formulation of simple constitutive models of ageing. It is hoped that they will form the basis for the design of new physical characterisation experiments for skin ageing and more advanced multi-physics material models that will be calibrated with data produced in the context of such experiments. We strongly believe that only inter- and multidisciplinary approaches integrating experimental characterisation, imaging, clinical observation and modelling from the outset will have a real chance to deliver predictive tools to account for skin ageing in the design of treatment solutions and products.

Acknowledgements Part of this work was funded through the award of a Royal Society Newton Fund grant (2014–2016) between the Universities of Southampton and Cape Town. The authors would like to gratefully acknowledge this financial support as well as the logistic and infrastructure support provided by their respective institutions for research visits of Damien Pond, Andrew McBride and Georges Limbert. Georges Limbert would also like to thank Procter & Gamble and L´Oréal for their financial support of his research over the last few years.

References

1. Burns T, Breathnach S, Cox N, Griffiths C (2004) Rook's textbook of dermatology, 7th edn. Blackwell Science, Oxford. ISBN 0632064293
2. Shimizu H (2007) Shimizu's textbook of dermatology. Hokkaido University Press/Nakayama Shoten Publishers, Sapporo/Tokyo
3. Tobin DJ (2006) Biochemistry of human skin — our brain on the outside. Chem Soc Rev 35(1):52–67
4. Assaf H, Adly MA, Hussein MR (2010) Aging and intrinsic aging: pathogenesis and manifestations, Section 13, pp 129–138
5. Naylor EC, Watson REB, Sherratt MJ (2011) Molecular aspects of skin ageing. Maturitas 69(3):249–256
6. Gilchrest BA, Yaar M (1992) Ageing and photoageing of the skin: observations at the cellular and molecular level. Br J Dermatol 127 Suppl 41:25–30
7. Goukassian D, Gad F, Yaar M, Eller MS, Nehal US, Gilchrest BA (2000) Mechanisms and implications of the age-associated decrease in DNA repair capacity. FASEB J 14(10):1325–1334
8. Fisher GJ, Wang Z, Datta SC, Varani J, Kang S, Voorhees JJ (1997) Pathophysiology of premature skin aging induced by ultraviolet light. N Engl J Med 337(20):1419–1429
9. Berneburg M, Plettenberg H, Krutmann J (2000) Photoaging of human skin. Photodermatol Photoimmunol Photomed 16(6):239–244

10. Kligman AM (1969) Early destructive effects of sunlight on human skin. J Am Med Assoc 210:2377–2380
11. Fisher GJ, Kang S, Varani J, Bata-Csorgo Z, Wan Y, Datta S, Voorhees JJ (2002) Mechanisms of photoaging and chronological skin aging. Arch Dermatol 138(11):1462–1470
12. Diffey BL (2003) A quantitative estimate of melanoma mortality from ultraviolet a sunbed use in the UK. Br J Dermatol 149(3):578–581
13. Sandby-Moller J, Poulsen T, Wulf HC (2003) Epidermal thickness at different body sites: relationship to age, gender, pigmentation, blood content, skin type and smoking habits. Acta Dermato Venereol 83(6):410–413
14. Vierkötter A, Krutmann J (2012) Environmental influences on skin aging and ethnic-specific manifestations. Dermato-endocrinology 4(3):227–231
15. Benedetto AV (1998) The environment and skin aging. Clin Dermatol 16(1):129–139
16. Sherratt MJ (2013) Age-related tissue stiffening: cause and effect. Adv Wound Care 2(1):11–17
17. Silver FH, Seehra G, Freeman JW, DeVore D (2002) Viscoelastic of young and old human dermis: a proposed moelcular mechanism for elastic energy storage in collagen and elastin. J Appl Polymer Sci 86:1978–1985
18. Leyva-Mendivil MF, Lengiewicz J, Page A, Bressloff NW, Limbert G (2017a) Skin microstructure is a key contributor to its friction behaviour. Tribol Lett 65(1):12
19. Leyva-Mendivil MF, Lengiewicz J, Page A, Bressloff NW, Limbert G (2017) Implications of multi-asperity contact for shear stress distribution in the viable epidermis – an image-based finite element study. Biotribology 11:110–123. https://doi.org/10.1016/j.biotri.2017.04.001
20. Leyva-Mendivil MF, Page A, Bressloff NW, Limbert G (2015) A mechanistic insight into the mechanical role of the stratum corneum during stretching and compression of the skin. J Mech Behav Biomed Mater 49:197–219
21. Hahnel E, Lichterfeld A, Blume-Peytavi U, Kottner J (2017) The epidemiology of skin conditions in the aged: a systematic review. J Tissue Viability **26**(1):20–28
22. Kligman AM, Koblenzer C (1997) Demographics and psychological implications for the aging population. Dermatol Clin 15(4):549–553
23. Morey P (2007) Skin tears: a literature review. Prim Intention 15(3):122–129
24. (2010) http://www.statistics.gov.uk/cci/nugget.asp?id=949
25. (2016) https://www.ons.gov.uk/peoplepopulationandcommunity/populationandmigration/populationestimates/articles/overviewoftheukpopulation/february2016
26. (2017) https://www.ons.gov.uk/peoplepopulationandcommunity/populationandmigration/populationestimates/articles/overviewoftheukpopulation/july2017
27. United Nations (2015) World population ageing. Department of Economic and Social Affairs Population Division, United Nations, New York, ((ST/ESA/SER.A/390)):(ST/ESA/SER.A/390)
28. Kelly E, Stoye G, Vera-Hernandez M (2015) Public hospital spending in England: evidence from National Health Service administrative records. Technical report, Institute for Fiscal Studies
29. Pond D, McBride A, Davids L, Reddy BD, Limbert G (2018) Microstructurally-based constitutive modelling of the skin. linking intrinsic ageing to microstructural parameters. J Theor Biol 444:108–123
30. Limbert G (2014) State-of-the-art constitutive models of skin biomechanics, chapter 4, pp 95–131. Pan Stanford Publishing Pte. Ltd, Singapore
31. Lanir Y (1987). Skin Mechanics. McGraw-Hill, New York
32. Chan LS (1997) Human skin basement membrane in health and autoimmune diseases. Front Biosci, 2(15):343–352
33. Silver FH, Freeman JW, DeVore D (2001) Viscoelastic properties of human skin and processed dermis. Skin Res Technol 7(1):18–23
34. Langton AK, Sherratt MJ, Griffiths CEM, Watson REB (2010) Review article: a new wrinkle on old skin: the role of elastic fibres in skin ageing. Int J Cosmet Sci 32(5):330–339

35. Lévêque JL, de Rigal J, Agache PG, Monneur C (1980) Influence of ageing on the in vivo extensibility of human skin at a low stress. Arch Dermatol Res 269(2):127–135
36. Reihsner R, Balogh B, Menzel EJ (1995) Two-dimensional elastic properties of human skin in terms of an incremental model at the in vivo configuration. Med Eng Phys 17(4):304–313
37. Oxlund H, Manschot J, Viidik A (1988) The role of elastin in the mechanical properties of skin. J Biomech 21(3):213–218
38. Oxlund H, Andreassen TT (1980) The roles of hyaluronic acid, collagen and elastin in the mechanical properties of connective tissues. J Anat 131(4):611–620
39. Pailler-Mattei C, Bec S, Zahouani H (2008) In vivo measurements of the elastic mechanical properties of human skin by indentation tests. Med Eng Phys 30(5):599–606
40. Ribeiro JF, dos Anjos EHM, Mello MLS, de Campos Vidal B (2013) Skin collagen fiber molecular order: a pattern of distributional fiber orientation as assessed by optical anisotropy and image analysis. PLOS One 8(1):e54724
41. Tonge TK, Atlan LS, Voo LM, Nguyen TD (2013a) Full-field bulge test for planar anisotropic tissues: Part I – experimental methods applied to human skin tissue. Acta Biomater 9(4):5913–5925
42. Gosline J, Lillie M, Carrington E, Guerette P, Ortlepp C, Savage K (2002) Elastic proteins: biological roles and mechanical properties. Philos Trans R Soc Lond Ser B: Biol Sci 357(1418):121–132
43. Langer K (1978) On the anatomy and physiology of the skin: II. Skin tension. Br J Plast Surg 31(2):93–106
44. Lapeer RJ, Gasson PD, Karri V (2010) Simulating plastic surgery: from human skin tensile tests, through hyperelastic finite element models to real-time haptics. Progr Biophys Mol Biol 103(2–3):208–216
45. Silver FH, Kato YP, Ohno M, Wasserman AJ (1992) Analysis of mammalian connective tissue: relationship between hierarchical structures and mechanical properties. J Long-Term Effects Med Implants 2(2–3):165–198
46. Tregear RT (1969) The mechanical properties of skin. J Soc Cosmet Chem 20:467–477
47. Oomens CW, van Campen DH, Grootenboer HJ (1987) In vitro compression of a soft tissue layer on a rigid foundation. J Biomech 20(10):923–935
48. Tobin DJ (2017) Introduction to skin aging. J Tissue Viability 26(1):37–46
49. Farage MA, Miller KW, Elsner P, Maibach HI (2007) Structural characteristics of the aging skin: A review. Cutan Ocul Toxicol 26(4):343–357
50. Montagna W, Carlisle K (1990) Structural changes in ageing skin. Br J Dermatol 122 Suppl 35:61–70
51. Fenske NA, Lober CW (1986) Structural and functional changes of normal aging skin. J Am Acad Dermatol 15(4(1)):571–585
52. Puizina-Ivić N (2008) Skin aging. Acta Dermatovenerol Alp Pannonica Adriat 17(2):47–54
53. Gragnani A, MacCornick S, Chominski V, Ribeiro de Noronha SM, Alves Corra de Noronha SA, Masako Ferreira L (2014) Review of major theories of skin aging. Adv Aging Res 3(4):265–284
54. Krutmann J, Bouloc A, Sore G, Bernard BA, Passeron T (2017) The skin aging exposome. J Dermatol Sci 85(3):152–161
55. Escoffier C, de Rigal J, Rochefort A, Vasselet R, Lévêque JL, Agache PG (1989) Age-related mechanical properties of human skin: an in vivo study. J Investig Dermatol 93(3):353–357
56. Pawlaczyk M, Lelonkiewicz M, Wieczorowski M (2013) Age-dependent biomechanical properties of the skin. Postepy Dermatologii i Alergologii 30(5):302–306
57. Diridollou S, Vabre V, Berson M, Vaillant L, Black D, Lagarde JM, Gregoire JM, Gall Y, Patat FQ (2001) Skin ageing: changes of physical properties of human skin in vivo. Int J Cosmet Sci 23(6):353–362
58. Oriba HA, Bucks DA, Maibach HI (1996) Percutaneous absorption of hydrocortisone and testosterone on the vulva and foreaarm: effect of the menopause and site. Br J Dermatol 134:229–233

59. Duncan KO, Lefell DJ (1997) Preoperative assessment of eth elderly patient. Dermatol Clin 15:583–593
60. Brincat MP, Kabalan S, Stud JW, Moniz CF, de Trafford J, Montgomery J (1987) A study of the decrease of skin collagen content, skin thickness, and bone mass in the postmeopausal women. Obstret Gynecol 70(6):840–845
61. Gilchrest BA (1982) Age-associated changes in the skin. J Am Geriatr Soc 30(2):139–143
62. Gilchrest BA (1989) Skin aging and photoaging: an overview. J Am Acad Dermatol 21:610–613
63. Rippke F, Schreiner V, Schwantitz H (2002) The acidic milieu of the horny layer: New findings on the physiology and pathophysiology of skin pH. Am J Clin Dermatol 3(4):261–272
64. Waller JM, Maibach HI (2005) Age and skin structure and function, a quantitative approach (I): blood flow, pH, thickness, and ultrasound echogenicity. Skin Res Technol 11(4):221–35
65. Alexander H, Cook T (2006) Variations with age in the mechanical properties of human skin in vivo. J Tissue Viability 16(3):6–11
66. Xu F, Lu T (2011) Introduction to skin biothermomechanics and thermal pain. Springer, Heidelberg/Dordrecht/London/New York
67. Henry F, Piérard-Franchimont C, Cauwenbergh G, Piérard GE (1997) Age-related changes in facial skin contours and rheology. J Am Geriatr Soc 45(2):220–222
68. Tagami H (2008) Functional characteristics of the stratum corneum in photoaged skin in comparison with those found in intrinsic aging. Arch Dermatol Res 300(1):S1–6
69. Silver FH, Siperko LM, Seehra GP (2003) Mechanobiology of force transduction in dermal tissue. Skin Res Technol 9(1):3–23
70. McCallion R, Li WPA (1993) Dry and photo-aged skin: manifestations and management. J Clin Pharmacol Ther 18:15–32
71. Yaar M, Eller MS, Gilchrest BA (2002) Fifty years of skin aging. J Investig Dermatol Symp Proc 7:51–58
72. Batisse D, Bazin R, Baldeweck T, Querleux B, Lévêque JL (2002) Influence of age on the wrinkling capacities of skin. Skin Res Technol 8(3):148–154
73. Wu KS, Van Osdol WW, Dauskardt RH (2002) Mechanical and microstructural properties of stratum corneum. Biol Biomim Mater-Properties Funct 724:27–33
74. Wu KS, van Osdol WW, Dauskardt RH (2006) Mechanical properties of human stratum corneum: effects of temperature, hydration, and chemical treatment. Biomaterials 27(5):785–795
75. Kligman LH (1986) Photoaging. manifestations, prevention and treatment (review). Dermatol Clin 4:517–528
76. Lavker RM (1979) Structural alterations in exposed and unexposed aged skin. J Investig Dermatol 73:59–66
77. Lagarrigue SG, George J, Questel E, Lauze C, Meyer N, Lagarde JM, Simon M, Schmitt AM, Serre G, Paul C (2012) In vivo quantification of epidermis pigmentation and dermis papilla density with reflectance confocal microscopy: variations with age and skin phototype. Exp Dermatol 21(4):281–286
78. Sauermann K, Clemann S, Jaspers S, Gambichler T, Altmeyer P, Hoffmann K, Ennen J (2002) Age related changes of human skin investigated with histometric measurements by confocal laser scanning microscopy in vivo. Skin Res Technol 8(1):52–56
79. Querleux B, Baldeweck T, Diridollou S, de Rigal J, Huguet E, Leroy F, Barbosa VH (2009) Skin from various ethnic origins and aging: an in vivo cross-sectional multimodality imaging study. Skin Res Technol 15(3):306–313
80. Kligman AM, Zheng P, Lavker RM (1985) The anatomy and pathogenesis of wrinkles. Br J Dermatol 113:37–42
81. Marks R (1999) Skin disease in old age, 2nd edn. Martin Dunitz, London
82. Grove GL (1989) Physiological changes in older skin. Clin Geriatr Med 5(1):115–125
83. Rabe JH, Mamelak AJ, McElgunn PJ, Morison WL, Sauder DN (2006) Photoaging: mechanisms and repair. J Am Acad Dermatol 55(1):1–19

84. Chung JH, Yano K, Lee MK, Youn CS, Seo JY, Kim KH, Cho KH, Eun HC, Detmar M (2002) Differential effects of photoaging vs intrinsic aging on the vascularization of human skin. Arch Dermatol 138(11):1437–42
85. Humbert P, Viennet C, Legagneux K, Grandmottet F, Robin S, Oddos T, Muret P (2012) In the shadow of the wrinkle: theories. J Cosmet Dermatol 11(1):72–78
86. Lovell CR, Smolenski KA, Duance VC, Light ND, Young S, Dyson M (1987) Type I and III collagen content and fibre distribution in normal human skin during ageing. Br J Dermatol 117(4):419–428
87. Gniadecka M, Nielsen OF, Wessel S, Heidenheim M, Christensen DH, Wulf HC (1998) Water and protein structure in photoaged and chronically aged skin. J Investig Dermatol 111(6):1129–1132
88. Uitto J (1989) Connective tissue biochemistry of the aging dermis. age-associated alterations in collagen and elastin. Clin Geriatr Med 5:127–147
89. Fisher GJ, Varani J, Voorhees JJ (2008) Looking older: Fibroblast collapse and therapeutic implications. Arch Dermatol 144(5):666–672
90. Varani J, Dame MK, Rittie L, Fligiel SE, Kang S, Fisher GJ, Voorhees JJ (2006) Decreased collagen production in chronologically aged skin: roles of age-dependent alteration in fibroblast function and defective mechanical stimulation. Am J Pathol 168(6):1861–1868
91. Lavker RM, Zheng P, Dong G (1987) Aged skin: a study by light, transmission electron, and scanning electron microscopy. J Investig Dermatol 88(3):44–51
92. Lavker RM, Zheng P, Dong G (1989) Morphology of aged skin. J Geriatr Dermatol 4(1):53–67
93. Varani J (2010) Fibroblast aging: intrinsic and extrinsic factors. Drug Discov Today Ther Strateg 7(3):65–70
94. Choi WS, Mitsumoto A, Kochevar IE (2009) Involvement of reactive oxygen species in tgf-β1-induced tropoelastin expression by human dermal fibroblasts. Photochem Photobiol 85(6):1425–1433
95. Ashworth JL, Murphy G, Rock MJ, Sherratt MJ, Shapiro SD, Shuttleworth CA, Kielty CM (1999) Fibrillin degradation by matrix metalloproteinases: implications for connective tissue remodelling. Biochem J 340(1):171–181
96. Yagi M, Yonei Y (2016) Glycative stress and anti-aging: what is glycative stress? Glycative Stress Res 3(3):152–155
97. Yagi M, Yonei Y (2018) Glycative stress and anti-aging: glycative stress and skin aging. Glycative Stress Res 5(1):50–54
98. Fisher GJ, Datta S, Wang Z, Li XY, Quan T, Chung JH, Kang S, Voorhees JJ (2000) c-Jun-dependent inhibition of cutaneous procollagen transcription following ultraviolet irradiation is reversed by all-trans retinoic acid. J Clin Investig 106(5):663–670
99. Chung JH, Kang S, Varani J, Lin J, Fisher GJ, Voorhees JJ (2000) Decreased extracellular-signal-regulated kinase and increased stress-activated map kinase activities in aged human skin in vivo. J Investig Dermatol 115(2):177–182
100. Daly CH, Odland GF (1979) Age-related changes in the mechanical properties of human skin. J Investig Dermatol 73(1):84–87
101. Quatresooz P, Thirion L, Piérard-Franchimont C, Piérard GE (2006) The riddle of genuine skin microrelief and wrinkles. Int J Cosmet Sci 28(6):389–395
102. Ruvolo Jr EC, Stamatas GN, Kollias N (2007) Skin viscoelasticity displays site- and age-dependent angular anisotropy. Skin Pharmacol Physiol 20(6):313–321
103. Vexler A, Polyansky I, Gorodetsky R (1999) Evaluation of skin viscoelasticity and anisotropy by measurement of speed of shear wave propagation with viscoelasticity skin analyzer. J Investig Dermatol 113(5):732–739
104. Kochevar IE, Taylor CR, Krutmann J (2008) Fundamentals of cutaneous photobiology and photoimmunology, chapter 88, 7th edn., pp 797–809. The McGraw-Hill Companies, New York
105. Anders A, Altheide H-J, Knälmann M, Tronnier H (1995) Action spectrum for erythema in humans investigated with dye lasers. Photochem Photobiol 61(2):200–205

106. de Gruijl FR, van der Leun JC (1994) Estimate of the wavelength dependency of ultraviolet carcinogenesis in humans and its relevance to the risk assessment of a stratospheric ozone depletion. Health Phys 67(4):319–325
107. Starcher B, Conrad M (1995) A role for neutrophil elastase in the progression of solar elastosis. Connect Tissue Res 31(2):133–140
108. Bernstein EF, Chen YQ, Tamai K, Shepley KJ, Resnik KS, Zhang H, Tuan R, Mauviel A, Uitto J (1994) Enhanced elastin and fibrillin gene expression in chronically photodamaged skin. J Investig Dermatol 103(2):182–186
109. Ramos-e Silva M, da Silva Carneiro SC (2007) Elderly skin and its rejuvenation: products and procedures for the aging skin. J Cosmet Dermatol 6(1):40–50
110. Watson RE, Griffiths CE, Craven NM, Shuttleworth CA, Kielty CM (1999) Fibrillin-rich microfibrils are reduced in photoaged skin. distribution at the dermal-epidermal junction. J Investig Dermatol 112(5):782–787
111. Fleischmajer R, Perlish JS, Gaisin A (1973) Comparative study of dermal glycosaminoglycans. J Investig Dermatol 61(1):1–6
112. Jenkins G (2002) Molecular mechanisms of skin ageing. Mech Ageing Dev 123(7):801–810
113. Jeyapalan JC, Sedivy JM (2008) Cellular senescence and organismal aging. Mech Ageing Dev 129(7):467–474
114. López-Otín, C, Blasco, MA, Partridge L, Serrano M, Kroemer G (2013) The hallmarks of aging. Cell 153(6):1194–1217
115. Hekimi S, Lapointe J, Wen Y (2011) Taking a "good" look at free radicals in the aging process. Trends Cell Biol 21(10):569–576
116. Merker K, Sitte N, Grune T (2000) Hydrogen peroxide-mediated protein oxidation in young and old human mrc-5 fibroblasts. Arch Biochem Biophys 375(1):50–54
117. Goriely A, Ben Amar M (2007) On the definition and modeling of incremental, cumulative, and continuous growth laws in morphoelasticity. Biomech Model Mechanobiol 6(5):289–296
118. Ambrosi D, Ateshian GA, Arruda EM, Cowin SC, Dumais J, Goriely A, Holzapfel GA, Humphrey JD, Kemkemer R, Kuhl E, Olberding JE, Taber LA, Garikipati K (2011) Perspectives on biological growth and remodeling. J Mech Phys Solids 59(4):863–883
119. Limbert G (2017) Mathematical and computational modelling of skin biophysics-a review. Proc R Soc A Math Phys Eng Sci 473(2203):1–39
120. Jor JWY, Parker MD, Taberner AJ, Nash MP, Nielsen PMF (2013) Computational and experimental characterization of skin mechanics: identifying current challenges and future directions. Wiley Interdiscip Rev Syst Biol Med 5(5):539–556
121. Li W (2015) Modelling methods for in vitro biomechanical properties of the skin: a review. Biomed Eng Lett 5(4):241–250
122. Flynn C (2014) Fiber-matrix models of the dermis. In: Querleux B (ed) Computational biophysics of the skin. Pan Stanford Publishing Pte. Ltd, Singapore, pp 133–159
123. Kuhl E, Garikipati K, Arruda E, Grosh K (2005) Remodeling of biological tissue: Mechanically induced reorientation of a transversely isotropic chain network. J Mech Phys Solids 53:1552–1573
124. Kuhl E, Holzapfel GA (2007) A continuum model for remodeling in living structures. J Mater Sci 42(21):8811–8823
125. Garikipati K, Arruda EM, Grosh K, Narayanan H, Calve S (2004) A continuum treatment of growth in biological tissue: the coupling of mass transport and mechanics. J Mech Phys Solids 52(7):1595–1625
126. Mazza E, Papes O, Rubin MB, Bodner SR, Binur NS (2005) Nonlinear elastic-viscoplastic constitutive equations for aging facial tissues. Biomech Model Mechanobiol 4(2–3):178–189
127. Mazza E, Papes O, Rubin MB, Bodner SR, Binur NS (2007) Simulation of the aging face. J Biomech Eng Trans ASME 129(4):619–623
128. Rubin MB, Bodner SR (2002) A three-dimensional nonlinear model for dissipative response of soft tissue. Int J Solids Struct 39(19):5081–5099
129. Maceri F, Marino M, Vairo G (2013) Age-dependent arterial mechanics via a multiscale elastic approach. Int J Comput Methods Eng Sci Mech 14(2):141–151

130. Marsden JE, Hughes TJR (1994) Mathematical foundations of elasticity. Dover, New-York
131. Arruda EM, Boyce MC (1993) A three-dimensional constitutive model for the large stretch behavior of rubber elastic-materials. J Mech Phys Solids 41(2):389–412
132. Flory PJ (1969) Statistical mechanics of chain molecules. Wiley, Chichester/New York
133. Bischoff JE, Arruda EA, Grosh K (2002) A microstructurally based orthotropic hyperelastic constitutive law. J Appl Mech Trans ASME 69(5):570–579
134. Kratky O, Porod G (1949) Röntgenuntersuchungen gelöster fadenmoleküle. Recueil des Travaux Chimiques des Pays-Bas et de la Belgique 68:1106–1122
135. Buganza Tepole A, Gosain AK, Kuhl E (2012) Stretching skin: The physiological limit and beyond. Int J Non-Linear Mech 47(8):938–949
136. Flynn C, Taberner AJ, Nielsen PMF, Fels S (2013) Simulating the three-dimensional deformation of in vivo facial skin. J Mech Behav Biomed Mater 28:484–494
137. Flynn C, McCormack BAO (2008) A simplified model of scar contraction. J Biomech 41(7):1582–1589
138. Flynn CO, McCormack BAO (2009) A three-layer model of skin and its application in simulating wrinkling. Comput Methods Biomech Biomed Eng 12(2):125–134
139. Bischoff JE, Arruda EM, Grosh K (2004) A rheological network model for the continuum anisotropic and viscoelastic behavior of soft tissue. Biomech Model Mechanobiol 3(1):56–65
140. Sáez P, Peña E, Martínez MA, Kuhl E (2013) Computational modeling of hypertensive growth in the human carotid artery. Comput. Mech. 53(6):1183–1196
141. Kuhl E, Menzel A, Steinmann P (2003) Computational modeling of growth - a critical review, a classification of concepts and two new consistent approaches. Comput Mech 32(1–2):71–88
142. Marko JF, Siggia ED (1995) Stretching dna. Macromolecules 28(26):8759–8770
143. Kielty CM, Sherratt MJ, Shuttleworth CA (2002) Elastic fibres. J Cell Sci 115(14):2817–2828
144. Tonge TK, Voo LM, Nguyen TD (2013b). Full-field bulge test for planar anisotropic tissues: Part II - a thin shell method for determining material parameters and comparison of two distributed fiber modeling approaches. Acta Biomat 9(4):5926–5942
145. Jor JWY, Nash MP, Nielsen PMF, Hunter PJ (2011) Estimating material parameters of a structurally based constitutive relation for skin mechanics. Biomech Model Mechanobiol 10(5):767–778
146. Kvistedal YA, Nielsen PMF (2009) Estimating material parameters of human skin in vivo. Biomech Model Mechanobiol 8(1):1–8
147. Himpel G, Kuhl E, Menzel A, Steinmann P (2005) Computational modelling of isotropic multiplicative growth. Comput Model Eng Sci 8(2):119–134
148. Menzel A, Kuhl E (2012) Frontiers in growth and remodeling. Mech Res Commun 42:1–14
149. Jacobs CR, Levenston ME, Beaupré GS, Simo JC, Carter DR (1995) Numerical instabilities in bone remodeling simulations: the advantages of a node-based finite element approach. J Biomech 28:449–459. https://doi.org/10.1016/0021-9290(94)00087-K
150. Jacobs CR, Simo JC, Beaupré GS, Cartert DR (1997) Adaptive bone remodeling incorporating simultaneous density and anisotropy considerations. J Biomech 30(96):603–613
151. Alastrué V, Rodríguez JF, Calvo B, Doblaré M (2007) Structural damage models for fibrous biological soft tissues. Int J Solids Struct 44(18–19):5894–5911
152. Kuhl E, Steinmann P (2003) Theory and numerics of geometrically non-linear open system mechanics. Int J Numer Methods Eng 58(11):1593–1615
153. Waffenschmidt T, Menzel A, Kuhl E (2012) Anisotropic density growth of bone - a computational micro-sphere approach. Int J Solids Struct 49(14):1928–1946
154. Lafortune P, Aris R (2015) Computational model of collagen turnover in carotid arteries during hypertension. Int J Numer Methods Biomed Eng 28(1):72–86
155. Humphrey JD, Rajagopal KR (2003) A constrained mixture model for arterial adaptations to a sustained step change in blood flow. Biomech Model Mechanobiol 2(2):109–126
156. Valentín A, Humphrey JD (2009) Evaluation of fundamental hypotheses underlying constrained mixture models of arterial growth and remodelling. Philos Trans R Soc A Math Phys Eng Sci 367(1902):3585–3606

157. Valentín A, Humphrey JD, Holzapfel GA (2011) A multi-layered computational model of coupled elastin degradation, vasoactive dysfunction, and collagenous stiffening in aortic aging. Ann Biomed Eng 39(7):2027–2045
158. Rouhi G, Epstein M, Sudak L, Herzog W (2007) Modeling bone resorbtion using mixture theory with chemical reactions. Mech Mater Struct 2(6):1141–1155
159. Valentín A, Holzapfel GA (2012) Constrained mixture models as tools for testing competing hypothesis in arterial biomechanics: survey. Mech Res Commun 29:126–133
160. Tang Y, Ballarini R, Buehler MJ, Eppell SJ (2010) Deformation micromechanisms of collagen fibrils under uniaxial tension. J R Soc Interface 7(46):839–850
161. Limbert G (2011) A mesostructurally-based anisotropic continuum model for biological soft tissues-decoupled invariant formulation. J Mech Behav Biomed Mater 4(8):1637–1657
162. Peng XQ, Guo ZY, Moran B (2005) An anisotropic hyperelasticconstitutive model with fiber-matrix shear interaction for the human annulus fibrosus. J Appl Mech 73(5):815–824
163. Maceri F, Marino M, Vairo G (2010) A unified multiscale mechanical model for soft collagenous tissues with regular fiber arrangement. J Biomech 43(2):355–363
164. Marino M, Vairo G (2013) Multiscale elastic models of collagen bio-structures: from cross-linked molecules to soft tissues, pp 73–102. Springer, Berlin/Heidelberg
165. Marino M, Vairo G, Wriggers P (2015) Multiscale hierarchical mechanics in soft tissues. Proc Appl Math Mech 15(1):35–38
166. Linka K, Khiém VN, Itskov M (2016) Multi-scale modeling of soft fibrous tissues based on proteoglycan mechanics. J Biomech 49(12):2349–2357
167. von Hoegen M, Skatulla S, Schröder J (2017) A generalized micromorphic approach accounting for variation and dispersion of preferred material directions. Comput Struct. https://doi.org/10.1016/j.compstruc.2017.11.013
168. Sack KL, Skatulla S, Sansour CC (2016) Biological tissue mechanics with fibres modelled as one-dimensional Cosserat continua. Applications to cardiac tissue. Int J Solids Struct 81:84–94
169. Holzapfel GA, Gasser TC, Ogden RW (2000) A new constitutive framework for arterial wall mechanics and a comparative study of material models. J Elast 61:1–48
170. Schröder J, Neff P (2003) Invariant formulation of hyperelastic transverse isotropy based on polyconvex free energy functions. Int J Solids Struct 40(2):401–445
171. Geers MGD, Kouznetsova VG, Brekelmans WAM (2010) Multi-scale computational homogenization: Trends and challenges. J Comput Appl Math 234(7):2175–2182

Inverse Methods

Johannes Weickenmeier and Edoardo Mazza

Abstract The mechanical properties of skin have been studied for several decades; yet, to this day reported stiffness values for full-thickness skin or individual layers such as the epidermis, papillary dermis, reticular dermis, and subcutis vary drastically. In vivo and ex vivo measurement techniques include extension, indentation, and suction tests. At the same time, several new imaging modalities emerged that visualize tissue microstructure at length scales ranging from the cell to the organ level. Informed by the experimental characterization of mechanobiological skin properties, computational skin models aim at predicting the soft tissue response under various physiological conditions such as skin growth, scar tissue formation, and surgical interventions. The identification of corresponding model parameters plays a major role in improving the predictive capabilities of such constitutive models. Here, we first provide an overview of the most common measurement techniques and imaging modalities. We then discuss popular methods used for model parameter identification based on inverse methods.

1 Introduction

Skin mechanics has been studied for several decades [1]. The medical field is interested in diagnosis, monitoring, and treating skin diseases [2], preventing excessive scar tissue formation [3], and facilitating fast wound healing in wound care [4, 5]. Biomechanics aims at characterizing mechanical properties to model

J. Weickenmeier (✉)
Department of Mechanical Engineering, Stevens Institute of Technology, Hoboken, NJ, USA
e-mail: johannes.weickenmeier@stevens.edu

E. Mazza
Department of Mechanical and Process Engineering, ETH, Zurich, Switzerland

Swiss Federal Laboratories for Materials Science and Technology, EMPA, Duebendorf, Switzerland

G. Limbert (ed.), *Skin Biophysics*, Studies in Mechanobiology,
Tissue Engineering and Biomaterials 22,
https://doi.org/10.1007/978-3-030-13279-8_6

skin deformation behavior, to provide criteria for developing artificial skin, or to simulate skin behavior in facial animations [6], skin wrinkling [7], analysis of congenital skin defects [8, 9], and personalized reconstructive surgery [10].

The multilayered anatomy of skin can be represented in corresponding biomechanical models and this leads to the requirement of determining layer specific constitutive equations [11]. Previous research provided a wide range of constitutive model formulations for skin, but to this day no generally accepted theory exists that translates microstructural tissue properties into corresponding model equations [12].

The comparability of models proposed in the literature is often limited due to significant differences in the representation of skin anatomy. Large discrepancies in predicted mechanical response are also linked with differences in the deformation modes considered for model development. In fact, model parameters are often determined based on data obtained from one specific experimental configuration. The range of validity of such parameter sets is inherently limited, in that an optimization may well reproduce the experiments for a particular loading condition but is likely to provide poor predictions for any generalized multiaxial, time dependent deformation state [13]. Skin literature presents several dedicated parameter identification schemes that combine a particular mechanical testing method with a skin model formulation representative of that experiment.

This review presents different procedures for skin characterization and associated model parameter identification schemes and discusses their limitations with regard to the development of a skin model of more general validity. The chapter briefly summarizes skin anatomy and outlines experimental methods suitable for a quantitative analysis of skin constituents at different length scales. We then describe common testing protocols for characterizing skin mechanical properties and outline corresponding structural and phenomenological models used for their analysis. Finally, we discuss inverse analysis procedures presented in skin literature addressing problems associated with the variability in experimental data, the contribution of individual skin layers, and the inherent coupling between model parameters.

2 Experimental Anatomy of Skin

The anatomy of skin has been studied extensively, and histochemical staining and dissection have led to a comprehensive description of cells and microstructure of individual skin layers; yet, to date the characterization of skin microstructure across spatial and temporal scales in its natural in vivo environment remains an active field of research. Many visualization techniques have been developed to study skin and its individual layers for a rich set of medically relevant applications and experimental investigations. Ultrasound and magnetic resonance imaging of skin at the organ level are common diagnostic tools in clinical practice and microscopy-based visualization methods are often used in research to study skin at the tissue and cellular level [14].

In view of skin modeling and the identification of corresponding parameters, it is relevant to differentiate between an anatomical description of skin and the actually experimentally observable microstructure with its associated properties [15]. Each imaging modality is generally limited to a specific length scale and it remains a major challenge to visualize skin anatomy in vivo from the organ level down to the cellular level [16].

In the following, we present a brief description of skin anatomy and summarize imaging modalities that visualize skin at the organ, tissue, and cellular level.

2.1 Anatomical Description

Figure 1 shows a representation of skin that consists of three main layers [18]: the outermost epidermis is typically 100 μm thick. The layer underneath, the dermis, is around 500 μm thick and consists of two sublayers: the papillary dermis and the reticular dermis. The deepest layer is the hypodermis with a thickness of around 1 mm. The actual size and microstructure of these individual layers varies with location in the body in order to provide optimal functionality, such as resilience in feet, grip in palms, and barrier function around the core body.

The epidermis protects the body against mechanical and microbacterial hazards and prevents the body from dehydration. The outermost layer, the stratum corneum, consisting of 5–10 layers of dead, keratin rich, and flat cells, represents a barrier impermeable to most biochemical and toxic compounds. The four additional layers underneath, often referred to as the viable or living epidermis, consist of cells that migrate from the dermal-epidermal junction and gradually die, whilst accumulating keratin and losing their nuclei. The dense cell layering gives the epidermis significant mechanical strength and often plays an important role in the response observed in skin tests.

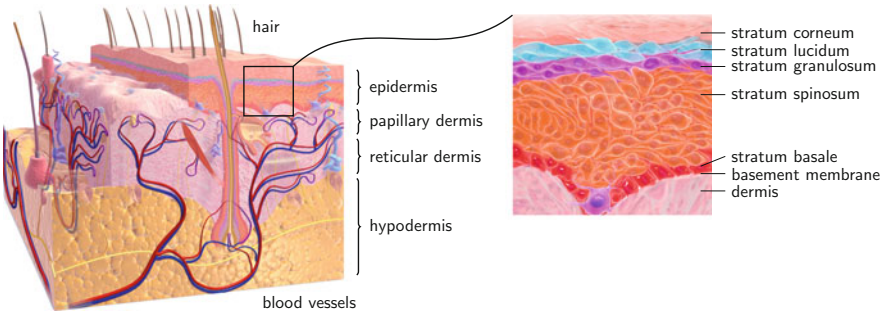

Fig. 1 Representation of the anatomical structure of skin. Skin has functionally different layers that contribute to the overall mechano-biochemical properties of what is the largest organ in the human body. Full thickness skin, left image, generally consists of three layers: the epidermis, dermis, and hypodermis. The epidermis, right image, is the outermost barrier between body and environment, and consists of five sublayers. Adapted from [17]

The dermis is the load-bearing layer in skin and is richly perfused with blood and lymph vessels, and hosts nerve endings. Cutaneous appendages, including sensory receptors, glands, and hair follicles, reside in the dermis which is mostly made up of type I and III collagen. The papillary layer has ridges consisting of thin collagen fibers and provides nutrients to the dermal-epidermal junction. The reticular dermis consists of a dense matrix of collagen bundles and elastin which gives skin its characteristic elastic extensibility.

The hypodermis, the deepest skin layer, primarily serves as a shock absorbing and insulating layer with a location-dependence specialized microstructure. It is located between the dermis and the fascia, which is a thin but strong membrane of connective tissue that encapsulates bones, muscles, and other organs underneath the skin. Fibrous septa running through the hypodermis anchor the dermis to fascial membranes and provide some degree of shear stiffness to the superficial layers of skin. The hypodermis itself contains primarily adipocytes and consists mainly of fat lobules embedded in a loose collagen network.

2.2 Imaging Modalities

In-vivo imaging modalities may generally be categorized by the length scales they resolve and their ability to identify individual pathologies [19]. MRI and US resolve organ and tissue structures at a submillimeter scale [20] and provide a full-thickness representation of skin [21]. High resolution ultrasound [22] and magnetic resonance imaging (MRI) at the organ-level [20] is used to determine layer thicknesses in different body regions and is gaining importance in clinical examinations, due to increased resolution of superficial tissue layers like epidermis and dermis [23]. The echogenicity of individual structures across full-thickness skin is proving useful to diagnose and monitor cysts, scleroderma, and solid, malignant, or inflammatory lesions [24]. It is important to note, however, that individual layers visible in MRI and ultrasound images may differ from medical anatomy. In sonography, and visible in the second row of Fig. 2, skin is often separated into the hyperechoic epidermis, the subepidermal low echogenic band (SLEB) representing the papillary dermis, the dermal echogenic band (DEB) showing reticular dermis, and the mostly hypoechogenic subcutis.

Imaging modalities that visualize skin features down to the cellular level are generally based on the reflective behavior of individual tissue constituents and use either light or lasers as a source for penetrating superficial skin layers [2]. Such non-invasive methods are limited to a penetration depth up to 1000 μm and are therefore primarily used for in vivo characterization of the epidermis and the dermis [28]. Most commonly used methods include reflectance confocal microscopy, optical coherence tomography (OCT), multi-photon microscopy, two-photon fluorescence, and second harmonic generation (SHG).

The characterization of the structural anatomy of the epidermis and dermis -and of the dermal collagen network in particular- is an active field of research [29]. The

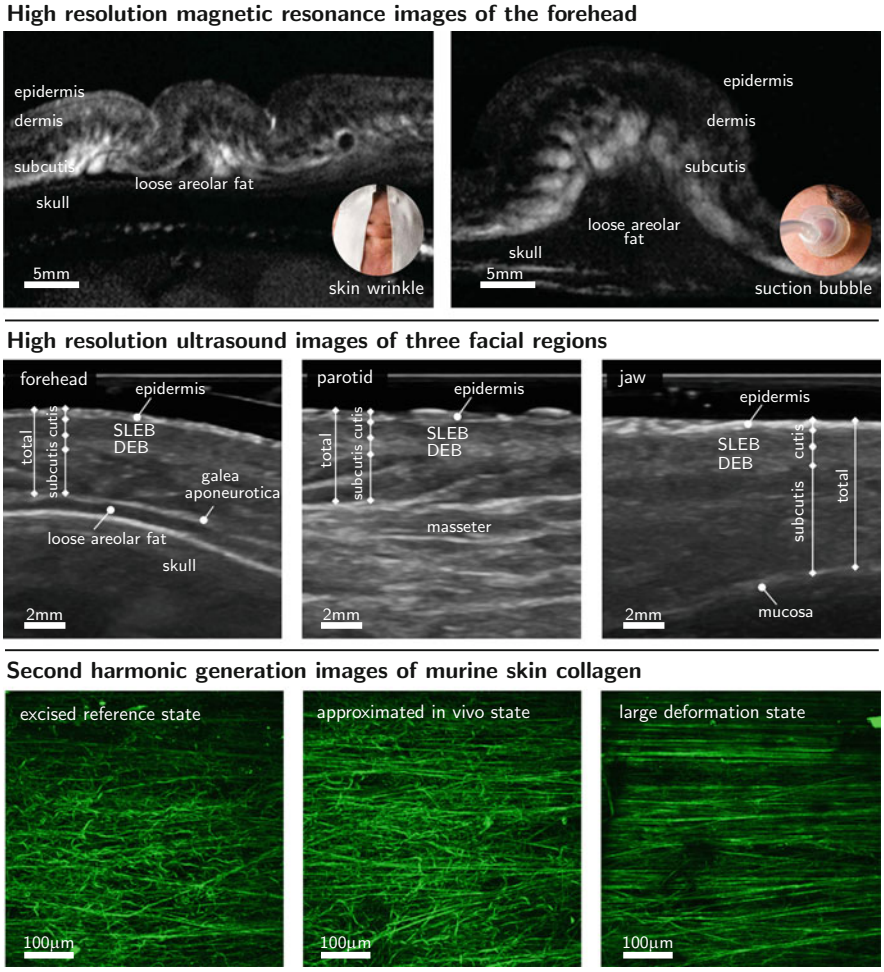

Fig. 2 High resolution magnetic resonance images of deformed skin in the forehead, top row; high resolution ultrasound images in facial regions, middle row. Each skin layer plays a particular role in providing skin its characteristic extensibility and region-specific mechanical response [25, 26]. Second harmonic generation visualizes the collagen network in excised skin samples: The bottom row shows collagen fibers undulated in the excised reference, and progressively aligned in approximated in vivo, and large deformation states [27]

assembly of collagen fibers into a highly functional network provides skin tissue its characteristic viscoelastic and anisotropic response [30]. The literature reports a rich set of studies investigating microstructure with respect to skin architecture [31, 32], inflammatory and blistering conditions [33], fiber orientation [30, 34], bundle thickness [35], tissue remodeling and skin diseases [36], and cutaneous vasculature [28, 37]. Acute changes of these properties cause structural alterations that may result in reduced extensibility, damage, and patient discomfort [14, 38].

3 Quantification of Mechanical Properties of Skin

Literature provides a rich body of work that investigated the mechanical behavior of skin or individual dermal and subdermal layers [1]. The range of data presented, however, has not led to a complete or consistent description of mechanical skin properties, and the findings continue to show a significant dependence on the testing method used. The biophysical response of skin is just too complex for a single experiment-or the aggregate of experimental data- to fully uncover the mechanisms governing the in vivo relation between local forces and deformations as a function of relevant biomarkers. Thus far, mechanical and biochemical properties are collected at a temporal and spatial scale most relevant to each individual application in medicine, biomechanical engineering, or for cosmetic industry. A comprehensive representation of the hierarchical structure of skin requires investigating the mechanical response across all relevant length and time scales and formulating model equations that allow bridging these scales.

Biomechanical testing methods are generally categorized as either in vivo, in vitro, or ex vivo. They are suitable for the characterization of intact skin or individual layers thereof. Traditionally, skin testing focused on ex-vivo measurements of global force-displacement curves under different loading conditions; recent experiments combine full-field deformation analysis, or tracking of complex 3D deformation of tissue structures, combined with local force measurement. These rich data sets are used to inform skin models of increased complexity which reflect microstructural characteristics. Measurements in many locations across the body illustrate the variation in skin compliance with varying microstructure. One major open question is the rationalization of skin stiffness measurements across several length scales which have provided values ranging from kPa, e.g. [40], to several MPa, e.g. [41].

The most common in vivo and ex vivo measurement methods in skin testing are suction, indentation, and (multiaxial) extension tests (see Fig. 3) and are discussed in the following.

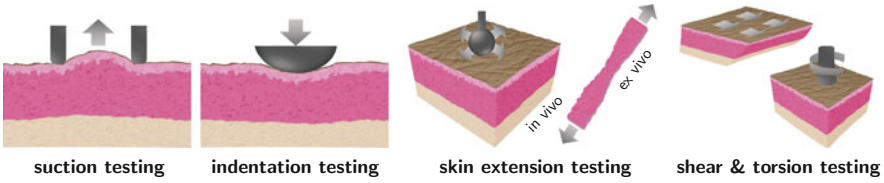

Fig. 3 The most common skin testing methods are suction, indentation, extension, shear, and torsion testing. Experimental setups for each method vary significantly across literature. In recent years, full-field in vivo methods have emerged, enabling the characterization of intact skin in its physiological state. Images adapted from [39]

3.1 Suction

Suction measurements are used to determine in vivo and in situ skin properties [1]. The negative pressure draws tissue into the probe opening where an optical system measures bulge height. The resulting relation between pressure and bulge height is directly related to the probe opening size and loading protocol. Most suction devices presented in literature use a 2–8 mm probe opening diameter and apply a negative suction pressure of up to 500mbars [11, 26]. Due to a wide range of possible loading profiles, suction measurements are particularly useful to determine the nonlinear, viscoelastic, and time- and location-dependent behavior of skin [11]. Immediate compliance, elastic recovery, creep, and permanent deformation are represented in corresponding parameters, which are used to quantify the influence of fatigue [42], ageing [43–45], sex [46], and body location [11, 26, 43, 46–49]. Commercially available devices, such as the Cutometer (Cutometer® MPA 580; Courage+Khazaka, Cologne, Germany), come with multiple probe types and a computer interface to prescribe customized loading protocols. Several custom-built devices apply the same principle and might have larger probe openings, like the Aspirator [11, 50], opening shapes [51], or include ultrasound imaging for a visualization of tissue deformation [52]. Although suction data are affected by significant variability, they demonstrate that skin properties vary across the body and are determined by local microstructure. Devices integrating the suction test with ultrasound imaging/optical coherence tomography visualize skin deformation during tissue loading [46, 53]. The results demonstrate that epidermis and dermis are tightly connected and are primarily responsible for skin's local stiffness [6, 53]. Variable probe opening size allows for the recruitment of individual skin layers [11, 54]. Small probe opening size of around 2 mm recruit the most superficial layers of skin, i.e. epidermis and the papillary dermis, while larger opening diameters of about 6–8 mm involve deeper layers, including the reticular dermis as well as the hypodermis or SMAS (superficial musculo aponeurotic system) [26, 53]. Inverse methods, which will be discussed further below, suggest stiffness ratios between superficial and deep skin layers of up to three orders of magnitude difference [11, 53].

Measurements across the body have shown that regions with a loose hypodermis or fatty subcutis, i.e. jaw, cheek, and neck, tend to respond more elastically [26, 44] than regions with a dense dermal matrix that connects the deep fascia with superficial skin layers, i.e. hands, forearm, and forehead [11, 44]. In fact, the face is a representative region of the body for which functionally driven microstructure characteristics can be linked with differences in skin mechanics, with the forehead being stiffest, followed by the parotid region and the jaw [26].

Suction experiments have well-known limitations. First, the mechanical analysis is based on the simplifying assumption that skin is isotropic. In fact, given the circular opening of typical suction probes, it is impossible to characterize the anisotropic properties of skin from these tests. Second, the measured response is dominated by the characteristics of the superficial layers, while the influence

of deeper layer diminishes with their distance from the surface, in particular for small probe openings. Third, the repeatability of suction measurements depends on accurate probe handling, especially for hand-held devices such as a the Cutometer. Repeated probe placement-including proper alignment of probe and skin and control of contact pressure are paramount to ensure reliable measurement results [55, 56]. The development of an experimental setup that minimizes movement between probe and skin surface and maintains constant contact pressure improved measurement results for multiple repetitions per measurement site and probe diameter size [11, 26].

3.2 Indentation

Indentation is another widely used in vivo testing method as it enables a non-invasive measurement. Unlike the suction method, indentation testing is restricted to flat body regions, such as the volar forearm or the calf [57, 58]. Direct mechanical interpretation of indentation tests is restricted to a linear analysis of the quasi-static or linear viscoelastic properties of skin. Combination of nonlinear analysis and an inverse scheme are necessary to inform more complex models [59]. A major challenge in indentation of soft biological tissues is the reliable identification of the initial contact point between indenter tip and skin surface during loading as well as the assessment of adhesion effects during unloading. Lastly, in-vivo indentation tests do not allow for a quantification of the anisotropic tissue response, since the unidirectional registration of force and displacement does not allow to detect a direction-dependent tissue response.

Indentation tests have shown that volar forearm skin softens with age and progressively loses elasticity, most likely due to microstructural changes in the dermis and hypodermis [58, 60, 61]. The same experimental setup was used to measure the dynamic response of superficial skin at an indentation depth of 200 ± 3 μm in a range of 10–60 Hz. At these low indentation depths, skin stiffness and viscosity were found to be frequency independent [57], which may suggest that the dermal matrix is not activated at a relevant length scale.

A more recent study investigated stiffness and viscosity in reconstructed skin [62]. A series of quasi-static, force-controlled indentation / creep experiments (including a hold time of 100 s after reaching a maximum indentation force of 0.5 mN) were conducted to assess differences in tissue properties at critical stages during the in vitro reconstruction of skin. It was found that skin substitutes stiffen significantly once keratinocytes are seeded on top of the reconstructed dermis to form an epidermal layer. This finding is very insightful in view of the generally accepted claim that skin stiffness is primarily originating from the dermis.

Atomic force microscopy (AFM) is an indentation-based measurement method and has been used to quantify the impact of hydration on the mechanical response of the stratum corneum and epidermis [60, 61]. Indentation depths of up to 200 nm are three orders of magnitude smaller than the previously described indentation

tests and therefore capture the mechanical response at a much smaller length scale. General observations from studies using AFM are that scar tissue is generally stiffer than healthy skin [63] and that the Young's modulus of stratum corneum is roughly twice as high as for the epidermis [64]. Latter study reported stiffness values in the range of 1–2 MPa in comparison to values reported for "skin" (varying due to age) between 5–10 kPa by [40, 57, 58]. Indentation experiments thus provide compelling evidence of the length scale influence on the mechanical properties of skin.

3.3 Skin Extension Tests

Skin extension tests have been used to characterize ex vivo mechanical properties of skin and individual layers thereof. Unlike suction and indentation, extension testing allows investigating the anisotropic response of skin as it relates to the Langer lines distributed across the body [65, 66]. Further, it is used to characterize the time and history dependent behavior of skin through monotonic and cyclic creep and relaxation experiments, e.g. [67].

In most studies, samples are cut from excised skin and clamped inside a uniaxial or multiaxial loading rig [41]. Inevitably, mechanical properties change upon excision and strongly depend on storage duration, storage conditions, and temperature. Sample preparation, often in the form of removing the epidermis as well as adipose tissue to isolate the dermal layer, represents a major interference with the physiological state of alive skin tissue [41, 68]. In fact, cutting away or peeling off of individual layers might damage the structural connections between individual layers. Extraction of skin from the body leads to the loss of in vivo multiaxial pre-tension, so that the peculiar in vivo tensioned configuration of collagen and elastin networks is lost thus leading to unphysiological stress-strain measurements.

Most skin extension studies interpret the experimental data on the basis of linear elasticity theory, extracting the slope of the linear regime of the overall nonlinear, J-shaped force-displacement curve [41, 69]. The most frequently reported parameters from uni- or multiaxial measurements are the ultimate tensile strength and the elastic modulus of the dermis [41]. Fewer studies derive non-linear model parameters through a finite element based inverse analysis [70]. Finite strain models usually require an inverse scheme to identify model parameters that match prediction and observation. Time-independent models are typically associated with quasi-static loading conditions, in the form of slow loading rates.

Flynn et al. [71] presented a setup to measure the three-dimensional force-displacement response of in vivo skin in multiple directions. The system captures the nonlinear and viscoelastic skin behavior at different measurement sites and allows to determine the anisotropic properties of skin by gradually changing the loading direction. As one of the few studies found in literature, the resulting data set is used to fit an anisotropic material model [72].

Recent studies were able to visualize local microstructural tissue deformation, often using Two-Photon Excited Fluorescence or second harmonic generation (SHG), while gradually loading the sample [29, 30]. Bancelin et al. [30] show that mice dermal collagen matrix undergoes three characteristic mechanisms in uniaxial tension experiments: (i) realignment of collagen fibers along the principal direction of stretch during the early loading phase; noticeable levels of stretch at low loads and low stiffness, (ii) tissue stiffening due to the recruitment of load bearing fibers aligned with the primary direction of loading, and (iii) a linear regime in the stress strain curve due to intra-and interfibrillar sliding in collagen fibers. Tissue loaded beyond its fracture point leads to widespread breakage of fibrils and their immediate recoil [70]. The distribution of fiber orientation is strongly coupled to the stiffness regime of the tissue and highlights the relevance of properly accounting for in vivo stress.

Pensalfini et al. [29] analyzed excised mice skin samples including a previously induced excisional wound. Uniaxial tension tests were performed to visualize the heterogeneity within the strain field of the wound region [29]. It was observed that skin tissue around the wound can be divided into mechanically distinct regions displaying microstructurally motivated stretch patterns. While skin in the core of the wound showed little extensibility, a highly compliant zone next to the wound accommodates the majority of tissue deformation. Concomitant histological analysis and SHG imaging demonstrated that the presence of the compliant region avoids the recruitment of newly deposited collagen fibers in the early phase of healing.

3.4 Other Testing Methods

Other, less common, skin testing methods include torsion testing, the bulge method, and static and dynamic shear load methods. Torsion experiments were among the earliest applied to characterize the in vivo response of skin [73, 74] and inspired the development of suction devices in later years. Bulge tests performed by [75] provided information on the macroscopic biaxial response of skin and reported stiffness values of around 11 MPa for the linear regime of the stress-strain curve; strikingly, a tenfold increase in skin stiffness was observed from the toe region to the linear regime with an average transition stretch value of 1.1. And lastly, full thickness shear measurements indicated a large variation of around 100% in the shear modulus depending on depth [76]. Epidermis was found to be almost two times stiffer than dermis in these large amplitude shear oscillatory tests, which is in contrast with the common claim that the mechanical response of the epidermis has negligible influence [53].

3.5 Summary

The review of experimental data on in vivo and ex vivo human skin highlights the complex nature of skin biophysics. Its mechanical behavior is nonlinear, viscoelastic, and anisotropic. Significant differences between in vivo and ex vivo measurements exist, and they might be linked with the level of in vivo tension of skin, which is difficult to quantify or reproduce in ex vivo settings. This poses a significant limitation, as most computational models assume a stress-free initial state. Knowledge of the physiological loading state of skin is relevant also for the assessment of the mechanical biocompatibility of tissue engineered skin substitutes and their scaffolds [27, 77].

4 Constitutive Modeling

Modeling of the mechanical behavior of skin has been the objective of biomechanics studies for several decades and remains an active field of research [1]. Given the highly complex mechanical response of individual skin structures as well as the interaction at the interface of sublayers, skin modeling requires not only the formulation of a material model, but a corresponding representation of skin anatomy as well. In most studies reported in literature, skin is homogenized into a single layer including epidermis, dermis, and potentially even hypodermis. Fewer studies apply a multilayered representation and differentiate between epidermis, papillary and reticular layer of dermis, and hypodermis or SMAS [11, 78].

The interpretation of experimental data using inverse analysis depends on the chosen mathematical description of the stress-strain relation, as well as on the anatomic reconstruction. Very often, application specific skin models are developed, such as e.g. for the simulation of skin response to cosmetic products [79], the role of skin in facial expressions or mastication [6, 7], or the prediction of scar tissue formation due to suture tension [80]. Chapter "Constitutive Modelling of Skin Mechanics" reviews constitutive model formulations for skin. In this section, we will briefly discuss the different type of material model equations, their parameters and how they relate to the inverse analysis of experimental data.

Early models focused on integrative strategies to represent the mechanical response of individual constituents of the extracellular matrix [81]. Such collagen-based models represent the degree of fibers undulation and its progressive reduction as the matrix deforms. Evidence based implementation of these models requires a thorough characterization of the microstructure for each sublayer of the skin. For most specific applications such level of detail is unknown, and experiments may not provide the information relevant to respective length scales and structures. Hence, most material models proposed in literature generally homogenize the tissues response and aim at reproducing the experimentally observed stress-strain curves [12]. Next to physically motivated formulations for structural models, commonly

used constitutive models are often based on phenomenological parameters. A common assumption is that skin behaves as incompressible, although no experimental evidence was reported on this property. Corresponding measurements are needed, since recent findings indicates that interstitial fluid motion might lead to significant volume changes in soft collagenous tissues [82]. The most relevant model equations applied for the analysis of experiments on skin are listed below. Many of these material models include a large number of parameters which cannot be measured directly and require an inverse identification scheme, as will be discussed in the following section. Table 1 summarizes material models frequently found in skin literature.

5 Parameter Identification Methods

Constitutive model parameter identification is a broad field of research and a variety of optimization schemes were proposed in the literature. Within the specific context of skin modeling, there are a few popular approaches that have proven useful for the identification of potentially large parameter sets. The following section provides a summary of these optimization schemes specific to skin models.

On the most abstract level, the choice of the appropriate optimization scheme depends on the availability of an analytical expression for the relation between stress and strain of the experiment providing the data. If skin is treated as a linear or nonlinear solid, such analytical solutions exists for all commonly applied loading conditions including uniaxial and planar biaxial tension/compression experiments [97]. Model parameters are then identified by a least-squares fit analysis which minimizes the sum of squared differences between the experimentally observed force-deformation (or stress-strain) curve and corresponding model predictions. These tests are usually performed on ex vivo or in vitro skin tissue samples. In vivo skin tissue measurements usually involve more complex deformation patterns for which no analytical expression exists. In these cases, the relation between material constants and experimental data is implicit and requires a numerical approach to determine a set of material parameters that minimizes the difference between the observed and predicted tissue response [11].

Optimization schemes minimize an objective function which may or may not explicitly depend on the model parameters. Two general classes of optimization algorithms exist: In one case, algorithms require an analytical or numerical evaluation of the objective function's gradients in the model parameter space [98]; the second class are derivative-free methods and include so called simplex algorithms [99].

Derivative-free methods have proven most useful in skin mechanics because they provide robust schemes for multidimensional parameter spaces [97]. Most skin models discussed in chapter "Constitutive Modelling of Skin Mechanics" have a large number of model parameters and assume a geometrically and structurally complex representation of skin, and therefore require the use of heuristic search

Table 1 Common constitutive models, main model features, number of parameters m, and accompanying experiments to identify model parameters

Model	Main features	m	Accompanying experiments
Neo–Hookean, Mooney–Rivlin, and Ogden (1)	Isotropic, hyperelastic	2–6	In vivo suction [53, 83]; in vivo indentation [59]; in vivo multiaxial extension [71, 72, 84]
Tong and Fung (2)	Anisotropic, nonlinear	13	Ex vivo uni- and biaxial tension and relaxation [85, 86]; in vivo multiaxial extension [87]
Lanir (3)	Anisotropic, viscoelastic	>11	Ex vivo uni- and biaxial tension and relaxation [85, 86]; in vivo uniaxial tension [88]
Weiss (4)	Transversely isotropic, hyperelastic	14	Ex vivo tensile tests [89]
Bischoff–Arruda–Grosh (5)	Anisotropic, viscoelastic	15	Ex vivo biaxial tension and relaxation [85, 86]
Rubin–Bodner (6)	Anisotropic, elastic-viscoplasticity	14	Ex vivo biaxial tension and relaxation [85, 86]; in vivo suction [11, 47]
Limbert (7)	Transversely isotropic, viscoelastic	23	Ex vivo biaxial tension and relaxation [85, 86]
Flynn–Rubin–Nielsen (8)	Discrete fiber model	11	Ex vivo biaxial tension [85, 86] ex vivo uniaxial tension

Labels in model column: 1—Rivlin [90], Ogden [91]; 2—Tong and Fung [92]; 3—Lanir [81]; 4—Weiss et al. [93]; 5—Bischoff et al. [94]; 6—Rubin and Bodner [67]; 7—Limbert [95]; 8—Flynn et al. [96]

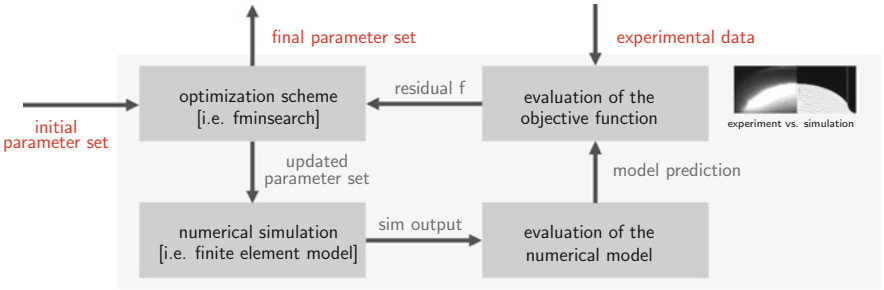

Fig. 4 Common implementation of inverse analysis algorithms (e.g. the *fminsearch* algorithm) for skin parameter identification schemes. The optimization scheme iteratively determines a model parameter set that minimizes the error between experimental data and the associated numerical simulation. During each iteration, a finite element simulation is necessary to predict the model response based on the updated parameter set

methods that are more likely to find a minimum of the objective function. Several implementations of derivative-free optimization schemes exist, and the fminsearch function in Matlab (The MathWorks Inc., Natick, Massachusetts, US) is widely used throughout skin literature. The fminsearch function uses the Nelder-Mead simplex algorithm [100, 101]: in an n-dimensional parameter space, the algorithm maintains n + 1 test points arranged as a simplex. The behavior of the objective function measured at each test point is used to extrapolate new test points and to replace those, that provide the worst response. Different strategies exist to update the test points and the algorithm will stop if the sample standard deviation of the objective function falls below a prescribed tolerance. As shown in Fig. 4, an initial parameter set is iteratively updated through an optimization algorithm, i.e. the *fminsearch* function, to minimize the error between experimental data and the associated numerical simulation. During each iteration, a finite element simulation is necessary to determine the model response based on the updated parameter set. The number of parameters, the number of simulations necessary per iteration, and the degree of coupling between parameters determine the required computation time and the uniqueness of the final parameter set.

Several groups working on skin mechanics have developed specialized optimization schemes, that range from a simultaneous fit of all model parameters to a sequential determination for individual layers and loading conditions. Weickenmeier et al. [11] performed suction experiments with varying probe opening diameters to recruit superficial and deeper skin layers individually. An initial sensitivity analysis of the accompanying multi-layered finite element skin model revealed strong coupling between material parameters as well as a significant influence of individual layers on the deformation field for different probe opening diameters. Sequential fitting of individual layers resulted in a stiffness ratio between the superficial and deep layer corresponding to two orders of magnitude difference [47]. The simultaneous fitting of superficial and deep material parameters using four different loading conditions to capture the instantaneous and transient response of

skin, provided more homogeneous results [11] which seem more reasonable in view of previously reported ex-vivo mechanical analysis of dermal tissue and SMAS [67].

Hendrik and co-authors presented a series of suction based skin experiments and corresponding model parameter fits [52, 53, 102]. While initially working with a single layer model [53, 102] and later extending skin to a two-layer model, Hendrik et al. used a constrained nonlinear optimization function based on Sequential Quadratic Programming (SQP), to determine all material parameters in parallel. Their two-layer model predicted three orders of magnitude difference between superficial and deeper layers. This outcome is motivated by the finite element model implementation and the weight of individual measurement curves on the overall cost function.

Flynn and co-authors' in vivo multi-axial skin loading device requires a finite element model for data analysis [96]. In a process similar to previously presented schemes, model parameters of a single layer skin model-including in vivo stress-are determined based on a nonlinear least-squares curve fitting algorithm. Based on the trust region method, a set of initial parameters is iteratively improved to minimize the error between experiment and model, while running a finite element simulation at each iteration to evaluate the model-based tissue response. Two different models were tested: an isotropic Ogden model [91] and the anisotropic Tong and Fung model [92]. The total number of parameters fit simultaneously were 4, 6, and 8, depending on the model formulation. The error function was calculated as the sum over all measurement directions and the in vivo stress level was used to represent the anisotropy of the tissue response. Jor et al. [103], using the same experimental setup, aimed at fitting a microstructurally motivated constitutive relation with 7 parameters.

With the emergence of experimental methods combining force measurements with video imaging of the accompanying deformation field, more elaborate and localized inversion schemes are presented in literature. The quantitative assessment of the heterogeneity of the deformation fields allows to determine material parameters at a local scale and are based on so called full-field methods. Avril et al. [104] presents an overview of corresponding inverse analysis schemes. In comparison to the above-mentioned methods, the new approaches solve the nonlinear elasticity equations based on the pointwise experimentally observed deformation field. This procedure allows using derivative-based methods, which are more reliable in that they are more likely to provide a global minimum. The associated increase in computational cost to evaluate the derivative of the objective function is often linked with the requirement of increased computational power.

6 Outlook

Skin is a complex biological system that is characterized by an intricate interplay between individual tissue layer and ECM components at different length scales. The interaction of the different components of the extracellular matrix and the different

layers depends on the state of deformation imposed to the skin, with different mechanisms influencing in-plane tension, in-plane or out-of-plane shear, and skin bending. Although a large number of mechanical tests has been conducted, our understanding of full-thickness skin behavior remains incomplete. New integrative testing methods, i.e. simultaneous visualization of tissue and microstructure kinematics during mechanical response to a wide range of loading conditions, as well as the analysis of skin properties in relation to observable microstructural parameters, represent promising approaches to improve our understanding of skin mechanics.

The range of mechanical properties reported in literature and the dependence of the mechanical response on the testing method used continues to represent a major challenge in determining a universal description of skin mechanics. In this context, a specific problem is represented by the mismatch in stiffness reported for different tissue length scales interrogated in the different experiments. The quantification of in vivo stress represents another critical question in skin mechanics: As most computational models assume a test specific stress-free initial state, existing parameter sets proposed in literature are likely to grossly misrepresent the actual in-vivo response of skin tissue.

Anatomy based skin models used in parameter identification schemes will become more reliable as we continue to improve our understanding of the relation between local microstructure and mechanical response. Essential input will be obtained through in vivo and ex vivo application of full field methods and the associated model parameter identification procedures. The systematic combination of computer-based modeling and multiscale experimental data acquisition will facilitate the development of biomechanical and mechanobiological models with enhanced predictive capabilities. Improved understanding of skin biomechanics will allow future research to focus on highly relevant medical questions, such as impaired wound healing, skin suturing, reconstructive surgery, skin tissue engineering, as well as diagnosis and monitoring of specific skin diseases.

References

1. Jor JWY, Parker MD, Taberner AJ, Nash MP, Nielsen PMF (2013) Computational and experimental characterization of skin mechanics: identifying current challenges and future directions. Wiley Interdiscip Rev Syst Biol Med 5(5):539–556
2. Hani AFM (2014) Surface imaging for biomedical applications. CRC, Boca Raton
3. Forbes SJ, Rosenthal N (2014) Preparing the ground for tissue regeneration: from mechanism to therapy. Nat Med 20(8):857
4. Murphy PS, Evans GRD (2012) Advances in wound healing: a review of current wound healing products. Plast Surg Int 2012:8. https://doi.org/10.1155/2012/190436
5. Rowan MP, Cancio LC, Eric A, Burmeister DM, Rose LF, Natesan S, Chan RK, Christy RJ, Chung KK (2015) Burn wound healing and treatment: review and advancements. Crit Care 19(1):243
6. Weickenmeier J, Wu R, Lecomte-Grosbras P, Witz J-F, Brieu M, Winklhofer S, Andreisek G, Mazza E (2014) Experimental characterization and simulation of layer interaction in facial soft tissues. In: Intrnational symposium on biomedical simulation. Springer, Cham, pp 233–241

7. Limbert G, Kuhl E (2018) On skin microrelief and the emergence of expression microwrinkles. Soft Matter 14(8):1292–1300
8. Buganza Tepole A, Joseph Ploch C, Wong J, Gosain AK, Kuhl E (2011) Growing skin: a computational model for skin expansion in reconstructive surgery. J Mech Phys Solids 59(10):2177–2190
9. Zöllner AM, Buganza Tepole A, Gosain AK, Kuhl E (2012) Growing skin: tissue expansion in pediatric forehead reconstruction. Biomech Model Mechanobiol 11(6):855–867
10. Lee T, Turin SY, Gosain AK, Tepole AB (2018) Multi-view stereo in the operating room allows prediction of healing complications in a patient-specific model of reconstructive surgery. J Biomech 74:202–206
11. Weickenmeier J, Jabareen M, Mazza E (2015) Suction based mechanical characterization of superficial facial soft tissues. J Biomech 48(16):4279–4286
12. Limbert G (2017) Mathematical and computational modelling of skin biophysics: a review. Phil Trans R Soc A 473(2203):20170257
13. Oomens C (2017) Mechanical behaviour of skin: the struggle for the right testing method. In: Avril S, Evans S (eds) Material parameter identification and inverse problems in soft tissue biomechanics. Springer, Cham, pp 119–132
14. Koehler MJ, Lange-Asschenfeldt S, Kaatz M (2011) Non-invasive imaging techniques in the diagnosis of skin diseases. Expert Opin Med Diagn 5(5):425–440
15. Wong R, Geyer S, Weninger W, Guimberteau J-C, Wong JK (2016) The dynamic anatomy and patterning of skin. Exp Dermatol 25(2):92–98
16. Weissleder R (2011) A clearer vision for in vivo imaging. Nat Biotechnol 19:316–317
17. Blausen Medical (2014) Dermal circulation. WikiJ Med 1(2):10
18. LaTrenta G (2004) Atlas of aesthetic face and neck surgery. W.B. Saunders, Philadelphia
19. Aspres N, Egerton IB, Lim AC, Shumack SP (2003) Imaging of Skin. Australas J Dermatol 44(1):19–27
20. Mirrashed F, Sharp JC (2004) In vivo morphological characterisation of skin by MRI microimaging methods. Skin Res Technol 10(3):149–160
21. Barral JK, Bangerter NK, Hu BS, Nishimura DG (2010) In vivo high-resolution magnetic resonance skin imaging at 1.5 T and 3 T. Magn Reson Med 63(3):790–796
22. Van Mulder TJS, de Koeijer M, Theeten H, Willems D, Van Damme P, Demolder M, De Meyer GRY, Beyers KCL, Vankerckhoven V (2017) High frequency ultrasound to assess skin thickness in healthy adults. Vaccine 35(14):1810–1815
23. Kleinerman R, Whang TB, Bard RL, Marmur ES (2012) Ultrasound in dermatology: principles and applications. J Am Acad Dermatol 67(3):478–487
24. Wortsman, Ximena, Jacobo Wortsman, Laura Carreño, Claudia Morales, Ivo Sazunic, Gregor B. E. Jemec 2013 Sonographic anatomy of the skin, appendages, and adjacent structures. Springer, New York. https://link.springer.com/chapter/10.1007/978-1-4614-7184-4_2. Accessed 29 Apr 2018
25. Weickenmeier J (2015) Investigation of the mechanical behavior of facial soft tissues. ETH Zurich, Zurich
26. Pensalfini M, Weickenmeier J, Rominger MB, Santoprete R, Distler O, Mazza E (2018) Location-specific mechanical response and morphology of facial soft tissues. J Mech Behav Biomed Mater 78:108–115
27. Pensalfini M, Ehret AE, Stüdeli S, Marino D, Kaech A, Reichmann E, Mazza E (2017) Factors affecting the mechanical behavior of collagen hydrogels for skin tissue engineering. J Mech Behav Biomed Mater 69:85–97
28. Chen Z, Rank E, Meiburger KM, Sinz C, Hodul A, Zhang E, Hoover E et al (2017) Non-invasive multimodal optical coherence and photoacoustic tomography for human skin imaging. Sci Rep 7(1):17975
29. Pensalfini M, Haertel E, Hopf R, Wietecha M, Werner S, Mazza E (2018) The mechanical fingerprint of murine excisional wounds. Acta Biomater 65:226–236
30. Bancelin S, Lynch B, Bonod-Bidaud C, Ducourthial G, Psilodimitrakopoulos S, Dokládal P, Allain J-M, Schanne-Klein M-C, Ruggiero F (2015) Ex vivo multiscale quantitation of skin

biomechanics in wild-type and genetically-modified mice using multiphoton microscopy. Sci Rep 5(1):17635–17635
31. Yasui T, Takahashi Y, Ito M, Fukushima S, Araki T (2009) Ex vivo and in vivo second-harmonic-generation imaging of dermal collagen fiber in skin: comparison of imaging characteristics between mode-locked Cr:forsterite and Ti:sapphire lasers. Appl Opt 48(10):D88–D95
32. Adabi S, Hosseinzadeh M, Noei S, Conforto S, Daveluy S, Clayton A, Mehregan D, Nasiriavanaki M (2017) Universal in vivo textural model for human skin based on optical coherence tomograms. Sci Rep 7(1):17912
33. Avanaki MR, Hojjatoleslami A, Sira M, Schofield JB, Jones CA, Podoleanu AG (2013) Investigation of basal cell carcinoma using dynamic focus optical coherence tomography. Appl Opt 52(10):2116–2124
34. Yasui T, Tohno Y, Araki T (2004) Characterization of collagen orientation in human dermis by two-dimensional second-harmonic-generation polarimetry. J Biomed Opt 9(2):259–264
35. Chen X, Nadiarynkh O, Plotnikov SV, Campagnola PJ (2012) Second harmonic generation microscopy for quantitative analysis of collagen fibrillar structure. Nat Protoc 7(4):654–669
36. Chen S-Y, Chen S-U, Hai-Yin W, Lee W-J, Liao Y-H, Sun C-K (2010) In vivo virtual biopsy of human skin by using noninvasive higher harmonic generation microscopy. IEEE J Sel Top Quantum Electron 13(3):478–492
37. Shirshin EA, Gurfinkel YI, Priezzhev AV, Fadeev VV, Lademann J, Darvin ME (2017) Two-photon autofluorescence lifetime imaging of human skin papillary dermis in vivo: assessment of blood capillaries and structural proteins localization. Sci Rep 7(1):1171
38. Koehler MJ, Hahn S, Preller A, Elsner P, Ziemer M, Bauer A, König K, Bückle R, Fluhr JW, Kaatz M (2008) Morphological skin ageing criteria by multiphoton laser scanning tomography: non-invasive in vivo scoring of the dermal fibre network. Exp Dermatol 17(6):519–523
39. Pond D, McBride AT, Davids LM, Reddy BD, Limbert G (2018) Microstructurally-based constitutive modelling of the skin – linking intrinsic ageing to microstructural parameters. J Theor Biol 444:108–123
40. Achterberg VF, Buscemi L, Diekmann H, Smith-Clerc J, Schwengler H, Meister J-J, Wenck H, Gallinat S, Hinz B (2014) The nano-scale mechanical properties of the extracellular matrix regulate dermal fibroblast function. J Investig Dermatol 134(7):1862–1872
41. Annaidh AN, Bruyère K, Destrade M, Gilchrist MD, Otténio M (2012) Characterization of the anisotropic mechanical properties of excised human skin. J Mech Behav Biomed Mater 5(1):139–148
42. Dobrev H (2005) Application of Cutometer area parameters for the study ofhuman skin fatigue. Skin Res Technol 11(2):120–122
43. Luebberding S, Krueger N, Kerscher M (2014) Mechanical properties of human skin in vivo: a comparative evaluation in 300 men and women. Skin Res Technol 20(2):127–135
44. Krueger N, Luebberding S, Oltmer M, Streker M, Kerscher M (2011) Age-related changes in skin mechanical properties: a quantitative evaluation of 120 female subjects. Skin Res Technol 17(2):141–148
45. Ryu HS, Joo YH, Kim SO, Park KC, Youn SW (2008) Influence of age and regional differences on skin elasticity as measured by the Cutometer. Skin Res Technol 14(3):354–358
46. Diridollou S, Black D, Lagarde JM, Gall Y, Berson M, Vabre V, Patat F, Vaillant L (2000) Sex-and site-dependent variations in the thickness and mechanical properties of human skin in vivo. Int J Cosmet Sci 22(6):421–435
47. Barbarino GG, Jabareen M, Mazza E (2011) Experimental and numerical study on the mechanical behavior of the superficial layers of the face. Skin Res Technol 17(4):434–444
48. Luboz V, Promayon E, Payan Y (2014) Soft tissue finite element modeling and calibration of the material properties in the context of computer-assisted medical interventions. Ann Biomed Eng 42(11):2369–2378

49. Kim MA, Kim EJ, Lee HK (2018) Use of SkinFibrometer® to measure skin elasticity and its correlation with Cutometer® and DUB® Skinscanner. Skin Res Technol 24(3):466–471
50. Nava A, Mazza E, Kleinermann F, Avis NJ, McClure J (2003) Determination of the mechanical properties of soft human tissues through aspiration experiments. In: International Conference on Medical Image Computing and Computer-Assisted Intervention. Springer, New York, pp 222–229
51. Iivarinen JT, Korhonen RK, Julkunen P, Jurvelin JS (2013) Experimental and computational analysis of soft tissuemechanical response under negative pressure in forearm. Skin Res Technol 19(1):356–365
52. Hendriks F, Brokken D, Oomens C, Bader D, Baaijens F (2006) The relative contributions of different skin layers to the mechanical behavior of human skin in vivo using suction experiments. Med Eng Phys 28(3):259–266
53. Hendriks F, Brokken D, Van Eemeren J, Oomens C, Baaijens F, Horsten J (2003) A numerical-experimental method to characterize the non-linear mechanical behaviour of human skin. Skin Res Technol 9(3):274–283
54. Schlangen LJM, Brokken D, Van Kemenade PM (2003) Correlations betwen small aperture skin suction parameter- statistical analysis and mechanical model. Skin Res Technol 9(2):122–130
55. Bonaparte JP, Chung J (2014) The effect of probe placement on inter-trial variability when using the Cutometer MPA 580. J Med Eng Technol 38(2):85–89
56. Bonaparte JP, Ellis DA, Chung J (2013) The effect of probe to skin contact force on Cutometer MPA 580 measurements. J Med Eng Technol 37(3):208–212
57. Boyer G, Laquièze L, Le Bot A, Laquièze S, Zahouani H (2009) Dynamic indentation on human skin in vivo: ageing effects. Skin Res Technol 15(1):55–67
58. Pailler-Mattei C, Debret R, Vargiolu R, Sommer P, Zahouani H (2013) In vivo skin biophysical behaviour and surface topography as a function of ageing. J Mech Behav Biomed Mater 28:474–483
59. Delalleau A, Josse G, Lagarde J-M, Zahouani H, Bergheau J-M (2006) Characterization of the mechanical properties of skin by inverse analysis combined with the indentation test. J Biomech 39(9):1603–1610
60. Zahouani H, Vargiolu R, Boyer G, Pailler-Mattéi C, Laquièze L, Mavon A (2009) Friction noise of human skin in vivo. Wear 267(2):1274–1280
61. Zahouani H, Boyer G, Pailler-Mattéi C, Ben Tkaya M, Vargiolu R (2011) Effect of human ageing on skin rheology and tribology. Wear 271:2364–2369
62. Tupin S, Molimard J, Cenizo V, Hoc T, Sohm B, Zahouani H (2016) Multiscale approach to characterize mechanical properties of tissue engineered skin. Ann Biomed Eng 44(9):2851–2862
63. Grant CA, Twigg PC, Tobin DJ (2012) Static and dynamic nanomechanical properties of human skin tissue using atomic force microscopy: effect of scarring in the upper dermis. Acta Biomater 8(11):4123–4129
64. Geerligs M, van Breemen L, Peters GWM, Ackermans PAJ, Baaijens FF, Oomens C (2011) In vitro indentation to determine the mechanical properties of epidermis. J Biomech 44(6):1176–1181
65. Langer K (1862) Zur Anatomie und Physiologie der Haut – II – Die spannung der cutis. Sitzungsberchte der Mathematisch-naturwissenschaftlicher Classe der. Kaiserlichen Akademie der Wissenschaften 45:133
66. Langer K (1978) On the anatomy and physiology of the skin: I. The cleavability of the cutis. Br J Plast Surg 31(1):3–8
67. Rubin MB, Bodner SR (2002) A three-dimensional nonlinear model for dissipative response of soft tissue. Int J Solids Struct 39(19):5081–5099
68. Har-Shai Y, Bodner SR, Egozy-Golan D, Lindenbaum ES, Ben-Izhak O, Mitz V, Hirshowitz B (1996) Mechanical properties and microstructure of the superficial musculoaponeurotic system. Plast Reconstr Surg 98(1):59–70

69. Shergold OA, Fleck NA, Radford D (2006) The uniaxial stress versus strain response of pig skin and silicone rubber at low and high strain rates. Int J Impact Eng 32(9):1384–1402
70. Yang W, Sherman VR, Gludovatz B, Schaible E, Stewart P, Ritchie RO, Meyers MA (2015) On the tear resistance of skin. Nat Commun 6:6649
71. Flynn C, Taberner AJ, Nielsen PMF (2011) Measurement of the force–displacement response of in vivo human skin under a rich set of deformations. Med Eng Phys 33(5):610–619
72. Flynn C, Taberner A, Nielsen P (2011) Modeling the mechanical response of in vivo human skin under a rich set of deformations. Ann Biomed Eng 39(7):1935–1946
73. Sanders R (1973) Torsional elasticity of human skin in vivo. Pflügers Archiv Eur J Phys 342(3):255–260
74. Escoffier C, de Rigal J, Rochefort A, Vasselet R, Lévêque J-L, Agache PG (1989) Age-related mechanical properties of human skin- an in vivo study. J Investig Dermatol 93(3):353–357
75. Tonge TK, Atlan LS, Voo LM, Nguyen TD (2013) Full-field bulge test for planar anisotropic tissues: part I–experimental methods applied to human skin tissue. Acta Biomater 9(4):5913–5925
76. Lamers E, T.H.S v K, F.P.T B, G.W.M P, C.W.J O (2013) Large amplitude oscillatory shear properties of human skin. J Mech Behav Biomed Mater 28:462–470
77. Mazza E, Ehret AE (2015) Mechanical biocompatibility of highly deformable biomedical materials. J Mech Behav Biomed Mater 48:100–124
78. Leyva-Mendivil MF, Page A, Bressloff NW, Limbert G (2015) A mechanistic insight into the mechanical role of the stratum corneum during stretching and compression of the skin. J Mech Behav Biomed Mater 49:197–219
79. Boissieux L, Kiss G, Thalmann NM, Kalra P 2000 Simulation of skin aging and wrinkles with cosmetics insight.https://link.springer.com/chapter/10.1007/978-3-7091-6344-3_2. Accessed 8 Apr 2018
80. Lee T, Vaca EE, Ledwon JK, Bae H, Topczewska JM, Turin SY, Kuhl E, Gosain AK, Buganza A (2018) Improving tissue expansion protocols through computational modeling. J Mech Behav Biomed Mater 82:224–234
81. Lanir Y (1983) Constitutive equations for fibrous connective tissues. J Biomech 16(1):1–12
82. Ehret AE, Bircher K, Stracuzzi A, Marina V, Zündel M, Mazza E (2017) Inverse poroelasticity as a fundamental mechanism in biomechanics and mechanobiology. Nat Commun 8(1):1002
83. Delalleau A, Josse G, Lagarde J-M, Zahouani H, Bergheau J-M (2008) A nonlinear elastic behavior to identify the mechanical parameters of human skin in vivo. Skin Res Technol 14(2):152–164
84. Evans SL, Holt CA (2009) Measuring the mechanical properties of human skin in vivo using digital image correlation and finite element modelling. J Strain Anal Eng Des 44(5):337–345
85. Lanir Y, Fung YC (1974) Two-dimensional mechanical properties of rabbit skin—II. Experimental results. J Biomech 7(2):171–174
86. Lanir Y, Fung YC (1974) Two-dimensional mechanical properties of rabbit skin—I. Experimental system. J Biomech 7(1):29–34
87. Kvistedal YA, Nielsen PMF (2009) Estimating material parameters of human skin in vivo. Biomech Model Mechanobiol 8(1):1–8
88. Meijer RR, Douven LL, Oomens CC (1999) Characterisation of anisotropic and non-linear behaviour of human skin in vivo. Comput Methods Biomech Biomed Eng 2(1):13–27
89. Groves RB, Coulman S, Birchall J, Evans SL (2013) An anisotropic, hyperelastic model for skin: experimental measurements, finite element modelling and identification of parameters for human and murine skin. J Mech Behav Biomed Mater 18:167–180
90. Rivlin R (1948) Large elastic deformations of isotropic materials. IV. Further developments of the general theory. Phil Trans R Soc A 241(835):379–397
91. Ogden R (1972) Large deformation isotropic elasticity – on the correlation of theory and experiment for incompressible rubberlike solids. Proc R Soc Lond A Math Phys Sci 326(1567):565–584
92. Tong P, Fung YC (1976) The stress-strain relationship for the skin. J Biomech 9(10):649–657

93. Weiss JA, Maker BN, Govindjee S (1996) Finite element implementation of incompressible, transversely isotropic hyperelasticity. Comput Methods Appl Mech Eng 135:107–128
94. Bischoff JE, Arruda EM, Grosh K (2000) Finite element modeling of human skin using an isotropic, nonlinear elastic constitutive model. J Biomech 33(6):645–652
95. Limbert G (2011) A mesostructurally-based anisotropic continuum model for biological soft tissues–decoupled invariant formulation. J Mech Behav Biomed Mater 4(8):1637–1657
96. Flynn C, Rubin MB, Nielsen PMF (2011) A model for the anisotropic response of fibrous soft tissues using six discrete fibre bundles. Int J Numer Meth Biomed Eng 27(11):1793–1811
97. Avril S (2017) Overview of identification methods of mechanical parameters based on full-field measurements. In: Avril S, Evans S (eds) Material parameter identification and inverse problems in soft tissue biomechanics, vol 573. Springer, Cham, pp 37–66
98. Koziel S, Yang X-S (2011) Computational optimization, methods and algorithms. Springer, Berlin Heidelberg
99. Conn AR, Scheinberg K, Vicente LN (2009) Introduction to derivative-free optimization. SIAM, Philadelphia
100. Lagarias JC, Reeds JA, Wright MH, Wright PE (1998) Convergence properties of the Nelder-Mead simplex method in low dimensions. SIAM J Optim 9(1):112–147
101. Nelder JA, Mead R (1965) A simplex method for function minimization. Comput J 7:308–313
102. Hendriks F, Brokken D, Oomens C, Baaijens F (2004) Influence of hydration and experimental length scale on the mechanical response of human skin in vivo, using optical coherence tomography. Skin Res Technol 10(4):231–241
103. Jor JWY, Nash MP, Nielsen PMF, Hunter PJ (2011) Estimating material parameters of a structurally based constitutive relation for skin mechanics. Biomech Model Mechanobiol 10(5):767–778
104. Avril S, Bonnet M, Bretelle A-S, Grédiac M, Hild F, Ienny P, Latourte F et al (2008) Overview of identification methods of mechanical parameters based on full-field measurements. Exp Mech 48:381–402

Experimental Characterisation: Rich Deformations

Cormac Flynn

Abstract Human skin is a complex material that exhibits a non-linear stress-strain response, anisotropy, and viscoelasticity. In addition, skin in vivo is under an anisotropic pre-stress, which varies according to location and person. While several methods have been developed to measure the in vivo mechanical response of skin, many of these are incapable of characterising the anisotropy. Few also attempt to measure the in vivo stress. To quantify the anisotropy, it is necessary to apply deformations to the skin in a number of directions. This chapter provides an overview of a method where a rich set of deformations are applied to the surface of the skin and the nonlinear, anisotropic, and viscoelastic response is characterised using finite element analyses and nonlinear optimisation. The in vivo stress is also estimated. Different constitutive models were tested as to their suitability to represent skin. Material parameters and pre-stresses were identified for points on the anterior forearm, upper arm, and the face.

1 Introduction

The mechanical characterisation of human skin is driven by its application in a broad range of disciplines. Better knowledge of skin properties would lead to improved identification and treatment of certain diseases [7, 20, 26]. The development of consumer products, such as razors, sanitary pads, nappies, and sticking plasters would benefit from better mechanical knowledge of the skin they are in contact with [8, 24, 42]. More recently, wearable sensors and trans-dermal patches are required to adhere to, stretch and deform with the skin they are attached to for long periods [22, 28]. Characterisation of facial skin is particularly important for the development of realistic computational social agents [37] and social-care robots [25]. A challenge for both these fields is the development of facial models that cross the 'uncanny

C. Flynn (✉)
Galway-Mayo Institute of Technology, Galway, Ireland
e-mail: cormac.flynn@gmit.ie

G. Limbert (ed.), *Skin Biophysics*, Studies in Mechanobiology,
Tissue Engineering and Biomaterials 22,
https://doi.org/10.1007/978-3-030-13279-8_7

valley'—a phenomenon that proposes the more realistic artificial faces become the more eerie and repulsive to a perceiver they are [31].

There are many studies in the literature that characterise some aspects of the mechanical response of skin. The approaches taken are manifold including applying suction, normal indentation, torsion, in-plane shear, uniaxial and biaxial tension to the skin surface. Several of these methods, including suction and normal indentation are unable to characterise the anisotropic nature of skin due to their axisymmetrical loading. To capture the multi-directional properties of skin, it is necessary to apply deformations to the skin in a number of directions.

Reihsner et al. [36] derived elastic constants for in vitro skin samples by stretching them in-plane in a multi-axial tester. The six elastic constants were determined for each of the 16 skin sites sampled. Jor et al. [23] estimated the material parameters for a structural model of porcine skin by a combination of multi-axial in vitro stretching and digital image correlation (DIC). Affagard et al. [1] proposed an experimental protocol to improve the identification of material parameters for a single skin assay ex vivo. The protocol included uniaxial loading, equibiaxial loading, and alternated biaxial loading all combined with DIC. DIC combined with bulge tests have been recently used to characterise the anisotropic mechanical properties of ex vivo human skin [41].

While in vitro or ex vivo tests are valuable in determining detailed relationships between microstructure and mechanical response, it is of interest to characterise the skin in vivo. For instance, a clinician may want to measure the mechanical response of a patient's skin to track the progression of disease such as lymphoedema. Kvistedal and Nielsen [27] used a similar experimental set up as Jor et al. [23] to characterise in vivo forearm skin of several volunteers. They used nonlinear optimisation techniques to estimate the material parameters that best fit the Tong and Fung [40] model to each volunteer's skin. This protocol included attaching the skin to 16 pads, each of which were attached to an actuator. It is the opinion of the author that this protocol would be difficult and time consuming to use in the clinical setting.

Coutts et al. [7] used a uniaxial extensometer in two directions to characterise the in vivo skin anisotropy in breast cancer related lymphoedema. More recently, Then et al. [39] used an extensometer device in multiple directions to characterise the in vivo response of facial skin. The use of an extensometer has the disadvantage of having to reconfigure the apparatus for each direction. The reconfiguration introduces a delay in the acquisition of the data and uncertainty of the position at the skin site. Evans and Holt [11] pulled a wire attached to in vivo forearm skin in different directions and tracked the displacements using digital image correlation. Optimisation using a finite element model estimated Ogden material parameters and the in vivo strain. Multi-view stereo techniques have also been used to track deformations and growth of living skin [38]. These approaches have the distinct advantage of not having to reconfigure the instrumentation to measure the response in different directions.

This chapter presents an approach to characterise in vivo human skin using a micro-robotic device. Firstly, details of the force-sensitive micro-robot are pre-

sented. Secondly, the protocols for applying a rich set of deformations to areas of the arm and face are detailed. Thirdly, the constitutive models, finite element model, and non-linear optimisation techniques used to identify material parameters and in vivo stresses are introduced. Results from these experiments are detailed. Lastly, current challenges in determining the mechanical properties of in vivo human skin are discussed and future opportunities are identified.

2 Multi-Directional Characterisation of Skin Using a Micro-Robotic Device

This section presents details of the force-sensitive micro-robot and how it is used to measure the force-displacement response of different points on the face and arm. The finite element model used to simulate the experiments is introduced along with the constitutive models used to represent the skin. The section concludes with the non-linear optimisation procedure to identify model parameters.

2.1 Method or Applications

2.1.1 Force-Sensitive Micro-Robot

The micro-robot consisted of three parallel axes, which were driven by voice-coil actuators (BEI KIMCO LA10-12-027A) Fig. 1. These moved a platform in three-dimensional space. The axes were guided by precison linear slides (IKO BSP 730SL). On top of each axis there was a vee-jewel bearing. Inside each bearing sat a steel pivot, which was connected to the platform via a linear slide. Small springs prevented the steel pivots from lifting out of the bearings.

Three force-transducers (FSS1500NC, Honeywell, Freeport, IL, USA) were fixed to the moving platform at the apices of a 15-mm equilateral triangle. The legs of a rigid frame sat upon each force transducer. Two neodymium magnets on the frame and platform kept the frame in place on the force transducers.

On the tip of the frame sat a 4-mm-diameter cylindrical probe. The force acting on the probe was determined from the measured forces acting on the force transducers according to the relation:

$$\begin{bmatrix} R_X \\ R_Y \\ R_Z \end{bmatrix} = \begin{pmatrix} -\sqrt{3}w/2h & 0 & \sqrt{3}w/2h \\ -w/2h & w/h & -w/2h \\ -1 & -1 & -1 \end{pmatrix} \begin{bmatrix} F_X \\ F_Y \\ F_Z \end{bmatrix} \tag{1}$$

where R_X, R_Y, R_Z are the components of the probe tip reaction force. F_A, F_B, F_C are the measured forces, w is the distance from the centroid to an apex of the triangle

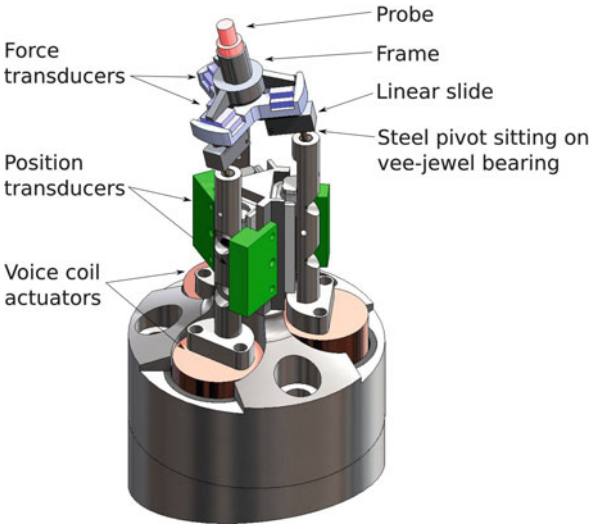

Fig. 1 Force-sensitive micro-robot. Reprinted by permission from Springer: Computer Methods in Biomechanics and Biomedical Engineering. Lecture Notes in Bioengineering, Gefen A., Weihs D., 2018

formed by the three force transducers, and h is the perpendicular distance between the probe tip and the base of the rigid frame.

Linear position transducers (RDC1014, ALPS, Campbell, CA, USA) measured the displacements of the parallel axes. Using a forward kinematics algorithm, the displacement of the probe tip was calculated. A LabView software interface (National Instruments, Austin, USA) controlled the motion of the probe and recorded the position and force data. Axes position feedback signals provide closed-loop position control. The integrated PID controller on the motion control card (NI 7358, National Instruments, Austin, USA) was used. The resolution of the probe tip displacement was 50 μm and the resolution of the measured force was 6 mN.

2.1.2 In vivo Experiments

The micro-robot applied a rich-set of deformations and measured the force response of different skin areas of the arms and faces of volunteers. On the right arm, areas on the posterior upper arm and anterior forearm were tested (Fig. 2a). On the face, six areas were tested: the centre of the right-hand cheek, the centre of the right-hand jaw, on the right-hand cheek near the lips, the right-hand parotideomasseteric region, the right-hand zygomatic region, and the centre of the forehead (Fig. 2b).

For each test, the relevant area of the face or arm was rested on a support plate positioned above the probe of the micro-robot. A hole in the support-plate allowed the probe to be attached to the skin using cyanoacrylate adhesive. A visual inspection after the tests indicated that the probe remained fixed to the surface of the skin throughout. For the arm experiments, double-sided tape was placed around the edge of the whole. As a result, skin in contact with the support plate did not move.

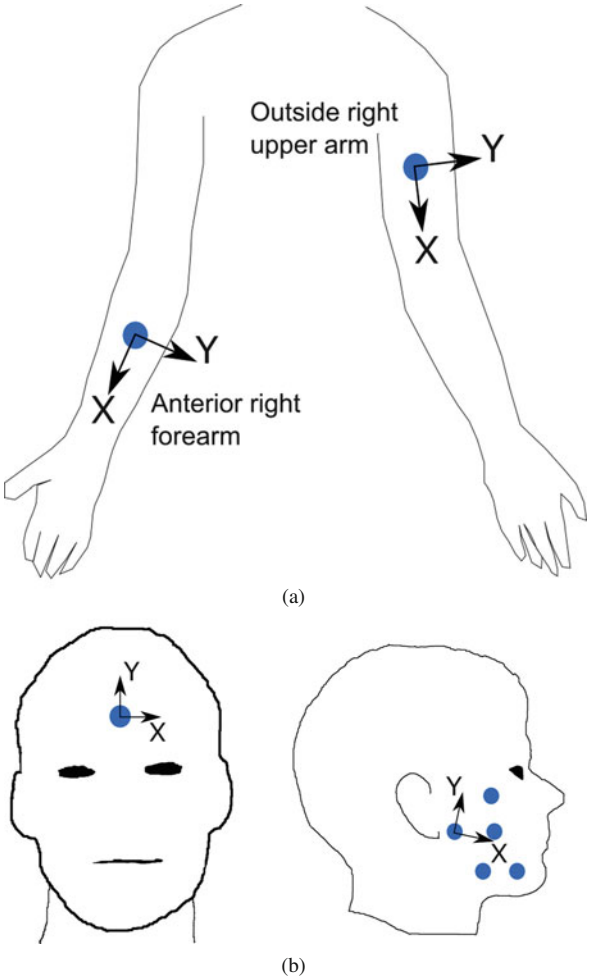

Fig. 2 Locations where the micro-robot probe was attached. (**a**) Arm locations; (**b**) face locations. X and Y axes indicate probe displacement coordinate axes (see Fig. 4). The orientation of the axes is the same for all locations on the face. Reprinted by permission from Springer: Computer Methods in Biomechanics and Biomedical Engineering. Lecture Notes in Bioengineering, Gefen A., Weihs D., 2018

This was verified through visual inspection. This provided a boundary condition for the finite element analyses described later. For the facial skin experiments, a boundary ring was attached using double-sided tape to the volunteer's face, centring it on the region of interest. The boundary ring slotted into a corresponding hole on the support plate in only one orientation. This ensured that the orientation of the face with respect to the micro-robot was known. Similar to the arm experiments, facial skin in contact with the boundary ring and support plate did not move (Fig. 3).

For all skin areas tested, the attached probe moved according to a rich set of deformations. For each direction, the probe moved according to three triangular wave cycles of frequency 0.1 Hz. Three cycles were used to precondition the skin. This was done to get a consistent skin response. It was found that the skin was pre-conditioned after one cycle. The probe was first moved in the plane of the skin

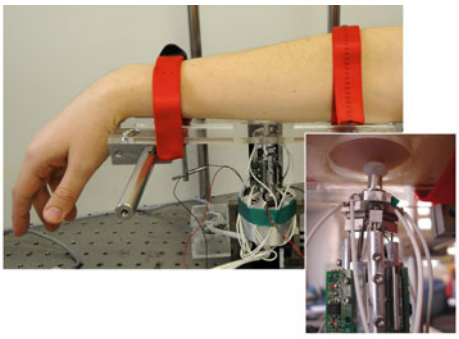

(a)

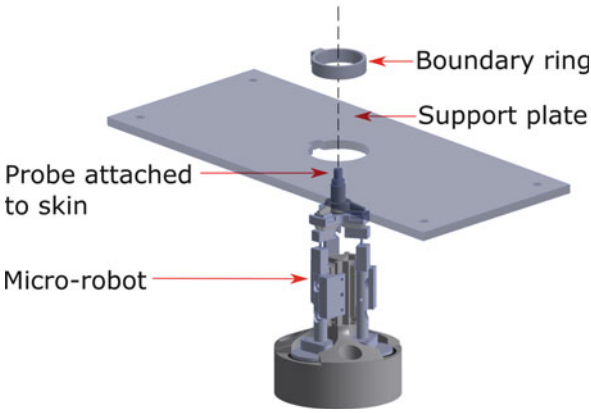

(b)

Fig. 3 Experimental set-up. (**a**) Arm experiments; (**b**) for the facial skin experiments, the boundary ring is attached to the volunteer's face and centred at one of the locations indicated in Fig. 2b. Reprinted by permission from Springer: Computer Methods in Biomechanics and Biomedical Engineering. Lecture Notes in Bioengineering, Gefen A., Weihs D., 2018

surface in a direction $\theta = 0°$ (Fig. 4). The amplitude of the displacement was approximately 1.2–1.4 mm depending on the local stiffness of the skin. The angle of the displacement was then increased in steps of 10°, 20°, or 30° up to $\theta = 180°$ for the arm locations and $\theta = 330°$ for the facial locations. Next a series of out-of-plane displacements were applied to the areas of interest, where $\theta = 0°$, 45°, and 90°, and $\phi = 45°$. The final displacement was in a direction normal to and away from the surface of the skin ($\theta = 0°, \phi = 90°$). There was no wait time between each direction.

The time, probe displacement, and probe reaction force was recorded for all tests on the arms and faces.

2.1.3 Finite Element Models

Finite element models simulated the in vivo arm and facial skin experiments. Different packages were used in the various studies. ABAQUS Version 6.7 (SIMULIA,

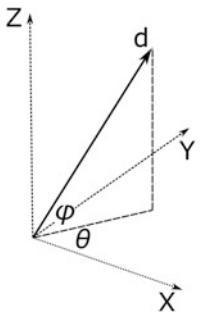

Fig. 4 The probe was displaced in different in-plane and out-of-plane directions. For the arm skin there were in-plane directions with $\theta = 0°, 30° \ldots 180°$ and $\phi = 0°$. For facial skin there were 12 in-plane directions with $\theta = 0°, 30° \ldots 330°$ and $\phi = 0°$. For all regions, there were three out-of-plane directions with $\theta = 0°, 45°, 90°$ and $\phi = 45°$, and one normal direction with $\theta = 0°$ and $\phi = 90°$. $d \approx 1.2$–1.4 mm for all directions. See Fig. 2 for orientation of axes at the arm and face locations. Reprinted by permission from Springer: Computer Methods in Biomechanics and Biomedical Engineering. Lecture Notes in Bioengineering, Gefen A., Weihs D., 2018

Providence, RI) was used for the arm studies, and ANSYS (Canonsburg, PA, USA) and FEBio [30] were used for the face studies. Different packages were used according to their availability in the institutes where the studies were conducted. There were some differences in the models due to functional differences between the packages. For example, the *INITIAL CONDITIONS keyword in ABAQUS allowed us to define a stress field in the reference configuration. This facility was not available in the other packages. The model for the facial skin study in Flynn et al. [14] is described here.

A square domain of side 50 mm represented the skin (Fig. 5). The inside edge of the hole in the support plate and the outside edge of the probe were represented by two circular partitions. The domain was meshed using 2432 quadrilateral shell elements of thickness 1.5 mm, which is representative of the thickness of skin in the relevant areas of the face and arm [18, 36]. Underlying layers of skin were ignored in this model. The implications of this assumption are addressed in the conclusions.

Two static analysis steps were performed. The first step applied a pre-stress to the skin. All four edges were fixed in the Z direction. Boundary conditions were applied to two adjacent edges such that they only shortened along their length when the domain was stretched (Fig. 5). Loads were applied normal to the edge of the opposite sides. The loads were linearly ramped from zero to the full load in 5 s. The magnitude of the loads varied according to the location on the body and were determined through the non-linear optimisation procedure described later. As it was assumed the skin outside the hole in the support plate did not move in the experiments, in the second static analysis step all nodes outside the larger circular partition were fixed in all degrees of freedom. The nodes inside the smaller circular partition were displaced according to the displacement of the probe in the

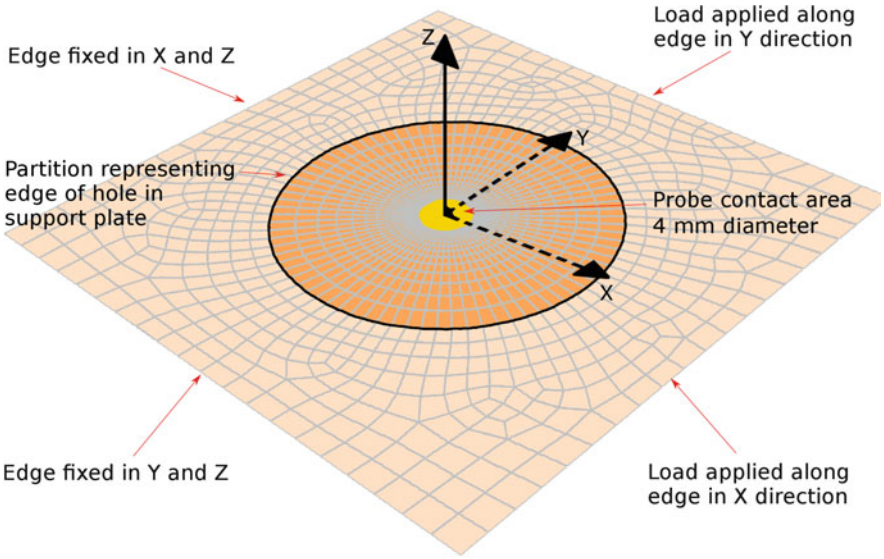

Fig. 5 Finite element model of the in vivo experiments. Reprinted by permission from Springer: Computer Methods in Biomechanics and Biomedical Engineering. Lecture Notes in Bioengineering, Gefen A., Weihs D., 2018

experiments. The magnitude and direction of the sum of the reaction forces within the probe region were calculated at each step.

2.1.4 Constitutive Models

For both arm and facial skin studies, several constitutive models were tested as to their suitability in representing skin. The models are briefly described here.

For the arm studies, the Ogden [32] model and the Tong and Fung [40] model were used to represent the skin. For the facial skin studies, in addition to the Ogden model, the Bischoff et al. [4] model, a frame invariant version of the Fung constitutive equation [2], and the Gasser et al. [17] model were tested as to their suitability to represent skin.

The Ogden [32] model was used to both represent arm and facial skin. Using this isotropic model with an anisotropic pre-stress field can capture the anisotropic response of skin in a manner similar to Bischoff et al. [3].

$$W_{\text{Ogden}} = \sum_{i=1}^{2} \frac{\mu_i}{\alpha_i} \left(\lambda_1^{\alpha_i} + \lambda_2^{\alpha_i} + \lambda_3^{\alpha_i} \right) + U(J) \tag{2}$$

where μ_i, and α_i are material parameters.

The volumetric component of the strain energy function is

$$U(J) = \frac{B}{2}(\ln J)^2 \tag{3}$$

where $B = 1$ MPa is the bulk modulus representing the near incompressibility of skin and $J = det\mathbf{F}$ is the volume ratio. $\mathbf{F}$ is the deformation gradient.

The anisotropic Tong and Fung [40] model was used to represent arm skin.

$$W_{\text{Tong}} = \alpha_1 E_{11}^2 + \alpha_2 E_{22}^2 + \alpha_3 E_{11} E_{22} + c e^{A_1 E_{11}^2 + A_2 E_{22}^2} + U(J) \tag{4}$$

where E_{11} and E_{22} are components of the Lagrangian strain tensor and α_1, α_2, α_3, c, A_1, and A_2 are material parameters. α_1, α_2, α_3, and c control the stiffness at low strains, while A_1, and A_2 control the stiffness of the response at high strains.

The Bischoff et al. [4] model was used to represent facial skin and was implemented into FEBio using the user material plug-in facility.

$$W_{\text{Bischoff}} = \frac{nk\theta}{4}\left(P^2 \sum_{i=1}^{4}\left[\frac{\rho^{(i)}}{P^2}\beta_\rho^{(i)} + \ln\frac{\beta_\rho^{(i)}}{\sinh\beta_\rho^{(i)}}\right] - \frac{\beta_P}{P}\ln\left[\bar{\lambda}_{\mathbf{a}}^{a^2}\bar{\lambda}_{\mathbf{b}}^{b^2}\bar{\lambda}_{\mathbf{c}}^{c^2}\right]\right) + U(J) \tag{5}$$

where a, b, and c are the lengths of a cell, n is the number of fibres per unit volume, $k = 1.38 \times 10^{-23}\,\text{JK}^{-1}$ is Boltzman's constant, and θ is the absolute temperature.

$\bar{\lambda}_{\mathbf{a}} = \sqrt{\mathbf{a}^T\bar{\mathbf{C}}\mathbf{a}}$, $\bar{\lambda}_{\mathbf{b}} = \sqrt{\mathbf{b}^T\bar{\mathbf{C}}\mathbf{b}}$, $\bar{\lambda}_{\mathbf{c}} = \sqrt{\mathbf{c}^T\bar{\mathbf{C}}\mathbf{c}}$ are the principal fibre stretches along the principal material axes of the cell, $(\mathbf{a}, \mathbf{b}, \mathbf{c})$. $\bar{\mathbf{C}}$ is the deviatoric right Cauchy tensor.

$P = \frac{1}{2}\sqrt{a^2 + b^2 + c^2}$ is the undeformed length of a fibre in the cell, while $\rho^{(i)}$ is the deformed length of the i^{th} fibre. $\beta_\rho^{(i)} = \mathscr{L}^{-1}\left(\frac{\rho^{(i)}}{N}\right)$, with $\mathscr{L}(x) = \coth x - \frac{1}{x}$ being the Langevin function.

A frame invariant version of the Fung constitutive equation proposed by Ateshian and Costa [2] was also tested for facial skin.

$$W_{\text{Fung}} = \frac{c}{2}(\mathrm{e}^Q - 1) + U(J) \tag{6}$$

$$Q = c^{-1}\sum_{a=1}^{3}\left[2\mu_a\mathbf{a}_a^0 \otimes \mathbf{a}_a^0 : \bar{\mathbf{E}}^2 + \sum_{b=1}^{3}\lambda_{ab}(\mathbf{a}_a^0 \otimes \mathbf{a}_a^0 : \bar{\mathbf{E}})(\mathbf{a}_b^0 \otimes \mathbf{a}_b^0 : \bar{\mathbf{E}})\right] \tag{7}$$

where c is a parameter representing the stiffness, and λ_{ab}, μ_a are Lamé parameters. All parameters have units of stress. $\bar{\mathbf{E}} = \frac{1}{2}(\bar{\mathbf{F}}^T\bar{\mathbf{F}} - \mathbf{I})$ is the deviatoric Green-Lagrange strain tensor. $\mathbf{a}_a^0$ defines an initial direction of a material axis a, which is prescribed in the X direction (Fig. 5). For the purposes of simplifying the parameter optimisation procedure, $\lambda_{11} = \lambda_{12} = \lambda_{23} = \lambda_{31}$, $\lambda_{22} = \lambda_{33}$, and $\mu_2 = \mu_3$.

An anisotropic model proposed by Gasser et al. [17] was the fourth model used for facial skin.

$$W_{\text{Gasser}} = \frac{\mu}{2}(\bar{I}_1 - 1) + \frac{k_1}{k_2}\{e^{k_2[\bar{I}_n(\theta)-1]^2} - 1\} + U(J) \tag{8}$$

where μ, k_1 control the stiffness of the skin at small strains and k_2 is a dimensionless parameter that controls the stiffness at large strains. $\tilde{I}_n(\theta) = \mathbf{N}\bar{\mathbf{C}}\mathbf{N}$ is the fibre stretch squared of the n^{th} family of fibres orientated in the direction $\mathbf{N}$ in the reference configuration.

In all the studies, a quasi-linear viscoelastic model proposed by Fung [15] characterised the time-dependent properties of skin.

$$\mathbf{T}(t) = \mathbf{T}_e(t) + \int_0^t \mathbf{T}_e(t-\tau)\frac{\partial g_R(\tau)}{\partial \tau}\,\mathrm{d}\tau, \tag{9}$$

where $\mathbf{T}(t)$ is the total Cauchy stress at time t, $\mathbf{T}_e = \frac{1}{J}\mathbf{F}\frac{\partial W}{\partial E}\mathbf{F}^T$ is the elastic Cauchy stress, and $g_R(t)$ is a Prony series relaxation function.

$$g_R(t) = 1 - \bar{g}_1^P(1 - e^{-t/\tau_1^G}) \tag{10}$$

where $\bar{g}_1^P = 0.4$ is a viscoelastic parameter and $\tau_1^G = 0.8\,\text{s}$ is the relaxation time. The same Prony parameters were used for all locations. The values were chosen such that the hysteresis level in the model matched the hysteresis level measured in the experiments.

2.1.5 Framework for Identification of Model Parameters

Constitutive material parameters and the pre-stress field that best fit the model probe reaction forces to the measured probe reaction forces from the in vivo experiments were determined. The optimisation procedure used the lsqnonlin function in MATLAB 2016a (The Mathworks, Inc., Natwick, MA, USA). This function minimised the following objective function in a least squares sense using a trust region method

$$F(\mathbf{x}) = \sum_{i=1}^{16}\sum_{j=1}^{N_i}\left\{\left(\frac{R_{X_j}^{model}(\mathbf{x}) - R_{X_j}^{exp}}{max\left(R_{X_j}^{exp}\right)}\right)^2 + \left(\frac{R_{Y_j}^{model}(\mathbf{x}) - R_{Y_j}^{exp}}{max\left(R_{Y_j}^{exp}\right)}\right)^2 + \left(\frac{R_{Z_j}^{model}(\mathbf{x}) - R_{Z_j}^{exp}}{max\left(R_{Z_j}^{exp}\right)}\right)^2\right\} \tag{11}$$

where $\mathbf{x}$ is the model parameter set, and N_i is the number of data points recorded for the i^{th} probe direction (16 directions for the face experiments and 8 directions for the arm experiments). $R_{X_j}^{model}(\mathbf{x})$, $R_{Y_j}^{model}(\mathbf{x})$, and $R_{Z_j}^{model}(\mathbf{x})$ are the model probe reaction forces in the X, Y, and Z directions at the j^{th} data point. $R_{X_j}^{exp}$, $R_{Y_j}^{exp}$, $R_{Z_j}^{exp}$ are the experiment probe reaction forces in the X, Y, and Z directions at the j^{th} data point. A customised MATLAB script assembled the input files for the finite element analyses. Upon completion of the analyses, the results were read and the objective function in Eq. (11) was calculated. The lsqnonlin function adjusted the material parameters and pre-loads and updates the input files for another round of finite element analyses. This iterative procedure continued until a local minimum in the objective function was found. Parameter sets were identified that fit the model data to the in vivo data for different points on the arm and face. The variance accounted for (VAF) was calculated for each set.

$$VAF = 1 - \frac{F(\mathbf{x})}{\sum_{i=1}^{16}\sum_{j=1}^{N_i}\left\{\left(\frac{R_{X_j}^{exp}}{max\left(R_{X_j}^{exp}\right)}\right)^2 + \left(\frac{R_{Y_j}^{exp}}{max\left(R_{Y_j}^{exp}\right)}\right)^2 + \left(\frac{R_{Z_j}^{exp}}{max\left(R_{Z_j}^{exp}\right)}\right)^2\right\}} \tag{12}$$

2.2 Results

For both the arm and face experiments, the mechanical response of the skin was nonlinear, anisotropic, and viscoelastic (sample results shown in Figs. 6 and 7). The experimental method demonstrated good repeatability with force-displacement responses from multiple tests on the cheek of one volunteer differing by less than 10%.

There were notable differences in the stiffness of the response between volunteers. The anisotropy of the skin of volunteers was similar. In general, the directions of the stiffest responses for all tested locations between volunteers were the same (Fig. 8). The stiffest response on the forearm was along the length of the arm, while for the upper arm the stiffest response was approximately perpendicular to the longitudinal axis of the arm. For the central cheek area, the stiffest response was approximately in the X direction indicated in Fig. 3b.

All six facial locations exhibited anisotropic characteristics (Fig. 9). For the central cheek, central jaw, near ear, and zygomatic regions, the in-plane force-displacement response was stiffest approximately along the 150–330° axis and least stiff approximately along the 60–240° axis. At the near lip and forehead locations, the in-plane responses were stiffest along the 0–180° axis and least stiff along the 90–270° axis.

The Ogden [32] model simulated the response of the anterior forearm with VAFs ranging from 98% to 99% (table 1). The Tong and Fung [40] model simulated the

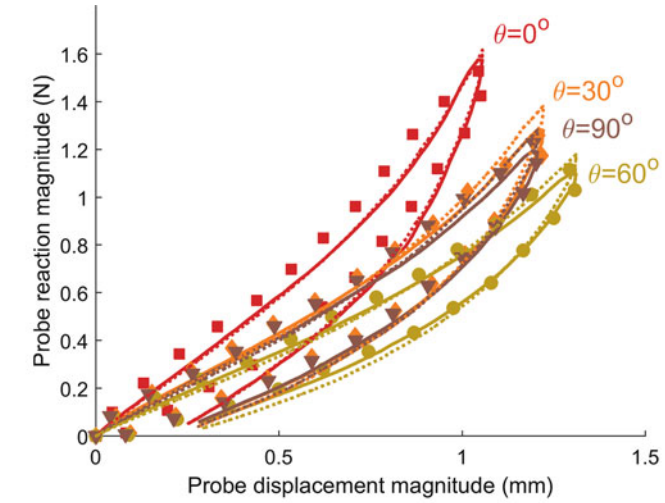

(a)

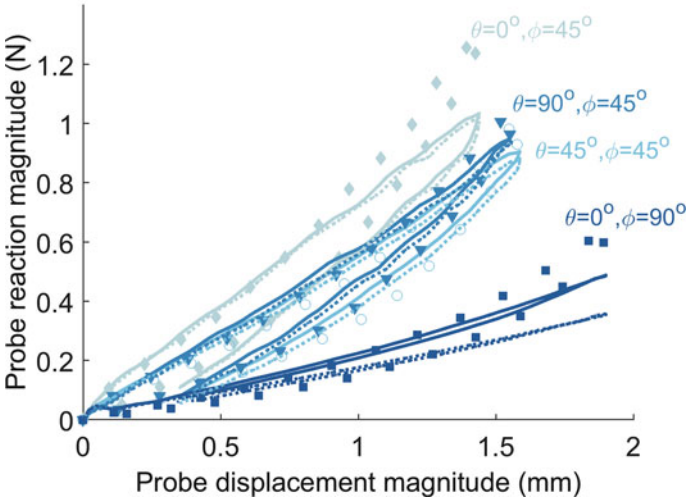

(b)

Fig. 6 Experimental and model force-displacement response for the stiffest anterior forearm skin. (**a**) In-plane response; (**b**) out-of-plane response. Experimental data indicated by symbols; Tong and Fung [40] model indicated by solid lines; Ogden [32] model indicated by dashed lines. See Table 1 for model parameters and pre-stresses. Reprinted by permission from Springer: Annals of Biomedical Engineering, Modeling the Mechanical Response of In Vivo Human Skin Under a Rich Set of Deformations, Cormac Flynn, Andrew Taberner, and Poul Nielsen, 2011

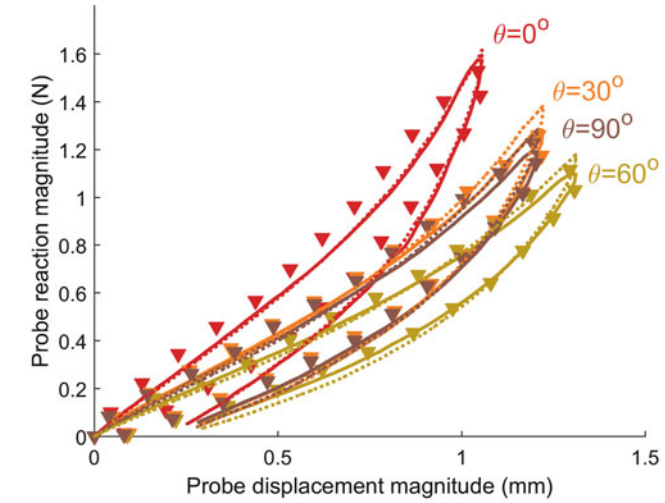

(a)

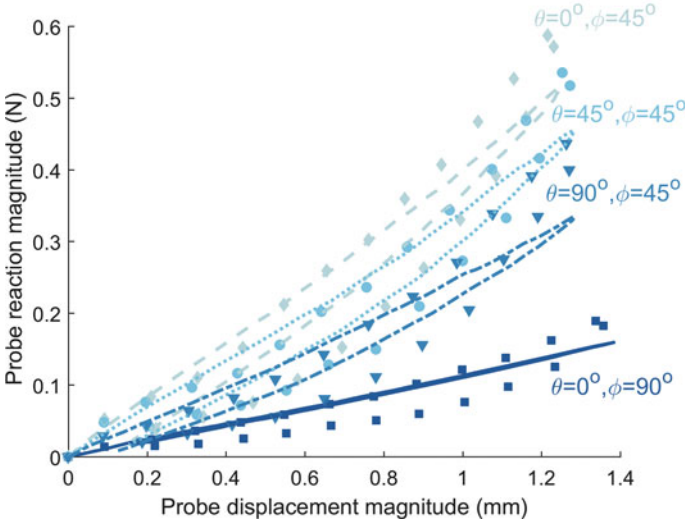

(b)

Fig. 7 Experiment and Bischoff et al. [4] model probe reaction-displacement response for forehead region. (**a**) In-plane response; (**b**) out-of-plane response. *VAF* for Bischoff et al. [4] was 94%. See Table 2 for model parameters and pre-stresses. Reprinted by permission from Springer: Computer Methods in Biomechanics and Biomedical Engineering. Lecture Notes in Bioengineering, Gefen A., Weihs D., 2018

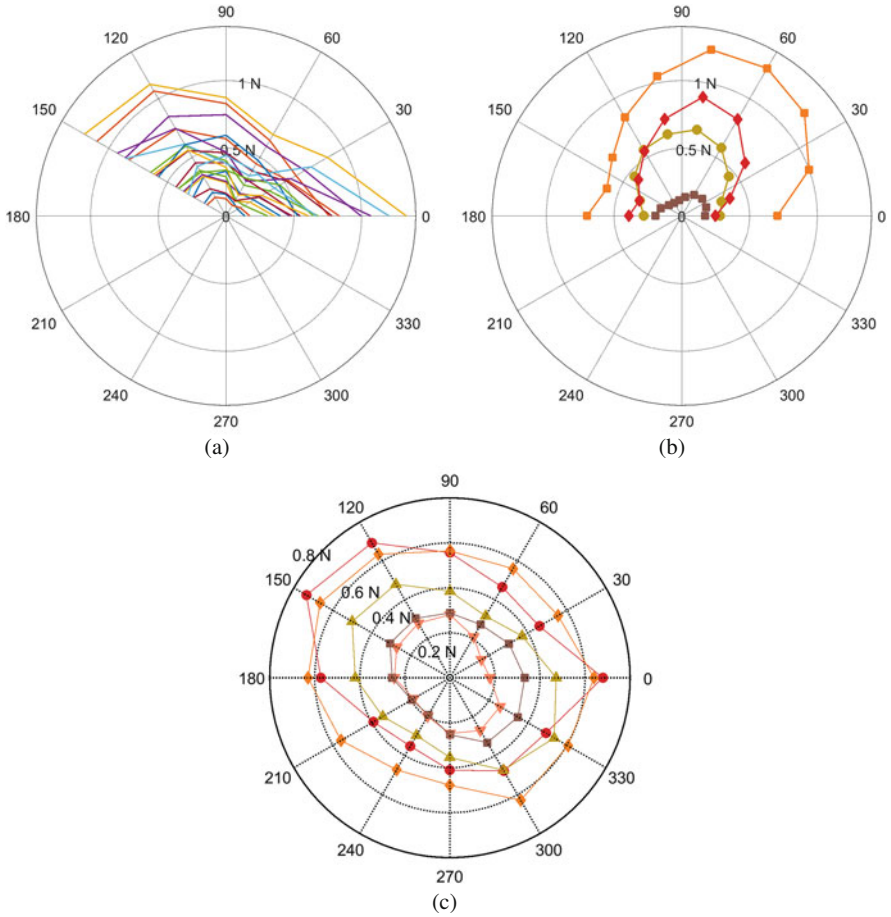

Fig. 8 In-plane force reaction for different directions for volunteers at (**a**) 0.9 mm displacement for anterior forearm; (**b**) 1.3 mm displacement for upper arm; (**c**) 1.1 mm displacement for central cheek. Note that forearm data was recorded up to 150° and upper arm data was recorded up to 180°. 0° is in the direction of the X-axis, which is defined for each location in Fig. 4. (c) Reprinted from Journal of the Mechanical Behavior of Biomedical Materials, 28, Cormac Flynn, Andrew J. Taberner, Poul M. F. Nielsen, and Sidney Fels, Simulating the three-dimensional deformation of in vivo facial skin, 484-494, 2013, with permission from Elsevier

response with similar VAFs. Both models simulated the response of the upper arm with a VAF of 98%.

The Ogden [32] model simulated the response of the facial skin with VAFs ranging from 93% to 96% (Table 2). The Bischoff et al. [4] and Ateshian and Costa [2] models simulated the response with similar agreements. The Gasser et al. [17] model had the smallest VAF (79%) when used to simulate forehead skin (Table 2). As a result, it was not used to simulate other regions of the face.

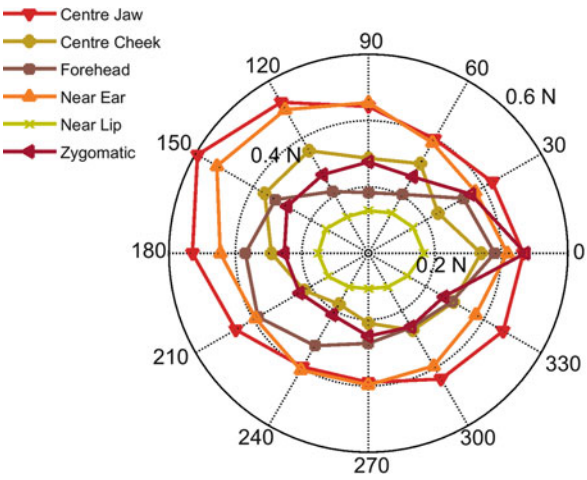

Fig. 9 In-plane force reaction at 0.7 mm displacement for different locations on one volunteer's face

3 Current Challenges and Future Directions

This chapter presented a method of characterising the mechanical response of in vivo human skin by applying a rich set of deformations using a micro-robotic device. The resulting force-displacement response from different points of the arm and face of volunteers exhibited non-linearity, anisotropy, and viscoelasticity. Qualitatively, the response of each volunteer's skin was similar. The direction of stiffest response corresponded, in general, to the direction of relaxed skin tension lines (RSTLs) in that area [5]. This in agreement with [34] in the central cheek region. However, the magnitude of the stiffness varied significantly according to volunteer [11]. This highlights the importance of getting patient-specific data for developing volunteer-specific models.

Using finite element analyses and non-linear optimisation, parameter sets were identified that best-fit the model responses to the experimental responses of different skin locations and different volunteers. VAFs ranging from 92% to 99 % were achieved for all the constitutive models tested except the Gasser et al. [17] model, which only achieved a VAF of 79% for the forehead region. The force-displacement response was too linear using this model. Overall, the anisotropic constitutive models did not perform better compared to the isotropic Ogden [32] model. Better knowledge of the structural characteristics of the skin through appropriate imaging in each case may guide the selection of anisotropic parameter values.

The optimisation procedure also estimated the in-vivo pre-stresses at the different locations. The pre-stresses ranged from 5 to 92 kPa, which is greater than values reported in the literature [9, 10, 21]. While this difference may be attributed to variations between individuals, it can also be due to the protocol used. Flynn et al. [12] demonstrated the importance of using out-of-plane deformations to estimate pre-stresses in skin. The normal response of skin is more dependent on the pre-stress than on the material parameters. With an application to cerebral aneursyms,

Table 1 Identified arm region material parameters, in vivo pre-stress field, and variance accounted for (*VAF*)

Region	Model	Model parameters	(σ_x, σ_y) (kPa)	*VAF* (%)
Anterior forearm (stiff)	Ogden [32]	$\mu_1 = 29.16$ kPa; $\mu_2 = 2.15$ Pa; $\alpha_1 = 1.71$; $\alpha_2 = 40.09$	(84, 61)	98
Anterior forearm (stiff)	Tong and Fung [40]	$c = 0.0107$ Pa; $A_1 = 40.636$; $A_2 = 21.837$; $a_1 = 12.754$ kPa; $a_2 = 6.057$ Pa; $a_3 = 38.046$ kPa	(92, 49)	99
Anterior forearm (medium)	Ogden [32]	$\mu_1 = 19.40$ kPa; $\mu_2 = 0.03$ Pa; $\alpha_1 = 1.00$; $\alpha_2 = 54.02$	(48, 39)	97
Anterior forearm (medium)	Tong and Fung [40]	$c = 0.0207$ Pa; $A_1 = 34.167$; $A_2 = 54.740$; $a_1 = 19.676$ kPa; $a_2 = 0.008$ Pa; $a_3 = 53.306$ kPa	(51, 31)	98
Anterior forearm (supple)	Ogden [32]	$\mu_1 = 10.06$ kPa; $\mu_2 = 0.001$ Pa; $\alpha_1 = 1.43$; $\alpha_2 = 37.62$	(39, 28)	98
Anterior forearm (supple)	Tong and Fung [40]	$c = 0.0221$ Pa; $A_1 = 26.772$; $A_2 = 40.846$; $a_1 = 20.956$ kPa; $a_2 = 0.390$ Pa; $a_3 = 31.675$ kPa	(38, 16)	98
Upper arm	Ogden [32]	$\mu_1 = 27.04$ kPa; $\mu_2 = 2.77$ Pa; $\alpha_1 = 3.79$; $\alpha_2 = 39.38$	(22, 48)	98
Upper arm	Tong and Fung [40]	$c = 0.1000$ Pa; $A_1 = 51.089$; $A_2 = 7.962$; $a_1 = 1.563$ kPa; $a_2 = 8772$ Pa; $a_3 = 12.355$ kPa	(17, 45)	98

The parameters are originally from Flynn et al. [12]. Reprinted by permission from Springer: Computer Methods in Biomechanics and Biomedical Engineering. Lecture Notes in Bioengineering, Gefen A., Weihs D., 2018

Lu et al. [29] showed that a normal load on a membrane structure can determine the wall tension without requiring accurate knowledge of the wall elastic properties. For the facial skin locations, some of the pre-stresses predicted using different constitutive models were similar. For example, using the Bischoff et al. [4] model the estimated pre-stress in the forehead region was 25 kPa, 23 kPa while using the Gasser et al. [17] model estimated the pre-stress in the same region to be 26 kPa, 18 kPa. The normal responses using both these models were similar to the experimental response [14]. In contrast, the Ateshian and Costa [2] model estimated a lower pre-stress of 7 kPa, 3 kPa for the forehead region but the predicted normal response was much lower than the experimental response. The pre-stress estimation may be improved by ensuring all the applied deformations have an out-of-plane component. The objective function would then have a greater weighting of out-of-plane responses.

Table 2 Identified facial region material parameters, in vivo pre-stress field, and variance accounted for (*VAF*)

Region	Model	Model parameters	(σ_x, σ_y) (kPa)	*VAF* (%)
Forehead	Bischoff et al. [4]	$n = 6.632 \times 10^{11}$ (mm^{-3}); $(a, b, c) =$ (0.8529, 1.272, 1.386)	(25, 23)	94
Forehead	Ateshian and Costa [2]	$c = 0.3118$ kPa; $\lambda_{11} = 0.9982$ kPa; $\lambda_{22} = 1.005$ kPa; $\mu_1 = 7.169$ kPa; $\mu_2 = 7.142$ kPa	(7, 3)	94
Forehead	Gasser et al. [17]	$\mu = 14.08$ kPa; $k_1 = 11.01$ kPa; $k_2 = 0.09188$; $\theta = 30.82^o$	(26, 18)	79
Forehead	Ogden [32]	$\mu_1 = 53.95$ kPa; $\mu_2 = 0.3012$ Pa; $\alpha_1 = 1.868$; $\alpha_2 = 69.00$	(34, 27)	94
Near lip	Bischoff et al. [4]	$n = 5.690 \times 10^{11}$ (mm^{-3}); $(a, b, c) =$ (0.6952, 1.276, 1.529)	(9, 8)	94
Near lip	Ateshian and Costa [2]	$c = 0.3291$ kPa; $\lambda_{11} = 1.0$ kPa; $\lambda_{22} = 6.387$ kPa; $\mu_1 = 4.556$ kPa; $\mu_2 = 2.352$ kPa	(9, 7)	91
Near lip	Ogden [32]	$\mu_1 = 41.29$ kPa; $\mu_2 = 0.16$ Pa; $\alpha_1 = 1.658$; $\alpha_2 = 54.964$	(24, 16)	93
Central cheek	Bischoff et al. [4]	$n = 1.246 \times 10^{12}$ (mm^{-3}); $(a, b, c) =$ (0.7880, 1.246, 1.446)	(53, 46)	92
Central cheek	Ateshian and Costa [2]	$c = 0.4421$ kPa; $\lambda_{11} = 1.0$ kPa; $\lambda_{22} = 1.0$ kPa; $\mu_1 = 6.121$ kPa; $\mu_2 = 4.353$ kPa	(10, 5)	93
Central cheek	Ogden [32]	$\mu_1 = 58.27$ kPa; $\mu_2 = 0.14$ Pa; $\alpha_1 = 2.334$; $\alpha_2 = 33.081$	(89, 72)	93
Central jaw	Bischoff et al. [4]	$n = 8.922 \times 10^{11}$ (mm^{-3}); $(a, b, c) =$ (0.8406, 1.224, 1.413)	(37, 32)	96
Central jaw	Ateshian and Costa [2]	$c = 0.5010$ kPa; $\lambda_{11} = 1.000$ kPa; $\lambda_{22} = 1.000$ kPa; $\mu_1 = 3.322$ kPa; $\mu_2 = 5.919$ kPa	(20, 16)	95
Central jaw	Ogden [32]	$\mu_1 = 57.73$ kPa; $\mu_2 = 0.42$ Pa; $\alpha_1 = 2.265$; $\alpha_2 = 34.689$	(81, 75)	96

The parameters are originally from Flynn et al. [13] and Flynn et al. [14]. Reprinted by permission from Springer: Computer Methods in Biomechanics and Biomedical Engineering. Lecture Notes in Bioengineering, Gefen A., Weihs D., 2018

The uniqueness of the parameter sets needs to be established. For simple uniaxial and biaxial tests on natural rubber, it is possible to identify several optimum parameter sets that result in the same quality of fit of model data to experimental data [33]. Using a richer set of deformations as was done for the arm and facial skin studies increases the identifiability of the material parameters and pre-

stresses. Flynn et al. [12] demonstrated improved identifiability when out-of-plane deformations were applied to the skin. This could be improved by enriching the data set further by tracking the displacement of the skin around the probe using DIC.

There are several opportunities to improve the finite element model used to simulate the experiments. For all the locations, the skin surface was assumed to be flat and underlying layers and connections were ignored. This assumption is weak in certain areas such as the zygomatic region of the face, whose surface is curved and is also the location of the zygomatic ligament, which anchors the facial skin to the underlying bone [16]. It is likely with probe displacements of 1.2–1.4 mm and an assumed skin thickness of 1.5 mm that the underlying layers of the skin would influence the force response. The influence of the underlying connections also may explain why the in-plane force in diametrically opposed directions differ (e.g. 330° and 150° in Fig. 8c). If there were no underlying connections, the response would be expected to be the same. Including the sub-dermal layers and ligaments is likely to improve the normal response of the skin. In general, the model simulated the response of arm skin (97–99%) better than the response of facial skin (91–96%). This could be attributed to the model assumptions being more realistic for arm skin than for facial skin.

The quasi-static loading of the skin surface is limiting in terms of full mechanical characterisation. Recently, Parker et al. [35] have used a revised version of the micro-robot to characterise the dynamic response of skin of the anterior forearm and hand using nonlinear stochastic system identification methods. Chen and Hunter [6] also used stochastic identification techniques with a dynamic indenter that needed to be reconfigured for each applied load direction.

The experimental protocol using the micro-robot and support plate is time consuming and sometimes uncomfortable for the volunteer. This is particularly true when testing facial skin. It is unlikely that this approach would be suitable for use in a clinical context where the comfort of the patient is important. Hand-held devices such as that proposed by HajiRassouliha et al. [19], which measures three-dimensional strain fields of skin, are likely to point the way forward to accessible characterisation of a patient's skin in the clinic.

References

1. Affagard J-S, Wijanto F, Allain J-M (2017) Improving the experimental protocol for a more accurate identification of a given mechanical behaviour in a single assay: Application to skin. Strain 53(5):e12236
2. Ateshian GA, Costa KD (2009) A frame-invariant formulation of Fung elasticity. J Biomech 42(6):781–785
3. Bischoff JE, Arruda EM, Grosh K (2000) Finite element modeling of human skin using an isotropic, nonlinear elastic constitutive model. J Biomech 33(6):645–652
4. Bischoff JE, Arruda EA, Grosh K (2002) A microstructurally based orthotropic hyperelastic constitutive law. J Appl Mech Trans ASME 69(5):570–579
5. Borges AF (1989) Relaxed skin tension lines. Dermatol Clin 7(1):169–177

6. Chen Y, Hunter IW (2009) In vivo characterization of skin using a weiner nonlinear stochastic system identification method. Conf Proc IEEE Eng Med Biol Soc 2009:6010–6013
7. Coutts LV, Miller NR, Mortimer PS, Bamber JC (2016) Investigation of In Vivo skin stiffness anisotropy in breast cancer related lymphoedema. J Biomech 49(1), 94–99
8. Cowley K, Vanoosthuyze K (2016) The biomechanics of blade shaving. Int J Cosmet Sci 38(S1):17–23
9. de Jong LAM (1995) Pre-tension and anisotropy in skin: modelling and experiments
10. Diridollou S, Patat F, Gens F, Vaillant L, Black D, Lagarde JM, Gall Y, Berson M (2000) In vivo model of the mechanical properties of the human skin under suction. Skin Res Technol 6(4):214–221
11. Evans SL, Holt CA (2009) Measuring the mechanical properties of human skin in vivo using digital image correlation and finite element modelling J Strain Anal Eng Des 44(5):337–345
12. Flynn C, Taberner A, Nielsen P (2011) Modeling the mechanical response of in vivo human skin under a rich set of deformations. Ann Biomed Eng 39(7):1935–1946
13. Flynn C, Taberner AJ, Nielsen PMF, Fels S (2013) Simulating the three-dimensional deformation of in vivo facial skin. J Mech Behav Biomed Mater 28:484–494
14. Flynn C, Taberner AT, Fels S, Nielsen PMF (2018) Comparison of anisotropic models to simulate the mechanical response of facial skin. In: Computer methods in biomechanics and biomedical engineering. Springer, NewYork, pp 43–55
15. Fung YC (1993) Biomechanics: mechanical properties of living tissues. Springer, New York
16. Furnas DW (1989) The retaining ligaments of the cheek. Plast Reconstr Surg 83(1):11–16
17. Gasser TC, Ogden RW, Holzapfel GA (2006) Hyperelastic modelling of arterial layers with distributed collagen fibre orientations. J R Soc Interface 3(6), 15–35
18. Ha RY, Nojima K, Adams WP, Brown SA (2005) Analysis of facial skin thickness: defining the relative thickness index. Plast Reconstr Surg 115(6):1769–1773
19. HajiRassouliha A, Kmiecik B, Taberner AJ, Nash MP, Nielsen PMF (2015) A low-cost, hand-held stereoscopic device for measuring dynamic deformations of skin in vivo. In: 2015 international conference on Image and Vision Computing New Zealand (IVCNZ) IEEE, New York, pp 1–6
20. Hsu C-C, Tsai W-C, Hsiao T-Y, Tseng F-Y, Shau Y-W, Wang C-L, Lin S-C (2009) Diabetic effects on microchambers and macrochambers tissue properties in human heel pads. Clin Biomech 24(8):682–686
21. Jacquet E, Josse G, Khatyr F, Garcin C (2008) A new experimental method for measuring skin's natural tension. Skin Res Technol 14(1):1–7
22. Jin X, Zhu DD, Chen BZ, Ashfaq M, Guo XD (2018) Insulin delivery systems combined with microneedle technology. Adv Drug Delivery Rev 127:119–137
23. Jor J, Nash M, Nielsen P, Hunter P (2011) Estimating material parameters of a structurally based constitutive relation for skin mechanics. Biomech Model Mechanobiol 10(5):767–778
24. Karwoski AC, Plaut RH (2004) Experiments on peeling adhesive tapes from human forearms. Skin Res Technol 10(4):271–277
25. Kelly R, Watts L (2017) Slow but likeable? Inefficient robots as caring team members. Robots in Groups and Teams, p 1
26. Killaars RC, Lopez Penha TR, Heuts EM, van der Hulst RRJW, Piatkowski AA (2015) Biomechanical properties of the skin in patients with breast cancer-related lymphedema compared to healthy individuals. Lymphat Res Biol 13(3):215–221
27. Kvistedal YA, Nielsen PMF (2009) Estimating material parameters of human skin in vivo. Biomech Model Mechanobiol 8(1):1–8
28. Liu L, Kuffel K, Scott DK, Constantinescu G, Chung H-J, Rieger J (2017) Silicone-based adhesives for long-term skin application: cleaning protocols and their effect on peel strength. Biomed Phys Eng Express 4(1):015004
29. Lu J, Zhou X, Raghavan ML (2008) Inverse method of stress analysis for cerebral aneurysms. Biomech Model Mechanobiol 7(6):477–486
30. Maas SA, Ellis BJ, Ateshian GA, Weiss JA (2012) FEBio: finite elements for biomechanics. J Biomech Eng 134(1):011005

31. Mori M, MacDorman KF, Kageki N (2012) The uncanny valley [from the field]. IEEE Robot Autom Mag 19(2):98–100
32. Ogden RW (1972) Large deformation isotropic elasticity - on the correlation of theory and experiment for incompressible rubberlike solids. Proc R Soc Lond A Math Phys Sci 326(1567):565–584
33. Ogden RW, Saccomandi G, Sgura I (2004) Fitting hyperelastic models to experimental data. Comput Mech 34(6):484–502
34. Ohshima H, Tada A, Kanamaru A, Akamatsu H, Sakai Y, Itoh M, Kanto H (2011) Relevance of the directionality of skin elasticity to aging and sagging of the face. Skin Res Technol 17(1):101–107
35. Parker MD, Jones LA, Hunter IW, Taberner AJ, Nash MP, Nielsen PMF (2017) Multidirectional in vivo characterization of skin using Wiener nonlinear stochastic system identification techniques. J Biomech Eng 139(1):011004
36. Reihsner R, Balogh B, Menzel EJ (1995) Two-dimensional elastic properties of human skin in terms of an incremental model at the in vivo configuration. Med Eng Phys 17(4):304–313
37. Sagar M, Bullivant D, Robertson P, Efimov O, Jawed K, Kalarot R, Wu T (2014) A neurobehavioural framework for autonomous animation of virtual human faces. In: SIGGRAPH Asia 2014 autonomous virtual humans and social robot for telepresence. ACM, New York, p. 2
38. Tepole AB, Gart M, Gosain AK, Kuhl E (2014) Characterization of living skin using multiview stereo and isogeometric analysis. Acta Biomater 10(11), 4822–4831
39. Then C, Stassen B, Depta K, Silber G (2017) New methodology for mechanical characterization of human superficial facial tissue anisotropic behaviour in vivo. J Mech Behav Biomed Mater 71:68–79
40. Tong P, Fung Y-C (1976) The stress-strain relationship for the skin. J Biomech 9(10):649–657
41. Tonge TK, Atlan LS, Voo LM, Nguyen TD (2013) Full-field bulge test for planar anisotropic tissues: part I - experimental methods applied to human skin tissue. Acta Biomater 9(4):5913–5925
42. Trowbridge MM, Wang B, Gutshall D, Rodenberg CA, Farage MA (2017) A randomized, controlled trial comparing skin health effects and comfort of two adult incontinence protective underwear. Skin Res Technol 23(2):202–211

Multiscale Characterisation of Skin Mechanics Through In Situ Imaging

Jean-Marc Allain, Barbara Lynch, and Marie-Claire Schanne-Klein

Abstract The complex mechanical properties of skin have been studied intensively over the past decades. They are intrinsically linked to the structure of the skin at several length scales, from the macroscopic layers (epidermis, dermis and hypodermis) down to the microstructural organization at the molecular level. Understanding the link between this microscopic organization and the mechanical properties is of significant interest in the cosmetic and medical fields. Nevertheless, it only recently became possible to directly visualize the skin's microstructure during mechanical assays, carried out on the whole tissue or on isolated layers. These recent observations have provided novel information on the role of structural components of the skin in its mechanical properties, mainly the collagen fibers in the dermis, while the contribution of others, such as elastin fibers, remains elusive. In this chapter we present current methods used to observe skin's microstructure during a mechanical assay, along with their strengths and limitations, and we review the unique information they provide on the link between structure and function of the skin.

J.-M. Allain (✉)
LMS, Ecole Polytechnique, CNRS, Palaiseau, France

Inria, Université Paris-Saclay, Palaiseau, France
e-mail: jean-marc.allain@polytechnique.edu

B. Lynch
LMS, Ecole Polytechnique, CNRS, Palaiseau, France
e-mail: blynch@rd.loreal.com

M.-C. Schanne-Klein
LOB, Ecole Polytechnique, CNRS, INSERM, Palaiseau, France
e-mail: marie-claire.schanne-klein@polytechnique.edu

G. Limbert (ed.), *Skin Biophysics*, Studies in Mechanobiology,
Tissue Engineering and Biomaterials 22,
https://doi.org/10.1007/978-3-030-13279-8_8

1 Introduction

Skin mechanics has been studied for over 50 years [1–3]. The mechanical properties of skin can be measured experimentally either ex vivo or in vivo.

Ex vivo measurements have covered almost all classical mechanical testing set-ups, and have been performed on humans as well as many types of animal. The references given here are just a few examples, as a complete review is out of the scope of this chapter. The tensile properties of skin have been extensively studied, in uniaxial, biaxial and multiaxial tests. Some examples can be found in [1, 3–6]. Less commonly used are the inflation [7], compression [8], shear [9] and even delamination [10] tests.

Despite an abundance of publications, no unique set of mechanical parameters has been determined since skin's mechanical properties vary strongly as a function of many factors, including but not limited to: species, age, anatomical location, orientation, but also sample preparation and storage, hydration level and even clamping set-up. Therefore, an enormous variability in skin's mechanical parameters has been reported in the literature.

Ex vivo tests present some serious advantages. They allow for the exploration of a wide range of parameters, up to breakage if so wanted. Skin is isolated from the subcutaneous tissues and can thus be studied as a material on its own. Ex vivo testing also permits to modify samples with chemicals to evaluate separately the contribution of each structural component. This method has been exploited for example to modulate the proportions of elastin [11] or proteoglycans [12] and study the resulting impact on mechanical properties.

The main drawback of ex vivo studies is related to their main advantage. Because the tissue is separated from the body, it is isolated from its natural environment and in particular natural pre-stress and hydration control and may be damaged during the isolation process.

In vivo measurements have been developed to characterise the mechanical properties of skin in its natural environment, mostly on humans. Four main categories of tests have been performed: torsion [13], tension [14], suction [15] and indentation [16]. For a more complete review of the literature on this subject, the reader may refer to [17]. Torsion and tensile assays apply mechanical stimulation in the skin surface's plane, while suction and indentation assays deform the skin perpendicularly to its surface. A small deformation will be selected to optimize sensitivity to the mechanical properties of skin upper layers (stratum corneum, epidermis, upper dermis), while a larger deformation will involve the whole thickness of skin and even some subcutaneous tissues.

From all these studies, a good knowledge of skin's mechanical properties at the macroscopic level has been acquired. These properties are comparable to those of other collagen-rich tissues, such as tendon [18], cornea [19] or aorta [20], although each of these tissues present very different microstructures.

For a wide range of applications, a sound and precise understanding of the mechanical properties of skin is essential in explaining causes and effects. For example, in the study of the etiology of alterations arising from genetic diseases (e.g. Ehlers-Danlos syndrome, Marfan syndrome, Cutis laxa) or from ageing, to study impact [21], to improve wound healing outcome [22], to improve drug and vaccine transepidermal delivery [17], to develop robot-assisted surgery [23], and to improve dermatological and cosmetic products and procedures [24].

Skin is a complex material because of its architecture as a layered structure and highly multiscale organization (e.g. fibrils form fibers, which form bundles and so on) (see chapter "Human Skin: Composition, Structure and Visualisation Methods" for a more detailed review of skin's hierarchical structure). From this observation, it is straightforward to infer that, in the mechanical aspects of the applications mentioned in the previous paragraph, the interplay of microstructural constituents within and across individual skin layer plays a pivotal role. Thus, the question of the relationship between microscopic organization and macroscopic mechanical properties has been raised from the very first studies of skin's mechanics [3]. However, technical difficulties in the observation of the microstructure during a mechanical assay have for a long time restricted the answers that could be provided to this "multiscale question". Hence, many studies have been limited to infer the link between microstructure and mechanics from separated mechanical measurements and static images of the tissue in an unloaded state. Two notable studies included a few SEM observations of samples observed post mortem in a given stretch state: one sample is stretched to a given stretch, fixed and then observed [25, 26]. The process is then repeated at different stretch levels with different samples. Due to the complexity of the protocol and inter-sample variation, these early approaches were however limited to a qualitative observation of the reorientation of collagen fibers.

Yet, a complex multiscale interpretation of skin mechanics is increasingly needed to link the microscopic scale, relevant to cells, proteins and chemicals to the macroscopic scale, relevant to patients and consumers.

Furthermore, the expanding field of mechanobiology has showed that the mechanical properties of tissues can greatly influence cell behavior and has opened up new research and translational opportunities in all the fields mentioned above.

Appropriate micro-mechanical experiments have been developed only in the last decade or so as the result of miniaturization of mechanical testing devices and improvement of imaging methods. As will be developed in this chapter, in situ imaging has proven useful for three main purposes: as a way to determine local strains, either to validate the mechanical testing protocol or to study the local response of the tissue, to identify the relative contribution of each layers and to identify the relative contribution of each microstructural components.

2 Skin Structure and Mechanical Properties

2.1 Skin Structure

Skin is a complex multilayered organ (see also chapter "Human Skin: Composition, Structure and Visualisation Methods" for a more complete description). It also encompasses hairs, sweat and sebaceous glands, nerves and blood vessels. The main part of the organ is usually separated into three layers. The following short description applies to human skin and is usually generalized to other mammalian species, up to a scale factor.

The outermost layer of skin is the epidermis. Its thickness ranges from 0.05 mm on the eyelids to 1.5 mm on soles and palms. The epidermis is made of layers of cells, called keratinocytes, stacked onto each other. These cells originate from the basal layer, at the junction between the epidermis and the dermis. This is where melanin is added to the keratinocytes by cells called melanocytes. No blood vessel goes through the epidermis. Some immune cells, such as the Langerhans' cells, migrate through the epidermis to detect antigens. The epidermal cells migrate from the basal membrane to the skin's surface while filling with keratin, a very resistant fibrous protein. The outermost layer of the epidermis is called the stratum corneum and is entirely composed of dead cells glued together with lipidic cement. The cells from the stratum corneum detach progressively with friction and cleansing, leaving space for new cells. The mean turnover time of the epidermis, required to renew the cells completely, is roughly 39 days. This time can be affected by various diseases, psoriasis for instance [27].

Under the epidermis lays the dermis, ranging from 0.3 to 3 mm in thickness. The epidermis-dermis junction presents a finger-like wavy structure, known to facilitate both adhesion of dermis to epidermis and exchange of nutrients. The cohesion between the two layers is ensured by anchoring filaments of proteins: proteoglycans (called hemidesmosomes) and type IV and VII collagen fibrils. The dermis is the most important layer of the skin for structural integrity and mechanical resistance. A few cells, called fibroblasts, can be found in the dermis. Their role is to synthetize the components of the extracellular matrix which constitutes the major part of the dermis. These components are collagen fibers of different types (mainly I but also III, V, VI, XII, XIV and XVI), elastic fibers and ground substance. The ground substance encompasses everything in the extracellular matrix that are not fibers, including, but not limited to, proteoglycans. The main component of the ground substance and of the dermis in general is water, which represents 64% of the whole skin. Sebaceous and sweat glands lay in the dermis. Small blood vessels run through the dermis and especially at the epidermis-dermis junction, to bring nutrients to the epidermal basal cells.

Under the dermis lays the hypodermis, the deepest layer of the skin, also called "sub-cutaneous" tissue. It is composed of loose connective tissue and lobules of fat. The hair follicles initiate there, and blood vessels run through the hypodermis.

The thickness of each layer, the geometry of interfaces, and the mechanical properties of skin are known to vary as a function of body site, age, gender, and lifestyle (UV exposure, moisturization, etc.). In animal skin, it also varies a lot depending on the species, which affects, amongst many other parameters, hair density.

2.2 *Mechanical Properties of Skin*

Skin can sustain large strains, of tens of percent. It presents a non-linear stress-stretch response: a typical example of stress-stretch curve for skin is shown on Fig. 1. This so-called "J-curve" is commonly separated into three regions: a toe-region, in which large stretches result in very little force, a heel-region, in which the force increases non-linearly with the stretch, and a linear-region, in which the force increases linearly with the stretch. After the linear-region, the skin breaks progressively. The stress-stretch response of skin is highly anisotropic [1].

Skin is also a viscoelastic material. An example of viscoelastic behavior is represented by the strong strain rate dependency of the non-linear mechanical response of skin [29] so that when a loading-unloading cycle is performed, hysteresis can be observed. The viscoelasticity of skin also leads to creep and relaxation responses: if

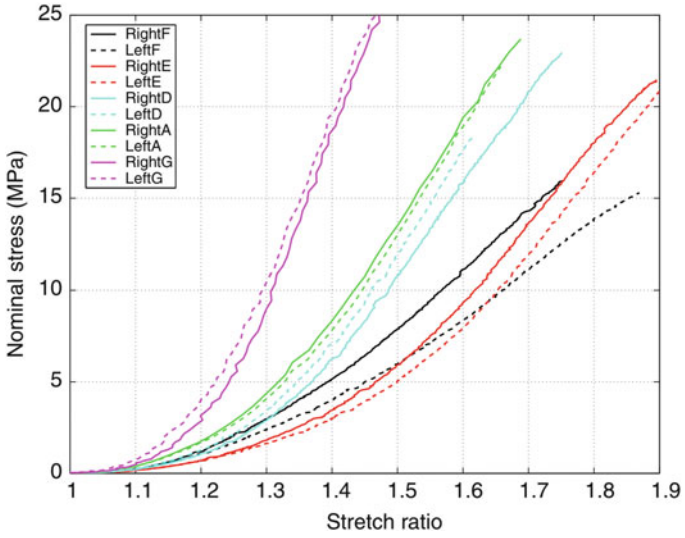

Fig. 1 Stress–stretch response of adjacent samples from the upper back of human cadavers with the same orientation (N = 10). Colors indicate different subjects while solid and dashed lines indicate samples to the right and left of the spinal line respectively. This illustrates the inter-subject and intra-subject variations between adjacent samples with the same orientation. Figure from Ní Annaidh et al. [28]

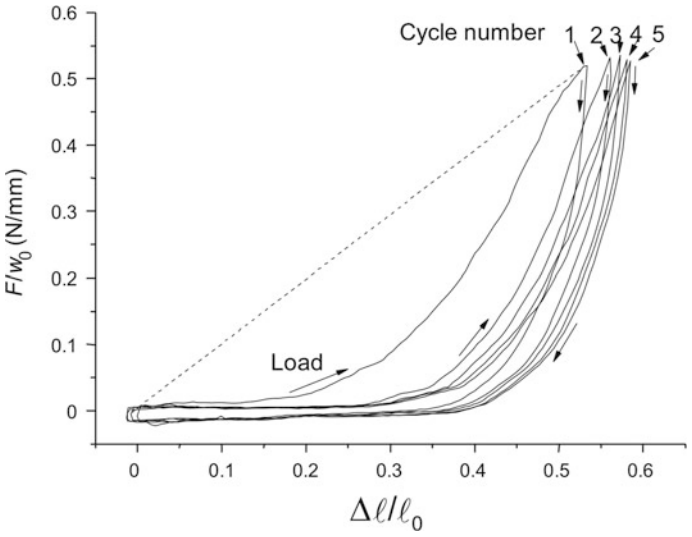

Fig. 2 Normalized force versus strain curves of skin showing the progressive shift towards a limit cycle after successive loading and unloading cycles. The experiments were performed in situ on canine cadavers. Figure from Bismuth et al. [31]

the stress is held constant, the strain increases with time (creep) while if the strain is held constant, stress decreases with time (relaxation) [30].

Another well-known macroscopic mechanical property of skin is the so-called preconditioning. When the skin is subjected to repeated cycles at the same loading level (in stretch or stress), the response will shift progressively (see Fig. 2), a clear demonstration of dissipative mechanisms. It is classically admitted that the response will converge towards a limit-cycle, and many authors consider that ten cycles are sufficient [31, 32], even if the convergence seems quite slow [33, 34]. The preconditioning effect is very similar to the Mullins effect observed in elastomers [35].

In vivo, skin is subjected to a natural pre-stressed state. This is manifested through a complex network of tension lines across the body whose orientation can be determined by puncturing circular holes in skin: the resulting holes are ellipsoidal as a consequence of the relaxation of the prestress. A mapping of the main directions of these tension forces in human cadavers was described in 1861 by K. Langer: these are the so-called Langer's lines [36], which are still used by surgeons nowadays [21] (see chapter "Tension Lines of the Skin" for a more detailed discussion of this topic).

2.3 Contribution of the Different Layers to the Mechanical Properties

The relative contribution of each of skin layers to the overall macroscopic mechanical properties strongly depends on the mechanical solicitation considered.

The dermis is usually considered to be skin's main load bearing layer and its mechanical behavior is indeed similar to that of the skin as described above. From a mechanical point-of-view, the dermis main function is to provide sufficient flexibility to allow movement while maintaining a very high resilience to protect the internal organs. Due to their small thicknesses, the stratum corneum and viable epidermis are mainly involved when the mechanical solicitations are targeted at the surface, for instance in tribological properties [37–40]. The main mechanical role of the hypodermis is considered to be that of a shock absorber, which dissipates excessive energy.

To study independently the mechanical properties of each layer, the most straightforward approach is to isolate each layer, which is obviously only possible in ex vivo experiments. This technique has been employed very commonly to characterise independently the stratum corneum [41], and the combination of dermis and hypodermis [42], and even to separate the dermis sublayers: papillary and reticular dermises [43]. Less often, it has also been used to evaluate the association of stratum corneum and viable epidermis (hence making it possible to isolate the properties of the viable epidermis on its own—[44]), and hypodermis [45].

Isolating skin layers presents one major drawback, which is the risk of damaging the tissue during the isolation process. In situ imaging of the whole skin can offer an interesting alternative to assess the relative contributions of different layers tested simultaneously, as illustrated by the ingenious combination of a shear test with digital image correlation by Gerhardt et al. [46, 47], in which the mechanical properties of the epidermis and dermis could be identified as a function of depth, see Fig. 3.

In vivo, it is particularly difficult to decorrelate the relative contributions of each layers. This has been done recently through two different approaches. The first one is to combine multiple mechanical tests at different solicitations with numerical methods [48]. The second one consists in using simultaneous mechanical loading and in situ image acquisitions, both being compatible with in vivo experiments [15, 46, 49]. In both approaches, the mechanical parameters of the different layers can then be determined through inverse methods assuming a particular formulation for the constitutive behavior of each layer (see chapter "Inverse Methods" for a review of inverse methods applied to skin characterisation).

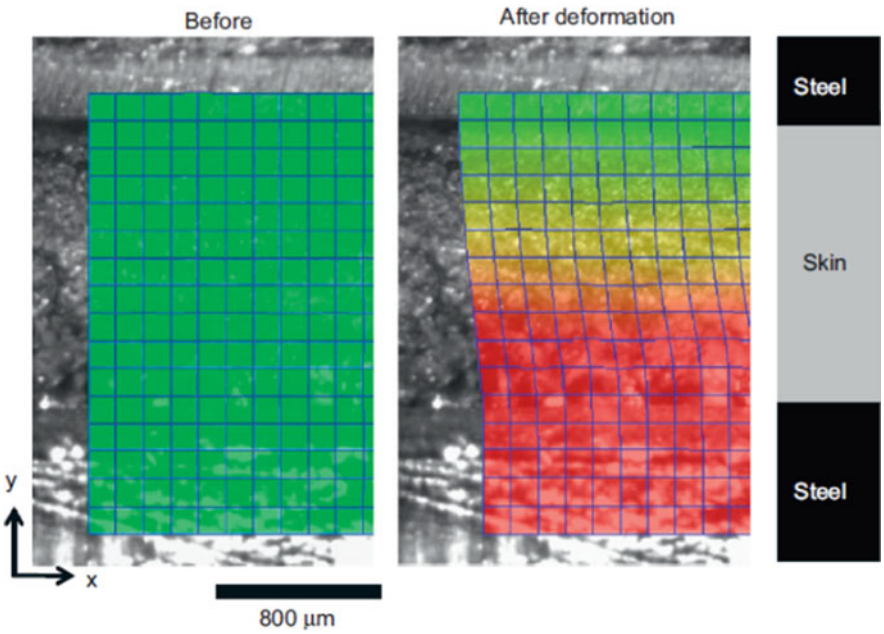

Fig. 3 Displacement fields of porcine skin under shear (left: undeformed image, right: 10% global deformation). Full thickness skin is placed between two steel plates, the lowest one being moved by an eccentric rotation stage. The images were obtained through a stereo-microscope. The displacement was obtained by Digital Image Correlation. One can observe less deformation of the upper skin layers (quantified in the original paper). Figure from Gerhardt et al. [46]

3 Dermis

The dermis is by far skin's most studied layer from a mechanical point of view since it is considered to be the main contributor to the mechanical properties [50]. The dermis is mainly composed of collagen and elastic fibers (elastin and fibrillin, often referred together as elastin), surrounded by a water-rich disorganized matrix of biomolecules (proteoglycans, etc.). The dermis is separated in two parts based on morphology of the collagen network: the papillary dermis and the reticular dermis. The papillary dermis is closest to the epidermis and consists of fairly small, curled and crimped collagen fibers, that are quite loosely arranged. The deepest layer of the dermis is called reticular dermis: it consists of fibers that are arranged in thick bundles stacked densely onto one another. The papillary dermis is much thinner than the reticular dermis, with a ratio of approximately 0.2/0.8. The dermis contains very few cells, the fibroblasts, which play a critical role in regenerating and repairing the tissue. The microstructure of the dermis changes drastically with time, as a result of both age (intrinsic ageing) and exposure to external factors such as UV light or pollution. The reader is referred to [51] for a comprehensive review of these changes or chapter "Constitutive Modelling of Skin Ageing".

To investigate the effect of each microstructural component on the skin's mechanical properties, two main types of approaches are possible: post-mortem and in-situ observations.

3.1 Role Classically Attributed to Each Microstructural Component of Skin

Hypotheses on the role of each of the dermis's microstructural components in the overall macroscopic mechanical properties have been discussed as early as the 1970s [3, 32]. At that time, the structure of some collagen-rich tissues had already been observed quite well, in particular that of tendons, which have a simpler structure than skin and no elastic fibers, and that of aortas.

Ever since, it has been classically considered that the main contributor to the mechanical properties of the dermis are the collagen fibers. These fibers are initially more or less randomly distributed in the skin plane and present a very wavy and coiled structure. In the toe region of a typical uniaxial tensile test stress-stretch curve, the fibers are believed to unfold gradually. The classical interpretation then states that in the heel region, they become progressively more and more aligned in the direction of traction. In the linear region, they are then mechanically loaded and stretched, leading to a strong increase of the reaction force.

Elastin is considered to play an important mechanical role at low forces and stretches, while at that point the collagen fibers are still undulated and thus unable to sustain load. However the main contribution of elastin is believed to be in giving skin the ability to recoil after being stretched, something the collagen network alone is not believed to be able to do by itself [11, 43]. The authors of the studies on elastin emphasize the key role of the entanglement of the elastin and collagen networks: it is because the elastic fibers are interconnected with the collagen fibers that they are able to pull back the collagen in its original configuration.

There is no classically accepted interpretation of the role of other non-fibrillar molecules, such as proteoglycans, in the dermis' mechanics. On one hand, a trypsin treatment degrading the non-fibrillar matrix has been found to have no effect on the mechanical properties [43]. On the other hand, a large part of the literature attributes to proteoglycans a key role in the change of mechanical properties with ageing [52, 53]. Alterations of the non-fibrillar matrix through genetic modifications has also been shown to change the mechanical response of skin [42], and in particular its preconditioning [12]. To this day, it remains difficult to understand the molecular origin of these changes in mechanical properties. The lack of consensus comes partly from the difficulty to image the organization of proteoglycans. In most modeling attempts, the contribution of the non-fibrillar matrix is either neglected or reduced to a pure incompressible medium or very soft incompressible elastic matrix.

3.2 Post-mortem Studies of the Relationship Between Microstructure and Mechanics

In post-mortem experiments, the microstructure is characterised at different stretch levels by observing different samples at each stretch level. However, due to intra-specimen variability, two different samples have different microstructural features, and thus the main drawback of this technique is that it can only be used to achieve statistical consideration. However, post-mortem observations do allow to use any imaging technique, including the most powerful ones. Destructive imaging approaches, such as histological cross-sectioning and scanning electron microscopy (SEM) are generally selected.

Histological cross-sectioning is the most classical approach to observe the microstructure of a biological tissue. A biopsy of the tissue is fixed, embedded in paraffin, and thin slices are cut (a few micrometers thick). The sections are then deparaffinised, colored with a chosen stain or combination of stains specific to the components sought and observed under an optical microscope. This approach allows for an easy identification of the various constituents of skin, for instance using hematoxylin-eosin staining of transverse sections. However, it remains strongly invasive, and limited to 2D sections. It has been used mainly to characterise the tissue in an unloaded state, and to infer the mechanical properties from the composition, for instance comparing skin from young and aged donors, from different ethnicities or different anatomical locations [54].

In **scanning electron microscopy**, the sample is imaged using an electron beam. SEM allows for incredible resolutions of about a few nanometers over a small field of view, and thus very small details can be observed at the surface of the sample. The price of that resolution is the need to put the sample into a vacuum environment, meaning that the sample has to be fixed, and the very small field of view and imaging depth. The obtained images are in grey levels and difficult to interpret for novice users. SEM has been performed on skin as early as the seventies to observe the rearrangement of collagen fibers under stretching [25, 26]. These observations agreed with the classical interpretation of the role of the collagen fibers in skin mechanics described above. Note that transmission electron microscopy (TEM) can also been used in ultra-thin sections and provide typically the same resolution and field of view.

The main limitation of the post-mortem approach is that it is not possible to track a unique region of interest during the mechanical assay. Thus, it cannot be used to quantify the evolution of the microstructure. This is why in situ approaches have been developed recently, taking advantages of the progresses of optical imaging techniques.

3.3 In Situ Exploration of the Relationship Between Microstructure and Mechanics

Quantifying the evolution of the microstructure during a mechanical assay requires a method that doesn't destroy the sample. Ideally, this method should also necessitate no staining, or only a simple one, so that the mechanical properties are not altered. It should also permit to observe a relatively large field of view, to correlate the observations with the macroscopic mechanical properties. Finally, it has to be fast enough so that it remains possible to preserve the sample during the whole assay, meaning that the whole experiment should last no more than a few hours.

Very few methods are compatible with all these criteria: X-rays and optical methods. However, skin is not sufficiently organized to be observed using X-rays, contrary to tendons [55] or muscles [56]. Optical methods can be applied to skin, which is partially transparent to light. The difficulty is then to observe specifically different constituents. Four types of optical methods can mainly be considered: confocal microscopy, polarimetric imaging, optical coherent tomography and multiphoton microscopy. We will present mainly studies performed with multiphoton microscopy, as it is the technique that has shown the most interest to study the dermis. We will afterwards briefly discuss the other three methods as possible alternatives.

3.3.1 Principle of Multiphoton Microscopy

Multiphoton microscopy is a laser-scanning imaging technique that uses non-linear optical effects as a source of contrast in biological samples. It means that it relies on the combination of two or more photons into one photon by the tissue, hence the term "non-linear". To image skin tissues the most adapted multiphoton techniques are second harmonic generation (SHG) microscopy and two-photon excited fluorescence (2PEF) microscopy. The two types of signals can be obtained simultaneously on the same microscope and both ex vivo and in vivo. They require an important light power to exploit the non-linear response of the material. Thus, pulsed lasers are typically used, with around 100 femtoseconds pulse duration, which deliver a high peak power for a low mean power and therefore low invasiveness for the tissue.

The principle of multiphoton microscopy is illustrated in Fig. 4a through electronic states diagrams (simplified Jablonski diagrams). The laser light excites the molecules of the tissue, which under the proper physical conditions emit light in return. SHG and 2PEF signals require two inbound photons for the excitation. Hence, the probability of occurrence of photon emission increases strongly with the number of photon present (precisely with the square of the number of photons). As the number of photons is maximal in the focal point of the laser, the multiphoton signal will be generated exclusively in this part of the laser beam, as shown for 2PEF on the right side of Fig. 4b. This so-called optical sectioning ensures an axial

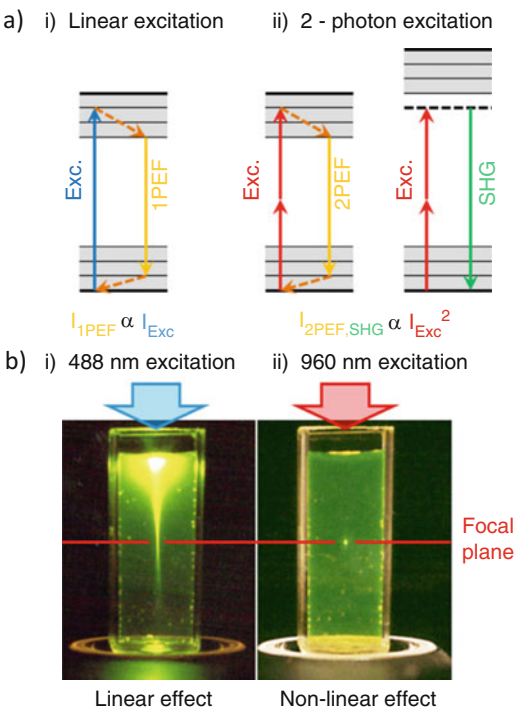

Fig. 4 Non-linear imaging. (**a**) Simplified Jablonski diagrams of (i) 1-photon and (ii) 2-photon excitation signals (left: 2PEF, right: SHG). Figure from Lynch [57]. (**b**) Spatial distribution of the emitted signal of a fluorescein solution, for (i) 1-photon and (ii) 2-photon excited fluorescence. Figure from Zipfel et al. [58]

resolution and enables three-dimensional imaging: once the signal is collected from a given point (voxel), a 3D image can be reconstructed by scanning the focal point at all the wanted positions. In contrast, for classical fluorescence, the signal intensity is proportional to the number of photons, as illustrated in the left image of Fig. 4b: the signal spreads everywhere in the beam path. Three-dimensional imaging is then obtained by imaging the focal volume on a pinhole in front of the detector, resulting in so-called confocal imaging (see below). In practice, both techniques (1-photon and 2-photon excited fluorescence) result typically in the same resolution: around 0.3 μm in the lateral direction and 1–2 μm in the axial direction, depending on the excitation wavelength and on the numerical aperture of the objective lens. However, the intrinsic 3D resolution obtained by optical sectioning in multiphoton microscopy is more robust than confocal imaging in scattering tissues such as skin. Micrometer resolution is therefore better preserved in depth and multiphoton microscopy advantageously ensures 3D imaging with better depth penetration than confocal microscopy.

The depth penetration of multiphoton microscopy strongly depends on the tissue optical properties. In a transparent tissue such as cornea, the full thickness of the tissue may be scanned. In skin however, scattering and absorption ultimately limit the imaging depth. Firstly, absorption reduces the quantity of laser light that penetrates the tissue, limiting the emission per focal point, and also reduces the quantity of photon reaching the detector. Similarly, scattering spreads the focal

point, reducing the emission and deteriorating the resolution in depth. In vivo, the whole epidermis can be imaged, as well as the very superficial layer of the dermis, typically a few tens of micrometers [59]. Ex vivo, when removing the epidermis, it is possible to image the dermis with good resolution up to a depth of typically 100–200 μm.

The **second harmonic generation** signal is generated when two photons of the same wavelength are combined to create a single photon of half that wavelength (see Fig. 4a). At the molecular scale, this signal originates in the excitation of electric dipoles along the peptide bonds. As such, it is an instantaneous and coherent process, which means that the phase of the emitted electric field is related to the phase of the excitation electric field and to the orientation of the dipole. The consequence of this coherence is that the signal is strong for dense and aligned objects, in which constructive interferences build up the signal quadratically. It is the case for collagen fibrils where all the peptide bonds are aligned in the same direction and exhibit a high density. On the contrary, the signal coming from random structure will not be amplified: destructive interferences will annihilate the signal because of centro-symmetry. Thus, fibrillar structures such as collagen fibers, cellulose or microtubules, will be easily visible with SHG, while a disorganized network will be lost in the background. This specificity allows SHG to have an excellent contrast for collagen fibers in skin (see Fig. 5).

Another strength of SHG is that the signal is not subject to photobleaching, contrary to fluorescence. This means that the signal doesn't decrease with time, making it perfect for repeated images. Moreover, it does not imply any absorption process and is therefore a low-invasive technique.

To the advantages of SHG, one can also add the possibility of using polarized light to obtain information on the local organization of the fibers in the focal volume. For linearly polarized light, the more aligned with the excitation light the fibers are, the lower the signal in the perpendicular direction will be. Despite the simplicity of

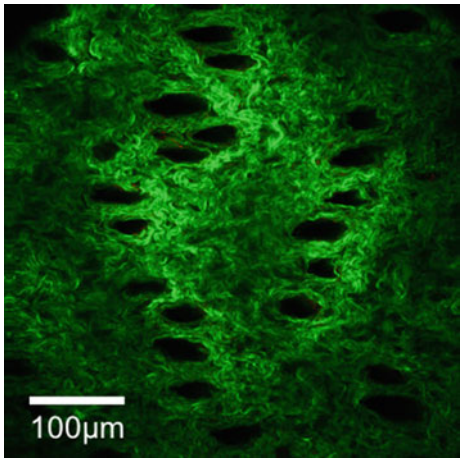

Fig. 5 Typical image of mice skin in rest state obtained with SHG microscopy. The SHG signal appears in green (false color). Black holes are hair follicles. Image from Lynch et al. [30]

this principle, extracting quantitative information from the polarization signal has to be done carefully because the light polarization may be affected by strong focusing and by in-depth propagation into heterogeneous and/or anisotropic tissues [60].

Of course, SHG also suffers from some limitations. The first one is that it is difficult to extract a quantitative information directly from the magnitude of the SHG signal. This magnitude is strongly related to the local organization of the molecules in the focal volume; fibrils oriented in an anti-parallel way in the focal volume exhibit no signal for instance. As a consequence, SHG images are often processed in a semi-quantitative way, exploiting only the pattern of the SHG signal rather than the intensity in every pixel. The second drawback is the acquisition time, as at each point the signal has to be acquired for long enough (few μs) to obtain a significant signal from endogenous molecules. Typically, it will take 1–4 s to scan a 2D area of 512 × 512 pixels, and a few minutes to scan a 3D volume with 100 different planes. During this time, the tissue has to be kept immobile. Thus, SHG can only image a small part of a tissue during a mechanical assay.

These limitations are clearly not important enough to outweigh the advantages of the SHG technique, and this type of microscopy has become more and more popular to study the mechanics of soft tissues since it was first used almost 10 years ago on tendon [61]. It has then been applied on many other biological tissues: aorta [62, 63], cornea [64], fetal membrane [65, 66], liver capsule [67, 68] or pericardium [69]. It is also classically, and has been for a longer time, used to study low density collagen gels [70, 71].

The **two-photon excited fluorescence (2PEF)** signal arises from the simultaneous absorption by a molecule of two photons of a given wavelength. In response, the molecule will emit a single photon at a wavelength slightly higher than half of the excitation wavelength (see Fig. 4a). The 2PEF signal is thus slightly red-shifted with respect to the SHG signal in terms of emitted wavelength, which makes it possible to separate the two signals.

The 2PEF signal can be generated by endogenous molecules in cells or in extracellular matrix, mainly in elastin or collagen. It is usually acquired on skin to observe the organization of elastin. 2PEF can also come from exogenous molecules, and most of the many fluorescent probes available for confocal microscopy do emit 2PEF signal. However, dying the tissue in depth is quite difficult, except by using fluorescent proteins expressed directly in genetically-modified animals. It is possible to target specific molecules in a cell, but the low number of cells in the dermis doesn't make this process effective, with the exception of inflammatory regions, in which cells are more numerous.

Contrary to SHG, the intensity of the 2PEF signal can be taken as a quantitative measure of the number of molecules, albeit with great caution: the magnitude of the signal is also dependent on the absorption properties of the tissue, which can change with depth or when the tissue is mechanically loaded, and it may vary with time due to photobleaching.

Photobleaching and phototoxicity are the main drawbacks of 2PEF microscopy. As the tissue photobleaches, the intensity of the signal decreases, which means that the observation of low-density structures such as elastin may be difficult after a

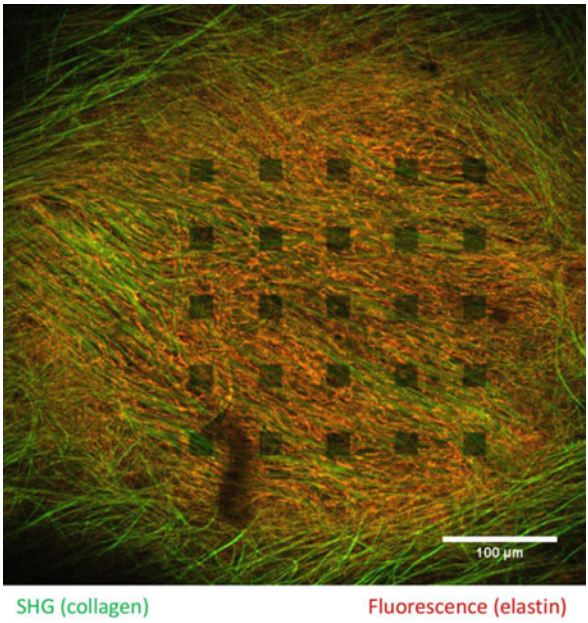

Fig. 6 Typical photobleached grid on a human liver Gilsson's capsule observed with multiphoton microscopy. The photobleached squares are on the 2PEF signal (magenta), emitted by elastin, while the SHG signal (green), emitted by collagen fibers, is not subjected to photobleaching and remains visible everywhere. Image from Jayyosi et al. [67]

while. High excitation power may also damage the tissue. However, these effects can be mitigated by use of low excitation power. Notably, photobleaching has been exploited in tendon and Gilsson's capsule to draw patterns on the tissue, which were then monitored during mechanical loading to measure the local strain field [72, 73], as illustrated in Fig. 6.

3.3.2 Quantitative Multiscale Mechanics of the Dermis with Multiphoton Microscopy

Collagen Network

SHG has been used to observe the rearrangement of the collagen network during a tensile test on skin [42, 74]. These experiments were performed on ex vivo skin from the back of mice. After preparation, including removal of hairs and removal of the epidermis to isolate the dermis, samples were attached to a uniaxial traction device placed under the microscope (see Fig. 7a, b), with a drop of immersion gel on top to preserve its hydration state.

The sample was then progressively stretched. The stretching was incremental and was paused during the SHG image acquisition. This resulted in a relaxation of the force, as expected from a viscoelastic material. Figure 7c shows a typical example of loading path and recorded force versus time curves. The strain rate has to be very slow (less than 10^{-4} s^{-1}) so that it is possible to follow the same region of interest (ROI) with the microscope. Indeed, even with a symmetric traction device, the ROI

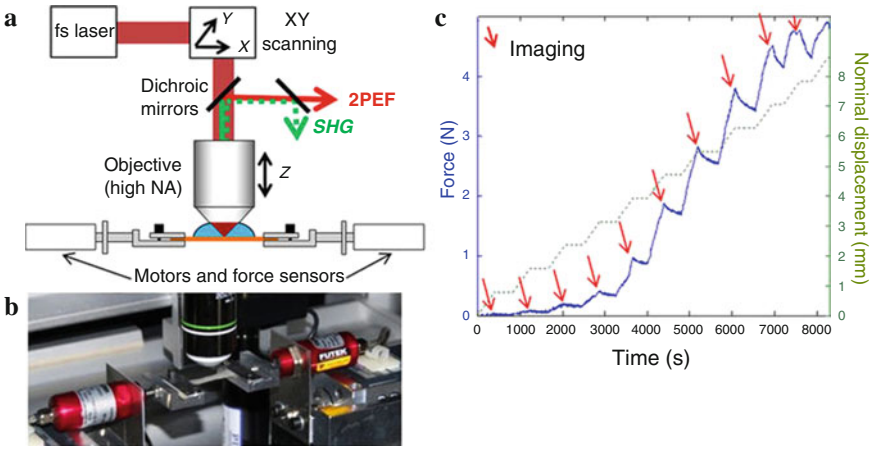

Fig. 7 Experimental set-up combining multiphoton microscopy with a uniaxial traction device. (**a**) Schematic representation and (**b**) photo of the set-up: a mice skin sample is maintained between the two grips of the symmetric traction device (**c**) Nominal displacement (green) and force (blue) versus time curves of a typical experiment, showing the incremental stretching of the skin sample and corresponding image acquisition after each displacement step (red arrows). Figure from Bancelin et al. [42]

will move slightly during stretching. These displacements have to be compensated manually.

Figure 8 shows typical SHG images obtained at different stretch levels. Qualitatively, the reorganization of the collagen network seems close to the one obtained with a post-mortem approach using SEM [25, 26]. The fibers appear more and more aligned in the direction of traction as the stretch increases. The holes of the hair follicles become more and more elliptical and aligned in the direction of traction.

Quantitative information can be extracted from such images. Firstly, local strains can be determined. Local strains quantification is useful to validate the testing set-up, evaluate the local homogeneity of the strain and observe the behavior of the sample in the direction perpendicular to traction (compressibility). [74] performed Digital Image Correlation (DIC) to measure a local strain field at different distances from hair follicles, as well as the strain at the scale of the field of view. As SHG image acquisition can only be performed semi-continuously, DIC is difficult to implement for large stretches, because the pattern of collagen fibers changes greatly between two stretch levels, hindering the correlation. Bancelin et al. [42] tracked the center of the hair follicles to measure the strain at the scale of the field of view. This approach is more robust for large stretches but doesn't allow to probe smaller scales. In the direction of stretching, the mesoscopic strain, at the scale of the field of view, was found to be similar to the imposed macroscopic one (see Fig. 9a), which means that the sample is homogeneous at this scale. In the direction perpendicular to traction, the stretch was found to be constant for small stretches, despite the mechanical loading imposed on the sample (see Fig. 9b). Surprisingly,

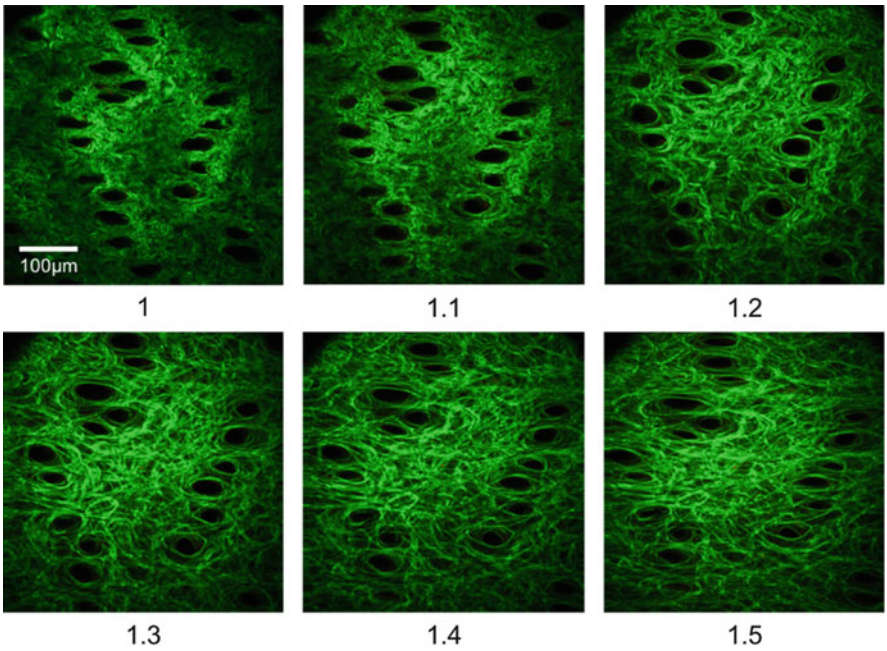

Fig. 8 Typical SHG images of a unique mice skin sample at different indicated stretch levels. The SHG signal is in green. Black holes are hair follicles. The traction is applied in the horizontal direction. The unstretched image is the same as Fig. 5

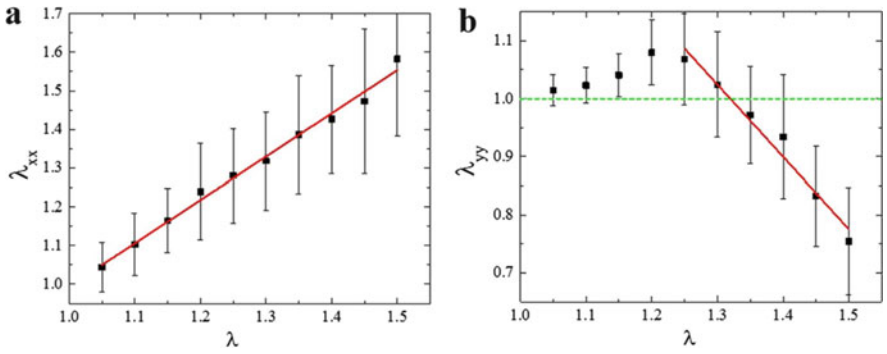

Fig. 9 Stretch measured at the scale of the SHG image versus applied macroscopic stretch on mice skin. (**a**) Stretch in direction of the traction. (**b**) Stretch in the perpendicular direction. Figure adapted from Bancelin et al. [42]

when the epidermis was removed the strain was even found to increase, meaning the sample swelled in the direction perpendicular to traction [42]. After a certain stretch level, the strain perpendicular to traction decreased linearly with the imposed stretch. This effect, attributed to a poroelastic phenomenon, has been reported since

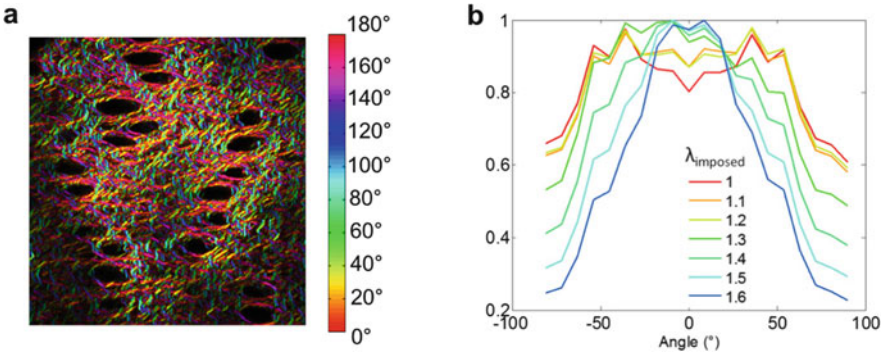

Fig. 10 Fiber orientation measured from the SHG images through a rotating element (**a**) Orientation map extracted from Fig. 5. (**b**) Associated orientation histogram at different stretch levels. Adapted from Lynch et al. [30]

the earliest measurement of skin's macroscopic mechanical properties [3]. No shear was observed.

More interestingly for a multiscale approach, another information that can be acquired from the SHG signal is the orientation of collagen fibers. To determine the collagen fiber orientation, Nesbitt et al. used a fast Fourier transform (FFT) analysis [74]. This approach is commonly implemented to analyze the orientation histogram of fibers. However, it presents the limitation of measuring all the spatial scales at the same time. This means that it is not possible to determine whether the increased organization observed has been generated by changes at smaller scales, for example due to fibers straightening, or larger scales, by fibers reorganizing at the scale of the image. Bancelin et al. [42] used a morphological approach: with a rotating element, one can determine the direction closest to the fiber orientation, pixel by pixel to obtain orientation maps (see Fig. 10a). This approach is more complex to implement and has a lower angular resolution. However, the selected size of the rotating element imposes the actual length scale that is probed. In these two approaches, the fiber orientation distribution is characterised by an orientation histogram (either extracted from the FFT or reconstructed from the map), which can be easily followed at different stretch levels (see Fig. 10b). It is even more convenient to use a scalar, the orientation index (OI), which is related to the width of the distribution. A reduction of this width, resulting in a higher OI, can be understood as an increase of the fraction of fibers aligned in the direction of traction.

During a typical uniaxial tensile test, the OI appears to evolve similarly to the stress (see Fig. 11). In the toe and heel regions of the stress-stretch curve it remains fairly constant, while it increases linearly with the stretch in the linear region.

This observation seems in contradiction with the classical interpretation of the role of the collagen network in the overall mechanics of the dermis. In this interpretation, the fibers realign with the direction of traction in the heel region while they are elongated in the linear part. Following this microstructural interpretation,

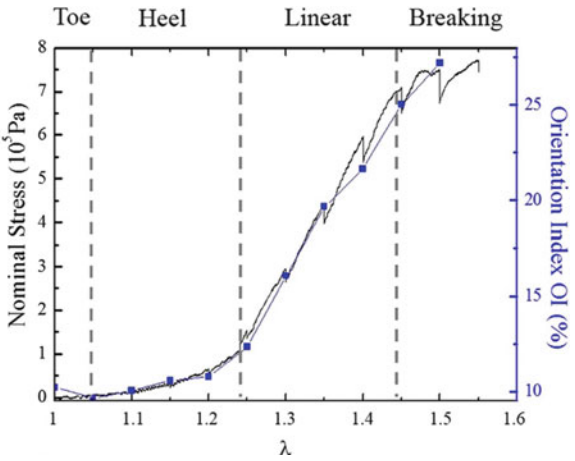

Fig. 11 Nominal stress (black) and Orientation Index (blue) versus the global stretch applied to mice skin. Figure from Bancelin et al. [42]

the OI should increase in the toe and heel regions and saturate in the linear part, resulting in a plateau. Some new interpretation appears to be needed to account for these experimental data, probably involving a more complex response of the network, such as a global contribution of the connected fibers and/or a plastic response of the fibers [30].

All microstructural mathematical models of skin include information about the collagen network orientation and mechanical contribution. For examples of the possible models, the reader is referred to the following references [6, 20, 75, 76], while a more complete description can be found in chapters "Constitutive Modelling of Skin Mechanics", "Constitutive Modelling of Skin Growth", "Constitutive Modelling of Skin Wound Healing" and "Constitutive Modelling of Skin Ageing".

These mathematical models all rely on the so-called affine assumption, which states that fiber stretches and rotations follow the deformations of the surrounding volume. This assumption has the major advantage to be purely kinematics. In SHG images one can measure simultaneously the strain and the fibers orientation at the scale of the field of view. Thus, it is possible to test the affine assumption by computing the theoretical evolution of the initial orientation histogram under the applied mechanical loading. The affine assumption satisfactorily predicts that the OI should remain almost constant in the toe and heel regions and should increase linearly in the linear part [67]. However, it systematically overestimates the OI in the linear part (see Fig. 12), implying that it overestimates fibers alignment. Consequently, the affine assumption is valid for the toe and heel regions but should be taken with caution in the linear region of the stress-stretch curve.

The combination of SHG and traction assays has also been adapted to altered skin states, for example, when skin is affected by genetic diseases [42], age [77] or wounds [48]. It explains, at least partially, how microstructural changes can

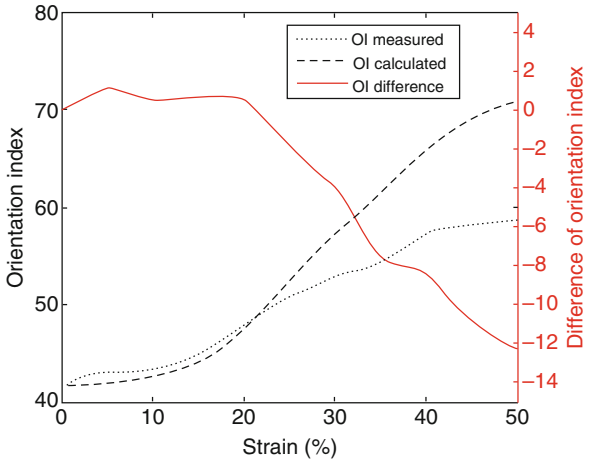

Fig. 12 Evolution of the OIs measured (dotted black line) and calculated (dashed black line), and their difference (measured minus calculated) (red), as a function of applied strain. Figure from Jayyosi et al. [67]

be associated with observable changes in the macroscopic mechanical properties.

Elastin Network

The 2PEF signal has been used to image the evolution of the elastin network during a mechanical loading in aorta [78], as illustrated on Fig. 13. The advantage of this signal is that it can be recorded simultaneously with the SHG signal, so that the two images can also be superimposed.

In skin, to the best of our knowledge, no experimental work has been carried out to follow the elastic network during a mechanical assay. This is likely due to the fact that the elastic network is not as dense in skin as it is in the aorta, making it difficult to observe without any labelling, at least in murine skin.

3.3.3 Other Types of Microscopy

Confocal Microscopy

Confocal microscopy is now widespread in biology since this technique allows for fluorescence or reflectance imaging in three dimensions. It typically offers the same 3D resolution as that obtained in multiphoton microscopy, and similar acquisition times (both of them being laser-scanning techniques). It often requires that the collagen fibers be stained, which can be complex for thick tissues and not perfectly specific or uses reflectance signals that are not specific. Moreover, confocal microscopy is more sensitive to scattering than multiphoton microscopy and therefore suffers from lower penetration depth in highly scattering tissues such as skin. In skin, examples can be found of combining confocal microscopy with collagen staining to determine the initial collagen organization [6]. In tendon, this

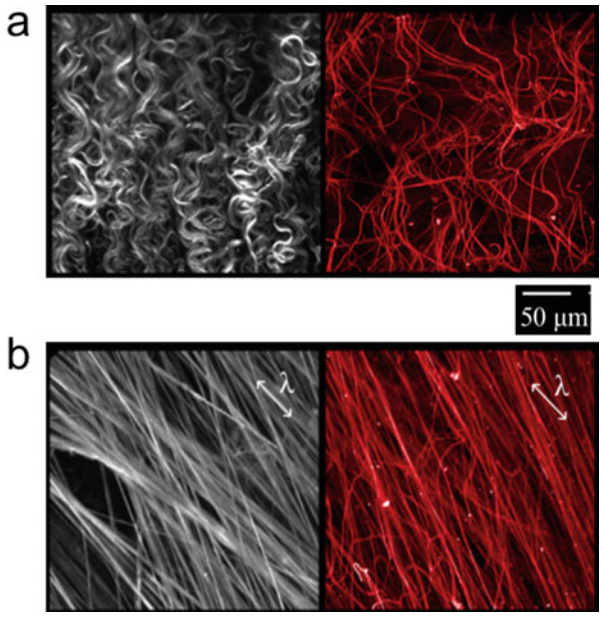

Fig. 13 Arterial microstructure imaged with a multiphoton microscope (adventitia layer). (**a**) Free load state and (**b**) diagonal load (stretch $\lambda = 1.9$). The collagen is colored in grey (left) and the elastin in red (right). Figure adapted from Krasny et al. [78]

approach has been used to determine the local strains during a mechanical assay [72, 79].

Optical Coherent Tomography

Optical coherent tomography (OCT) is an interferometric technique sensitive to the contrast of reflectance (due to variation of the refractive index). Thus, it allows imaging the interfaces between skin's different layers in 3D.

Different approaches can be used to obtain OCT image. Mainly, one can list the full field OCT (FF-OCT) and the spectral domain OCT (SD-OCT). SD-OCT uses a spectral decomposition of the optical signal to determine the information in depth: one acquisition point gives access to the information on the whole accessible depth. Then, the image is reconstructed by moving the acquisition points on the surface. The main advantage of the SD-OCT is that it is very fast. However, its resolution is typically limited to 10 μm in the axial (depth) direction, and few micrometers (around 3–4) in the lateral direction. FF-OCT images directly one horizontal plane of the sample through a camera. The reconstruction in depth is obtained by changing the lengths of the interferometer arm. This approach requires a very good signal to noise ratio, and thus is significantly slower than the SD-OCT. However, it allows to use objectives with high numerical aperture, and thus has much better resolutions (typically, 1 μm in each direction).

OCT has the drawback of being non-specific, so that it can observe only the different skin layers, and doesn't give access to the microstructure. However, it has strong advantages for in situ experiments, in particular the SD-OCT. Firstly, it has a good spatial resolution, even with lenses with long working distances and not immerged. It could even be used to image individual cells or their aggregates in the stratum corneum (see Sect. 4). Secondly, it is cheap (with respect to other optical methods) and fast. These advantages are of great interest for in situ assays and especially in vivo ones.

To the best of our knowledge, it appears that OCT has not been used in skin for the measurement of strain fields, but it has already been used to measure skin's thickness and surface shape during suction experiments [80].

Polarimetric Imaging

In its basic implementation, polarimetric imaging uses linearly polarized light to investigate the optical response of the tissue in this specific orientation. If the oriented light interacts with a non-aligned medium, it will be partly deviated, creating a light signal split between the initial orientation and the perpendicular one. Then, by rotating the initial orientation, it is possible to determine the effect on all orientations [81]. In a more complex implementation (Mueller imaging), different states of polarization are used, including circular and elliptical ones, and the reflected light is also analyzed along all these states. These complex implementations provide more information than the basic one, at the expense of an increased acquisition time and complex image processing [82].

In uterine cervical cones, another type of collagen-rich tissue, it has been shown that the main orientation determined through polarimetric techniques is related to the collagen fibers orientation [82]. Polarimetric imaging has also been performed on skin for cancer diagnostic [83].

This approach is a reflection technique limited to bi-dimensional surface images, while the polarimetric signal still comes from the light penetration along a certain depth in the sample. Thus, it is not straightforward to determine the origin of the evolution of the polarization without other analysis methods. However, it is a bright-field technique that allows for short acquisition times (depending on the number of images acquired at different polarizations). If used complementarily to more specific imaging methods, the short acquisition time of this technique could be very useful for in vivo observations as each image only requires a few seconds.

4 Viable Epidermis and Stratum Corneum

The epidermis plays a fundamental role in skin physiology and biomechanics. In particular, its outermost layer, the stratum corneum, has to be an efficient barrier against injuries and pathogen invasion. The stratum corneum also maintains skin hydration by limiting water evaporation.

Because it is the most external layer of skin, the stratum corneum is easily accessible for in vivo experiments. And because it is a rather stiff layer, it is also

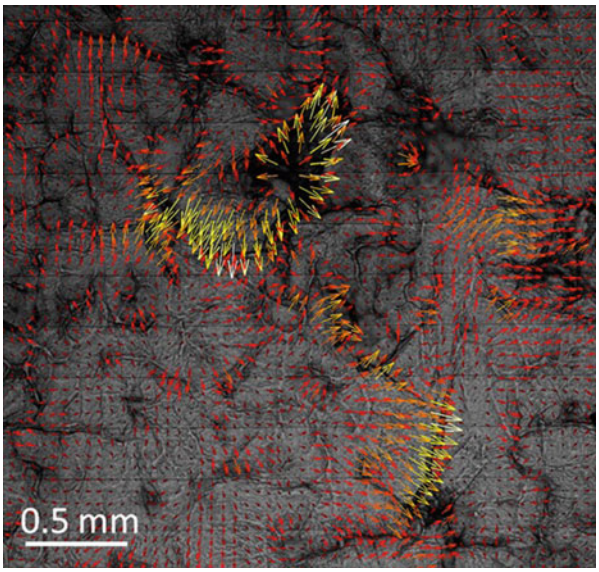

Fig. 14 Stratum corneum topography (grey) and force distribution (arrow). Forces are generated after drying the stratum corneum from 99 to 54% relative humidity. Figure from German et al. [84]

easy to isolate for in vitro experiments. Thus, quite a few studies have reported in situ experiments to measure the mechanical properties of the last few layers of skin, with a special focus on the impact of the hydration level [84–86]. For large scale measurements of displacement, multiphoton microscopy (2PEF) and confocal microscopy were also used. Much more local information was obtained through Raman spectroscopy [87], in order to relate hydration level to molecular structure and mechanical properties.

From these studies, we know that the stratum corneum is homogeneous at macroscopic scales but that heterogeneous strain fields can be observed at the scale of cell aggregates, around 100 μm, during the drying process (see Fig. 14). The stratum corneum shows strong variations in stiffness with the relative humidity, and thus presents a depth gradient: the stiffness is almost similar to the subjacent epidermal layers when saturated in water, while it strongly increases when approaching the skin surface.

5 Hypodermis

The hypodermis is mainly made of fat lobules, surrounded by weakly organized collagen-rich structures, called septa. Thus, it has a low stiffness (a few kPa to 100 kPa) and is difficult to separate from the dermis. As a consequence, the mechanical properties of the hypodermis have barely been studied [23, 88–91].

To the best of our knowledge, the link between mechanics and microstructure has never been explored in ex vivo hypodermis. However, a few interesting ideas have been tested in cultivated in vitro adipocytes, in particular by using atomic force microscopy (AFM) to locally probe the stiffness of adipocytes [92] or by using magnetic resonance imaging (MRI) to measure deformations in the subcutaneous tissue in vivo when applying a macroscopic strain [93].

6 Conclusion

Skin mechanical properties are considered to be deeply related to the microstructure of its layers, with a main contribution of the dermis. While many techniques are available to image skin's microstructure, it remains difficult to attribute a specific contribution to each microstructural component without observing them simultaneously during a mechanical assay. This limits the range of suitable imaging techniques to non-destructive approaches, which also need to have sufficient resolution and specificity in identifying particular structural components (e.g. collagen fibers).

This explains why the number of in situ multiscale mechanical studies has been limited in the past. However, nowadays, this trend is reversed with the advent of novel advanced optical microscopy. In particular, the combination of second harmonic generation microscopy with mechanical assays made it possible to probe the specific role of collagen in the mechanics of the dermis. This approach also highlighted limitations associated with the assumption of affinity of deformations, which is used in most constitutive models of skin mechanics.

Still, despite notable progress, much work remains to be done. In the dermis, the roles of the elastic network and that of other non-fibrillar components remain to be explored. Similarly, very little information is available on the epidermis and hypodermis. These layers are considered less important for skin's overall macroscopic mechanical properties but do play key roles in the biological functions of the skin.

References

1. Lanir Y, Fung YC (1974) Two-dimensional mechanical properties of rabbit skin—II. Experimental results. J Biomech 7:171–182. https://doi.org/10.1016/0021-9290(74)90058-X
2. Tong P, Fung Y-C (1976) The stress-strain relationship for the skin. J Biomech 9:649–657. https://doi.org/10.1016/0021-9290(76)90107-X
3. Veronda DR, Westmann RA (1970) Mechanical characterization of skin—finite deformations. J Biomech 3:111–124
4. Affagard J-S, Wijanto F, Allain J-M (2017) Improving the experimental protocol for a more accurate identification of a given mechanical behaviour in a single assay: application to skin. Strain 53:e12236. https://doi.org/10.1111/str.12236

5. Edwards C, Marks R (1995) Evaluation of biomechanical properties of human skin. Clin Dermatol 13:375–380. https://doi.org/10.1016/0738-081X(95)00078-T
6. Jor JWY, Nash MP, Nielsen PMF, Hunter PJ (2010) Estimating material parameters of a structurally based constitutive relation for skin mechanics. Biomech Model Mechanobiol 10:767–778. https://doi.org/10.1007/s10237-010-0272-0
7. Edsberg LE, Mates RE, Baier RE, Lauren M (1999) Mechanical characteristics of human skin subjected to static versus cyclic normal pressures. J Rehabil Res Dev 36(2):133–141
8. Wang Y, Marshall KL, Baba Y et al (2013) Hyperelastic material properties of mouse skin under compression. PLoS One 8:e67439. https://doi.org/10.1371/journal.pone.0067439
9. Hollenstein M, Ehret AE, Itskov M, Mazza E (2011) A novel experimental procedure based on pure shear testing of dermatome-cut samples applied to porcine skin. Biomech Model Mechanobiol 10:651–661. https://doi.org/10.1007/s10237-010-0263-1
10. Bonod-Bidaud C, Roulet M, Hansen U et al (2012) In vivo evidence for a bridging role of a collagen V subtype at the epidermis–dermis interface. J Investig Dermatol 132:1841–1849
11. Oxlund H, Manschot J, Viidik A (1988) The role of elastin in the mechanical properties of skin. J Biomech 21:213–218. https://doi.org/10.1016/0021-9290(88)90172-8
12. Eshel H, Lanir Y (2001) Effects of strain level and proteoglycan depletion on preconditioning and viscoelastic responses of rat dorsal skin. Ann Biomed Eng 29:164–172. https://doi.org/10.1114/1.1349697
13. Agache PG, Monneur C, Leveque JL, De Rigal J (1980) Mechanical properties and Young's modulus of human skin in vivo. Arch Dermatol Res 269:221–232. https://doi.org/10.1007/BF00406415
14. Kvistedal YA, Nielsen PMF (2009) Estimating material parameters of human skin in vivo. Biomech Model Mechanobiol 8:1–8. https://doi.org/10.1007/s10237-007-0112-z
15. Hendriks FM, Brokken D, Oomens CWJ, Baaijens FPT (2004) Influence of hydration and experimental length scale on the mechanical response of human skin in vivo, using optical coherence tomography. Skin Res Technol 10:231–241. https://doi.org/10.1111/j.1600-0846.2004.00077.x
16. Pailler-Mattéi C, Zahouani H (2006) Analysis of adhesive behaviour of human skin in vivo by an indentation test. Tribol Int 39:12–21. https://doi.org/10.1016/j.triboint.2004.11.003
17. Groves RB (2011) Quantifying the mechanical properties of skin in vivo and ex vivo to optimise microneedle device design. Cardiff University, Cardiff
18. Abrahams M (1967) Mechanical behaviour of tendon in vitro. Med Biol Eng 5:433–443
19. Elsheikh A, Alhasso D, Rama P (2008) Biomechanical properties of human and porcine corneas. Exp Eye Res 86:783–790. https://doi.org/10.1016/j.exer.2008.02.006
20. Holzapfel GA, Sommer G, Gasser CT, Regitnig P (2005) Determination of layer-specific mechanical properties of human coronary arteries with nonatherosclerotic intimal thickening and related constitutive modeling. Am J Physiol Heart Circ Physiol 289:H2048–H2058. https://doi.org/10.1152/ajpheart.00934.2004
21. Ottenio M, Tran D, Ní Annaidh A et al (2015) Strain rate and anisotropy effects on the tensile failure characteristics of human skin. J Mech Behav Biomed Mater 41:241–250. https://doi.org/10.1016/j.jmbbm.2014.10.006
22. Pensalfini M, Haertel E, Hopf R et al (2018) The mechanical fingerprint of murine excisional wounds. Acta Biomater 65:226–236. https://doi.org/10.1016/j.actbio.2017.10.021
23. Samani A, Zubovits J, Plewes D (2007) Elastic moduli of normal and pathological human breast tissues: an inversion-technique-based investigation of 169 samples. Phys Med Biol 52:1565–1576. https://doi.org/10.1088/0031-9155/52/6/002
24. Diridollou S, Vabre V, Berson M et al (2001) Skin ageing: changes of physical properties of human skin in vivo. Int J Cosmet Sci 23:353–362
25. Belkoff SM, Haut RC (1991) A structural model used to evaluate the changing microstructure of maturing rat skin. J Biomech 24:711–720
26. Brown IA (1973) Scanning electron-microscope study of effects of uniaxial tension on human skin. Br J Dermatol 89:383–393

27. Hoath SB, Leahy DG (2003) The organization of human epidermis: functional epidermal units and phi proportionality. J Investig Dermatol 121:1440–1446. https://doi.org/10.1046/j.1523-1747.2003.12606.x
28. Ní Annaidh A, Bruyère K, Destrade M et al (2012) Characterization of the anisotropic mechanical properties of excised human skin. J Mech Behav Biomed Mater 5:139–148. https://doi.org/10.1016/j.jmbbm.2011.08.016
29. Shergold OA, Fleck NA, Radford D (2006) The uniaxial stress versus strain response of pig skin and silicone rubber at low and high strain rates. Int J Impact Eng 32:1384–1402. https://doi.org/10.1016/j.ijimpeng.2004.11.010
30. Lynch B, Bancelin S, Bonod-Bidaud C et al (2016) A novel microstructural interpretation for the biomechanics of mouse skin derived from multiscale characterization. Acta Biomater 50:302–311. https://doi.org/10.1016/j.actbio.2016.12.051
31. Bismuth C, Gerin C, Viguier E et al (2014) The biomechanical properties of canine skin measured in situ by uniaxial extension. J Biomech 47:1067–1073. https://doi.org/10.1016/j.jbiomech.2013.12.027
32. Fung YC (1993) Biomechanics. Mechanical properties of living tissues, 2nd edn. Springer, New York
33. Kang G, Wu X (2011) Ratchetting of porcine skin under uniaxial cyclic loading. J Mech Behav Biomed Mater 4:498–506. https://doi.org/10.1016/j.jmbbm.2010.12.015
34. Kiss M-O, Hagemeister N, Levasseur A et al (2009) A low-cost thermoelectrically cooled tissue clamp for in vitro cyclic loading and load-to-failure testing of muscles and tendons. Med Eng Phys 31:1182–1186. https://doi.org/10.1016/j.medengphy.2009.06.008
35. Diani J, Fayolle B, Gilormini P (2009) A review on the Mullins effect. Eur Polym J 45:601–612. https://doi.org/10.1016/j.eurpolymj.2008.11.017
36. Langer K (1978) On the anatomy and physiology of the skin – I. The cleavability of cutis. Br J Plast Surg 31:3–8
37. Leyva-Mendivil MF, Lengiewicz J, Limbert G (2018) Skin friction under pressure. The role of micromechanics. Surf Topogr Metrol Prop 6:014001. https://doi.org/10.1088/2051-672X/aaa2d4
38. Leyva-Mendivil MF, Lengiewicz J, Page A et al (2017) Skin microstructure is a key contributor to its friction behaviour. Tribol Lett 65. https://doi.org/10.1007/s11249-016-0794-4
39. Leyva-Mendivil MF, Lengiewicz J, Page A et al (2017) Implications of multi-asperity contact for shear stress distribution in the viable epidermis – an image-based finite element study. Biotribology 11:110–123. https://doi.org/10.1016/j.biotri.2017.04.001
40. Leyva-Mendivil MF, Page A, Bressloff NW, Limbert G (2015) A mechanistic insight into the mechanical role of the stratum corneum during stretching and compression of the skin. J Mech Behav Biomed Mater 49:197–219. https://doi.org/10.1016/j.jmbbm.2015.05.010
41. Park AC, Baddiel CB (1972) Rheology of stratum corneum. A molecular interpretation of the stress-strain curve. J Soc Cosmet Chem 23:3–12
42. Bancelin S, Lynch B, Bonod-Bidaud C et al (2015) Ex vivo multiscale quantitation of skin biomechanics in wild-type and genetically-modified mice using multiphoton microscopy. Sci Rep 5:17635. https://doi.org/10.1038/srep17635
43. Ventre M, Mollica F, Netti PA (2009) The effect of composition and microstructure on the viscoelastic properties of dermis. J Biomech 42:430–435. https://doi.org/10.1016/j.jbiomech.2008.12.004
44. Geerligs M, van Breemen L, Peters G et al (2011) In vitro indentation to determine the mechanical properties of epidermis. J Biomech 44:1176–1181. https://doi.org/10.1016/j.jbiomech.2011.01.015
45. Geerligs M, Peters GWM, Ackermans PAJ et al (2010) Does subcutaneous adipose tissue behave as an (anti-)thixotropic material? J Biomech 43:1153–1159. https://doi.org/10.1016/j.jbiomech.2009.11.037
46. Gerhardt L-C, Schmidt J, Sanz-Herrera JA et al (2012) A novel method for visualising and quantifying through-plane skin layer deformations. J Mech Behav Biomed Mater 14:199–207. https://doi.org/10.1016/j.jmbbm.2012.05.014

47. Lamers E, van Kempen THS, Baaijens FPT et al (2013) Large amplitude oscillatory shear properties of human skin. J Mech Behav Biomed Mater 28:462–470. https://doi.org/10.1016/j.jmbbm.2013.01.024
48. Pensalfini M, Weickenmeier J, Rominger M et al (2018) Location-specific mechanical response and morphology of facial soft tissues. J Mech Behav Biomed Mater 78:108–115. https://doi.org/10.1016/j.jmbbm.2017.10.021
49. Vogt M (2005) Development and evaluation of a high-frequency ultrasound-based system for in vivo strain imaging of the skin. IEEE Trans Ultrason Ferroelect Freq Contr 52:11
50. Montagna W, Parakkal PF (1974) The structure and function of skin, 3rd edn. Academic Press, New York. https://doi.org/10.1016/C2012-0-01604-3
51. Naylor EC, Watson REB, Sherratt MJ (2011) Molecular aspects of skin ageing. Maturitas 69:249–256. https://doi.org/10.1016/j.maturitas.2011.04.011
52. Carrino DA, Önnerfjord P, Sandy JD et al (2003) Age-related changes in the proteoglycans of human skin: specific cleavage of decorin to yield a major catabolic fragment in adult skin. J Biol Chem 278:17566–17572. https://doi.org/10.1074/jbc.M300124200
53. Li Y, Liu Y, Xia W et al (2013) Age-dependent alterations of decorin glycosaminoglycans in human skin. Sci Rep 3:2422. https://doi.org/10.1038/srep02422
54. Langton AK, Graham HK, McConnell JC et al (2017) Organization of the dermal matrix impacts the biomechanical properties of skin. Br J Dermatol 177:818–827. https://doi.org/10.1111/bjd.15353
55. Puxkandl R, Zizak I, Paris O et al (2002) Viscoelastic properties of collagen: synchrotron radiation investigations and structural model. Philos Trans R Soc B Biol Sci 357:191–197. https://doi.org/10.1098/rstb.2001.1033
56. Reconditi M, Brunello E, Linari M et al (2011) Motion of myosin head domains during activation and force development in skeletal muscle. Proc Natl Acad Sci 108:7236–7240. https://doi.org/10.1073/pnas.1018330108
57. Lynch B (2016) Multiscale biomechanics of skin: experimental investigation of the role of the collagen microstructure. Ecole polytechnique
58. Zipfel WR, Williams RM, Webb WW (2003) Nonlinear magic: multiphoton microscopy in the biosciences. Nat Biotechnol 21:1369–1377. https://doi.org/10.1038/nbt899
59. Decencière E, Tancrède-Bohin E, Dokládal P et al (2013) Automatic 3D segmentation of multiphoton images: a key step for the quantification of human skin. Skin Res Technol 19:115–124. https://doi.org/10.1111/srt.12019
60. Gusachenko I, Tran V, Goulam Houssen Y et al (2012) Polarization-resolved second-harmonic generation in tendon upon mechanical stretching. Biophys J 102:2220–2229. https://doi.org/10.1016/j.bpj.2012.03.068
61. Goulam Houssen Y, Gusachenko I, Schanne-Klein M-C, Allain J-M (2011) Monitoring micrometer-scale collagen organization in rat-tail tendon upon mechanical strain using second harmonic microscopy. J Biomech 44:2047–2052. https://doi.org/10.1016/j.jbiomech.2011.05.009
62. Keyes JT, Haskett DG, Utzinger U et al (2011) Adaptation of a planar microbiaxial optomechanical device for the tubular biaxial microstructural and macroscopic characterization of small vascular tissues. J Biomech Eng 133:075001
63. Krasny W, Magoariec H, Morin C, Avril S (2017) Kinematics of collagen fibers in carotid arteries under tension-inflation loading. J Mech Behav Biomed Mater 77:718–726. https://doi.org/10.1016/j.jmbbm.2017.08.014
64. Benoit A, Latour G, Schanne-Klein M-C, Allain J-M (2015) Simultaneous microstructural and mechanical characterization of human corneas at increasing pressure. J Mech Behav Biomed Mater 60:93–105. https://doi.org/10.1016/j.jmbbm.2015.12.031
65. Mauri A, Ehret AE, Perrini M et al (2015) Deformation mechanisms of human amnion: quantitative studies based on second harmonic generation microscopy. J Biomech 48:1606–1613. https://doi.org/10.1016/j.jbiomech.2015.01.045

66. Mauri A, Perrini M, Mateos JM et al (2013) Second harmonic generation microscopy of fetal membranes under deformation: normal and altered morphology. Placenta 34:1020–1026. https://doi.org/10.1016/j.placenta.2013.09.002
67. Jayyosi C, Affagard J-S, Ducourthial G et al (2017) Affine kinematics in planar fibrous connective tissues: an experimental investigation. Biomech Model Mechanobiol 16(4):1459–1473. https://doi.org/10.1007/s10237-017-0899-1
68. Jayyosi C, Coret M, Bruyère-Garnier K (2016) Characterizing liver capsule microstructure via in situ bulge test coupled with multiphoton imaging. J Mech Behav Biomed Mater 54:229–243. https://doi.org/10.1016/j.jmbbm.2015.09.031
69. Alavi SH, Ruiz V, Krasieva T et al (2013) Characterizing the collagen fiber orientation in pericardial leaflets under mechanical loading conditions. Ann Biomed Eng 41:547–561. https://doi.org/10.1007/s10439-012-0696-z
70. Ban E, Franklin JM, Nam S et al (2018) Mechanisms of plastic deformation in collagen networks induced by cellular forces. Biophys J 114:450–461. https://doi.org/10.1016/j.bpj.2017.11.3739
71. Vader D, Kabla A, Weitz D, Mahadevan L (2009) Strain-induced alignment in collagen gels. PLoS One 4:e5902. https://doi.org/10.1371/journal.pone.0005902
72. Cheng VWT, Screen HRC (2007) The micro-structural strain response of tendon. J Mater Sci 42:8957–8965. https://doi.org/10.1007/s10853-007-1653-3
73. Jayyosi C, Fargier G, Coret M, Bruyère-Garnier K (2014) Photobleaching as a tool to measure the local strain field in fibrous membranes of connective tissues. Acta Biomater 10:2591–2601. https://doi.org/10.1016/j.actbio.2014.02.031
74. Nesbitt S, Scott W, Macione J, Kotha S (2015) Collagen fibrils in skin orient in the direction of applied uniaxial load in proportion to stress while exhibiting differential strains around hair follicles. Materials 8:1841–1857. https://doi.org/10.3390/ma8041841
75. Bischoff JE (2006) Reduced parameter formulation for incorporating fiber level viscoelasticity into tissue level biomechanical models. Ann Biomed Eng 34:1164–1172. https://doi.org/10.1007/s10439-006-9124-6
76. Manschot JFM, Brakkee AJM (1986) The measurement and modelling of the mechanical properties of human skin *in vivo*—II. The model. J Biomech 19:517–521
77. Lynch B, Bonod-Bidaud C, Ducourthial G et al (2017) How aging impacts skin biomechanics: a multiscale study in mice. Sci Rep 7:13750. https://doi.org/10.1038/s41598-017-13150-4
78. Krasny W, Morin C, Magoariec H, Avril S (2017) A comprehensive study of layer-specific morphological changes in the microstructure of carotid arteries under uniaxial load. Acta Biomater 57:342–351. https://doi.org/10.1016/j.actbio.2017.04.033
79. Screen HR, Bader DL, Lee DA, Shelton JC (2004) Local strain measurement within tendon. Strain 40:157–163
80. Hendriks FM, Brokken D, Oomens CWJ et al (2006) The relative contributions of different skin layers to the mechanical behavior of human skin in vivo using suction experiments. Med Eng Phys 28:259–266. https://doi.org/10.1016/j.medengphy.2005.07.001
81. Qi J, Elson DS (2017) Mueller polarimetric imaging for surgical and diagnostic applications: a review. J Biophotonics 10:950–982. https://doi.org/10.1002/jbio.201600152
82. Bancelin S, Nazac A, Ibrahim BH et al (2014) Determination of collagen fiber orientation in histological slides using Mueller microscopy and validation by second harmonic generation imaging. Opt Express 22:22561. https://doi.org/10.1364/OE.22.022561
83. Jacques SL, Ramella-Roman JC, Lee K (2002) Imaging skin pathology with polarized light. J Biomed Opt 7:329. https://doi.org/10.1117/1.1484498
84. German GK, Engl WC, Pashkovski E et al (2012) Heterogeneous drying stresses in stratum corneum. Biophys J 102:2424–2432. https://doi.org/10.1016/j.bpj.2012.04.045
85. Liang X, Graf BW, Boppart SA (2011) In vivo multiphoton microscopy for investigating biomechanical properties of human skin. Cell Mol Bioeng 4:231–238. https://doi.org/10.1007/s12195-010-0147-6

86. Wu KS, van Osdol WW, Dauskardt RH (2006) Mechanical properties of human stratum corneum: effects of temperature, hydration, and chemical treatment. Biomaterials 27:785–795. https://doi.org/10.1016/j.biomaterials.2005.06.019
87. Vyumvuhore R, Tfayli A, Biniek K et al (2015) The relationship between water loss, mechanical stress, and molecular structure of human *stratum corneum ex vivo*: Relationship between SC water loss, mechanical stress, and molecular structure. J Biophotonics 8:217–225. https://doi.org/10.1002/jbio.201300169
88. Geerligs M (2010) Skin layer mechanics. Technische Universiteit Eindhoven, Eindhoven
89. Geerligs M, Peters GW, Ackermans PA et al (2008) Linear viscoelastic behavior of subcutaneous adipose tissue. Biorheology 45:677–688. https://doi.org/10.3233/BIR-2008-0517
90. Gefen A (2007) Viscoelastic properties of ovine adipose tissue covering the gluteus muscles. J Biomech Eng 129:924. https://doi.org/10.1115/1.2800830
91. Patel PN, Smith CK, Patrick CW (2005) Rheological and recovery properties of poly(ethylene glycol) diacrylate hydrogels and human adipose tissue. J Biomed Mater Res A 73A:313–319. https://doi.org/10.1002/jbm.a.30291
92. Shoham N, Girshovitz P, Katzengold R et al (2014) Adipocyte stiffness increases with accumulation of lipid droplets. Biophys J 106:1421–1431. https://doi.org/10.1016/j.bpj.2014.01.045
93. Shoham N, Levy A, Shabshin N et al (2017) A multiscale modeling framework for studying the mechanobiology of sarcopenic obesity. Biomech Model Mechanobiol 16:275–295. https://doi.org/10.1007/s10237-016-0816-z

Tension Lines of the Skin

Aisling Ní Annaidh and Michel Destrade

Abstract Skin tension lines are natural lines of tension that occur within the skin as a result of growth and remodeling mechanisms. Researchers have been aware of their existence and their surgical implications for over 150 years. Research in the twentieth century showed clearly, through destructive mechanical testing, that the orientation of skin tension lines greatly affects the mechanical response of skin in situ. More recent work has determined that this anisotropic response is, at least in part, due to the structural arrangement of collagen fibres within the dermis. This observation can be incorporated into mathematical and mechanical models using the popular Gasser-Ogden-Holzapfel constitutive equation. Advances in non-invasive measurement techniques for the skin, such as those based on elastic wave propagation, have enabled patient-specific identification of skin tension lines in an accurate and rapid manner. Using this technique on humans, we show that there is considerable variation in the level of anisotropy as the skin ages. Furthermore, we identify that both the structural arrangement of fibres and the in vivo levels of pre-strain play a significant role in the anisotropic behavior of skin.

A. Ní Annaidh
School of Mechanical & Materials Engineering, University College Dublin, Dublin 4, Ireland

UCD Charles Institute of Dermatology, School of Medicine and Medical Science, University College Dublin, Dublin, Ireland
e-mail: aisling.niannaidh@ucd.ie

M. Destrade (✉)
Stokes Centre for Applied Mathematics, School of Mathematics, Statistics and Applied Mathematics, NUI Galway, Galway, Ireland

School of Mechanical & Materials Engineering, University College Dublin, Dublin 4, Ireland
e-mail: michel.destrade@nuigalway.ie

G. Limbert (ed.), *Skin Biophysics*, Studies in Mechanobiology,
Tissue Engineering and Biomaterials 22,
https://doi.org/10.1007/978-3-030-13279-8_9

1 Historical Beginnings and Clinical Significance

As is the case for most biological soft tissues, an inherent residual stress exists in the skin [1–3]. It is due to growth and remodelling mechanisms [4] and is, in general, very complex to model and evaluate [5]. In human skin, the presence of residual stress has important implications for surgical planning and forensic science, as it can affect significantly the extent of gaping following a cut, and then the resulting healing time. The so-called *Langer Lines* are often considered to be the lines of maximum in vivo tension in the skin. They form an involved map over the body. To minimise the likelihood of excessive wound tension, wound rupture and subsequent unsightly scars, surgical incisions should be made parallel to Langer lines, which lie along the path of maximum skin tension [6].

The discovery of tension lines in skin is widely attributed to a nineteenth Century Austrian surgeon, Karl Langer, after whom the lines are named. The conventional wisdom is that Langer identified the existence of skin tension lines in 1861. In fact, Guillaume Dupuytren, a French anatomist and military surgeon, had made this observation earlier, as early as 1834. Langer's contribution was to systematically puncture the skin of cadavers with multiple circular wounds and indicate the major axes of the resulting ellipses [7]. When viewed together, these ellipses form a map of the natural lines of skin tension, see Fig. 1. Kocher explicitly linked the direction of Langer lines, or cleavage lines, to recommended orientations for surgical incisions and observed that incisions made along these lines will cause little or no scarring, whereas incisions transverse to them will gape and result in unsightly scars [9].

While Langer lines are the best known skin tension lines, many variations on the original lines proposed by Langer have been made over the years. In 1951, for example, Kraissl [10] suggested that surgeons should incise along natural wrinkle lines rather than along the Langer lines. In 1984, Borges [6] defined the Relaxed

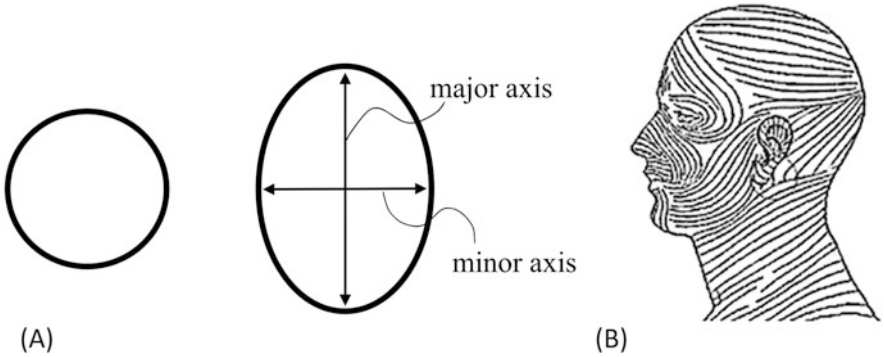

Fig. 1 (**a**) Original circular wound geometry and deformed ellipsoidal wound geometry due to skin tension (**b**) Langer Lines of the face created by joining the major axis of each deformed wound. Reproduced from [8]

Skin Tension Lines (RSTL). These lines follow furrows when the skin is relaxed and can be identified visually by pinching the skin. In his historical account, Carmichael [11] identified a non-exhaustive list of no less than 46 different types of skin lines, folds and planes of the skin recorded in the literature from 1861 [7] to 2004 [12]. Most of these lines have similarities with the original Langer Lines in that they are related to the natural lines of skin tension and seek to assist in surgical planning to ensure the best outcomes in terms of the aesthetics of the resulting scar. To avoid confusion, for the remainder of this chapter, we will use the term "skin tension lines" (STL) to refer to the orientation of maximum skin tension.

Until recently, the orientation of the STLs could not be identified with certainty unless the skin was punctured by a circular punch, an option which is generally neither feasible nor practical. In the first part of this chapter, we show how destructive, invasive techniques have been used to determine the orientation of the STLs and to develop a fundamental understanding of the skin's structure. By now, it is well accepted that the STLs vary with location on the body, age, ethnicity, body mass index, health, gender, etc., and that no fully universal pattern of maximum tensions exists [13]. Given the importance of STLs on the mechanical properties of skin and wound closure, there is a pressing need for patient-specific maps to be established in vivo and in real time. In this respect, recent advances in elastic wave propagation techniques have facilitated non-invasive, in vivo identification of skin tension lines [14, 15]. In the second part of this chapter, we show that a simple device, based on elastic wave propagation, can perform these tasks without damaging the skin.

2 Invasive Investigation of the Skin Tension Lines

2.1 Mechanical Behaviour with Respect to Skin Tension Lines

Early tensile tests suggested that the deformation characteristics of skin are dependent on specimen orientation with respect to the STLs. Ridge et al. [16] carried out uniaxial tensile tests on human cadavers both parallel and perpendicular to the STLs and found that the samples parallel to the STLs had higher stiffness, as shown in Fig. 2a. On the basis of this observation, an idealised collagen fibre mesh structure was proposed, as shown in Fig. 2b. The fibres were assumed to form an interweaving lattice structure with a mean angle less than 45°. Later, Lanir and Fung [17] performed biaxial tests on skin samples taken from the abdomen of rabbits, confirming that skin is strongly anisotropic and probably possessing orthotropic symmetry. It was also reported that during stress-relaxation tests there were considerable alterations to the transverse dimensions, indicating that relaxation behaviour may also be orthotropic. On the basis of these findings, researchers now

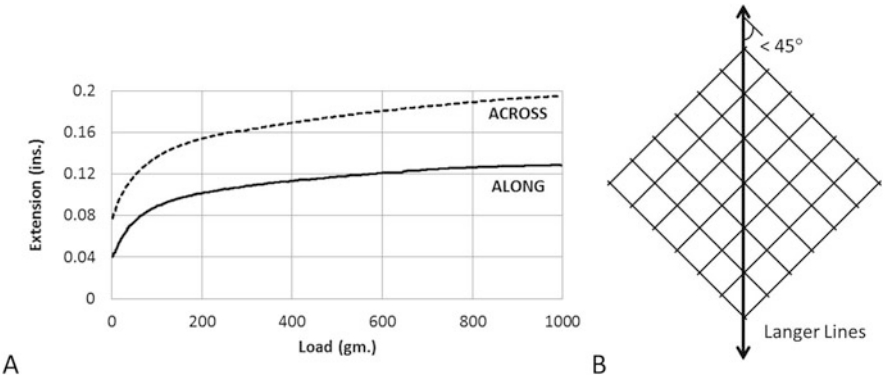

Fig. 2 (**a**) Load-extension curve along and across the Langer lines. (**b**) The proposed lattice structure of collagen fibres. Reproduced from [16]

commonly use the plane containing the STLs as a reference plane, as opposed to e.g., the sagittal plane.

While uniaxial tensile tests alone are not sufficient to determine multi-dimensional material models for soft tissues, they remain important because they serve to evaluate the level of anisotropy and provide data which can later be used as validation for models constructed using more complicated testing methods [18]. Moreover, constitutive model parameters can be determined directly from a histological study of the collagen fibre alignment in the dermis, which allows for reasonable determination of material responses [19].

In [20] human skin was excised from the backs of seven human subjects: three male, four female, with the average age of the subjects being 89 ± 6 years. A total of 56 specimens were excised in various orientations with respect to the perceived orientation of STLs, shown in Fig. 3a, and each sample was grouped into one of three categories: parallel, perpendicular, or at 45° to the STLs. Uniaxial tensile tests were performed at a strain rate of 0.012/s. A number of characteristics from nominal stress vs. stretch ratio curves were identified as descriptive parameters. They are illustrated in Fig. 3b.

A multiway analysis of variance found the orientation of STLs to have a significant effect on the ultimate tensile strength ($P < 0.0001$), the strain energy ($P = 0.0101$), the elastic modulus ($P = 0.0002$), the initial slope ($P = 0.0375$), and the failure stretch ($P = 0.046$). The interaction between orientation and location was also tested i.e., whether the effect of orientation was dependent upon location. This interaction between orientation and location was found to be significant only for the failure stretch ($P = 0.0118$). These results are illustrated in Fig. 4 and reproduced in Table 1. From these experimental studies, it is clear that the mechanical behaviour of skin varies with respect to the STLs.

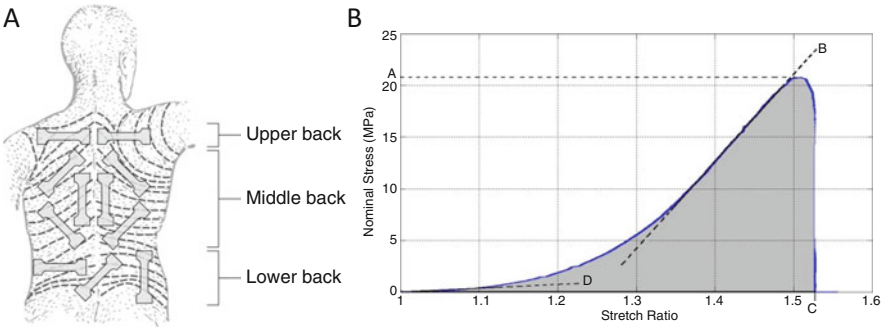

Fig. 3 (**a**) Orientation of samples from the back with respect to the STLs [7]. (**b**) Typical stress-stretch graph for uniaxial tension experiments. The ultimate tensile strength is the maximum stress until failure of the specimen and is indicated by A. The elastic modulus is defined as the slope of the linear portion of the curve shown by B. The failure stretch is the maximum stretch obtained before failure and is shown by C. The initial slope is the slope of the curve at infinitesimal strains and is shown by D. The strain energy is the energy per unit volume consumed by the material during the experiment and is represented by the area under the curve [20]

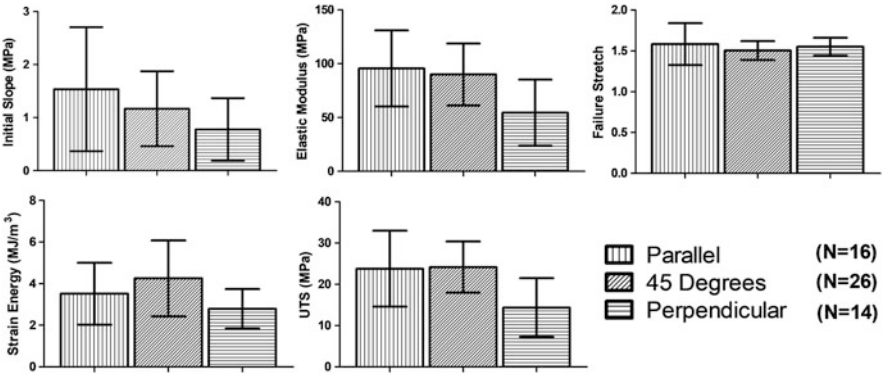

Fig. 4 Influence of orientation on the initial slope, elastic modulus, failure stretch, strain energy and ultimate tensile strength (UTS). Values given include mean and standard deviation [20]

2.2 Shrinkage and Expansion with Respect to Skin Tension Lines

It is known that both shrinkage and expansion of specimens can occur upon excision from the body [16, 17, 21, 22]. This is due to the release of residual stresses within the skin. What remains unclear is the level of residual stress present within the skin and how this may vary with the orientation of specimens. Upon excision of skin samples from the body, Ridge and Wright [16] observed that the greatest shrinkage occurred in the direction of Langer lines, with a shrinkage of 9% parallel to the Langer lines and 5% perpendicular to the Langer lines. They also observed a

Table 1 Summary of uniaxial tensile test results on human skin with respect to sample orientation and location (mean ± standard deviation for each orientation/location group) [20]

STL orientation	Location	N	UTS (MPa)	Strain energy (MJ/m^3)	Failure stretch	Elastic modulus (MPa)	Initial slope (MPa)
Parallel	Middle	9	28.64 ± 9.03	4.28 ± 1.49	1.46 ± 0.07	112.47 ± 36.49	1.21 ± 0.97
Parallel	Bottom	7	17.60 ± 4.77	2.54 ± 0.76	1.74 ± 0.32	73.81 ± 19.41	1.95 ± 1.34
45°	Top	12	22.7 ± 3.61	3.80 ± 0.92	1.52 ± 0.10	82.62 ± 17.36	0.99 ± 0.51
45°	Middle	9	28.85 ± 7.87	5.38 ± 2.59	1.52 ± 0.15	103.49 ± 41.20	1.33 ± 0.96
45°	Bottom	5	20.23 ± 4.18	3.31 ± 0.67	1.43 ± 0.04	82.81 ± 18.43	1.30 ± 0.60
Perpendicular	Middle	9	16.53 ± 5.71	2.98 ± 0.89	1.52 ± 0.08	63.75 ± 24.59	0.91 ± 0.68
Perpendicular	Bottom	5	10.56 ± 8.41	2.44 ± 1.04	1.61 ± 0.14	37.66 ± 36.41	0.54 ± 0.33

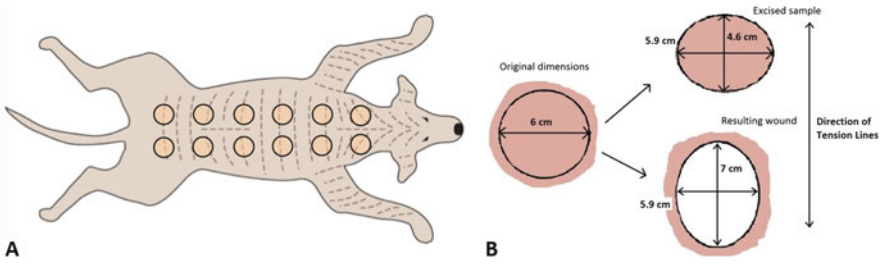

Fig. 5 (**a**) Sample locations of circular samples removed from dog cadaver (**b**) Illustration of average contraction and expansion levels with respect to the skin tension lines for (1) an isolated excised sample (2) an originally excise wound [14]

large difference in the level of shrinkage between males and females. Reihmer and Menzel [23] carried out multiaxial tension tests using a customised device, where excised circular samples were radially stretched by a ring of pullers placed at 30° intervals around the circumference, restoring the in vivo shape of the excision. They confirmed that the axes of minimum and maximum shrinkage after excision were correlated with the orientation of STLs and that the in vivo were determined by restoring the original shape of the specimen.

More recently, Deroy et al. [14], using a dog cadaver model, showed that the average area expansion of the circular wounds was 9%, corresponding to a line expansion of 16% parallel to the STLs (by image analysis), but a line contraction of 10% perpendicular to the STLs. Similarly, the area of the excised sample shrank by 33% overall, shrinking 23% parallel to the STLs and shrinking 10% perpendicular to the STLs. Figure 5 provides a summary of the levels of expansion and contraction of both the excised skin sample and the resulting wound.

2.3 Structural Basis of Skin Tension Lines

Cox [21] and Stark [24] both illustrated that the orientations of STLs are preserved even after the skin is removed from the body and the skin tension released, and concluded that the lines must have an anatomical basis. However until the publication of papers by Ní Annaidh et al. [25] and Deroy et al. [14], it was unclear in the literature whether the STLs had a structural basis, and to the authors' knowledge there was no previous quantitative data published on this point. Van Zuijlen et al. [26] and Noorlander et al. [27] used Fourier analysis to measure the level of anisotropy of collagen in the skin but failed to provide information on the mean orientation of the fibres. While in Jor et al. [28], histology techniques provided quantitative results on the orientation of collagen fibres in porcine skin, but results were presented in the plane normal to the epidermis/skin surface (i.e.

through-the-thickness direction) while the preferred orientation of collagen fibres in skin is known to be parallel to the epidermis surface [5, 25].

It is well known that collagen fibres govern many of the mechanical properties of soft tissues, in particular their anisotropic behaviour (at least partly, as strain-induced anisotropy can also play a role, as we will see later.) A number of authors have sought to incorporate their influence in constitutive models of soft tissues. Gasser at al. [29] developed a now widely accepted structural model for arterial layers which includes a parameter representing the dispersion of collagen fibres. The inclusion of the collagen dispersion factor is particularly useful for application to human skin, since the orientations of collagen fibres there are more dispersed than say in the tendon or media layer of the artery [25]. The corresponding Gasser-Ogden-Holzapfel (GOH) strain energy function, Ψ, is given by

$$\Psi = \frac{\mu}{2}(I_1 - 3) + \mu\frac{k_1}{k_2}\left\{e^{k_2[\kappa I_1 + (1-3\kappa)I_4 - 1]^2} - 1\right\}$$

where μ, k_1 and k_2 are positive material constants, κ is the dispersion factor, and I_1 and I_4 are strain invariants, with I_1 related to the isotropic behaviour of the tissue matrix and I_4 related to the anisotropic behaviour due to the fibre contribution.

Using automated image processing of histological skin sections summarised in Fig. 6, Ní Annaidh et al. [25] determined the quantitative structural parameters of the GOH model for the human dermis. Two distinct peaks are evident from Fig. 6c. It is assumed that these two peaks correspond to the preferred orientation of two crossing families of fibres and are distributed according to a π-periodic von Mises distribution. The standard π-periodic von Mises distribution is normalized and the resulting density function, $\rho(\theta)$, reads as follows,

$$\rho(\theta) = 4\sqrt{\frac{b}{2\pi}}\frac{\exp\left[b\left(\cos\left(2\theta\right)\right)+1\right]}{erfi\left(\sqrt{2b}\right)}$$

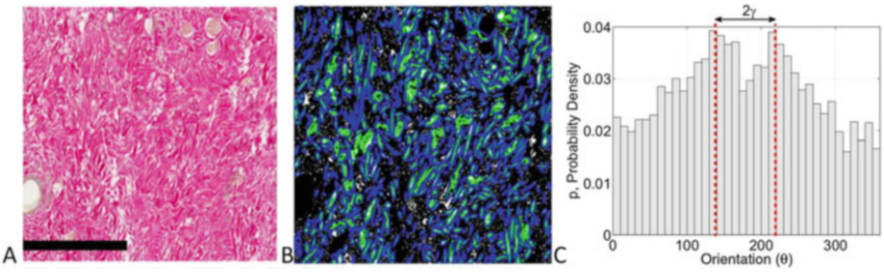

Fig. 6 (**a**) Original histology slide sectioned parallel to the epidermis and stained with Van Gieson to highlight collagen fibres as pink. Scale bar is 1 mm. (**b**) After morpholigical operations, the predominant orientations of fibres bundles are identified by determining the orientation of best fit ellipses. (**c**) The predominant orientations of fibre bundles are plotted on a histogram and fit to a π-periodic Von Mises distribution

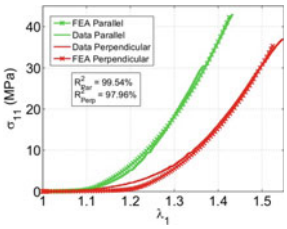

Sample	μ (MPa)	k_1	k_2	γ (°)	Θ (°)	κ	R^2 (%)
Parallel	0.2014	243.6	0.1327	41	88	0.1535	99.5
Perpendicular	0.2014	243.6	0.1327	41	0	0.1456	98.0

Fig. 7 FEA simulation of tensile test compared with experimental data of sample parallel and perpendicular to the STLs. Material parameters used in the simulation. Note that structural parameters (γ, θ, κ) were evaluated from histological data [25]

where b is the concentration parameter associated with the von Mises distribution and θ is the mean orientation of fibres. The parameters b and θ were evaluated using maximum likelihood estimates (MLE) and κ was calculated by numerical integration of the integral given by [29],

$$\kappa = \frac{1}{4}\int_0^{\pi} \rho\,(\theta)\, sin^3\theta d\theta$$

The fibres were assumed to form an interweaving lattice structure as first postulated by Ridge and Wright [30]. Those authors suggested that the mean angle of the two families of fibres indicates the direction of the Langer lines. More recently, in vitro [28] and in vivo [31] studies have also supported this hypothesis. The lattice structure proposed by Ridge and Wright [30] is an idealised one, and the adoption here of the dispersion factor creates a more realistic scenario. Using the identified structural constitutive parameters for both a sample parallel and perpendicular to the STLs, Fig. 7 illustrates the potential of the GOH model to predict the mechanical behaviour of a sample, given known structural parameters.

3 Noninvasive Investigation of the Skin Tension Lines

In this second part of the chapter, we will see how the orientation of STLs can be determined accurately, locally, rapidly, non-destructively, and non-invasively. This possibility is highly desirable for planned surgery, because STLs are known to be patient-specific and can depend on a multitude of factors, including location, age, health, body mass index, ethnicity, hydration, gender, corpulence, etc., and of course, differ from one species to another. Minimizing scalpel cutting force, wound healing time, and scar tissue extent are goals of prime importance to surgeons and patients alike. Here we show how a small acoustic device can determine the directions of STLs, based on some simple principles and on logic.

We use the Reviscometer® RVM600 (Courage & Khazaka Electronic GmbH, Köln, Germany), a commercial device aimed primarily at the cosmetic and derma-

tology industry [31–33], and based on a simple operating principle. Basically it is a probe consisting of two small indenters, 2 mm apart, coming into contact with the skin. One hits the skin with a force of 1 N, and the other receives the resulting mechanical signal generated and travelling in the skin. The machine returns the time it took to travel the 2 mm distance, the so-called RRT ("resonance running time"), although this measurement is provided in arbitrary units and its relationship with standard units, i.e. seconds, is not provided by the manufacturer. The probe can then be rotated by 10° increments, to give the variations of the RRT with angle. With this information, we can actually address the following questions, using experimental observations and logic:

- Is the skin anisotropic?
- How many directions of preferred orientation does it possess?
- Do the mechanical properties of skin change with age?
- What is the orientation of the STLs at a given location?
- Is the anisotropy due to stretch alone, to fibres alone, or a combination?
- How many families of parallel fibres are there?

First, we conduct a series of 36 measurements on the lower volar forearm area of a 21 year old human female. Figure 8 shows the apparatus and displays the results given by the measurements, averaged over the 36 series.

This simple experiment clearly shows that *skin is anisotropic*. On inspection, we see that the results reveal *two preferred directions*: one where the acoustical signal generated by the probe travels at its fastest in the skin (blue minima at 60° and at $60 + 180 = 240°$) and another where it travels at its slowest (green maxima at 150° and 330°). Those *two directions are at right angle* to one another.

Next we may use the Reviscometer® to investigate the *influence of age and gender on the mechanical properties of skin*. The measured values of the RRT are not useful from the point of view of physics, because it proves difficult to calibrate the Reviscometer against an engineering material with known properties. Nonetheless, we can use the ratio $A = RRT_{max}/RRT_{min}$ of its highest to its smallest value as a dimensionless measure of the skin anisotropy, and track if and how it

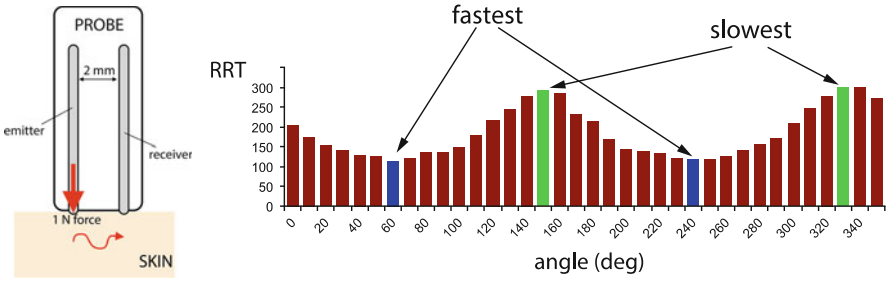

Fig. 8 The Reviscometer applied on skin in the lower volvar forearm area. Its measurements clearly show two directions at right angle one to the other, where the acoustic signal travels at its fastest and at its slowest

Table 2 Age distribution of the cohort of 78 volunteers tested on their volar forearm skin

Age (years)	0–10	10–20	20–30	30–40	40–50	50–60	60–70	70+
Sample size	7	10	16	11	7	10	7	10

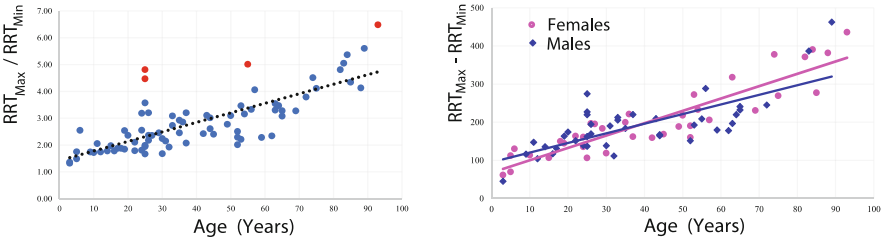

Fig. 9 (left) Variation of the anisotropic index RRT_{max}/RRT_{min} with age for the skin on the volar forearm skin of 78 volunteers. (right) Variation of the anisotropic range RRT_{max}-RRT_{min} with age, with gender distinction (circles: females, squares: males)

evolves with age and gender. To this end, we tested a total of 78 volunteers (37 female, 41 male), aged 3–93 years of age, see Table 2. We conducted the tests at University College Dublin, having secured ethical approval (LS-15-65-NiAnnaidh).

We found a significant linear relationship between the Anisotropic Index, A (where the Anisotropic Index refers to the ratio of the maximum RRT: minimum RRT about a full 360° for a given site) and age ($P < 0.0005$), as shown in Fig. 9. An R^2 value of 0.59 indicates that age accounted for a significant amount of the explained variability in the Anisotropic Index, but it suggests that the linear model is merely adequate. There were a number of unusual observations with large standardised residual values, as some outliers (in red) do not fit the model. We noted that these outliers belong to Asian ethnic groups while the remainder of the cohort were Caucasian Irish, but we did not have enough volunteers to account for this factor. When we accounted for gender, we did not find significant differences for the data on the volar forearm skin.

So far, we have seen that the Reviscometer® indicates two distinct orthogonal on in vivo skin, but how are these directions of fast and slow mechanical wave propagation related to the Skin Tension Lines? To address that question, we simply compare those directions to those resulting from the original protocol devised by Langer.

For these experiments, we used the skin of dog cadavers. Although designed to work optimally on human skin, the Reviscometer® also works well on dog skin, even though dog skin is known to be stiffer and somewhat thicker than human skin [14, 20]. We performed the testing at the University College Dublin School of Veterinary Medicine on the cadavers of two healthy young adult dogs. First, we drew circles on the skin of one dog, and used the Reviscometer® to determine the direction of fastest wave at each location. Then we excised 6 mm circular discs from the skin at those locations and watched them change shape due to the in situ skin tension. Using image analysis, we fitted the wounds to ellipses and determined the

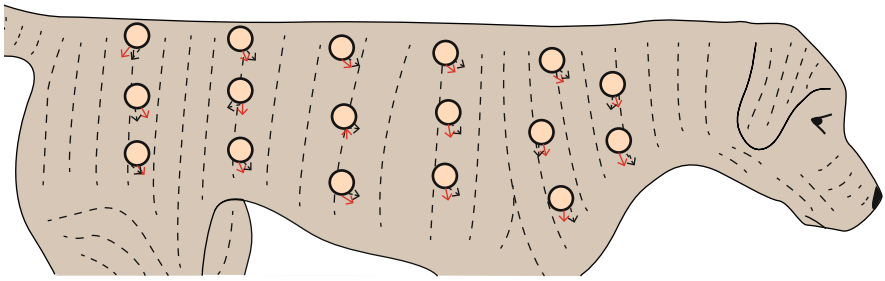

Fig. 10 Comparing the local lines of fastest mechanical wave propagation given by the Reviscometer (black arrows) to the orientation of the Skin Tension Lines (red arrows) as determined by Langer's original protocol of cutting a circular hole out of the skin and recording the direction of the major axis in the resulting elliptical shape. The experiments were conducted on a 5-year-old female, mixed-breed, medium sized dog cadaver at University College Dublin

orientation of their major axis. We found a significant statistical correlation between the orientation of the major axes of the resulting elliptical wounds and the direction of fastest wave propagation. In other words, the Reviscometer® device provides *a non-invasive, non-destructive way of determining the STLs locally*. Of course, this study is limited in its scope and the experimental uncertainty is still an issue, but these limitations can be addressed with further and wider trials. The results of the two techniques are compared directly in Fig. 10.

At this stage, we can contemplate several scenarios to explain the anisotropy of the RRT response. It could be due to

i. Fibres only;
ii. Strain only;
iii. A combination of both.

We can safely exclude (i) straightaway, because it is obvious that skin is stretched in the body, as shown by our and Langer's experiments, and as attested by anyone who has cut themselves and seen their wound gape open. On the other hand, deciding between the second and third possibility is not so obvious.

Resorting now to *modelling*, we can make the reasonable assumption that the probe is sensitive to vertical displacements only, based on its working principle. To model these vertical motions, we focus on homogeneous, linearly polarised plane waves, for which the components of the mechanical displacement $\boldsymbol{u}$ are of the form

$$u_1 = 0, u_2 = 0, u_3 = ae^{ik(\boldsymbol{n}.\boldsymbol{x}-vt)},$$

where a is the amplitude, k is the wavenumber, $\boldsymbol{n} = \cos\theta\ \boldsymbol{i} + \sin\theta\ \boldsymbol{j}$ is the unit vector in the direction of propagation, and v is the wave speed. Here we took the skin to be normal to the x_3-axis, and the x_1, x_2 axes to be aligned with the principal axes of strain. We assume that the fibres, if they exist, are lying in the (x_1, x_2) plane. Because the surface of the skin in the upper arm volar area and on the

chosen locations in the dog cadaver is flat and smooth, we can also assume that it is deformed homogeneously and not subject to shear forces, which would create wrinkles at rest [34]. It follows that if there is only one family of parallel fibres, then they must be aligned with one of the principal directions of strain. If there are two families of parallel fibres, then they must either be at right angle and aligned with the principal axes, or be mechanically equivalent with their bisectors aligned with the principal axes [25]. Whether the anisotropy is due to strain only or to a mixture of strain and fibres (Cases ii and iii above), the wave speed is given by the same formula, as follows,

$$\rho v^2 = \mathcal{A}_{01313}(\cos\theta)^2 + \mathcal{A}_{02323}(\sin\theta)^2,$$

where ρ is the mass density and the $\mathcal{A}_0$'s are the instantaneous shear moduli, computed from the second derivatives of the strain energy density with respect to the strain [35]. In either case—whether fibres are present or not—the variation of RRT with angle resulting from the equation above is compatible with the RRT profiles found, see Fig. 8.

To settle the question, we rely on the Reviscometer® again. On the skin of the second dog cadaver, we repeated the procedure of identifying the Langer Lines by determining the fastest wave direction and matching it to the principal minor axis of the resulting elliptical wound. This time, however, we cut out larger discs (6 cm diameter). Then, on those ex-vivo discs, which were completely free of initial stress and had turned into ellipses, we *again* made measurements with the Reviscometer® device. The results were again anisotropic, see Fig. 11, and this observation can only be attributed to the presence of oriented fibres.

The other insight that came out of the latter experiments was that we found the directions of anisotropy for the unstressed discs to be the same as those noted

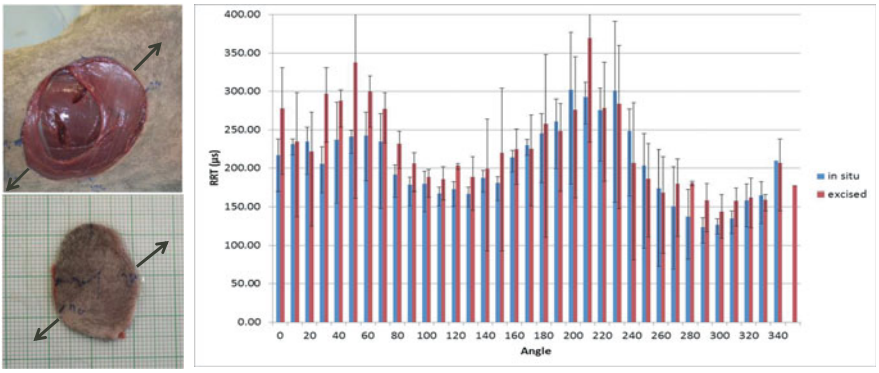

Fig. 11 RRT measurements before (red) and after (blue) excision of a 6 cm disc. The excised sample displays anisotropy and thus demonstrates the presence of fibres in the skin. Both samples indicate the same direction of fastest wave, and thus show that fibres are aligned with Langer lines in situ

when in situ. This observation is proof that *in the body, fibres are aligned with the principal axes of strain.* Hence we can exclude the possibility of anisotropy due to two families of parallel fibres, mechanically equivalent, with their bisectors aligned with the principal axes of strain. We also recorded that the amplitude of the RRT anisotropy was noticeably reduced once the discs had been removed, while the RRT itself had increased, confirming that in vivo tension plays a significant mechanical role in the skin, of the same order as the contribution from the fibres. The only question that our investigation could not address was whether there was one or two families of parallel fibres aligned with the principal axes of strain. Here we must rely on the indications given by the destructive testing described in the first part of the chapter, which tell us that there are indeed two families of parallel fibres in the skin. Making the reasonable assumption that the fibres orthogonal to the directions of tension are contracted, we can ignore their mechanical contribution and conclude that in the body at rest, *active fibres are aligned with the Langer Lines.*

4 Conclusion

Assessing the body of literature examining *destructive* testing of skin, we have confirmed that its mechanical properties, in particular the stiffness and the level of shrinkage once excised from the body, depend heavily on their orientation with respect to skin tension lines. Histological investigations have supported the hypothesis that the STLs have a structural basis, while recent *non-invasive* testing of skin has shed further light on this matter. It is now clear that in the body, fibres are aligned with the principal axes of strain and that both the alignment of collagen fibres and the in vivo strain play a significant role in the mechanical response of the skin. Since it is non-invasive, in vivo evaluation techniques such as elastic wave propagation offer significant potential in the investigation of the ageing of skin and in the patient specific planning of surgical procedures. Further research should seek to develop models to accurately reflect the mechanical environment.

References

1. Alexander H, Cook TH (1977) Accounting for natural tension in the mechanical testing of human skin. J Invest Dermatol 69(3):310–314
2. Holzapfel GA (2005) Similarities between soft biological tissues and rubberlike materials. In: Austrell P-E, Kari L (eds) Constitutive models for Rubber IV. Taylor & Francis, London, pp 607–618
3. Flynn C, McCormack BAO (2010) Simulating the wrinkling and aging of skin with a multi-layer finite element model. J Biomech 43(3):442–448
4. Rodriguez EK, Hoger A, McCulloh AD (1994) Stress dependent finite growth in soft elastic tissues. J Biomech 27:455–467

5. Holzapfel GA (2001) Biomechanics of soft tissue. In: Lemaitre J (ed) Handbook of materials behavior models. Academic Press, Burlington, pp 1057–1071
6. Borges AF (1984) Relaxed Skin Tension Lines (RSTL) versus other skin lines. Plast Reconstr Surg 73(1):144–150
7. Langer K (1861) On the anatomy and physiology of the skin. The Imperial Academy of Science, Vienna. Reprinted in (1978). Br J Plast Surg 17(31):93–106
8. Fagan J (2014) Open Access Atlas of Otolaryngology, Head & Neck Operative Surgery. Cape Town University. http://doer.col.org/handle/123456789/6513
9. Kocher T (1892) Chirurgische operationslehre. G. Fischer, Jena
10. Kraissl CJ (1951) The selection of appropriate lines for elective surgical incisions. Plast Reconstr Surg 8(1):1–28
11. Carmichael SW (2014) The tangles web of langer's lines. Clin Anat 27:162–168
12. Sarıfakıoğlu N et al (2004) A new phenomenon: "sleep lines" on the face. Scand J Plast Reconstr Surg Hand Surg 38(4):244–247
13. Brown IA (1973) A scanning electron microscope study of the effects of uniaxial tension on human skin. Br J Dermatol 89:383–393
14. Deroy C et al (2017) Non-invasive evaluation of skin tension lines with elastic waves. Skin Res Technol 23(3):326–335
15. Liang X, Boppart SA (2010) Biomechanical properties of in vivo human skin from dynamic optical coherence elastography. IEEE Trans Biomed Eng 57(4):953–959
16. Ridge MD, Wright V (1966) The directional effects of skin. A bio-engineering study of skin with particular reference to Langer's lines. J Invest Dermatol 46(4):341–346
17. Lanir Y, Fung YC (1974) Two-dimensional mechanical properties of rabbit skin. II. Experimental results. J Biomech 7(2):171–174
18. Holzapfel GA, Ogden RW (2009) On planar biaxial tests for anisotropic nonlinearly elastic solids. A continuum mechanical framework. Math Mech Solids 14(5):474–489
19. Holzapfel GA (2006) Determination of material models for arterial walls from uniaxial extension tests and histological structure. J Theor Biol 238(2):290–302
20. Ní Annaidh A et al (2012) Characterising the anisotropic mechanical properties of excised human skin. J Mech Behav Biomed Mater 5:139–148
21. Cox HT (1941) The cleavage lines of the skin. Br J Surg 29(114):234–240
22. Jansen LH, Rottier PB (1958) Some mechanical properties of human abdominal skin measured on excised strips. Dermatologica 117:65–83
23. Reihsner R, Menzel EJ (1996) On the orthogonal anisotropy of human skin as a function of anatomical region. Connect Tissue Res 34(2):145–160
24. Stark HL (1977) Directional variations in the extensibility of human skin. Br J Plast Surg 30(2):105–114
25. Ni Annaidh A et al (2012) Automated estimation of collagen fibre dispersion in the dermis and its contribution to the anisotropic behaviour of skin. Ann Biomed Eng 40(8):1666–1678
26. Van Zuijlen PPM et al (2002) Morphometry of dermal collagen orientation by Fourier analysis is superior to multi-observer assessment. J Pathol 198:284–291
27. Noorlander ML et al (2002) A quantitative method to determine the orientation of collagen fibers in the dermis. J Histochem Cytochem 50(11):1469–1474
28. Jor JWY et al (2011) Modelling collagen fibre orientation in porcine skin based upon confocal laser scanning microscopy. Skin Res Technol 17(2):149–159
29. Gasser T, Ogden RW, Holzapfel G (2006) Hyperelastic modelling of arterial layers with distributed collagen fibre orientations. J R Soc Interface 3:15–35
30. Ridge MD, Wright V (1966) Mechanical properties of skin: a bioengineering study of skin structure. J Appl Physiol 21:1602–1606
31. Ruvolo JEC, Stamatas GN, Kollias N (2007) Skin viscoelasticity displays site- and age-dependent angular anisotropy. Skin Pharmacol Physiol 20:313–321
32. Paye M et al (2007) Use of the Reviscometer for measuring cosmetics-induced skin surface effects. Skin Res Technol 13:343–349

33. Quatresooz P et al (2008) Laddering melanotic pattern of Langer's lines in skin of colour. Eur J Dermatol 5:575–578
34. Ciarletta P, Destrade M, Gower AL (2013) Shear instability in skin tissue. Q J Mech Appl Math 66(2):273–288
35. Destrade M (2015) Incremental equations for soft fibrous materials. In: Dorfmann L, Ogden RW (eds) Nonlinear mechanics of soft fibrous materials. Springer, Vienna, pp 233–267

Experimental Tribology of Human Skin

Marc A. Masen, Noor Veijgen, and Michel Klaassen

Abstract The interaction behavior of the human skin is of relevance for the functional performance of a wide range of products and, as a result, the topic is widely studied in both industry and academia. However, the key underlying mechanisms determining the interaction behavior of skin are at present not well understood.

Skin is a living material and thus will respond and may adapt to mechanical interaction, for instance by producing sweat, releasing biomarkers and even developing a blister or a wound. In addition, the properties of skin strongly depend on personal traits and characteristics. This makes predictive modelling of the interaction behaviour of skin challenging, and therefore there is a continued need for experimental investigations.

In literature a large range of experimentally obtained friction values have been reported. These have been measured using a wide variety of tribometers. When commencing tribological testing it is essential to ensure that the investigations are performed using the appropriate tribo-system, meaning that contact conditions such as pressures, sliding velocities and environmental conditions are representative for the final application, as any of these factors will have a significant effect on the obtained tribological result. Additionally, many studies use the volar forearm as measurement site; whilst this area provides ease of measurement, it may not always be highly representative of the actual skin site of interest.

Because of the complex nature of skin interactions, much of the underlying fundamental physical mechanisms remain to be discovered. Focused in-depth experimental investigations will be key to achieving a better understanding in skin tribology.

M. A. Masen (✉)
Tribology Group, Department of Mechanical Engineering, Imperial College London, London, UK
e-mail: m.masen@imperial.ac.uk

N. Veijgen · M. Klaassen
Laboratory for Surface Technology and Tribology, University of Twente, Enschede, The Netherlands

G. Limbert (ed.), *Skin Biophysics*, Studies in Mechanobiology, Tissue Engineering and Biomaterials 22,
https://doi.org/10.1007/978-3-030-13279-8_10

1 Introduction

Our skin is the outermost layer of the human body and is in continuous interaction with the outside world. This interaction comes in the form of a large range of cues, of which the field of tribology covers those aspects related to contact mechanics. This includes normal and shear forces and the resulting pressures as well as shear stresses and friction.

Tribology is defined as the science and engine?ering of interacting surfaces in relative motion, and in that respect 'skin tribology' can be loosely defined as the study of interacting surfaces in which one of the interacting surfaces is the human skin or, alternatively, a substitute for human skin. The latter is pertinent when investigating damage mechanisms. The tribological behavior of skin is important for a wide variety of applications, ranging from touch perception and haptics of products such as consumer electronics and personal care and cosmetics, to the prevention of damage following more intense contact conditions, such as in the case of a sliding tackle during sports or the in the contact of skin with medical devices.

2 Tribological System

It is essential to recognize that the tribology of skin, or any other material, is not a material property, but depends strongly on the entire system of two materials in contact, the presence of a lubricating medium (gaseous, liquid or solid), the loading conditions in terms of forces and sliding velocities as well as the (micro-) environment in which the contact operates. For a skin tribo-system this is schematically illustrated in Fig. 1.

As briefly mentioned before, output parameters of the tribological system include shear forces that are the result of the friction between the two bodies, and the

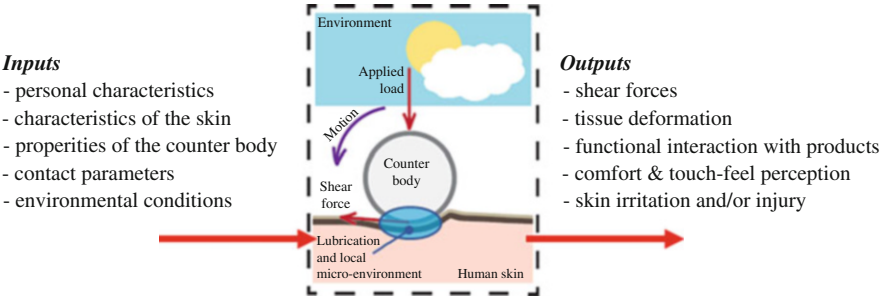

Fig. 1 The tribological system for skin-object interaction; the observed interaction phenomena depend on a multitude of inputs that include the mechanical and geometrical properties of both bodies in contact, the motion and loading characteristics and the surrounding environmental conditions, both globally and locally (after Veijgen [1])

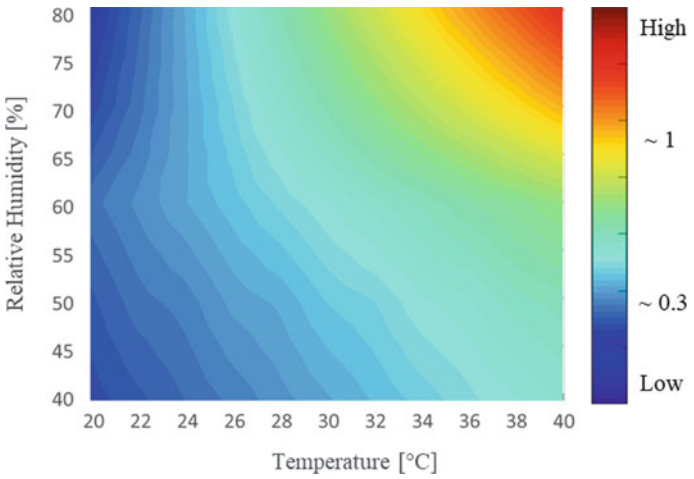

Fig. 2 Effect of temperature and humidity on friction [2]

response of the tissue to interaction. Other outputs are more affective and perception based and include touch/feel as triggered through strains and vibrations in the mechanoreceptors in the skin, and related to these, the perceived comfort or lack thereof. Another possible output is irritation and or damage to skin. It needs to be noted that any of these effects can be triggered as a result of either static friction, which is sometimes referred to as 'grip', or in medicine as 'shear', and dynamic friction, which involves macroscopic sliding and relates to the rubbing contact between two bodies.

An illustrative example of the importance of this system approach is the effect of the environment on skin interactions: compare the stickiness experienced during a hot and humid summer day to the dryness of a cold day in the winter. Whilst the skin and the counter surface may be (more or less) the same, the contact and friction behavior has completely changed due to the change in temperature and humidity. This is also illustrated in Fig. 2, from Klaassen [2], which shows the measured static coefficient of friction (represented as a heat-map) as a function of the temperature and the relative humidity.

An additional factor to consider when dealing with living tissue is the response of the tissue to the physical contact. Such responses may occur at the subject level, the tissue level as well as at the cell level: the subject may respond to interaction by preventing it from (re-)occurring, such as when someone feels discomfort because of a blister developing and subsequently adapts their gait. The response of the tissue to interaction will be deformation, possibly resulting in the restriction of blood flow through the capillary vessels, but also in the release of sweat. At the cells level the response to loading could be an anti-inflammatory reaction Cornelissen [3]. Any of these will have a marked effect on the tribo-system and thus on the output as

they affect the loads, sliding velocities, the (micro-environment in which the contact operates and/or the characteristics of the two interacting bodies.

3 Experimental Methods Used in Skin Tribology

The main focus in most published skin tribology studies has been on friction, even though friction itself (maximizing, minimizing or optimizing) is hardly ever the main topic of interest in skin interactions. However, in many cases, friction is seen as a key determining component of the final objective, which could be the perception and comfort experienced whilst handling a product, the grip between the hand and a grabrail or the prevention of damage to tissue during prolonged contact.

A wide range of tribometers with corresponding have been utilized for tribological studies of the skin. Some examples are shown in Fig. 3. These tribometers can be classified into four groups based on the type of relative motion they employ, as listed below and shown in Fig. 4:

- Linear sliding or linearly reciprocating tribometers, as shown in Fig. 4a and the top row of Fig. 3. Naylor [4] was one of the first to use a linear reciprocating probe sliding against the skin. In such a configuration the alignment of the skin with the plane of motion may present a challenge, however this can be overcome to a certain degree by measuring the friction in both directions of motion. Obviously, the length of a stroke is limited. Additionally, this reciprocating configuration allows studying the point at which full sliding motion is initiated, and as such the possible occurrence of a static friction peak.
- Rotating tribometers with the axis of rotation perpendicular to the skin surface, Fig. 4b and the second row of Fig. 3, see e.g. Prall. Early versions of these tribometers were based on rotational rheometers. An obvious characteristic of such a measurement set-up is that the in-plane anisotropy of the skin cannot be assessed. Additionally, the sliding velocity in the contact increases with radial distance from the centre of motion with a zero-velocity pole at the centre of rotation. An annulus or ring-shaped specimen will prevent this from happening. Two examples of small hand-held versions of such a configuration were presented by Comaish [13] and Hendriks [9].
- Rotating tribometers with the axis of rotation parallel to the skin surface, Fig. 4c and the third row of Fig. 3. Highley [10] employed a configuration where the probe rotates against the skin with the axis of rotation parallel to the surface of the skin. Such a setup allows for continuous motion in one direction, meaning the in-plane anisotropic properties of the skin can also be taken into account. Veijgen [1] built a small, handheld version for use outside of the laboratory.
- A fourth type of set-up was introduced in the early nineties by Dinç [14], who employed a force transducer to measure the friction between the tip of the finger

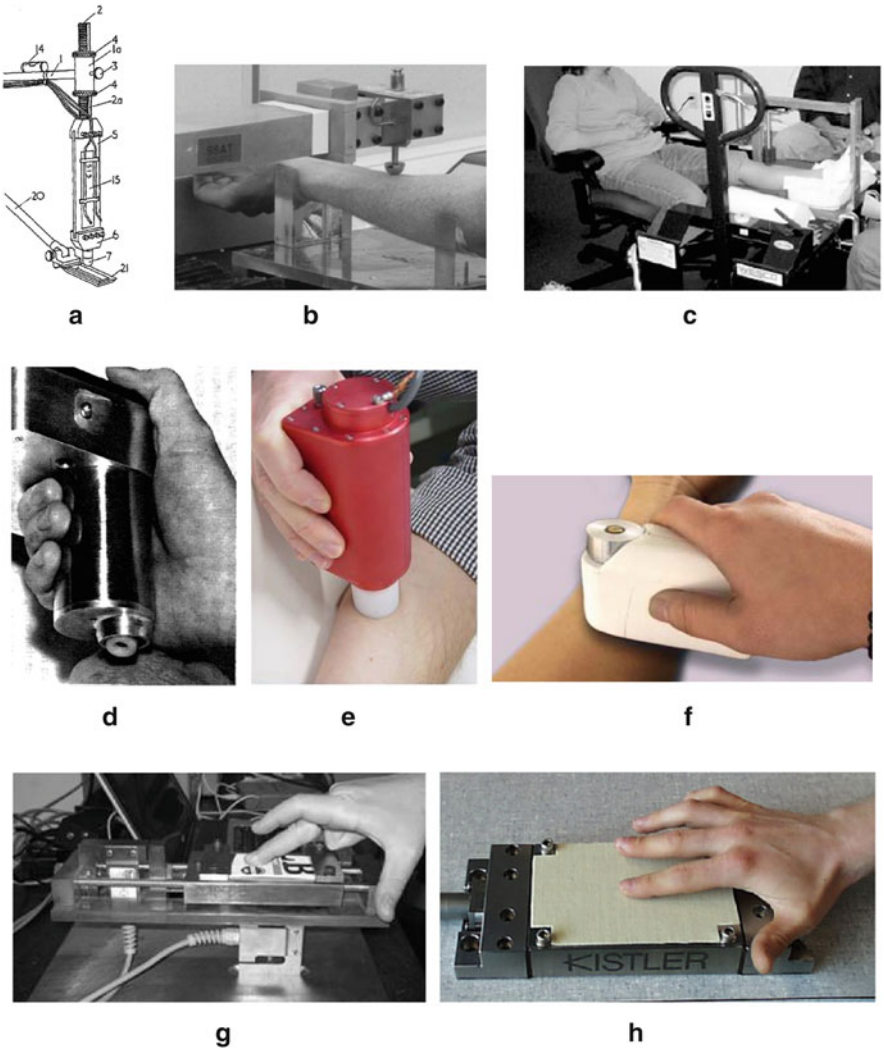

Fig. 3 A selection of skin tribometers reported in literature. (**a**) Naylor [4]. (**b**) Adams [5]. (**c**) Polliack [6]. (**d**) Comaish [8]. (**e**) Hendriks [9]. (**f**) Veijgen [1]. (**g**) Lewis [11]. (**h**) Derler [12]

sliding over a flat sample of material. Often a specimen made of a certain material is fixed onto the force transducer and the subject is asked to slide or rub the skin (often the finger, but hand, arm and feet have also been tested) against the specimen. The force transducer measures both the applied load and the resulting shear load. The input conditions such as applied load and the sliding velocity in these set-ups depend strongly on the subject and are therefore typically not very accurately controlled, or constant during the test. This means that such

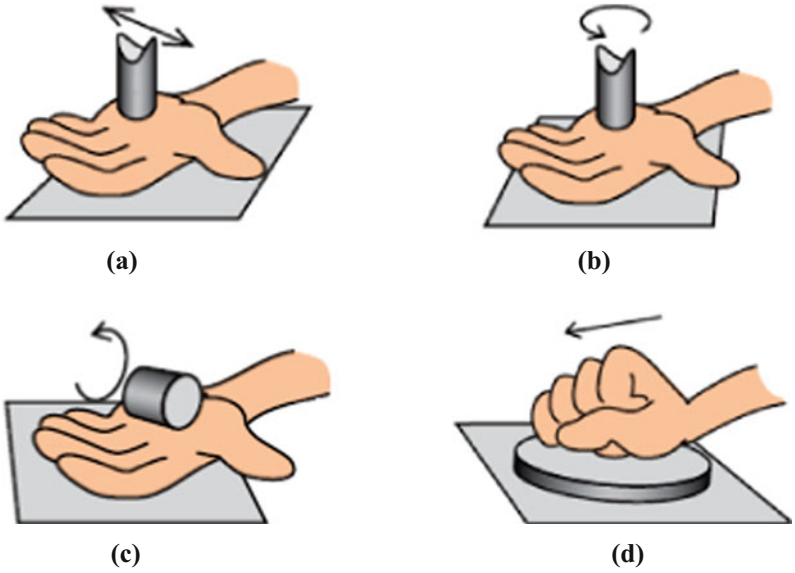

Fig. 4 Various contact configurations used in tribometry [1]. (**a**) Linear contact. (**b**) Perpendicular rotating contact. (**c**) Parallel rotating contact. (**d**) User controlled motion

a set-up is less suited for investigations focused to understanding of the basic interaction phenomena. However, they provide a testing methodology that is often somewhat closer to the application that the previously mentioned three set-ups, and therefore can provide highly relevant information. Similar setups have been successfully applied in psychophysics investigations, see e.g. Smith [15] and Gee [16].

Next to these tribometers, which are often based on traditional tribometers, but customized for use on skin and on life subjects, e.g. by reducing the applied load and velocity as well as enabling insertion of body parts, a range of commercial tribometers, in various states of development are now available for use on skin and artificial skin substitutes. A prototype version of a 'BioTriboMeter' (BTM, PCS Instruments Ltd., London, UK) is shown in Fig. 5. Biotribometers typically allow more complex motion profiles than traditional tribometers, whilst allowing a dynamic applied load and recording forces at high (>100 Hz) temporal resolution, to match the triggering frequencies of the mechanoreceptors in the skin.

Given the wide range of set-ups used by various researchers, results reported in the literature for skin friction measurements are obtained using a large range of measurement conditions: besides the possible variations in the motion type of the tribometer that were discussed above, a fairly large range for both the applied load and the sliding velocity have been used. Loads vary between 10 mN and 100 N whilst velocities range from the order of 100 μm/s to several metres per second. As

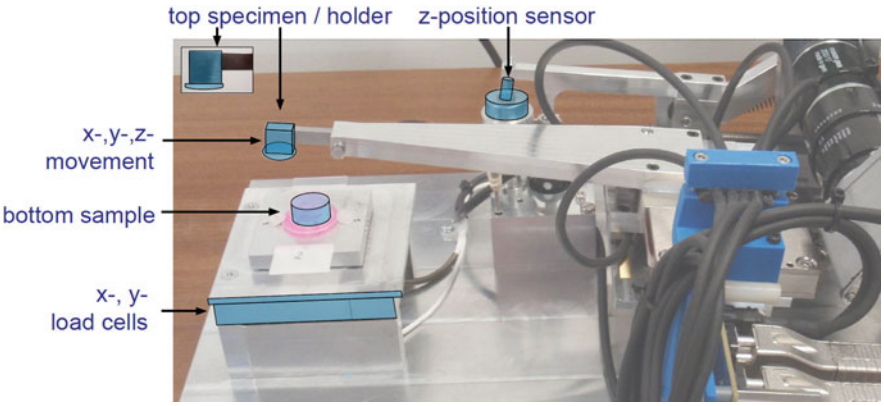

Fig. 5 Prototype biotribometer for use on a variety of tissue and tissue mimics, Porte [17]

discussed by Sivamani [18, 19], Derler [20] and Veijgen [1], coefficient of friction values for skin reported in literature range from less than 0.2 to over 2.

4 Key Factors Affecting Dynamic Friction

An excellent overview of the key factors and their effects on the friction behavior of skin that have been reported in literature has been provided by Derler [20]. A brief overview of their findings is provided in Table 1. From this overview it can be concluded that many of the key underlying factors in skin tribology are at present still not very well understood, and that many investigators obtained conflicting results.

5 Hydration of the Skin

Although there currently is no clear consensus between researchers on which parameters are affecting the tribological behavior of skin, most researchers agree that the moisture content, or the hydration, of the skin appears to be one of the most important parameters determining friction. This also aligns with intuition and everyday experience that, preventing full film lubrication or '*aquaplaning*', the friction under moist or damp conditions is significantly higher than in dry conditions.

A range of researchers, including Comaish [13], Highley [10], Wolfram [21], Johnson et al. [22] and Adams [5] studied the friction under 'dry' and 'wet' conditions and found a significant increase in wet conditions. El-Shimi [23] and Sivamani [18, 19] observed a correlation between the hydration level and the coefficient of friction. Gerhardt [24] showed that this correlation was indeed valid for individuals when the moisture content of the skin is carefully controlled, but also

Table 1 Factors affecting the friction of skin, as reported in a review paper by Derler [20] and experiments by Veijgen [1]

Factor	Effect on friction		
	Derler [20]		Veijgen [1]
Hydration of the skin	Increase or increase up to a maximum, followed by a decrease		Positive correlation
Temperature of the skin	Not mentioned		Negative correlation
Ambient temperature	Not mentioned		Positive correlation
Amount of sebum on the skin	No effect or a slight increase		No significant effect
Skin surface roughness	No effect		Not included
Roughness of counter body	Unclear: Decrease, increase or decrease until a minimum followed by increase all reported		Negative correlation
Surface free energy of counter body	Unclear, both increase and decrease reported		Positive correlation
Age of subject	No effect, constant		Positive correlation
Height of subject	Not mentioned		Negative correlation
Body region	*High*:	Forehead and behind ear	Finger pad significantly higher than other sites
	↓	Volar forearm and upper back	
		Dorsal forearm	
		Ankle and palm	
		Lower back	
		Thigh	
	Low:	Abdomen	Temple significantly lower than other sites

that the moisture content of a person's skin as measured using capacitive methods appears not to be a generally applicable predictive parameter for the friction of the skin. This is further evidenced by the large deviations for the friction for each value of the moisture content in Fig. 6.

It appears reasonable to suspect the moisture content of the skin to be one of the driving factors behind friction. Indeed, Johnson [22] already identified the role of water, and Adams investigated the effects of occlusion to the friction. Klaassen [2], suggested that the amount of water available to the contact drives the observed friction coefficient. Klaassen [25] employed an alternative characterization of the moisture content of skin, based on the work of Bomannan [26] and Lucassen [27] in which he employed Fourier Transform InfraRed (FTIR) spectroscopy using an Attenuated Total Reflectance (ATR) crystal to ensure appropriate measurements on the skin.

They found a high correlation between the friction and the moisture content of the skin as expressed in terms of the ratio of the Amide I and Amide 2 peaks in

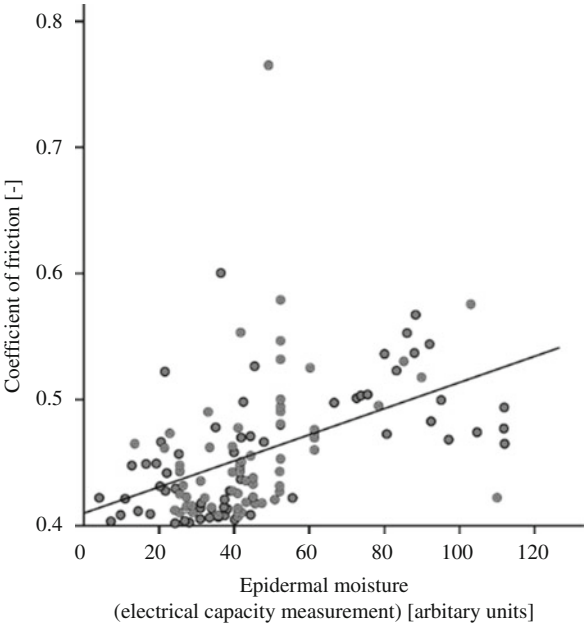

Fig. 6 Skin moisture content or hydration related to friction for 50 people, as reported by Veijgen [1]

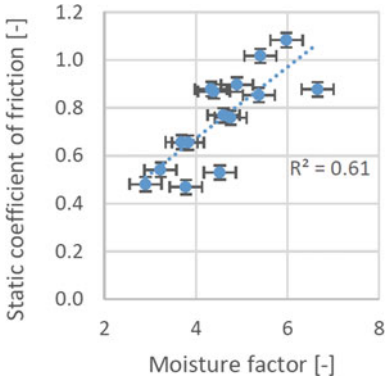

Fig. 7 Friction as a function of in-vivo measured skin moisture factor, defined as the ATR-FTIR Amide I to Amide II ratio

an ATR-FTIR spectrum of the skin (Fig. 7). The coefficient of friction correlates well to this skin moisture factor, with a coefficient of determination of $R^2 = 0.61$. Whilst for most engineering application this value would be considered fairly low, for applications involving living subjects, this value is reasonable.

6 Static Friction and Dynamic Friction

As stated before, the static friction has a close relationship with aspects such as grip and the contact between medical devices and skin, whereas the dynamic friction relates to rubbing and the perception of touch and feel. There is an ongoing

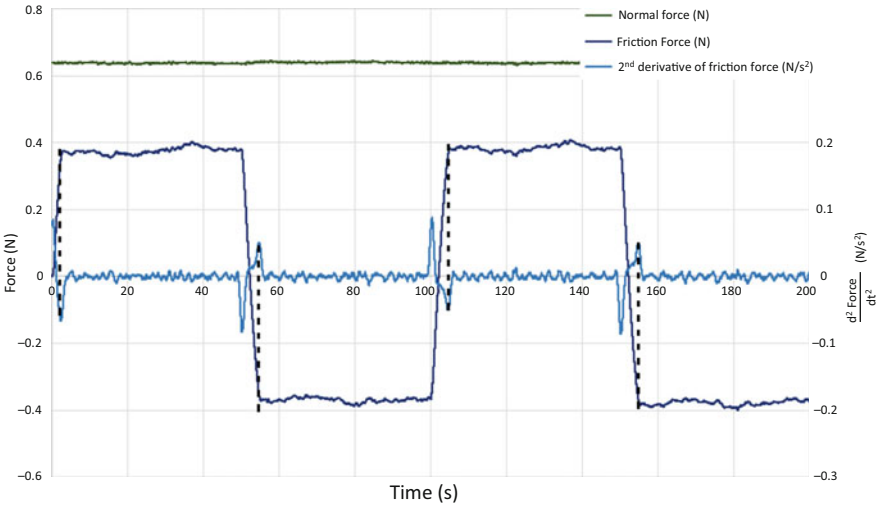

Fig. 8 Measured friction force signal obtained in a linear reciprocating tribometer, and the second time derivative of the friction force to define the onset of macroscopic sliding

debate if skin actually exhibits a 'traditional' static friction peak and if so, how to define this phenomenon unambiguously. As a result, many researchers develop their own definition of a static and a dynamic friction and how to deduce this from a measured signal. At present, there appears a significant amount of ambiguity, and any differences in values for the coefficients of friction reported in literature based may very well be based on non-similar definitions, compare e.g. Gitis [28], Koudine [29] and Klaassen [25]. A more firm definition of the reported friction values would be extremely useful.

Gitis [28] defined the static coefficient of friction as the maximum value in their measured signal and take the mean value as the dynamic coefficient of friction. They also use the ratio between the amplitude and the mean as a measure for the 'stickiness' of the skin. Koudine [29] refers to the fluctuation in the frictional force which they attribute the variation to the non-uniformity of the skin's surface Klaassen [25] suggests defining the transition between the static and the dynamic regime by taking the second time derivative of the friction signal (Fig. 8), and defining the maximum static friction as the maximum friction value measured in a period of 0.2 s around this transition point. Although the use of a 0.2 s band might be random, this is a fairly unambiguous definition.

Finally, Veijgen [30] observed that the dynamic coefficient of friction for skin contact is on average 0.85 times the static coefficient of friction, as shown in Fig. 9.

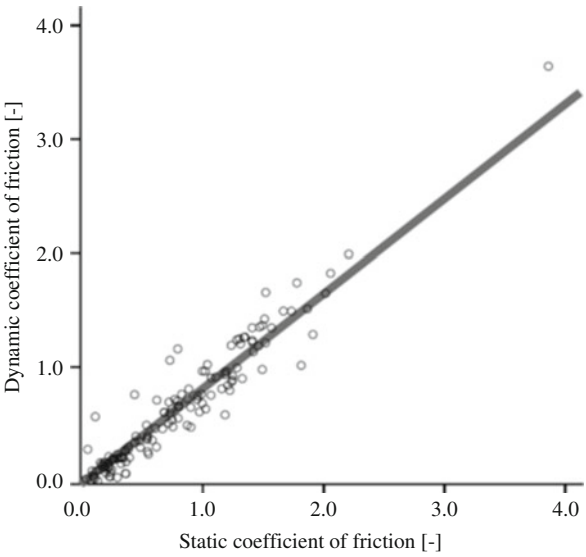

Fig. 9 Statistical relationship between static and dynamic coefficient of friction

7 Concluding Remarks

Interest in the tribology of skin is growing and over the past two decades an abundance of research papers has been published discussing the frictional behavior of skin. However, much remains to be discovered as the key underlying mechanisms are still not well understood. A large range of friction values have been reported in literature. In various cases the volar forearm has been assumed to be representative for skin on other body sites, but this appears to be an assumption that is mainly focused towards an ease of measurement. Recently, several small tribometers have been developed that can be used on multiple body sites, and a small selection was shown in Fig. 3. Additionally, a number of commercial tribometers allow testing of tissue and tissue mimics under a wide range of conditions. These devices also allow friction measurements to be recorded at high temporal resolution, typically in the order of 1000 Hz, linking the measurement with the typical trigger rates of the mechanoreceptors that are distributed in the skin.

A complicating factor in skin friction research is that many studies do not fully define the tribological system in unambiguous terms: many studies will lack information about the subjects, normal load or pressure, the relative velocity, the properties or finish of the contact material and the environmental conditions. Quite often the skin is rather simplistically described in terms of the anatomical location and the age of the subject. However, the skin is a living material and its properties depend on many more variables, including, but not limited to the thickness of the skin layers, gender, ethnicity, dietary habits, the season as well as the ambient temperature and the humidity. Indeed, scientific literature shows a broad range of results with a variety of, often conflicting, conclusions. It seems likely that this may

result from differences in materials, methods and/or experimental conditions. It is rather obvious that two studies cannot use the exact same skin samples, as even when experiments are done on the same subjects, a range of other parameters will have changed. Therefore, it is impossible to exactly reproduce studies and results, even when measured under the same circumstances.

When commencing tribological testing it is absolutely essential to ensure that experimental investigations are done using the appropriate tribo-system, meaning contact conditions such as pressures, sliding velocities and environmental conditions are representative for the final application, as any of these factors could have a significant effect on the tribological result.

Because of the complex nature of skin interactions, much of the underlying fundamental mechanisms remains to be discovered. Focused in-depth experimental investigations will be key to achieving a better understanding in skin tribology.

Bibliography

1. Veijgen NK (2013) Skin friction: a novel approach to measuring, in vivo human skin. PhD Thesis, University of Twente, The Netherlands
2. Klaassen M, Schipper DJ, Masen MA (2016) Influence of the relative humidity and the temperature on the in-vivo friction behaviour of human skin. Biotribology 6:21–28
3. Cornelissen LH, Bronneberg D, Gibbs S, Bouten CV, Oomens CW (2010) Cytokine release in tissue-engineered epidermal equivalents after prolonged mechanical loading. Methods Mol Biol 585:335–344
4. Naylor PFD (1955) The skin surface and friction. Br J Dermatol 67(7):239–248
5. Adams MJ, Briscoe BJ, Johnson SA (2007) Friction and lubrication of human skin. Tribol Lett 26(3):239–253
6. Polliack AA, Scheinberg S (2006) A new technology for reducing shear and friction forces on the skin: implications for blister care in the wilderness setting. Wilderness Environ Med 17(2):109–119
7. Prall JK (1973) Instrumental evaluation of the effects of cosmetic products on skin surfaces with particular reference to smoothness. J Soc Cosmet Chem 24:693–707
8. Comaish JS (1973) Epidermal fatigue as a cause of friction blisters. Lancet 301(7794):81–83
9. Hendriks CP, Franklin SE (2010) Influence of surface roughness, material and climate conditions on the friction of human skin. Tribol Lett 37:361–373
10. Highley DR, Comey M, DenBeste M, Wolfram LJ (1977) Frictional properties of skin. J Invest Dermatol 69(3):303–305
11. Lewis R, Carré MJ, Tomlinson SE (2014) Skin friction at the interface between hands and sports equipment. Process Eng 72:611–617
12. Derler S, Schrade U, Gerhardt LC (2007) Tribology of human skin and mechanical skin equivalents in contact with textiles. Wear 263:1112–1116
13. Comaish JS, Bottoms E (1971) The skin and friction: deviations from Amonton's laws, and the effects of hydration and lubrication. Br J Dermatol 84:37–43
14. Dinç OS, Ettles CM, Calabrese SJ, Scarton HA (1991) Some parameters affecting tactile friction. J Tribol 113(3):512–517
15. Smith AM, Chapman CE, Deslandes M, Langlais JS, Thibodeau MP (2002) Role of friction and tangential force variation in the subjective scaling of tactile roughness. Exp Brain Res 144(2):211–223

16. Gee MG, Tomlins P, Calver A, Darling RH, Rides M (2005) A new friction measurement system for the frictional component of touch. Wear 259:1437–1442
17. Porte E, Cann PME, Masen MA (2018) Fluid load support does not explain tribological performance of PVA hydrogels. J Mech Behav Biomed Mat 90:284–294
18. Sivamani RK, Goodman J, Gitis NV, Maibach HI (2003) Friction coefficient of skin in real-time. Skin Res Technol 9:235–239
19. Sivamani RK, Goodman J, GItis NV, Maibach HI (2003) Coefficient of friction: tribological studies in man-an overview. Skin Res Technol 9:227–234
20. Derler S, Gerhardt LC (2012) Tribology of skin: review and analysis of experimental results for the friction coefficient of human skin. Tribol Lett 45:1–27
21. Wolfram LJ (1983) Friction of skin. J Soc Cosmet Chem 34:465–476
22. Johnson SA, Gorman DM, Adams MJ, Briscoe BJ (1993) The friction and lubrication of human stratum corneum. In: Dowson D (ed) Thin films in tribology. Proceedings of the 19th Leeds-Lyon symposium on tribology. Elsevier, Amsterdam, pp 663–672
23. El-Shimi AF (1977) In vivo skin friction measurements. J Soc Cosmet Chem 28(2):37–52
24. Gerhardt LC, Strässle V, Lenz A, Spencer ND, Derler S (2008) Influence of epidermal hydration on the friction of human skin against textiles. J R Soc Interface 5(28):1317–1328
25. Klaassen M (2018) The static friction behaviour of skin with relevance to pressure ulcer prevalence. PhD Thesis University of Twente, The Netherlands
26. Bomannan D, Potts RO, Guy RH (1990) Examination of stratum corneum barrier function in vivo by infrared spectroscopy. J Invest Dermatol 95(4):403–408
27. Lucassen GW, van Veen GN, Jansen JA (1998) Band analysis of hydrated human skin stratum corneum attenuated total reflectance fourier transform infrared spectra in vivo. J Biomed Opt 3(3):267–280
28. Gitis N, Sivamani R (2004) Tribometrology of skin. Tribol Trans 47:461–469
29. Koudine AA, Barquins M, Anthoine P, Aubert L, Lévèque JL (2000) Frictional properties of skin: proposal of a new approach. Int J Cosmet Sci 22:11–20
30. Tomlinson SE, Lewis R, Liu X, Texier C, Carre MJ (2011) Understanding the friction mechanisms between the human finger and flat contacting surfaces in moist conditions. Tribol Lett 41(1):283–294
31. Asserin J, Zahouani H, Humbert P, Couturaud V, Mougin D (2000) Measurement of the friction coefficient of the human skin in vivo. Quantification of the cutaneous smoothness. Colloids Surf B Biointerfaces 19:1–12
32. Anderson RR, Parrish JA (1981) The optics of human skin. J Invest Dermatol 77:13–19
33. André T, Lefèvre P, Thonnard JL (2010) Fingertip moisture is optimally modulated during object manipulation. J Neurophysiol 103:402–408
34. Barnes CJ, Childs THC, Henson B, Southee CH (2004) Surface finish and touch – a case study in a new human factors tribology. Wear 257:740–750
35. Besser M, Marpet M, Medoff H (2008) Barefoot-pedestrian tribometry: in vivo method of measurement of available friction between the human heel and the walkway. Ind Health 46:51–58
36. Bettley FR (1960) Some effects of soap on the skin. Br Med J 5187:1675–1679
37. Bobjer O, Johansson SE, Piguet S (1993) Friction between hand and handle. Effects of oil and lard on textured and non-textured surfaces; perception of discomfort. Appl Ergon 24(3):190–202
38. Bouwstra JA, Groenink WW, Kempenaar JA, Romeijn SG, Ponec M (2008) Water distribution and natural moisturizer factor content in human skin equivalents are regulated by environmental relative humidity. J Invest Dermatol 128:378–388
39. Briggaman RA, Wheeler CE (1975) The epidermal-dermal junction. J Invest Dermatol 65:65–71
40. Brody I (1962) The ultrastructure of the epidermis in psoriasis vulgaris as revealed by electron microscopy. J Ultrastruct Res 6:304–323
41. Burger B, Fuchs D, Sprecher E, Itin P (2011) The immigration delay disease: adermatoglyphia-inherited absence of epidermal ridges. J Am Acad Dematol 64:974–980

42. Cal K, Zakowiecki D, Stefanowska J (2010) Advanced tools for in vivo skin analysis. Int J Dermatol 49:492–499
43. Chang WR, Grönqvist R, Leclercq S, Myung R, Makkonen L, Strandberg L (2001) The role of friction in the measurement of slipperiness, part 1: friction mechanisms and definition of test conditions. Ergon 44(13):1217–1232
44. Childs THC, Henson B (2007) Human tactile perception of screen-printed surfaces: self-report and contact mechanics experiments. Proc Inst Mech Eng J J Eng Tribol 221(J3):427–441
45. Comaish JS, Harborow PRH, Hofman DA (1973) A hand-held friction meter. Br J Dermatol 89(1):33–35
46. Crevecoeur F, Giard T, Thonnard JL, Lefèvre P (2011) Adaptive control of grip force to compensate for static and dynamic torques during object manipulation. J Neurophysiol 106:2973–2981
47. Cua AB, Wilhelm KP, Maibach HI (1990) Frictional properties of human skin: relation to age, sex and anatomical region, stratum corneum hydration and transepidermal water loss. Br J Dermatol 123:473–479
48. Cua AB, Wilhelm KP, Maibach HI (1995) Skin surface lipid and skin friction: relation to age, sex and anatomical region. Skin Pharmacol 8(5):246–251
49. Davis BL (1993) Foot ulceration: hypotheses concerning shear and vertical forces acting on adjacent regions of skin. Med Hypotheses 40(1):44–47
50. Dick JC (1947) Observations on the elastic tissue of the skin with a note on the reticular layer at the junction of the dermis and epidermis. J Anat 81(3):201–211
51. Dowson D (1997) Tribology and the skin surface. In: Wilhelm KP, Elsner P, Berdardesca E, Maibach HI (eds) Bioengineering of the skin: skin surface imaging and analysis. CRC Press, Boca Raton, pp 159–179
52. Edwards C, Marks R (1995) Evaluation of biomechanical properties of human skin. Clin Dermatol 13:375–380
53. Elkhyat A, Courderot-Masuyer C, Gharbi T, Humbert P (2004) Influence of the hydrophobic and hydrophilic characteristics of sliding and slider surfaces on friction coefficient: in vivo human skin friction comparison. Skin Res Technol 10:215–221
54. Fagiani R, Massi F, Chatelet E, Berthier Y, Akay A (2011) Tactile perception by friction induced vibrations. Tribol Int 44:1100–1110
55. Gerhardt LC, Lenz A, Spencer ND, Münzer T, Derler S (2009) Skin-textile friction and skin elasticity in young and aged persons. Skin Res Technol 15:288–298
56. James WD, Davis LB, Quick CM, Siegel SE (eds) (1994) Military dermatology. Office of the Surgeon General at TMM Publications, Washington
57. Johansson RS (1978) Tactile sensibility in the human hand: receptive field characteristics of mechanoreceptive units in the glabrous skin area. J Physiol 281:110–123
58. Klaassen M, de Vries EG, Masen MA (2017) The static friction response of non-glabrous skin as a function of surface energy and environmental conditions. Biotribology 11:124–131
59. van Kuilenburg J, Masen MA, Groenendijk MNW, Bana V, van der Heide E (2012) An experimental study on the relation between surface texture and tactile friction. Tribol Int 48:15–21
60. Kvistedal YA, Nielsen MF (2007) Estimating material parameters of human skin in vivo. Biomech Model Mechanobiol 8(1):1–8
61. Lewis R, Menardi C, Yoxall A, Langley J (2007) Finger friction: grip and opening packaging. Wear 263:1124–1132
62. Li FX, Margetts S, Fowler I (2001) Use of chalk in rock climbing: sine qua non or myth? J Sports Sci 19:427–432
63. Li W, Qu SX, Zhou ZR (2006) Reciprocating sliding behaviour of human skin in vivo at lower number of cycles. Tribol Lett 23(2):165–170
64. Li W, Kong M, Liu XD, Zhou ZR (2007) Tribological behavior of scar skin and prosthetic skin in vivo. Tribol Int 41(7):640–647
65. Madison KC (2003) Barrier function of the skin: “la raison d’être” of the epidermis. J Invest Dermatol 121:231–241

66. Masen MA (2011) A system based experimental approach to tactile friction. J Mech Behav Biomed Mater 4:1620–1626
67. Matlin MW, Foley HJ (2010) Sensation and perception. Allyn and Bacon, Boston
68. Mossel WP, Roosen CPG (1994) Friction and the skin. In: Robertson SA (ed) Contemporary ergonomics. Proceedings of the annual conference of the Ergonomics Society, 19–22 April 1994. Taylor & Francis, Warwick, London, UK, pp 353–358
69. Mossel WP (1996) The measurement of skin friction. In: Robertson SA (ed) Contemporary ergonomics. Proceedings of the annual conference of the Ergonomics Society, 10–12 April 1996. Taylor & Francis, Leicester, London, UK, pp 69–75
70. Nakazawa N, Ikeura R, Inooka H (2000) Characteristics of human fingertips in the shearing direction. Biol Cybern 82:207–214
71. Nakagawa N, Sakai S, Matumoto M, Yamada K, Nagano M, Yuki T, Sumida Y, Uchiwa H (2004) Relationship between NMF (lactate and potassium) content and the physical properties of the stratum corneum in healthy subjects. J Invest Dermatol 122:755–763
72. Neerken S, Lucassen GW, Bisschop MA, Lenderink E, Nuijs AM (2004) Characterization of age-related effects in human skin: a comparative study that applies confocal laser scanning microscopy and optical coherence tomography. J Biomed Opt 9(2):274–281
73. Nonomura Y, Fujii T, Arashi Y, Miura T, Maeno T, Tashiro K, Kamikawa Y, Monchi R (2009) Tactile impression and friction of water on human skin. Colloids Surf B Biointerfaces 69:264–267
74. Pailler-Mattéi C, Pavan S, Varigiolu R, Pirot F, Falson F, Zahouani H (2007) Contribution of stratum corneum in determining bio-tribological properties of the human skin. Wear 263:1038–1043
75. Pasumarty S, Johnson S, Watson S, Adams M (2011) Friction of the human finger pad: influence of moisture, occlusion and velocity. Tribol Lett 44:117–137
76. Porte E (2019) Friction and lubrication of hydrogels as articular cartilage mimics. PhD thesis, Imperial College London
77. Ramalho A, Silva CL, Pais AACC, Sousa JJS (2007) In vivo friction study of human skin: influence of moisturizers on different anatomical sites. Wear 263:1044–1049
78. Rawlings AV, Harding CR (2004) Moisturization and skin barrier function. Dermatol Ther 17:43–48
79. Rawlings AV (2006) Ethnic skin types: are there differences in skin structure and function. Int J Cosmet Sci 28:79–93
80. Sivamani RK, Maibach HI (2006) Tribology of skin. Proc Inst Mech Eng J J Eng Tribol 220(J8):729–737
81. Sjövall P, Skedung L, Gregoire S, Biganska O, Clément F, Luengo G (2018) Imaging the distribution of skin lipids and topically applied compounds in human skin using mass spectrometry. Sci Rep 8:16683
82. Uygur M, de Freitas PB, Jaric S (2010) Frictional properties of different hand skin areas and grasping techniques. Ergon 53(6):812–817
83. Veijgen NK, Masen MA, van der Heide E (2013) Variables influencing the frictional behaviour of in vivo human skin. J Mech Behav Biomed Mat 28:448–461
84. Veijgen NK, van der Heide E, Masen MA (2013) A multivariable model for predicting the frictional behaviour and hydration of the human skin. Skin Res Technol 19(3):330–338
85. Venus M, Waterman J, McNab I (2010) Basic physiology of the skin. Surgery 28(10):469–472
86. Wickett RR, Visscher MO (2006) Structure and function of the epidermal barrier. Am J Infect Control 34(10):S98–S110
87. Wilmore JH, Costill DL (2004) Physiology of sport and exercise. Human Kinetics, Campaign
88. Yoxall A, Janson R, Bradbury SR, Langley J, Wearn J, Hayes S (2006) Openability: producing design limits for consumer packaging. Packag Technol Sci 19:219–225
89. Zahouani H, Boyer G, Pailler-Mattéi C, Tkaya MB, Vargiolu R (2011) Effect of human ageing on skin rheology and tribology. Wear 271:2364–2369
90. Zhang M, Mak AFT (1999) In vivo friction properties of human skin. Prosthetics Orthot Int 23:135–141